Západočeská univerzita v Plzni
Fakulta aplikovaných věd

ROBUSTNÍ ŘÍZENÍ POHYBU PRUŽNÝCH ELEKTROMECHANICKÝCH SOUSTAV

Ing. Martin Goubej

disertační práce
k získání akademického titulu
Doktor
v oboru Kybernetika

Školitel: Prof. Ing. Miloš Schlegel, CSc.

Katedra: Katedra Kybernetiky

Plzeň 2014

University of West Bohemia
Faculty of applied sciences

ROBUST MOTION CONTROL OF FLEXIBLE ELECTROMECHANICAL SYSTEMS

Ing. Martin Goubej

A dissertation submitted in partial fulfillment
of the requirements for the degree of
Doctor of Philosophy
(Cybernetics)

Supervised by: Prof. Ing. Miloš Schlegel, CSc.

Department of Cybernetics

Pilsen 2014

Abstract

The main topic of the thesis is a problem of motion control of electromechanical systems with oscillatory dynamics caused by a mechanical compliance of the driven load. The goal is to develop effective and reliable algorithms for automatic system identification and robust controller synthesis applicable to a wide range of industrial motion control systems. Achieved theoretical results are described in three distinct sections devoted to automatic identification, passive vibration damping using input shaping method and active feedback vibration control. Numerical simulations and experimental results demonstrate successful employment of the developed methods.

Abstrakt

Dizertační práce se zabývá problematikou řízení pohybu elektromechanických systémů s kmitavou dynamikou způsobenou poddajností poháněné soustavy. Cílem je vyvinout efektivní a spolehlivé algoritmy pro automatickou identifikaci systému a návrh robustního regulátoru použitelné pro široké spektrum průmyslových aplikací systémů řízení pohybu. Dosažené teoretické výsledky jsou popsány ve třech sekcích věnovaných automatické identifikaci, pasivnímu tlumení vibrací s použitím metody tvarování vstupní veličiny a aktivního zpětnovazebního tlumení. Použití navržených metod je demonstrováno řadou numerických simulací a experimentálních výsledků.

Poděkování

Na tomto místě bych rád poděkoval svému školiteli Prof. Ing. Miloši Schlegelovi, CSc. za poskytnuté vedení, rady, inspiraci a nadšení pro obor automatického řízení, jež se mu podařilo na mě přenést. Díky patří i všem kolegům z výzkumného týmu za neopakovatelnou atmosféru na pracovišti, která působí jako podhoubí pro vznik nových myšlenek a nápadů a která mi dala poznat, jak zábavná a naplňující může být vědecká práce. Velký dík si zaslouží moje rodina, partnerka a blízký okruh přátel za podporu, toleranci a shovívavost i ve chvílích, kdy čísla a rovnice pro mě byly důležitejší než společně strávený čas. Díky všem...

Contents

List of Figures

LIST OF FIGURES

List of Tables

Glossary

H_2	2-norm of linear system
H_∞	infinity norm of linear system
AC	alternating current
ACIM	alternating current induction motor
ARE	Algebraic Riccati Equation
Back EMF	back electromotive force, voltage induced in rotor or stator windings according to Lenz's law due to the rotation of the motor shaft
BIBO	Bounded-Input Bounded-Output stability of a dynamic system
CNC	Computer numerical control, last generation of digital controlled machine tools
DC	direct current
DoF	Degrees-of-freedom, number of independent parameters or coordinates of the system that may vary independently
DTC	Direct torque control, method for current control of AC drives
EC motor	electronically commutated three-phase motor
EI	Extra-insensitive input shaping filter
FFT	Fast Fourier Transform, numerical algorithm for computationally efficient derivation of discrete time Fourier transform
FOC	Field-oriented control, method for current/torque control of AC drives
G-code	Programming language used in machine-tools
LMS	Linear Mean Squares
LQG	Linear quadratic regulator with Gaussian noise model
LQR	Linear quadratic regulator
LTI	Linear time-invariant system
LTV	Linear time-variant system
MEMS	micro electromechanical systems, technology of very small devices made up from components between 1 to 100 micrometers in size
ODE	Ordinary differential equation
PDE	Partial differential equation
PID	Proportional-inetgral-derivative controller
PLC	Programmable logic controller, common notation for industrial system performing logical or regulatory control
PMSM	permanent magnet synchronous motor
PWM	pulse width modulation
rpm	revolutions per minute, auxiliary SI unit for measuring of rotational velocity
SNR	Signal-to-noise ratio
THD	Total harmonic distortion
UWB	University of West Bohemia in Pilsen, Czech Republic
ZV	Zero-vibration input shaping filter
ZVD	Zero-vibration-derivative input shaping filter

1

Introduction

We are currently witnessing technological progress that strongly affects our daily lives. Rapid development in electronics, computer technology and embedded systems which has been observed in the last few decades has brought a new generation of products in various application fields such as consumer electronics, automotive, aerospace and manufacturing. The term ”mechatronics” was first used by Tetsuro Mori, the senior engineer of the Japanese company Yaskawa in 1969, to describe new types of advanced systems which contain aspects of mechanics, electronics and intelligent computer control. This term became commonplace and is currently seen as a synergistic combination of different disciplines of technology and science which are used to create sophisticated, economical and reliable devices. An example of a mechatronic system is an industrial robot, digital camera or a car equipped with driver assistance functions [1, 2, 3, 4].

The theory of automatic control plays a key role in the process of mechatronic engineering. The introduction of feedback and insertion of the control law in the form of a computer algorithm allows for significant changes in the dynamical behavior of the controlled system and the implementation of completely new functional properties that would otherwise be unattainable. If we imagine for example the levitation of a shaft in magnetic bearing or the change of mechanical stiffness in a flexible structure we may even state that the feedback control can change the ordinary laws of physics (in the sense of an outside observer). Therefore, such systems are often called *active mechanical structures*, because the properties of the original passive system are altered by actively using some auxiliary source of energy.

This thesis deals with the specific problem of precise motion control of electromechanical systems with flexible structure which is often encountered in modern industrial automation. Various manufacturing applications of mechatronic systems such as CNC machining, assembling, welding, packaging or material handling require highly

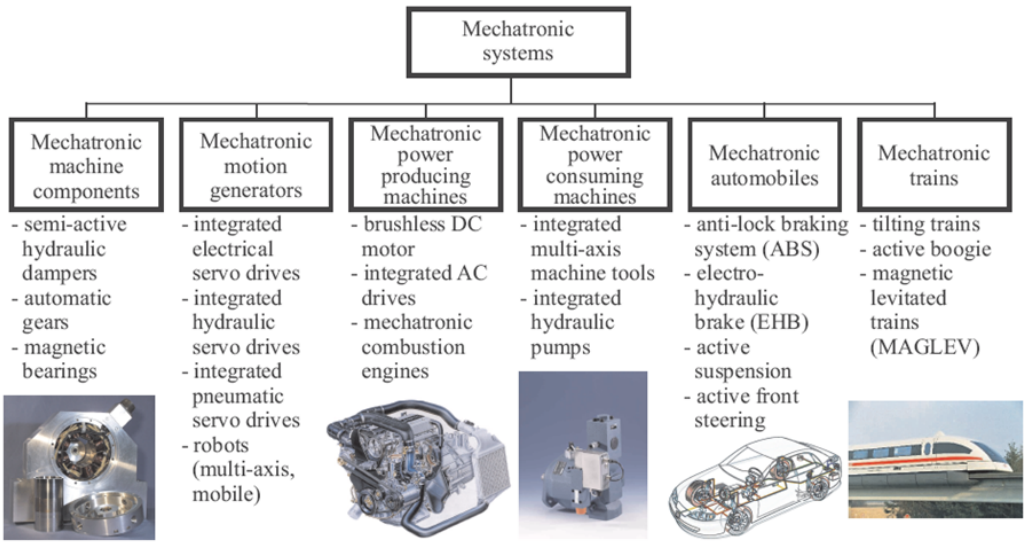

Figure 1.1: Examples of mechatronic systems - survey of R. Isermann [3]

dynamic motions which have to be precisely executed by a machine (simple manipulator, conveyor belt, industrial robot or machine-tool). The increasing demands for efficiency, precision and dynamics of the controlled motion lead to a higher desired bandwidth of the control loops. New types of lightweight constructions are introduced in order to reduce the inertial masses and enhance the energy efficiency and mass to load ratio. However, rapid motions and reduced stiffness of the mechanical construction often lead to excitation of unwanted mechanical vibrations. Such vibrations significantly reduce the overall quality of control and are recognized as the most limiting factor for the achievable bandwidth. The motion induced oscillations complicate and prolong the process of machine commissioning and handmade controller tuning which is often performed by process engineers in practice becomes almost impossible. There is a strong demand from industry for assisting software tools which would provide some functions for automatic or semi-automatic identification and motion control loop settings. Some of the major manufacturers of the servo drives offer an auto-tuning function in their frequency-inverter firmware. However, its functionality is often limited to rigid mechanical loads and may fail in the presence of oscillatory dynamics. Moreover, the controller structure is often fixed to a basic cascade PID algorithm which may be unsatisfactory for complex flexible systems with multiple resonance modes. The goal

of this thesis is to provide effective and reliable algorithms for automatic identification and robust tuning of motion control loops in industrial electrical drives.

The thesis is structured as follows. Chapter 2, which is a preliminary chapter, introduces some important results of modern control system theory which are used further in the text. Chapter 3 deals with state-of-the-art motion control systems explaining some fundamental problems and known methods for their solution. Chapter 4 formulates the aims of the thesis. Chapter 5 introduces a novel approach to frequency identification of oscillatory electromechanical systems. Chapter 6 deals with passive vibration control using input shaping methods. Chapter 7 is devoted to active feedback vibration control and a problem of robust velocity and position controller synthesis. Chapter 8 demonstrates the use of the proposed methods in several laboratory setups and industrial applications. The last part is devoted to discussion and final conclusions.

2

Preliminary chapter

This chapter provides a summary of some important methods of control system theory which are used further in the thesis. To be concise, only the main results are presented. The full derivation including proofs can be found in the referenced literature.

2.1 Norms of signals and linear systems

For a quantitative measurement of performance and robustness of a control system, appropriate signals and system norms have to be introduced. The following section presents the most important norms which are often used in optimal and robust control methods [5, 6].

Definition 1. L_p**-norm of a signal**
For any $1 \leq p \leq \infty$ the L_p*-norm* $\|z\|_p$ or *p-norm* of a continuous-time scalar-valued signal $z(t)$ is defined by:

$$\|z\|_p = (\int_{-\infty}^{\infty} |z(t)|^p \, dt)^{1/p}. \tag{2.1}$$

The definition can be generalized for a n-dimensional vector $\boldsymbol{z}(t)$ with values in $\mathbb{R}^n$ or $\mathbb{C}^n$ to:

$$\|\boldsymbol{z}\|_p = (\int_{-\infty}^{\infty} \|\boldsymbol{z}(t)\|^p \, dt)^{1/p}. \tag{2.2}$$

where $\|\boldsymbol{z}(t)\|$ is any vector norm on space $\mathbb{R}^n$ or $\mathbb{C}^n$.

As $p \to \infty$ the L_p norm tends to the so called $\infty - norm$ which is characterized as:

$$\|\boldsymbol{z}\|_\infty = \sup_t \|\boldsymbol{z}(t)\|. \tag{2.3}$$

The L_∞ norm expresses *amplitude* or *peak value* of the signal. For a particular choice $p = 2$ we get the L_2 norm:

$$\|\boldsymbol{z}\|_2 = (\int_{-\infty}^{\infty} \|\boldsymbol{z}(t)\|^2 \, dt)^{1/2} = (\int_{-\infty}^{\infty} \boldsymbol{z}(t)^T \, \boldsymbol{z}(t) \, dt)^{1/2}. \tag{2.4}$$

The square of the L_2 norm ${\|\boldsymbol{z}\|_2}^2$ has physical interpretation of *total energy* associated with the signal.

The L_2 norm can be defined analogously in the frequency domain for the Laplace-transformed signal $\boldsymbol{z}(s)$ on the imaginary axis. We obtain

$$\|z\|_2 = (\frac{1}{2\pi} \int_{-\infty}^{\infty} |z(j\omega)|^2 \, d\omega)^{1/2}, \tag{2.5}$$

for the scalar case and

$$\|\boldsymbol{z}\|_2 = (\frac{1}{2\pi} \int_{-\infty}^{\infty} \boldsymbol{z}(-j\omega)^T \boldsymbol{z}(j\omega) \, d\omega)^{1/2}, \tag{2.6}$$

for vector-valued $z(s)$.

Definition 2. **H_2-norm of linear system**
Consider SISO linear system. The linear mapping from the scalar input $u(t)$ to the output signal $y(t)$ is defined by the convolution integral

$$y(t) = \int_{-\infty}^{\infty} h(\tau) u(t - \tau) d\tau; \; t \in \mathbb{R}, \tag{2.7}$$

where $h(t)$ is impulse response function. In the Laplace domain, the input-output relation is defined by the transfer function $H(s)$ by:

$$Y(s) = H(s)U(s), \tag{2.8}$$

where $H(s)$ is the Laplace transform of $h(t)$.

The H_2 norm is defined analogously to 2.5 as:

$$\|H\|_2 = (\frac{1}{2\pi} \int_{-\infty}^{\infty} |H(j\omega)|^2 \, d\omega)^{1/2}. \tag{2.9}$$

For the *multivariable* case with an impulse response matrix $\boldsymbol{h}(t)$ and a transfer matrix $\boldsymbol{H}(s) = [h_{kl}(s)]$ we obtain a generalization in the form of

$$\begin{aligned} \|H\|_2 &= (\sum_{kl} \|h_{kl}\|_2{}^2)^{1/2} = \\ &= (\frac{1}{2\pi} \int_{-\infty}^{\infty} \sum_{kl} |h_{kl}(j\omega)|^2 \, d\omega)^{1/2} = (\frac{1}{2\pi} \int_{-\infty}^{\infty} tr[\boldsymbol{H}(-j\omega)^T \boldsymbol{H}(j\omega)] \, d\omega)^{1/2}. \end{aligned} \tag{2.10}$$

The integral is finite only for stable transfer functions of $\boldsymbol{H}(s)$ with no right half-plane poles. Thus, the norm is defined only for stable systems. The notation H_2 which is often used instead of L_2 is a reference to Hardy spaces of bounded and analytic functions in the right-half plane.

The H_2 norm of the system can be interpreted in terms of norms of generated output signals. Consider for example a SISO system with input signal $U(j\omega) = 1$ (Dirac's delta function δ). From (2.8) and (2.5) we get

$$\|y\|_2 = (\frac{1}{2\pi} \int_{-\infty}^{\infty} |H(j\omega)|^2 \, d\omega)^{1/2} = \|H\|_2 \tag{2.11}$$

Therefore, the H_2 norm can be interpreted as energy of the system output excited by wideband Dirac's impulse or in other words as *average system gain taken over all frequencies*. These results can be easily generalized for the multivariable case (see e.g. [6]).

Similar physical interpretation is possible in the framework of stochastic systems. Supposing that the vector input $\boldsymbol{u}(t)$ is a white noise signal with the covariance function $E[\boldsymbol{u}(t)^T \boldsymbol{u}(s)] = \boldsymbol{I}\delta(t-s)]$, the system output $\boldsymbol{y}(t)$ is a stationary stochastic process and its mean square value is defined as:

$$E[\boldsymbol{y}(t)^T \boldsymbol{y}(t)] = tr \int_{-\infty}^{\infty} \boldsymbol{H}(-j\omega)^T \boldsymbol{H}(j\omega) \, d\omega = 2\pi \|H\|_2{}^2. \tag{2.12}$$

Thus, the mean square output of the system which is excited by the wideband unitary white noise signal is determined by the H_2 system norm. The H_2 norm is often used as a measure of performance in the closed loop system.

Definition 3. **H_∞-norm of linear system**
For a stable linear SISO system with transfer function $H(s)$, the H_∞ norm is defined as

$$\|H\|_\infty = \sup_\omega |H(j\omega)|. \tag{2.13}$$

This measure provides a value of the *worst case system gain* in the frequency domain in the sense of maximum amplification of the harmonic input signal over the whole frequency range. Another useful interpretation follows from the observation of the following inequality. Considering the system (2.8) and definition (2.5) we may write:

$$\begin{aligned}(\frac{1}{2\pi}\int_{-\infty}^{\infty}|H(j\omega)U(j\omega)|^2\,d\omega)^{1/2} &\leq \sup_{\omega}|H(j\omega)|(\frac{1}{2\pi}\int_{-\infty}^{\infty}|U(j\omega)|^2\,d\omega)^{1/2} \\ \Rightarrow \|Y\|_2 &= \|HU\|_2 \leq \|H_\infty\|\|U\|_2.\end{aligned} \tag{2.14}$$

Therefore, the H_∞ norm can be defined as:

$$\|H\|_\infty = sup\left\{\frac{\|HU\|_2}{\|U\|_2};\ U \neq 0\right\}. \tag{2.15}$$

Hence, the H_∞ norm also gives the maximum system gain in the sense of amplification of L_2 norm of an arbitrary input signal. From the operator theory, it follows that H_∞ is an operator norm induced by the L_2 signal norm.

For the multivariable system, the H_∞ norm is generalized for the transfer matrix $H(s)$ in the following manner

$$\|H\|_\infty = \sup_{\omega}\bar{\sigma}(\boldsymbol{H}(j\omega)), \tag{2.16}$$

where $\bar{\sigma}$ denotes the largest singular value of the matrix. The inequality (2.15) holds as well for the vector valued input and output signal and the physical interpretation remains the same. The $\infty - norm$ provides the *maximal system gain in all output directions over the frequency range* or *peak amplification of input signal* in the sense of the L_2 signal norm. The H_∞ is an useful measure for the evaluation of robust stability of a closed loop system.

2.2 Linear quadratic optimal control

The procedure of controller or estimator design can be formulated as an optimization problem with respect to a proper criterion function. Important results of optimal control theory are related to quadratic cost functions which try to achieve a suitable compromise between controller or estimator bandwidth and the corresponding control effort and noise sensitivity [5, 7, 8, 9, 10]. The *Linear Quadratic Regulator* (LQR) problem is defined as follows.

A given LTI system having a state space model is considered in the form:

$$\dot{\boldsymbol{x}}(t) = \boldsymbol{A}\boldsymbol{x}(t) + \boldsymbol{B}\boldsymbol{u}(t), \tag{2.17}$$

$$\boldsymbol{y}(t) = \boldsymbol{C}\boldsymbol{x}(t) + \boldsymbol{D}\boldsymbol{u}(t), \tag{2.18}$$

where $\boldsymbol{x}(t) \in \mathbb{R}^n$ is state vector, $\boldsymbol{u}(t) \in \mathbb{R}^m$ is input vector, $\boldsymbol{y}(t) \in \mathbb{R}^p$ is measurement output vector, $\boldsymbol{A}, \boldsymbol{B}, \boldsymbol{C}, \boldsymbol{D}$ are constant real matrices with corresponding dimensions, the pair $(\boldsymbol{A}, \boldsymbol{B})$ is controllable and the pair $(\boldsymbol{A}, \boldsymbol{C})$ is observable. The goal is to find a control law which steers the system from an arbitrary initial state $\boldsymbol{x}(0)$ to a very small value as quick as possible without spending too much control effort. Therefore, the performance index which introduces a compromise between closed-loop dynamics and magnitude of control is defined as:

$$J = \int_0^\infty (\boldsymbol{x}^T \boldsymbol{Q}\boldsymbol{x} + \boldsymbol{u}^T \boldsymbol{R}\boldsymbol{u}) dt. \tag{2.19}$$

The optimal regulator should minimize the quadratic cost function (2.19) for all possible trajectories of the system.

The steady-state solution of this problem for an infinite horizon of control leads to the control law in the form of the state feedback:

$$\boldsymbol{u}(t) = -\boldsymbol{K}\boldsymbol{x}(t), \tag{2.20}$$

where the $m \times n$ state feedback gain matrix $\boldsymbol{K}$ is given by equation

$$\boldsymbol{K} = \boldsymbol{R}^{-1}\boldsymbol{B}^{\boldsymbol{T}}\boldsymbol{P}. \tag{2.21}$$

The symmetric nonnegative-definite $n \times n$ matrix $\boldsymbol{P}$ is a solution of the *Algebraic Riccati Equation* (ARE):

$$\boldsymbol{A}^{\boldsymbol{T}}\boldsymbol{P} + \boldsymbol{P}\boldsymbol{A} - \boldsymbol{P}\boldsymbol{B}\boldsymbol{R}^{-1}\boldsymbol{B}^{\boldsymbol{T}}\boldsymbol{P} + \boldsymbol{Q} = 0. \tag{2.22}$$

The Riccati equation has to be solved numerically. Special methods based on matrix factorizations or iterative computation have been developed for this purpose. The LQR problem assumes that all of the system states are accessible for measurement. A more realistic formulation of the control problem which considers an output feedback controller and introduces an uncertainty in both modelling and measurement is given by the *Linear Quadratic Gaussian* (LQG) design in the framework of stochastic systems. The plant model is assumed in form:

$$\begin{aligned} \dot{\boldsymbol{x}}(t) &= \boldsymbol{A}\boldsymbol{x}(t) + \boldsymbol{B}\boldsymbol{u}(t) + \boldsymbol{G}\boldsymbol{w}(t), \\ \boldsymbol{y}(t) &= \boldsymbol{C}\boldsymbol{x}(t) + \boldsymbol{D}\boldsymbol{u}(t) + \boldsymbol{v}(t), \end{aligned} \tag{2.23}$$

where $\boldsymbol{w}, \boldsymbol{v}$ are white process and measurement noise signals satisfying $E[\boldsymbol{w}(t)] = E[\boldsymbol{v}(t)] = 0,\ E(\boldsymbol{w}\boldsymbol{w}^{\boldsymbol{T}}) = \boldsymbol{W},\ E(\boldsymbol{v}\boldsymbol{v}^{\boldsymbol{T}}) = \boldsymbol{V}$ with appropriate covariance matrices $\boldsymbol{W}, \boldsymbol{V}$ which specify the noise intensity. Since the state and output variables are now defined as random processes due to the stochastic noises, the criterion function is formulated as the integrated expected value:

$$J = \lim_{T\to\infty} \frac{1}{T}\{\int_0^\infty E(\boldsymbol{x}^T\boldsymbol{Q}\boldsymbol{x} + \boldsymbol{u}^T\boldsymbol{R}\boldsymbol{u})dt\}. \tag{2.24}$$

It was shown that the *optimal stochastic controller* for the system (2.23) and cost function (2.24) is composed from the LQR state feedback (2.21) for the noiseless system and an optimal state estimator in a form:

$$\dot{\hat{\boldsymbol{x}}}(t) = \boldsymbol{A}\hat{\boldsymbol{x}}(t) + \boldsymbol{B}\boldsymbol{u}(t) + \boldsymbol{L}\{\boldsymbol{y}(t) - \boldsymbol{C}\hat{\boldsymbol{x}}(t) - \boldsymbol{D}\boldsymbol{u}(t)\}, \tag{2.25}$$

where the estimator gain $\boldsymbol{L}$ is given by

$$\boldsymbol{L} = \boldsymbol{Y}\boldsymbol{C}^{\boldsymbol{T}}\boldsymbol{V}^{-\boldsymbol{1}}, \tag{2.26}$$

and the symmetric nonnegative-definite $n \times n$ matrix Y, is a solution of the ARE:

$$\boldsymbol{A}\boldsymbol{Y} + \boldsymbol{Y}\boldsymbol{A}^{\boldsymbol{T}} - \boldsymbol{Y}\boldsymbol{C}^{\boldsymbol{T}}\boldsymbol{V}^{-\boldsymbol{1}}\boldsymbol{C}\boldsymbol{Y} + \boldsymbol{G}\boldsymbol{W}\boldsymbol{G}^{\boldsymbol{T}} = \boldsymbol{0}. \tag{2.27}$$

The observer (2.25) is known as the Kalman-Bucy filter [11]. In the case of uncorrelated, white and stationary noises with known intensities, the filter is an optimal causal estimator which minimizes the steady-state error covariance

$$\lim_{t\to\infty} E\{(\boldsymbol{x} - \hat{\boldsymbol{x}})(\boldsymbol{x} - \hat{\boldsymbol{x}})^T\}. \tag{2.28}$$

The problem of optimal controller and estimator design is dual. It can be observed that the substitution of $\boldsymbol{A} \to \boldsymbol{A}^{\boldsymbol{T}}, \boldsymbol{P} \to \boldsymbol{Y}, \boldsymbol{B} \to \boldsymbol{C}^{\boldsymbol{T}}, \boldsymbol{Q} \to \boldsymbol{G}\boldsymbol{W}\boldsymbol{G}^{\boldsymbol{T}}, \boldsymbol{L} \to \boldsymbol{K}^{\boldsymbol{T}}$ into the *control Riccati equation* (2.22) leads to the dual *filtering Riccati equation* (2.27).

The noise model is usually unknown in practical situations and the covariance matrices $\boldsymbol{V}, \boldsymbol{W}$ are used merely as tuning parameters of the observer to achieve a reasonable compromise between observer bandwidth and amplification of the measurement noise. It was shown that a deterministic explanation can be derived [12] and the Kalman filter is in fact a least squares estimator which minimizes objective function

$$J = \int_0^\infty (\boldsymbol{w}^T\boldsymbol{W}^{-1}\boldsymbol{w} + \boldsymbol{v}^T\boldsymbol{V}^{-1}\boldsymbol{v})dt, \tag{2.29}$$

subject to the constraints given by the dynamic model of the observed system. Therefore, the goal is to use as little state and output disturbance as possible to explain the measured outputs. From this point of view, the matrices $\boldsymbol{V}, \boldsymbol{W}$ serve as a scaling factors which emphasize the relative confidence in prediction (system model) and observation (measurement).

Spectral properties of the linear quadratic regulators and observers

The linear quadratic regulators and observers are known for their guaranteed spectral properties. It was shown that regardless of the choice of weighting matrices $\boldsymbol{Q}, \boldsymbol{R}$, following relation holds for any scalar LQR controlled system:

$$|1 + L(i\omega)| \geq 1;\ L(i\omega) = \boldsymbol{K}(i\omega\boldsymbol{I} - \boldsymbol{A})^{-1}\boldsymbol{B}, \tag{2.30}$$

where $L(i\omega)$ is the loop transfer function given as the open loop connection of the system and the LQ optimal state feedback $\boldsymbol{K}$. The relation (2.30) is known as the *Kalman inequality* and its consequence is, that the Nyquist curve of the system does not enter a unitary radius circle centered in $[-1, i0]$ point of the complex plane. This leads to a guaranteed robustness of the closed loop in terms of minimum phase margin $p_m \geq 60^o$, gain margin in the interval $g_m \in \langle -0.5, \infty)$ and stability margin $s_m = |1 + L(i\omega)| \geq 1$. This result was generalized for multivariable systems with dynamic uncertainties in the individual input channels [13]. The property of strong robustness in stability is unfortunately lost in the case of the output feedback and LQG control. It was shown, that arbitrary poor performance may be achieved in this case [14].

A dual property can be obtained for the steady-state Kalman filter. For the optimal observer case, the inequality (2.30) changes into:

$$|1 + L(i\omega)| \geq 1;\ L(i\omega) = \boldsymbol{C}(i\omega\boldsymbol{I} - \boldsymbol{A})^{-1}\boldsymbol{L}, \tag{2.31}$$

where $L(i\omega)$ is the loop transfer function from estimation error to the observed output. The guaranteed gain and phase margins of the observer loop leads to the smooth shape of the observer frequency response. This topic is discussed in detail in chapter 5, which deals with optimal observer design for mechanical system identification.

Similar results related to optimal control and filtering were derived for linear discrete-time systems [7, 9, 10].

Symmetrical Root Locus

Particular result of optimal control exists for SISO systems and special choice of quadratic cost function [8, 15]. The performance index of the LQR (2.19) may be simplified to a form:

$$J = \int_0^\infty \{\varrho z^2(t) + u(t)\}dt, \tag{2.32}$$

where z is a properly chosen scalar output given as a linear combination of system states

$$z(t) = \boldsymbol{H}x(t), \tag{2.33}$$

and ϱ is a user-specified weighting parameter.

The corresponding optimal LQ controller (2.21) assigns the closed-loop poles at the stable roots of the symmetric root-locus (SRL) equation:

$$1 + \varrho G_c(-s)G_c(s) = 0, \tag{2.34}$$

where $G_c(s)$ is the open loop transfer function from the input u to the weighted output z:

$$G_c(s) = \frac{Z(s)}{U(s)} = \boldsymbol{H}(s\boldsymbol{I} - \boldsymbol{A})^{-1}\boldsymbol{G}. \tag{2.35}$$

A dual result is achieved for the optimal estimator. In the case of SISO system and scalar process noise w in the model (2.23), the optimal estimator poles are obtained from SRL equation:

$$1 + qG_o(-s)G_o(s) = 0, \tag{2.36}$$

where $G_o(s)$ is the transfer function from the noise to the sensor output

$$G_o(s) = \frac{Y(s)}{W(s)} = \boldsymbol{C}(s\boldsymbol{I} - \boldsymbol{A})^{-1}\boldsymbol{G}. \tag{2.37}$$

The SLR equations can be used for systematic determination of optimal closed-loop pole location of the estimator and state controller. The complexity of the LQ algorithm and the corresponding Riccati equation which has to be solved numerically is significantly reduced as well as number of degrees of freedom (compared to the full pole-placement problem). The root locus may be plotted graphically in the complex plane as a function of weights ϱ, q to get an insight into the shape of the optimal pole patterns.

2.3 Modal control using parametric Jordan form assignment

Modal control can be defined as the design of a control which changes the modes (eigenvalues) of the system to achieve desired closed loop performance. Soon after the introduction of modern state space methods of optimal control theory, it was found that engineering specifications in practical control problems can rarely be summarized in a single quadratic criterion. Rosenbrock [16] suggested modal control as an alternative and powerful design aid and since the first important results of Wohnham, Anderson and Luenberger [17, 18] further theoretical works have been published [19, 20, 21, 22, 23]. It is well known that the solution of pole assignment problem is not unique for a multivariable system. Therefore, great emphasis was put on the search for a non-redundant parametrization of the eigenstructure assignment with a

minimum set of free parameters which could be used to fulfil additional important design specifications (e.g. stability radius, feedback gain norm, decentralized or symmetrical feedback). In this section, some recent results achieved at the Department of Cybernetics of University of West Bohemia are briefly summarized. For full references, see [21, 22, 23, 24, 25].
Considering a linear time invariant system defined by state space representation:

$$\dot{\boldsymbol{x}}(t) = \boldsymbol{A}\boldsymbol{x}(t) + \boldsymbol{B}u(t), \tag{2.38}$$

$$\boldsymbol{y}(t) = \boldsymbol{C}\boldsymbol{x}(t), \tag{2.39}$$

where $\boldsymbol{x}(t) \in \mathbb{R}^n$ is state vector, $\boldsymbol{u}(t) \in \mathbb{R}^m$ is input vector, $\boldsymbol{y}(t) \in \mathbb{R}^p$ is measurement output vector, $\boldsymbol{A}, \boldsymbol{B}, \boldsymbol{C}$ are constant real matrices with corresponding dimensions and the pair $(\boldsymbol{A}, \boldsymbol{B})$ is controllable.

Our first goal is to find all state feedbacks $\boldsymbol{F} \in \mathbb{R}^{m\times n}$ in the form of

$$\boldsymbol{u}(t) = \boldsymbol{F}\boldsymbol{x}(t), \tag{2.40}$$

which assign a chosen Jordan form $\boldsymbol{L} \in \mathbb{R}^{s\times s}$ and therefore fulfil condition $\boldsymbol{A} + \boldsymbol{B}\boldsymbol{F} \sim \boldsymbol{L}$. Such feedback matrices form a set $\mathcal{F}_s$

$$\mathcal{F}_s(\boldsymbol{A}, \boldsymbol{B}, \boldsymbol{L}) \triangleq \left\{ \boldsymbol{F} \in \mathbb{R}^{m\times n} : \ (A + BF) \sim \begin{bmatrix} \boldsymbol{L} & * \\ 0 & * \end{bmatrix} \right\}, \tag{2.41}$$

where $*$ denotes an arbitrary real matrix of proper dimension. If $s < n$ we call it partial Jordan form assignment. From definition of similar matrices it follows:

$$\begin{aligned} &\boldsymbol{A} + \boldsymbol{B}\boldsymbol{F} = \boldsymbol{T}\boldsymbol{M}\boldsymbol{T}^{-1} \\ \Rightarrow\ &\boldsymbol{A}\boldsymbol{T} - \boldsymbol{T}\boldsymbol{M} + \boldsymbol{B}\boldsymbol{F}\boldsymbol{T} = 0, \end{aligned} \tag{2.42}$$

where

$$\boldsymbol{M} = \begin{bmatrix} \boldsymbol{L} & \boldsymbol{R} \\ \boldsymbol{0} & \boldsymbol{S} \end{bmatrix},$$

and $\boldsymbol{R}, \boldsymbol{S}$ are matrices of proper dimensions. Next we consider $\boldsymbol{T} = [\boldsymbol{X}, \boldsymbol{V}]$, $\boldsymbol{X} \in \mathbb{R}^{n\times s}$, $\boldsymbol{V} \in \mathbb{R}^{n\times(n-s)}$. From (2.42) we get

$$\boldsymbol{A}\boldsymbol{X} - \boldsymbol{X}\boldsymbol{L} + \boldsymbol{B}\boldsymbol{H} = \boldsymbol{0}, \tag{2.43}$$

where $\boldsymbol{H} \triangleq \boldsymbol{F}\boldsymbol{X} \in \mathbb{R}^{m\times s}$. It clearly holds that for $\boldsymbol{F} \in \mathcal{F}_s(\boldsymbol{A}, \boldsymbol{B}, \boldsymbol{L})$, the matrices $\boldsymbol{H}$ and $\boldsymbol{X}$ exist which fulfil the equation (2.43). Now the process can be reversed to derive an algorithm for computing the state feedback $\boldsymbol{F}$. If we choose the matrix $\boldsymbol{H}$ we can

solve the Sylvester equation (2.43). Supposing that the eigenvalues of matrices $\boldsymbol{A}$ and $\boldsymbol{L}$ are different, a general solution exists in form

$$\boldsymbol{F} = \boldsymbol{H}\left[\boldsymbol{X}^{\boldsymbol{T}}(\boldsymbol{H})\boldsymbol{X}(\boldsymbol{H})\right]^{-1}\boldsymbol{X}^{\boldsymbol{T}}(\boldsymbol{H}) + \boldsymbol{F_0}, \tag{2.44}$$

where $\boldsymbol{F}_0$ is an arbitrary matrix fulfilling condition $\boldsymbol{F_0 X(H)} = \boldsymbol{0}$. It can be shown that the solution (2.44) holds for almost any chosen $\boldsymbol{H}$. In case of a multi-input system ($m > 1$), there is an infinite number of state feedbacks which assign a specified Jordan form. Thus, there is a freedom in choice of $\boldsymbol{H}$, which may be used to fulfill some additional design specification e.g. robustness in stability or control effort. Moreover, the number of free parameters in $\boldsymbol{H}$ can be reduced by replacing it by a so called parametric matrix $\boldsymbol{Q}(\boldsymbol{\alpha})$ where the parametric vector $\boldsymbol{\alpha}$ contains a minimum set of design parameters.

Now the problem of Jordan form assignment using static output feedback is to find a set of all the matrices $\mathcal{K}_s$ fulfilling

$$\mathcal{K}_s(\boldsymbol{A},\boldsymbol{B},\boldsymbol{C},\boldsymbol{L}) \triangleq \left\{\boldsymbol{K} \in \mathbb{R}^{m\times p} :\ (\boldsymbol{A}+\boldsymbol{BKC}) \sim \begin{bmatrix}\boldsymbol{L} & * \\ 0 & *\end{bmatrix}\right\}. \tag{2.45}$$

Again, if $s < n$ we call it partial Jordan form assignment. From the previous section it follows that for any $\boldsymbol{K} \in \mathcal{K}_s(\boldsymbol{A},\boldsymbol{B},\boldsymbol{C},\boldsymbol{L})$ there has to be $\boldsymbol{F} \in \mathcal{F}_s(\boldsymbol{A},\boldsymbol{B},\boldsymbol{L})$ such that $\boldsymbol{F} = \boldsymbol{KC}$. Thus, there exists $\boldsymbol{H} \in \mathbb{R}^{m\times s}$ and $\boldsymbol{F}_0$ and the relation

$$\boldsymbol{H}\left[\boldsymbol{X}^{\boldsymbol{T}}(\boldsymbol{H})\boldsymbol{X}(\boldsymbol{H})\right]^{-1}\boldsymbol{X}^{\boldsymbol{T}}(\boldsymbol{H}) + \boldsymbol{F_0} = \boldsymbol{KC}, \tag{2.46}$$

where $\boldsymbol{X}(\boldsymbol{H})$ is the solution of the Sylvester equation (2.43). By multiplying (7.151) with $\boldsymbol{X}(\boldsymbol{H})$ from the right we get

$$\boldsymbol{H} = \boldsymbol{KCX}(\boldsymbol{H}). \tag{2.47}$$

Again, we can replace $\boldsymbol{H}$ by a parametric matrix $\boldsymbol{Q}(\boldsymbol{\alpha})$ with a minimum set of free parameters and obtain a bilinear system of equations

$$\boldsymbol{Q}(\boldsymbol{\alpha}) = \boldsymbol{KCX}(\boldsymbol{\alpha}), \tag{2.48}$$

for the unknown $\boldsymbol{\alpha}$ and $\boldsymbol{K}$. An analytical method which can solve a set of polynomial equations is needed in order to find all the real solutions. To accomplish this, Gröbner basis method can be used [26]. A freely available toolbox for Maple software which solves this problem was developed at Department of Cybernetics of University of West Bohemia (UWB). Of course, this approach is limited to small dimension problems due

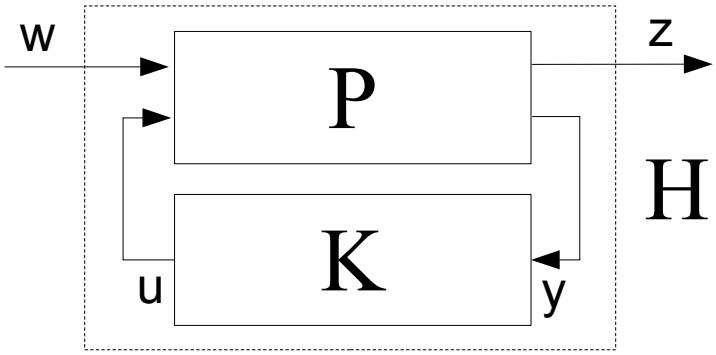

Figure 2.1: General H_2/H_∞ optimization problem - closed-loop scheme where $\boldsymbol{P}$ denotes a generalized plant, $\boldsymbol{K}$ feedback controller, $\boldsymbol{u}$ plant inputs, $\boldsymbol{y}$ measured outputs, $\boldsymbol{w}$ external signal/disturbances, $\boldsymbol{z}$ controlled or penalized outputs, $\boldsymbol{H}$ closed-loop transfer matrix

to the fact that computational complexity grows exponentially with the number of free parameters. Secondary numerical optimization of a set of free parameters α can be performed to meet some specific design requirements (maximum complex or real stability radius, H_∞ norm of suitable transfer matrix etc.). More details can be found in [24, 25].

2.4 H_2 and H_∞ optimal control

The procedure of feedback compensator design can be formulated as an optimization problem of minimizing a properly chosen norm of the closed-loop system. The general H_2/H_∞ problem is defined for the block diagram of Fig. (2.1). The goal is to find a controller $\boldsymbol{K}$ which:

1. Stabilizes the closed-loop system
2. Minimizes the H_2 or H_∞ norm of the closed-loop system $\boldsymbol{H}$ with $\boldsymbol{w}$ chosen as inputs and $\boldsymbol{z}$ as outputs of a generalized plant $\boldsymbol{P}$

The generalized plant $\boldsymbol{P}$ can be represented in the state-space form:

$$\begin{aligned} \dot{\boldsymbol{x}}(t) &= \boldsymbol{A}\boldsymbol{x}(t) + \boldsymbol{B_1}\boldsymbol{w}(t) + \boldsymbol{B_2}\boldsymbol{u}(t), \\ \dot{\boldsymbol{z}}(t) &= \boldsymbol{C_1}\boldsymbol{x}(t) + \boldsymbol{D_{11}}\boldsymbol{w}(t) + \boldsymbol{D_{12}}\boldsymbol{u}(t), \\ \boldsymbol{y}(t) &= \boldsymbol{C_2}\boldsymbol{x}(t) + \boldsymbol{D_{21}}\boldsymbol{w}(t) + \boldsymbol{D_{22}}\boldsymbol{u}(t), \end{aligned} \tag{2.49}$$

where $\boldsymbol{w}$ is a vector of exogenous signals, usually reference commands, input or output disturbances and measurement noise, $\boldsymbol{z}$ is a vector of generalized outputs, typically controlled and manipulating variables. The general formulation allows precise customization of the design problem by properly selecting the input and output signals and by adding some additional weighting functions which allow specification of the design requirements.

The solution of the $\boldsymbol{H_2}$ **problem** is obtained as follows [5]. Assuming that

- the system $\dot{\boldsymbol{x}}(t) = \boldsymbol{A}\boldsymbol{x}(t) + \boldsymbol{B_2}\boldsymbol{u}(t),\ \boldsymbol{y}(t) = \boldsymbol{C_2}\boldsymbol{x}(t)$ is stabilizable and detectable,
- the matrix $\begin{bmatrix} \boldsymbol{A} - s\boldsymbol{I} & \boldsymbol{B_1} \\ \boldsymbol{C_2} & \boldsymbol{D_{12}} \end{bmatrix}$ has full row rank for every $s = i\omega$ and $\boldsymbol{D_{21}}$ has full row rank,
- the matrix $\begin{bmatrix} \boldsymbol{A} - s\boldsymbol{I} & \boldsymbol{B_2} \\ \boldsymbol{C_1} & \boldsymbol{D_{12}} \end{bmatrix}$ has full column rank for every $s = i\omega$ and $\boldsymbol{D_{12}}$ has full column rank,

the optimal output feedback controller is obtained in the observer plus state feedback form as:

$$\begin{aligned} \dot{\hat{\boldsymbol{x}}}(t) &= \boldsymbol{A}\hat{\boldsymbol{x}}(t) + \boldsymbol{B_2}\boldsymbol{u}(t) + \boldsymbol{L}\{\boldsymbol{y}(t) - \boldsymbol{C_2}\hat{\boldsymbol{x}}(t) - \boldsymbol{D_{22}}\boldsymbol{u}(t)\}, \\ \boldsymbol{u}(t) &= -\boldsymbol{K}\hat{\boldsymbol{x}}(t). \end{aligned} \tag{2.50}$$

The observer and state feedback gain matrices are computed from

$$\boldsymbol{K} = (\boldsymbol{D_{12}^T}\boldsymbol{D_{12}})^{-1}(\boldsymbol{B_2^T}\boldsymbol{X} + \boldsymbol{D_{12}^T}\boldsymbol{C_1}),\ \boldsymbol{L} = (\boldsymbol{Y}\boldsymbol{C_2^T} + \boldsymbol{B_1}\boldsymbol{D_{21}^T})(\boldsymbol{D_{21}}\boldsymbol{D_{21}^T})^{-1}, \tag{2.51}$$

where $\boldsymbol{X}$ and $\boldsymbol{Y}$ are positive-definite solutions of the algebraic Ricati equations

$$\begin{aligned} \boldsymbol{A^T X} + \boldsymbol{X A} + \boldsymbol{C_1^T C_1} - (\boldsymbol{X B_2} + \boldsymbol{C_1^T D_{12}})(\boldsymbol{D_{12}^T D_{12}})^{-1}(\boldsymbol{B_2^T X} + \boldsymbol{D_{12}^T C_1}) = 0, \\ \boldsymbol{AY} + \boldsymbol{AY^T} + \boldsymbol{B_1 B_1^T} - (\boldsymbol{Y C_2^T} + \boldsymbol{B_1 D_{21}^T})(\boldsymbol{D_{21} D_{21}^T})^{-1}(\boldsymbol{C_2 Y} + \boldsymbol{D_{21} B_1^T}) = 0. \end{aligned} \tag{2.52}$$

The solution of the H_2 optimization problem is unique. It was shown that the LQG controller design is a special case of the general H_2 problem for a particular choice of the generalized plant [5]. Therefore, the original time-domain stochastic formulation of the problem is transformed to an equivalent deterministic optimization problem in the frequency domain.

Optimal solution of the $\boldsymbol{H_\infty}$ **problem** cannot be found directly. However, solutions of so called *suboptimal* problem which leads to a stabilizing controller that achieves

$\|H\|_\infty < \gamma$ for a specified nonnegative number γ are known. The most popular is the one based on the state space realization of the generalized plant (2.49) [5, 27]. The required assumptions are formulated as:

- the system $\dot{\boldsymbol{x}}(t) = \boldsymbol{A}\boldsymbol{x}(t) + \boldsymbol{B_2}\boldsymbol{u}(t),\ \boldsymbol{y}(t) = \boldsymbol{C_2}\boldsymbol{x}(t)$ is stabilizable and detectable,
- $\begin{bmatrix} \boldsymbol{A} - s\boldsymbol{I} & \boldsymbol{B_1} \\ \boldsymbol{C_2} & \boldsymbol{D_{12}} \end{bmatrix}$ has full row rank for every $s = i\omega$,
- $\begin{bmatrix} \boldsymbol{A} - s\boldsymbol{I} & \boldsymbol{B_2} \\ \boldsymbol{C_1} & \boldsymbol{D_{12}} \end{bmatrix}$ has full column rank for every $s = i\omega$,
- $\boldsymbol{D_{12}}$ and $\boldsymbol{D_{21}}$ have full rank.

A stabilizing controller for which $\|H\|_\infty < \gamma$ exists if and only if the following three conditions hold:

1. $\boldsymbol{AQ} + \boldsymbol{QA^T} + \boldsymbol{Q}(\frac{1}{\gamma^2}\boldsymbol{C_1^T C_1} - \boldsymbol{C_2^T C})\boldsymbol{Q} + \boldsymbol{B_1 B_1^T} = 0$ has a stabilizing solution $\boldsymbol{Q} \geq 0$
2. $\boldsymbol{PA} + \boldsymbol{A^T P} + \boldsymbol{P}(\frac{1}{\gamma^2}\boldsymbol{B_1 B_1^T} - \boldsymbol{B_2 B_2^T})\boldsymbol{P} + \boldsymbol{C_1^T C_1} = 0$ has a stabilizing solution $\boldsymbol{P} \geq 0$
3. All eigenvalues of $\boldsymbol{Q}$ and $\boldsymbol{P}$ have magnitude less than γ

Under these conditions, the suboptimal controller can be obtained in the form of:

$$\dot{\hat{\boldsymbol{x}}}(t) = (\boldsymbol{A} + [\frac{\boldsymbol{1}}{\boldsymbol{\gamma^2}}\boldsymbol{B_1 B_1^T} - \boldsymbol{B_2 B_2^T}]\boldsymbol{P})\hat{\boldsymbol{x}}(t) + (\boldsymbol{I} - \frac{\boldsymbol{1}}{\boldsymbol{\gamma^2}}\boldsymbol{QP})^{-\boldsymbol{1}}\boldsymbol{QC_2^T}\big(\boldsymbol{y}(t) - \boldsymbol{C_2}\hat{\boldsymbol{x}}(t)\big),$$
$$\boldsymbol{u}(t) = -\boldsymbol{B_2}\hat{\boldsymbol{x}}(t). \tag{2.53}$$

The *suboptimal solution* is non-unique and all solutions parametrized by a free stable contraction map can be found. The *optimal* solution is approached by iterating the value of γ to the lowest possible value for which the suboptimal solution exists. The H_∞ optimization is useful for the controller design using the loopshaping technique. Proper compensator can be found by introducing some weighting filters which allow to gain control over the shape of important closed-loop frequency response functions. A version of what is known as the *Mixed sensitivity problem* is used for derivation of H_∞ controllers. Detailed description is provided in Chapter 7.

2.5 Data fitting and least-squares optimization

Many practical engineering problems lead to a search for a suitable function which approximates a set of measured data points. The problem of synthesis of an optimal fitting function is formalized as follows.
For a given vector of measured data

$$\boldsymbol{y} = \begin{bmatrix} y_1 \\ y_2 \\ \vdots \\ y_m \end{bmatrix}, \tag{2.54}$$

and some a priori chosen parametric function

$$f(\boldsymbol{p}) = \hat{y}(\boldsymbol{p}), \tag{2.55}$$

where $\boldsymbol{p} = [\ p_1 \quad p_2 \quad \dots \quad p_k\ ]$ is a vector of unknown parameters, find an optimal solution $\boldsymbol{p}^*$ which minimizes a criterion function given as the sum of squares of the residuals

$$\chi^2(\boldsymbol{p}) = \frac{1}{2}\sum_{i=1}^{m}\left[\frac{r_i(\boldsymbol{p})}{w_i}\right]^2 = \frac{1}{2}\|\sqrt{\boldsymbol{W}}\boldsymbol{r}(\boldsymbol{p})\|^2 = \frac{1}{2}\boldsymbol{r}(\boldsymbol{p})^{\boldsymbol{T}}\boldsymbol{W}\boldsymbol{r}(\boldsymbol{p}), \tag{2.56}$$

where $\boldsymbol{W} = diag\{\frac{1}{w_i^2}\}$ is a diagonal weighting matrix which introduces a relative confidence in the individual data points and $\boldsymbol{r(p)}$ is the residual vector defined as

$$\boldsymbol{r}(\boldsymbol{p}) = \begin{bmatrix} r_1 \\ r_2 \\ \vdots \\ r_m \end{bmatrix};\ r_i(\boldsymbol{p}) = y_i - \hat{y}_i(\boldsymbol{p}). \tag{2.57}$$

The weighting matrix $\boldsymbol{W}$ may be obtained from a known statistics of the measurement process (e.g. a standard deviation of the individual measurements) or it is set as the identity matrix when no individual weighting is necessary. The criterion (2.56) evaluates the overall quality of the data approximation and the optimal solution is defined as:

$$\boldsymbol{p}^* = \underset{\forall \boldsymbol{p}}{argmin}\{\chi^2(\boldsymbol{p})\}. \tag{2.58}$$

Linear least-squares

In the case of a approximating function which is *linear with respect to the unknown parameters* and may be expressed as $\hat{y}_i = \boldsymbol{\varphi_i p}$, the problem may be formulated by means of a linear regression model which is written in the matrix form:

$$\boldsymbol{y} = \boldsymbol{\Phi p} + \boldsymbol{r};\ \boldsymbol{\Phi} = \begin{bmatrix} \boldsymbol{\varphi_1} \\ \boldsymbol{\varphi_2} \\ \vdots \\ \boldsymbol{\varphi_m} \end{bmatrix}. \tag{2.59}$$

The optimal parameter vector is obtained analytically by setting

$$\frac{\partial \chi^2(\boldsymbol{p})}{\partial \boldsymbol{p^T}} = \frac{1}{2}(\boldsymbol{y} - \boldsymbol{\Phi p})^T \boldsymbol{W}(\boldsymbol{y} - \boldsymbol{\Phi p}) = 0, \tag{2.60}$$

which leads to a set of normal equations

$$\boldsymbol{\Phi^T W \Phi p^*} = \boldsymbol{\Phi^T W y}. \tag{2.61}$$

Nonlinear least-squares

In many cases, the approximating function is nonlinear in the unknown parameters and the data fitting problem leads to a nonlinear least-squares optimization. Analytical solution does not exist and a numerical method has to be used to find a solution [28, 29].

Standard gradient methods assume that the cost function (2.56) has continuous second partial derivatives and it can be written using the *Taylor expansion* as:

$$\chi^2(\boldsymbol{p} + \boldsymbol{h}) = \chi^2(\boldsymbol{p}) + \boldsymbol{h^T g(p)} + \frac{1}{2}\boldsymbol{h^T H(p) h} + O(\|h\|^3), \tag{2.62}$$

where $\boldsymbol{g}$ is the $m \times 1$ *gradient vector* and $\boldsymbol{H}$ is the $m \times m$ *Hessian matrix*.
The gradient contains the partial derivatives of the cost function with respect to the individual parameters:

$$\boldsymbol{g(p)} = \begin{bmatrix} g_1(\boldsymbol{p}) \\ g_2(\boldsymbol{p}) \\ \vdots \\ g_m(\boldsymbol{p}) \end{bmatrix}; g_j(\boldsymbol{p}) = \frac{\partial \chi^2}{\partial p_j}(\boldsymbol{p}) = \frac{\partial}{\partial p_j}\{\frac{1}{2}\boldsymbol{r(p)^T W r(p)}\} = \sum_{i=1}^{m} \frac{1}{w_i^2} r_i(\boldsymbol{p}) \frac{\partial r_i}{\partial p_j}(\boldsymbol{p}). \tag{2.63}$$

The gradient can be expressed in a compact matrix form:

$$\boldsymbol{g(p)} = \boldsymbol{J(p)^T W r(p)} \tag{2.64}$$

by means of the $m \times k$ *Jacobian matrix* $\boldsymbol{J}$ which contains the first partial derivatives of the cost function components and which is defined as

$$[\boldsymbol{J}(\boldsymbol{p})]_{i,j} = \frac{\partial r_i}{\partial p_j}(\boldsymbol{p}). \tag{2.65}$$

The Hessian matrix contains second partial derivatives and the individual elements are given as:

$$[\boldsymbol{H}(\boldsymbol{p})]_{j,k} = \frac{\partial^2 \chi^2}{\partial p_j \partial p_k}(\boldsymbol{p}) = \sum_{i=1}^{m} \left\{ \frac{\partial r_i}{\partial p_j}(\boldsymbol{p}) \frac{1}{w_i^2} \frac{\partial r_i}{\partial p_k}(\boldsymbol{p}) + r_i(\boldsymbol{p}) \frac{1}{w_i^2} \frac{\partial^2 r_i}{\partial p_j \partial p_k}(\boldsymbol{p}) \right\}. \tag{2.66}$$

Again, the Hessian can be written in a compact matrix form with use of the Jacobian:

$$\boldsymbol{H}(\boldsymbol{p}) = \boldsymbol{J}^{\boldsymbol{T}}(\boldsymbol{p}) \boldsymbol{W} \boldsymbol{J}(\boldsymbol{p}) + \sum_{i=1}^{m} \frac{r_i(\boldsymbol{p}) \boldsymbol{r}''(\boldsymbol{p})}{w_i^2}. \tag{2.67}$$

The gradient methods use the model of the objective function $\boldsymbol{\chi^2}$ to iteratively approach a local minimum from a given initial point $\boldsymbol{p_0}$.

Gradient Descent method

The steepest descent methods updates the parameter values in each step of the algorithm in the direction which is opposite to the gradient of the cost function. Therefore, the perturbation of the actual parameter estimate $\boldsymbol{h}$ is computed as:

$$\boldsymbol{h_{GD}} = -\alpha \boldsymbol{g}(\boldsymbol{p}) = -\alpha \boldsymbol{J}(\boldsymbol{p})^{\boldsymbol{T}} \boldsymbol{r}(\boldsymbol{p}), \tag{2.68}$$

where the positive scalar value α determines the length of the step. *Line-search procedure* is usually employed for determination of the proper step length in order to prevent from overshooting the local minimum of the cost function. The optimal value of α is computed from:

$$\alpha^* = \underset{\forall \alpha > 0}{argmin} \{ \chi^2(\boldsymbol{p} + \alpha \boldsymbol{h_{GD}}) \}. \tag{2.69}$$

The steepest gradient method combined with the line-search procedure converges a local minimum of the objective function. However, the final convergence is linear and often very slow and the method may fail under some circumstances [28]. However, it performs well in the initial stage of the optimization for many problems.

Gauss-Newton method

The Gauss-Newton method is based on a linear approximation of the residual functions in the vicinity of actual parameter values $\boldsymbol{p}$. For a small $\|h\|$, the Taylor expansion of the residual vector is assumed as:

$$\boldsymbol{r}(\boldsymbol{p}+\boldsymbol{h}) = \boldsymbol{r}(\boldsymbol{p}) + \boldsymbol{J}(\boldsymbol{p})\boldsymbol{h}. \tag{2.70}$$

Therefore, the objective function for the perturbed residuals is obtained as:

$$\chi^2(\boldsymbol{p}+\boldsymbol{h}) = \chi^2(\boldsymbol{p}) + \boldsymbol{h}^{\boldsymbol{T}}\boldsymbol{J}(\boldsymbol{p})^{\boldsymbol{T}}\boldsymbol{W}\boldsymbol{r}(\boldsymbol{p}) + \frac{1}{2}\boldsymbol{h}^{\boldsymbol{T}}\boldsymbol{J}(\boldsymbol{p})^{\boldsymbol{T}}\boldsymbol{W}\boldsymbol{J}(\boldsymbol{p})\boldsymbol{h}. \tag{2.71}$$

This corresponds to the quadratic model of χ^2 (2.62), the only difference is in the approximation of the Hessian matrix

$$\boldsymbol{H}(\boldsymbol{p}) \approx \boldsymbol{J}^{\boldsymbol{T}}(\boldsymbol{p})\boldsymbol{W}\boldsymbol{J}(\boldsymbol{p}), \tag{2.72}$$

which is valid for the close vicinity of the local minimums of the cost function in which $r_i \approx 0$ and second term of (2.67) is negligible.
The optimum perturbation $\boldsymbol{h}$ is found by setting

$$\frac{\partial}{\partial \boldsymbol{p}}\chi^2(\boldsymbol{p}+\boldsymbol{h}) = \boldsymbol{J}(\boldsymbol{p})^{\boldsymbol{T}}\boldsymbol{W}\boldsymbol{r}(\boldsymbol{p}) + \boldsymbol{J}(\boldsymbol{p})^{\boldsymbol{T}}\boldsymbol{W}\boldsymbol{J}(\boldsymbol{p})\boldsymbol{h} = 0, \tag{2.73}$$

which leads to solution in the form of normal equations

$$[\boldsymbol{J}^{\boldsymbol{T}}(\boldsymbol{p})\boldsymbol{W}\boldsymbol{J}(\boldsymbol{p})]\boldsymbol{h}_{\boldsymbol{GN}} = -\boldsymbol{J}^{\boldsymbol{T}}(\boldsymbol{p})\boldsymbol{W}\boldsymbol{r}(\boldsymbol{p}). \tag{2.74}$$

Again, the line-search procedure may be employed to find an optimal step length in the computed direction $\boldsymbol{h}_{\boldsymbol{GN}}$. In the case that the Jacobian $\boldsymbol{J}(\boldsymbol{p})$ has full rank in all steps of, the Hessian matrix $\boldsymbol{H}(\boldsymbol{p}) = \boldsymbol{J}^{\boldsymbol{T}}(\boldsymbol{p})\boldsymbol{W}\boldsymbol{J}(\boldsymbol{p})$ is positive definite and the algorithm converges to a local minimum. The Gauss-Newton algorithm provides quadratic convergence in special cases (when $\chi^2(\boldsymbol{p}^*) = 0$), see e.g. [28]) and generally converges very fast in the vicinity of the local minimums. The convergence may be poor in the initial phase or in the locations of the parametric space for which the linear model of the residual function (2.70) does not hold.

Levenberg-Marquardt method

The Levenberg-Marquardt (LM) method combines the steepest gradient and Gauss-Newton iterations to a hybrid algorithm which tries to improve the convergence rate

both in the initial and final phase and to reduce the sensitivity to the initial conditions. The normal equations of the Gauss-Newton method (2.74) are modified to the form:

$$[\boldsymbol{J^T(p)WJ(p)} + \lambda \boldsymbol{I}]\boldsymbol{h_{LM}} = -\boldsymbol{J^T(p)Wr(p)}. \tag{2.75}$$

Small values of the positive scalar λ result in a Gauss-Newton update and large values leads to a step in the steepest descent direction as can be seen from equations (2.74,2.68). The level of λ is adapted in each iteration according to a *gain ratio*

$$\rho = \frac{\chi^2(\boldsymbol{p}) - \chi^2(\boldsymbol{p} + \boldsymbol{h_{LM}})}{\chi^2(\boldsymbol{p}) - \hat{\chi}^2(\boldsymbol{p} + \boldsymbol{h_{LM}})}, \tag{2.76}$$

where the denominator is composed from the assumed cost function model (2.71)

$$\begin{aligned}\chi^2(\boldsymbol{p}) - \hat{\chi}^2(\boldsymbol{p} + \boldsymbol{h_{LM}}) &= -\boldsymbol{h_{LM}^T J(p)^T W r(p)} - \frac{1}{2}\boldsymbol{h_{LM}^T J(p)^T W J(p) h_{LM}} \\ &= \frac{1}{2}\boldsymbol{h_{LM}^T}(\lambda \boldsymbol{h_{LM}} - \boldsymbol{g(p)}).\end{aligned} \tag{2.77}$$

Large values of ρ indicate good approximation of χ^2 by the linear model and the λ is decreased to perform a larger step in the Gauss-Newton direction. On the other side, low or even negative values of ρ signalize poor validity of the model and lead to an increase of λ which results in a smaller step closer to the steepest descent direction. Since both step size and direction are adjusted, no explicit line search is needed in this case and the LM procedure interpolates smoothly between the Gauss-Newton and gradient descent steps based on the local behaviour of the objective function.
The algorithm is summarized in the following steps:

1. Set the initial values for $\lambda = \lambda_0$ and parameter estimate $\boldsymbol{p} = \boldsymbol{p_0}$
2. Solve the normal equations $[\boldsymbol{J^T(p)WJ(p)} + \lambda \boldsymbol{I}]\boldsymbol{h_{LM}} = -\boldsymbol{J^T(p)Wr(p)}$ to obtain the perturbation $\boldsymbol{h_{LM}}$
3. Evaluate the gain ratio ρ. If $\rho > \epsilon_\rho$, accept the new parameters $\boldsymbol{p} = \boldsymbol{p} + \boldsymbol{h_{LM}}$ and reduce λ by a chosen factor, otherwise increase λ by a factor and go to the next iteration.
4. Repeat steps 2) and 3) until an occurrence of one of the stopping conditions

The stopping conditions are usually chosen as:

- *Parameters convergence*, $max\{h_i/p_i\} < \epsilon_1$
- *Cost function convergence*, $\chi^2 < \epsilon_2$
- *Gradient convergence*, $max\{|g|\} < \epsilon_3$
- *Maximum number of iterations*

The convergence of the algorithm is difficult to prove theoretically as it depends on the chose of initial values and the algorithm for the update of the λ parameter. However, the method is generally considered as a robust algorithm which outperforms the simpler gradient descent and Gauss-Newton methods and which works well in many practical applications.

3

Motion control - state of the art

This chapter provides a brief introduction to motion control systems. The first section explains the general concepts, specifies the basic components and architecture of the control system and defines typical tasks and problems encountered in industrial applications. The second section deals with flexible mechanical systems in detail, presenting the common approaches to modelling, identification and control of vibrations.

3.1 Basic motion control concepts

The problem of motion control is one of the key issues in mechatronic systems and occurs in a wide range of applications including robotics, industrial production lines, transportation, aviation, bio-medical applications or space research . The basic principle is an interconnection of mechanical and electronic components and insertion of intelligence in the form of a control system. This combination provides increased reliability and performance, reduces production and maintenance costs and allows an implementation of advanced features and functions which would be unattainable through the use of a purely mechanical design. Motion control system design links several different science and engineering disciplines (drives and power electronics, sensors , control theory, computer science and programming, mechanical engineering etc.). The basic structure of the system is shown in Fig. 3.1. Various sensors acquire information about actual values of certain physical quantities (position, velocity, acceleration, force...) which are necessary for the control. Such a sensor can be either a physical measuring device in the form of a transducer or a virtual sensor - state observer that estimates values of unknown variables whose measurement is not directly available. Based on the data from the sensors, necessary control actions are computed and executed by actuators (usually linear or rotary drives) which apply force or torque on the

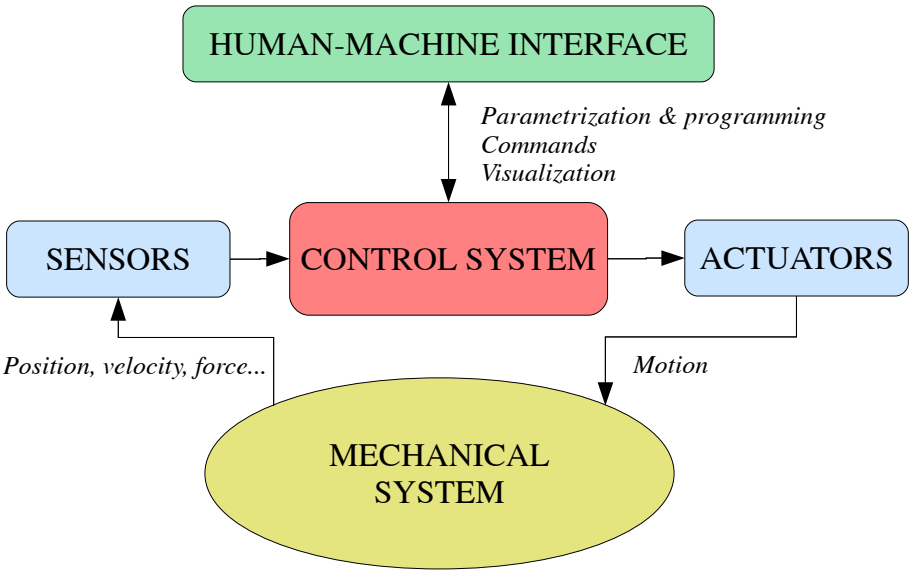

Figure 3.1: Structure of motion control system

work mechanism causing its movement in a desired manner.

A key role is played by the control system. The quality of the implemented algorithms and control laws significantly affects the functionality and overall performance of the device. Important properties of the system including its controllability have to be taken into consideration in the initial phases of design. Achievable dynamics, range of motion or possibility of occurrence of unwanted vibrations due to limited stiffness are directly affected by mechanical construction and selection of hardware components of the system. Therefore, the procedure of mechanical design cannot be separated from the development of control system. Only the consistent application of principles of so-called *simultaneous engineering* which respects the internal relationships between individual subsystems can lead to optimal results. However, there are numerous situations in industry when a finished machine has to be controlled and any problems in the mechanical design have to be resolved by proper algorithms of the control system.

3.1.1 Sensors

A sensor is a device which measures a physical quantity and converts it into an analog or digital signal which can be used as feedback in the control system. Basic types of sensors which can be found in typical motion control systems include [1, 2, 3, 30, 31, 32]:

Position sensors

These are used in applications where precise positioning of the work mechanism is required. The sensor can be integrated into the motor housing and beside the function of indirect detection of load position, it is often used as feedback for electronic commutation in current/torque control loop of AC drives. Resolvers or optical encoders are used in most cases. *Resolver* acts as a positional transformer with primary and secondary windings. The stationary primary part is excited by a harmonic voltage of high frequency. Due to changes in the mutual inductance between the two windings caused by their angular displacement, the rotor angle can be evaluated by measuring the voltage on the attached secondary part. Resolvers can be equipped with an integrated circuit, so-called R/D converter (resolver-to-digital), which provides the information about the absolute position in digital format, usually with 10 to 12 bits precision. *Optical sensors* operate on the principle of a transmitter and a receiver of light signal that passes through the optical grating. Alternating matt and transparent sections causes changes in the amount of light detected by measured voltage in the receiver. By evaluating two mutually phase-shifted signals in the form of rectangular pulses or harmonic signals, the direction of rotation can be determined. Sensors are manufactured as absolute (single and multi-turn) or incremental encoders. Typical resolution is of the order of 10 to 20 bits per revolution . A simple Hall magnetic sensor, which detects the magnet mounted on the rotor can be used for low-cost applications. In addition to internal drive sensors, auxiliary transducers can be used for direct measurement of load position. The additional sensor can provide valuable feedback for precise positioning of the load (e.g. tip of a robot end-effector or spindle of a machine-tool) because the direct measurement is not affected by mechanical imperfections, static and dynamical deformations of the kinematic chain between the actuator and load. In this case, linear encoders, optical cameras, laser or magnetostrictive sensors are often used.

Velocity sensors

Information about the actual linear or angular velocity is often used in the lowest regulatory level of motion control system. Instead of special velocity sensors such as formerly used DC tachogenerators, the speed is usually calculated from the continuous measurement of the position. The velocity can be obtained by simply differentiating the position signal However, this brings an error in form of high-frequency quantization noise due to the finite resolution of the position sensor and discrete time sampling. Therefore, the calculated value is usually additionally processed by a digital filter with

low-pass characteristics. An alternative method is to use a suitable interpolation algorithm or to deploy a state observer.

Acceleration sensors

These sensors on principle of accelerometers, are often manufactured by MEMS (micro electromechanical systems) technology. They can be combined with gyroscopes and magnetometers in a single *inertial measurement unit* which provides measurement of position,velocity and acceleration in up to three linear and three rotational axes. They are often employed in mobile applications (drive stability systems of a car, navigation of ships, aircrafts, spacecrafts or mobile robots). In industrial manufacturing systems, accelerometers and gyros can be used for detection and control of vibrations in a machine.

Sensors of force and torque

Haptic sensors based on tensometers are often used for applications of robots which come into direct contact with its surroundings (obstacles, human operator, patient of assisting robot, contact motion during assembly or manufacturing). Strain-gauge sensors can be installed to detect and control vibrations of the work mechanism.

Auxiliary sensors

Additional sensors providing information about temperature, pressure, flow etc. which do not necessarily relate to motion control but which for example may be used for the monitoring of machine condition and the purpose of safety functions.

Usually, there is an effort to integrate all the necessary equipment on a single chip resulting in so-called intelligent or *smart sensors*. All the processing of the measured signal such as noise filtering, linearization, hysteresis and drift correction or calibration is carried out inside the sensor and the resulting values are directly transferred in a digital form to the control system using a standard communication bus.

The physical sensor is often replaced by a virtual sensor in the form of a state observer in order to reduce costs for instrumentation or in cases where sensor installation is physically unfeasible. Various filtering and state estimation techniques are used for the calculation of unmeasured quantities [11, 33, 34, 35, 36].

3.1.2 Actuators

Actuators in mechatronic systems work as controlled electromechanical transducers. Their purpose is to transfer energy from any source (usually electric, pneumatic or hydraulic) to mechanical motion in the form of force, torque, angle, position, etc. based on the input commands from the control system. Three basic actuator categories can be defined according to their operating principle [3]:

- ***Electromagnetic actuators*** - the fundamental principle of operation is an interaction of two magnetic fields between fixed and moving parts of the drive. This group includes electric motors (DC, AC, synchronous and asynchronous, stepper, switched reluctance ...) or actuators working on the principle of an electromagnet (voice coil motors). Huge advances have been made in the field of electrical drives in the last few decades, mainly due to rapid development in the technology of semiconductors, power electronics, microprocessor technology and methods of automatic control. Because of their dominant position in industrial applications, they are given a special section below.

- ***Pneumatic and hydraulic actuators*** - they work on the principle of a compressed working medium in the form of air or hydraulic oil which is supplied via a control valve to a piston or other similar mechanism. The problem with air compressibility brings difficulties with accurate control of power or speed / position of the pneumatic actuators. Therefore, they are often used for simple movements between two end positions without a necessity for precise trajectory tracking (simple manipulators, stacker machines, clamping end-effectors of robots). By adding a pressure sensor in the working chamber, continuous positioning of the piston can be achieved by implementing proper feedback control. However, motion accuracy is much worse compared to electrical drives. On the contrary, hydraulic actuators can be used for precise positioning due to limited compressibility of hydraulic fluid and direct proportionality between its volume and extension of the piston in the cylinder. They are often used in applications where it is necessary to develop large forces, such as hydraulic presses, brakes, high-power robots, construction machinery, etc. The disadvantage of hydraulic and pneumatic actuators is expensive operation and maintenance costs, large power losses and the necessity of a hydraulic power unit or air compressor for the supply of working fluid.

- ***Unconventional actuators*** - they work on different physical principles than the previous two groups. These include magnetostrictive microactuators based on changes in the structure of solid material in the magnetic field or piezoelectric motors that use reverse piezoelectric effect. Voltage applied to the ceramic piezoelectric material causes its mechanical deformation. By connecting a large number of such elements in series, a progressive wave which is mechanically transmitted to the moving part of the actuator can be generated by proper excitation signal. The result is a rotary or linear movement. They are sometimes referred as ultrasonic motors, because of excitation of mechanical vibrations in the ultrasonic frequency (hundreds of kHz). Although the displacement of each individual piezo-element is very small (of the order of micrometers) the overall range of motion is much higher due to large number of elements. High-speed movements can be generated by using high frequency excitation. The small dimensions of these actuators make them suitable for microelectromechanical systems. They can be found in various optical devices (microscopes, cameras, camcorders, etc.) performing lens focus and stabilization functions. Another use is in micro-teleoperation systems where a human operator performs remote-controlled movements using a haptic interface such as in medical operations.

There is a general trend of decentralization and development of so called smart-drives equipped with embedded control which are able to work independently as a drive unit. All functions required for motion control are integrated inside the actuator. Communication interface provides a connection to a supervisory control system using a fast serial fieldbus. Recent development of modern Ethernet-based standards such as EtherCAT, Ethernet Powerlink, Profinet, SERCOS and others bring new possibilities in the implementation of high-performance motion control systems. Short cycle times (tens to hundreds of microseconds), high baudrates with deterministic data transfer and low communication jitter due to robust mechanisms for synchronization of individual nodes in the network (tens to hundreds of nanoseconds synchronicity) makes them suitable for large scale automation of complex technological lines with dozens of actuators or precise control of multi-axis machines. The network can be used to close the velocity, position or force control loops due to a fast update rate and low communication delay which allow the implementation of sophisticated and computationally demanding algorithms in the supervisory control system.

3.1.3 Electrical drives in industrial applications

Electrical drives are dominant in the industrial applications thanks to their versatility, scalability of performance, dynamic properties and possibility of control (see [37, 38, 39]). The main advantages can be summarized as follows:

- Wide range of rated power ranging from milliwatts to tens of kilowatts in typical applications
- Wide range of rated torque (units of millinewtonmeters to hundreds of newton-meters) and speed (units to thousands of rpm's (revolutions per minute))
- Possibility of precise position or velocity control using high-resolution feedback sensors
- Accurate torque control using modern controlled semiconductor amplifiers
- Low noise, no waste products
- High efficiency, low no-load losses, high overloading capacity
- Possiblity of four-quadrant operation, i.e., capability of energy recuperation in both direction of rotation
- Long lifetime (dozens of years) - basically limited only by the lifespan of the bearings in modern maintenance-free drives
- Simple supply of energy from the grid or a battery

The term *electrical drive* is usually understood as a whole set of actuator elements including the motor, sensors, power electronics, microprocessor-based control circuit and auxiliary electrical components such as circuit breakers, contactors or relays. The drive can be equipped with an electromechanical brake which prevents from unwanted movements of the load in steady state or in case of a system failure. A gear may be added for adapting output speed and torque.

Basic motor types

DC motors are historically the oldest electric machines. Nowadays, they are largely replaced by AC drives. In the past, they were widely used in applications of mechatronic systems with necessity for precise motion control because of their very good

regulatory properties and relative simplicity of control and excitation circuits. The basic structural component of these motors is a commutator - a mechanical device that ensures the maintenance of the orthogonal relative orientation of the rotor and stator magnetic flux. The most common type of construction uses permanent magnets in the stator housing and movable armature with a winding supplied by electrical current using brushes. Gradual mechanical wear of the brushes is inevitable due to the sliding contacts. Therefore, occasional cleaning or replacement is necessary. Electrical sparks which arise at the point of contact during high motor speeds lead to electromagnetic interference, shortens engine life and can cause a short circuit. For these reasons, DC motors are gradually being replaced by modern, AC electronically commutated drives.

AC induction motors use the principle of electromagnetic induction. The three-phase stator winding which is stored in the stator housing and powered by harmonic voltage from the mains or controlled frequency inverter. The rotor is made in the form of a cylindrical cage, which consists of several electrically connected metal rods. The phase shift between the harmonic voltages in each individual motor phase creates a rotating magnetic field that intersects the rotor conductors. This creates a secondary rotor magnetic field that responds to the stator field and generates a torque on the motor shaft. The secondary field can exist only if the relative speed of rotation between the stator field and the moving armature is nonzero. Therefore, the motor speed is always lower than the frequency of the supply voltage leading to a so called slip and asynchronous speed of rotation relative to the mains frequency. The ACIM are known for their reliability due to their simple and robust construction. In the past, their application was limited due to the complicated control of torque, speed and position (compared to DC motors). However, development of semiconductors, power electronics and microprocessor technology as well as the development of new control techniques (vector control, direct torque control, see eg. [39]) has led to an extensive boom in the utilization of these drives, especially in industrial applications and traction.

Stepper motors are characterized by a special design of stator with salient poles and coils forming the magnetic field. The rotor is equipped with either permanent magnets or also includes salient poles made from ferromagnetic material. Such an actuator is known as a switched reluctance motor, because the mechanical torque arises in consequence of the so-called reluctance phenomenon where the magnetic circuit of the stator and rotor are trying to take position with smallest reluctance. The gradual switching of energized coils causes stepping of the motor, i.e., rotation of the shaft by a defined angle (about 100 to 20,000 steps per revolution). The gradual winding

switching is performed by a special electronic circuit. The advantage of these actuators is simple and inexpensive construction as well as the ability to operate without a feedback sensor. The disadvantage is increased noise and pulsation torque which follows from the discrete manner of movement. Dynamic properties are strongly affected by the load and unstable operation may occur in certain modes of operation. Stepper motors are widely used in scanners and printers or to drive simple robots and cheaper CNC machine tools.

Permanent magnets synchronnous motors (PMSM) are currently the most advanced type of electrical motor used in motion control applications. Its dynamics, high power to weight ratio, short term overloading capability, range and precision control or high starting torque surpasses all other types of drives. The special design of the motor housing, usually with its own cooling, and internal structure allows it to achieve a very compact motor shape with a small moment of inertia of the rotor. The advantage is the use of permanent magnets mounted on the rotor. They ensure a constant excitation of the magnetic field, which is immediately available and does not have to be created indirectly as in the case of the induction motor. Again, their rapid extension was allowed by rapid development of technology and control techniques. Instead of a mechanical commutator which is used in DC machines, the orthogonal orientation of stator and rotor fields is maintained electronically by the control circuit equipped with high-res position sensor. Synchronous motors are used in applications where with the highest demands on precision of motion such as robotics or CNC machine tools.

Electronically commutated DC motors, commonly designated as EC motors or brushless DC motors, are basically very similar to PMSM's by their internal construction. The only difference is in the distribution of cooper in the stator windings leading to quasi trapezoidal profile of back electromotive voltage. This simplifies the process of commutation which can be done in limited number of discrete steps (so called six-step commutation [39]). Cheaper low-resolution position feedback (usually magnetic Hall sensor) and a simpler control algorithm can be used compared to PMSM at the cost of mild torque pulsation due to the discrete commutation. This type of motor is suitable for low-cost applications with limited demands for motion precision.

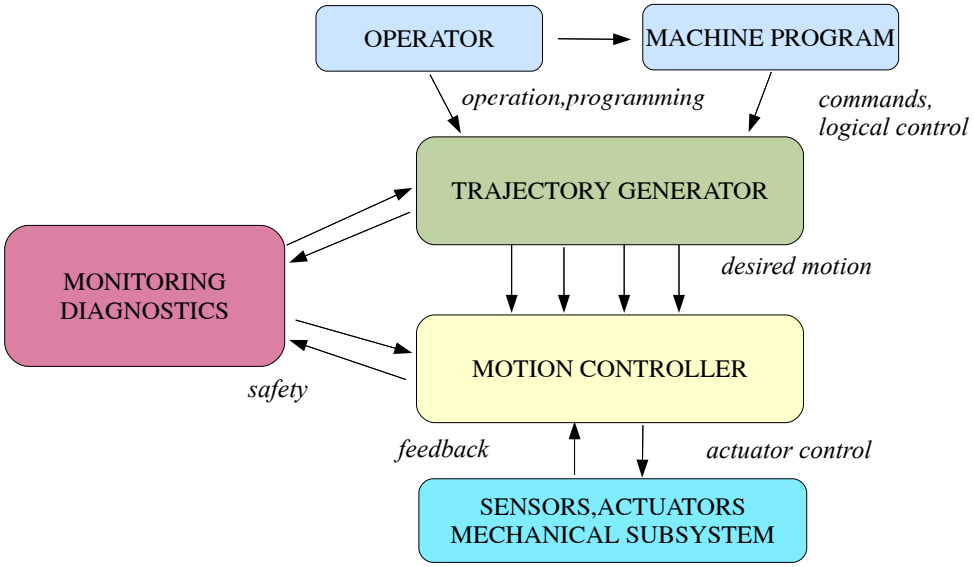

Figure 3.2: Levels of motion control system

3.2 Typical motion control problems

The motion control system can be divided into four distinct layers according to their main functionality (3.2):

- **Low level - motion controller** - This layer is responsible for the control of actuators and execution of motions defined in the higher levels. The motion controller deals with problems of feedback stabilization, reference trajectory tracking, disturbance rejection, mechanical nonlinearities compensation etc.

- **Higher level - trajectory generator** - This layer performs calculations necessary for generation of desired trajectories of motion based on the instructions from the operator or pre-defined sequence of commands entered in machine program. The motion command can have a form of point-to-point movement of the manipulator, tracking of a defined spatial curve or a machining of a desired shape from the workpiece. Desired motion can be represented as a function of acceleration, speed, position or torque / force in time. Setpoint values of these individual variables are passed to the motion controller which ensures accurate tracking.

- **Monitoring and diagnostics -** This level deals with issues of safety operation of the machine. The goal is to prevent, detect and solve any faults and emergency

conditions such as sensor or actuator failure, obstacle collision, working fluid leaks, non-standard operation due to severe mechanical wear etc. Methods for diagnostics and fault detection may be used (see e.g. [40]).

- **Human-machine interface -** This layer provides a visual feedback of important system quantities for the human operator. It allows important commands or machine programme to be entered.

The first two layers, which are the most important for the control system design, are discussed in detail in the next section, presenting some common tasks and problems encountered in industrial applications.

3.2.1 Trajectory generator

Typical motion control problems which are to be solved in the trajectory generator level include:

- **Trajectory planning in an unknown space with obstacles** - This kind of task is typically found in applications of mobile robots. The robot or mobile platform is equipped with limited range sensors such as lasers, radar or sonar, which allow detection of obstacles in an unknown environment. The aim is to move from an initial to a final position in the shortest time possible or by taking a smallest travel distance without any collision with obstacles [41, 42]. Methods of machine perception and artificial intelligence are often used and analytical solution can not usually be found. In industrial manufacturing systems such as automated lines, robots or machine tools, the shape of the motion trajectory is well known in advance and is predefined in a machine program.

- **Trajectory generation with respect to physical limitations of machinery** - The shape of the desired trajectory has to respect physical limits of the actuators and mechanical subsystem. The construction of the machine always imposes restrictions on maximum speed, acceleration or torque / force. Other constraints arise from a permissible range of motion due to machine kinematics (e.g. danger of collision of individual links in robotic manipulator, singular points in machine workspace etc.). Violation of the physical limits can cause severe damage or excessive wear of some mechanical elements. The generator must respect these limitations and provide physically realizable motion [43, 44, 45, 46]).

- **Time-optimal control** - In certain tasks (eg. pick-and-place manipulators, high-speed CNC machining), the execution of a movement in the shortest time possible may be requested. This leads to the problem of time-optimal control with constraints both on the input and the state of the system due to physical limitations of the mechanics [47, 48, 49, 50, 51]. Additional restrictions on smoothness of the generated motion such as limited jerk (time derivative of acceleration) which has a positive effect on the amount of motion induced oscillations may be added. The problem can be solved analytically for one-dimensional motions [52]. However, the complexity rises dramatically for the case of general multi-axis machine kinematics leading to a problem of nonlinear optimization with nonlinear constraints. No analytical solution exist and usually some suboptimal or numerical results have to be used.

- **Damping of residual vibrations in mechanical construction** - Rapid movement of the machine parts can excite mechanical oscillations due to limited stiffness of mechanical construction. These vibration may result in deterioration of the quality of control or even damage the equipment. Suitable shaping of the reference trajectory using special shaping filters can reduce these undesired oscillations [53, 54, 55, 56, 57]. The problem of vibration damping generally extends into the lower motion control level (e.g. in active feedback compensation of vibrations). This topic is discussed in detail further in the thesis.

- **Smooth connection of different trajectories** - In many practical cases, the executed motion command is interrupted before it is finished e.g. due to an intervention of machine operator or in case of a system failure. The control system has to be able to re-plan the desired trajectory instantly and to provide a smooth transition to a new reference trajectory (so-called motion blending, see [58]).

- **Synchronized multi-axis motions - electronic cam and gearbox** - An electronic gearbox replaces its mechanical counterpart. The goal of the control system is to keep a constant speed ratio between the two or more drives. One of the drive is controlled independently (virtual input of the gearbox) and the other derive their movement relatively to the first with the constant gear ratio (similar to gearbox output shaft). The electronic cam can be employed for the sake of cost reduction compared to complicated mechanical solution or in cases of difficulties with the realization of a physical connection between the two or more drives at larger distance. This concept is generalized in an electronic cam. Instead of a constant

speed ratio, the relative position of independent (master) and controlled (slave) axis is preserved. The aim is to replace mechanical cams which act as mechanical transducers, usually transmitting a rotational motion of central shaft to multiple linear motions of the working mechanism (e.g. crankshaft of a combustion engine). This type of mechanical transmission is often used in manufacturing machines with a large number of auxiliary drives that have to be mutually synchronized (textile, printing, marking or cutting machines). The master- slave position dependence (so called cam profile) is entered manually from desired shape of the slave motion or by conversion of mechanical cam contour in a suitable software tool. The function which describes a cam profile should be smooth, at least in the first two derivatives for fluent execution of physically feasible movement without excessive changes in acceleration and jerk. Methods of piece-wise polynomial interpolation using various kinds of spline curves is often used for the calculation of an optimal cam profile [59, 60, 61, 62, 63, 64]. The advantage of an electronic cam is the ability to easily change the machine program by simply adjusting the cam profile. Higher motion accuracy can be achieved compared to a mechanical cam which is influenced by mechanical wear.

- **Coordinated multi-axis motion** - Various spatial curves are used for the definition of machine motions in the task space from simple lines, circles or spirals to general rational spline functions which offer a high degree of freedom in the shaping of the trajectory [62, 65, 66]. One of the problems associated with the use of general parametric spatial curves is violation of the natural requirement for arc-length parametrization, i.e., the travelled distance is a nonlinear function of the curve parameter leading to unwanted fluctuations in velocity, acceleration and jerk during the motion execution. This can be a particularly disturbing feature e.g. in CNC machine tools as these fluctuations can cause visible flaws of the machined surfaces. This inherent nonlinearity needs to be corrected leading to a problem of so-called *feedrate control* [45, 46, 62]. Time-optimal execution may be requested to achieve the fastest time of machining or manipulation (so-called *feedrate optimization problem* in the literature). Another issue of multi-axis motion control is derivation of kinematic transforms. The desired motion commands are usually specified in a so-called *task space* as a time function of general coordinates vector $\boldsymbol{X}$. This vector is usually defined as a Cartesian coordinate system which determines position and orientation of important machine parts (end-effector of a robot or spindle of a machine tool) with respect to a workpiece or stationary

base. The trajectory generator has to transform this movement to so-called *joint space* of individual actuator coordinates described by vector $\boldsymbol{\Theta}$. Therefore, computation of direct and inverse kinematic transforms ($\boldsymbol{X} = G(\boldsymbol{\Theta}), \boldsymbol{\Theta} = G^{-1}(\boldsymbol{X})$) is necessary. In many cases, the solution of kinematic transforms cannot be determined analytically and a proper numerical method has to be used. Derivation of kinematic models and their transforms is one of the fundamental problems in robotics [43, 44, 67, 68, 69].

In an effort to unify the user interface and functionality of motion control systems, PLCopen association of world's leading automation manufacturers has developed a *Motion Control* standard, which is intended to ensure compatibility between different hardware and software platforms [58]. This standard defines the form of function blocks for motion control system in terms of their inputs, outputs and desired behaviour from the user point of view. It deals only with the part of the trajectory generation layer. The lower control level is already vendor specific due to its close connection to the system hardware.

In the specific field of CNC machine tools, normalized language called *G-code* is used for the description of the machining process. Programming is usually performed using specialized software tools for computer-aided manufacturing (CAM) [65, 66, 70, 71].

3.2.2 Motion controller

The motion control layer is responsible for the accurate tracking of reference trajectories obtained from the generator level. Control of position, velocity, torque/force or their combination (e.g. position control with force constraints) is typically performed in industrial applications. Feedback of controlled physical quantities is acquired from actuator sensors or an auxiliary instrumentation installed on the machine. A typical three-level cascade structure which is implemented in most of today's industrial motion controllers and electrical drives can be seen in Fig. 3.3. The innermost current loop controls the generated torque or force (which is proportional to motor current) by driving the power-electronics components of the actuator, typically a voltage-source three-phase inverter in case of an AC electrical drive. Higher level velocity loop controls the speed of motion by setting a current/torque setpoint for the inner loop. A feedback filter with lowpass characteristics is often used to remove high-frequency noise which is usually present (electrical noise in DC tacho signal or quantization noise due to differentiation of position sensor data). A torque reference filter with low-pass, notch or

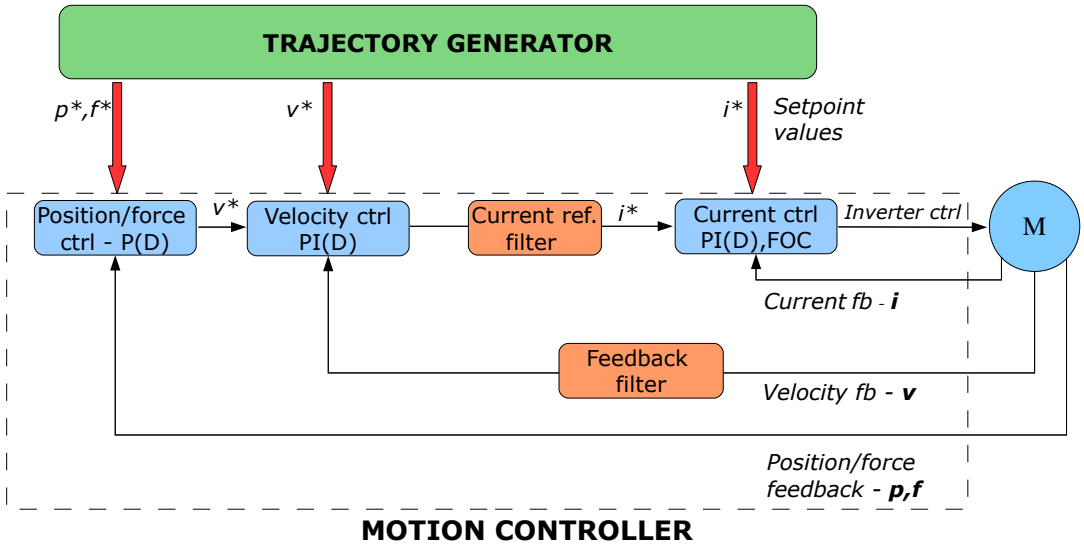

Figure 3.3: Cascade PID structure of industrial motion controller

lead-leg dynamics may be added in order to attenuate a specific frequency band or generally high-frequency portion in the manipulating variable that could excite mechanical vibrations in the machine. The last outer loop performs position or force control and generates velocity setpoint values for the speed controller.

The advantage of the cascade structure is the minimization of the influence of various disturbances acting in different parts of the system and gradual linearization of dynamics in subsequent control loops. The inner torque loop suppresses disturbances in the actuator subsystem (e.g. in electrical part of the motor such as changes in resistance and inductance due to temperature fluctuations of stator winding, back-EMF acting against the voltage source, nonlinear dynamics in magnetic circuit). Speed loop compensates any external mechanical disturbances in the form of a load torque or nonlinear friction and deals with uncertainty in system dynamics (change in weight/moment of inertia of the system, shift in resonant frequencies of the mechanics within the workspace...). Position loop ensures precise positioning of the mechanics and zero steady-state error. Another advantage of the cascade structure is the possibility of introducing maximum limits for position, speed and current/torque due to physical restrictions of the actuator or controlled system. Moreover, step by step tuning of individual loops is easier than a design of complex centralized controller.

The procedure of motion controller design involves the following problems:

- **Selection of a suitable algorithm for feedback control** - Most of the industrial motion control systems use the above presented cascade structure with linear PID controllers implemented in the individual loops (Fig. 3.3). The reason for this is the mass extension of PID controllers in the field of process control (and generally in automation) and a small number of free parameters which is a desirable feature for the possibility of manual tuning. Many advanced and more complex control strategies have been reported in the literature including robust, predictive, adaptive or sliding mode control [72, 73, 74, 75, 76, 77, 78], or methods of artificial intelligence such as neural networks or fuzzy logic [79, 80]. These advanced techniques often bring some improvement to performance and quality of control in a specific application. However, wider extension of these methods is problematic mainly due to the lack of proper software tools for assisted commissioning of motion control loops and because of the diversity of tasks that occur in industrial applications.

- **Reference trajectory tracking** - The motion controller is responsible for accurate tracking of reference values transmitted from the trajectory generator level in the form of desired position, velocity, acceleration, force/torque or their combination.

- **Compensation of nonlinearities in the mechanical part of the system** - Typical mechatronic system includes some nonlinear elements. An example can be nonlinear static characteristics (e.g. force to voltage ratio in electromagnetic or pneumatic actuator), nonlinear friction, backlash or hysteresis in joints, transmissions or in the working mechanism etc. All these factors have a negative impact on the achievable motion accuracy and the motion controller must take some appropriate actions to eliminate or suppress them sufficiently. Methods of model-based feed-forward compensation, dithering, nonlinear or adaptive control, or special modifications of standard linear controllers have been reported in the literature [72, 81, 82, 83, 84, 85].

- **Robustness against disturbances and modelling errors** - the control system often works in the presence of uncertainty and external disturbances (e.g. reaction forces during machining or interaction with the environment, effect of gravity), system dynamics may change in time (manipulation with variable load, change of effective inertia due to nonlinear kinematics of the machine). The technique of so-called *disturbance observer* has received much attention in the field of motion control, due to its simplicity and good performance [72, 73, 86]. The idea is to

design an observer which estimates unknown external disturbances acting on the mechanical system. The disturbance is usually modelled as a general polynomial signal and the estimated value is used for its direct cancelation by the actuators. In the case of complex multi-axis machines such as robotic manipulators, an idea of global decoupling and linearization of system dynamics is usually used to achieve precise tracking. An accurate system model is necessary for successful implementation of this technique. An adaptive or robust approach may be used to cope with the uncertainty in the model. [43, 44, 67, 68, 69].

- **Damping of mechanical vibrations** - the process of mechatronic system design involves conflicting demands on mechanical properties of the mechanical construction. On one hand, sufficient robustness and rigidity is required to prevent motion induced oscillations. On the contrary, there is an effort to minimize overall mass to reduce material costs, decrease the inertias to improve power efficiency and enhance achievable dynamics of motion. There are many practical situations when oscillatory dynamics is inevitable due to the use of elastic components (e.g. tooth-belts, harmonic gears, ropes or cables, long manipulator arms etc.) or a mistake was done in the phase of mechanical design and the correction must be done by means of the control system. The mechanical stiffness can be increased through the implementation of appropriate control algorithms. Two distinct approaches to vibration control are recognized. *Passive vibration control* tries to minimize actuator gain in the range of resonant frequencies of the system to prevent the excitation of oscillations. This can be done by implementing a proper frequency filter with lowpass, notch or lead-leg characteristics, or special structure FIR filters [54, 55, 56, 57, 87, 88, 89, 90]. The filter may be implemented in the velocity feedback loop to shape the torque command (see Fig. 3.3), or in the trajectory generator to modify the reference values. No feedback sensor is required and the only prerequisite is known location of the system resonances. Adaptive filtering or gain-scheduling methods can be used if the resonance frequency varies in time [91]. No additional energy is supplied to the system and vibrations caused by an external disturbance cannot be controlled. *Active vibration control* methods are used for synthesis of a feedback controller which actively suppresses the resonant dynamics. The feedback is acquired directly from physical sensors or indirectly by means of state observer [73, 89, 92]. The compensator actively delivers mechanical power from an external source to the load and

there is a risk of instability. Both passive and active vibration control methods are discussed in detail further in the thesis.

- **Automatic commissioning** - The individual motion controller loops have to be tuned for each particular mechanical system to achieve high-quality control. In case of a new mechatronic device intended for a serial production (such as a new model of hard disk drive, industrial robot or digital camera), the design of embedded control system is usually a part of long-term product development cycle. Therefore, the motion control layer can be highly optimized for the particular system. Advanced methods for system identification and controller synthesis as well as various software tools may be used and this work is usually done by specialized control system engineers. Proper mechanical design can be done with respect to the controllability of the system mechanics and the desired motion dynamics (co-design principle). On the contrary, many industrial applications require rapid commissioning of a motion control system which is a part of a larger technology or a complex machine. The motion control is usually built from a set of standard components (e.g. central PLC controller plus electrical drives and servo-amplifiers) giving a limited possibility of control structure choice. Very often, the mechanical design of the machine cannot be changed in any way and any potential problems have to be corrected by means of the control system. The time available for the commissioning is usually very short (e.g. due to a production deadlines or enforced shutdown of surrounding technology in a factory). No model of the system may be available and use of physical modelling approach can be troublesome due to complex dynamics and lack of knowledge of exact parameter values. The tuning of the controller gains is often performed manually leading to sub-optimal or conservative results, unsatisfactory performance and time-consuming commissioning. Hence, any assistance which could simplify and speed-up this process in form of advanced software tools for automatic or semi-automatic identification and controller synthesis is highly appreciated in practice [90, 93, 94, 95, 96, 97, 98]. Some of the major manufacturers of electrical drives offer an auto-tuning capability in the firmware of the drive amplifiers. However, from the author's experience, the performance of such systems is quite poor (agreement with this opinion can be found in related literature [90, 94]). Most of them fail in case of oscillatory dynamics of the system, they lack the feature of closed loop identification (which is fundamental for unstable structures), conditions of the identification experiment are difficult to control (there is a danger of

an unpredictable motion of the load which may excess a permissible range) and the tuning process is not described well in the user manual. The resulting performance is usually worse compared to precise manual tuning done by a skilled engineer which is experienced in the field of motion control. The goal of this thesis is to provide simple, reliable and effective methods for automatic identification and controller tuning which could be used in such applications.

3.3 Motion control of rigid mechanical systems

The previous section presented general concepts of motion control systems and defined the most important topics and practical tasks. This thesis deals with the problem of vibration control, therefore, the motion control layer is studied in more detail. This section presents basic approaches for torque control in electrical drives, which are dominant in industrial applications. Methods for motion control of idealized rigid systems with single or multiple degrees-of-freedom (DoF) are discussed followed by an introduction to modelling and control methods for flexible systems.

3.3.1 Current/torque control in electrical drives

From the perspective of a mechanical load, the controlled electrical drive may be viewed as a source of torque or force. Due to the electromagnetic principle of operation, the generated torque is directly proportional to actual current which influences the magnitude of magnetic flux generated by stator or rotor winding (based on motor construction). Therefore, the control of motor current is equal to the control of the electromagnetic torque generated on its shaft. Basic principles of current control are briefly explained in this section.

The problem is relatively simple for DC motors. The armature circuit can be modelled as a serial connection of ideal resistor and inductance leading to first order differential equation

$$\begin{aligned} \frac{di(t)}{dt} &= \frac{1}{L}\{v(t) - Ri(t) - e(t)\}, \\ e(t) &= k_b\omega_r(t), \\ T_m &= k_t i(t), \end{aligned} \tag{3.1}$$

where $i(t)[A]$ is armature current,
$u(t)[V]$ applied voltage,
$e(t)[V]$ induced back electromotive force (back EMF),

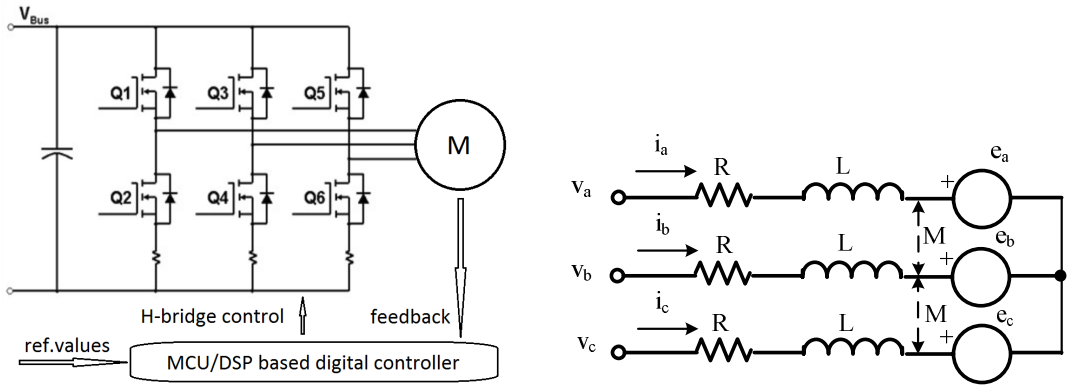

Figure 3.4: a) Digital controlled 3-Phase H-Bridge inverter b)Equivalent stator circuit of AC machine

$k_b[\frac{V.s}{rad}]$ back EMF constant,
$\omega_r[rad/s]$ rotor speed,
$R[\Omega], L[H]$ armature resistance and inductance, respectively,
$k_t[\frac{Nm}{A}]$ torque constant,
$T_m[Nm]$ motor torque.

The back EMF may be treated as an unknown external disturbance or cancelled directly from the known values of k_b and ω_r by applying an opposite voltage. Transfer function from armature voltage to current is

$$P(s) = \frac{I(s)}{V(s)} = \frac{1}{Ls + R}. \tag{3.2}$$

Simple PI current controller can be employed leading to second order closed loop transfer function with two freely assignable poles. The controller may be implemented by an analog circuit or by using a digital pulse-width modulation (PWM) controlled H-Bridge inverter (Fig. 3.5); only two inverter legs will be used for DC motor connection). Four quadrant operation is possible with a proper modulation method. The current control of EC motor is similar. When using a six-step commutation method [39], the electrical revolution of the motor is divided into six regions, each corresponding to a range of 60 degrees. In each region, only two phases of the motor are connected to the voltage source and driven by the H-bridge in the same manner as a DC motor. The third remains inactive by opening the two transistors in the appropriate inverter leg (Fig. 3.5). The equivalent circuit of serial connection of two phases lead to the

following dynamics and plant transfer function describing one step of commutation

$$\begin{aligned} \frac{di(t)}{dt} &= \frac{1}{2(L-M)}\{v(t) - 2Ri(t) - 2e(t)\}, \\ P(s) &= \frac{I(s)}{V(s)} = \frac{1}{2(L-M)s + 2R} = \frac{1}{L_{2p}s + R_{2p}}, \end{aligned} \tag{3.3}$$

where M[H] is the mutual inductance of two phases. The actual rotor position which is necessary for the choice of a proper commutation step is determined by a simple Hall magnetic sensor or by measuring the voltage induced in the inactive phase in case of sensorless operation.

The situation is more complicated in the case of AC machines (PMSM or ACIM) due to their inherently multivariable nonlinear dynamics. We limit ourselves to the simpler case of PMSM to explain the basic idea of *field oriented control*(FOC) which is used in most of the industrial servodrives. The dynamics of the stator circuit is described using physical laws for electromagnetic induction:

$$\begin{aligned} \boldsymbol{U} &= \boldsymbol{RI} + \frac{\boldsymbol{d\Psi}}{\boldsymbol{dt}}, \\ \boldsymbol{\Psi} &= \boldsymbol{LI} + \boldsymbol{\Psi_M}, \end{aligned} \tag{3.4}$$

where $\boldsymbol{U},\ \boldsymbol{I}$ and $\boldsymbol{\Psi}$ denote vector of voltage, current and flux
$\boldsymbol{R}$, $\boldsymbol{L}$ are matrices of phase resistance and inductance and $\boldsymbol{\Psi}_M$ is flux vector caused by permanent magnets. By assuming balanced stator windings, we get the following set of equations:

$$\frac{d}{dt}\begin{bmatrix} i_a(t) \\ i_b(t) \\ i_c(t) \end{bmatrix} = \frac{1}{L-M}\left\{ \begin{bmatrix} u_a(t) \\ u_b(t) \\ u_c(t) \end{bmatrix} - R\begin{bmatrix} 1 & 0 & 0 \\ 0 & 1 & 0 \\ 0 & 0 & 1 \end{bmatrix} \begin{bmatrix} i_a(t) \\ i_b(t) \\ i_c(t) \end{bmatrix} - \begin{bmatrix} e_a(t) \\ e_b(t) \\ e_c(t) \end{bmatrix} \right\} \tag{3.5}$$

where back EMF's induced in each phase $e_{a,b,c}$ can be determined by taking a time derivative of magnetic flux of permanent magnets due to the shaft rotation. Since the flux of the magnets is determined as

$$\begin{aligned} \Psi_{ma} &= k_b \cos\varphi_e, \\ \Psi_{mb} &= k_b \cos\left(\varphi_e - 2\pi/3\right), \\ \Psi_{mc} &= k_b \cos\left(\varphi_e + 2\pi/3\right), \end{aligned} \tag{3.6}$$

we obtain instant back EMF values

$$\begin{aligned} e_a &= \frac{d\Psi_{ma}}{dt} = -k_b\omega_e \sin\varphi_e, \\ e_b &= \frac{d\Psi_{mb}}{dt} = -k_b\omega_e \sin\left(\varphi_e - 2\pi/3\right), \\ e_b &= \frac{d\Psi_{mc}}{dt} = -k_b\omega_e \sin\left(\varphi_e + 2\pi/3\right), \end{aligned} \tag{3.7}$$

where φ_e[rad] is electrical rotor position,
$\varphi_m = \frac{1}{p}\varphi_e$[rad] mechanical rotor position,
p number of rotor pole-pairs and
ω_e[rad/s] electrical shaft speed.

The generated torque is given by

$$T_m = \frac{P}{\omega_r} = \frac{e_a i_a + e_b i_b + e_c i_c}{\omega_r} = -pk_b\left(i_a \sin\varphi_e + i_b \sin\left(\varphi_e - 2\pi/3\right) + i_c \sin\left(\varphi_e + 2\pi/3\right)\right), \tag{3.8}$$

where $P[W]$ is mechanical power and $\omega_r[rad/s]$ mechanical shaft speed.

The obtained model gives a set of coupled nonlinear equations which can be hardly used for common linear methods of controller synthesis. Nonlinear techniques e.g. sliding mode control can be used directly to cope with the nonlinearities and obtain robust solution [77, 99]. Instead of this, field oriented control uses an idea of coordinate transformation of the nonlinear model to a simpler form of equations. The voltage, flux and current vectors of star connected three-phase machine are not independent quantities and have to obey the balance conditions:

$$\begin{aligned} i_a(t) + i_b(t) + i_c(t) &= 0, \\ u_a(t) + u_b(t) + u_c(t) &= 0, \\ \Psi_a(t) + \Psi_b(t) + \Psi_c(t) &= 0. \end{aligned}$$

Therefore, there is a redundancy in the model and and simpler two-phase representation may be obtained. By using so-called *Clarke* and *Park* transforms, the currents, flux and voltages vectors can be defined in coordinates which rotate synchronously with the rotor shaft. Without going into too much detail about the derivation (see [39, 77] for full reference), the model reduces to the form:

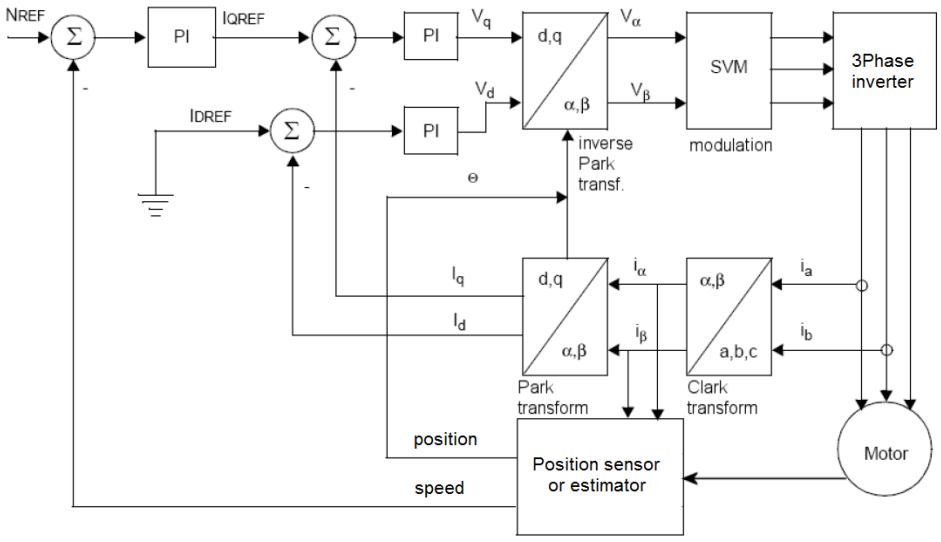

Figure 3.5: Principle of Field oriented control

$$
\begin{aligned}
\begin{bmatrix} v_d \\ v_q \end{bmatrix} &= R \begin{bmatrix} 1 & 0 \\ 0 & 1 \end{bmatrix} \begin{bmatrix} i_d \\ i_q \end{bmatrix} + \frac{d}{dt} \begin{bmatrix} L_d & 0 \\ 0 & L_q \end{bmatrix} \begin{bmatrix} i_d \\ i_q \end{bmatrix} + \begin{bmatrix} \omega_e L_q i_q \\ e_q + \omega_e L_d i_d \end{bmatrix}, \\
e_d &= 0, \\
e_q &= \lambda \omega_e, \\
T_m &= \frac{3p}{2} \left[k_b i_q + (L_d - L_q)\, i_d i_q \right], \qquad (3.9)
\end{aligned}
$$

where subindexes d, q denote two orthogonal axes of the coordinate system rotating with the shaft and therefore direct and quadrature components of the voltage, current and flux vectors. The nonlinear cross-coupling terms of the equation can be cancelled by appropriate control actions in the form of applied voltages u_d, u_q and the resulting two linear first order systems can be controlled in the same manner as in the case of DC motor e.g. by a PI controller. By setting a setpoint value for $i_d = 0$, the motor torque becomes directly proportional to quadrature current $T_m = k_t i_q$. The obtained manipulating variables v_d, v_q are transformed back to phase coordinates and realized by a proper modulation algorithm for the H-bridge (e.g. space vector modulation [39]). Hence, the idea of field oriented control is to decouple the nonlinear system dynamics to obtain linear system similar to DC motor. An alternative technique used in industry is *direct torque control* which essentially estimates motor flux from the measured currents

and uses a hysteresis controller which selects the proper control action from the set of permissible configuration of H-bridge switches in each sampling instant [100, 101]. The control of ACIM is more complicated due to the fact that magnitude and direction of the rotor flux cannot be directly measured. A flux observer is usually designed to estimate the unknown quantities; the idea of FOC remains the same.

Modern digital controlled electrical servo drives equipped with fast microcontrollers or digital signal processors with high sampling rate (typically 1 to 40kHz sampling frequency or even more with DTC) represent highly dynamical and efficient actuators which are being employed in the most demanding applications. Due to the fast time constants of the current control loop (typical rise time in hundreds of microseconds) which is usually negligible compared to dynamics of the mechanical subsystem, the closed loop actuator system can be reasonably approximated by first order lag or simple static gain

$$P(s) = \frac{T_m(s)}{i^*(s)} \approx \frac{k_t}{\tau_i s + 1} \approx k_t, \tag{3.10}$$

where i^* is current setpoint, τ_i is time constant of the closed current loop. Therefore, the drive becomes a controlled source of torque or force in the mechanical system.

3.3.2 Speed/position control of rigid mechanical systems

The simplest problem of single DoF speed control of a rigid mechanical system can be formulated as follows. Considering a fast current/torque control loop with negligible time constant (with respect to much slower dynamics of the mechanical subsystem), the system can be modeled by first order equation according to Newton's second law of motion as

$$\begin{aligned} \frac{d\omega(t)}{dt} &= \frac{1}{I}\{T_m(t) - T_f(t) - T_l(t)\}, \\ T_m(t) &\approx k_t i(t), \\ I &= I_m + I_g + \frac{I_l}{n^2}, \end{aligned} \tag{3.11}$$

where $\omega[rad/s]$ is motor angular velocity, $T_m, T_f, T_l[Nm]$ denote motor, friction and external load disturbance torque, respectively, $I[kg.m^2]$ is total moment of inertia computed to actuator side which consists of motor shaft inertia I_m, gear inertia I_g (if applied), reduced load inertia I_l and gear ratio n.

Although a nonlinear friction phenomenon is often observed in practical mechanical systems, it is usually approximated by a linear viscous term $T_f(t) = B\omega(t)$ in order

to obtain linear model which is suitable for common control design methods. The resulting transfer function from motor torque to angular velocity is a first order system

$$P_1(s) = \frac{\omega(s)}{T_m(s)} = \frac{1}{Is + B}. \tag{3.12}$$

Secondary dynamics is presented in the velocity loop due to the actuator lag and feedback filtering. For modern servo-drives equipped with high bandwidth digital control, the current loop dynamics is negligible and the second dominant delay is introduced by a low-pass filter which attenuates the high frequency measurement noise and which can be modeled by first order lag with a filter time constant τ_f

$$F(s) = \frac{\omega_f(s)}{\omega(s)} = \frac{1}{\tau_f s + 1}. \tag{3.13}$$

The open loop dynamics from motor torque to filtered velocity feedback is second order plant

$$P_2(s) = \frac{\omega_f(s)}{T_m(s)} = \frac{1}{(Is + B)(\tau_f s + 1)}. \tag{3.14}$$

A simple PI velocity controller is implemented in most of industrial servoamplifiers as it provides the integrating part which is necessary for zero-steady state error compensation and a minimum set of two free parameters simplifying the procedure of hand tuning. Its dynamics can be defined in the s-domain by the following equation:

$$T_m(s) = \{K_p + \frac{K_i}{s}\}(\omega^*(s) - \omega_f(s)), \tag{3.15}$$

where ω^* is velocity setpoint.

The resulting closed-loop transfer function of plant 3.14 and controller 3.15 is

$$T(s) = \frac{K_p s + K_i}{I\tau_f s^3 + (I + B\tau_f)s^2 + (K_p + B)s + K_i}. \tag{3.16}$$

The closed-loop dynamics cannot be assigned freely due to limited order of the PI compensator. Location of the two poles can be chosen arbitrarily while the third pole value depends on controller and plant parameters.

Optimal controller tuning

Several methods can be used to cope with the limited degree of freedom and obtain a suitable solution. Methods of *modulus optimum* and *symmetrical optimum* are often used in practice due to the simple tuning formulas and relatively good performance and robustness [89, 102, 103, 104]. The basic idea is to obtain the highest possible closed

loop bandwidth which is achievable with the low order compensator. The *modulus optimum method* (sometimes referred as absolute value criterion) tries to cancel the slowest time constant of the plant, usually the one of the mechanical system which is defined as $\tau_m = \frac{I}{B}$, with the compensator zero by choosing:

$$\frac{K_p}{K_i} = \tau_m = \frac{I}{B}. \tag{3.17}$$

This results in the following open-loop and closed-loop transfer functions:

$$\begin{aligned} L(s) &= \frac{\omega_f(s)}{T_m(s)} = \frac{K_i}{B}\frac{1}{s(\tau_f s+1)}, \\ T(s) &= \frac{\omega_f(s)}{\omega^*(s)} = \frac{1}{\frac{\tau_f B}{K_i}s^2 + \frac{B}{K_i}s + 1} = \frac{1}{b_2 s^2 + b_1 s + 1}. \end{aligned} \tag{3.18}$$

The goal of the maximum achievable bandwidth ω_{bw} can be formulated in the frequency domain by requirement $|T(i\omega)| \approx 1$ for $\omega < \omega_{bw}$. Moreover, a flat shape of magnitude of the frequency response $|T(i\omega)|$ without any resonant peaks caused by weakly damped poles is required to obtain reasonable transient closed loop dynamics without any excessive overshoot. Considering the square of magnitude

$$|T(i\omega)|^2 = \frac{1}{1 + (b_1^2 - 2b_2)\omega^2 + b_2^2\omega^4}, \tag{3.19}$$

we can see, that the bandwidth can be maximized by choice $b_1^2 = 2b_2$ which minimizes the decay ratio of the magnitude and extends the flat range of $|T(i\omega)| \approx 1$. This leads to controller gains in the form of:

$$K_i = \frac{B}{2\tau_f},\ K_p = \frac{I}{2\tau_f}, \tag{3.20}$$

where the proportional gain was computed from the condition of pole zero cancelation (3.17). Substitution in (3.18) results in the closed-loop transfer function

$$T(s) = \frac{1}{2{\tau_f}^2 s^2 + 2\tau_f s + 1} = \frac{(\frac{1}{\sqrt{2}\tau_f})^2}{s^2 + \frac{1}{\tau_f}s + (\frac{1}{\sqrt{(2)}\tau_f})^2} = \frac{\omega_{bw}^2}{s^2 + \sqrt{2}\omega_{bw}s + \omega_{bw}^2}, \tag{3.21}$$

which has a form of second order Butterworth filter with cutoff frequency $\omega_{bw} = \frac{1}{\sqrt{2}\tau_f}$ and damping ratio $\xi = \frac{\sqrt{2}}{2}$. Well behaved and fast setpoint response is achieved due to the maximal flatness property of the Butterworth filter. However, the pole-zero cancelation does not occur in the plant sensitivity function from external disturbance torque to the controlled velocity (see Fig. 3.6)

$$PS(s) = \frac{\omega_f(s)}{T_l(s)} = (-\frac{s\omega_{bw}^2}{s^2 + \sqrt{2}\omega_{bw}s + \omega_{bw}^2})(\frac{2\tau_f}{Is + B}). \tag{3.22}$$

Therefore, the disturbance rejection is poor in the case of a slow mechanical constant and the design procedure fails for systems with unknown or negligible friction ($B \approx 0$). For this case, the *symmetrical optimum* method is often used. Open and closed-loop transfer functions have the form of:

$$\begin{aligned} L(s) &= \frac{\omega_f(s)}{T_m(s)} = (\frac{K_p s + K_i}{s})(\frac{1}{Is})(\frac{1}{\tau_f s + 1}), \\ T(s) &= \frac{\omega_f(s)}{\omega^*(s)} = \frac{K_p s + K_i}{I\tau_f s^3 + Is^2 + K_p s + K_i}. \end{aligned} \tag{3.23}$$

The optimal controller gains for maximum achievable bandwidth are found similarly to the previous case by analyzing the magnitude of the closed loop frequency response $|T(i\omega)|$. The optimal gains are defined as:

$$K_p = \frac{I}{2\tau_f},\ K_i = \frac{I}{8\tau_f^2}, \tag{3.24}$$

leading to closed loop transfer functions:

$$\begin{aligned} T(s) &= \frac{4\tau_f s + 1}{8\tau_f^3 s^3 + 8\tau_f^2 s^2 + 4\tau_f s + 1}, \\ PS(s) &= \frac{\frac{8\tau_f^2}{I} s}{8\tau_f^3 s^3 + 8\tau_f^2 s^2 + 4\tau_f s + 1}. \end{aligned} \tag{3.25}$$

The resulting closed-loop poles correspond to the third order Butterworth filter:

$$p_1 = -\frac{1}{2\tau_f},\ p_{2,3} = -\xi\omega_n \pm \omega_n\sqrt{1-\xi^2}i;\ \xi = 0.5,\ \omega_n = \frac{1}{2\tau_f}. \tag{3.26}$$

Fast settling time (approx. $16\tau_f$) and good disturbance rejection is achieved in this case. There is quite a large overshoot in the setpoint step response (about 43%, see Fig. 3.6) which is often reduced by adding a lowpass velocity reference filter with a properly chosen time constant.

The above mentioned methods have become very popular in practice due to their simple closed form formulas and good nominal performance. Their main disadvantage is, that no procedure for manual adjustment or re-tuning is offered in case that they fail in reality. Moreover, the demand for maximum bandwidth often leads to excessive gains which can excite additional unmodeled dynamics in the loop. Although some modified versions with variable parameters have been proposed in the literature [103, 104], the obtained parameterizations lack some clear physical meaning and trial and error procedure has to be used to fulfill particular design requirements.

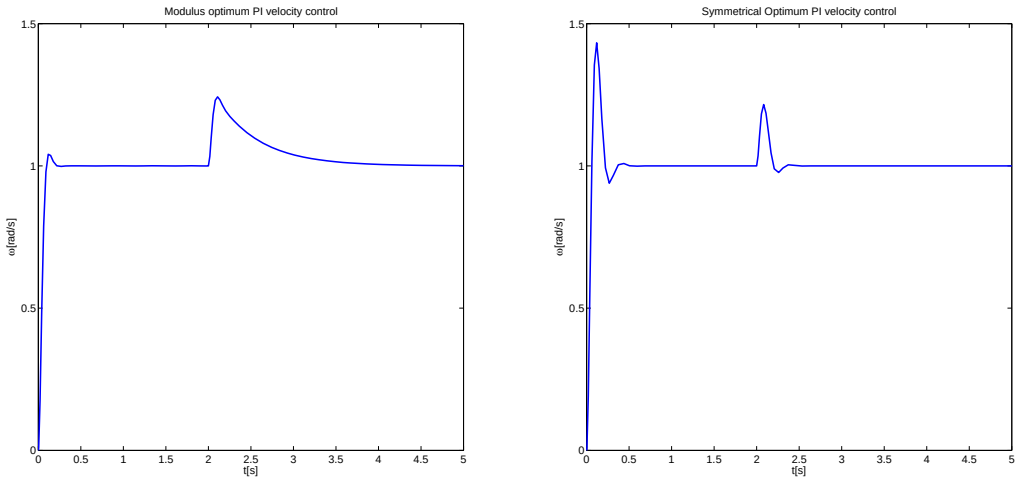

Figure 3.6: Modulus and symmetrical optimum velocity PI control, setpoint and disturbance response for $P(s) = \frac{1}{(0.5s+1)(0.02s+1)}$

Partial and full pole placement

The pole placement method can often be used to obtain proper tuning rules with a set of physically feasible parameters. In many practical cases, the mechanical time constant is dominant compared to that of the feedback filter ($\frac{I}{B} >> \tau_f$) and the plant can be reasonably approximated by first order dynamics

$$P(s) \approx \frac{1}{Is + B}. \tag{3.27}$$

The PI controller in the 2DoF form is assumed with the control law given as

$$T_m(s) = K_p(b\omega^*(s) - \omega_f(s)) + \frac{K_i}{s}(\omega^*(s) - \omega_f(s)), \tag{3.28}$$

where $b \in < 0, 1 >$ is setpoint weighting factor, can be used to assign poles and zeros of the closed-loop system

$$T(s) = \frac{\omega(s)}{\omega^*(s)} = \frac{\frac{K_p b}{I}s + \frac{K_i}{I}}{s^2 + \frac{b+K_p}{I}s + \frac{K_i}{I}} = \frac{b_1 s + w_n^2}{s^2 + 2\xi\omega_n s + w_n^2}. \tag{3.29}$$

Closed loop bandwidth and the shape of the transient response can be directly determined by a proper choice of ω_n and ξ leading to controller gains

$$K_p = 2\xi\omega_n I - B, K_i = I\omega_n^2. \tag{3.30}$$

Independent shaping of the setpoint and disturbance response can be performed by choice of setpoint weight b which alters location of the system zero. For the particular choice $b = 1$, the controller reduces to standard 1 DoF form (3.15) and the zero is location is fixed. For $b = 0$ (feedback proportional gain), the zero vanishes. Providing that the desired bandwidth is low with respect to unmodeled high-frequency dynamics (feedback filter, actuator lag, elasticity of the mechanical subsystem), the two assigned poles are dominant and the approximation of the closed-loop dynamics by second-order system holds well.

A simple procedure for model-free step-by-step tuning can be derived from the formulas (3.30). Considering that $\xi = \frac{K_p+B}{2I\omega_n}$, $\omega_n = \sqrt{\frac{K_i}{I}}$, the following rules can be formulated:

1. Set $K_i = 0$ and raise K_p until small steady state error and reasonable damping is achieved. This moves the dominant real pole of the plant to the left on the real axis of complex plane as can be seen from the root locus plot.

2. Raise K_i to obtain moderate settling time. This completes the initial rough setting.

3. For precise tuning of the shape of transient response, damping of dominant closed loop poles is altered by the change of K_p. The bandwidth remains unaffected.

4. For precise tuning of the bandwidth given by natural frequency ω_n, change K_i and simultaneously adjust K_p to maintain the ratio $\frac{K_p^2}{K_i}$ and keep constant level of damping.

5. Repeat the last two steps until the bandwidth cannot be raised any more with a desired level of damping due to secondary dynamics in the loop.

In the case that the impact of secondary dynamics is significant with respect to the mechanical time constant (e.g. low friction, slow actuator or noisy feedback measurement requiring low bandwidth filtering), the concept of **partial pole placement** can be employed. Consider second order plant with unitary static gain (without loss of generality)

$$P(s) = \frac{1}{(\tau_1 s + 1)(\tau_2 s + 1)}. \tag{3.31}$$

The complementary sensitivity function of system (3.31) controlled by PI compensator (3.15) is defined as:

$$T(s) = \frac{K_p s + K_i}{\tau_1\tau_2 s^3 + (\tau_1 + \tau_2)s^2 + (K_p + 1)s + K_i} = \frac{b(s)}{a(s)}. \tag{3.32}$$

The desired characteristic polynomial can be chosen in the form of:

$$a^*(s) = (s+a)(s^2 + 2\xi\omega_n + \omega_n^2). \tag{3.33}$$

The pole placement problem is formed by setting $a(s) \stackrel{!}{=} a(s)^*$ and solving the corresponding set of polynomial equations for the unknowns K_p, K_i, a. The obtained solution is:

$$\begin{aligned} K_p &= (\tau_1\tau_2 - 4\xi^2\tau_1\tau_2)\omega_n^2 + (2\xi(\tau_1+\tau_2))\omega_n - 1, \\ K_i &= \omega_n^2(\tau_1 + \tau_2 - 2\xi\omega_n\tau_1\tau_2), \\ a &= \frac{\tau_1 + \tau_2 - 2\xi\omega_n\tau_1\tau_2}{\tau_1\tau_2}. \end{aligned} \tag{3.34}$$

The two chosen poles cannot be assigned freely because of the third pole a which moves on the real axis, based on the plant parameters and chosen values of ω_n, ξ (see Fig. 3.7). The maximum achievable bandwidth ω_n^{max} for this parameterization can be found by setting $a = \omega_n$ which gives the solution:

$$\omega_n^{max} = \frac{\tau_1 + \tau_2}{\tau_1\tau_2(1+2\xi)}. \tag{3.35}$$

This gives a set of three poles located on a circle with the radius ω_n^{max}. For the choice $\xi = 0.5$, we get a third order Butterworth filter and the closed loop is optimal in the sense of an absolute value criterion. By further increasing the desired bandwidth, the third pole a closes to the imaginary axis which results in degradation of closed loop performance due to slow dominant time constant. For the choice $\omega_n > \frac{\tau_1+\tau_2}{2\xi\tau_1\tau_2}$, the pole a enters right-half plane and integral gain $K_i < 0$ leading to unstable compensator and closed loop dynamics. Lower bound of applicable gains in the sense of a minimal ω_n^{min} can be found from requirement $K_p > 0$ which gives a minimum phase controller.

The presented concept of partial pole placement is used in a similar way further in the thesis for the case of a flexible system. The advantage of this approach is so called *feature-based parametrization* providing a set of free parameters with clear physical meaning (closed loop bandwidth ω_n and shape of transient response ξ). The analytical formulas can be used for smooth tuning of the real plant and the determination of the range of applicable gains. The disadvantage of polynomial synthesis is exponential rise of complexity with an increasing number of plant and compensator parameters. A numerical solution is often necessary for high order plants.

Full pole-placement can be performed for the second-order system 3.31 by using a PID controller with the control law given as:

$$T_m(s) = \{K_p + \frac{K_i}{s} + \frac{K_d s}{\tau_d s + 1}\}(\omega^*(s) - \omega_f(s)), \tag{3.36}$$

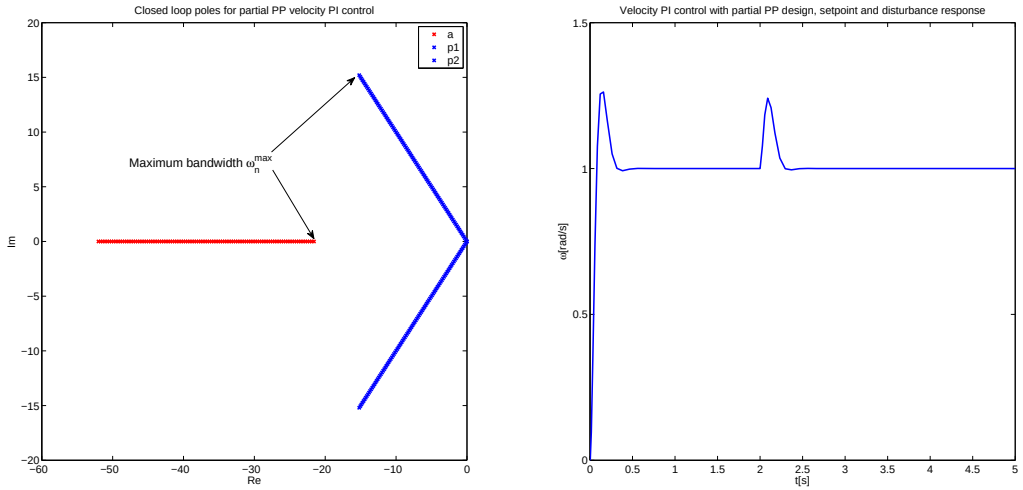

Figure 3.7: Partial pole placement velocity PI control, closed loop poles, setpoint and disturbance response for $P(s) = \frac{1}{(0.5s+1)(0.02s+1)}$, $\omega_n = \omega_n^{max}$, $\xi = \frac{\sqrt{2}}{2}$

where K_d is derivative gain and τ_d a derivative filter time constant.

Four closed loop poles can be arbitrarily assigned and higher bandwidth can be theoretically achieved compared to PI control. However, the range of applicable gains is limited in practice due to amplification of high-frequency noise in the derivative part of the controller and increased sensitivity to uncertainty in the plant model.

Robustness regions method

A much more general approach to PI(D) controllers tuning was developed at the Department of Cybernetics at UWB [105, 106, 107]. Most of the practical design requirements can be formulated in frequency domain by imposing some restrictions on the shape of the Nyquist plot of the open loop plant $L(iw)$. The typical specifications include:

- *Robustness in stability* in the sense of minimum distance of $L(i\omega)$ to point $(-1, i0)$ in the complex plane which can be formulated as the peak of the sensitivity function $S(i\omega)$ as

$$\|\frac{1}{1+L}\|_\infty = \sup_\omega |S(i\omega)| \leq M_S \tag{3.37}$$

- *Closed loop performance* in the sense of oscillatory response of the system which can be determined by maximum overshoot of the complementary sensitivity func-

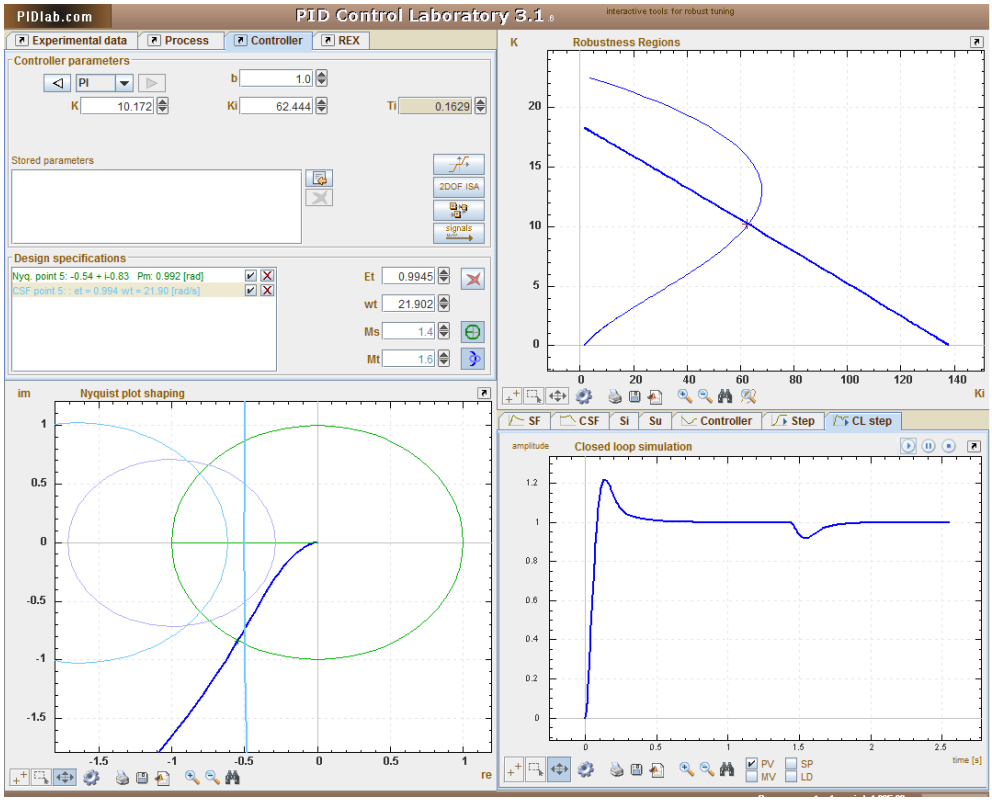

Figure 3.8: PID Control Laboratory - www.pidlab.com, robustness region method for PI velocity controller design

tion $|T(i\omega)|$ and corresponding M-circle in the Nyquist plane

$$\|T\|_\infty = \sup_\omega |T(i\omega)| \leq M_T \tag{3.38}$$

- *Rejection of low frequency disturbances* which can be defined as:

$$|S(i\omega)| \leq \epsilon_S;\ \omega \in < 0, \omega_S > \tag{3.39}$$

- *Robustness to model uncertainty* in the form of unmodeled high frequency dynamics leading to limitation of the maximum bandwidth

$$|T(i\omega)| \leq \epsilon_T;\ \omega \in < \omega_T, \infty > \tag{3.40}$$

An analytical solution for the specified design problem cannot be found and a numerical method has to be used for higher order plants. For each design specification,

a set of admissible controller parameters can be found numerically for each $\omega \in \mathbb{R}$ by computing a set of roots of a polynomial equation. The set of all solutions form a region in a parametric plane $K_p - K_i$. For a PID controller, the values of K_d, τ_d are fixed in appropriate ratio to other controller parameters according to common practical recommendations. The final set of controller gains can be found in the intersection of the regions. This set can be empty as the design specifications are contradictory and appropriate adjustment of the specifications may be needed to obtain a suitable solution. An interactive graphical user interface (GUI) in the form of Java applet which performs all the necessary calculations is available online (*www.pidlab.com*). An example of a particular design can be seen in Fig.(3.8). Velocity PI controller is designed for the plant from the previous examples ($P(s) = \frac{1}{(0.5s+1)(0.02s+1)}$) according to specifications: $M_s = 1.4, M_T = 1.6, \epsilon_T = 1, \omega_T = 20$. One interpolation point of $L(i\omega)$ located on the unit circle is added to impose minimum phase margin $p_m > 57\,^\circ$. The set of optimal compensator gains is found in the intersection of computed robustness regions. The plot of $L(i\omega)$ shows fulfillment of the design limits given by the M-circles. Simulation is available for evaluating the closed loop performance in the time domain.

The advantage of this method is its applicability to arbitrary order of the system including time-delay due to the frequency-domain specification of the design problem. Therefore, a full order system model including mechanics and actuator dynamics, feedback or torque reference filters and time delays (e.g. due to communication lag) can be used without simplification. Unfortunately, no analytical solution which would provide closed-form formulas for controller tuning is available. However, the controller can be tuned interactively with the offered GUI. Robust identification experiment and automatic controller tuning can be performed for aperiodic plants [108].

Position control loop

Once the velocity loop has been properly tuned, the outer position controller synthesis is relatively straightforward. The inner torque loop rejects fast disturbances in the actuator system, the velocity loop linearizes the dynamics of the mechanical subsystem and compensates any external forces. The objective of the position loop is to follow of the reference trajectory. The velocity loop usually contains integrator part ensuring zero steady state error. Therefore, a simple proportional position controller is used in most cases. It can be tuned experimentally by gradually increasing the proportional gain until a limit of maximum bandwidth with an aperiodic setpoint response is reached. The process of closing the position loop can be viewed in terms of the root locus plot

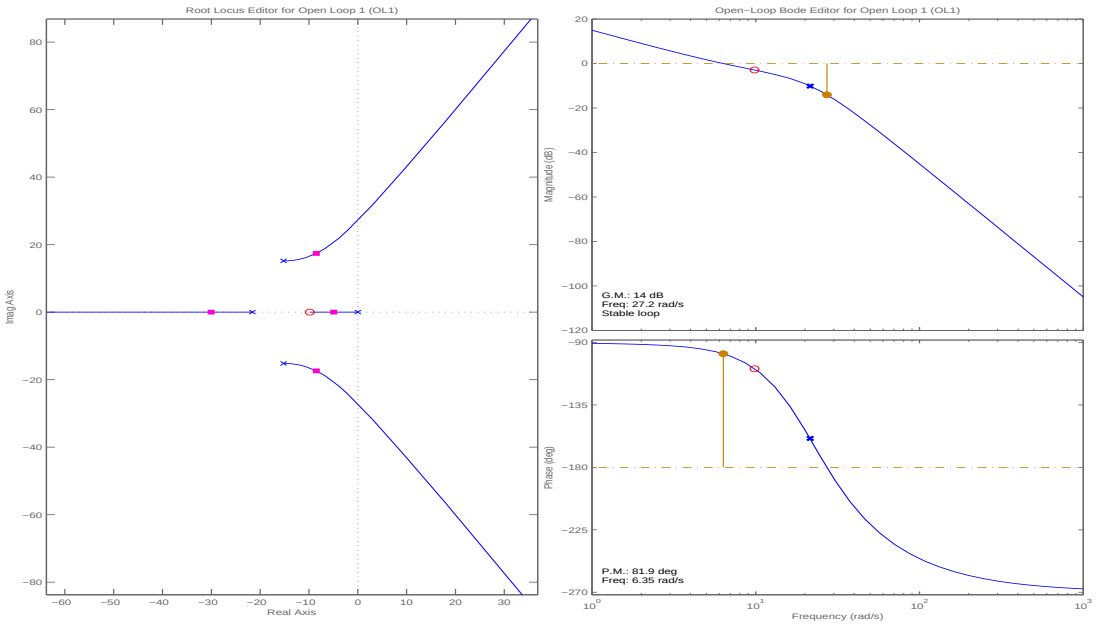

Figure 3.9: Example of root locus design of position control loop

(Fig. 3.9). Closed loop root locus and open loop bode plot is displayed. Maximum gain of the position controller is limited by the location of closed loop poles of the inner velocity loop. The real zero which is introduced by the velocity PI controller has a stabilizing effect due to the corresponding phase lead around the crossover frequency of the open loop. Higher bandwidth can be achieved with a 2DoF velocity controller which can be tuned to cancel the slowest real pole of the velocity loop with the variable zero at cost of reduced robustness in stability. The position controller is replaced by a force/torque compensator in certain applications, usually in the form of a linear PD controller. The overall bandwidth of the position loop can be further increased by introducing the feed-forward signal of desired velocity and torque, which is obtained from a trajectory generator, in the velocity and current loops (see Fig. 3.3).

Satisfactory performance is usually achieved with well tuned cascade PID control provided that no oscillatory dynamics is present and dynamics of the mechanical subsystem does not change significantly. Alternative control strategies have been proposed in the literature. A disturbance observer or sliding mode controller is recommended in the case of highly dynamical positioning, variable inertia of the load or large amount of external disturbances [72, 73, 76, 77, 78]. Adaptive methods can be used in case of slowly varying dynamics or disturbances [75, 79, 80, 91]. Techniques of stable dynamic

inversion (zero phase error tracking control and its variations) can be used for design of a pre-filter which can extend closed loop bandwidth [109, 110, 111]. However, the standard PID structure is still prevalent in industrial motion control systems.

3.3.3 Multivariable motion control

A large number of mechatronic devices perform coordinated movements of several axes resulting in multiple degree of freedom motions. A typical example is an industrial robotic manipulator or 5-axis CNC machine tool. Proper mathematical models for description of motion dynamics are needed for the purpose of analysis, optimization, simulation and control design. A common way of modelling is the idea of a *rigid multibody system*. The mechanical system is viewed as a set of interconnected rigid bodies which may undergo various translational and rotational displacements. The body represents an atomic part of the machine such as one link of the robotic arm. Individual bodies are connected via *joints* which impose kinematical constraints on admissible motion. Basic types of joints are revolute (relative rotation of connected bodies), prismatic (relative displacement along one axis), spherical (free movement in two planes) and cardan (transmission of rotary motion in any direction). The bodies can form an open or closed kinematic chain. Two basic approaches of Newton-Euler and Lagrange's equations are usually used for the systematic derivation of dynamic models of multibody systems. The first one forms a set of balance conditions for forces and torques acting in the mechanical system, whereas the second one is an energy-based approach [43, 68, 69, 112, 113].

The latter Lagrange's equations method can be briefly summarized as follows. Kinetic energy of i-th body is defined by the equation

$$T_i = \frac{1}{2} m_i \boldsymbol{v_i^T} \boldsymbol{v_i} + \frac{1}{2} \boldsymbol{\omega_i^T} \boldsymbol{I_i} \boldsymbol{\omega_i}, \tag{3.41}$$

where $m_i[kg]$ is mass of the body,
$\boldsymbol{v_i}[m/s]$ is absolute velocity of the center of mass (with respect to a stationary base reference frame RF_0),
$\boldsymbol{\omega_i}[rad/s]$ denote the vector of absolute angular velocity of the body and
$\boldsymbol{I_i}$ is the symmetric 3×3 inertia matrix describing distribution of the body mass relative to its the center of gravity.

Total kinetic energy T of the system is simply the sum of the contributions of N individual bodies and it can be expressed in terms of properly chosen *generalized coordinates* $\boldsymbol{q}$ which describe the actual machine configuration (usually a set of joint

variables in the form of actuator displacements):

$$T(\boldsymbol{q}, \dot{\boldsymbol{q}}) = \sum_{i=1}^{N} T_i = \frac{1}{2} \dot{\boldsymbol{q}}^{\boldsymbol{T}} \boldsymbol{M}(\boldsymbol{q}) \dot{\boldsymbol{q}}, \tag{3.42}$$

where $\boldsymbol{M}(\boldsymbol{q})$ is a configuration dependent symmetric positive definite inertia matrix of the system.

Potential energy U of the system due to the gravity effect is computed in a similar manner as

$$U(\boldsymbol{q}) = \sum_{i=1}^{N} U_i. \tag{3.43}$$

The potential energy of the body is usually expressed in the stationary base reference frame. Its computation is straightforward for an open kinematic chain as it can be expressed with use of homogenous coordinate transformations between reference frames of individual bodies:

$$U_i = -m_i \boldsymbol{g}^{\boldsymbol{T}} \boldsymbol{r}_{\boldsymbol{0},\boldsymbol{i}}(\boldsymbol{q}); \begin{pmatrix} \boldsymbol{r}_{\boldsymbol{0},\boldsymbol{i}} \\ 1 \end{pmatrix} = \boldsymbol{A}_{\boldsymbol{1}}^{\boldsymbol{0}}(q_1) \boldsymbol{A}_{\boldsymbol{2}}^{\boldsymbol{1}}(q_2) ... \boldsymbol{A}_{\boldsymbol{i}}^{\boldsymbol{i-1}}(q_i) \begin{pmatrix} \boldsymbol{r}_{\boldsymbol{i},\boldsymbol{i}} \\ 1 \end{pmatrix}, \tag{3.44}$$

where $\boldsymbol{g}$ is a gravity vector,
$\boldsymbol{r}_{\boldsymbol{0},\boldsymbol{i}}(\boldsymbol{q})$ is the position of the center of mass of the body in RF_0,
$\boldsymbol{A}_{\boldsymbol{i}}^{\boldsymbol{i-1}}$ is homogenous transformation matrix between reference frames of two adjacent bodies and
$\boldsymbol{r}_{\boldsymbol{i},\boldsymbol{i}}$ is a constant vector of the center of gravity position in reference to the frame of i-th body. The so called *Lagrangian* of the system is formed as

$$L(\boldsymbol{q}, \dot{\boldsymbol{q}}) = T(\boldsymbol{q}, \dot{\boldsymbol{q}}) - U(\boldsymbol{q}). \tag{3.45}$$

By using some fundamental laws of physics and mechanics (Newton's second law, principle of d'Alembert, virtual works principle etc.), a set of Euler-Lagrange equation is derived in the form

$$\frac{d}{dt} \frac{\partial L}{\partial \dot{q}_k} - \frac{\partial L}{\partial q_k} = u_k; \; k = 1, ..., N, \tag{3.46}$$

where $\boldsymbol{u} = [u_1 ... u_N]^T$ is a vector of generalized forces performing work on $\boldsymbol{q}$ (usually actuator torques/forces). By computing the partial derivatives and performing some algebra, the equations of motion can be derived in compact matrix form

$$\boldsymbol{M}(\boldsymbol{q}) \ddot{\boldsymbol{q}} + \boldsymbol{C}(\boldsymbol{q}, \dot{\boldsymbol{q}}) \dot{\boldsymbol{q}} + \boldsymbol{g}(\boldsymbol{q}) = \boldsymbol{u}; \; \boldsymbol{u} = \boldsymbol{u_a} - \boldsymbol{u_f} - \boldsymbol{u_l}, \tag{3.47}$$

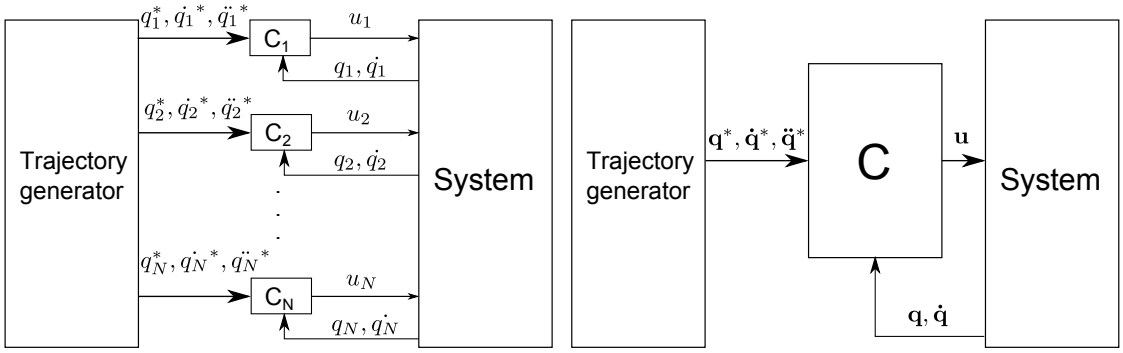

Figure 3.10: Multivariable motion control - decentralized vs centralized approach

where $\boldsymbol{M(q)}_{N\times N}$ is an inertia matrix,
$\boldsymbol{C(q,\dot{q})\dot{q}}_{N\times 1}$ is the vector of centrifugal and Coriolis forces,
$\boldsymbol{g(q)_{N\times 1}} = (\frac{\partial \boldsymbol{U}}{\partial \boldsymbol{q}})^T$ is the vector of gravity forces.

The vector of generalized forces $\boldsymbol{u}$ is formed by actuator torques/forces $\boldsymbol{u_a}$, friction terms $\boldsymbol{u_f}$ and external load terms $\boldsymbol{u_l}$.

It can be shown that the variation of the total energy is equal to the work of the generalized forces acting on the system:

$$\frac{d}{dt}(T+U) = \boldsymbol{\dot{q}^T u}. \tag{3.48}$$

The equations of motion can alternatively be defined in some proper task coordinates (e.g. position and orientation of a tool-tip or end-effector) by using kinematic transforms from the joint variables.

Two basic approaches can be used for the design of a motion controller (Fig. 3.10). A *decentralized* method considers N separated SISO control loops of individual actuators. Nonlinear coupling terms of the dynamics are treated as external disturbances. This can be justified by taking a closer look at the particular motion equation corresponding to each actuator:

$$\sum_{\forall j} m_{k,j}(\boldsymbol{q})\ddot{q}_j + \sum_{\forall i,j} c_{k,i,j}(\boldsymbol{q})\dot{q}_i\dot{q}_j + g_k(\boldsymbol{q}) = u_k;\ k = 1, ..., N. \tag{3.49}$$

The diagonal terms of the inertia matrix $m_{k,k}(\boldsymbol{q}) > 0$ represent an actual moment of inertia at $k-th$ joint when other joints are not accelerating. The nondiagonal terms $m_{k,j}(\boldsymbol{q})$ describe inertia seen at $k-th$ joint due to $i-th$ joint acceleration. The $c_{k,i,i}(\boldsymbol{q})$ terms denote centrifugal force at $k-th$ joint due to joint i velocity and $c_{k,i,j}(\boldsymbol{q})$ describe Coriolis force at joint k because of joints i and j motion. Considering that the dynamics of desired motion is relatively low, the inertial, centrifugal and Coriolis

terms are negligible with respect to the static part of the model - the gravity vector and diagonal part of the inertia matrix. Thus the model can be reduced to a simplified form

$$m_{k,k}(\boldsymbol{q})\ddot{q}_j + g_k(\boldsymbol{q}) = u_k - u_l;\ k = 1, ..., N, \tag{3.50}$$

where u_l is an equivalent disturbance torque/force which contains all the neglected parts of the system dynamics. For a particular system configuration $\boldsymbol{q}$, N independent SISO motion controllers can be designed as described in the previous section. In case the inertia varies significantly over the machine workspace, set of multiple gain-scheduled controllers can be used to enhance the overall robustness. The gravity term can be compensated by the feed-forward action or it can be treated as a slowly varying disturbance torque which is rejected by the integrator part of the controller. Sufficient performance can be achieved even with a single set of linear PID controllers in the case of moderate requirements for motion dynamics and trajectory tracking precision [69, 114].

Centralized methods use a global model of the system and try to design a multivariable controller (which is often nonlinear, due to nature of the motion equations). The usual approach is to perform a global linearization of the system dynamics through the introduction of the control law in the following form:

$$\boldsymbol{u_a} = \boldsymbol{C}(\boldsymbol{q}, \dot{\boldsymbol{q}})\dot{\boldsymbol{q}} + \boldsymbol{g}(\boldsymbol{q}) + \boldsymbol{u_f} + \boldsymbol{M}(\boldsymbol{q})\boldsymbol{v}, \tag{3.51}$$

where $\boldsymbol{v}_{N\times 1}$ is newly introduced input vector. Substitution of control (3.51) to the system model (3.47) and neglecting the external load terms leads to closed-loop dynamics

$$\ddot{\boldsymbol{q}} = \boldsymbol{v}, \tag{3.52}$$

which is linear and decoupled with respect to the vector $\boldsymbol{v}$. The obtained N double integrator loops can be stabilized by a simple PD controller (or equivalent state feedback from joint variables $\boldsymbol{q}, \dot{\boldsymbol{q}}$)

$$\begin{aligned} \boldsymbol{v} &= \boldsymbol{K_p}(\boldsymbol{q}^* - \boldsymbol{q}) + \boldsymbol{K_d}(\dot{\boldsymbol{q}}^* - \dot{\boldsymbol{q}}) + \ddot{\boldsymbol{q}}^* \quad , \\ \boldsymbol{K_p} &= diag\{\omega_1, \omega_2, ..., \omega_N\}, \boldsymbol{K_d} = diag\{2\xi_1\omega_1, 2\xi_2\omega_2, ..., 2\xi_N\omega_N\} \quad , \end{aligned} \tag{3.53}$$

leading to closed loop dynamics:

$$\ddot{\tilde{\boldsymbol{q}}} + \boldsymbol{K_d}\dot{\tilde{\boldsymbol{q}}} + \boldsymbol{K_p}\tilde{\boldsymbol{q}} = \boldsymbol{0};\ \tilde{\boldsymbol{q}} = \boldsymbol{q}^* - \boldsymbol{q}. \tag{3.54}$$

However, perfect compensation of nonlinear dynamics is seldom achievable in practice due to modeling errors. Incorrect rejection of gravity, friction or load terms leads to

steady-state positioning error. A more complex compensator which includes integrating part such as PID control or disturbance observer is recommended for such cases ([72, 115]). Alternatively, robust or adaptive controller can be employed to deal with model uncertainty [43, 69, 113]. Proof of global stability can be done for certain multivariable control schemes using Lyapunov function analysis.

Higher bandwidth and better precision of motion tracking can be achieved by using the centralized approach, provided that a sufficiently precise model of the system can be obtained. The improvement can be seen especially during highly dynamical motions which emphasize the nonlinear and coupled nature of system dynamics. The disadvantage is higher computational burden compared to decentralized methods. Development of a special motion control system is usually needed as the commercial servoamplifiers implement only the standard SISO PID control algorithm.

3.4 Flexible mechanical systems

Every real world mechanical system has a flexible structure. This results from inevitable physical laws which state that forces acting on a solid material cause its deformation. A simple equation which describes a linear relation between the tensile force acting on a body and resulting change of its length was formulated by British physicist Robert Hooke in 17^{th} century as

$$\epsilon = \frac{\triangle l}{l} = \frac{\sigma}{E}, \tag{3.55}$$

where ϵ is the relative change of length (engineering normal strain),
$\sigma = \frac{F_n}{S}[Pa]$ is tensile or compressive stress due to normal force $F_n[N]$ applied to a surface $S[m^2]$,
$E[GPa]$ is Young's modulus, which is a measure of the stiffness of the material.

The assumption of linearity between the stress and strain holds only for small forces and displacement. Any real material will break when stretched over a large distance due to the excessive force applied. This behaviour is captured by a stress-strain curve which can be obtained experimentally (Fig. 3.11). However, Hooke's law is a reasonable approximation of the elastic behaviour of many materials under typical operating conditions and it is widely used in many disciplines of science and engineering. It describes the linear part of the stress-strain curve and defines the amount of applicable force which causes reversible elastic deformation. From the perspective of motion control, every mechatronic system should operate in this region to avoid damage to the mechanical components. Therefore, the approximation of an elastic material by an

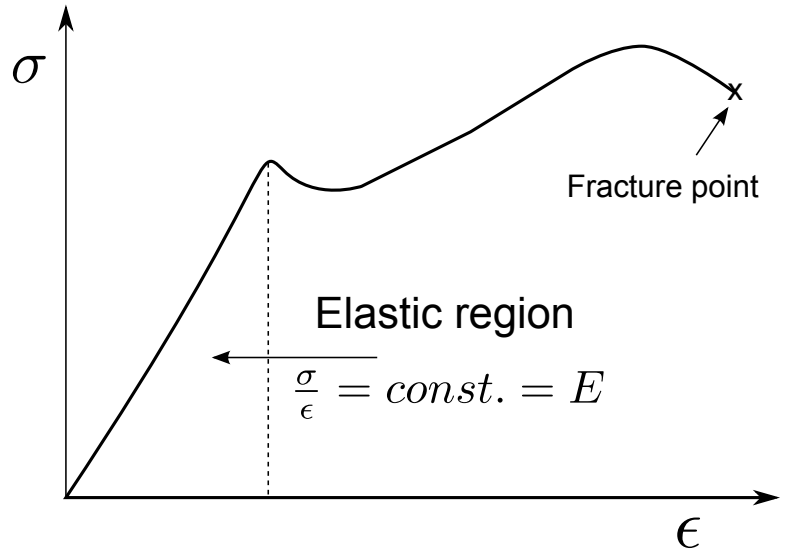

Figure 3.11: Stress-strain curve - typical shape for ductile metal materials

idealized linear spring can be justified in many practical cases. The obtained strain-stress linearity is advantageous as it allows the construction of linear dynamic models of flexible mechanical systems or considerable reduction in the complexity of nonlinear models. Similar simplifications can be done in an effort to develop models of complex spatial motions of flexible multibody systems which undergo elastic deformations. Some of the common approaches to modelling flexible systems are presented further in this section.

Elasticity of the mechanical components can cause severe difficulties in motion control applications. A rapid motion of the actuator can excite resonant modes of the system in the form of transient or residual vibrations which reduce the overall quality of control and cause increased wear of the machine. The important consequence of Hooke's law and theory of elasticity is that the occurrence of the unwanted vibration phenomenon is related to the amplitude of the applied forces and torques. This amplitude is directly affected by the closed-loop bandwidth of the motion control loops. In the case of a low bandwidth controller, the mechanic subsystem resembles an idealized rigid body system whereas an excessive increase of the controller gains leads to inevitable excitation of oscillatory dynamics. Therefore, *the mechanics of the system should always be designed according to the desired achievable dynamics of motion to avoid problems in the phase of the control system implementation*.

There are several factors which can lead to difficulties with vibrations:

- **Wrong mechanical design with respect to desired performance** - improper sizing and dimensioning of mechanical elements can lead to unwanted oscillatory behaviour. This can be avoided by using modern model-based design software tools equipped with powerful functions for structural analysis and finite element simulations. However, such tools may not be available and eventual mistakes have to be corrected by means of the control system.

- **Flexible elements of an otherwise stiff system** - in many practical systems, the use of flexible components is inevitable for their proper operation. An example is an industrial robotic manipulator which is constructed as a stiff system, but may include parts with elastic behaviour such as flexsplines of the harmonic drives, toothed belts or long shafts. The elasticity is *lumped* from the perspective of system dynamics. The elasticity of machine parts may results from the desirable properties of the system (e.g. assistance robots equipped with compliant arms by virtue of safety).

- **Lightweight systems with distributed elasticity** - very long and slender components or the use of lightweight materials may lead to oscillatory dynamics. This phenomenon is typical for skyscrapers, tendon bridges or space structures (long and lightweight manipulator arms, flexible components of satellites due to extensive use of lightweight composite materials etc.). Distributed deformation complicates the process of modeling and control system design due to complex nonlinear dynamics.

3.4.1 Modeling of flexible systems

Relevant dynamic models are needed for the purpose of analysis and motion control design. There are conflicting requirements for model accuracy in the range of desired bandwidth and a low order of closed-form expressions suitable for control synthesis. Three distinct approaches can be used for the derivation of mathematical models:

1. **Spatial discretization based on the Finite element method**
   Complex dynamics of a flexible system with distributed elasticity which is generally infinite-dimensional can be split into a collection of subdomains (usually called elements or nodes) which represent small physical parts of the real system. Each element is described by a set of equations and boundary conditions. The

distributed elasticity which typically leads to complex partial differential equations (PDE's) is approximated by a large number of simpler ordinary differential equations (ODE's) which can be solved numerically. The advantage of this approach is the ability to model the dynamics of complex mechanical structures with complicated geometry consisting from components made from various materials [116, 117, 118, 119]. Commercially available software tools for finite element analysis and structural simulation can be used in the phase of mechanical design. The disadvantage is dependence on a particular mechanical structure and the high order of resulting models (typically hundreds of node equations) making them impractical for the purpose of control design.

2. **Analytical modeling of flexible elements**
   Several simplifying assumptions can be used to develop suitable analytical models which can approximate global system behaviour with reasonable accuracy. Lumped elasticity in flexible joints can be added to the models of multibody systems [119, 120, 121]. Slender arms of the robot can be approximated by idealized models of elastic beams (e.g. Timoshenko or Euler-Bernoulli beam theory [122]) and resulting PDE's describing the motion dynamics can be approximated by a limited number of ODE's by truncation of high frequency dynamics (e.g. assumed modes method [119, 123]). Models with reasonable complexity applicable for control design can be constructed using the standard framework of Lagrange's equations [124, 125]. A wider class of systems can usually be described with a properly chosen model structure, a proper identification procedure is needed to match the model parameters with a real mechanical system.

3. **Local problem oriented models**
   Local dynamics of flexible systems can often be described by relatively simple linear models [86, 126, 127, 128]. Acceptable accuracy can be achieved by considering a limited range of desired bandwidth and close vicinity around some operating point. The oscillatory dynamics can naturally be expressed with frequency domain models in form of plant transfer functions by means of weakly damped poles and zeros resulting in peaks in frequency response. Powerful methods for system identification and control design which are available in the linear theory make it suitable for the purpose of automatic controller tuning. This thesis deals with the class of linear flexible multi-mass models which can represent a large variety of motion control problems encountered in industrial applications, as will be shown further in the text. Care must be taken in relation to the local validity

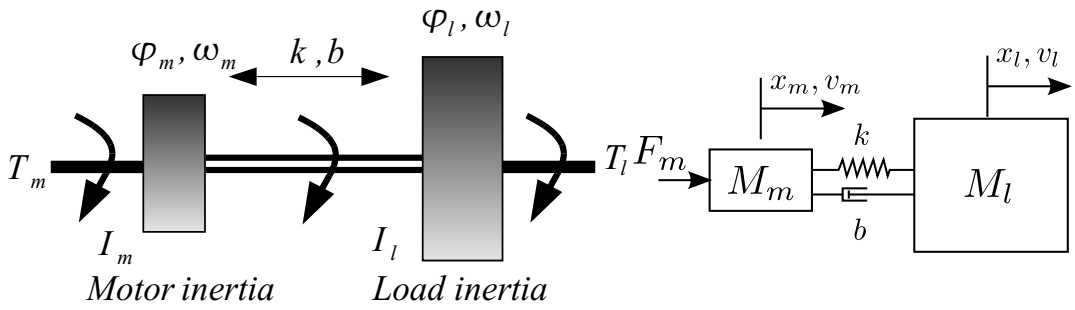

Figure 3.12: Two-mass model - rotor and load inertia coupled by a flexible shaft, equivalent linear motion system

of the model and the possibility of the occurrence of nonlinear effects typical for mechanical systems such as friction, backlash or hysteresis. Robust, adaptive or gain-scheduled controllers should be used in the case of large variations in the system dynamics. The global stability of nonlinear closed-loop system is usually difficult to prove.

3.4.2 Linear structural dynamics approach

Examples of dynamic models which are suitable for motion control design are presented in this section. It is shown that a proper class of linear models with assumed lumped elasticity can be used to model oscillatory behaviour of large class of practical systems encountered in industrial applications.

Two-mass and multi-mass resonant system

The two-mass model is a basic representation of a mechanical system with a single resonant mode (Fig. 3.12). A rotary actuator with inertia I_m is connected to a load inertia I_L by a flexible shaft. The motion of the actuator causes elastic deformation of the shaft which may be modeled as a linear torsional spring described by the stiffness constant k and internal viscous friction coefficient b. Equations of motion can be formed using Newton's laws:

$$\begin{aligned} \varepsilon_m = \dot{\omega}_m &= \frac{1}{I_m}\{T_m - k(\varphi_m - \varphi_l) - b(\omega_m - \omega_l)\}, \\ \varepsilon_l = \dot{\omega}_l &= \frac{1}{I_l}\{T_l + k(\varphi_m - \varphi_l) + b(\omega_m - \omega_l)\}. \end{aligned} \tag{3.56}$$

The corresponding state space model can be derived in the form of

$$\begin{aligned}\dot{\boldsymbol{x}} &= \begin{bmatrix} \dot{\varphi}_m \\ \dot{\omega}_m \\ \dot{\varphi}_l \\ \dot{\omega}_l \end{bmatrix} = \begin{bmatrix} 0 & 1 & 0 & 0 \\ -\frac{k}{I_m} & -\frac{b}{I_m} & \frac{k}{I_m} & \frac{b}{I_m} \\ 0 & 0 & 0 & 1 \\ \frac{k}{I_l} & \frac{b}{I_l} & -\frac{k}{I_l} & -\frac{b}{I_l} \end{bmatrix} \boldsymbol{x} + \\ &+ \begin{bmatrix} 0 & 0 \\ \frac{1}{I_m} & 0 \\ 0 & 0 \\ 0 & \frac{1}{I_l} \end{bmatrix} \begin{bmatrix} T_m \\ T_l \end{bmatrix}, \; \boldsymbol{y}= \begin{bmatrix} 0 & 1 & 0 & 0 \\ 0 & 0 & 0 & 1 \end{bmatrix} \boldsymbol{x}, \end{aligned} \tag{3.57}$$

where $\varphi_{m,l}, \omega_{m,l}$ denote motor and load angular position and velocity and T_m is electromagnetic torque produced by the motor. Only motor side measurement is usually available in typical industrial applications. Additional load sensors can be added to improve positioning accuracy and control performance.

Transfer functions from motor torque to motor and load speed can be obtained as

$$\begin{aligned} P_1^{\omega}(s) &= \frac{\omega_m(s)}{T_m(s)} = \frac{I_l s^2 + bs + k}{s[I_m I_l s^2 + b(I_m + I_l)s + k(I_m + I_l)]} = \frac{K_1}{s} \frac{s^2 + 2\xi_z \omega_z s + \omega_z^2}{s^2 + 2\xi \omega_n s + \omega_n^2}, \\ P_2^{\omega}(s) &= \frac{\omega_l(s)}{T_m(s)} = \frac{bs + k}{s[I_m I_l s^2 + b(I_m + I_l)s + k(I_m + I_l)]} = \frac{K_2}{s} \frac{s + \frac{\omega_z}{2\xi_z}}{s^2 + 2\xi \omega_n s + \omega_n^2}, \end{aligned} \tag{3.58}$$

where the corresponding gains, natural frequencies and damping factors can be expressed in terms of system parameters

$$\begin{aligned} K_1 &= \frac{\omega_n^2}{(I_l + I_m)\omega_z^2}, \; \omega_n = \sqrt{\frac{k(I_l + I_m)}{I_l I_m}}, \; \omega_z = \sqrt{\frac{k}{I_l}}, \\ K_2 &= \frac{2\xi_z \omega_n^2}{(I_l + I_m)\omega_z}, \; \xi = \sqrt{\frac{b^2(I_l + I_m)}{4kI_l I_m}}, \; \xi_z = \sqrt{\frac{b^2}{4kI_l}}. \end{aligned} \tag{3.59}$$

A so called *resonance ratio* parameter is defined as

$$r = \frac{\omega_n}{\omega_z} = \sqrt{1 + \frac{I_l}{I_m}}. \tag{3.60}$$

Transfer functions to motor and load position are obtained by simply adding an integrator term $\frac{1}{s}$ to expressions (3.58). Equivalent linear motion model can be obtained by direct substitution of appropriate physical quantities ($m \to I, \; F \to T, x \to \varphi, v \to \omega$, see Fig. 3.12). A viscous friction model can be added to both motor and load side by

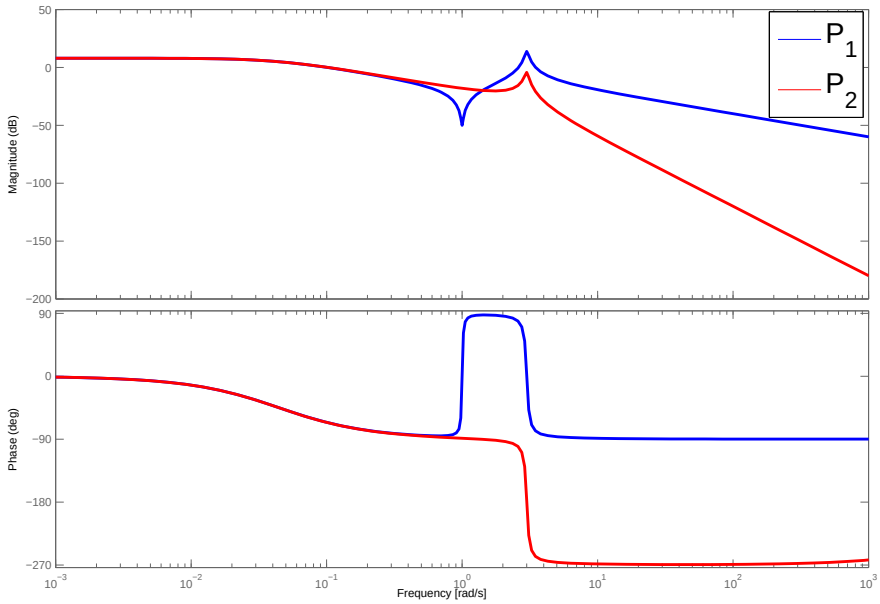

Figure 3.13: Bode plot of two-mass system - typical shape

modifying the state matrix of system (3.57) to

$$\boldsymbol{A} = \begin{bmatrix} 0 & 1 & 0 & 0 \\ -\frac{k}{I_m} & -\frac{b+b_m}{I_m} & \frac{k}{I_m} & \frac{b}{I_m} \\ 0 & 0 & 0 & 1 \\ \frac{k}{I_l} & \frac{b}{I_l} & -\frac{k}{I_l} & -\frac{b+b_l}{I_l} \end{bmatrix}, \tag{3.61}$$

where b_m, b_l denote motor and load friction coefficients. This leads to transfer functions:

$$\begin{aligned} P_1^{\omega}(s) = \frac{\omega_m(s)}{T_m(s)} &= \frac{I_l s^2+(b+b_l)s+k}{a_3 s^3+a_2 s^2+a_1 s+a_0}, \\ P_2^{\omega}(s) = \frac{\omega_l(s)}{T_m(s)} &= \frac{bs+k}{a_3 s^3+a_2 s^2+a_1 s+a_0}, \\ a_3 = I_l I_m,\ a_2 &= \{I_l(b+b_m)+I_m(b+b_l)\}, \\ a_1 = \{b_m(b_l+b)+k(I_m+I_l)+b_l b\},\ a_0 &= k(b_l+b_m). \end{aligned} \tag{3.62}$$

Analytical expressions of corresponding resonance and antiresonance frequencies and damping requires computation of roots of characteristic polynomial and leads to complicated equations which are omitted for sake of brevity. However, the exact dependence of pole locations on plant parameters is not as important, as the model can be viewed as a *general representation of dynamics of rigid and first resonance mode*. The nature of the system behaviour is better understood in the frequency domain by plotting

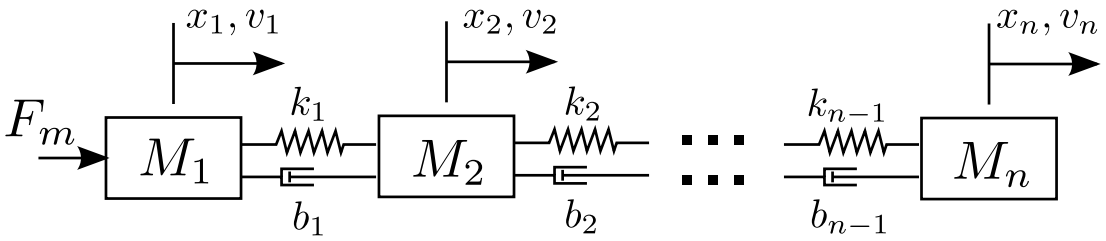

Figure 3.14: Multi-mass linear system

the Bode response of the plant transfer functions (3.62). The typical shape observed in practice can be seen in Fig.3.13. Low-frequency dynamics is determined by the rigid mode of the system (stable real pole of transfer function or an integrator in the case of negligible friction). Sharp peaks of resonance and antiresonance regions due to weakly damped pairs of poles and zeros appear in high frequency region. In the case of low desired bandwidth, the system dynamics can be approximated by the rigid body model. Increase in the controller gains leads to excitation of the oscillatory dynamics and problems with stability and closed-loop performance. An extended model which includes the high frequency behaviour is needed for an appropriate compensator design.

The nature of dynamic behaviour of multi-mass resonant systems can be seen more clearly after the application of so called *modal transform* [118, 126]. The equations of motion of a general multiple DoF system can be written in compact matrix form of mass-spring damper format:

$$\begin{aligned} \boldsymbol{M}\ddot{\boldsymbol{x}} + \boldsymbol{B}\dot{\boldsymbol{x}} + \boldsymbol{K}\boldsymbol{x} &= \boldsymbol{L_u} F_m, \\ \boldsymbol{y} &= \boldsymbol{L_u}\boldsymbol{x}, \end{aligned} \tag{3.63}$$

where $\boldsymbol{M}_{n\times n}$ is diagonal positive definite mass or inertia matrix,
$\boldsymbol{B}_{n\times n},\ \boldsymbol{K}_{n\times n}$ are symmetric semi-positive definite damping and stiffness matrices,
$\boldsymbol{L_u}_{n\times 1}$ is input matrix, $\boldsymbol{L_y}_{n_y\times n}$ output matrix, where n_y is the number of measured outputs.

For the case of linear configuration in Fig (3.14) we get:

$$\boldsymbol{M} = \begin{bmatrix} M_1 & 0 & 0 & \cdots & 0 \\ 0 & M_2 & 0 & \cdots & 0 \\ 0 & 0 & M_3 & \cdots & 0 \\ \vdots & \vdots & \vdots & \ddots & 0 \\ 0 & 0 & 0 & 0 & M_n \end{bmatrix}, \boldsymbol{B} = \begin{bmatrix} b_1 & -b_1 & 0 & \cdots & 0 \\ -b_1 & b_1+b_2 & -b_2 & \cdots & 0 \\ 0 & -b_2 & b_2+b_3 & \cdots & 0 \\ \vdots & \vdots & \vdots & \ddots & -b_{n-1} \\ 0 & 0 & 0 & -b_{n-1} & b_{n-1} \end{bmatrix},$$

$$\boldsymbol{K} = \begin{bmatrix} k & -k_1 & 0 & \cdots & 0 \\ -k_1 & k_1+k_2 & -k_2 & \cdots & 0 \\ 0 & -k_2 & k_2+k_3 & \cdots & 0 \\ \vdots & \vdots & \vdots & \ddots & -k_{n-1} \\ 0 & 0 & 0 & -k_{n-1} & k_{n-1} \end{bmatrix}, \boldsymbol{L_u} = \begin{bmatrix} 1 \\ 0 \\ 0 \\ \vdots \\ 0 \end{bmatrix}. \tag{3.64}$$

The output matrix of appropriate dimensions is defined according to the location and type of sensors installed (position, velocity or acceleration). The usual configuration in motion control systems is motor side (first mass of the model) velocity and position sensing (so called *colocated feedback*) and optional load-side measurement (last mass in the chain, *noncolocated feedback* in this case).

Natural frequencies of the system can be found by inspection of the undamped conservative system:

$$\boldsymbol{M\ddot{x} + Kx = 0}. \tag{3.65}$$

Expecting a solution in form $\boldsymbol{x} = \boldsymbol{\phi_k} e^{i\omega_k t}$, eigenvalue equation for matrices $\boldsymbol{K}, \boldsymbol{M}$ has to be fulfilled in the form:

$$(\boldsymbol{K} - \omega_k^2 \boldsymbol{M})\boldsymbol{\phi_k} = 0. \tag{3.66}$$

Since M is symmetric positive definite and K is symmetric positive semi-definite, eigenvalues ω_k^2 are real and nonnegative. The non-trivial solution of (3.66) can be found from the equation

$$det(\boldsymbol{K} - \omega_k^2 \boldsymbol{M}) = 0, \tag{3.67}$$

which leads to n values of natural frequencies ω_k. Corresponding eigenvectors $\boldsymbol{\phi_k}$ which describe the shape of individual system modes can be obtained by substitution to (3.66). Rigid body mode is computed from the condition of zero strain energy for $\omega_k = 0$.The set of eigenvectors form a orthogonal matrix of the mode shapes $\boldsymbol{\Phi} = [\boldsymbol{\phi_1}, \boldsymbol{\phi_2}, ..., \boldsymbol{\phi_n}]$ which is also orthogonal with respect to matrices M, K (follows directly from 3.66). Seeing that matrix $(\boldsymbol{K} - \omega_k^2 \boldsymbol{M})$ is singular, solutions of the particular eigenvectors are linearly dependent. Thus, it is convenient to scale them according

to mass matrix to obtain its diagonalization due to orthogonality relationship. Therefore, we may write the following:

$$\begin{aligned} \boldsymbol{\Phi^T M \Phi} &= \boldsymbol{I_n}, \\ \boldsymbol{\Phi^T K \Phi} &= diag\{\omega_k^2\} = \boldsymbol{\Omega^2}, \\ \boldsymbol{\Phi^T B \Phi} &= diag\{2\xi_k\omega_k\} = \boldsymbol{2\xi\Omega}. \end{aligned} \tag{3.68}$$

The orthogonality equation does not hold generally for an arbitrary $\boldsymbol{B}$. However, the dissipation matrix is often chosen in *Rayleigh damping* form $\boldsymbol{B} = \alpha\boldsymbol{M} + \beta\boldsymbol{K}$ which makes the equality valid.

The obtained modal matrix is used for the transition from physical (nodal) to modal coordinates. By setting

$$\boldsymbol{x = \Phi z}, \tag{3.69}$$

where $\boldsymbol{z}$ is the vector of modal amplitudes, we get

$$\boldsymbol{M\Phi\ddot{z} + B\Phi\dot{z} + K\Phi z = L_u} F_m. \tag{3.70}$$

Multiplication from left by $\boldsymbol{\Phi^T}$ and use of the orthogonality equations (3.68) leads to the *modal form of the system*:

$$\begin{gathered} \boldsymbol{I_n\ddot{z} + 2\xi\Omega\dot{z} + \Omega^2 z = \Phi^T L_u} F_m = \boldsymbol{\Phi_u} F_m \\ \boldsymbol{y = L_y \Phi z = \Phi_y z}, \end{gathered} \tag{3.71}$$

where $\boldsymbol{\Phi_u}$ is $n \times 1$ modal input vector and $\boldsymbol{\Phi_y}$ $n_y \times n$ modal output matrix. The obtained model has a form of n decoupled second order systems excited by new input vector $\boldsymbol{\Phi^T L_u}$. The modal form is useful for evaluation of the contribution of each individual mode to the overall system behaviour and for eventual truncation of high frequency dynamics which may be negligible with respect to desired closed-loop bandwidth.

This can be illustrated by the example of a two-mass system. The system matrices of mass-spring-damper model (3.64) are defined as:

$$\boldsymbol{M} = \begin{bmatrix} M_1 & 0 \\ 0 & M_2 \end{bmatrix}, \boldsymbol{B} = \begin{bmatrix} b & -b \\ -b & b \end{bmatrix}, \boldsymbol{K} = \begin{bmatrix} k & -k \\ -k & k \end{bmatrix}, L_u = \begin{bmatrix} 1 \\ 0 \end{bmatrix}. \tag{3.72}$$

Two eigenfrequencies corresponding to one rigid and one oscillatory mode are found from (3.66):

$$\omega_1 = 0,\ \omega_2 = \sqrt{\frac{k(M_1 + M_2)}{M_1 M_2}}. \tag{3.73}$$

The modal matrix composed from eigenvectors which are normalized with respect to the mass matrix has the form:

$$\mathbf{\Phi} = \begin{bmatrix} \frac{1}{\sqrt{M_1+M_2}} & -\frac{M_2}{M_1\sqrt{\frac{M_2{}^2}{M_1}+M_2}} \\ \frac{1}{\sqrt{M_1+M_2}} & \frac{1}{\sqrt{\frac{M_2{}^2}{M_1}+M_2}} \end{bmatrix} = \begin{bmatrix} \phi_{11} & \phi_{12} \\ \phi_{21} & \phi_{22} \end{bmatrix}. \tag{3.74}$$

Application of the modal transform leads to the dynamic model in the form:

$$\begin{bmatrix} 1 & 0 \\ 0 & 1 \end{bmatrix} \ddot{\boldsymbol{z}} + \begin{bmatrix} 0 & 0 \\ 0 & \frac{b(M_1+M_2)}{M_1M_2} \end{bmatrix} \dot{\boldsymbol{z}} + \begin{bmatrix} 0 & 0 \\ 0 & \frac{k(M_1+M_2)}{M_1M_2} \end{bmatrix} \boldsymbol{z} = \begin{bmatrix} \phi_{11} \\ \phi_{12} \end{bmatrix} F_m. \tag{3.75}$$

Damping of the resonant mode can be computed from corresponding diagonal terms as $\xi_2 = \sqrt{\frac{b^2(M_1+M_2)}{4kM_1M_2}}$. Transfer functions from input force to measured outputs can be obtained by application of the Laplace transform to the modal equations in model (3.75). Assuming motor side position feedback, the output matrix becomes $\mathbf{\Phi_y} = [\mathbf{1\ 0}]\mathbf{\Phi} = [\phi_{11}\ \phi_{12}]$ and the resulting transfer function is

$$\begin{aligned} P_1^x(s) &= \frac{x_1(s)}{F_m(s)} = \frac{\phi_{11}^2}{s^2} + \frac{\phi_{12}^2}{s^2+2\xi_2\omega_2 s+\omega_2^2} = \frac{\phi_{11}^2(s^2+2\xi_2\omega_2 s+\omega_2^2)+\phi_{12}^2 s^2}{s^2(s^2+2\xi_2\omega_2 s+\omega_2^2)} = \\ &= \frac{\phi_{11}^2}{s^2}\frac{r^2(s^2+\frac{2\xi_2\omega_2}{r^2}s+\frac{\omega_2^2}{r^2})}{s^2+2\xi_2\omega_2 s+\omega_2^2} = \frac{\phi_{11}^2}{s^2}\frac{r^2(s^2+2\xi_{z2}\omega_{z2}s+\omega_{z2}^2)}{s^2+2\xi_2\omega_2 s+\omega_2^2}, \end{aligned} \tag{3.76}$$

where $r^2 = 1+\frac{\phi_{12}^2}{\phi_{11}^2}$ is square of the resonance ratio.

Since $r^2 > 1$, both natural frequency ω_{z1} and damping ξ_{z1} of complex zero pair decreases with respect to complex poles in a defined rate:

$$\frac{\xi_2}{\xi_{z2}} = \frac{\omega_2}{\omega_{z2}} = r = \sqrt{1+\frac{M_2}{M_1}}. \tag{3.77}$$

The last two terms of (3.76) show, that the system can be partitioned to system

$$P_r(s) = \frac{\phi_{11}^2}{s^2} = \frac{1}{(M_1+M_2)s^2}, \tag{3.78}$$

which corresponds to the rigid mode of P_1 and matches the dynamics of ideal stiff connection of two masses, and additional high frequency oscillatory dynamics $P_o(s)$ with unit static gain describing the behaviour of first resonant mode:

$$P_o(s) = \frac{r^2(s^2+2\xi_{z2}\omega_{z2}s+\omega_{z2}^2)}{s^2+2\xi_2\omega_2 s+\omega_2^2}. \tag{3.79}$$

For a low excitation bandwidth $\omega << \omega_{z2}$, the system dynamics can be approximated by the rigid model.

In the case of the load side feedback, the output matrix has the form $\boldsymbol{\Phi_y} = [\mathbf{0}\ \mathbf{1}]\boldsymbol{\Phi} = [\phi_{21}\ \phi_{22}]$ and we obtain transfer function in form:

$$P_2^x(s) = \frac{x_2(s)}{F_m(s)} = \frac{\phi_{11}\phi_{21}}{s^2} + \frac{\phi_{12}\phi_{22}}{s^2 + 2\xi_2\omega_2 s + \omega_2^2} = \tag{3.80}$$

$$= \frac{\phi_{11}\phi_{21}(s^2 + 2\xi_2\omega_2 s + \omega_2^2) + \phi_{12}\phi_{22}s^2}{s^2(s^2 + 2\xi_2\omega_2 s + \omega_2^2)}. \tag{3.81}$$

From the property of orthogonality of the modal matrix $\boldsymbol{\Phi^T\Phi} = \boldsymbol{I_n}$, it follows that $\phi_{11}\phi_{21} + \phi_{12}\phi_{22} = 0$. The first eigenvector corresponding to the rigid mode contains terms with the same magnitude, therefore $\phi_{11}\phi_{21} = \phi_{11}^2$ and the system is reduced to:

$$P_2^x(s) = \frac{x_2(s)}{F_m(s)} = \frac{\phi_{11}^2}{s^2}\frac{2\xi_2\omega_2 s + \omega_2^2}{s^2 + 2\xi_2\omega_2 s + \omega_2^2} = \frac{\phi_{11}^2}{s^2}\frac{r^2(2\xi_{z2}\omega_{z2}s + \omega_{z2}^2)}{s^2 + 2\xi_2\omega_2 s + \omega_2^2}. \tag{3.82}$$

Again, the dynamics is split to rigid low frequency and resonant high-frequency resonant parts. Transfer functions to measured velocity or acceleration can be obtained through simple multiplication by s or s^2. Substitution of the computed frequencies, dampings and terms of modal matrix leads naturally to the same transfer functions which were obtained from the nodal state space model (3.57):

$$\begin{aligned} P_1^v(s) &= \frac{v_1(s)}{F_m(s)} = \frac{M_2 s^2 + bs + k}{s[M_1M_2s^2 + b(M_1 + M_2)s + k(M_1 + M_2)]}, \\ P_2^v(s) &= \frac{v_2(s)}{F_m(s)} = \frac{bs + k}{s[M_1M_2s^2 + b(M_1 + M_2)s + k(M_1 + M_2)]}. \end{aligned} \tag{3.83}$$

Some of the derived results can be extended to the n-th order multi-mass system (3.64). Considering the collocated feedback case, the transfer function becomes

$$P_1^x(s) = \frac{x_1(s)}{F_m(s)} = \sum_{i=1}^{n}\frac{\phi_{1i}^2}{s^2 + 2\xi_i\omega_i s + \omega_i^2} = \frac{\phi_{11}^2}{s^2} + \sum_{i=2}^{n}\frac{\phi_{1i}^2}{s^2 + 2\xi_i\omega_i s + \omega_i^2} = \tag{3.84}$$

$$= \frac{\phi_{11}^2\prod_{i=2}^{n}(s^2 + 2\xi_i\omega_i s + \omega_i^2) + s^2\sum_{i=2}^{n}\phi_{1i}^2\prod_{i\neq j}^{n}(s^2 + 2\xi_j\omega_j s + \omega_j^2)}{s^2\prod_{i=2}^{n}(s^2 + 2\xi_i\omega_i s + \omega_i^2)} =$$

$$= \frac{1}{\sum_{i=1}^{n}M_i s^2}\frac{s_1\prod_{i=2}^{n}(s^2 + 2\xi_{zi}\omega_{zi}s + \omega_{zi}^2)}{\prod_{i=2}^{n}(s^2 + 2\xi_i\omega_i s + \omega_i^2)};\ s_1 = \frac{\prod_{i=2}^{n}\omega_i^2}{\prod_{i=2}^{n}\omega_{zi}^2},$$

where the scaling factor s_1 is introduced to emphasize the partitioning of system dynamics to rigid and oscillatory part.

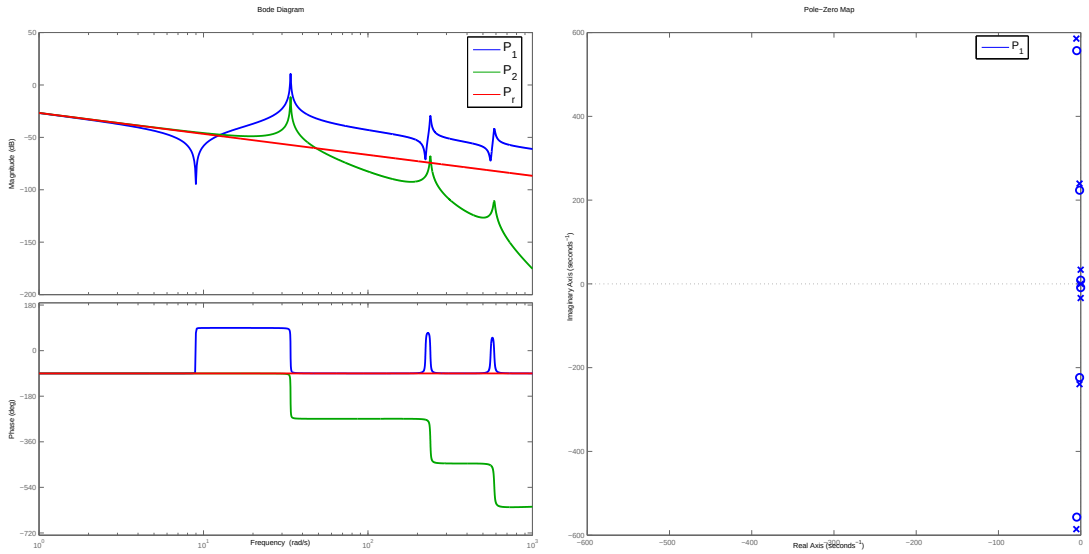

Figure 3.15: Multi-mass system example ($n = 4$) - Bode plots for motor and load side velocity feedback ($P_{1,2}$), rigid body dynamics P_r, pole-zero map of P_1

An example of the typical shape of Bode plot can be seen in Fig.(3.15). A repeating pattern of alternating pairs of weakly damped zeros and poles is observed in the high frequency region, rigid mode dynamics is dominant for low frequencies. The usual values of damping achieved in industrial motion control applications are $\xi \simeq 0.01..0.1$. Resonance frequencies vary from tens to hundreds of Hertz. Lower damping can be seen in the dynamics of space structures due to the extensive use of composite materials and absence of aero-dynamical damping [126].
The load side dynamics can be described by the transfer function:

$$\begin{aligned} P_n^x(s) &= \frac{x_n(s)}{F_m(s)} = \sum_{i=1}^{n} \frac{\phi_{1i}\phi_{ni}}{s^2 + 2\xi_i\omega_i s + \omega_i^2} = \frac{\phi_{11}\phi_{n1}}{s^2} + \sum_{i=2}^{n} \frac{\phi_{1i}\phi_{ni}}{s^2 + 2\xi_i\omega_i s + \omega_i^2} = \\ &= \frac{\phi_{11}^2 \prod_{i=2}^{n}(s^2 + 2\xi_i\omega_i s + \omega_i^2) + s^2 \sum_{i=2}^{n} \phi_{1i}\phi_{ni} \prod_{i\neq j}^{n}(s^2 + 2\xi_j\omega_j s + \omega_j^2)}{s^2 \prod_{i=2}^{n}(s^2 + 2\xi_i\omega_i s + \omega_i^2)} = \\ &= \frac{1}{\sum_{i=1}^{n} M_i s^2} \frac{s_2 \prod_{i=1}^{n-1}(b_i s + k_i)}{\prod_{i=2}^{n}(s^2 + 2\xi_i\omega_i s + \omega_i^2)};\ s_2 = \frac{\prod_{i=2}^{n}\omega_i^2}{\prod_{i=1}^{n-1} ki^2}. \end{aligned} \tag{3.85}$$

The structure of system zeros comes from the property of the orthogonality of the modal matrix as was shown in the two-mass case and it has a clear physical interpretation. Every pair of masses introduces one transmission zero which is influenced by stiffness and damping of the spring-damper connection regardless of the weight of adjacent nodes (3.83). Considering the load-side output feedback, the property of blocking

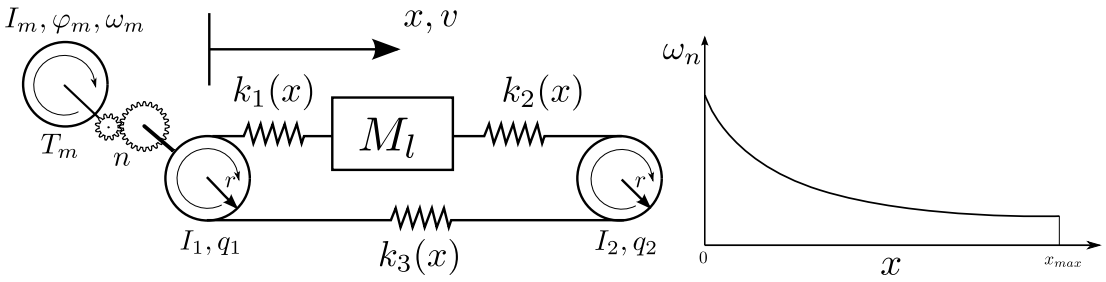

Figure 3.16: Flexible tooth-belt drive system - system structure, nonlinear function of resonance frequency with respect to load position

certain mode of input signal has to be naturally inherited by each following node of the chain. For lightly damped systems, the resulting zeros appear in high frequency region and their influence is negligible with respect to the dominant part caused by the poles. Therefore, the transfer function can approximated as:

$$P_n^x(s) \approx \frac{1}{\sum_{i=1}^{n} M_i s^2} \frac{\prod_{i=2}^{n} \omega_i^2}{\prod_{i=2}^{n} (s^2 + 2\xi_i \omega_i s + \omega_i^2)}. \tag{3.86}$$

The insight into the dynamics of lightly damped systems gained from analysis of the modal form leads to the conclusion that a **limited number of modal coordinates can be considered for the purpose of system identification and control law design. Particular physical structure of the system is irrelevant from the control point of view and low order frequency domain models can be used to capture dominant oscillatory behaviour of the system needed for the vibration control**. The truncation of high frequency dynamics is valid when performed correctly with respect to the desired excitation bandwidth. Significant reduction of model order compared to the nodal representation is often achieved, especially in the case of FEM models of complex geometry structures.

Approximation of nonlinear dynamics

The linear multi-mass models can be used for local approximation of dynamical behaviour of otherwise nonlinear systems in the vicinity of an operating point. Another useful application is a description of a system with distributed elasticity by a low-order lumped parameter model. Two examples are presented to explain these approaches.

Example 1 - Flexible tooth-belt drive system

Belt drive systems are used in many industrial motion control applications as an alternative to more expensive screw-ball drives. The typical structure of the system can be seen in Fig. (3.16). The actuator is connected to the driving pulley via a gear-box. A flexible tooth-belt connects the manipulated load to driving and driven pulleys. The elasticity of the belt can cause problems with mechanical vibrations which can occur in a high-speed operation. Assuming stiff connection of drive, gearbox and driving pulley, the system can be modeled as a nonlinear three-mass structure [129]:

$$\begin{aligned}(I_1 + n^2(I_g + I_m))\ddot{q}_1 + T_{f1} &= nT_m - r[k_1(x)(rq_1 - x) - k_3(x)(rq_2 - rq_1)],\\ I_2\ddot{q}_2 + T_{f2} &= r[k_2(x)(x - rq_2) - k_3(x)(rq_2 - rq_1)],\\ M_l\ddot{x} + F_f &= k_1(x)(rq_1 - x) - k_2(x)(x - rq_2),\end{aligned} \tag{3.87}$$

where I_m, I_g, I_1, I_2 are moments of inertia of the motor, gear and pulleys,
q_1, q_2 are angular displacements of the pulleys,
$k_{1,2,3}(x)$ are position dependent spring constants of the belt parts,
r is the pulley radius,
T_m, T_{f1}, T_{f2} are driving and friction torques,
n is gear ratio and F_f is load side friction force.

Considering that the pulley inertias are negligible compared to equivalent load and load-side motor inertias, ie. $I_{1,2} << \{(I_m+I_g)n^2,\ M_l\}$, the system can be approximated by an equivalent nonlinear two-mass model

$$\begin{aligned}(I_m + I_g)\ddot{\varphi}_m &= T_m - T_f - \tfrac{r}{n}k_{eq}(x)(\tfrac{r}{n}\varphi_m - x),\\ M_l\ddot{x} &= k_{eq}(x)(\tfrac{r}{n}\varphi_m - x) - F_f,\end{aligned} \tag{3.88}$$

where the equivalent spring constant $k_{eq}(x) = f(k_1(x), k_2(x), k_3(x))$ can be estimated analytically or obtained from an experimental measurement [130].

The system can be linearized around arbitrary working point x leading to a standard LTI two-mass model (3.56). Natural frequency of the system depends on the value of nonlinear stiffness $k_{eq}(x)$ and varies with load position in a nonlinear manner. Usual dependence observed in practice can be seen in Fig. (3.16). Techniques of robust control, linear or nonlinear gain-scheduling can be employed for the design of a proper compensator which could cope with the varying dynamics [35, 129, 130].

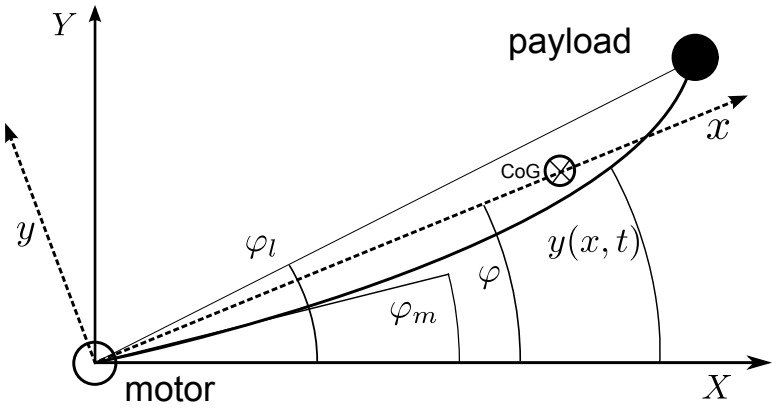

Figure 3.17: Flexible beam - motion of system with distributed elasticity

Example 2 - Planar motion of flexible robotic arm

A light-weight robotic arm with distributed flexibility can be modeled as a slender beam using the *Euler-Bernoulli* beam theory [124, 126, 131]. Dynamics of a pinned-free flexible beam (see Fig. 3.17) can be modeled by the partial differential equation:

$$\frac{\partial^2}{\partial x^2}(EI(x)\frac{\partial^2 y(x,t)}{\partial x^2}) + \mu\frac{\partial^2 y(x,t)}{\partial t^2} = f(x,t), \tag{3.89}$$

where EI is flexural stiffness, μ is distributed mass, $y(x,t)$ is flexible beam deflection, $f(x,t)$ is the sum of all external forces.

In the free evolution and under assumption of constant EI, the PDE can be solved by separation of variables

$$y(x,t) = \phi(x)S(t), \tag{3.90}$$

which leads to differential equation

$$\phi^{(IV)}(x) = \lambda^4\phi(x);\ \lambda^4 = \frac{\mu\omega^2}{EI}, \tag{3.91}$$

for the eigenfunctions $\phi_i(x)$ and flexible beam eigenfrequencies ω_i.

After fairly lengthy calculations (see [131] for full derivation), a set of computed eigenvectors and frequencies for a properly chosen set of boundary conditions can be used to form the following result:

$$y(x,t) = \sum_{i=1}^{\infty}\phi_i(x)q_i(t) \approx \sum_{i=1}^{n}\phi_i(x)q_i(t). \tag{3.92}$$

Truncation of the high-frequency dynamics by assuming a limited number of orthogonal modes can be performed in the same manner as for the previously analyzed linear

multi-mass system. The overall dynamic model with separated rigid and oscillatory parts is defined as

$$I\ddot{\varphi} = T_m, \qquad (3.93)$$
$$\ddot{q}_i + 2\xi_i\omega_i\dot{q}_i + \omega_i^2 q_i = \phi_i^{'}(0)T_m;\ i = 2..n,$$

where $\phi_i^{'}(0)$ is tangent of each bending mode at the link base,
I is overall moment inertia with respect to link base and
φ is rigid mode angular displacement of center of gravity,
q_i is modal amplitude of $i-th$ bending mode.

Transfer functions with a structure similar to lumped parameter systems can be obtained. For the collocated motor feedback, the output of system (3.94) is chosen as the clamped angle of the link base which is measured by motor encoder $\varphi_m = \varphi + \sum_{i=2}^{n}\phi_i^{'}(0)q_i$, which leads to the transfer function:

$$\begin{aligned} P_m(s) &= \frac{\varphi_m(s)}{T_m(s)} = \sum_{i=1}^{n}\frac{\phi_i^{'}(0)^2}{s^2+2\xi_i\omega_i s+\omega_i^2} = \qquad (3.94)\\ &= \frac{1/I\prod_{i=2}^{n}(s^2+2\xi_i\omega_i s+\omega_i^2) + s^2\sum_{i=2}^{n}\phi_i^{'}(0)^2\prod_{i\neq j}^{n}(s^2+2\xi_j\omega_j s+\omega_j^2)}{s^2\prod_{i=2}^{n}(s^2+2\xi_i\omega_i s+\omega_i^2)}. \end{aligned}$$

The resulting pole-zero pattern with alternating weakly damped pairs is similar to that of discrete systems (3.84). The system is always minimum phase [120]. The link tip dynamics (can be measured by an optical device) with the output chosen as $\varphi_t = \varphi + \sum_{i=2}^{n}\phi_i(l)q_i$ is described as:

$$\begin{aligned} P_t(s) &= \frac{\varphi_t(s)}{F_m(s)} = \sum_{i=1}^{n}\frac{\phi_i^{'}(0)\phi_i(l)}{s^2+2\xi_i\omega_i s+\omega_i^2} = \qquad (3.95)\\ &= \frac{1/I\prod_{i=2}^{n}(s^2+2\xi_i\omega_i s+\omega_i^2) + s^2\sum_{i=2}^{n}\phi_i^{'}(0)\phi_i(l)\prod_{i\neq j}^{n}(s^2+2\xi_j\omega_j s+\omega_j^2)}{s^2\prod_{i=2}^{n}(s^2+2\xi_i\omega_i s+\omega_i^2)}. \end{aligned}$$

Although the same structure is obtained (compared to the multi-mass lumped parameter model), the internal dynamics is different as unstable zeros typically appear, making the problem of tip stabilization more difficult [124].

Multi-mass resonant models in practical applications

The presented approach of modeling of flexible systems with oscillatory dynamics using multi-mass models can be applied in various engineering applications. The structure of

system matrices of the mass-spring-damper model may differ depending on the particular method of analytical or numerical modeling. However, the important properties of the modal transform and general characteristics of the resulting dynamics are preserved. The idea of modal coordinates and approximation of overall dynamics of the system by limited number of oscillatory modes is beneficial for the synthesis of low order controllers which are easier for design and implementation. The linearity of the model allows for the utilization of powerful techniques of linear control theory. Numerous examples of successful exploitation of linear multi-mass models can be found in related literature. The most important applications can be found in:

- **Industrial motion control systems** - The two-mass flexible model has a direct physical interpretation of a stiff system connected to the actuator by a compliant element (e.g. long shaft or harmonic gear). Representation of the first oscillatory mode is often satisfactory for the purpose of passive or active damping. Higher resonant modes can be added to capture more complex structure of the system or approximate a distributed elasticity. Wide ranges of applications can be found ranging from electrical drives control [90, 127, 128, 129, 130, 132, 133, 134], robotics [43, 68, 131], CNC machining [135], rolling mills [136], paper machines [137] or vibration control of rotor systems [91].

- **Active vibration control of weakly damped structures** - Tendon bridges, large telescopes, tall buildings or space satellites are examples of weakly damped systems with potential for the application of active vibration control [126, 138, 139]. Models obtained from FEM analysis or experimental data of higher order compared to industrial systems are usually needed to capture complex multivariable dynamics. The control system is often tailored to a particular application.

- **Automotive** - Multi-mass linear models can be used for the description of the dynamics of car suspension for the purpose of active or semi-active vibration control [126, 140, 141].

- **Micro-positioning systems** - Vibration damping problems arise in micro-actuator control of hard disk drives and other optical devices [72, 142, 143, 144], atomic force microscopy [35, 145] or medical applications.

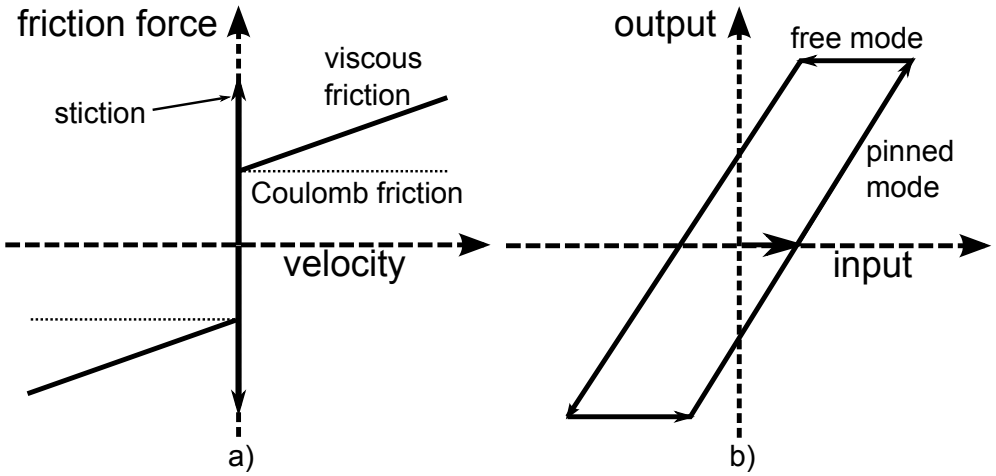

Figure 3.18: Nonlinear mechanics effects - a) friction b) backlash

3.4.3 Nonlinear dynamics in motion control systems

The assumption of linearity of the system dynamics is often violated by various imperfections in the mechanics of the controlled machine. The most typical nonlinear effects observed in the motion control systems are friction and backlash.

Friction is a physical phenomenon which appears at the interface of two surfaces which are in contact during a motion. It arises from fundamental electromagnetic interactions between the particles of the contacting bodies and manifests itself as a reactive force or torque which resists the relative motion. The basic properties of friction can be explained using a static characteristics which describes the magnitude of the resisting force as a function of relative velocity [146]. Typical shape of friction characteristics is shown in Fig. (3.18a). The overall friction force usually consists of Coulombic (or "dry") part which is constant for a given direction of motion and a viscous friction component which is growing proportionally with the rising velocity. Certain amount of stiction, a minimum level of a driving force which is needed to break the interface loose and start the motion, is usually observed in mechanical system. The viscous friction is generally advantageous for the motion control system as it naturally provides an additional damping which may improve stability of the closed loop or reduce the level of mechanical vibration in case of an oscillatory system. A system with viscous friction characteristics still behaves as a linear one and does not pose any problem for use of standard linear controllers. On the contrary, higher levels of Coulomb friction and stiction considerably affect the dynamics of the mechanical system. The introduced discontinuity causes problems with successful implementation of linear controllers in

the motion control loops and usually lead to a loss of precision of motion. While the Coulomb friction may have some stabilizing effect in the sense of vibration damping, the stiction typically causes a hunting phenomenon and rise of unwanted limit cycles (so called *stick-slip* effect).

Backlash is a lost motion or clearance caused by gaps between the mechanical elements of the machine such as teeth of gear trains or tappets found in valves. Its effect can be illustrated by input-output displacement diagram (Fig. 3.18b). Once a contact has been achieved between the individual elements and the motion direction is maintained, the mechanical coupling behaves as a rigid connection (so called pinned mode). Change of the direction of the driving force results in disconnection of the coupling causing a free motion of the input side mechanism. The position of the output side is indeterminate within the range of backlash. Large amount of backlash complicates precise positioning of the working mechanism and typically leads to steady state oscillations due to infinite alternation of pinned and free modes of motion in a controllers effort to reach the setpoint position. The negative influence of backlash is emphasized in the case of oscillatory mechanical system. Sudden acceleration during the free motion due to reduced inertia followed by hard hit at the moment of clearance adjustments can excite significant amount of vibrations.

The occurrence of significant amount of nonlinear friction and backlash can lead to severe deterioration of the closed loop performance in motion control systems. Their influence should be minimized by a proper mechanical design. However, re-design of the machine is often impossible or cost-ineffective and a correction has to be performed by means of the control system algorithms. Several methods has been proposed in the literature. The effect of stiction and dry friction can be reduced by adjustment of the pulse-width modulation of the actuator driving voltage or by dithering method [3, 146, 147, 148]. The goal is to maintain the motion before the stiction level is reached by injecting an additional high-frequency input signal. In the case that a good friction model (static or dynamic) is available, a model-based compensation scheme may be used. The friction model estimates the actual value of the friction force which is added to the control signal of a linear controller [89, 148, 149]. The friction characteristics may vary in time, usually due to changing temperature, normal force or mechanism position. An adaptive algorithm may be needed to cope with such fluctuations [150, 151]. The direct friction compensation is difficult in case of additional dynamics between the control input and the disturbance (typically flexible multi-mass system with load-side friction). The influence of backlash may be reduced by proper tuning of the feedback controller. Well damped response which prevents from frequent changes

in driving force direction results in smoother motion. The limit cycling due to friction or backlash may be avoided by a proper adjustment of the linear controller. Typical modifications include insertion of a dead-band to the feedback signal, controlled reset of the integrator during the slip phase or an additional logic which limits the velocity of the actuator in the steady state [133, 147].

3.4.4 Identification of flexible electro-mechanical systems

There is a wide variety of identification methods which have been developed for both time and frequency domain models [152, 153]. However, there are some specific issues which have to be taken into consideration in the case of mechanical systems identification:

1. Most of the methods assume a linear system to be identified. Mechanical systems typically contain some nonlinearities such as friction, backlash or hysteresis which may distort the expected linear response causing an error in the obtained linear models.

2. The identification experiment has to be planned carefully as the range of permissible motion is often limited.

3. Bandwidth of the excitation signal has to be chosen correctly with respect to desired closed loop bandwidth. Excitation of unmodelled high-frequency dynamics (e.g. higher nonlinear bending modes of the construction) can cause modelling errors.

4. Amplitude of the excitation signal has to be controlled precisely in the vicinity of the system resonance frequencies. Large amplitudes can excite a high amount of vibrations which can lead to damage of the equipment. Nonlinear characteristics of the compliant parts of the system can be emphasized causing modelling errors. On the contrary, low amplitudes can lead to the loss of information due to sensor noise or system nonlinearities.

5. A large number of typical industrial systems are unstable due to their working principle (robotic arms, vertical axes of CNC machine tools, manipulators with hanging loads) and their identification has to be performed in the closed loop. This can lead to problems with observability of the system dynamics and the experiment planning is more complicated.

The procedure of experimental identification consists of several subsequent steps:

- **Exciting signal selection**
- **Experiment & data collection**
- **Model selection & data fitting**
- **Validation**

Exciting signal selection

Two basic types of exciting signals are used extensively for motion control systems [94, 154, 155, 156]. **Pseudo-random binary sequence** (PRBS, sometimes called maximum length sequence) is a sequence of alternating steps with defined amplitude and varying length. It can be generated in hardware by means of shift register and properly chosen feedback from XOR gates (see Fig. 3.19a) or in software by programming the corresponding generator algorithm. The resulting binary sequence can be scaled to a proper amplitude $\pm A$ to produce a symmetrical excitation signal. Other important parameters of the generator are number of shift registers N and generator frequency $f_s[Hz]$. The PRBS has some important statistical properties advantageous for system identification:

- The signal is deterministic and periodic, its length is given by the number of registers as $P = 2^N - 1$. The property of periodicity allows to use averaging and windowing techniques of signal processing to achieve high precision of system response measurement.
- The autocorrelation function $R_{xx}(k)$ is a periodic unit impulse sequence which approaches periodic Kronecker delta function for large values of P. Therefore, the impulse function of an identified LTI system can be approximated as crosscorrelation function $g(k) \approx R_{xy}(k)$ between input and output signals. The frequency response of the system can be computed by performing the Fast Fourier Transform algorithm for the windowed impulse response.
- The spectral power density of the PRBS has a quasi-flat shape and is given by $S_{xx}(\omega) = \frac{A^2(P+1)sin^2(\pi k/P)}{P^2(\pi k/P)^2}$, where k is integer number defining the discrete line spectrum at frequencies $f = \frac{kf_s}{P}$ according to the chosen generator frequency [154]. The power at first harmonic is $A^2(P+1)/P^2$ and falls 3 dB at approximately at $f_s/3$. Proper choice of generator sampling f_s and amplitude A can be used for specification of effective excitation bandwidth.

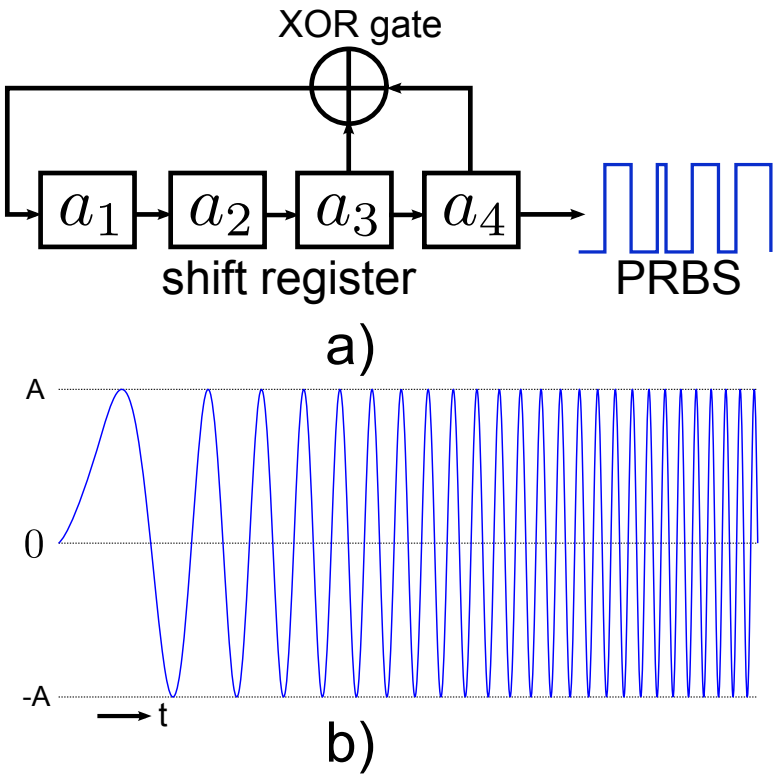

Figure 3.19: Suitable wideband excitation signals - a) pseudo-random binary sequence b) chirp signal

The produced PRBS is a broadband excitation signal which speeds up the execution of the experiment (compared to direct measurement of frequency response using harmonic inputs with varrying frequency). Various signal processing methods can be used for the computation of LTI models from the masured response. Correct setting of the generator with respect to system dynamics (location of resonance frequencies) is necessary in order to obtain suitable results [155].

Swept sine (or *chirp*) signal is a second type of wideband excitation signal which is suitable for identification of mechanical systems (Fig. 3.19b). It is described in the time-domain as $u(t) = Asin\{\omega(t)t\}$. The excitation bandwidth as well as the rate of frequency sweep is given by the choice of the time-varying function $\omega(t)$ (usually linear or logarithmic rate of change). When the sweep is sufficiently slow compared to system transient response, the actual frequency $\omega(t)$ may be considered as constant and one point of frequency response can be measured directly. The experiment is typically longer compared to the PRBS. However, the identification system designer has a larger freedom in determination of power spectrum of the excitation signal as the amplitude

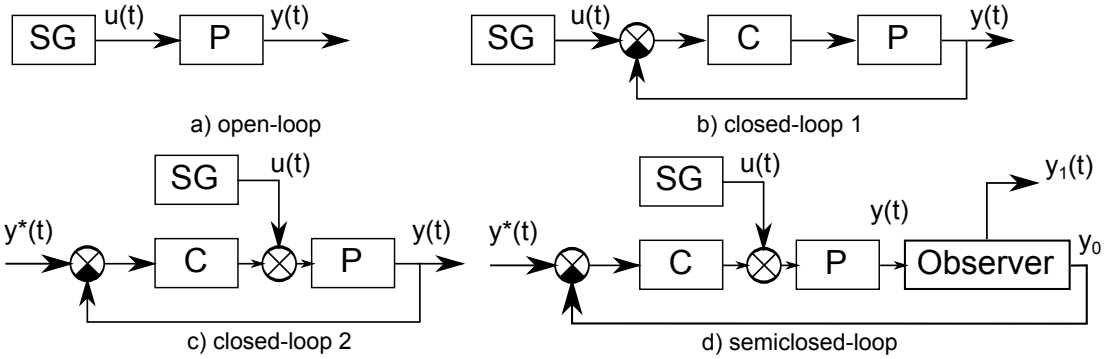

Figure 3.20: Different identification schemes (SG - signal generator, P - plant, C - compensator)

can be also varied in time as a function of frequency $A(t) = f(\omega)$. This is especially important for lightly damped mechanical systems because their gain changes considerable due to resonance and antiresonance behaviour. This topic is discussed in detail in the next chapter which deals with frequency identification using swept sine signals with varying amplitude. Multi-sine broadband signals in form $u(t) = \sum_{i=1}^{n} A_i cos(\omega_i t + \phi_i)$ are sometimes used as an alternative to chirp waveform.

Experiment and data collection

The experiment can be performed in open-loop or closed-loop configuration (3.20). Open-loop scheme (3.20a) is suitable for free-running systems (e.g. conveyor belts) or systems with large admissible range of motion. The signal generator produces the exciting signal (usually desired actuator torque/force), the system response in form of position or velocity signal is recorded for further processing and model synthesis. The open-loop scheme may be impractical for many other systems with limited workspace due to a danger of a collision of machine parts or in the case of unstable mechanical structures which would collapse due to the effect of gravity force (robotic manipulator arms). Closed-loop scheme with feedback compensator which stabilizes the system is preferable for such cases; the signal generator is connected to the feedback loop and produces the input disturbance or setpoint command signal (3.20b,c). Particular problem of the closed-loop scheme is, that the feedback compensator affects the harmonic content of input signal which is acting on the system and condition of sufficient excitation in a desired bandwidth may be violated leading to modelling errors. This drawback could be overcome with use of so-called *semi-closed loop scheme* (3.20d) which is proposed in the next chapter of the thesis. Only the DC value y_0 of the measured output

signal which is obtained from an observer is fed-back to the compensator such that the control actions do not counteract the excitation signal and the power spectrum density of the system input remains unaffected.

Model selection & data fitting

Most of the control design methods for motion control systems assume linear and time invariant dynamics of the system. Thus, linear time-domain or frequency domain models are usually chosen for data fitting. Discrete-time models are convenient for direct processing of sampled data from the identification experiment. General linear polynomial model can be described as

$$y(k) = \boldsymbol{G}(q, \boldsymbol{\Theta})u(k) + \boldsymbol{H}(q, \boldsymbol{\Theta})e(k), \tag{3.96}$$

where $u(k), y(k)$ is the input and output signal at time k, $e(k)$ is a disturbance signal (typically described as a sequence of random variables), q is the shift operator, $\boldsymbol{G}, \boldsymbol{H}$ are rational transfer functions in q which describe system and noise dynamics and $\boldsymbol{\Theta}$ is the vector of model parameters.

Particular choice of system model in the form of $\boldsymbol{G}(q, \boldsymbol{\Theta}) = \frac{\boldsymbol{B}(q)}{\boldsymbol{A}(q)}$ and noise model as $\boldsymbol{H}(q, \boldsymbol{\Theta}) = \frac{1}{\boldsymbol{A}(q)}$ leads to the well known ARX model structure which can be used for simple estimation by linear mean squares (LMS) algorithms. However, the LMS estimators give biased estimates of parameters $\boldsymbol{\Theta}$ in the presence of coloured measurement noise which is usually occuring in practical motion control applications. The measurement signal has to be filtered properly or a higher order model has to be used to reduce the error. Another option is to model the stochastic part of the system separately. Three basic model structures are widely used; ARMAX ($\boldsymbol{H}(q, \boldsymbol{\Theta}) = \frac{\boldsymbol{C}(q)}{\boldsymbol{A}(q)}$), Output-Error ($\boldsymbol{H}(q, \boldsymbol{\Theta}) = 1$) and Box-Jenkins models ($\boldsymbol{H}(q, \boldsymbol{\Theta}) = \frac{\boldsymbol{C}(q)}{\boldsymbol{D}(q)}$). Proper numerical method which estimates the noise model such as general *prediction error method* has to be used in this case. Alternatively, *instrumental variable* approach which does not require any specific noise model may be used. A suitable artificial signal which should be correlated with noise-free measurement signal and uncorelated with the noise has to be found to acquire nearly bias free estimates of model parameters.

Application of discrete polynomial models for identification of motion control systems can be found in the literature. The paper [157] compares LMS, IV and PEM algorithms for automatic commisioning of electrical drives. The works [156, 158] discuss the choice of proper model structure. The paper [159] proposes automatic identification procedure for the two-mass system. Three-mass system and recursive least

square identification algorithm is studied in [160]. The obtained discrete time models can be transformed to continuous time for utilization of continuous time control design methods. Typical order of discrete polynomial models varies from 10 to 20 to achieve sufficient precision and order reduction techniques are usually applied prior to controller synthesis [93, 157].

An alternative to time-domain modelling is a computation of the frequency response of the system from the measured data and its fitting to a properly chosen transfer function. The frequency response of the system can be defined by means of spectral density functions of the input and output signals

$$G(i\omega) = \frac{S_{uy}(i\omega)}{S_{uu}(i\omega)}, \tag{3.97}$$

where $S_{uu}(i\omega)$ is the power spectral desinty of the input excitation signal and $S_{uy}(i\omega)$ is cross-spectral density of the input and output signals.

Several signal processing methods can be used for the spectral analysis of the sampled signals. Corellogram methods use the results of the Wiener-Khinchin theorem which states that the power spectral density and the autocorrelation functions form a Fourier transform pair:

$$\begin{aligned} S_{uu}(i\omega) &= \int_{-\infty}^{\infty} R_{uu}(\tau)e^{-i\omega\tau}d\tau = \mathcal{F}\{R_{uu}(\tau)\}, \\ S_{uy}(i\omega) &= \int_{-\infty}^{\infty} R_{uy}(\tau)e^{-i\omega\tau}d\tau = \mathcal{F}\{R_{uy}(\tau)\}, \end{aligned} \tag{3.98}$$

where $R_{uu}(\tau) = \frac{1}{T}\int_0^T u(t)u(t+\tau)dt$ is the autocorrelation function of the input and $R_{uy}(\tau) = \frac{1}{T}\int_0^T u(t)y(t+\tau)dt$ is the cross-correlation of the input-output pair. The same relation holds for the discrete-time signals. The correlation functions can be computed from the sampled data and the Fourier transform is computed using the FFT (Fast Fourier Transform) algorithm. Technique of averaging can be used for periodic excitation signals to improve the signal-to-noise ratio (SNR). Application of windowing functions may be necessary for prevention of spectrum leakage due to finite length of the sampled sequences [155, 157, 161].

Periodogram methods use an alternative way of estimation of the spectral density functions. The periodogram of the sampled time sequence of input and output signals $u(k), y(k); k = 0..N$ is defined as:

$$\begin{aligned} P_{uu}(i\Omega) &= \frac{1}{N}|U(e^{i\Omega})|^2 = \frac{1}{N}U(e^{i\Omega})U^*(e^{i\Omega}), \\ P_{uy}(i\Omega) &= \frac{1}{N}Y(e^{i\Omega})U^*(e^{i\Omega}), \end{aligned} \tag{3.99}$$

where $\Omega = \omega T_s$ is the normalized angular frequency with respect to sampling time T_s and $U(e^{i\Omega}), Y(e^{i\Omega})$ is discrete Fourier transform of the input and output signals and the index * denote the conjugated complex frequency spectrum.

It can be shown, that the periodogram is an asymptotically unbiased estimator for the power spectral density for $N \to \infty$. Therefore the frequency response can be estimated as:

$$G(i\Omega) \approx \frac{P_{uy}(i\Omega)}{P_{uu}(i\Omega)}, \tag{3.100}$$

A smoothing of the computed periodograms is necessary in practice in order to reduce the spectral bias caused by sharp truncation of the signal sequences and high variance of the estimate. Averaging of multiple periodograms for higher number of data segments (known as Barlett's methods) or further improvement by overlapping of the segments and appllications of windowing functions (Welch method) are commonly used [162, 163].

The obtained set of frequency response points $\hat{G}(i\omega_k), k = 0..M$ can be used for computation of parameters of properly chosen transfer function $G(i\omega)$. This can be formulated as a nonlinear least squares problem of minimization of criterion

$$J = \sum_{k=0}^{M} |\hat{G}(i\omega_k) - G(i\omega_k)|^2 \tag{3.101}$$

with respect to the coefficients of the model $G(i\omega)$. Application of this method for the automatic commisioning of electrical drives can be found in [157, 161, 164, 165].

Standard time and frequency-domain methods assume linearity of the identified system. They may fail in the case of imperfect mechanics of the system and occurence of some typical nonlinearities such as friction, backlash or hysteresis. Special identification methods have been proposed in the literature for such cases. The survey [157] proposes a multistep procedure for subsequent identification of linear and nonlinear parts of the system dynamics. Extraction of typical characteristics of known nonlinearities from the obtained experimental data is performed in time and frequency domain. The resulting physical parameters of the system mechanics such as overal inertia, eigenfrequencies, shaft stiffness, backlash width or friction characteristics are computed and used for proper controller synthesis. The drawback of this approach is computational complexity and necessity of apriori specification of model structure. Special classification techniques such as self organizing feature maps may be used for determination of dominant nature of the system dynamics leading to decision about further steps of parametric identification [166]. Neural networks can be used as an

alternative [167, 168, 169]. The network is trained to match the input-output characteristics of the plant using the obtained experimental data. However, it is difficult to extract some knowledge about the system structure and dynamics from the computed network parameters (basis functions and their weights) and their use is usually limited to representation of static nonlinearity at the system input (mechanical friction). The basis function network can be used for direct friction compensation or for estimation of the unknown state variables of the nonlinear system [157, 169, 170, 171].

Model validation

Validity of the model is usually evaluated by comparison of measured and predicted output values $(y(k), \hat{y}(k))$ due to the excitation input signal which was used during the identification experiment. Simple measure is the root-mean-square of the output prediction error:

$$J_{RMS} = \sqrt{\frac{1}{N}\sum_{k=1}^{N}(y(k) - \hat{y}(k))^2} = \sqrt{\frac{1}{N}\sum_{k=1}^{N}\varepsilon(k)^2} \tag{3.102}$$

Statistical properties of the residuals $\varepsilon(k)$ may be evaluated to get a better insight to the model accuracy. In the casse of correct modelling, the autocorrelation function

$$R_{\varepsilon\varepsilon}(\tau) = \frac{1}{N}\sum_{k=1}^{N}\varepsilon(k)\varepsilon(k-\tau) \tag{3.103}$$

should ressemble a white noise signal while the cross-corelation

$$R_{\varepsilon u}(\tau) = \frac{1}{N}\sum_{k=1}^{N}\varepsilon(k)u(k-\tau) \tag{3.104}$$

should be small as possible [152].

3.4.5 Vibration control methods

The unwanted mechanical oscillations encountered in motion control applications can lead to a deterioration of quality of control and may cause an increased wear of the mechanical components of the system. They should be avoided by proper mechanical design of the machine or by appropriate adjustment of the control system during the commissioning phase. Three main approaches are used in practice to deal with the vibrations.

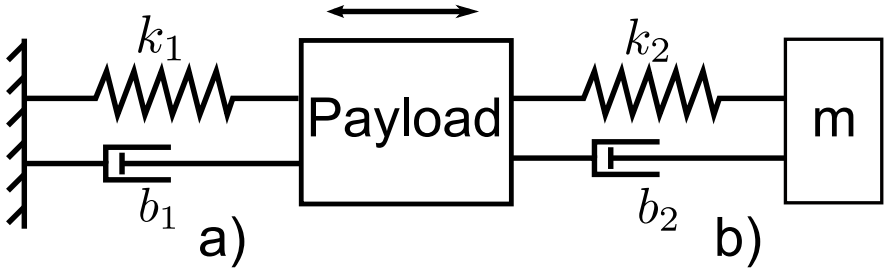

Figure 3.21: Mechanical damping - a) vibration isolator b) vibration absorber

Mechanical damping

Suitable adjustment of machine construction can be used to suppress the vibrations [172]. The resonance frequencies of the system may be shifted to higher values outside of the expected excitation bandwidth by increasing the stiffness of the critical parts of the mechanics. However, increase of the overall mass leads to higher construction costs, lower energy efficiency, slower dynamics of motion due to high inertias etc. Reinforcement of the machine construction can be problematic in certain cases due to inevitable use of flexible components such as ropes, gears with elastic parts or long manipulator arms. Additional mechanical elements which improve the suspension may be used. Passive isolation systems or *vibration isolators* contain mass, spring and damping elements which are inserted between a moving payload and a rigid frame or ground. The mass and spring cause energy dissipation and provide additional damping. They can be seen as a mechanical low-pass filters. Another approach is use of *vibration absorbers* which consist of a secondary inertia-spring system coupled to the payload. They generally act as a mechanical notch-filters. Proper tuning of the absorber parameters according to the resonance frequencies of the machine is needed for proper operation. Another issue is a proper placement of the machine with respect to stifness of the foundation and sub-soil.

Passive vibration control

Vibration damping may be provided by means of the motion control system. *Passive vibration control* (sometimes called *gain stabilization*) reduces the amplitude of the excitation signal (actuator force/torque) in the frequency range of the system resonances to prevent from excitation of vibrations. This is performed by implementing a low-pass or notch-filter in the motion control loop. The low-pass filters are easy to use as only the cut-off frequency has to be set. However, the phase-lag introduced by the filter

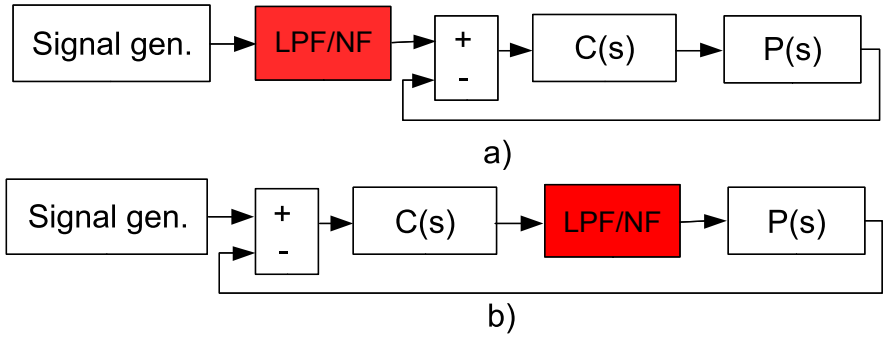

Figure 3.22: Passive vibration control (P - plant, C - compensator, LPF/NF - low-pass or notch filter) - a) open-loop b) close-loop configuration

limits the achievable bandwidth of the closed loop. Therefore, notch filters may be advantageous for low frequency resonances. The filter may operate in the open-loop configuration to shape the setpoint command which is obtained from the trajectory generator (see Fig. 3.22a) or it is connected in series with the feedback compensator (Fig. 3.22b). Most of the commercial servo-drive units offer this capability. Usually a two-pole two-zero IIR filter is imlemented in the feedback loop. Its transfer function is defined as:

$$NF_1(s) = \frac{s^2 + 2\xi\omega_n s + \omega_n^2}{s^2 + 2\xi_d\omega_n s + \omega_n^2},\ \xi_d > \frac{\sqrt{2}}{2}. \tag{3.105}$$

The filter zeros are set to cancel the weakly damped poles of the system given by the corresponding values of ω_n, ξ and they are replaced by the well damped pole-pair with specified damping ξ_d. The feedback compensator is designed for the resulting damped system to obtain a stable closed loop. Higher degree-of-freedom is available with use of so-called bi-quad filter. Its transfer function is given as

$$NF_2(s) = K\frac{s^2 + 2\xi_z\omega_z s + \omega_z^2}{s^2 + 2\xi_d\omega_d s + \omega_d^2}, \tag{3.106}$$

with arbitrarly chosen gain, zero and pole location. Complete zero-pole cancelation of the bi-quad terms of the system resonance and antiresonance can be achieved (see transfer function of the two-mass and multimass systems 3.58). However, vibration damping is effective only at the motor side whereas the attached load motion remains oscillatory. The bi-quad filter may be alternatively used as an extension of the feedback compensator (usually a simple PI controller in the velocity loop) which increases a number of free parameters allowing a higher-order compensator design.

An alternitave way of the notch filter design is a so called *input shaping method* or *zero-vibration shaping*. The goal is to design a FIR shaping filter which modifies

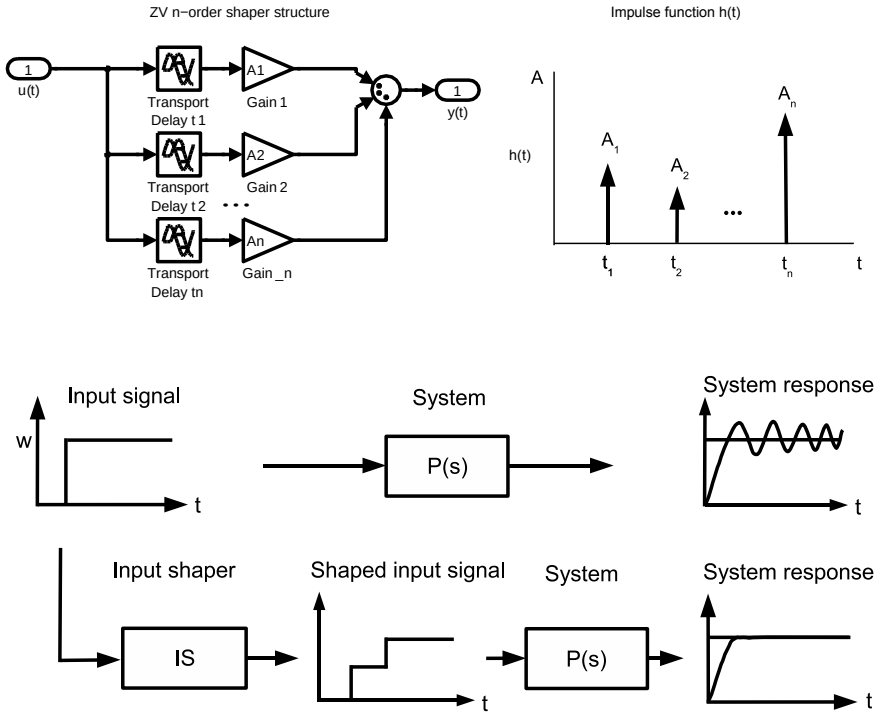

Figure 3.23: Zero Vibration input shaping filter - structure, impulse function and principle of operation

an input signal of an underdamped oscillatory system in such a way that the level of excited vibrations is minimal (3.23) The idea of shaping filter consisting of time delay elements was presented by Smith [173], followed by number of works which further extended this concept [54, 56, 174, 175, 176]. A general n-pulse input shaping filter can be described in the form of impulse function

$$h_s(t) = \sum_{i=1}^{n} A_i \delta(t - t_i), 0 \leqslant t_1 < t_{i+1}, A_i \neq 0, \tag{3.107}$$

where A_i means amplitude of the i-th pulse and δ is dirac function with time shift t_i.

The response of the shaper in time domain can be determined by performing the convolution operation with the continuous input signal:

$$v(t) = \int_{-\infty}^{\infty} h_s(\tau) u(t-\tau) d\tau = \int_{-\infty}^{\infty} \left(\sum_{i=1}^{n} A_i \delta(\tau - t_i) \right) u(t-\tau) d\tau = \sum_{i=1}^{n} A_i u(t - t_i). \tag{3.108}$$

It can be seen, that the filter has the form of sum of time delayed values of the input weighted by coefficients A_i. The goal of the filter design is to choose the values of amplitudes A_i and time delays t_i in such a way that after the last pulse has been led to the system, the amplitude of the excited residual vibrations is equal to zero. This can be illustrated for the simplest 2-pulse ZV filter and a second-order underdamped system.

Consider a linear system described by transfer function $P(s)$ and impulse function $h_p(t)$:

$$P(s) = \frac{\omega^2}{s^2 + 2\xi\omega s + \omega^2},\ h_p(t) = \frac{\omega}{\sqrt{1-\xi^2}} e^{-\xi\omega t} \sin(\omega_d t). \tag{3.109}$$

The two-pulse shaper impulse function is

$$h_s(t) = A_1\delta(t - t_1) + A_2\delta(t - t_2), \tag{3.110}$$

leading to overall impulse response of serial connection of the shaper and plant $P(s)$ in the form

$$h(t) = A_1 h_p(t - t_1) \cdot \mathbb{1}(t - t_1) + A_2 h_p(t - t_2) \cdot \mathbb{1}(t - t_2), \tag{3.111}$$

where $\mathbb{1}(t)$ is the Heaviside step function.

For the time $t > t_2$, it holds

$$h(t) = A_1 h_p(t - t_1) + A_2 h_p(t - t_2) = \frac{\omega}{\sqrt{1-\xi^2}} e^{-\xi\omega t} \sqrt{C^2 + S^2} \sin(\omega_d t - \psi), \tag{3.112}$$

where

$$C = \sum_{i=1}^{2} A_i e^{\xi\omega t_i} \cos(\omega_d t_i),\ S = \sum_{i=1}^{2} A_i e^{\xi\omega t_i} \sin(\omega_d t_i),\ \psi = \arctan\frac{S}{C}. \tag{3.113}$$

It can be seen, that for minimizing the level of residual vibrations after the second pulse, the following expression has to be fulfilled:

$$C^2 + S^2 = 0. \tag{3.114}$$

With proper choice of time delay values $t_1 = 0,\ t_2 = \frac{\pi}{\omega_d}$, the equation reduces to the condition

$$\left(A_1 - A_2 e^{\xi\omega\frac{\pi}{\omega_d}}\right)^2 = 0. \tag{3.115}$$

A next condition for unitary static gain $A_1 + A_2 = 1$ in conjunction with (3.115) give a set of algebraic equations which lead to the solution in the form of filter parameters:

$$\begin{gathered} A_1 = \frac{1}{1+K},\ A_2 = \frac{K}{1+K},\ K = e^{-\frac{\xi\pi}{\sqrt{1-\xi^2}}} \\ t_1 = 0,\ t_2 = \frac{\pi}{\omega_d},\ \omega_d = \omega\sqrt{1-\xi^2}. \end{gathered} \tag{3.116}$$

For the proper function of the ZV filter, the exact value of natural frequency and damping coefficient of the oscillatory part of the system has to be known. The error in the system model results in non-zero residual oscillations. If the model of the system cannot be determined exactly, additional robustifying condition can be added in the form $\frac{\partial}{\partial\omega}\left[C^2 + S^2\right] = 0$ leading to a three-pulse ZVD (zero vibration derivative) filter. The drawback is an increased filter length causing more delay in the signal path. Other types of robust shapers as well as generalisations of this approach have been reported in the literature [175, 177, 178]. Multimode input shapers can be designed for higher number of resonance modes [176].

The zero vibration filters have been used in various motion control applications such as overhead cranes, flexible robotic manipulators, CNC machine tools, voice-coil motors or spacecrafts [118, 176, 177, 179, 180]. The main advantage compared to conventional notch filters is the finite impulse response which is advatageous for the setpoint command shaping (the overall duration of the motion is known in advance), possibility of infinite damping of certain frequency in case of disrete time implementation and lower phase-lag introduced in the signal path [89, 181]. A particular disadvantage of the standard signal shapers is a limited degree of freedom for the control system engineer. For a chosen filter type, the natural frequency and damping of the system are usually the only design parameters. This thesis presents a novel approach to four-impulse signal shaper parameterization which covers a whole set of admissible filters. Set of two design parameters with clear physical meaning is provided for the filter tuning.

The notch-filtering methods generally require precise knowledge of the location of the system resonance frequencies. Modelling errors can lead to detuning of the controller and loss of the vibration damping functionality. There is a phenomenon of so called *pole-flipping* which occurs in the case of imperfect cancelation of system poles and filter zeros in the closed-loop configuration [126]. The weakly damped poles enter the right half-plane causing the instability of the closed loop. Even when correctly

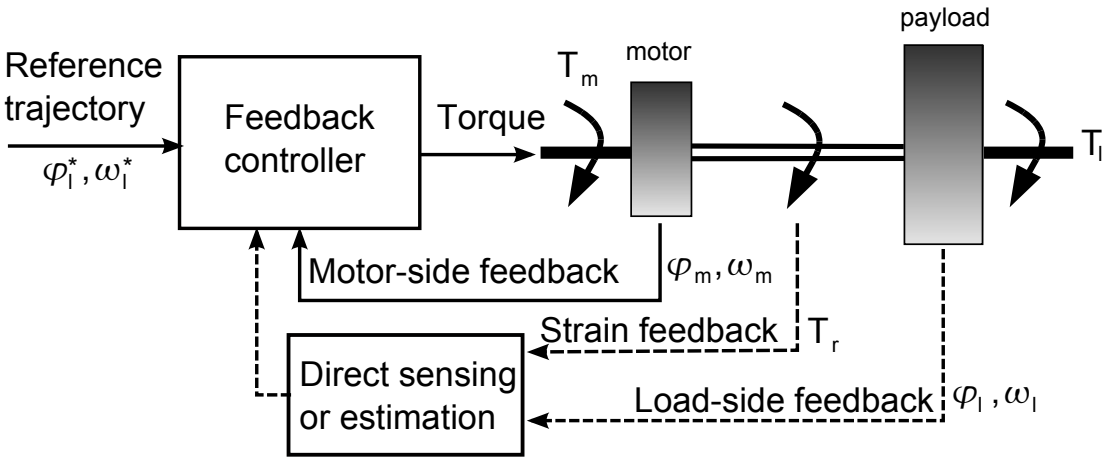

Figure 3.24: Active vibration control - flexible mechanical system (dashed line - optional feedback)

tuned, the vibrations excited by an exogennous sources (e.g. a cutting force of a machine tool or a friction load torque) cannot be damped because of loss of controllability due to pole cancelation by the filter.

Active vibration control

Active vibration control methods try to alter the oscillatory dynamics of a flexible mechanical system by means of a proper feedback controller (Fig. 3.24). Provided that the full state information is available (i.e. both motor and load position and velocity and/or the shaft reaction torque in the case of the two-mass system), state feedback controller may be used to relocate the weakly damped poles of the system and suppress the resonance behaviour. This requires the shaft sensors to be installed at both motor and load side. Only motor-side measurement is available in most practical applications which complicates the procedure of the controller design. The inaccessible states of the system may be reconstructed using an observer. However, its application may be difficult due to model uncertainty, time-varying dynamics, measurement noise effects (quantization, electromagnetic disturbances due to motor PWM or sensor electronics) or nonlinearities in the mechanical subsystem. The advantage compared to the passive methods is ability to actively suppress the vibrations caused by external disturbances (load torque/force). The disadvantage is a risk of instability due to introduction of the feedback. Typical problem related to flexible systems is so called *spill-over effect*. The unmodeled high-frequency dynamics (typically higher resonance modes) may be

excited by the feedback controller causing the instability of the closed loop. Therefore, the goal is to suppress a certain number of resonances and achieve a sufficient high-frequency roll-off of the compensator in order to prevent from excitation of unmodeled dynamics.

Numerous approaches to active vibration control have been proposed in the literature for the motion control of flexible mechanical systems. Systematic redesign of velocity PID controller using partial pole-placement method is presented in [182]. One of three closed-loop pole pattern is chosen based on system resonance ratio, good vibration damping is achieved for certain range of plant parameters. Nonlinear H_∞ optimization is used for computation of PID gains in [183]. Use of direct measurement of shaft torque or load-side variables as an additional feedback signal was used in [92, 184, 185, 186], comparative study of these methods is presented in [187] and [188]. Improvement of robustness and performance is reported compared to conventional PID control. State space feedback and LQR control in conjunction with Kalman filter for estimation of load motion is proposed in [134]. Good closed-loop performance is achieved provided that proper weighting matrices of the quadratic criterion function have been chosen. Output feedback H_∞ controller is designed in [133, 189]. Again, the weighting scheme used in H_∞ optimization is crucial for proper function of the compensator. Modification of standard disturbance observer method for flexible system called *resonance-ratio control* uses the measured or estimated reaction torque feedback to suppress the vibrations [86, 190]. The vibration damping works well provided that the reaction torque can be measured or estimated effectively, maximum achievable closed-loop bandwidth is limited by the value of system anti-resonance frequency. Sliding-mode control can be used as well. The most difficult task is a design of chattering-free algorithm suitable for discrete-time implementation and estimation of the unavailable states which are necessary for computation of the switching function [129, 191, 192]. Model-based predictive control is designed and compared to PID control in [193, 194]. Advantage in closed-loop performance comparable to the state space methods is reported, there is no need for additional observer design and the actuator limits are handled directly in the control algorithm. The drawback is a sensitivity to modelling errors and high computational complexity of the predictive controller. Soft-computing methods including neural networks, fuzzy logic and expert systems have also been proposed for the motion control problems [195, 196, 197]. Neural network can be used as a nonlinear mapping function for modelling and compensation of nonlinearities such as friction or as an nonlinear estimator of the unknown states. Its learning

capability may be usefull for online adaptation of control algorithm in the case of time-varying dynamics of the system. The main problem is the chose of network structure and its training. Global stability of the closed loop is difficult to prove compared to the analytical methods. Occurrence of significant nonlinearities in the mechanical system can deteriorate the performance of the model-based controllers counting on linear plant models. Systematic design for a more complex nonlinear model may bring an improvement in quality of control [133, 198]. Extensive survey of existing methods is given in [199].

3.5 Summary

Elasticity of the materials and components which are being used for construction of the motion control systems can cause severe difficulties with mechanical vibrations. The phenomenon of oscillations is emphasized with increasing demands for motion precision and higher bandwidth of the control loops which may overlap with the resonance frequencies of the mechanical construction. Approximation of system behaviour by an idealized rigid dynamic model is insufficient and more sophisticated methods are needed for a systematic design of the mechanics and control system algorithms.

4

Thesis aims and objectives

The main goal of the thesis is a development of robust and reliable methods for automatic commissioning of velocity and position motion control loops applicable for electromechanical systems with oscillatory dynamics. This fundamental problem is encountered in numerous industrial applications of motion control systems and it is not sufficiently solved in the commercially available automation products. The aim is to provide algorithms for automatic identification and robust controller synthesis suitable for direct implementation in today's power electronics and real-time control systems. Individual research goals are formulated further in this chapter.

Automatic identification of oscillatory electromechanical systems

Advanced vibration control methods require precise information about the system dynamics. The idealization in form of a rigid multi-body model is insufficient for a design of suitable model-based compensators. Especially the location of system resonance and antiresonance frequencies is fundamental for successful implementation of vibration damping techniques. The physical modelling approach usually fails due to the a priori unknown physical properties of the controlled mechanical system (e.g. friction characteristics or stiffness of the construction and drivetrain components). An automatic identification procedure which considerably simplifies and speeds up the machine commissioning is essential for industrial applications.

Most of the academic methods for the system identification rely on linearity of the observed system. The presence of nonlinearities typical for mechanical systems such as friction or backlash may lead to unsatisfactory results. Identification of linear part of the system dynamics may be advantageous even in the case of nonlinear mechanics

as the linearity of the acquired model makes it suitable for a consequent step of robust compensator design in a powerful framework of linear systems. The newly developed method should be applicable for a closed-loop identification which is necessary for certain applications of mechanical systems with hanging loads.

The main goals may be summarized as follows:

- Development of an automatic identification method suitable for oscillatory mechanical systems which can be described by a proper class of linear models
- Computation of the linear part of the system dynamics
- Adaptation of the algorithm for the case of nonlinear mechanics
- Closed-loop identification scheme for unstable mechanical configurations
- Implementation of the method in the form of a functional block suitable for direct application in a real-time control system

Feedforward vibration control using input-shaping method

As was explained in the previous chapter, the feed-forward passive vibration control methods using the command-shaping techniques may be applied to a large variety of motion control problems. The main advantage is a simple implementation in the control system and no requirement for additional instrumentation or observer design for the load-side feedback. A simpler compensator may be used for the actuator control leading to a faster commissioning of the motion control loop.

The Zero Vibration shapers offer an interesting alternative to the conventional low-pass and notch-filters with many advantages such as lower phase-lag, finite impulse response and a higher level of achievable damping. However, standard design methods offer a limited possibility of shaper parameterization which is usual in the case of standard IIR filters, i.e. specification of the width and shape of the stop-band in the frequency-domain. Most of the theoretical works describe the continuous-time filters and do not focus on the real-time implementation aspects. Therefore, in regards to this problem, the main goals of the thesis are:

- Development of a robust input shaping filter with a set of suitable design parameters with a clear physical meaning
- Discrete-time implementation of the algorithm in the form of a functional block

Active vibration control of multi-mass systems

The feedback vibration control methods are necessary for high-fidelity systems with demanding requirements for the closed-loop bandwidth and motion precision. They are inevitable for the implementation of the active vibration damping functionality (compensation of exogenous disturbances). Traditional design methods which were developed for rigid mechanical systems such as symmetric or modulus optimum fail in the case of oscillatory dynamics and a systematic model-based approach is needed to obtain suitable results.

Although the PID cascade control structure is still used in the overwhelming majority of commercial motion control systems, this control scheme has received quite a little attention in the academic research community. The goal of this thesis is to provide an analysis of the capability of this control strategy in terms of active vibration control and a development of a systematic procedure for the tuning of the PID gains which could be used for the existing motion control systems. An advantage of using more complex controllers should be evaluated as well.

The thesis is focused on the motor-side feedback control with no additional load-side instrumentation as this is the most frequent case in industrial applications. However, the advantage of additional load feedback signal is studied as well.

An important aspect of practical usability of control design method is a simple tuning procedure. It is unrealistic to suppose that an average engineer working in the industrial practice has a deep understanding of modern control theory and is able to tune the weighting filters of the H_∞ optimization algorithm, adjust the weights of the quadratic criterion of the LQ regulator or estimate the noise model in the Kalman filter. The goal is to provide a reliable methods which would automate most of the tasks involved in the procedure of controller design and which offer a minimum number of physically intuitive parameters for a simple fine-tuning on the real plant. The main objectives are summarized as follows:

- Analysis of achievable quality of control of the oscillatory multi-mass systems using the conventional cascade PID control structure
- Automatic procedure for PID gains tuning
- Analysis of performance improvement with use of higher order controllers
- Feature-based parameterization of the proposed closed control schemes

4. THESIS AIMS AND OBJECTIVES

The following chapters of the thesis present new theoretical and practical results achieved in the field of motion control of flexible electro-mechanical systems. The individual parts are devoted to automatic system identification, feed-forward vibration damping using input-shaping filters and active vibration control methods applied to oscillatory multi-mass systems, respectively.

5

Automatic identification of oscillatory electromechanical systems

The system identification procedure is a key part of the automatic commissioning system as it provides a suitable mathematical model for the consequent step of compensator design. Particular issues related to mechanical system identification were discussed in the previous chapter. This chapter presents a new approach to frequency identification of oscillatory electromechanical systems. Algorithms for the generation of the excitation signal, data acquisition and model synthesis are described in detail. Continuous-time description of the proposed method is also presented for the sake of clarity. The problem of discrete-time implementation of the algorithms is discussed in a separate subsection. The presented methods extend a former work of [200]. Some of the achieved results were published in [201].

5.1 Exciting signal generation

The first step of an identification experiment is the selection of a proper excitation signal. Various suitable testing signals such as pseudo-random binary sequence, other step series, chirp signal or multiple harmonics sine waves were proposed in the literature (see the survey of methods provided in Chapter 3). The main advantage of such signals is the wideband excitation of the system dynamics which reduces the amount of time necessary for the execution of the experiment. However, this advantage can be fully exploited only in the case of a linear plant. The presumption of linearity is often violated by the occurrence of nonlinearities such as friction, backlash or hysteresis. These nonlinearities may distort the frequency spectrum generated by the system and the advantage of a broadband input is lost because the information about the frequency response of the linear part of the system is corrupted. The input signal can

excite a high-frequency dynamics (higher resonance modes, feedback filters, actuator lag, nonlinear bending modes of the mechanics) which can complicate a procedure of data-fitting to low order models suitable for controller design. Typical property of weakly damped resonant mechanical systems is the shape of its frequency response which contains sharp peaks and notches related to resonance and antiresonance frequencies. Its magnitude changes significantly over the important frequency range and the exciting signal should deal with these changes by adapting its amplitude in order to extract most of information from the experiment. Low amplitude wideband signal can lead to loss of information in the vicinity of system antiresonance due to measurement noise whereas high amplitudes can excessively excite the resonance dynamics leading to violation of velocity or position limits or a physical damage to the system.

All the issues discussed above are taken into consideration in the proposed algorithm. **A swept sine wave with variable amplitude, frequency and DC component is selected as the exciting signal**. The signal generator can be described by state space model

$$\begin{aligned} \begin{bmatrix} \dot{x}_1 \\ \dot{x}_2 \end{bmatrix} &= \begin{bmatrix} 0 & \omega(t) \\ -\omega(t) & 0 \end{bmatrix} \begin{bmatrix} x_1 \\ x_2 \end{bmatrix}; x(0) = \begin{bmatrix} 0 \\ 1 \end{bmatrix}, \\ y(t) &= [A(t)\ 0]\, x(t) + u_0(t), \\ \omega(t) &= \omega_b e^{s_c t} \in \langle \omega_b, \omega_f \rangle, \end{aligned} \tag{5.1}$$

where $\omega(t)$ is actual frequency of the generated sinusoidal output,
$A(t)$ is output amplitude,
$\langle \omega_b, \omega_f \rangle$ defines the interval for the frequency sweep,
s_c is a sweep coefficient which defines the rate of frequency variation and
u_0 is a DC component of the output.

The frequency of the generated output is varied in time in the logarithmic scale over the chosen frequency range. The resulting output of the generator is given by the equation:

$$y(t) = A(t) sin\{\int_0^t \omega(\tau) d\tau\} + u_0(t). \tag{5.2}$$

The generated excitation signal is used as a setpoint value for the actuator (usually the commanded torque or current for the inner loop of the electrical drive). The amplitude $A(t)$, frequency $\omega(t)$ and mean value $u_0(t)$ of the generated signal is varied in time by an *adaptation algorithm* which controls the identification experiment (see Fig. 5.1). The measured output signal (actual motor or load position/velocity) is processed

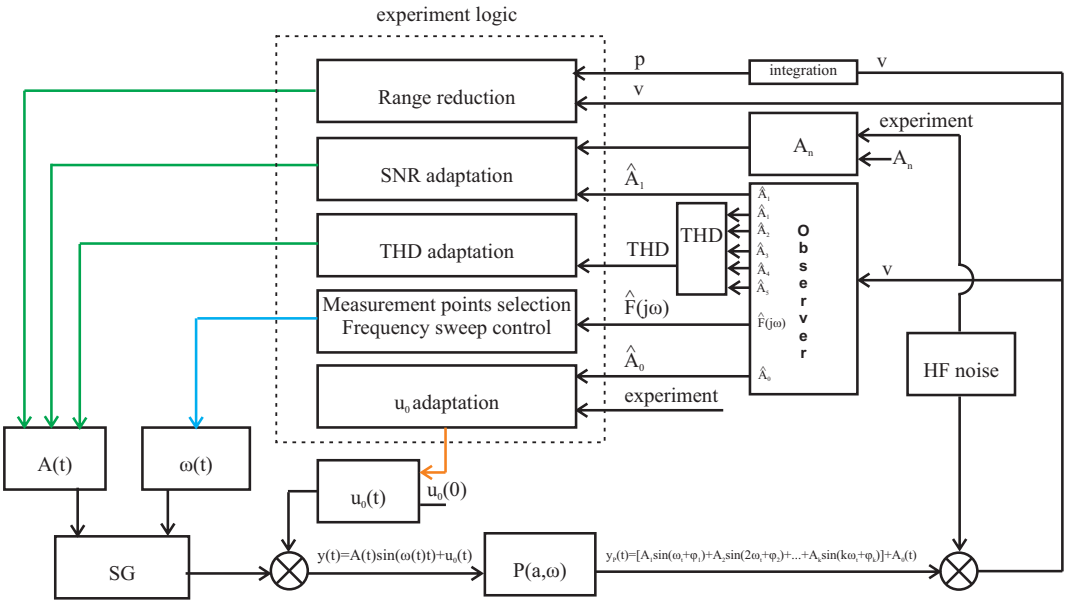

Figure 5.1: Proposed frequency identification algorithm

in an observer which estimates the system frequency response. The presence of higher harmonics which is measured by the total harmonic distortion index (THD) is used for the detection of nonlinearities and proper adaptation of the generator amplitude. The range of the excited motion is watched and the amplitude is also adjusted to avoid a possible collision in the system mechanics. Signal to noise ratio (SNR) is computed to estimate the quality of the excitation at a particular frequency. The algorithm which controls the experiment selects proper time instants at which the frequency sweep stops for a measurement. A user-specified number of points of the frequency response is acquired for further processing in a model fitting algorithm.

5.2 Estimation of system frequency response

Provided that the adaptation of the generated excitation signal (5.2) is stopped in a particular moment, the variables A, u_0, ω become constant resulting in steady state output response of the system y_p (after a transient state excited by the input signal variation has vanished). This response is periodic and for the case of an ideal linear plant, we may write:

$$y_p(t) = A_0 + A_1 sin(\omega t + \varphi_1), \tag{5.3}$$

where A_0 denotes the DC component of the output and A_1, φ_1 express the amplitude and phase shift of plant response with respect to the excitation signal.

For a general nonlinear system, the output signal may contain an arbitrary number of higher harmonics due to the effects of the nonlinear mechanics. The periodic response can be expressed by the Fourier series in the amplitude-phase form:

$$y_p(t) = A_0 + A_1 sin(\omega t + \varphi_1) + \sum_{k=2}^{\infty} A_k sin(k\omega t + \varphi_k), \tag{5.4}$$

where ω is the fundamental frequency of the exciting input signal and A_k, φ_k correspond to the amplitude and phase of the higher harmonics.

The mechanical systems typically behave as low-pass filters due to physical properties of the inertial loads on the motor and load side which attenuate high-frequency portion of the driving torques or forces. Therefore, it is reasonable to assume that the output signal is band-limited and a finite number of lowest harmonics can be considered for its approximation. The equation (5.4) reduces to a finite series and an observer can be designed to reconstruct a limited number of first harmonics of the signal.

State observer with an inner model of the first five harmonics and the DC component is proposed. It can be described by a linear state space model in the form of:

$$\begin{bmatrix} \dot{\hat{z}}_1 \\ \dot{\hat{z}}_2 \\ \dot{\hat{z}}_3 \\ \dot{\hat{z}}_4 \\ \dot{\hat{z}}_5 \\ \dot{\hat{z}}_6 \\ \dot{\hat{z}}_7 \\ \dot{\hat{z}}_8 \\ \dot{\hat{z}}_9 \\ \dot{\hat{z}}_{10} \\ \dot{\hat{z}}_{11} \end{bmatrix} = \begin{bmatrix} 0 & \omega(t) & 0 & 0 & \cdots & 0 & 0 \\ -\omega(t) & 0 & 0 & 0 & \cdots & 0 & 0 \\ 0 & 0 & 0 & 2\omega(t) & \cdots & 0 & 0 \\ 0 & 0 & -2\omega(t) & \ddots & \cdots & 0 & 0 \\ \vdots & \vdots & \vdots & & 0 & 5\omega(t) & 0 \\ 0 & 0 & 0 & 0 & -5\omega(t) & 0 & 0 \\ 0 & 0 & 0 & 0 & 0 & 0 & 0 \end{bmatrix} \begin{bmatrix} \hat{z}_1 \\ \hat{z}_2 \\ \hat{z}_3 \\ \hat{z}_4 \\ \hat{z}_5 \\ \hat{z}_6 \\ \hat{z}_7 \\ \hat{z}_8 \\ \hat{z}_9 \\ \hat{z}_{10} \\ \hat{z}_{11} \end{bmatrix} +$$

$$+\begin{bmatrix} k_1\{\omega(t)\} \\ k_2\{\omega(t)\} \\ k_3\{\omega(t)\} \\ k_4\{\omega(t)\} \\ k_5\{\omega(t)\} \\ k_6\{\omega(t)\} \\ k_7\{\omega(t)\} \\ k_8\{\omega(t)\} \\ k_9\{\omega(t)\} \\ k_{10}\{\omega(t)\} \\ k_{11}\{\omega(t)\} \end{bmatrix} \epsilon, \hat{y} = \begin{bmatrix} 1 & 0 & 1 & 0 & 1 & 0 & 1 & 0 & 1 & 0 & 1 \end{bmatrix} \begin{bmatrix} \hat{z}_1 \\ \hat{z}_2 \\ \hat{z}_3 \\ \hat{z}_4 \\ \hat{z}_5 \\ \hat{z}_6 \\ \hat{z}_7 \\ \hat{z}_8 \\ \hat{z}_9 \\ \hat{z}_{10} \\ \hat{z}_{11} \end{bmatrix}, \epsilon = y_p - \hat{y}, \tag{5.5}$$

with a corresponding matrix notation

$$\begin{aligned} \dot{\hat{\boldsymbol{z}}} &= \boldsymbol{A_o}(t)\hat{\boldsymbol{z}} + \boldsymbol{k}(t)\epsilon, \\ \hat{y} &= \boldsymbol{C_o}\hat{\boldsymbol{z}}, \end{aligned} \tag{5.6}$$

where $\hat{\boldsymbol{z}} = [\hat{z}_1, \hat{z}_2, ..., \hat{z}_{11}]^T$ is the vector of observed states,
$\boldsymbol{A_o}, \boldsymbol{C_o}$ denote state and output matrices,
$\hat{y}$ is observer output which tracks the measured signal,
ϵ is the observer output error and
$\boldsymbol{k}(t) = [k_1, k_2, ..., k_{11}]^T$ is the time-varying vector of innovation feedback gains.

The estimator has a structure of a linear time-varying system which adapts its dynamics in order to keep synchronization with the observed plant output due to variable frequency of the excitation signal generator. The properties of the observer are discussed separately for the measurement and sweep phase of the identification experiment.

Measurement phase algorithm

In the phase of frequency response measurement, the generator stops the frequency sweep and the variable ω remains constant and the estimator dynamics reduces to a linear time-invariant system. Considering the first five harmonics of the plant output (5.4), the observer error dynamics of the estimator (5.5) is governed by the equation:

$$\dot{\boldsymbol{\varepsilon}} = (\boldsymbol{A_o} - \boldsymbol{k}\boldsymbol{C_o})\boldsymbol{\varepsilon} = \boldsymbol{A_o^{cl}}\boldsymbol{\varepsilon}, \tag{5.7}$$

where $\boldsymbol{\varepsilon} = \hat{\boldsymbol{z}} - \boldsymbol{z}$ is the observer error vector and $\boldsymbol{A_o^{cl}}$ is the closed-loop state matrix.

Since the pair $[\boldsymbol{A_o}, \boldsymbol{C_o}]$ is observable, arbitrary error dynamics may be assigned by appropriate choice of the observer gains. The goal of the estimator design is to select a

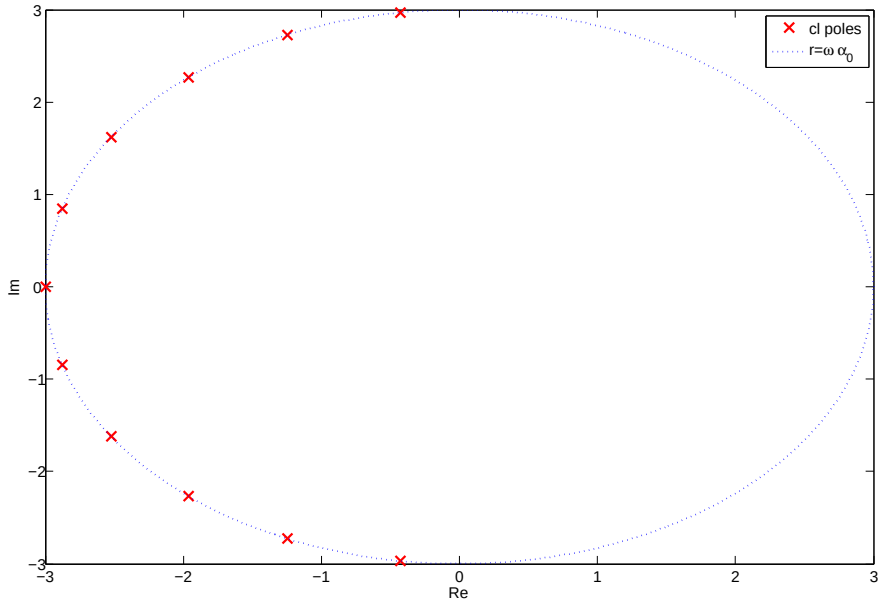

Figure 5.2: Observer closed-loop poles - Butterworth pattern

suitable location of the closed-loop poles for the system (5.7). The number of degrees of freedom should be reduced for the practical implementation, preferably to a single design parameter. Two alternatives for the observer synthesis are proposed.

Butterworth pattern offers a possible scheme for the closed-loop pole placement. The motivation for this choice comes from the fact that the observer dynamics between measured and estimated output should resemble low-pass filter characteristics in the frequency domain. Low frequency component of the measured signal should pass to the estimated output without significant change in phase and amplitude to ensure good tracking and convergence of the state estimates to their true values. The high frequency part of the signal should be attenuated as the measurement noise is usually dominating in this frequency band. Therefore, the Butterworth low-pass filter offers a natural choice for the closed loop poles due to its property of maximum flatness of the frequency response and smooth transition between the pass-band and stop-band. The number of user-specified design variables is reduced to a single parameter which specifies the filter bandwidth.

The Butterworth pattern of closed-loop poles s_m for the observer (5.5) is obtained in the form of:

$$s_m = \alpha_0 \omega e^{\frac{i(2m+11-1)\pi}{2 \cdot 11}};\ m = 1, 2, 3, ..., 11. \tag{5.8}$$

The poles are located on a circle in the complex plane with the radius given by the product of actual value of frequency ω and the coefficient α_0 which defines the relative observer bandwidth with respect to fundamental frequency of the measured signal (Fig. 5.2). The observer gain vector $\boldsymbol{k}$ which assigns the given structure of poles (10.1) can be computed analytically using the pole-placement method. This leads to closed-form formulas in the form:

$$k_m = k_m^0(\alpha_0)\omega;\ m = 1, 2, 3, ..., 11, \tag{5.9}$$

where $k_m^0(\alpha_0)$ are 11^{th} order polynomials of α_0. A complete printout of the analytical solution can be found in the appendix (10.1). Thus, the observer gains are linear with respect to the actual value of frequency ω for a particular choice of α_0. The polynomials $k_m^0(\alpha)$ can be evaluated only once in the initialization phase of the algorithm and the values of observer gains are obtained from simple multiplication by actual frequency ω. This leads to significant reduction of computational burden in the real-time implementation of the algorithm.

The frequency spectrum of the measured periodic output signal $y_p(t)$ and consequently an estimate of the system frequency response can be computed from the observed states $\hat{\boldsymbol{z}}(t)$. From the equations of the signal generator (5.1) and observer (5.5) we obtain:

$$\begin{aligned} x_1(t) &= \sin \omega t, \\ x_2(t) &= \cos \omega t, \\ \hat{z}_1(t) &= A_1 \sin(\omega t + \varphi_1) = A_1(x_1 \cos \varphi_1 + x_2 \sin \varphi_1), \\ \hat{z}_2(t) &= A_1 \cos(\omega t + \varphi_1) = A_1(x_1 \cos \varphi_1 - x_2 \sin \varphi_1), \end{aligned} \tag{5.10}$$

where A_1 is the amplitude of the first harmonics in the measured signal and φ_1 is the phase shift with respect to the generated exciting signal (5.2).
This leads to the formulas in the form of:

$$\begin{aligned} A_1 &= \sqrt{\hat{z}_1^2 + \hat{z}_2^2}, \\ \cos \varphi_1 &= \frac{1}{A_1}(x_1 \hat{z}_1 + x_2 \hat{z}_2), \\ \sin \varphi_1 &= \frac{1}{A_1}(x_2 \hat{z}_1 - x_1 \hat{z}_2), \\ \varphi_1 &= atan2(\cos \varphi_1, \sin \varphi_1). \end{aligned} \tag{5.11}$$

Therefore, the estimate of the frequency response is given as:

$$\hat{P}(i\omega) = \frac{A_1}{A} e^{i\varphi_1}. \tag{5.12}$$

The estimate (5.12) is valid only in the case of an ideal linear response of the identified system. A potential occurrence of nonlinearities may lead to distortion of the generated frequency spectrum which can be observed as an excitation of higher harmonics in the measured output signal. The amplitudes of higher harmonics can be computed from the observed states analogous to (5.11) as:

$$A_i \;=\; \sqrt{\hat{z}_{2i-1}^2 + \hat{z}_{2i}^2};\; i = 2, 3, 4, 5. \tag{5.13}$$

An algorithm which uses this information for a proper adaptation of the identification experiment is proposed in the next section.

A particular problem of the observer design according to the Butterworth pattern is the possibility of an unwanted distortion of the estimator frequency response due to transfer zeros. The transfer function from measured to estimated output can be obtained in the form of:

$$\begin{aligned} F_{\hat{y}y}(s) = \frac{\hat{Y}(s)}{Y(s)} &= -\boldsymbol{C_o}(s\boldsymbol{I} - \boldsymbol{A_o} - \boldsymbol{k_{BW}}\boldsymbol{C_o})^{-1}\boldsymbol{k_{BW}} \\ &= \frac{-\boldsymbol{C_o} adj(s\boldsymbol{I} - \boldsymbol{A_o^{cl}})\boldsymbol{k_{BW}}}{det(s\boldsymbol{I} - \boldsymbol{A_o^{cl}})}, \end{aligned} \tag{5.14}$$

where $\boldsymbol{k_{BW}} = [k_1, k_2, ..., k_{11}]^T$ is the observer innovation gain vector comptuted from (5.9).

The property of maximum flatness of the Butterworth type low-pass filter is guaranteed only for the transfer functions with no zeros. On the contrary, the filter (5.14) contains transmission zeros, which are given as the roots of the polynomial

$$-\boldsymbol{C_o} adj(s\boldsymbol{I} - \boldsymbol{A_o^{cl}})\boldsymbol{k_{BW}}. \tag{5.15}$$

The relative order of the system (5.14) is one, because the first nonzero Markov parameter can be computed as:

$$M_1 = \boldsymbol{C_o}\boldsymbol{k_{BW}} = k_1 + k_3 + k_5 + k_7 + k_9 + k_{11} = -\frac{17567}{2500}\omega\alpha_0 \neq 0 \;\forall \omega, \alpha_0 > 0. \tag{5.16}$$

Therefore, ten transmission zeros appear in the transfer function (5.14) and a high frequency roll-off of -20dB per decade is achieved. Since the value of the actual frequency ω serves only as a time scaling parameter, the location of the system zeros is directly

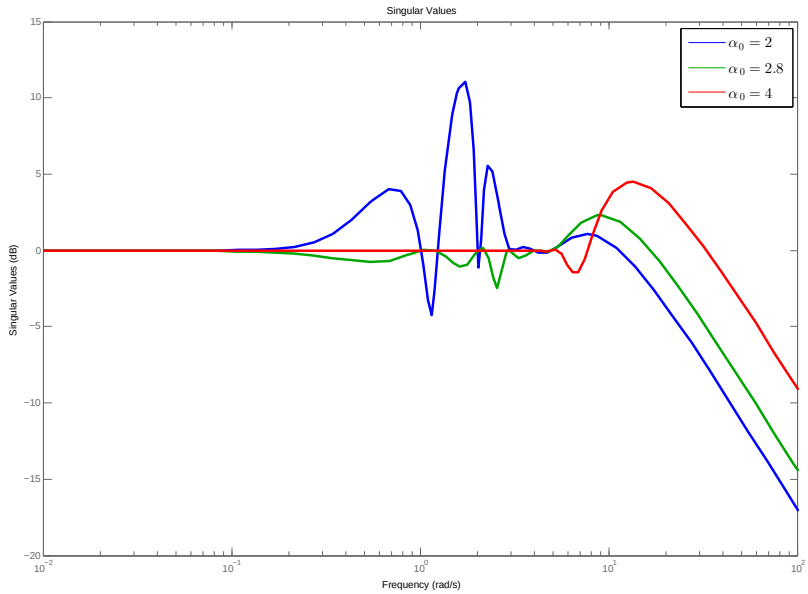

Figure 5.3: Amplitude frequency response - $|F_{\hat{y}y}(i\omega)|$ for the Butterworth pole distribution and chosen $\alpha_0 = 2, 2.8, 4$

determined only by the specification of the relative observer bandwidth α_0. **Improper choice of this parameter may lead to degradation of the estimator performance** due to the inadmissible shape of the resulting frequency response. Figure (5.3) shows the amplitude frequency response of the observer $|F_{\hat{y}y}(i\omega)|$ with the Butterworth pole distribution and three different choices of the relative bandwidth α_0. Regardless of the observer settings, the frequency response has to fulfill the interpolation conditions given by the inner model of the signal generator in the form of five harmonics and the DC component:

$$\begin{aligned} F_{\hat{y}y}(ik\omega) &= 1;\ k = 1, 2, ..5 \\ F_{\hat{y}y}(0) &= 1. \end{aligned} \tag{5.17}$$

However, the shape of the pass-band which affects the observer performance may differ considerably due to changes in the relative position of the transfer zeros. Whereas a smooth frequency response with small overshoot is obtained for the choice $\alpha_0 = 2.8$, significant peaking phenomenon is observed for lower and higher setting of the

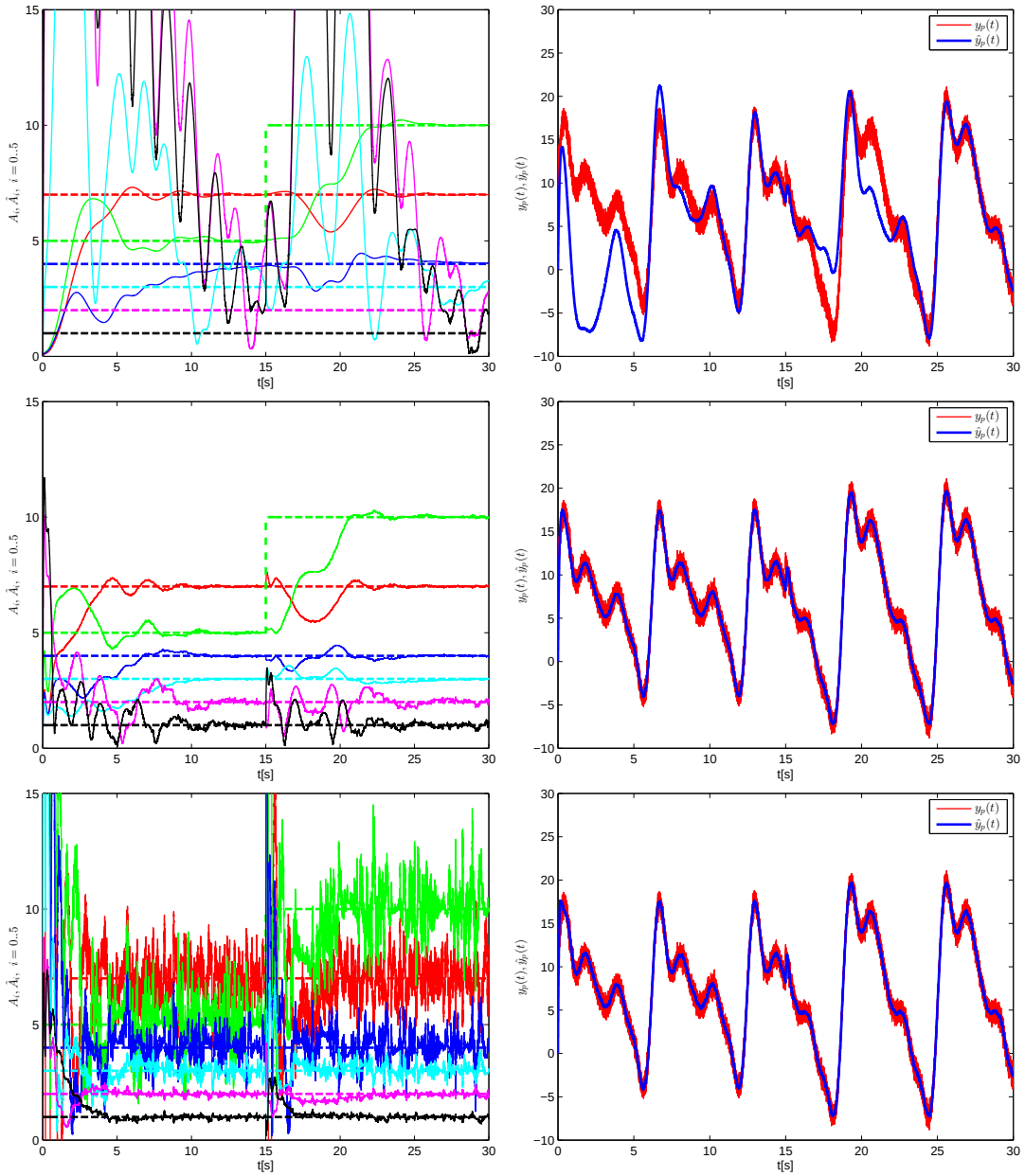

Figure 5.4: Time domain observer performance - Butterworth pole distribution: left - estimation of DC component and amplitudes of five harmonics, right - output signal tracking; each row corresponds to the different choice of observer bandwidth $\alpha_0 = 2, 2.8, 4$

observer bandwidth. The peaks in the frequency response can significantly affect the performance of the estimator as can be seen in Fig. (5.4).

The simulation experiment shows the estimator outputs during the tracking of a multiple harmonics sine-wave signal contaminated by an additive high-frequency measurement noise for the three different choices of α_0.
The measured signal is given by equation:

$$y(t) = A_0 + A_1(t)sin(\omega t) + A_2 sin(2\omega t) + A_3 sin(3\omega t) + A_4 sin(4\omega t) + A_5 sin(5\omega t) + \xi(t),$$
$$A_0 = 7, A_1(t) = \begin{cases} 5 & \text{for } t \leq 15 \\ 10 & \text{for } t > 15 \end{cases}, A_2 = 4, A_3 = 3, A_2 = 2, A_1 = 1, \omega = 1, \xi \sim \mathcal{N}(0, 0.3), \tag{5.18}$$

where $\xi(t)$ is a normally distributed white noise with covariance $\sigma^2 = 0.3$ and zero mean. Step change of the amplitude of first harmonics to a new value $A_1 = 10$ is performed at time $t = 15s$ to show the transient response.

It can be seen that the observer performs well for the setting $\alpha_0 = 2.8$. The output signal is tracked without an excessive amplification of the measurement noise in the estimates which converge to the true values with a consistent speed. Lower value $\alpha_0 = 2$ leads to severe degradation of performance. The convergence rate is poor, especially for the amplitudes of the higher harmonics. This is caused by the steep peaks in the pass-band which may be observed in the frequency responses of the estimated output and state variables corresponding to the individual harmonics and DC component (Fig. 5.3,5.6). On the other side, the increase of the observer bandwidth to $\alpha_0 = 4$ results in a strong amplification of the noise, mostly in the estimates of DC portion and first three harmonics. Although the mean value of the estimates converge rapidly to the true values, the obtained signals could not be used directly in an automatic identification procedure without a further processing (e.g. by an additional low-pass filter).

Generally speaking, *any peaks in the frequency response of the observer indicate a potential problem with the performance*. A significant overshoot in the pass-band inevitably causes long settling times of certain estimated states when excited by a wideband signal. On the contrary, high gain in the transition and stop band regions may lead to unacceptable amplification of the measurement noise. Therefore, the worst-case gain of the observer output frequency response may serve as a valuable performance index:

$$J_{\hat{y}}(\alpha_0) \triangleq \|F_{\hat{y}y}(s)\|_\infty = \sup_\omega |F_{\hat{y}y}(i\omega)|. \tag{5.19}$$

The values of $J_{\hat{y}}$ for $\alpha_0 \in \langle 1, 5\rangle$ are plotted in the left figure (5.5). It can be seen, that best output tracking is achieved for $\alpha_0 \approx \langle 2.5, 3\rangle$. Peaking is observed outside of this region as shown in figure (5.3). Further insight into the problem is gained by

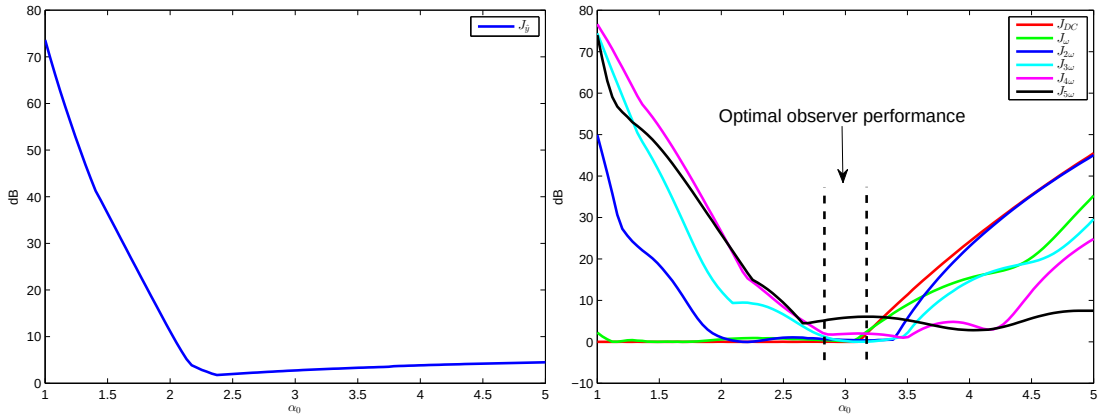

Figure 5.5: Observer performance indices - Butterworth pole distribution: worst-case gain of the frequency responses as a function of bandwidth α_0; left $J_{\hat{y}}$, right $J_{DC}, J_{i\omega}$

observation of the frequency responses of the states corresponding to the individual five harmonics and DC component (Fig. 5.6). An additional set of performance indices is introduced as follows:

$$J_{DC}(\alpha_0) \triangleq \|F_{DCy}(s)\|_\infty = \sup_\omega |\frac{\hat{Z}_{11}(i\omega)}{Y(i\omega)}|, \tag{5.20}$$

$$J_{\omega}(\alpha_0) \triangleq \|F_{\omega y}(s)\|_\infty = \sup_\omega |\frac{\hat{Z}_{1}(i\omega)}{Y(i\omega)}|,$$

$$J_{2\omega}(\alpha_0) \triangleq \|F_{2\omega y}(s)\|_\infty = \sup_\omega |\frac{\hat{Z}_{3}(i\omega)}{Y(i\omega)}|,$$

$$J_{3\omega}(\alpha_0) \triangleq \|F_{3\omega y}(s)\|_\infty = \sup_\omega |\frac{\hat{Z}_{5}(i\omega)}{Y(i\omega)}|,$$

$$J_{4\omega}(\alpha_0) \triangleq \|F_{4\omega y}(s)\|_\infty = \sup_\omega |\frac{\hat{Z}_{7}(i\omega)}{Y(i\omega)}|,$$

$$J_{5\omega}(\alpha_0) \triangleq \|F_{5\omega y}(s)\|_\infty = \sup_\omega |\frac{\hat{Z}_{9}(i\omega)}{Y(i\omega)}|.$$

The individual transfer functions are computed analogous to (5.14) by substituting a corresponding output matrix to the state space model. Evaluation of these indices is shown in (Fig. 5.5 right). It can be seen that the low values of $\alpha_0 < 3$ affect mostly the performance of the estimation of higher harmonics due to the occurrence of peaking in the corresponding frequency responses while the first harmonics and DC component estimates remain unaffected. This is consistent to the experimental results shown in (Fig.5.4, first row). On the other hand, high values of $\alpha_0 > 3$ leads to overshoots in frequency responses corresponding to DC value and the first two harmonics whereas

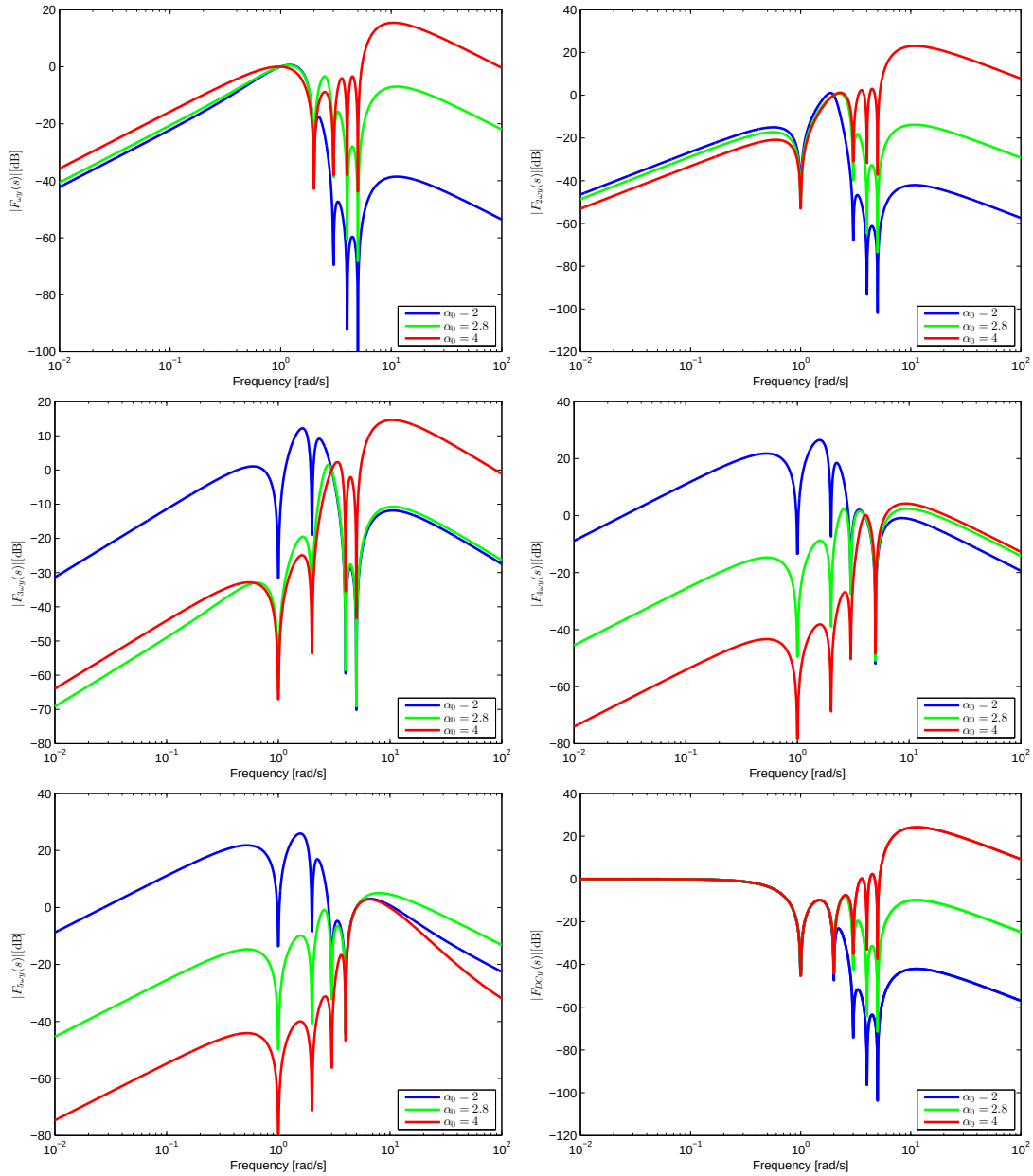

Figure 5.6: Observer performance in the frequency domain - Butterworth pole distribution: amplitude frequency response of the five harmonics and DC component estimates for the varying observer bandwidth $\alpha_0 = 2, 2.8, 4$

the influence on the higher harmonics is relatively lower. Therefore, the high-frequency noise is propagated mainly in the channels of the DC component and the first two harmonics estimates. This was indeed observed in the simulation (Fig.5.4, third row).

Optimal observer performance with a smooth shape of all the transfer function without excessive peaking is achieved in range $\alpha_0 \approx \langle 2.8, 3.2 \rangle$.

The performed analysis showed that a naive choice of the observer closed-loop poles may lead to a poor performance due to the influence of the transfer zeros. *The observer designed with the Butterworth closed-loop pole distribution performs well in a relatively narrow range of the chosen bandwidth*. A second observer design is introduced to overcome this disadvantage and offer a higher flexibility in the specification of the estimator dynamics.

A systematic approach to the observer synthesis is given in the framework of quadratic optimal theory by means of the **Kalman-Bucy filter**. The problem of reconstructing the spectrum of a signal consisting of five harmonics and a DC component is formulated as follows. The model of the signal generator is given by the state space model in the form of:

$$\begin{aligned} \dot{\boldsymbol{z}}(t) &= \boldsymbol{A_o z}(t) + \boldsymbol{G w}(t), \\ y(t) &= \boldsymbol{C_o z}(t) + v(t), \end{aligned} \tag{5.21}$$

where $\boldsymbol{A_o}, \boldsymbol{C_o}$ denote state and output matrices which were defined in (5.5),
$\boldsymbol{G}$ is a process disturbance input matrix,
$\boldsymbol{w}$ is a process disturbance vector
$v(t)$ is an output disturbance.

Classical stochastic formulation of the problem models the process and output disturbances as normally distributed Gaussian white noises with zero mean and intensity given by the appropriate covariances $\boldsymbol{W}, V$:

$$E(\boldsymbol{w w^T}) = \boldsymbol{W},\ E(v^2) = V. \tag{5.22}$$

Under these assumptions, an optimal causal observer which minimizes the steady-state error covariance $\lim_{t\to\infty} E\{(\boldsymbol{z} - \hat{\boldsymbol{z}})(\boldsymbol{z} - \hat{\boldsymbol{z}})^T\}$ is given as:

$$\begin{aligned} \dot{\hat{\boldsymbol{z}}}(t) &= \boldsymbol{A_o}\hat{\boldsymbol{z}}(t) + \boldsymbol{k}\{y(t) - \hat{y}(t)\}, \\ \hat{y}(t) &= \boldsymbol{C_o}\hat{\boldsymbol{z}}(t). \end{aligned} \tag{5.23}$$

The innovation gain vector $\boldsymbol{k} = [k_1, k_2, ..., k_{11}]^T$ is computed as

$$\boldsymbol{k} = \boldsymbol{Y C_o^T} V^{-1}, \tag{5.24}$$

and the symmetric nonnegative-definite $n \times n$ matrix $\boldsymbol{Y}$, is a solution of the Algebraic Riccati Equation:

$$\boldsymbol{A_o Y} + \boldsymbol{Y A_o^T} - \boldsymbol{Y C_o^T} V^{-1} \boldsymbol{C_o Y} + \boldsymbol{G W G^T} = \boldsymbol{0}. \tag{5.25}$$

The steady-state solution of the stochastic optimal estimator leads to the LTI system with the structure of the full-state Luenberger observer. The difference is that the observer error dynamics which is given by the location of the closed-loop poles is obtained indirectly from the specification of the process and output noise model. The problem of the stochastic formulation is, that *the noise statistics can be seldom obtained in practice*. The disturbances acting on the system usually does not resemble the assumed white noise model or their intensities are a priori unknown. Whereas the variance of the output noise $v(t)$ represents the uncertainty of the measurement and may be obtained experimentally or from the known sensor precision, the white noise model of the process disturbance in the signal generator does not have a clear physical meaning. As was stated in the preliminary chapter, a deterministic explanation of the Kalman filter leads to the conclusion, that, the noise intensity parameters can be used merely as a tuning parameters of the observer, which pose a relative confidence in the system model and measurement accuracy. The Kalman filter is a least squares estimator which minimizes objective function

$$J = \int_0^\infty \{\boldsymbol{w}^T (\boldsymbol{G W G^T})^{-1} \boldsymbol{w} + V^{-1} v^2\} dt, \tag{5.26}$$

subject to the constraints given by the dynamic model of the observed system. The observer uses the least possible quadratic norm of the state and output disturbances to "explain" the observations and the weighting factors $\boldsymbol{W}, V$ may be used to find a compromise between the estimator bandwidth and sensitivity to the measurement noise.

The goal of the observer design for the problem of system identification is to find a *suitable weighting scheme* in terms of the choice of parameters $\boldsymbol{G}, \boldsymbol{W}, V$ which would lead to practically applicable estimators. The number of design parameters should be reduced to a single user-specified value which determines the observer bandwidth. At first, dimension of the process disturbance $\boldsymbol{w}$ and the direction of its injection has to be chosen. Considering that the amplitudes of the individual observed harmonics and the level of the DC component may generally change in time independently, the disturbance dimension is set to the number of the generator states ($n = 11$) and the disturbance input is chosen as the identity matrix $\boldsymbol{G} = I_{11}$. Assumption of mutually independent disturbances lead to the diagonal weighting matrix $\boldsymbol{W} =$

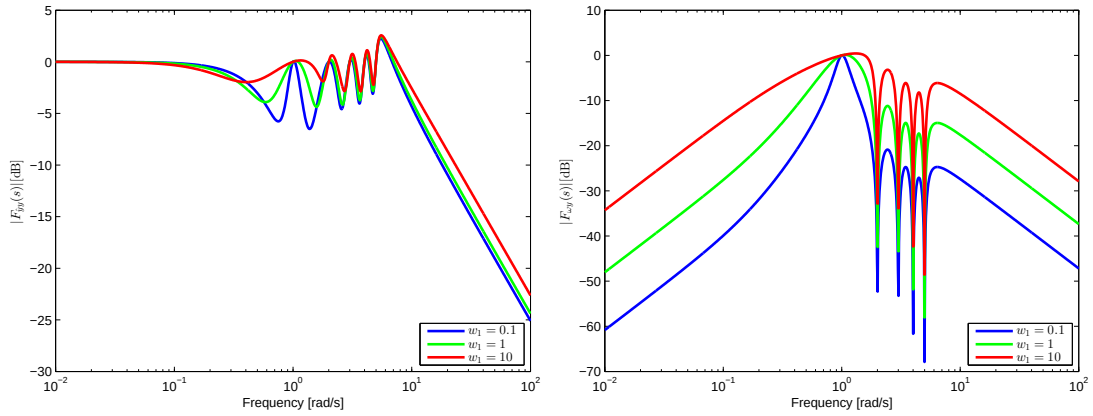

Figure 5.7: Adjustment of the weighting scheme for the Kalman filter: amplitude frequency response of the observer output (left) and first harmonics estimates (right) for various setting of the relative weight w_1

$diag\{w_1, w_1, w_2, w_2, w_3, w_3, w_4, w_4, w_5, w_5, w_6\}$. The relative weights of its individual elements determine *how much energy the estimate of the corresponding harmonics will receive* from the measurement. The influence of this setting can be easily observed in the observer frequency response (Fig. 5.7).

Amplitude frequency response of the output and first harmonics estimates $|F_{\hat{y}y}(i\omega)|$, $|F_{\omega y}(i\omega)|$ are shown for the three different choices of relative weight w_1:

$$\boldsymbol{W} = diag\{w_1, w_1, 1, 1, 1, 1, 1, 1, 1, 1, 1\}, V = 1;\ w_1 = [0.1, 1, 10]. \tag{5.27}$$

It can be seen, that the change of the relative weight of the individual harmonics affects the shape of the transfer function in the close vicinity of the corresponding resonance frequency. Higher relative weight leads to a wider pass-band of the harmonics estimate which has the shape of a peak filter. At the same time, a more flat profile is obtained in the appropriate part of the output response. This property is used in the following proposed weighting scheme. The process disturbance weighting matrix is chosen as:

$$\boldsymbol{W} = diag\{0.4, 0.4, 0.6, 0.6, 0.8, 0.8, 0.9, 0.9, 1, 1, 0.6\}. \tag{5.28}$$

The relative weights of the individual elements reflect the fact, that the *first harmonics and DC component estimates should be less sensitive to the high-frequency measurement noise* as they are primarily used for the system identification and eventually for the closed-loop control during the experiment. Moreover, narrow pass-band of the peak filter is desirable for the first harmonics transfer function to make the estimation insensitive to an eventual occurrence of subharmonic frequencies in a wideband signal which

may be generated by a generally nonlinear system. On the contrary, higher harmonics estimates are used for detection of nonlinearities in the system dynamics. Therefore, the pass-band of the corresponding state transfer functions *should be relatively wide to improve the sensitivity to high-frequency disturbances* which may occur at frequencies which do not perfectly match the five integer multiples of the fundamental frequency ω contained in the signal generator model. Particular values of the weights ω_i were found by performing extensive simulations with the models of typical mechanical systems to be identified. The only remaining design parameter is the output disturbance weighting factor V which is considered as a user-specified value of the observer bandwidth.

The important advantage of the Kalman filter based observer design is its **guaranteed gain and phase margins** which come from the spectral properties of the Riccati equation. A well known robustness margins of the linear quadratic regulator (infinite gain margin and phase margin greater than 60) may alose be derived for the dual problem of the optimal estimator. The observer Riccati equation (5.25) may be rewritten in the form of

$$\boldsymbol{Y}(s\boldsymbol{I_n} - \boldsymbol{A_o^T}) + (-s\boldsymbol{I_n} - \boldsymbol{A_o})\boldsymbol{Y} + \boldsymbol{k}V\boldsymbol{k^T} = \boldsymbol{GWG^T}, \tag{5.29}$$

which was obtained by addition and subtraction of $s\boldsymbol{I_n}$, substitution of the observer gain vector $\boldsymbol{k}$ from (5.24) and rearrangement of the individual terms. Multiplication from the left by $\boldsymbol{C_o}(-s\boldsymbol{I_n} - \boldsymbol{A_o})^{-1}$, from the right by $(s\boldsymbol{I_n} - \boldsymbol{A_o^T})^{-1}\boldsymbol{C_o^T}$, addition of V to both sides and substitution $\boldsymbol{YC_o^T} = \boldsymbol{k}V, \boldsymbol{CY} = V\boldsymbol{k^T}$ from from (5.24) leads to:

$$\begin{aligned} V + \boldsymbol{C_o}(-s\boldsymbol{I_n} - \boldsymbol{A_o})^{-1}\boldsymbol{k}V + V\boldsymbol{k^T}(s\boldsymbol{I_n} - \boldsymbol{A_o^T})^{-1}\boldsymbol{C_o^T} + \\ \boldsymbol{C_o}(-s\boldsymbol{I_n} - \boldsymbol{A_o})^{-1}\boldsymbol{k}V\boldsymbol{k^T}(s\boldsymbol{I_n} - \boldsymbol{A_o^T})^{-1}\boldsymbol{C_o^T} \\ = V + \boldsymbol{C_o}(-s\boldsymbol{I_n} - \boldsymbol{A_o})^{-1}\boldsymbol{GWG^T}(s\boldsymbol{I_n} - \boldsymbol{A_o^T})^{-1}\boldsymbol{C_o^T}. \end{aligned} \tag{5.30}$$

A factorization of (5.30) with definition $\boldsymbol{GWG^T} = \boldsymbol{H^TH}$ is possible in the form of:

$$[1 + L(-s)]v[1 + L(s)]^T = V + \boldsymbol{C}(-s)\boldsymbol{C^T}(s), \tag{5.31}$$

where $L(s) = \boldsymbol{C_o}(s\boldsymbol{I_n} - \boldsymbol{A_o})^{-1}\boldsymbol{k}$ is the loop transfer function and
$\boldsymbol{C}(s) = \boldsymbol{C_o}(s\boldsymbol{I_n} - \boldsymbol{A_o})^{-1}\boldsymbol{H^T}$ is the 1×11 cost function matrix. Further rearrangement and substitution $s = i\omega$ leads to:

$$\begin{aligned} [1 + L(-i\omega)][1 + L(i\omega)]^T = 1 + \tfrac{\boldsymbol{C}(-i\omega)\boldsymbol{C^T}(i\omega)}{V}, \\ \Rightarrow |1 + L(i\omega)| \geq 1 \end{aligned} \tag{5.32}$$

The system $L(s)$ is defined as the open loop transfer function from observer error $y(t) - \hat{y}(t)$ to estimated output $\hat{y}$. It can be seen from the observer equations (5.23) that the

closed-loop dynamics is obtained by simply closing a unitary feedback around $L(s)$:

$$F_{\hat{y}y}(s) = \frac{\hat{y}(s)}{y(s)} = \frac{L(s)}{1+L(s)} = \boldsymbol{C_o}(s\boldsymbol{I_n} - \boldsymbol{A_o} + \boldsymbol{k}\boldsymbol{C_o})^{-1}\boldsymbol{k}. \tag{5.33}$$

The inequality (5.32) implies that the Nyquist plot of $L(i\omega)$ does not enter the unitary circle centered around the $[-1, i0]$ point of the complex plane giving the guaranteed stability margin $s_m \geq 1$, phase margin $p_m \geq 60\,^\circ$ and gain margin $g_m = \langle 0.5, \infty)$. Since the open-loop frequency response does not enter the unitary circle, there is also a guaranteed maximum overshoot in the closed-loop amplitude frequency response:

$$|F_{\hat{y}y}(i\omega)| = \frac{|L(i)\omega|}{|1+L(i)\omega|} = \frac{\sqrt{(u^2+v^2)}}{\sqrt{(1+u)^2+v^2}} = M. \tag{5.34}$$

The points of the complex plane with a constant closed loop amplitude define a set of M-contours which are given as circles parameterized by the number M as:

$$(u - \frac{M^2}{1-M^2})^2 + v^2 = (\frac{M}{1-M^2})^2. \tag{5.35}$$

Substitution of $[u, v] = [-2, 0]$ to (5.35) and solution of the resulting quadratic equation gives the result $M = 2$ which defines the M-circle of maximum radius which fits into the unitary circle given by the inequality (5.32). Therefore, there is a guaranteed maximum overshoot in the observer frequency response which was chosen as the performance index in (5.19):

$$J_{\hat{y}}(V) = \|F_{\hat{y}y}(s)\|_\infty = \underset{\omega}{sup}|F_{\hat{y}y}(i\omega)| \leq 2(\approx 6dB)\ \forall V > 0. \tag{5.36}$$

Consequently, *no unwanted peaking phenomenon which was observed in the case of the Butterworth closed-loop pole distribution can occur for an arbitrary choice of observer bandwidth* V. Since the inequality (5.36) defines a worst-case gain for any observed system and arbitrary choice of the weighting scheme, considerably better results are achieved for the particular case of the proposed observer (5.23). Figure (5.8) shows the peak values of the frequency responses in the output and individual harmonics channels which were defined as the performance indices in (5.19,5.20). The plots are shown for the varying scalar weight $V \in \langle 0.005, 0.5\rangle$ which determines the observer bandwidth. The chosen range is equivalent to the setting of $\alpha_0 \in \langle 1, 5\rangle$ in the sense of the resulting bandwidth in order to make the results directly comparable with the Butterworth pole distribution (Fig. 5.5).

It can be seen that there is no unwanted peaking in the frequency response functions. The worst case output gain is $J_{\hat{y}} \leq 2.35dB$ and there is no overshoot in the individual harmonics and DC channels ($J_{i\omega}, J_{DC} \approx 0dB$ - small values observed in the right plot occurred due to the numerical computation of the corresponding ∞-norms). The shape of the pass-band in the individual channels remains very similar over the whole range of the desired bandwidth and the estimator is able to achieve consistent

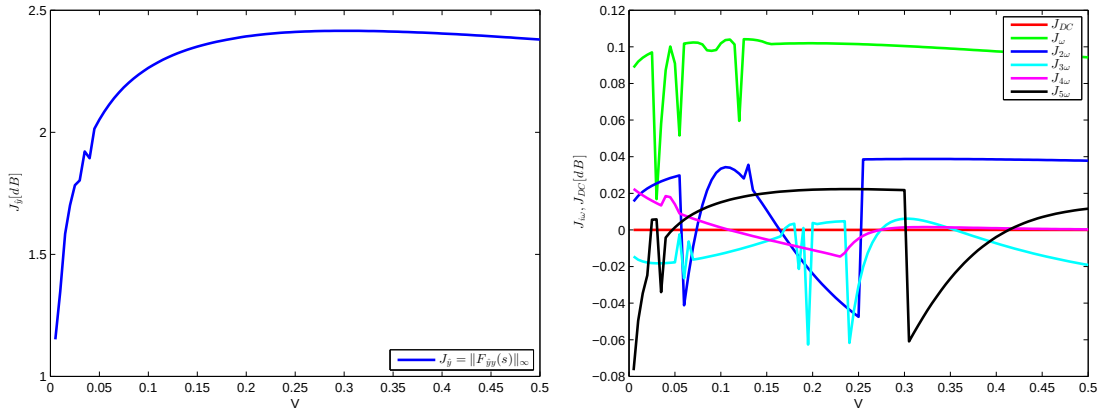

Figure 5.8: Observer performance indices - Kalman filter: worst-case gain of the frequency responses as a function of observer bandwidth V; left $J_{\hat{y}}$, right $J_{DC}, J_{i\omega}$

performance without the undesirable peaking (Figures 5.9,5.10). This is confirmed by means of a simulation experiment (Fig. 5.11) which is identical to the one performed with the Butterworth observer design (Fig. 5.4).

Direct comparison of the results shows that the second estimator design based on the Kalman-Bucy filter offers much higher variability in the specification of the observer bandwidth and thus is preferable for the real-time implementation in the automatic identification algorithm. The non-dimensional scalar weight V should be replaced by another user-specified parameter with a clear physical meaning. The estimator bandwidth ω_{BW} in the standard -3dB sense of $|F_{\hat{y}y}(i\omega)|$ is a suitable candidate for this purpose.

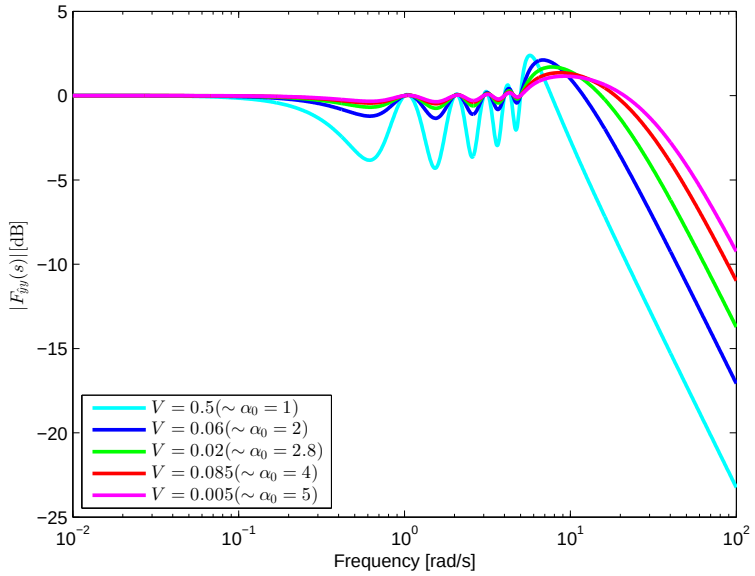

Figure 5.9: Amplitude frequency response - $|F_{\hat{y}y}(i\omega)|$ for the Kalman filter design and chosen $V = 0.5, 0.06, 0.02, 0.085, 0.005$ (bandwidth is equivalent to the settings $\alpha_0 = 1, 2, 2.8, 4, 5$ for the Butterworth pole distribution)

Two possible approaches are considered for the observer tuning:

1. The user specifies the desired relative observer bandwidth and the correct value of scalar weight V is computed from a nonlinear mapping function $V = f(\omega_{BW})$ or from a lookup table. The observer gains are consequently computed from the Algebraic Riccati equation.

2. A finite set of the observer bandwidth values is offered for the user setting. For each option, the innovation gains may be precomputed off-line and stored in the identification algorithm which is deployed to a target real-time platform.

The first alternative offers a higher flexibility at the cost of the requirement of numerical solution of the corresponding ARE in the target control system. The second option reduces the computational complexity while limiting the freedom in the selection of the observer bandwidth to a finite set of values. It can be observed that the system matrix $\boldsymbol{A_o}(\omega)$ of the signal generator model (5.5,5.23) can be written as a product of a constant matrix and scalar value of actual frequency as follows:

$$\boldsymbol{A_o}(\omega) = \omega \boldsymbol{A_o}(1) \tag{5.37}$$

Substitution of (5.37) to the ARE (5.25) leads to the equation:

$$\boldsymbol{A_o}(1)\boldsymbol{Y}\omega + \omega \boldsymbol{Y}\boldsymbol{A_o}(1)^{\boldsymbol{T}} - \omega \boldsymbol{Y}\boldsymbol{C_o^T}V^{-1}\boldsymbol{C_o}\boldsymbol{Y}\omega + \boldsymbol{G}\boldsymbol{W}\boldsymbol{G^T} = 0. \tag{5.38}$$

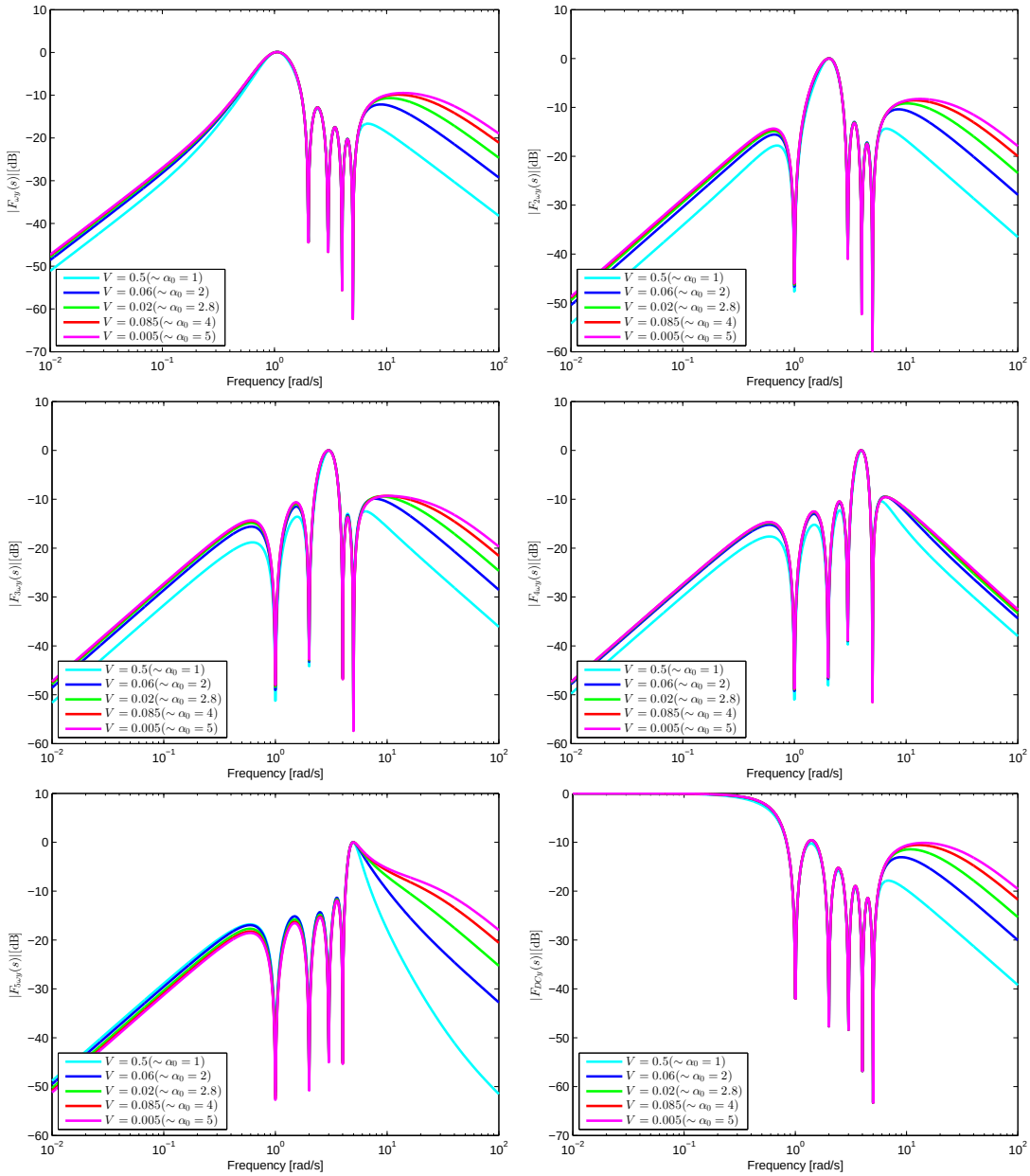

Figure 5.10: Observer performance in the frequency domain - Kalman filter design: amplitude frequency response of the five harmonics and DC component estimates for the varying observer bandwidth $V = 0.5, 0.06, 0.02, 0.085, 0.005$ (equivalent to the settings $\alpha_0 = 1, 2, 2.8, 4, 5$ for the Butterworth pole distribution)

The choice $V(\omega) = V(1)/\omega^2$ leads to the solution of the ARE in the form of:

$$\boldsymbol{Y}(\omega) = \boldsymbol{Y}(1)/\omega. \tag{5.39}$$

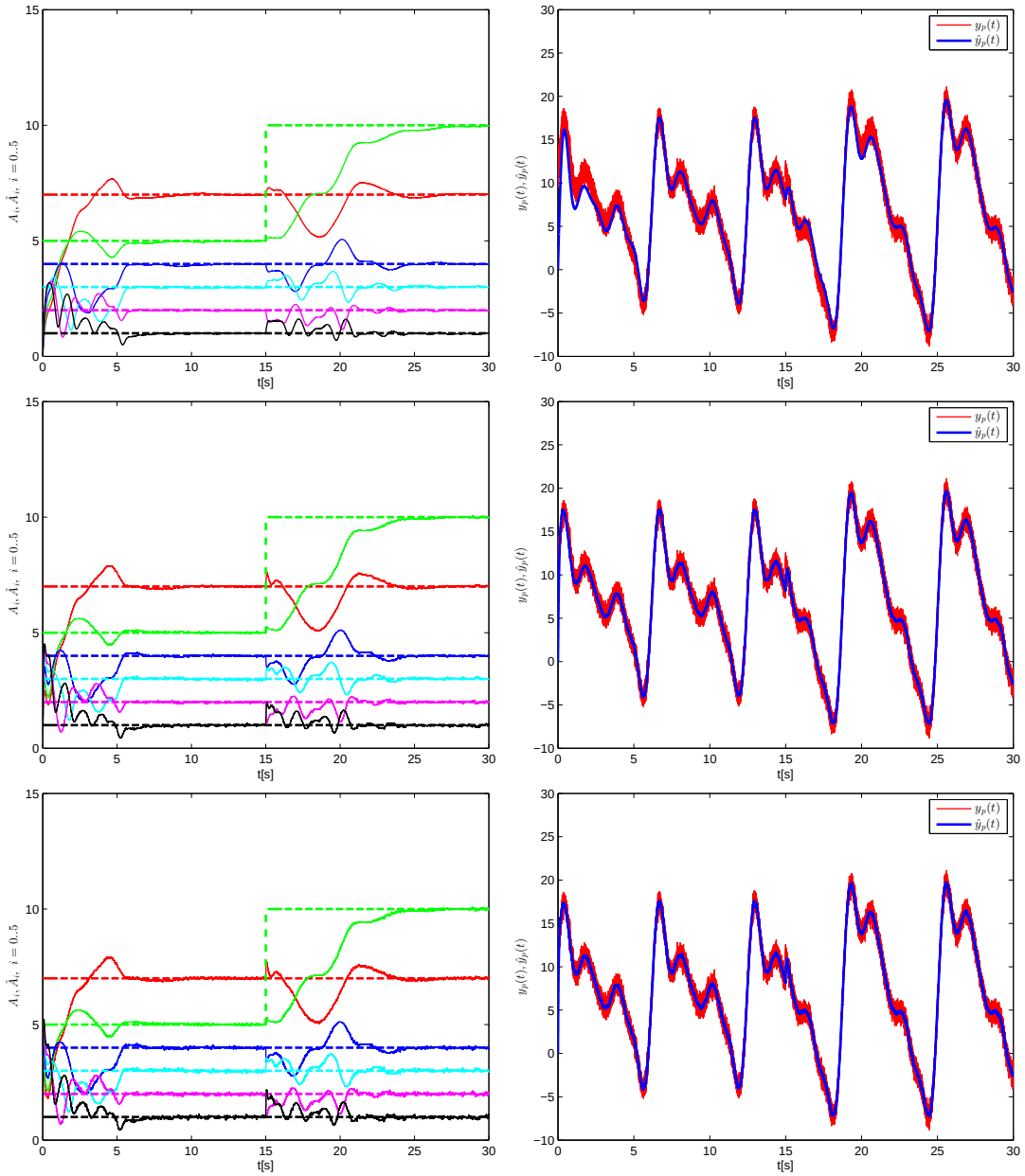

Figure 5.11: Time domain observer performance - Kalman filter design: left - estimation of DC component and amplitudes of five harmonics, right - output signal tracking; each row corresponds to the different choice of observer bandwidth $V = 0.5, 0.02, 0.005$ (equivalent to the settings $\alpha_0 = 1, 2.8, 5$ for the Butterworth pole distribution)

Consequently, the observer gain vector is obtained as:

$$\boldsymbol{k}(\omega) = \boldsymbol{Y}\boldsymbol{C}_{\boldsymbol{o}}^{\boldsymbol{T}} V^{-1} = \frac{\boldsymbol{Y}(1)}{\omega}\boldsymbol{C}_{\boldsymbol{o}}^{\boldsymbol{T}}\boldsymbol{V}(1)^{-1}\omega^2 = \boldsymbol{k}(1)\omega. \tag{5.40}$$

Therefore, *the actual frequency ω serves only as the time scaling parameter*. The innovation gain vector $\boldsymbol{k}(\omega, V)$ of the observer can be computed for $\omega = 1$ without loss of generality and the values for a particular frequency $\omega \neq 1$ are obtained from simple multiplication. The observer dynamics and thus the shape of the frequency responses remains equal for an arbitrary ω.

Sweep phase algorithm

The measurement phase serves for the estimation of one point of the system frequency response. It is alternated with the sweep phases in which the signal generator (5.1) varies the frequency of the exciting harmonic input until a new measurement phase starts for the sake of another point acquisition. In order to keep synchronization of the observer with the measured output, its structure is continuously adapted to the varying frequency ω. The observer (5.23) is altered to the following time-varying system:

$$\begin{aligned} \dot{\hat{\boldsymbol{z}}}(t) &= \boldsymbol{A_o}(t)\hat{\boldsymbol{z}}(t) + \boldsymbol{k}(t)\{y(t) - \hat{y}(t)\}, \\ \hat{y}(t) &= \boldsymbol{C_o}\hat{\boldsymbol{z}}(t). \end{aligned} \tag{5.41}$$

Considering the structure of the system matrix and innovation gain vector which consist from the constant part and scalar perturbation $\omega(t)$ as in (5.37,5.40), the state space model (5.41) can be rewritten in the form of

$$\begin{aligned} \dot{\hat{\boldsymbol{z}}}(t) &= \omega(t)\{[\boldsymbol{A_o}(1) - \boldsymbol{k}(1)\boldsymbol{C_o}]\hat{\boldsymbol{z}}(t) + \boldsymbol{k}(1)y(t)\} \\ &= \omega(t)\{\boldsymbol{A_o^{cl}}\hat{\boldsymbol{z}}(t) + \boldsymbol{B_o^{cl}}y(t)\}, \\ \hat{y}(t) &= \boldsymbol{C_o}\hat{\boldsymbol{z}}(t), \end{aligned} \tag{5.42}$$

where $\boldsymbol{A_o^{cl}}, \boldsymbol{B_o^{cl}}$ denote the constant part of the closed-loop state and input matrices.

The observation error dynamics is described by the state space system:

$$\dot{\boldsymbol{\varepsilon}}(t) = \omega(t)\{\boldsymbol{A_o}(1) - \boldsymbol{k}(1)\boldsymbol{C_o}\}\boldsymbol{\varepsilon}(t) = \omega(t)\boldsymbol{A_o^{cl}}\boldsymbol{\varepsilon}(t);\ \boldsymbol{\varepsilon}(t) = \hat{\boldsymbol{z}}(t) - \boldsymbol{z}(t), \boldsymbol{\varepsilon}(t_0) = \boldsymbol{\varepsilon}_0. \tag{5.43}$$

General solution of the homogenous equation

$$\dot{\boldsymbol{x}}(t) = \boldsymbol{A}(t)\boldsymbol{x}(t);\ \boldsymbol{x}(t_0) = \boldsymbol{x}_0 \tag{5.44}$$

can be written in the form of an infinite series which is obtained by applying successive approximation of the integral equation $\boldsymbol{x}(t) = \boldsymbol{x}_0 + \int_{t_0}^{t} \boldsymbol{A}(\tau)\boldsymbol{x}(\tau)d\tau$ as:

$$\begin{aligned} \boldsymbol{x}(t) &= \boldsymbol{x}_0 + \int_{t_0}^{t} \boldsymbol{A}(u_1)du_1\boldsymbol{x}_0 + \int_{t_0}^{t} \boldsymbol{A}(u_1)\int_{t_0}^{u_1} \boldsymbol{A}(u_2)du_2du_1\boldsymbol{x}_0 + ... \\ &= [\boldsymbol{I_n} + \int_{t_0}^{t} \boldsymbol{A}(u_1)du_1 + \int_{t_0}^{t} \boldsymbol{A}(u_1)\int_{t_0}^{u_1} \boldsymbol{A}(u_2)du_2du_1 + ...]\boldsymbol{x}_0 \\ &= \boldsymbol{\Phi}(t, t_0)\boldsymbol{x}_0, \end{aligned} \tag{5.45}$$

where the $n \times n$ matrix function $\boldsymbol{\Phi}(t,\tau)$ is referred to as the *state transition matrix*. It can be shown that the solution (5.45) is unique and the matrix $\boldsymbol{\Phi}(t,\tau)$ has two important properties [202]:

$$\boldsymbol{\Phi}(t,t) = \boldsymbol{I_n},\ \frac{\partial}{\partial t}\boldsymbol{\Phi}(t,\tau) = \boldsymbol{A}(t)\boldsymbol{\Phi}(t,\tau). \tag{5.46}$$

Thus, it can be seen that the solution (5.45) satisfies the homogenous equation (5.44). It may be difficult to find a closed-form analytical solution of the state transition matrix for a general LTV system and often a numerical approximation has to be used. However, the problem simplifies considerably for the case of commuting state matrix

$$\boldsymbol{A}(t)\boldsymbol{A}(\tau) = \boldsymbol{A}(\tau)\boldsymbol{A}(t)\ \forall t,\tau. \tag{5.47}$$

In this case, the state transition matrix can be obtained in the form

$$\boldsymbol{\Phi}(t,\tau) = exp[\int_{\tau}^{t} \boldsymbol{A}(u)du] = \sum_{k=0}^{\infty} \frac{1}{k!}\int_{\tau}^{t} \boldsymbol{A}(u)du, \tag{5.48}$$

where exp denotes the matrix exponential function. This result can be easily verified by substitution to the solution (5.45) and the equation (5.44). It can be seen that the observer error system (5.43) fulfills the condition (5.47) as we may write:

$$\boldsymbol{A}(t)\boldsymbol{A}(\tau) = \omega(t)\boldsymbol{A_o^{cl}}\omega(\tau)\boldsymbol{A_o^{cl}} = \boldsymbol{A}(\tau)\boldsymbol{A}(t)\ \forall t,\tau. \tag{5.49}$$

The matrix $\boldsymbol{\Phi}(t,\tau)$ can be computed as follows:

$$\boldsymbol{\Phi}(t,\tau) = exp[\boldsymbol{A_o^{cl}}\lambda];\ \lambda(t) = \int_{\tau}^{t} \omega(u)du. \tag{5.50}$$

The resulting trajectory of the observer error system (5.43) is given as:

$$\boldsymbol{\varepsilon}(t) = \boldsymbol{\Phi}(t,t_0)\boldsymbol{\varepsilon}_0 = exp[\boldsymbol{A_o^{cl}}\lambda(t)]\boldsymbol{\varepsilon}_0;\ \lambda(t) = \int_{t_0}^{t} \omega(u)du. \tag{5.51}$$

Since the closed loop matrix $\boldsymbol{A_o^{cl}}$ has stable eigenvalues due to the observer design procedure, $\omega(t) > 0\ \forall t$ and consequently $\lambda(t), \dot{\lambda}(t) > 0\ \forall t$, the individual entries of the exponential matrix decay to zero and the system is asymptotically stable as we may write:

$$\|\boldsymbol{\varepsilon}(t)\| \leq \|\boldsymbol{\Phi}(t,t_0)\|\|\boldsymbol{\varepsilon}_0\| \leq c_1 e^{-c_2(t-t_0)}\|\boldsymbol{\varepsilon}_0\|,\ \forall t \geq t_0, \tag{5.52}$$

for some positive constants $c_1, c_2 > 0$ which depend on chosen closed-pole location of the matrix $\boldsymbol{A_o^{cl}}$ and values of $\omega(t)$. The function $\lambda(t)$ serves only as a time scaling parameter and the assumption $\omega(t) > 0\ \forall t$ gives the sufficient condition for the asymptotic stability. Therefore, the LTV system (5.42) is **the asymptotic observer** for the time-varying signal generator given by the pair $(\boldsymbol{A_o}\{\omega(t)\}, \boldsymbol{C_o})$.

Unfortunately, the condition of asymptotic tracking does not hold for the output of a general unknown plant measured during the sweep phase. The response of the system

excited by the swept sine signal inherently contains a transient response which is not included in the signal generator model which leads to an estimation error. Property of *Bounded-Input Bounded-Output (BIBO) stability* of the observer (5.42) for an arbitrary measured output is required to make sure that the estimation error does not grow unbounded between the two consecutive measurement steps.

Theorem 5.2.1. The LTV observer (5.42) is stable in the BIBO sense for an arbitrary measured output signal $y(t)$ and initial conditions $\hat{\boldsymbol{z}}(t_0)$ provided that $\omega(t) > 0 \; \forall t > t_0$ during the sweep phase of the identification experiment.

Proof. Let the time instant t_0 define the start of the sweep phase at the beginning of the identification experiment or the moment of transition from the measurement phase. The output response of the observer is given by the integral equation:

$$\hat{y}(t) = \boldsymbol{C_o}\boldsymbol{\Phi}(t,t_0)\hat{\boldsymbol{z}}(t_0) + \int_{t_0}^{t} \boldsymbol{C_o}\boldsymbol{\Phi}(t,\tau)\omega(\tau)\boldsymbol{B_o^c}y(\tau)d\tau. \tag{5.53}$$

Since the state matrix of the observer $\boldsymbol{A}(t) = \omega(t)\boldsymbol{A_o^{cl}}$ corresponds to the state matrix of the homogenous system (5.43), the properties of the transition matrix (5.50,5.51) and the condition of exponential stability (5.52) implicate the property of *asymptotic internal stability* of the estimator at the same time. Assuming that:

$$\begin{aligned} &\|\boldsymbol{\Phi}(t,t_0)\| \leq c_1 e^{-c_2(t-t_0)}, \|\boldsymbol{\Phi}(t,\tau)\| \leq c_1 e^{-c_2(t-\tau)}, \|\omega(t)\boldsymbol{B_o^{cl}}\| \leq c_3, \\ &\|\boldsymbol{C_o}\| \leq c_4, \|y(t)\| \leq c_5; \; \forall t > t_0, \end{aligned} \tag{5.54}$$

we may write:

$$\begin{aligned} \|\hat{y}(t)\| &\leq \|\boldsymbol{C_o}\|\|\boldsymbol{\Phi}(t,t_0)\|\|\hat{\boldsymbol{z}}(t_0)\| + \int_{t_0}^{t} \|\boldsymbol{C_o}\|\|\boldsymbol{\Phi}(t,\tau)\|\|\omega(\tau)\boldsymbol{B_o^{cl}}\|\|y(\tau)\|d\tau \\ &\leq c_4c_1\|\hat{\boldsymbol{z}}(t_0)\| + \int_{t_0}^{t} c_4c_1e^{-c_2(t-\tau)}c_3c_5d\tau \\ &= c_4c_1\|\hat{\boldsymbol{z}}(t_0)\| + \frac{c_4c_1c_3c_5}{c_2}\{1 - e^{-c2(t-t_0)}\} \\ &\leq c_4c_1\|\hat{\boldsymbol{z}}(t_0)\| + \frac{c_4c_1c_3c_5}{c_2}. \end{aligned} \tag{5.55}$$

□

Therefore, the observer is BIBO stable for any measured signal during the sweep phase and both its output and the estimation error is bounded. Provided that the rate of change of the excitation frequency $\dot{\omega}(t)$ is sufficiently low with respect to the transient dynamics of the identified system, the measured response is *approximately equal to the steady state frequency response of the system excited by the constant frequency sine wave input* and the observer states may be used for its estimation according to the equations (5.12,5.13). The influence of the sweep rate on the accuracy of these estimates is evaluated further in the thesis. This approximate information is only used for the

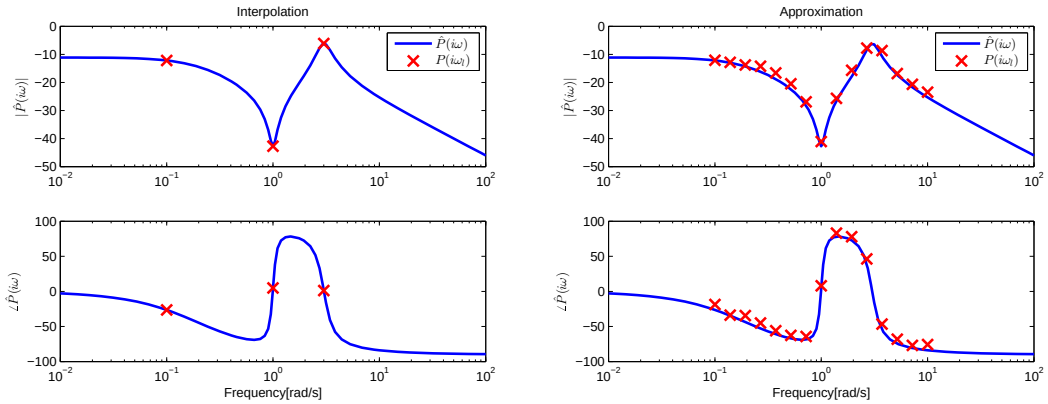

Figure 5.12: Frequency response fitting: interpolation vs approximation

control of the identification experiment and it does not affect the measurements which are used for the model synthesis. Once the frequency sweep stops, the observer moves to the regular LTI system and estimates the true frequency response of the system. Synchronization of the observer with the measured signal during the sweep phase leads to very fast convergence during the measurement phase since the inner states are already properly tracked to the measured output.

5.3 Data fitting and model computation

The proposed observer is used for the acquisition of an arbitrary number of points of the plant frequency response

$$\hat{P}(i\omega_l);\ l = 1, ..., n, \tag{5.56}$$

which are consequently used for a data-fitting to a chosen system model. Two distinct approaches to model synthesis are possible (Fig. 5.12).

Interpolation algorithm uses a limited number of specifically chosen data points which are exactly interpolated by a pre-described transfer function. This is demonstrated on the example of two-mass compliant system. The transfer function from motor torque T_m to motor velocity v_m is given in the form of

$$P(s) = \frac{v_m(s)}{T_m(s)} = \left(\frac{K}{s+a}\right)\left(\frac{s^2 + 2\xi_z\omega_z s + \omega_z^2}{s^2 + 2\xi_n\omega_n s + \omega_n^2}\right) = \frac{b_2 s^2 + b_1 s + b_0}{s^3 + a_2 s^2 + a_1 s + a_0}. \tag{5.57}$$

Six unknown coefficients of this transfer function can be sorted in the parametric vector

$$\boldsymbol{p} = \begin{bmatrix} a_0 & a_1 & a_2 & b_0 & b_1 & b_2 \end{bmatrix}. \tag{5.58}$$

The values of plant parameters can be computed from the three measured points of the frequency response $\hat{P}(i\omega_l)$ which give six values of real and imaginary parts. The

closed form analytical solution can be found from the set of polynomial equations:

$$\begin{aligned} \Re(P(i\omega_l)) &= \Re(\hat{P}(i\omega_l)), \\ \Im(P(i\omega_l)) &= \Im(\hat{P}(i\omega_l));\ l = 1,..,3. \end{aligned} \tag{5.59}$$

The resulting estimates of the transfer function coefficients are obtained in the form of rational functions of the measured points of $\hat{P}(i\omega_l)$:

$$p_k = \frac{num_k\{\Re[P(i\omega_{1,2,3})], \Im[P(i\omega_{1,2,3})]\}}{den_k\{\Re[P(i\omega_{1,2,3})], \Im[P(i\omega_{1,2,3})]\}};\ k = 1..6. \tag{5.60}$$

The physical parameters of the plant (5.57) can be determined from equations:

$$K = b_2, \xi_z = \frac{1}{2}\frac{b_1}{b_2\sqrt{\frac{b_0}{b_2}}}, w_z = \sqrt{\frac{b_0}{b_2}}, \tag{5.61}$$

the remaining parameters $\{a, \xi_n, \omega_n\}$ are obtained from the roots of the cubic equation in the denominator of transfer function (5.57). A complete print-out of the solution can be found in the appendix (10.2).

In order to capture the shape of the frequency response precisely, the three points has to be chosen carefully. One point should catch the low frequency behaviour determined by static gain and first order lag part. The other two are naturally chosen in the vicinity of the resonance and antiresonance peaks to get precise values of their frequency and damping. These points can be automatically selected by the identification algorithm. Typical frequency response of a flexible mechanical system contains several peaks in amplitude which are accompanied by steep changes of the phase shift. Thus, *observation of the actual phase lag, along with determination of the local extremes in the amplitude during the sweep phase can be used to get the information about the location of the important resonance and antiresonance regions of the frequency response*. As an alternative, the measurement points can be chosen manually by the user after an initial sweep from the plotted Bode curves or from an a priori knowledge about the system dynamics.

Approximation algorithm uses an arbitrary number of data points $\hat{P}(i\omega_l)$ (typically much higher than the number of the unknown parameters) to construct an approximating transfer function. This leads to a nonlinear least squares optimization since the frequency response data are nonlinear with respect to the plant parameters. The model-fitting problem is formulated as a minimization of a cost function $\chi^2(\boldsymbol{p})$ which is defined as the sum of squares of the residuals:

$$\begin{aligned} \boldsymbol{r(p)} &= \left[\ r_1(\boldsymbol{p}) \quad r_2(\boldsymbol{p}) \quad \dots \quad r_m(\boldsymbol{p})\ \right]^T;\ r_l(\boldsymbol{p}) = |P(i\omega_l) - \hat{P}(i\omega_l, \boldsymbol{p})|, l = 1..m \\ \chi^2(\boldsymbol{p}) &= \tfrac{1}{2}\sum_{i=1}^{m}\left[\tfrac{r_i(\boldsymbol{p})}{w_i}\right]^2 = \tfrac{1}{2}\boldsymbol{r(p)^T W r(p)}, \boldsymbol{p}^* = \underset{\forall \boldsymbol{p}}{argmin}\{\chi^2(\boldsymbol{p})\}, \end{aligned} \tag{5.62}$$

where $\boldsymbol{W} = diag\{\frac{1}{w_i^2}\}$ is a diagonal weighting matrix which introduces a relative confidence in the measurement of the individual data points, $\boldsymbol{p}$ is the vector of unknown

parameters (transfer function coefficients) and $\boldsymbol{p}^*$ is the optimal solution of the data fitting problem.

The nonlinear least-squares optimization has no analytical solution and a proper numerical algorithm has to be used. The Levenberg-Marquardt (LM) method [28, 29] which is considered as a standard for the nonlinear least squares problem and which is described in the preliminary chapter (2.5) is a suitable candidate for this purpose.

The LM algorithm starts with an initial estimate of the parametric vector and performs an iterative search of the local minimum of the objective function. The actual parameters are updated in each step by addition of a perturbation vector $\boldsymbol{h_{LM}}$ which is obtained as a solution of the normal equations:

$$[\boldsymbol{J^T(p)WJ(p)} + \lambda \boldsymbol{I}]\boldsymbol{h_{LM}} = -\boldsymbol{J^T(p)Wr(p)}, \boldsymbol{p}_{i+1} = \boldsymbol{p}_i + \boldsymbol{h_{LM}}, \tag{5.63}$$

where $\boldsymbol{J}$ is the $m \times k$ *Jacobian matrix* which contains the first partial derivatives of the residual functions ($[\boldsymbol{J(p)}]_{i,j} = \frac{\partial r_i}{\partial p_j}(\boldsymbol{p})$) and λ is an adaptation parameter which is automatically updated in each iteration according to the local behaviour of the cost function. The algorithm smoothly interpolates between Gauss-Newton and Gradient-descent iterations based on the local validity of the quadratic model of the objective function (see section 2.5 for detailed description):

$$\chi^2(\boldsymbol{p}+\boldsymbol{h}) = \chi^2(\boldsymbol{p}) + \boldsymbol{h^T J(p)^T W r(p)} + \frac{1}{2}\boldsymbol{h^T J(p)^T W J(p) h}. \tag{5.64}$$

The Jacobian matrix can be computed analytically from the a priori chosen transfer function of the system model $\hat{P}(i\omega)$. Considering that

$$P(i\omega_l) = a_l + ib_l,\ \hat{P}(i\omega_l, \boldsymbol{p}) = \hat{a}_l(\boldsymbol{p}) + i\hat{b}_l(\boldsymbol{p}), \tag{5.65}$$

the residual function can be rewritten in terms of the real and imaginary part of the measured and estimated data points of the transfer function as:

$$r_l(\boldsymbol{p}) = |P(i\omega_l) - \hat{P}(i\omega_l, \boldsymbol{p})| = \sqrt{\triangle a_l^2(\boldsymbol{p}) + \triangle b_l^2(\boldsymbol{p})}; \triangle a_l(\boldsymbol{p}) = a_l - \hat{a}_l, b_l(\boldsymbol{p}) = b_l - \hat{b}_l. \tag{5.66}$$

Therefore, the $m \times k$ Jacobian matrix is constructed from the partial derivatives of the residual functions (5.66) as follows:

$$[\boldsymbol{J(p)}]_{l,j} = \frac{\partial r_l}{\partial p_j}(\boldsymbol{p}) = -\frac{1}{\sqrt{\triangle a_l^2 + \triangle b_l^2}}[\triangle a_l \frac{\partial \hat{a}_l}{\partial p_j} + \triangle b_l \frac{\partial \hat{b}_l}{\partial p_j}]. \tag{5.67}$$

A numerical example of the proposed approximation algorithm is given for the oscillatory two-mass system (5.57). Fifteen measured points of the system frequency response were used for the computation of the approximation function. A measurement error in the form of normally distributed random numbers with the zero mean and standard deviation $\sigma = 0.3$ was added both to the amplitude and phase data. Relatively large errors were introduced intentionally in the chosen initial guess of the plant parameters in order to demonstrate the robustness of the LM algorithm. The actual plant parameters as well as their initial guess and the obtained estimates are listed in the table (5.1).

	P_{true}	$\hat{P}_{init}$	$\hat{P}_{fit}$	$\lvert\frac{p_{fit}-p_k}{p_k}\rvert$
K	0.5	500	0.5025	0.5%
a	0.2	0.01	0.233	16.5%
ω_n	3	15	3.02	0.7%
ξ_n	0.15	0.1	0.142	5.3%
ω_z	1	0.1	1.0356	3.6%
ξ_z	0.06	0.1	0.0462	23%

Table 5.1: Numerical example - true and estimated parameters of the two-mass system, application of the approximation algorithm using the Levenberg-Marquardt method

Figure (5.13) shows the Bode plots of the actual plant P_{true}, set of measured data points P_{meas}, initial model P_{init} and the obtained approximating transfer function P_{fit}. It can be seen that the resulting model closely fits the measured data points and the true plant transfer function in spite of the measurement errors and large initial deviation of the estimated parameter values. The lower plots show the evolution of the parameter estimates (coefficients of the model transfer function) and the values of the cost function χ^2 and the adaptation parameter λ. It can be seen, that the LM algorithm quickly converges towards the local minimum point during the first 50 iterations. About 30 steps which are close to the Gauss-Newton update are observed in the initial phase with λ starting at the chosen initial value $\lambda_0 = 1e-7$. Further improvement is observed in the final stage in which the λ increases to achieve more gradient-descent directions of the parameter updates.

Despite the robustness of the LM method, the initial estimate of the plant parameters $\boldsymbol{p_0}$ should be chosen as close to their real values as possible in order to improve the chance of convergence to the optimal fitting function. Several approaches or their combination can be used to obtain some proper initial guess:

- Computation of the *interpolating function* from the limited number of data points in the first step and utilization of the obtained parameters as the initial values for the second step of approximation function fitting.
- Determination of the physical plant parameters from the shape of the measured frequency response (local extremes of the amplitude response along with the steep changes in the phase shift etc.).
- Random search in a properly chosen parameter subspace using the Monte Carlo method, selection of a best initial guess candidate which minimizes the value of the $\chi^2(\boldsymbol{p_0})$ criterion function.

Interpolation vs approximation

The two presented approaches have specific advantages and drawbacks which have to be taken into consideration. The **interpolation method** offers an analytic solution

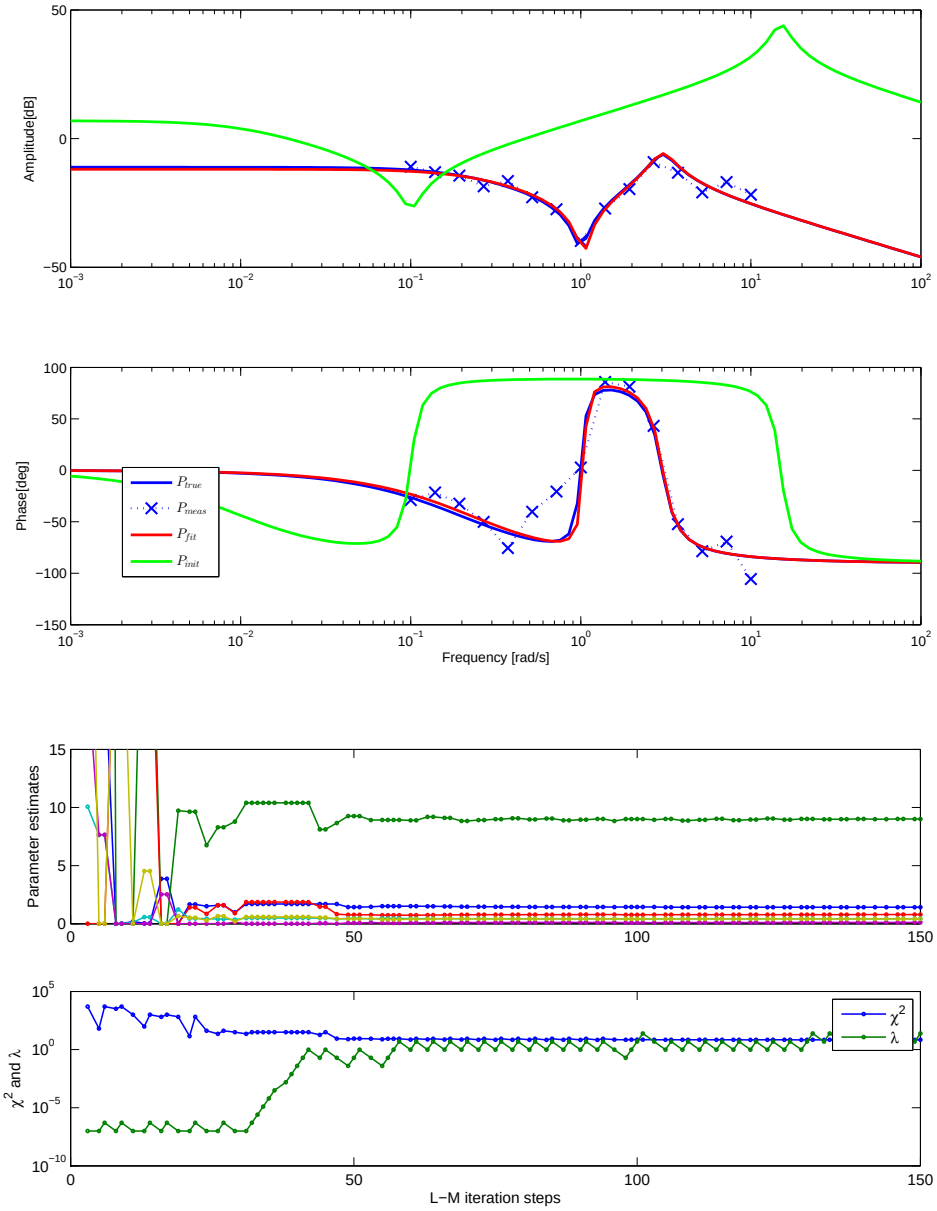

Figure 5.13: Frequency response fitting: approximation algorithm using the LM method; up - Bode plots of true plant transfer function P_{true}, measured data points P_{meas}, initial parameters transfer function P_{init} and final approximating function P_{fit}, down - convergence of the LM iterations - parameter estimates, cost function χ^2 and adaptation parameter λ

and direct computation of the plant parameters from the measured data which can be carried out on the target real-time control platform. However, the complexity of the

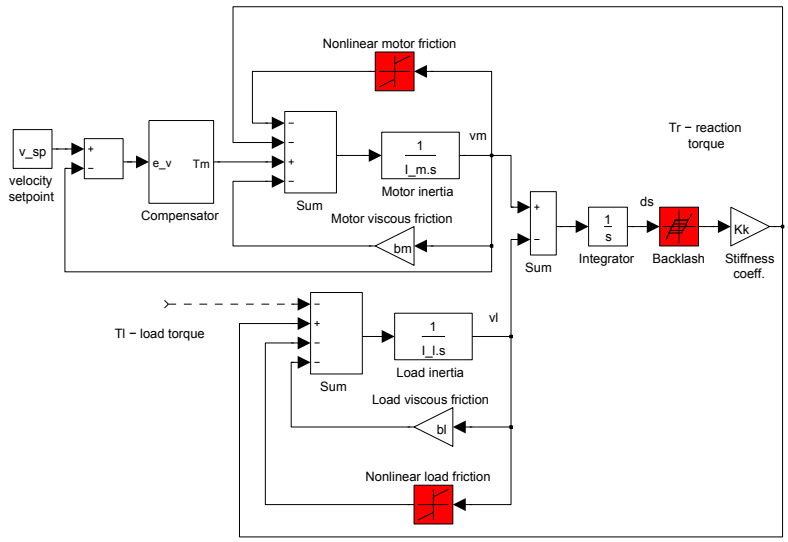

Figure 5.14: Nonlinear mechanics - diagram of the velocity control loop with a flexible two-mass system and the typical sources of nonlinear dynamics - friction and backlash

solution of the corresponding polynomial equations rises exponentially with the number of the plant parameters. Its use is practically limited to a fourth order system (rigid plus one resonance mode and an additional first order dynamics) for which the closed-form formulas may be obtained using the standard tools for symbolic computations. A correct choice of measurement points is needed in order to capture the shape of the frequency response in the presence of a measurement errors.

On the contrary, the **approximation method** uses numerical algorithms for the solution of the nonlinear least-squares problem. More computing power is required for the numerical optimization which may lead to the necessity of its execution in the drive commissioning software running on a personal computer. The convergence is generally not guaranteed and only a local minimum of the cost function may be found. A proper initial parameter estimate is needed to improve the accuracy of the results. The approximation algorithm is less sensitive to the measurement errors as a large number of the frequency response points can be involved in the computations. The order of the system is not limited in this case since the LM method works well even for the large scale problems. Proper combination of the proposed interpolation and approximation methods may be used to achieve suitable results of the frequency identification.

5.4 Identification of nonlinear mechanics

As was explained in the previous chapter (see section 3.4.3), a nonlinear behaviour of mechanical systems is often observed in practice. A significant amount of back-

lash, hysteresis or a nonlinear friction complicates the process of the commissioning of the motion control loops and affects the stage of identification as well as the performance of the implemented control algorithms. Proper adaptation of the methods for the automatic controller synthesis is needed to cope with the nonlinearities and obtain a suitable solution which can be employed in practical applications.

The nonlinear friction and backlash are usually recognized as the most significant sources of nonlinearity [81, 146, 157]. The way they affect the otherwise linear dynamics of a mechanism is illustrated in Fig. (5.14) on the example of a nonlinear flexible two-mass system. The friction arises at the boundary of the contacting bodies during their relative motion and causes an external disturbance torque or force acting on the drive or load. A well designed actuator with a suitable amount of lubrication, flawless bearings and proper mounting typically exhibits a linear curve of the viscous friction which is directly proportional to the operating speed. In contrast, a nonlinear load-side friction characteristics with stiction and Coulomb effects are often encountered in practice due to the higher mass and surface of the contacting bodies. The effect of the nonlinear friction on the otherwise linear dynamics of the controlled plant are pronounced in the vicinity of the zero velocity of the load and drive due to the introduction of various types of discontinuities. The typical result is the *stick-slip effect* which is observed as an irregular running during the reversing of a motion direction or as a hunting phenomenon which arises during the precise positioning. The nonlinear system response complicates the use of the identification methods which are based on the assumption of the plant linearity and often leads to the occurrence of limit cycles in the closed position loops. The backlash is usually caused by the utilization of gears which introduce a small amount of clearance in the drivetrain. Steep changes in the amplitude and direction of the driving torque or force brings a repeating disconnection of the mechanical coupling between the actuator and the driven load and may lead to a jerky motion, excitation of vibrations and occurrence of steady-state limit cycles.

Even in the case of a nonlinear mechanics with a significant influence of the friction or backlash, there are strong arguments for the importance of the identification of the *linear part* of the system dynamics:

- The nonlinear friction affects the system mainly in the low-speed region. It may be insignificant for velocity loops which operate mainly in non-zero velocities (e.g. conveyor-belts or point-to-point manipulators). For the position control loops, the nonlinearity is prevalent in the steady-state for which some friction compensation method may be used to improve the positioning accuracy.

- The acquisition of the complete nonlinear model may be difficult as the friction characteristics typically vary in time due to the change of a payload, variations in the system operating point, temperature or lubrication fluctuations, or due to the increasing wear of the mechanical components. The problem may be solved by a proper design of a robust or adaptive controller based on the linear model of the plant. Alternatively, the parameters of the nonlinearities may be obtained in the second step of the system identification and used for a model-based compensation

or for the estimation of the unknown state variables.

- There are many powerful methods for design of robust and adaptive controllers in the framework of linear systems which can cope with eventual nonlinearities in the loop.
- The effect of the backlash can be reduced by proper tuning of the controller. Well damped transient response without steep changes in the driving torque and a reduction of the closed-loop bandwidth may improve the quality of control.

Exciting signal adaptation

The influence of the nonlinearities on the identification of the linear part of the system dynamics can be reduced by a proper *adaptation of the amplitude of the generated excitation signal*. Whether a static or dynamic model of the nonlinear friction is assumed, the corresponding friction force/torque can be considered as an external disturbance acting on the linear system. Its magnitude is always limited since the viscous component of the friction may be incorporated in the identified model and the relative influence of the nonlinearity is inversely proportional to the magnitude of the driving force or torque which is generated by the actuator. This can be explained for a static nonlinear load-side friction model using the method of *describing function analysis*. Considering that the actuator delivers a harmonic excitation signal with a sufficient amplitude (in order to overcome the stiction and Coulomb effects of the friction), the load is put in a periodic motion. Supposing that the load inertia acts as a low-pass filter which allows only the first harmonics of the excitation input to pass to load velocity output $v_l = A\sin(\omega t)$ which drives the nonlinearity (see the load-side part of the diagram 5.14), the resulting friction T_f is a periodic function $T_f(t) = T_f(t+T)$ which can be expressed as a Fourier series expansion:

$$\begin{aligned} T_f(t) &= \frac{a_0}{2} + \sum_{n=1}^{\infty}[a_n(\sin n\omega t) + b_n(\cos n\omega t)],\ \omega = \frac{2\pi}{T}, \\ a_n(A,\omega) &= \frac{1}{\pi}\int_0^{2\pi} T_f(t)\sin(n\omega t)d(\omega t),\ b_n(A,\omega) = \frac{1}{\pi}\int_0^{2\pi} T_f(t)(\cos n\omega t)d(\omega t), \end{aligned} \tag{5.68}$$

where a_n, b_n are the Fourier coefficients. Assuming only the first harmonics, the nonlinear friction function is approximated by an amplitude dependent **describing function** which is defined as the ratio of the Fourier images of the input and output signals:

$$N(A,\omega) = \frac{\mathfrak{F}[T_f(t)]}{\mathfrak{F}[v_l(t)]} \triangleq \frac{T_f(A,\omega)}{V_l(A,\omega)} = \frac{a_1(\omega) + ib_1(\omega)}{A}. \tag{5.69}$$

For the simplest Coulomb friction model $T_f(t) = -Msign\,[v_l(t)]$, we obtain:

$$b_1 = 0,\ a_1 = -\frac{4M}{\pi} \Rightarrow N(A,\omega) = -\frac{4M}{\pi A}, \tag{5.70}$$

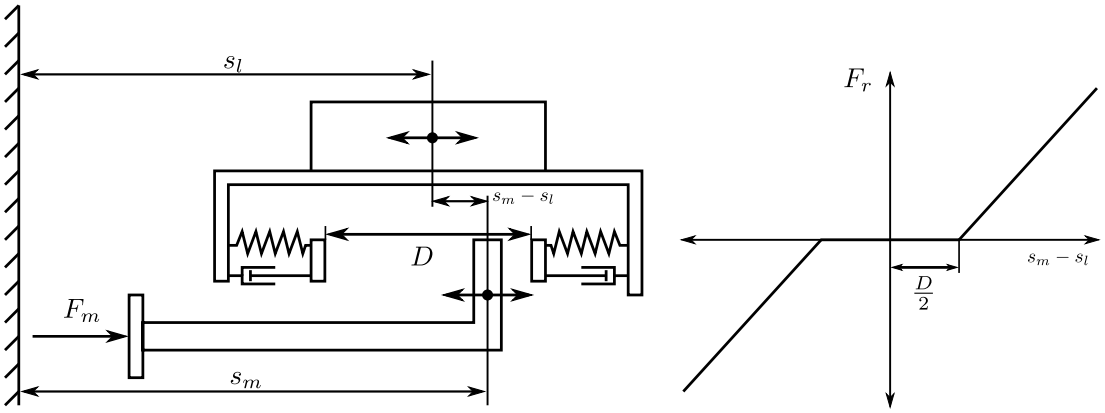

Figure 5.15: Flexible drive-train including the backlash model: left - schematics of the mechanical configuration, right - dead-zone type nonlinearity generating the reaction force/torque; s_m - actuator displacement, s_l - load displacement, D - backlash range, F_m - actuator force, F_r - reaction force

which clearly indicates that the contribution of the nonlinearity is inversely proportional to the magnitude of the load velocity and therefore the driving torque as well. This holds generally for a more complex friction models which can be described as an odd static nonlinearity without a dead zone or hysteresis. In this, case, the imaginary part of the describing function and the corresponding Fourier coefficient is computed as $b_1 = 0$ since the nonlinear function does not introduce any phase shift and the real part coefficient a_1 is frequency independent. Thus the describing function model reduces to the form:

$$N(A,\omega) = \frac{T_f(A,\omega)}{V_l(A,\omega)} = \frac{a_1(A)}{A}. \tag{5.71}$$

Further assuming that the nonlinearity output is limited in magnitude, we may write

$$\forall t : T_f(t) < k_1 \Rightarrow a_1(A) < k_2 \tag{5.72}$$

for some positive scalars $k_1, k_2 > 0$. Therefore, it may be concluded that the relative influence of the nonlinearity decreases with the increasing level of the excitation input. More complex analysis should be performed in the case of dynamic friction models. However, assuming that the driving torque generated by the actuator and consequently the reaction torque which drives the load are dominating with respect to the friction disturbance ($T_m, T_r >> T_f$), the response of the plant is very close to the output of the linear part of the system dynamics and the influence of the nonlinearity is becoming insignificant.

Similar conclusions may be derived for the *backlash nonlinearity*. Traditional models of backlash in mechanical systems usually consider an ideal rigid connection of the actuator and load during the pinned mode (contact movement after the backlash has been taken out). The trajectory of motion is described by the input-output displacement

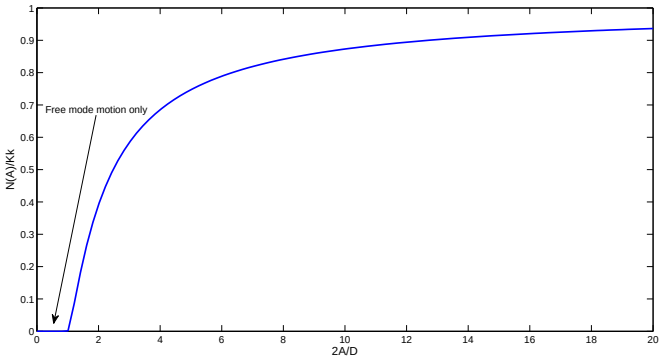

Figure 5.16: Describing function of the dead-zone nonlinearity: model of a flexible mechanical coupling with backlash

diagram with a hysteresis shape (see Fig. 3.18b). However, this model is not applicable for the flexible systems with compliant loads. For such cases, a correct description of the backlash phenomenon may be obtained in the following way. The assumed compliant mechanical connection of the actuator and load including the backlash is depicted in Fig. (5.15). For a small relative displacement $|s_m - s_l| < D/2$ of the two connected bodies in the range of the backlash D, there is no mechanical coupling between the actuator and load (free mode of motion). The reaction force F_r which drives the load and counteracts the actuator movement is zero. In the pinned mode which is valid for $|s_m - s_l| > D/2$, the reaction is directly proportional to the relative displacement and the stiffness constant which models the flexible coupling as an ideal linear spring. Eventually, a modal damping term may be added. The motion dynamics of the pinned mode is identical to that of the backlash-free flexible multi-mass system (see equations 3.56 for the two-mass case). Therefore, *the backlash may by modelled as a dead-zone type nonlinearity* which relates the resulting reaction force or torque with the relative displacement of the actuator and load bodies (Fig. 5.15 right). The describing function analysis may be applied to evaluate the influence of the nonlinearity with respect to the amplitude of the excitation signal.

The output of the dead-zone function under a harmonic excitation signal $u(t) = s_m(t) - s_l(t) = A\sin(\omega t)$ has a shape of a shifted sinusoidal function with three dead periods which correspond to the free motion. It is given as [203]:

$$F_r(t) = \begin{cases} 0 & \text{if } |u| < D/2 \Rightarrow \omega t \in \langle k\pi - \gamma, k\pi + \gamma \rangle \\ K_k[A\sin(\omega t) - D/2] & \text{if } |u| > D/2 \Rightarrow \omega t \notin \langle k\pi - \gamma, k\pi + \gamma \rangle \end{cases} \quad (5.73)$$
$$k = 0, 1, 2, ..., n$$
$$\gamma = \sin^{-1}(\tfrac{D}{2A}),$$

where K_k is the stiffness coefficient. The dead-zone is a static odd nonlinearity which leads to $b_1 = 0$ in the Fourier expansion. The coefficient a_1 and the corresponding integration may be performed for the interval $\omega t \in \langle 0, \pi/2 \rangle$ and multiplied by four due

to the symmetrical shape of the output as:

$$a_1 = \frac{4}{\pi}\int_0^{\pi/2} F_r(t)\sin(\omega t)d(\omega t) \tag{5.74}$$

$$= \frac{4}{\pi}\int_\gamma^{\pi/2} K_k[A\sin(\omega t) - D/2]\sin(\omega t)d(\omega t)$$

$$= \frac{2K_kA}{\pi}\left(\frac{\pi}{2} - \gamma - \frac{D}{2A}\sqrt{1-\frac{D^2}{4A^2}}\right). \tag{5.75}$$

Therefore, the describing function is obtained in the form of:

$$N(A) = \frac{2K_k}{\pi}\left(\frac{\pi}{2} - \gamma - \frac{D}{2A}\sqrt{1-\frac{D^2}{4A^2}}\right). \tag{5.76}$$

The describing function is zero for $A < \frac{D}{2}$ (free mode within the backlash region without any mechanical coupling to the load) and converges asymptotically to $N(A) = K_k$ (purely linear output response without the backlash) for the increasing amplitude of the input $A >> \frac{D}{2}$, see Fig. 5.16). This corresponds to an intuitive physical explanation - higher amplitude of the excitation signal allows a faster cleardown of the backlash during the motion reversal and causes less distortion of the resulting waveform of the reaction torque.

A valuable insight into the qualitative behaviour of the typical nonlinearities was obtained despite the approximate nature of the describing function method. The conclusion is that **an increase of the amplitude of the exciting signal during the identification suppresses the effects of the nonlinear friction and backlash to the overall output response**. Proper adaptation of the amplitude allows the utilization of the standard techniques for the estimation of the linear part of the system dynamics.

A nonlinear behaviour of the system may be detected during the identification procedure using the observer which was proposed in the previous section. An ideal linear response of the system contains only the first harmonic frequency which corresponds to the excitation signal (see equation 5.3). Occurrence of higher harmonics in the measured output response signalizes an influence of some nonlinearity which may be quantified by the **total harmonic distortion** index (THD):

$$THD(t) = \frac{\sqrt{\{A_2(t)^2 + A_3(t)^2 + A_4(t)^2 + A_5(t)^2\}}}{A_1(t)}, \tag{5.77}$$

where A_i correspond to the estimated amplitudes of the first five harmonics in the measured output. As the goal is to identify the linear part of the system dynamics, the THD can indicate the validity of the estimated point of the frequency response $\hat{F}(i\omega)$. During the experiment, the actual value of THD is monitored. If it exceeds a user specified level, the amplitude of the harmonic excitation signal $u(t) = A(t)\sin(\omega t)$ is smoothly increased. A simple integrator combined with a relay can be used to implement this

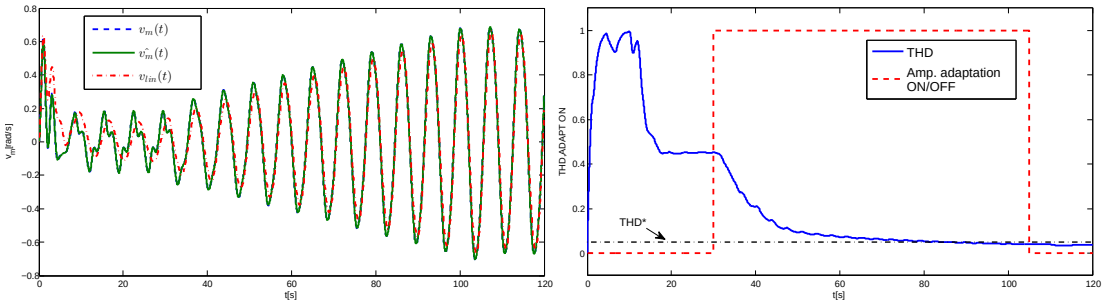

Figure 5.17: THD adaptation - response of the nonlinear two-mass system including friction and backlash, left - true and estimated motor velocity $v_m, \hat{v}_m$, response of the linear part of the system without the nonlinearities v_{lin}, right - measured THD index

adaptation law:

$$\begin{aligned} A(t) &= A(t_0) + \int_{t_0}^{t} \frac{1}{T_i} r(t)dt; T_i = \frac{2\pi}{r_c A(t_0)\omega} \\ r(t) &= \begin{cases} 1 & \text{if } THD > THD^* + h \\ 0 & \text{if } THD < THD^* - h \end{cases} \end{aligned} \tag{5.78}$$

where $r(t)$ is output of relay with hysteresis h, THD^* is setpoint threshold for THD and T_i is integral time constant defining the rate of adaptation. Recommended value for THD^* which was obtained from practical experiments is approximately 5-10%. The time constant T_i is defined relatively to the actual frequency with the relative change of $r_c = \frac{A}{A(t_0)}$ in amplitude during one period of the excitation input $T = \frac{2\pi}{\omega}$.

The process of adaptation is demonstrated by means of a numerical simulation in Fig. (5.17). A flexible two-mass system with the parameters from the table 5.1 is excited by a harmonic input. Nonlinear load-side friction is added in the form of Karnopp model [204]:

$$T_f = \begin{cases} T_R - T_l = T_e & \text{if } |T_e| < T_S \cap |v_l(t)| \leq dv \\ T_S sign\left[T_e(t)\right] & \text{if } |T_e| \geq T_S \cap |v_l(t)| \leq dv \\ T_C sign\left[v_l(t)\right] & \text{if } |v_l(t)| > dv \end{cases} \tag{5.79}$$

where T_f is the friction torque, T_e is the total external torque acting on the load which comprises of reaction torque T_R and external load torque T_l (see Fig.5.14). The external torque has to overcome the stiction T_S in the vicinity of zero velocity for $|v_l(t)| \leq dv$ in order to move the load. The lower value of T_C which corresponds to the Coulomb friction is applied for the higher load velocities $|v_l(t)| > dv$. Therefore, the stiction and Coulomb effects are considered in the model.

The friction model parameters were chosen as $\{T_s = 3, T_C = 0.5, dv = 0.02\}$. Stick-slip motion of the load introduces some higher harmonics in the response of the

measured drive velocity. This corresponds to the value $THD = 45\%$, which is obtained at $t = 17$ after an initial transient. The acquisition of the frequency response estimate $\hat{F}(i\omega)$ under these operating conditions would lead to a significant error in the magnitude and phase as can be seen from comparison of the estimated velocity $\hat{v}_m$ and the velocity obtained from a concurrently running linear model without the nonlinear friction ($v_{lin}(t)$ which is excited by the same input signal. The amplitude adaptation is enabled at $t = 30$ according to the equation (5.78). The increase of the amplitude of the exciting input leads to the vast reduction of the friction effect. The resulting output response is almost linear as indicated by the computed THD level which crosses the chosen maximum threshold $THD^* = 8\%$ at $t = 104$. The measurement of the frequency response can be done at this moment from the observer states (equations 5.11). Similar results were obtained for the backlash nonlinearity and for more complex friction models (e.g. LuGre and Maxwell slip models) which covers other nonlinear phenomenons such as hysteresis and the Stribeck effect [81, 84].

The same adaptation mechanism can be used for the control of the **signal to noise ratio (SNR)** which is defined as a power ratio between a signal and a measurement noise:

$$SNR(t) = \frac{P_{signal}}{P_{noise}}. \tag{5.80}$$

The wideband high frequency noise corrupts the ideal sinusoidal waveform of the measured plant output which results in excitation of the estimates of the higher harmonics. Therefore, the THD value may be used as a measure of the relative power of the noise at higher frequencies with respect to the fundamental frequency estimate which contains the meaningful information about the frequency response. Therefore, we may write:

$$SNR(t) \approx \frac{A_1(t)}{\sqrt{\{A_2(t)^2 + A_3(t)^2 + A_4(t)^2 + A_5(t)^2\}}} = \frac{1}{THD(t)}, \tag{5.81}$$

In the case that the noise level of the measurement channel is known in advance, the SNR may be alternatively estimated as:

$$SNR(t) \approx \frac{A_1(t)}{A_n}, \tag{5.82}$$

where A_n is the level of the measurement noise which can be specified from the known accuracy rating of the feedback sensor or it is obtained experimentally by measuring the steady-state variance of the output signal.

In the case that the computed SNR value violates the minimum defined treshold, the quality of the estimate of $F(i\omega)$ is low and the amplitude of the input signal has to be incremented. This can especially happen in the antiresonance region of the frequency response where the amplitude of the motor speed decays rapidly and information about the system dynamics can be lost in the measurement noise.

The demand for a large amplitude of the excitation signal with respect to the SNR and THD indices may lead to an overshoot of the physical limits imposed by the system

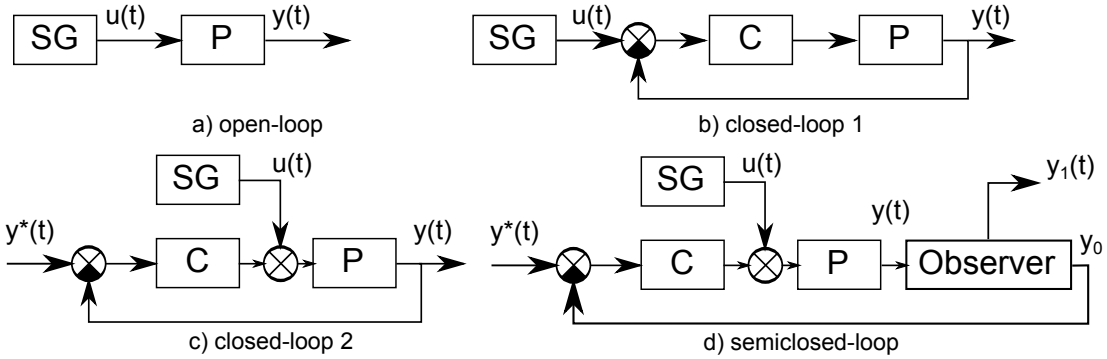

Figure 5.18: Open-loop and closed-loop identification - different identification schemes (SG - signal generator, P - plant, C - compensator)

(a bounded range of motion, saturation of the actuator or a velocity limit). This is important especially in the vicinity of the resonance frequencies of the system. When the measured output gets close to the physical limits, another adaptation rule decreases or holds the level of the input amplitude. An algorithm which decides whether an increment or a decrease is actually needed has to be implemented in the experiment logic (see the *range reduction, SNR and THD adaptation* modules in Fig. (5.1). Naturally, there may be some situations in which the physical limits do not allow a sufficient excitation in order to sufficiently suppress the effects of nonlinearities and an error is introduced in the obtained estimate of the frequency response.

5.5 Closed-loop identification

As was explained in the previous chapter, the *standard open-loop identification scheme (Fig. 5.18a) may be inapplicable for certain mechanical configurations*. Unstable systems such as robotic arms or mechanisms with hanging loads could collapse due to the gravity effect. Even for stable systems, it may be advantageous to keep the velocity or position around some defined working point during the identification experiment (e.g. a nonnegative average velocity of a free-running system to overcome the friction effects or a center position in the middle of the available range of motion for a positioning system).

The usual solution is to implement one of the standard closed-loop schemes (5.18b,c) with a feedback compensator which stabilizes the system and the signal generator which produces the input disturbance or the setpoint command. The main drawback of these configurations is that the controller counteracts the excitation signal in an effort to stabilize the system. This may *significantly affect the power spectrum density of the overall system input* which should sufficiently excite the plant dynamics in the desired frequency range.

Considering a plant and compensator dynamics which can be expressed in the form of transfer function polynomials $C(s) = \frac{d(s)}{c(s)}$, $P(s) = \frac{b(s)}{a(s)}$, we can derive the closed-loop

transfer functions from the exciting signal generator u_g to the overall plant input u_p for the closed-loop schemes (5.18b,c):

$$\begin{aligned} F_{cl1}(s) &= \frac{u_p(s)}{u_g(s)} = \frac{C(s)}{1+C(s)P(s)} = \frac{a(s)d(s)}{a(s)c(s)+b(s)d(s)}, \\ F_{cl2}(s) &= \frac{1}{1+C(s)P(s)} = \frac{a(s)c(s)}{a(s)c(s)+b(s)d(s)}. \end{aligned} \tag{5.83}$$

Assuming that we deal with an oscillatory mechanical system, the weakly damped complex poles from the polynomial $a(s)$ appear as zeros in both transfer functions F_{cl1}, F_{cl2} and introduce an antiresonance stop-band region in the frequency response. For a well tuned closed loop with properly damped poles given by the characteristic polynomial $a(s)c(s)+b(s)d(s)$, the **compensator prevents from the excitation of the system on its eigenfrequencies even if a wideband or large amplitude signal is produced by the generator**. This can significantly affect the precision of system identification in the frequency range which is the most important for the synthesis of vibration damping controllers. The only solution to overcome this effect is to actually detune the feedback controller and place the closed loop poles close to the vicinity of the weakly damped poles of the open-loop system $a(s)$ and compensate the antiresonance in the corresponding frequency responses (5.83). However, this may cause problems with the stability of the closed-loop and excessive transient response of the system may occur during the identification procedure. *There are conflicting requirements for sufficient excitation of the system for the purpose of identification and the requirement of system stabilization by means of the feedback compensator which tries to minimize the variance of the plant output*.

A so called **semi-closed loop scheme** is proposed to overcome these problems (Fig. 5.18d). In the first phase, a low-bandwidth compensator which stabilizes the system is designed. Either a velocity or position controller may be used based on the particular application demands. A simple integral or proportional-integral controller in the velocity loop and a proportional controller in the position loop is satisfactory for most applications. Only rigid dynamics of the system may be assumed for a low desired closed-loop bandwidth and the procedure for velocity or position control design which was discussed in the previous chapter may be used. In the phase of the identification experiment, the feedback is switched from the actual measured output $y(t)$ to its mean value $y_0(t)$, which is estimated using the proposed observer. In the steady state, the compensator controls only the mean value of the output signal which is kept constant around a chosen operating point and it does not react to the high frequency components of the measured response which are caused by the excitation by the harmonic disturbance. Provided that the observer bandwidth ω_{BW}^0 in the DC component channel is sufficiently large with respect to the closed loop bandwidth of the stabilizing feedback loop ω_{BW}^{cl} we may write:

$$|F_{DCy}(i\omega)| = \left|\frac{Y_0(i\omega)}{Y(i\omega)}\right| \approx 1 \; \forall \omega < \omega_{BW}^0, \; \omega_{BW}^0 >> \omega_{BW}^{cl}. \tag{5.84}$$

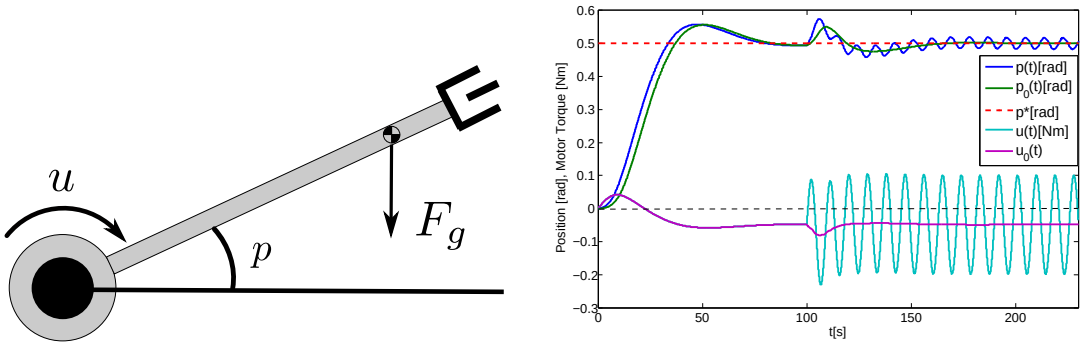

Figure 5.19: Unstable position controlled system - flexible robotic arm during the semiclosed-loop identification; $p(t)$ - actual measured motor side position,$p_0(t)$ estimated DC component of the output, p^* setpoint command for the feedback position controller, $u(t)$ overall input (motor torque), $u_0(t)$ input generated by the feedback controller, the experiment starts at t=100s

The frequency response of a properly designed observer and the corresponding transfer function to the mean value estimate $F_{DCy}(i\omega)$ has low-pass characteristics with the stop-band regions around the fundamental frequency and the higher harmonics (see the last Bode plot in Fig.5.10). Therefore, the high frequency dynamics of the observer as well as the injection of the exciting harmonic signal does not affect the slow stabilizing loop whose behaviour remain unchanged with the introduction of the observer into the feedback and the switch-over from the measured output to its estimated mean value. On the contrary, slow variations in the measured output which may be excited by a low-bandwidth feedback controller do not affect the measurement process due to the band-pass shape of the frequency response in the individual observer channels (first five plots in Fig.5.10). **The system frequency response can be identified in the same way as in the open loop configuration, the feedback compensator does not influence the identification experiment and vice-versa**. The stabilizing low bandwidth compensator and the high-bandwidth observer operate in a different frequency range and under assumption of slow variation of the frequency of the signal generator output they do not influence each other.

The principle of the proposed method is illustrated in (Fig. 5.19) which shows a simulation experiment with an unstable position controlled system. A flexible robotic arm is stabilized by the cascade control scheme with a simple integral controller in the velocity loop and a proportional controller in the position loop. The velocity and position control gains were computed for a low frequency approximation of the arm dynamics $P(s) = \frac{P(s)}{U(s)} \approx \frac{1}{Is^2}$ where I is the overall inertia of the arm with respect to the axis of rotation. At the beginning of the simulation, the system is stabilized at the operating point $p = 0.5rad$. The harmonic excitation signal is introduced as the input disturbance at time $t = 100s$. The compensator uses the mean value position feedback p_0 to stabilize the system. After a short initial transient, the mean value reaches the

steady state and the identification experiment proceeds the same the same way as in the open-loop configuration while compensating the effect of the gravity force and stabilizing the system around the specified working point.

5.6 Discrete-time implementation

The identification algorithms which were proposed in the previous sections have to be discretized for the possibility of direct implementation in a sampled data system.

Excitation signal generator

The discrete-time version of the harmonic signal generator (5.1) which was described in the previous section is obtained in the state space form as:

$$\begin{aligned} \begin{bmatrix} x_1(k+1) \\ x_2(k+1) \end{bmatrix} &= \begin{bmatrix} \cos\left(\omega(k)T_s\right) & \sin\left(\omega(k)T_s\right) \\ -\sin\left(\omega(k)T_s\right) & \cos\left(\omega(k)T_s\right) \end{bmatrix} \begin{bmatrix} x_1(k) \\ x_2(k) \end{bmatrix}; \boldsymbol{x}(0) = \begin{bmatrix} 0 \\ 1 \end{bmatrix} \\ y(k) &= [A(k)\ 0]\,\boldsymbol{x}(k) + u_0(k), \end{aligned} \tag{5.85}$$

where T_s is the sampling period and $A(k), \omega(k), u_0(k)$ denote the actual values of amplitude, frequency and DC component, respectively. The chosen state coordinates allow bumpless changes of the generator frequency in each step of the algorithm during the sweep phase of the identification. The actual amplitude is obtained from the proposed adaptation rules by monitoring the THD and SNR indices (direct discrete-time equivalents of the equations 5.77,5.78,5.80) and the range of motion is kept in the allowable range. The DC component u_0 is set by a feedback compensator in the case of the semi-closed loop identification.

Frequency response observer

There are two possible approaches for the discrete-time implementation of the proposed estimator:

1. **Direct discrete-time synthesis** - The observer can be designed directly for the discrete-time description of the signal generator model (5.5). The innovation gain vector can be computed analogously to the continuous time case either from the pole-placement problem or using the Kalman filter design procedure.
2. **Computation of a discrete equivalent of the continuous-time observer** - The developed continuous observer and the analytical formulas for the innovation vector gains may be used for derivation of an equivalent sampled-data algorithm. A proper discretization method has to be chosen in order to preserve important characteristics of the observer dynamics.

The drawback of the first approach is, that the observer gain values are nonlinear with respect to the sampling period and the actual value of the fundamental frequency

ω. It is not possible to derive analytical closed-form formulas as in the case of the continuous time and the observer gains have to be computed numerically. Either the pole-placement problem or the discrete algebraic Riccati equation (in the case of the Kalman filter design) would have to be solved in each step of the identification algorithm during the sweep phase in which the excitation frequency $\omega(k)$ varies in time. This would lead to a high computational burden. Moreover, complex numerical routines would have to be implemented in a target platform of a real-time control system.

The second approach requires a careful selection of the discretization algorithm. The zero or first-order-hold methods would cause an inaccurate conversion of the open-loop observer poles and violation of the inner model principle leading to an imperfect frequency response at the fundamental frequency and its higher harmonics, i.e.

$$F_{k\omega y}(e^{ik\omega T_s}) \neq 1;\ k = 1, 2, ..., 5, \tag{5.86}$$

where $F_{k\omega y}(e^{i\omega T_s})$ is the discrete-time frequency response of the estimates of the individual harmonics $k\omega$ (analogous to the continuous time observer, see eq. 5.20).

Tustin transform is a suitable method for this case as it provides guaranteed stability of the resulting discrete equivalent, it leads to good matching in the frequency domain between the continuous and discrete-time representations and the discretization can be computed quickly in each iteration of the identification algorithm. Frequency pre-warping may be used to ensure that the observer response is correct for the fundamental frequency ω.

The starting point is a continuous LTI system given in the state space form:

$$\begin{aligned} \dot{\boldsymbol{x}}(t) &= \boldsymbol{A}\boldsymbol{x}(t) + \boldsymbol{B}\boldsymbol{u}(t), \\ \boldsymbol{y}(t) &= \boldsymbol{C}\boldsymbol{x}(t). \end{aligned} \tag{5.87}$$

The discrete-time equivalent is obtained from the application of the bilinear transform

$$s = \frac{\omega_{pw}}{\tan(\omega_{pw} T_s/2)} \frac{z-1}{z+1}, \tag{5.88}$$

which relates the s-domain and z-domain transfer functions, where T_s is the sampling period of the discrete system and ω_{pw} is the pre-warp frequency. The change of variables (5.88) leads to the following equality:

$$\boldsymbol{H_c}(i\omega_{pw}) = \boldsymbol{H_d}(e^{i\omega_{pw}T_s}), \tag{5.89}$$

with $\boldsymbol{H_c}, \boldsymbol{H_d}$ denoting the transfer matrices of the continuous and discrete equivalents. The discrete-time state space model is obtained in the form:

$$\begin{aligned} \boldsymbol{x}(k+1) &= \boldsymbol{\Phi}\boldsymbol{x}(k) + \boldsymbol{\Gamma}\boldsymbol{u}(k), \\ \boldsymbol{y}(k) &= \boldsymbol{H}\boldsymbol{x}(k) + \boldsymbol{J}\boldsymbol{u}(k), \end{aligned} \tag{5.90}$$

where $\boldsymbol{\Phi}$, $\boldsymbol{\Gamma}$, $\boldsymbol{H}$, $\boldsymbol{J}$ are given as follows [7]:

$$\begin{aligned}
\boldsymbol{\Phi} &= \left(\boldsymbol{I} + \frac{\boldsymbol{A}T'}{2}\right)\left(\boldsymbol{I} - \frac{\boldsymbol{A}T'}{2}\right)^{-1}, \\
\boldsymbol{\Gamma} &= \left(\boldsymbol{I} - \frac{\boldsymbol{A}T'}{2}\right)^{-1}\boldsymbol{B}\sqrt{T'}, \\
\boldsymbol{H} &= \sqrt{T'}\boldsymbol{C}\left(\boldsymbol{I} - \frac{\boldsymbol{A}T'}{2}\right)^{-1}, \\
\boldsymbol{J} &= \boldsymbol{C}\left(\boldsymbol{I} - \frac{\boldsymbol{A}T'}{2}\right)^{-1}\boldsymbol{B}T'/2, \\
T' &= \frac{2\tan(\omega_{pw}T_s/2)}{\omega_{pw}}.
\end{aligned} \tag{5.91}$$

The continuous linear time-varying observer which was derived in the previous section is given as:

$$\begin{aligned}
\dot{\hat{\boldsymbol{z}}}(t) &= \omega(t)\{\boldsymbol{A}_{\boldsymbol{o}}^{\boldsymbol{cl}}\hat{\boldsymbol{z}}(t) + \boldsymbol{B}_{\boldsymbol{o}}^{\boldsymbol{cl}}y(t)\}, \\
\boldsymbol{w}(t) &= \boldsymbol{I}\hat{\boldsymbol{z}}(t),
\end{aligned} \tag{5.92}$$

where the matrices $\boldsymbol{A}_{\boldsymbol{o}}^{\boldsymbol{cl}}, \boldsymbol{B}_{\boldsymbol{o}}^{\boldsymbol{cl}}$ were defined in (5.42,5.41) and $y(t)$ is the measured plant output. The output matrix of the system (5.92) is chosen as the identity matrix for the purpose of discretization since all the observer states are required for the spectral analysis and they have to be included in the computations of the matrices $\boldsymbol{H}, \boldsymbol{J}$ in (5.91). The discrete-time equivalent is computed in each sampling period of the identification algorithm during the sweep phase for the actual value of generator frequency $\omega(t)$. Substitution of the continuous time model (5.92) to the transform (5.91) leads to the time-varying system in the form of:

$$\begin{aligned}
\boldsymbol{x}(k+1) &= \boldsymbol{\Phi}(k)\boldsymbol{x}(k) + \boldsymbol{\Gamma}(k)y(k), \\
\hat{\boldsymbol{z}}(k) &= \boldsymbol{H}(k)\boldsymbol{x}(k) + \boldsymbol{J}(k)y(k),
\end{aligned} \tag{5.93}$$

where the time-varying matrices $\boldsymbol{\Phi}(k), \boldsymbol{\Gamma}(k), \boldsymbol{H}(k), \boldsymbol{J}(k)$ are obtained as:

$$\begin{aligned}
\boldsymbol{\Phi}(k) &= \left(\boldsymbol{I} + \frac{\omega(k)\boldsymbol{A}_{\boldsymbol{o}}^{\boldsymbol{cl}}T'(k)}{2}\right)\left(\boldsymbol{I} - \frac{\omega(k)\boldsymbol{A}_{\boldsymbol{o}}^{\boldsymbol{cl}}T'(k)}{2}\right)^{-1} \triangleq \boldsymbol{M}_{\boldsymbol{1}}(k)\boldsymbol{M}_{\boldsymbol{2}}(k), \\
\boldsymbol{\Gamma}(k) &= \left(\boldsymbol{I} - \frac{\omega(k)\boldsymbol{A}_{\boldsymbol{o}}^{\boldsymbol{cl}}T'(k)}{2}\right)^{-1}\boldsymbol{B}_{\boldsymbol{o}}^{\boldsymbol{cl}}\omega(k)\sqrt{T'(k)} \triangleq \boldsymbol{M}_{\boldsymbol{3}}(k)\sqrt{T'(k)}, \\
\boldsymbol{H}(k) &= \sqrt{T'(k)}\boldsymbol{M}_{\boldsymbol{2}}(k), \\
\boldsymbol{J}(k) &= \boldsymbol{M}_{\boldsymbol{3}}(k)T'(k)/2, \\
T'(k) &= \frac{2\tan\left(\omega(k)T_s/2\right)}{\omega(k)}.
\end{aligned} \tag{5.94}$$

The *pre-warp frequency* is naturally chosen as the fundamental frequency of the generator in order to obtain the correct estimate of the system frequency response. Although the matching condition (5.88) does not hold exactly for the frequencies of the higher harmonics, the error introduced by the discretization is negligible in practice. Moreover, their precise reconstruction is not necessary as only the approximate values of the higher harmonics amplitudes are used for the detection of nonlinearities.

Very fast computation of the transform (5.94) is achieved due to the recursive application of the repeating terms $\boldsymbol{M_1}, \boldsymbol{M_2}, \boldsymbol{M_3}$ which are involved in the calculations of the system matrices. The most time-demanding part is the evaluation of the the matrix inverse in the term $\boldsymbol{M_2}(k) = \left(\boldsymbol{I} - \frac{\omega(k)\boldsymbol{A_o^c}T'(k)}{2}\right)^{-1}$. Analytical computation is possible instead of the explicit numerical inversion. We may write:

$$\boldsymbol{M_2}(k) = \frac{Adj\left(\boldsymbol{I} - \frac{\omega(k)\boldsymbol{A_o^{cl}}T'(k)}{2}\right)}{det\left(\boldsymbol{I} - \frac{\omega(k)\boldsymbol{A_o^{cl}}T'(k)}{2}\right)}. \tag{5.95}$$

For a chosen closed-loop pole pattern, the determinant and the individual elements of the adjugate matrix in (5.95) are obtained as constant coefficients polynomials of variable $\omega(k)T'(k)$ which can be simply evaluated for a particular $\omega(k)$ in each sampling period. Therefore, the inverse matrix $\boldsymbol{M_2}$ is given in the form of:

$$[\boldsymbol{M_2}(k)]_{i,j} = \frac{c_0^{i,j} + c_1^{i,j}\big(\omega(k)T'(k)\big) + c_2^{i,j}\big(\omega(k)T'(k)\big)^2 + ... + c_{11}^{i,j}\big(\omega(k)T'(k)\big)^{11}}{d_0^k + d_1^k\big(\omega(k)T'(k)\big) + d_2^k\big(\omega(k)T'(k)\big)^2 + ... + d_{11}^k\big(\omega(k)T'(k)\big)^{11}}, \tag{5.96}$$

where $c^{i,j}$ denote the position dependent coefficients of the adjugate matrix and d^k are coefficients of the determinant polynomial. This procedure reduces the computational time to about one third compared to the direct numerical enumeration of the inverse. The observer matrices are kept constant in the measurement phase for a particular value $\omega(k) = const.$ and the observer (5.93) reduces to the LTI system.

A complete iteration of the discrete-time observer in the sweep phase including the discretization requires about 6500 floating point operations. A benchmark was performed in the Matlab environment with a single-core 2.5Ghz Pentium 4 CPU. The average running time of the algorithm was about 40 microseconds, 92% of the time is required for the discretization. Half of this time is needed for the computation of $\boldsymbol{M_2}$ and the other half for the evaluation of the system matrices. The remaining 8% lasts for the update of the observer states. For the comparison, the direct computation of the discrete-time observer using the pole-placement method took approximately 1.8 millisecond with the same computer which is about 40x more. The discrete Kalman filter calculation needed approximately 12 milliseconds (300x more).

The computational power of today's industrial computers equipped with multi-core processors allow us to implement the proposed algorithm in a realtime control system for the online estimation of the frequency response with fast sampling rates up to 10kHz or more. Considering the corresponding Nyquist frequency and dividing it by a factor of ten to obtain a reasonable number of samples per oscillation period, we get

the approximate maximum frequency 500 Hz which may be detected in the measured signal. This is satisfactory for most of the industrial motion control systems with resonance frequencies varying typically from dozens to a few hundreds of Herzes. Since the individual matrices entries can be evaluated separately, the computational time could be further reduced by proper parallelization of the calculations by means of a multicore processor or using a FPGA hardware. Another option is a decrease in the number of the estimated harmonics to allow a realtime implementation with fast update rates even in low performance HW platforms.

Stability analysis of the discrete-time algorithm

Stability analysis of the proposed time-varying observer which is used in the sweep phase should be performed analogous to the continuous-time case to make sure that the estimation error cannot grow excessively in time between two consecutive measurement points.

Theorem 5.6.1. The discrete LTV observer (5.93) is uniformly asymptotically stable for an arbitrary sequence of the chosen excitation frequencies provided that $\omega(k) \in (0, \frac{\pi}{T_s})\ \forall k > 0$.

Proof. Consider the autonomous system which is obtained from (5.93) as

$$\boldsymbol{x}(k+1) = \boldsymbol{\Phi}(k)\boldsymbol{x}(k). \tag{5.97}$$

Define $\boldsymbol{S}(k,j)$ to be the state transition matrix of $\boldsymbol{\Phi}$ such that

$$\boldsymbol{S}(k,j) = \begin{cases} \boldsymbol{\Phi}(k-1)\boldsymbol{\Phi}(k-2)...\boldsymbol{\Phi}(j) & \text{for } k > j \\ \boldsymbol{I} & \text{for } k = j \end{cases} \tag{5.98}$$

The solution of the difference equation (5.97) is given as

$$\boldsymbol{x}(k) = \boldsymbol{S}(k,k_0)\boldsymbol{x}(0). \tag{5.99}$$

The following inequality holds for the Euclidean norm of the state vector

$$\|\boldsymbol{x}(k)\| \leq \|\boldsymbol{S}(k,k_0)\|\|\boldsymbol{x}(0)\|. \tag{5.100}$$

Therefore, the system is uniformly exponentially stable on $[k_0, \infty)$ if

$$\|\boldsymbol{S}(k,j)\| \leq M\alpha^{k-j} \text{ for arbitrary } k_0 \leq j \leq k < \infty \tag{5.101}$$

for some scalar constants $M > 0, 0 < \alpha < 1$ [202].

Assuming a set of stable eigenvalues of $\boldsymbol{A_o^{cl}}$ without any multiplicity, the system matrix $\boldsymbol{\Phi}(k)$ can be rewritten in the form of:

$$\begin{aligned}\boldsymbol{\Phi}(k) &= \left(\boldsymbol{I} + \frac{\omega(k)\boldsymbol{A_o^{cl}}T'(k)}{2}\right)\left(\boldsymbol{I} - \frac{\omega(k)\boldsymbol{A_o^{cl}}T'(k)}{2}\right)^{-1} \\ &= \left(\boldsymbol{VIV^{-1}} + \gamma(k)\boldsymbol{VDV^{-1}}\right)\left(\boldsymbol{VIV^{-1}} - \gamma(k)\boldsymbol{VDV^{-1}}\right)^{-1} \\ &= \left(\boldsymbol{V}\left[\boldsymbol{I}+\gamma(k)\boldsymbol{D}\right]\boldsymbol{V^{-1}}\right)\left(\boldsymbol{V}\left[\boldsymbol{I}-\gamma(k)\boldsymbol{D}\right]\boldsymbol{V^{-1}}\right)^{-1} \\ &= \boldsymbol{V}\left(\frac{\boldsymbol{I}+\gamma(k)\boldsymbol{D}}{\boldsymbol{I}-\gamma(k)\boldsymbol{D}}\right)\boldsymbol{V^{-1}};\ \boldsymbol{A_o^{cl}} = \boldsymbol{VDV^{-1}},\ \gamma(k) = \frac{\omega(k)T'(k)}{2}\end{aligned} \tag{5.102}$$

where $\boldsymbol{D}$ is the diagonal matrix of eigenvalues of $\boldsymbol{A_o^{cl}}$ and $\boldsymbol{V}$ is the corresponding matrix of eigenvectors. The pair $\boldsymbol{D}, \boldsymbol{V}$ forms the Jordan normal form of $\boldsymbol{A_o^{cl}}$ which is constant for a chosen closed-loop pole distribution of the continuous observer (see section 1.1.2 for the full derivation). The state transition matrix (5.98) is obtained in the form of:

$$\boldsymbol{S}(k,j) = \boldsymbol{V}\prod_{i=j}^{k}\left(\frac{\boldsymbol{I}+\gamma(i)\boldsymbol{D}}{\boldsymbol{I}-\gamma(i)\boldsymbol{D}}\right)\boldsymbol{V^{-1}} = \boldsymbol{V}\bar{\boldsymbol{D}}(k,j)\boldsymbol{V^{-1}} \text{ for } k > j. \tag{5.103}$$

Upper bound for the norm of the transition matrix is obtained as:

$$\|\boldsymbol{S}(k,j)\| \leq \|\boldsymbol{V}\|\|\bar{\boldsymbol{D}}(k,j)\|\|\boldsymbol{V^{-1}}\|. \tag{5.104}$$

The diagonal matrix $\bar{\boldsymbol{D}}(k,j) = diag\{d_1(k,j), d_2(k,j), ..., d_{11}(k,j)\}$ contains products of the closed-loop eigenvalues z_i of the observer obtained from the bilinear transform which is performed in each discretization step:

$$d_i(k,j) = \prod_{l=j}^{k} z_i(l). \tag{5.105}$$

Considering that the Euclidean induced matrix norm of $\bar{\boldsymbol{D}}$ corresponds to its spectral radius, we may write

$$\|\bar{\boldsymbol{D}}\|_2 = \sqrt{\lambda_{max}(\bar{\boldsymbol{D}}^*\bar{\boldsymbol{D}})} = \max_{\forall i}\{|d_i|\}; i = 1, ..., 11 \tag{5.106}$$

The Tustin transform guarantees the stability of the discrete-time equivalents computed in each step of the algorithm and thus it holds that

$$|d_i(k,j)| < 1 \text{ for any } 0 \leq j \leq k < \infty,\ 0 < \omega(k) < \frac{\pi}{T_s}. \tag{5.107}$$

Since $\omega(k)$ can take only finite range of values during the sweep phase due to the limitation by the Nyquist frequency, there definitely exists some time instant k_{max} which gives a maximum spectral radius of $\boldsymbol{\Phi}(k)$ such that:

$$\rho\big(\boldsymbol{\Phi}(k)\big) = \max_{\forall i}\{|z_i(k)|\} \leq \rho\big(\boldsymbol{\Phi}(k_{max})\big) = \rho_{max} < 1;\ \forall k > 0. \tag{5.108}$$

Therefore, the norm of the transition matrix is bounded by the exponential function

$$\|\boldsymbol{S}(k,j)\| \leq \|\boldsymbol{V}\|\|\bar{\boldsymbol{D}}(k,j)\|\|\boldsymbol{V^{-1}}\| \leq \|\boldsymbol{V}\|\|\boldsymbol{V^{-1}}\|\rho_{max}^{k-j}, \forall k > j \tag{5.109}$$

which gives the necessary condition for the asymptotic stability (5.101). Stability for the case of $\boldsymbol{A_o^{cl}}$ follows directly from continuity. □

Theorem 5.6.2. The discrete LTV observer (5.93) is stable in the BIBO sense for arbitrary values of the measured plant output $y(k)$ and any sequence of the chosen excitation frequencies provided that $\omega(k) \in (0, \frac{\pi}{T_s})\ \forall k > 0$.

Proof. The solution of the difference equation of the observer (5.93) is obtained in the form of:

$$\boldsymbol{x}(k) = \boldsymbol{S}(k,k_0)\boldsymbol{x_0} + \sum_{j=k_0}^{k-1} \boldsymbol{S}(k,j+1)\boldsymbol{\Gamma}(j)y(j) \tag{5.110}$$

$$\hat{\boldsymbol{z}}(k) = \boldsymbol{H}(k)\boldsymbol{S}(k,k_0)\boldsymbol{x_0} + \boldsymbol{H}(k)\sum_{j=k_0}^{k-1} \boldsymbol{S}(k,j+1)\boldsymbol{\Gamma}(j)y(j) + \boldsymbol{J}(k)y(k).$$

Since the $\omega(k) \in (0, \frac{\pi}{T_s})\ \forall k > 0$, the norms of the matrices $\boldsymbol{\Gamma}, \boldsymbol{H}, \boldsymbol{J}$ are bounded and the following inequalities may be assumed:

$$\begin{gathered} \|\boldsymbol{\Gamma}(k)\| \leq c_1,\ \|\boldsymbol{H}(k)\| \leq c_2,\ \|\boldsymbol{J}(k)\| \leq c_3, \\ \|\boldsymbol{x}(0)\| \leq c_4,\ \|\boldsymbol{V}\|\|\boldsymbol{V^{-1}}\| \leq c_5,\ \|y(k)\| \leq c_6;\ \forall k > 0. \end{gathered} \tag{5.111}$$

The upper bound for the observer output norm may be obtained in the form of:

$$\|\hat{\boldsymbol{z}}(k)\| \leq \|\boldsymbol{H}(k)\|\|\boldsymbol{S}(k,k_0)\|\|\boldsymbol{x_0}\| + \|\boldsymbol{H}(k)\|\sum_{j=k_0}^{k-1}\|\boldsymbol{S}(k,j+1)\|\|\boldsymbol{\Gamma}(j)\|\|y(j)\| + \|\boldsymbol{J}(k)\|\|y(k)\|. \tag{5.112}$$

From the result of the exponential stability (5.109) and conditions (5.111), we get:

$$\begin{aligned} \|\hat{\boldsymbol{z}}(k)\| &\leq c_2c_5\rho_{max}c_4 + c_2c_1c_6\sum_{j=k_0}^{k-1}\|\boldsymbol{S}(k,j+1)\| + c_3c_6 \\ &\leq c_2c_5\rho_{max}c_4 + c_2c_1c_6\left\{1 + c_5(\rho_{max} + \rho_{max}^2 + \rho_{max}^3 + ... + \rho_{max}^{k-1})\right\} + c_3c_6 \\ &\leq c_2c_5\rho_{max}c_4 + c_6\left(c_2c_1\left(1 + \frac{\rho_{max}c_5}{1-\rho_{max}}\right) + c_3\right). \end{aligned} \tag{5.113}$$

Therefore, the system is BIBO stable and the observer error is bounded during the sweep phase. □

Practical experiments with the time-varying observer show that the algorithm is able to track fast varying signals even for the high sweep rates. The tracking performance is demonstrated in Fig. (5.20). The plots present the ability of the observer

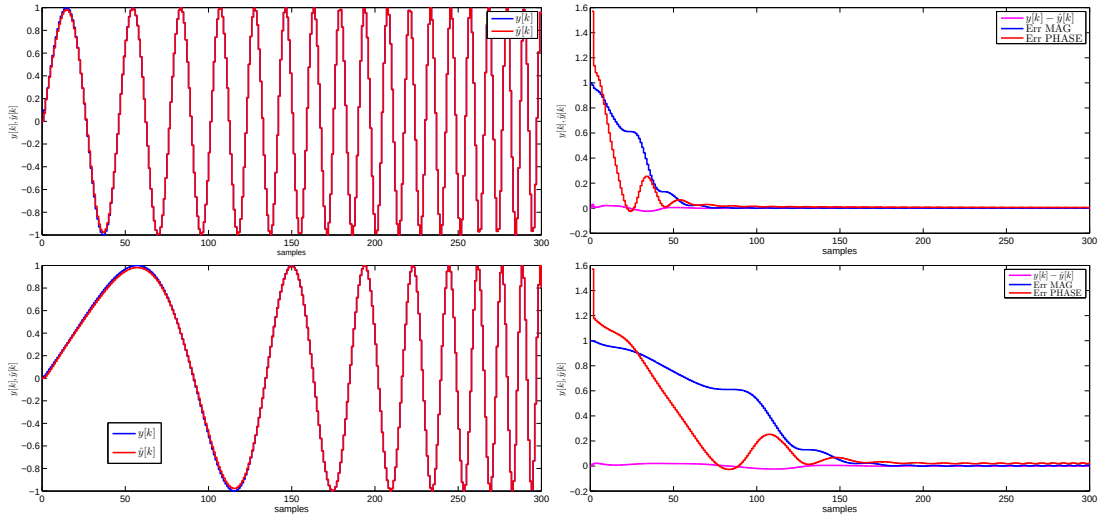

Figure 5.20: Sweep phase tracking performance of the discrete LTV observer - first row - linear frequency sweep, second row - exponential sweep, left - measured and estimated signal $y[k], \hat{y}[k]$, right - tracking error (magenta output following error $y[k] - \hat{y}[k]$, blue estimated magnitude error, red estimated phase error)

to follow swept harmonic signals which are used in the identification experiment. The frequency of the observed chirp signal is varied in the range $\omega(k) \in \langle 0.1, \frac{\pi}{5} \rangle [rad/s]$. The sampling period is set to $T_s = 1$ without loss of generality. The upper bound is chosen as the Nyquist frequency divided by five to obtain the maximum value for which the five harmonics may be detected. The first row corresponds to the linear increase of the frequency, the second one is obtained for the exponential sweep. The left column shows the measured and estimated signals, the right one represents the tracking errors. It can be seen that the observer estimates converge towards the true values after approximately 1.25 period of the measured signal for both linear and exponential sweep. The estimation errors does not tend to zero asymptotically, since the open-loop observer poles do not correspond exactly with the inner model of the signal generator due to the discretization by the bilinear transform. However, the steady-state values of the errors are in the order of 0.1% and they are negligible with respect to the errors which would be caused by a measurement noise and an excited transient dynamics of the identified system in practice. Moreover, the LTV observer is used only for the approximate measurement of the frequency response during the sweep phase of the identification. Therefore, the performance of the algorithm is more than satisfactory.

5.7 Integration into real time control system

The proposed identification method was implemented in the form of a functional block in the C language. The algorithms were integrated into the REX control system, which

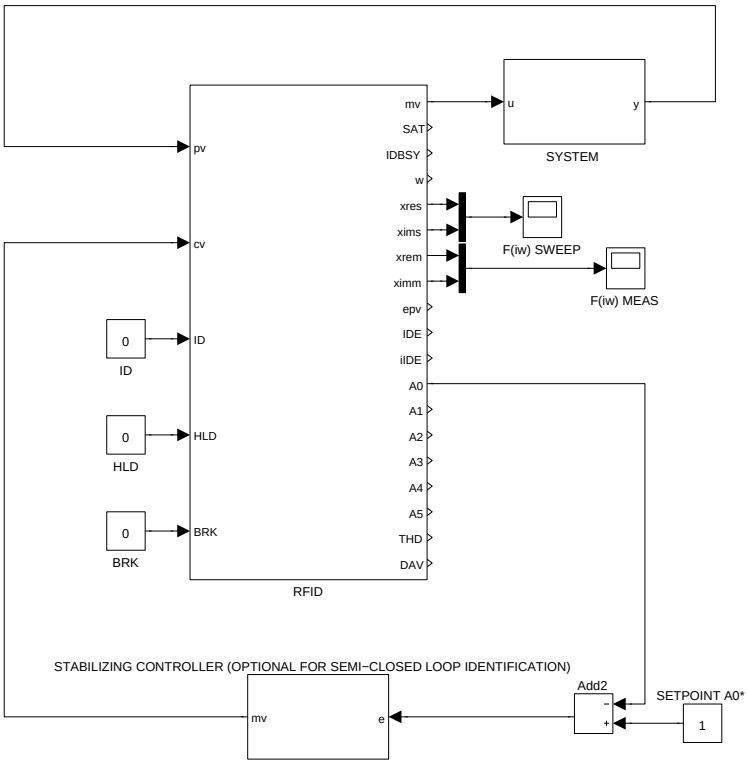

Figure 5.21: Robust frequency identification (RFID) functional block - Simulink diagram showing the user interface and the principle of interconnection with the identified system and feedback controller

is being used at the UWB. Matlab version in the form of C-MEX S-function was also developed for the purpose of numerical simulations. The universal format of the algorithm makes it suitable for an arbitrary platform which supports the C language.

The functional block interface and principle of interconnection with the identified system is depicted in Fig. (5.21). The user specifies the following set of parameters:

- Desired frequency range of the excitation signal $\omega \in \langle \omega_b, \omega_f \rangle$
- Initial amplitude $A(0)$ and static component $u_0(0)$ of the harmonic signal generator
- Rate of change of the actual generator frequency in the sweep mode (linear or logarithmic scale)
- Settling time for the measurement mode
- Desired values of the excitation frequency for the acquisition of the frequency response estimates

- Desired estimator bandwidth
- Optional parameters of the maximum desired threshold for the THD index, allowed range of the measured output variable and maximum generator amplitude for the adaptive algorithm

The identification procedure starts with the rising edge of the binary input `ID`. The signal generator produces the swept harmonic signal which is fed to the input of the identified system (`mv` output in the diagram 5.21). The measured output response of the system is acquired from the `pv` input of the block. The generator smoothly varies the actual frequency of the generated harmonic signal and estimates the actual point of the frequency response $\hat{F}(i\omega)$ whose real and imaginary parts are copied to the outputs `xres,xims`. The frequency sweeping stops at the user specified frequency values or when an important point of the frequency response is detected (resonance and antiresonance regions). The block proceeds to the measurement mode, waits for the steady state and acquires one point of the frequency response which is set to the `xrem,ximm` outputs. Successful acquisition of a sample of the frequency response is signalized by the binary input `DAV` (data valid). The procedure is repeated until the end of the desired frequency range ω_f is achieved. The estimation algorithm performs smooth transition between the time-varying observer which is synchronized with the actual generator frequency during the sweep mode and the linear time-invariant observer which operates in the measurement mode. The user can enable the amplitude adaptation algorithm which monitors the actual value of the THD index and adjusts the amplitude of the generated excitation signal in order to achieve consistent performance even in the presence of a measurement noise and occurence of nonlinearities in the system dynamics. Amplitudes of the estimated five harmonics and the static component of the measured signal are available at the outputs `A0-A5`. The DC component output `A0` is used as a feedback signal for a stabilizing controller when the closed-loop identification is required in a particular application. The manipulating variable of the compensator is fed to the `cv` input of the block and is added to the excitation signal produced by the generator. This type of interconnection implements the proposed *semi-closed loop identification* scheme.

Simulation example

The functionality of the block is demonstrated by means of the numerical simulation in the Matlab environment. A three-mass system with two dominant resonance frequencies is used for demonstration of the abilities of the developed algorithms. The plant transfer function of the identified system is chosen as:

$$F(s) = \frac{(s^2 + 0.06339s + 0.06057)(s^2 + 0.1129s + 2.064)}{(s + 0.04544)(s^2 + 0.04541s + 0.9985)(s^2 + 0.9854s + 9.12)}. \tag{5.114}$$

The transfer function represents an oscillatory mechanical system with the rigid and two dominant weakly damped oscillatory modes ($\omega_{n1} = 1\ rad/s, \xi_1 = 0.02, \omega_{n2} =$

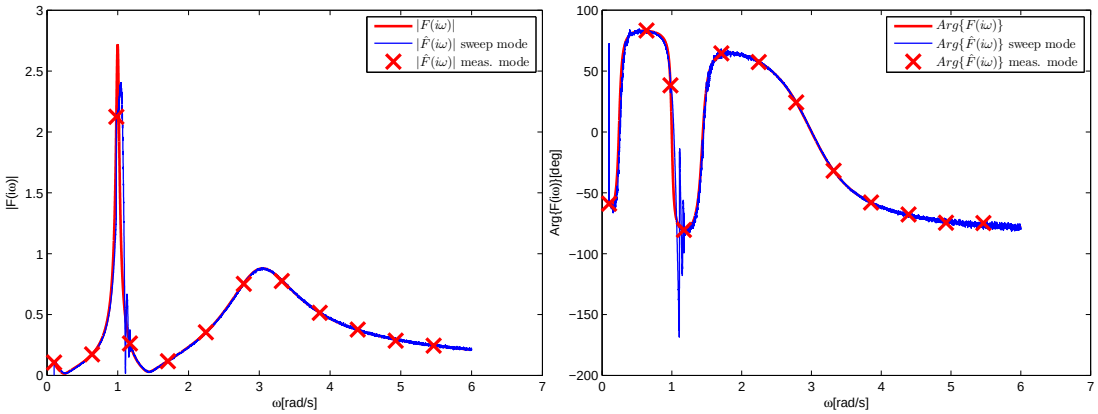

Figure 5.22: RFID block performance - estimation of the plant frequency response (left amplitude, right phase), red - true frequency response, blue - estimated response during the sweep mode, red cross - samples acquired during the measurement mode

$3\ rad/s, \xi_1 = 0.16$). The identification procedure is executed in the frequency range $\omega \in \langle 0.1, 6\rangle\ rad/s$ with the sampling period $T_s = 0.1s$. The obtained frequency response data are shown in Fig. (5.22). The red line denotes the true amplitude and phase characteristics of the system (5.114). The red crosses mark the data points which are acquired in the measurement mode. The blue line shows the estimated frequency response during the sweep mode. It can be seen that it tracks the real values closely except for the region of the first resonance around $\omega \approx 1\ rad/s$. The slight mismatch of the estimate in this range is caused by the transient dynamics of the system which is excited by the frequency sweeping. The estimation error is most significant especially before the fourth sampled data point at $\omega = 1.17 rad/s$ because of the excitation of the first resonance mode which needs a longer time to damp out. However, the estimation error in the sweep mode does not affect the accuracy of the samples obtained in the measurement mode for a constant excitation frequency provided that a long enough settling time is allowed to reach a steady state response.

The influence of the chosen frequency sweeping rate on the estimation error during the sweep mode is studied closer in Fig. (5.23). Estimates of the amplitude frequency response are shown for three different settings of the linear sweep rate coefficient cp. Higher sweep rates lead to stronger excitation of the transient dynamics and a larger estimation error. The estimates converge to the true values in the measurement mode when the sweeping stops.

The functionality of the adaptation algorithm is shown in Fig. (5.24). The first plot shows the manipulating variable generated by the RFID block. The identification is performed in the semi-closed loop configuration. A feedback compensator in the form of a PI controller is used to keep the mean value of the plant output at the constant level $A0^* = 1$. The experiment begins at time $k = 1000$ and the block starts with the generation of the excitation signal. The amplitude is automatically increased in the first

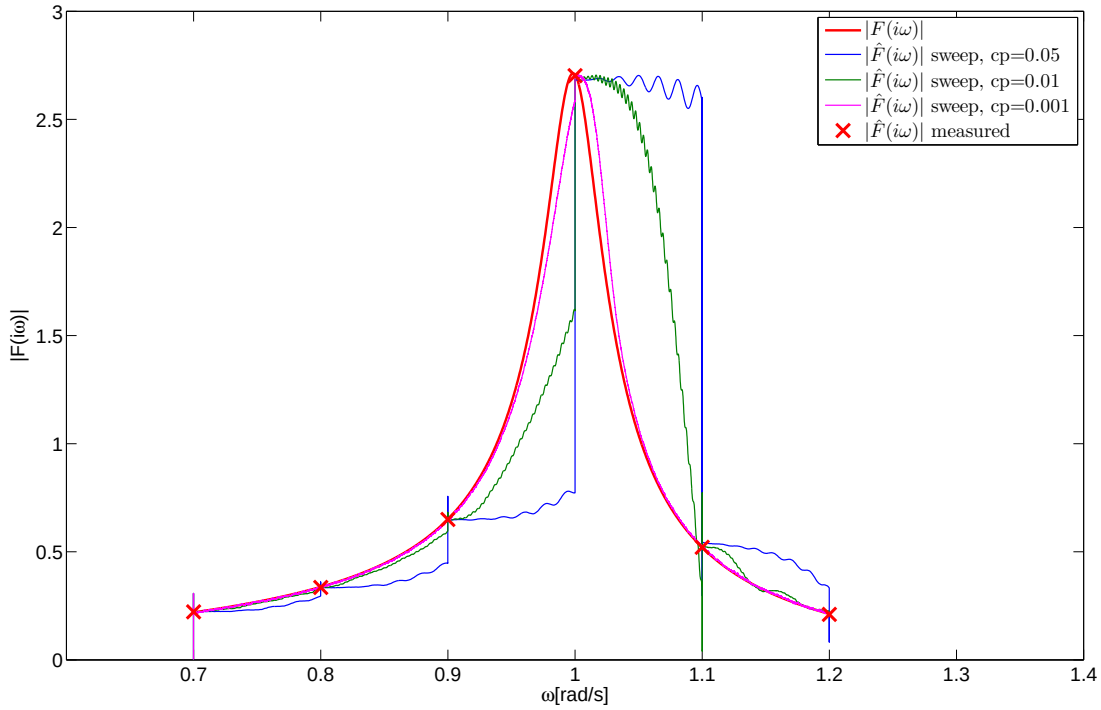

Figure 5.23: Sweep mode performance in the vicinity of the system resonance depending on the frequency sweeping rate, red - true frequency response, blue, green, magenta - estimated response during the sweep mode for three different choices of linear sweep rate cp[rad/s per sampling period], red cross - samples acquired during the measurement mode

phase as the actual frequency approaches the first antiresonance peak of the system at $\omega \approx 0.2\,rad/s$. The measured output is corrupted by a wideband noise and the increase in the generator amplitude is necessary to keep the desired value of the measured THD index under the desired value $THD^* = 0.1$. Once the excitation frequency approaches the first resonance, the amplitude needs to be reduced to keep the plant output in the chosen range $|pv| < 8$. The amplitude is increased again in the second antiresonance region and decreases in the vicinity of the second resonance. The red lines in the THD plot in Fig. (5.24) indicate the moment of acquisition of the frequency response points in the measurement mode. It can be seen that the desired maximum value of THD is fulfilled for all the measured points. The last plot in Fig. (5.24) shows the desired and actual values of the DC component of the plant output. It is shown that the proposed semi-closed loop scheme performs well. The feedback compensator does not influence the identification experiment and the DC value is kept at the setpoint value. The obtained samples of the plant frequency response are consequently used in the data-fitting routines which compute the model of the plant dynamics.

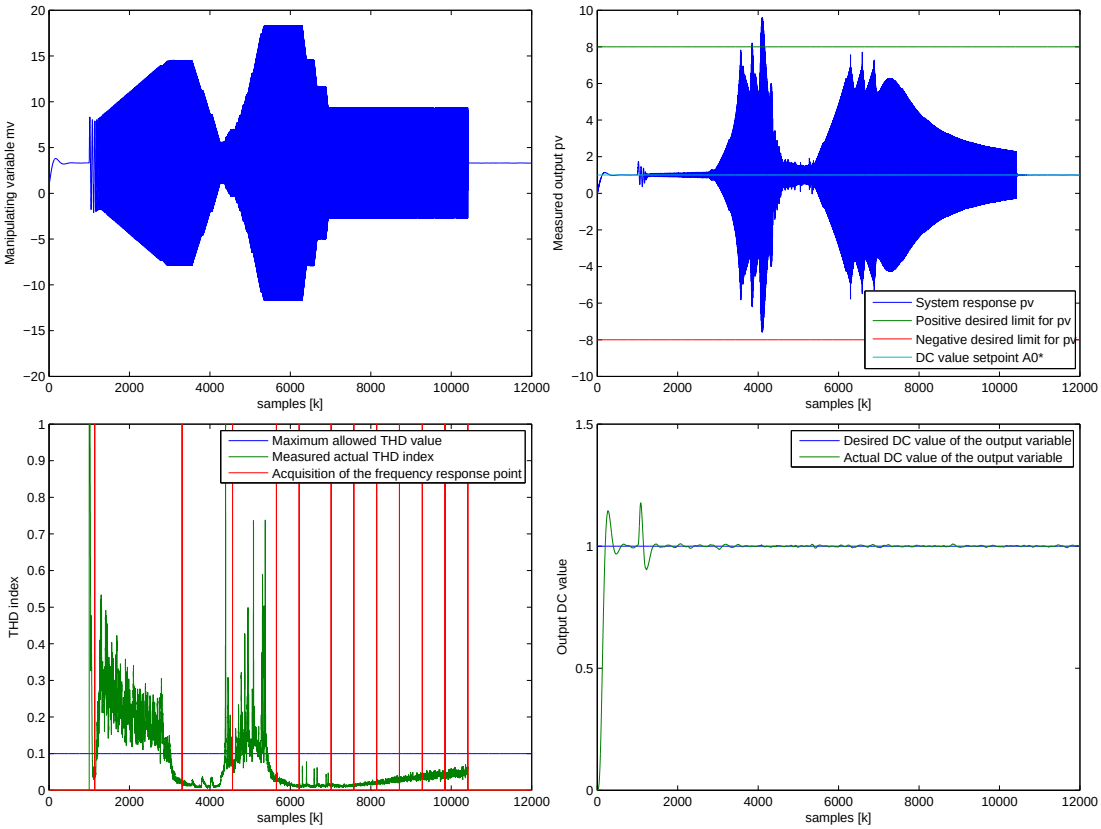

Figure 5.24: RFID adaptation algorithm - a) manipulating variable, b) measured plant output, c) measured THD index and time instants of frequency response acquisition, d) measured DC component of the plant output

5.8 Summary

This chapter presented a new approach to the frequency identification of electromechanical systems. The main idea is generation of a swept harmonic signal and real-time estimation of the plant frequency response using a properly designed linear time-varying observer. Quadratic optimal control theory is used for the computation of the innovation gains. Stability of the estimator is analyzed using the theory of time-varying systems. The estimator is supplemented by an adaptive algorithm which adjusts the amplitude of the generated excitation signal in order to cope with the measurement noise and eventual occurrence of nonlinearities typical for mechanical systems. The semiclosed-loop identification scheme is introduced for the possibility of feedback stabilization around a chosen working point. A computationally efficient discrete-time algorithm which can be used for real-time estimation with high sampling rates is developed. The proposed method is implemented in the form of a functional block in the C language.

6

Passive vibration damping using input-shaping method

The general concept of passive vibration control was introduced in the introductory chapter. The main goal is to constraint the amount of energy that the mechanical system receives from the actuators in the vicinity of its resonance frequencies. The passive approach may be advantageous in several situations:

- **Vibration damping of oscillatory loads without additional instrumentation**
  Many practical motion control systems do not use separate load-side measurement which could serve as a feedback information. The transmission of the reaction forces or torques from the load to the motor side sensor may be insufficient for a successful implementation of a feedback active vibration damping compensator. A typical example is an overhead crane with a hanging load or a high gear ratio ball screw drive system of a CNC machine tool.

- **Use of a fixed structure feedback compensator which cannot provide the active damping functionality**
  The majority of commercial motion control systems do not allow any customization of the compensator structure in the position and velocity control loops. The standard cascade PID structure may be inefficient for certain mechanical configuration and the passive damping is the only way of reducing of the unwanted oscillations.

- **Performance improvement of conservatively tuned loops**
  The addition of a proper shaping filter may extend the achievable closed-loop bandwidth or increase the robustness in stability by improving the high-frequency roll-off of the feedback compensator in the vicinity of the system resonance.

- **Composite vibration control**
  A setpoint command shaping filter may be used in conjunction with a properly tuned feedback compensator. The feedback controller provides active compensation of vibrations due to external disturbances whereas the feed-forward filter prevents excitation of the oscillations owing to setpoint variations.

Thus, *proper shaping of the setpoint command or the manipulating variable of the actuator may significantly reduce the amount of motion induced oscillations* which arise in the flexible load and improve the quality of control. The previous chapter presented the concept of **Zero-vibration filters** with time delays which are suitable for this purpose. They offer some important advantages compared to the conventional notch filters which are implemented in some industrial motion control systems:

- **Finite impulse response of the shaper**
  The usual approach to passive vibration damping is to use a continuous IIR filter which is designed according to a demanded shape of the stop-band and compute its discrete-time equivalent for the implementation in a sampled data system. The infinite impulse response may be impractical for the purpose of setpoint commands shaping as the resulting desired trajectories of motion do not converge to a steady state in a finite time. Moreover, there may be stability issues of the IIR filter due to improper discretization [89, 205].

- **Ability of infinite damping of a certain frequency**
  A very high sampling frequency may be needed for the discrete-time implementation of the IIR notch filters especially when highly a selective shape of the stop-band with a large amount of attenuation of a certain frequency is required. Problems with instability or limit cycling of the filter due to quantization may occur. On the contrary, the Zero-vibration shapers can provide an infinite damping and zero transmission at a particular frequency which has to be canceled. The stability of the filter is guaranteed due to its finite impulse response structure.

- **Monotone step response of the filter** A highly selective IIR filter with a narrow notch in the stopband region requires a setting of a very low damping of the filter poles. This leads to a highly oscillatory step response which makes it inapplicable for the open loop shaping of the command signals. A proper design method of a Zero-vibration signal can guarantee the desired monotone shape of the filter step response.

- **Smaller amount of delay introduced in the signal path**
  The Zero-vibration shapers can provide a higher amount of damping and a lower delay compared to the conventional notch filters (see e.g. an extensive comparison of various filter types presented in the survey [179]).

- **Analytical design of the shaping filter**
  Analytical closed-form formulas may be derived for certain types of the shaping filters for a known model of a system resonance. On the contrary, conventional FIR notch filter require complex numerical methods for the computation of the filter coefficients [205].

- **Direct specification of robustness to modelling errors**
  Direct specification of sensitivity of a Zero-vibration shaper to modelling errors

can be formulated by means of so called *sensitivity function* which expresses an amount of motion induced residual oscillations. The sensitivity function shaping is a more direct approach to the definition of the filter performance compared to the shaping of the filter amplitude response which is commonly used in the field of signal processing.

- **Simple discrete-time implementation and low order of the filter**
  Although the design of a Zero-vibration shaper is usually accomplished in the continuous time domain it can be easily implemented in a sampled data system. The thesis presents a simple technique for the discretization of the shaper algorithm which compensates a round-off errors due to a finite sampling resolution. The computational complexity of the shaper algorithm is much lower compared to the conventional FIR notch filters which require a very high order, typically in hunderds of samples per impulse response, in order to achieve a desired shape of the filter frequency response.

The concept of passive vibration damping using the zero vibration input shapers is well established both in the academic field and industrial practice. However, most of the theoretical works which have been published use a *fixed structure of the filter*. Its parameters are determined only by the location of the system resonances, i.e. the oscillatory poles of the system which need to be canceled out. The control system engineer has no additional options to affect the behavior of the filter in the control loop to perform a fine-tuning of the algorithm for a particular application. This is the main difference compared to the conventional notch filter design methods where, for example, the width of the stop band and the level of attenuation at the desired frequency may be defined to find a suitable trade-off between robustness of the filter and the delay it introduces into the signal path. The paper [57] is the only work known to the author which deals with a general parametrization of the shaping filters. Here the set of three-pulse shapers is completely determined by two parameters which can be adjusted manually or by some optimization method which minimizes a chosen criterion function. The following section presents an algorithm for a generalized parametrization of an input shaper with a minimum set of user parameters. A four-impulse filter which is described by two user-defined parameters with clear physical meaning was chosen for practical implementation in a real-time control system. The results published in author's papers [87, 206] are presented and further elaborated.

6.1 ZV4 Input Shaper

The starting point is a mathematical representation of a system resonance which is described by a second order underdamped system with transfer function:

$$P(s) = \frac{\omega_n^2}{s^2 + 2\xi\omega_n s + \omega_n^2};\ \xi < 1,\ \omega_d = \omega_n\sqrt{1-\xi^2}, \tag{6.1}$$

with natural frequency ω_n, damping coefficient ξ and damped frequency ω_d. This model represents a single oscillatory mode of a controlled plant which has to be attenuated by the shaping filter.

A four-impulse sequence input shaper is proposed with the transfer function given in the form of:

$$\begin{aligned} IS(s) &= \sum_{i=1}^{4} A_i e^{-t_i s};\ A_i \geq 0,\ \sum_{i=1}^{4} A_i = 1, \\ 0 &= t_1 < t_2 < t_3 < t_4, \end{aligned} \tag{6.2}$$

where A_i are amplitudes of the shaper pulses and t_i are the values of time-delays of the filter. Their sum has to be equal to one because of the demand for unitary static gain. Furthermore, the amplitudes have to be non-negative in order to achieve monotonous step response which is needed for the smooth shaping of the reference trajectories. The filter should cancel the unwanted oscillations in a reasonable time with respect to the damped period of the system $T_d = \frac{2\pi}{\omega_d}$.

The common procedure of input shaper design was presented in the previous chapter on the example of the two pulse ZV filter. The derivation was performed in the time domain from the analysis of impulse response of the serial connection of the shaper and the controlled plant (equation 3.112). A suitable choice of filter amplitudes and time-delays leads to the exact cancelation of the induced vibrations provided that the values of the resonance frequency and damping are known. The requirement of resonance cancelation can be formulated equivalently in the frequency domain as the condition of zero transmission of the filter at the corresponding frequency:

$$IS(s)\,|_{s=-\xi\omega_n \pm j\omega_n\sqrt{1-\xi^2}} = 0. \tag{6.3}$$

Therefore, transmission zeros of the shaper have to be placed in the location of the system resonance.

The goal is to find a general parametrization of all the four-pulse shapers with structure (6.2) fulfilling the condition (6.3) with a minimum set of free parameters with a clear physical interpretation. The equation (6.3) can be rewritten by substituting $\sigma = -\xi\omega_n$ and $\omega = \omega_n\sqrt{1-\xi^2}$ as:

$$IS(\sigma + j\omega) = \sum_{i=1}^{4} A_i e^{-t_i(\sigma+j\omega)} \stackrel{\triangle}{=} \sum_{i=1}^{4} a_i e^{-j\kappa_i}, \tag{6.4}$$

where $a_i = A_i e^{-t_i\sigma}$, $\kappa_i \stackrel{\triangle}{=} \omega t_i$, $\kappa_0 = 0$, $i = 1, ..., 4$.

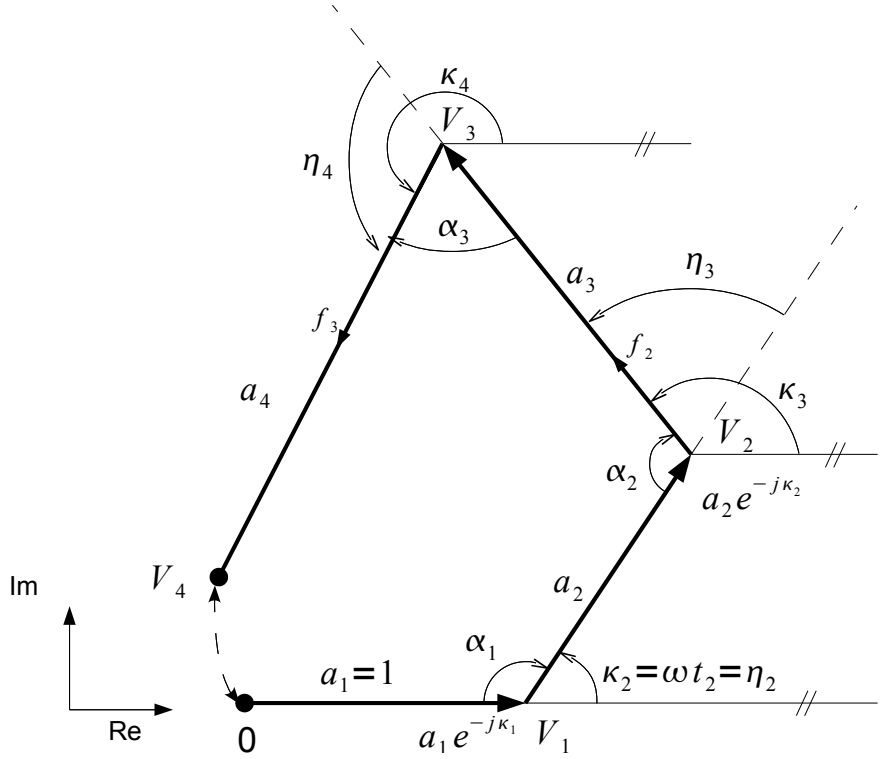

Figure 6.1: Vector diagram of the four impulse shaper

Now we define the following complex numbers:

$$\begin{aligned} V_k &\stackrel{\triangle}{=} \sum_{i=1}^{k} a_i e^{-j\kappa_i};\ k = 1, ..., 4 \\ \alpha_k &\stackrel{\triangle}{=} \pi - \eta_{k+1} = \pi - \omega_d \left(t_{k+1} - t_k\right);\ k = 1, \ldots, 3, \\ \alpha_k &\in \langle -\pi, \pi \rangle , \end{aligned} \tag{6.5}$$

where $\eta_i = \kappa_i - \kappa_{i-1}$.

The equations (6.5) form a vector diagram which can be displayed in the complex plane (Fig. 6.1). The complex numbers V_k represent the vertices of a tetragon with the edges of length a_k. The values of α_k have the meaning of the corresponding inner angles. The angles κ_i are defined by the time instants of the shaper pulses (see (6.4)) and η_{k+1} is the incremental angle of the side belonging to the *k-th* vertex. Therefore, *the problem of synthesis of the input shaping filter may be formulated as a geometric problem of construction of a tetragon in a plane*.

By analyzing the geometrical relationships of the tetragon, following formulas can be derived:

$$\begin{aligned} V_1 =& a_1 \stackrel{!}{=} 1, \\ V_2 =& (1 - a_2 \cos\alpha_1) + j a_2 \sin\alpha_1, \\ V_3 =& (1 - a_2 \cos\alpha_1) + a_3 \cos(\alpha_1 + \alpha_2) + \\ & + j\left[a_2 \sin\alpha_1 - a_3 \sin(\alpha_1 + \alpha_2)\right], \\ V_4 =& \left[(1 - a_2 \cos\alpha_1) + a_3 \cos(\alpha_1 + \alpha_2) - a_4 \cos(\alpha_1 + \alpha_2 + \alpha_3)\right] + \\ & + j\left[a_2 \sin\alpha_1 - a_3 \sin(\alpha_1 + \alpha_2) + a_4 \sin(\alpha_1 + \alpha_2 + \alpha_3)\right]. \end{aligned} \tag{6.6}$$

For the sake of convenience in further analysis, the length of the first edge a_1 is set equal to one without loss of generality. It can be seen that the demand for the zero transmission of the filter (6.4) is fulfilled only if the last vertex V_4 lies in the origin of complex plane. Thus, the following relation holds:

$$V_4 = 0 \Leftrightarrow Re\, V_4 = 0 \wedge Im V_4 = 0. \tag{6.7}$$

Now a set of four free parameters a_2, α_1, α_2, α_3 together with the given $a_1 = 1$ is sufficient to fully describe the tetragon $V_1V_2V_3V_4$ which exists if and only if the origin of the complex plane lies inside the affine cone defined by $(V_2, \{f_2, f_3\})$. The proof of this statement is clear from the figure (6.1). The remaining two parameters a_3, a_4 can be calculated from the equation (6.6) and condition (6.7) as:

$$a_3 = \frac{a_2 \sin(\alpha_2 + \alpha_3) - \sin(\alpha_1 + \alpha_2 + \alpha_3)}{\sin(\alpha_3)} \stackrel{!}{\geq} 0, \tag{6.8}$$

$$a_4 = \frac{a_2 \sin(\alpha_2) - \sin(\alpha_1 + \alpha_2)}{\sin(\alpha_3)} \stackrel{!}{\geq} 0. \tag{6.9}$$

The inequalities (6.8) and (6.9) follow from (6.2) and their fulfillment needs to be inspected in order to find a complete set of admissible values for the free parameters. The analysis of conditions (6.8) and (6.9) in a general case for the parameters a_2, α_1, α_2, α_3 is extremely complicated because of many degenerative conditions which have to be distinguished. For a practical implementation of the filter, the special case with equidistant shaper times t_1, t_2, t_3, t_4 may be considered. From (6.5) it follows that this demand leads to equal inner angles $\alpha_1, \alpha_2, \alpha_3$:

$$\alpha_1 = \alpha_2 = \alpha_3 = \alpha,\ \alpha \in < -\pi, \pi > . \tag{6.10}$$

This choice reduces the number of parameters to be specified (inner angles α and length a_2) and the problem of finding a complete parametrization of the filter is simplified significantly. Now the inequalities (6.8) and (6.9) have to be examined to find a set of admissible values for the parameter a_2.

If we consider positive inner angles $0 < \alpha < \pi$, the following conditions can be derived. From (6.8) we get:

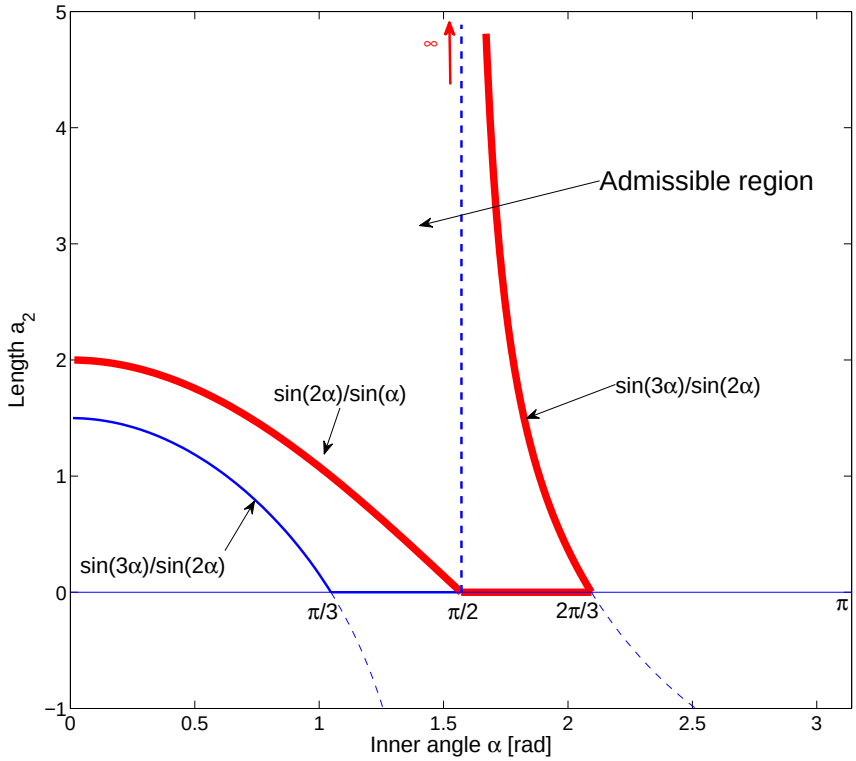

Figure 6.2: Parametric plane of the ZV4 shaper - admissible region for the shaper parameters

- For $0 < \alpha < \frac{\pi}{2}$:

$$a_3 \overset{!}{\geq} 0 \Rightarrow a_2 \geq \frac{\sin(3\alpha)}{\sin(2\alpha)} \Rightarrow a_2 \geq \max\{0, \frac{\sin(3\alpha)}{\sin(2\alpha)}\} \triangleq a_2^+ \tag{6.11}$$

- For $\frac{\pi}{2} < \alpha < \pi$:

$$0 \leq a_2 \leq \frac{\sin(3\alpha)}{\sin(2\alpha)} \tag{6.12}$$

From (6.9) it holds:

- For $0 < \alpha < \pi$:

$$a_4 \overset{!}{\geq} 0 \Rightarrow a_2 \geq \frac{\sin(2\alpha)}{\sin(\alpha)} \Rightarrow a_2 \geq \max\{0, \frac{\sin(2\alpha)}{\sin(\alpha)}\} \triangleq a_2^- \tag{6.13}$$

The intersection of the regions defined by (6.11), (6.12) and (6.13) defines a set of permissible values of a_2 with respect to the chosen angle $\alpha \in (0, \frac{2\pi}{3})$. This set can

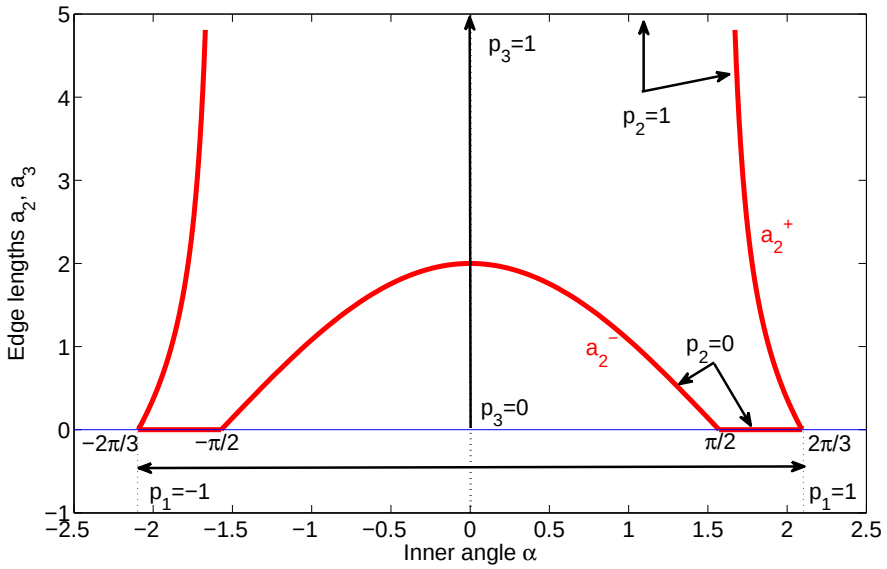

Figure 6.3: Complete parametric plane of the ZV4 shaper

be displayed in the parametric plane (Fig. 6.2). The analysis for the negative angle $\alpha \in (-\pi, 0)$ leads to the symmetrical constraint with respect to the vertical axis a_2 (Fig. 6.3).

Limit cases for special choice of α

For the choice of the angle α, two special cases can occur:

1. For $\alpha_1 = \alpha_2 = \alpha_3 = \alpha = 0$ the vector diagram (6.1) degenerates to a set of lines lying on the real axis. The condition (6.7) reduces to:

$$1 - a_2 + a_3 - a_4 = 0 \Rightarrow a_4 = 1 - a_2 + a_3. \tag{6.14}$$

   It can be seen that the choice of a_2 does not suffice for the complete parametrization of the filter. In this case, another user parameter for the length a_3 needs to be introduced. Its value can be chosen in the following way:

$$a_4 = 1 - a_2 + a_3 \overset{!}{\geq} 0 \Rightarrow a_3 \geq a_2 - 1. \tag{6.15}$$

2. For $\alpha_1 = \alpha_2 = \alpha_3 = \alpha = \frac{\pi}{2}$ the diagram (6.1) reduces to a rectangle. The lengths of its sides can be computed from (6.7):

$$\begin{aligned} a_2 - a_4 = 0 &\Rightarrow a_4 = a_2, \\ 1 - a_3 = 0 &\Rightarrow a_3 = 1, \\ a_2 &\overset{!}{\geq} 0. \end{aligned} \tag{6.16}$$

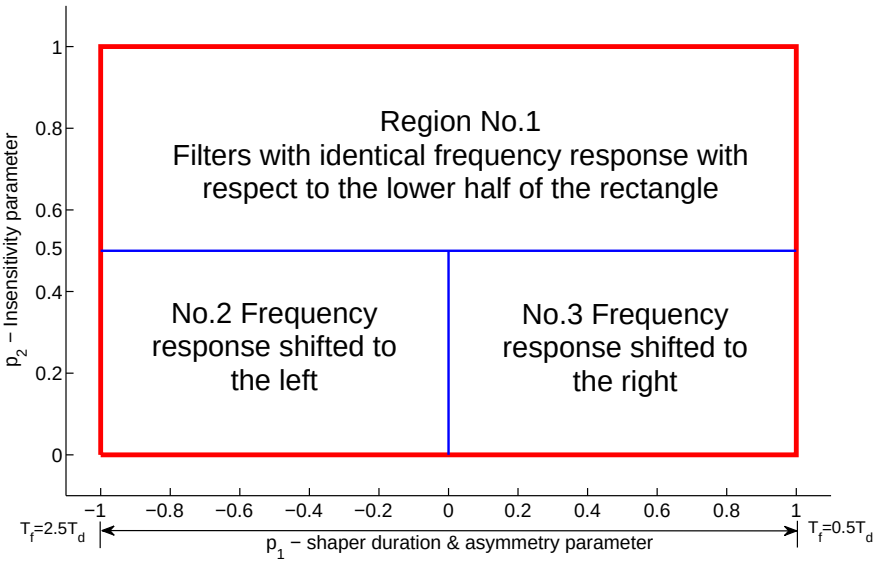

Figure 6.4: Transformed parametric plane of the asymmetric filter for $p_1 <> 0$

Complete algorithm for shaper design

The shape of the admissible region for the filter parameters defined by the inequalities (6.11)-(6.13) is quite irregular. Moreover, the range for a_2 and a_3 extends to infinity. Therefore, a nonlinear transformation is introduced for the sake of user convenience. Instead of directly specifying the angle α and side length a_2 (plus eventually a_3 for $\alpha = 0$), the user sets three values:

$$p_1, p_2, p_3;\ p_1 \in <-1, 1>,\ p_2 \in <0, 1>,\ p_3 \in <0, 1>\ . \tag{6.17}$$

The filter parameters (6.2) are calculated as follows:

1. If $p_1 <> 0$ then:

$$\alpha = p_1 \frac{2\pi}{3} \tag{6.18}$$

$$a_2 = \begin{cases} a_2^- + \frac{p_2}{1-p_2};\ for\, 0 < \alpha \leq \frac{\pi}{2}, \\ a_2^+ p_2;\ for\, \frac{\pi}{2} < \alpha \leq \frac{2\pi}{3} \end{cases}, \tag{6.19}$$

$$a_3 = \frac{a_2 \sin(2\alpha) - \sin(3\alpha)}{\sin(\alpha)}, \tag{6.20}$$

$$a_4 = \frac{a_2 \sin(\alpha) - \sin(2\alpha)}{\sin(\alpha)}, \tag{6.21}$$

where a_2^+, a_2^- were defined in (6.11) and (6.13).

If $p_1 = 0$ then:

$$\alpha = 0, \tag{6.22}$$

$$a_2 = \frac{p_2}{1-p_2}, \tag{6.23}$$

$$a_3 = \min\{a_2 - 1, \frac{p_3}{1-p_3}\}, \tag{6.24}$$

$$a_4 = 1 - a_2 + a_3. \tag{6.25}$$

The equations (6.19)-(6.25) transform the irregularly shaped admissible region for parameters α, a_2, a_3 into a rectangle in the parametric plane $\{p_1, p_2\}$ in the case of $p_1 <> 0$ (Fig. 6.4) and into a square in the plane $\{p_2, p_3\}$ for $p_1 = 0$ (Fig. 6.5). This provides much more comfortable selection of the filter parameters for the user.

2. The shaper pulses are equidistantly spaced in time and the values of the time instants t_i can be derived from (6.4) and (6.5):

$$\begin{aligned} &T = \frac{(\pi - \alpha)}{\omega_d}, \\ &t_1 = 0,\ t_2 = t_1 + T,\ t_3 = t_2 + T,\ t_4 = t_3 + T. \end{aligned} \tag{6.26}$$

3. The amplitudes of the pulses A_i can be obtained from substitution (6.4). Because of the fixed choice of the first side length ($a_1 = 1$) which was made in (6.5) the tetragon $\{V_1, V_2, V_3, V_4\}$ needs to be rescaled to fulfill the demand for unitary gain of the filter ($\sum_{i=1}^{4} A_i = 1$):

$$\begin{aligned} &\bar{a}_1 = a_1 = 1,\ \bar{a}_2 = a_2 e^{-\xi\omega_n t_2}, \\ &\bar{a}_3 = a_3 e^{-\xi\omega_n t_3},\ \bar{a}_4 = a_4 e^{-\xi\omega_n t_4}, \\ &\bar{k} = \bar{a}_1 + \bar{a}_2 + \bar{a}_3 + \bar{a}_4, \\ &A_1 = \frac{\bar{a}_1}{\bar{k}},\ A_2 = \frac{\bar{a}_2}{\bar{k}},\ A_3 = \frac{\bar{a}_3}{\bar{k}},\ A_4 = \frac{\bar{a}_4}{\bar{k}}. \end{aligned} \tag{6.27}$$

By using the above-mentioned algorithm, an arbitrary Zero vibration shaping filter with equidistantly spaced pulses can be designed. The important result is that **all the standard two, three or four-pulse shapers that have already been described in the literature can be obtained for a special choice of parameters** p_1, p_2, p_3. This statement holds for example for the Zero Vibration (ZV), Zero Vibration Derivative (ZVD), Zero Vibration Double Derivative (ZVDD) and two-hump Extra Insensitive (2HEI) filters (Fig. 6.5). In the case of two or three-pulse shapers, the corresponding number of pulse amplitudes is set to zero, thus for example for any two-pulse ZV filter the algorithm computes $A_3 = A_4 = 0$. The table 6.1 shows the values of parameters p_1, p_2, p_3 which lead to the standard filter types. Three examples are shown for 2HEI filter and different

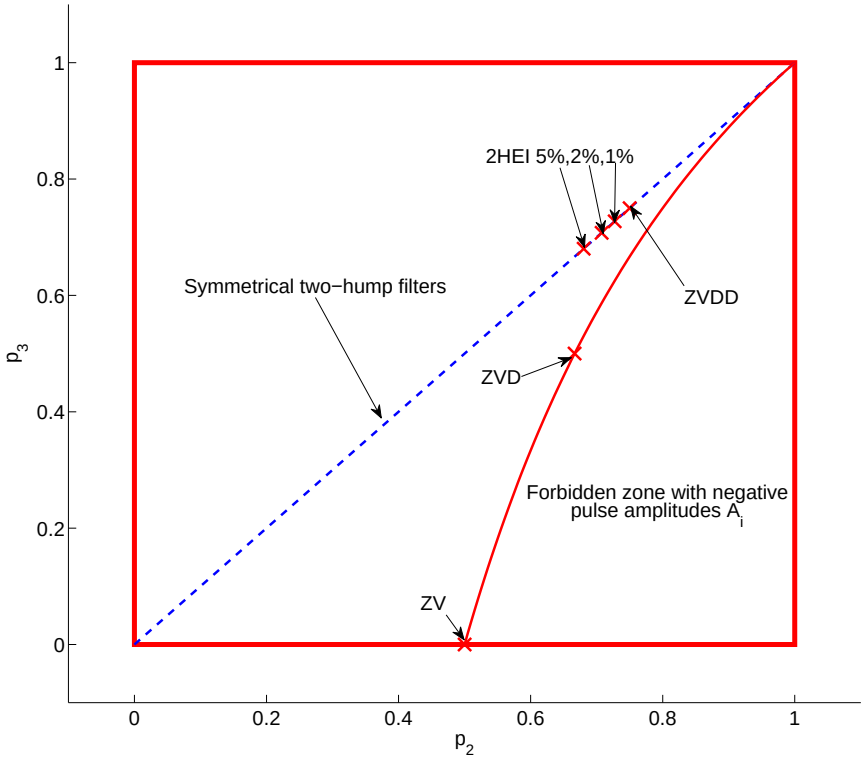

Figure 6.5: Transformed parametric plane of the symmetric filter for $p_1 = 0$

values of tolerated relative amplitude of excited oscillations $V_{tol} = 1\%, 2\%, 5\%$. For the 2HEI filters, the parametrization shown in (6.1) is valid only for an undamped oscillatory mode model ($\xi = 0$). The reason is that the 2HEI filter cannot be expressed in an explicit form for a nonzero damping. In this case, the filter parameters are functions of system damping and need to be calculated numerically. However, some corresponding values of p_1, p_2, p_3 can be found for each computed filter. The Extra Insensitive (EI) filter does not fulfill the zero vibration condition (6.3) and therefore it cannot be obtained directly using the proposed algorithm. Nevertheless, the same filter with shifted frequency response may be found and this shift can be adjusted by moving the desired ω_n to get the filter equal to EI. More details about the basic filter types and their properties can be found in [175].

Physical interpretation of shaper parameters

The main advantage of the proposed parametrization is that a clear physical meaning can be found for the user parameters. Each of the chosen values modifies the shape of the frequency response of the filter in a different way.

Filter type	p_1	p_2	p_3
ZV	0	0.5	0
ZVD	0	2/3	0.5
ZVDD	0	3/4	3/4
2HEI 5%	0	0.6803	0.6803
2HEI 2%	0	0.7075	0.7075
2HEI 1%	0	0.7274	0.7274

Table 6.1: Parameter setting for basic filter types

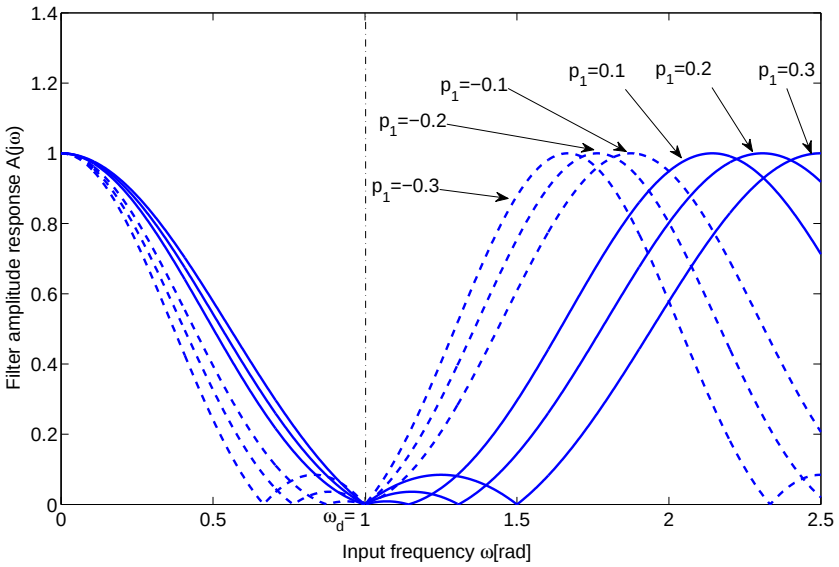

Figure 6.6: Asymmetric filter amplitude response for various values of p_1

The constant p_1 is called *Duration and asymmetry parameter*. From (6.26) it can be seen that α and therefore p_1 directly determines the overall length of the filter impulse function $T_f = t_4$. By substituting from (6.18) it follows that T_f takes values between $2.5T_d$ for $p_1 = -1$ and $0.5T_d$ for $p_1 = 1$. From (6.2) it holds that the zero transmission point of the frequency response repeats periodically with cycle $\omega_p = \frac{6\pi}{T_f}$. The result is that the parameter p_1 shifts the filter frequency response with respect to the damped frequency of the controlled system ω_d. This effect is demonstrated on figure (6.6) where different values of p_1 were chosen for fixed $p_2 = 0.1$ and system parameters $\omega_n = 1$, $\xi = 0$. For a positive choice of $p_1 \in (0, 1)$, an asymmetric filter with a right-shifted frequency response is obtained. For a negative $p_1 \in (-1, 0)$, we get a displacement to the left. The choice $p_1 = 0$ results in a symmetric frequency response. For the limit values $p_1 = \pm 1$ the filter degenerates to the two-pulse ZV shaper.

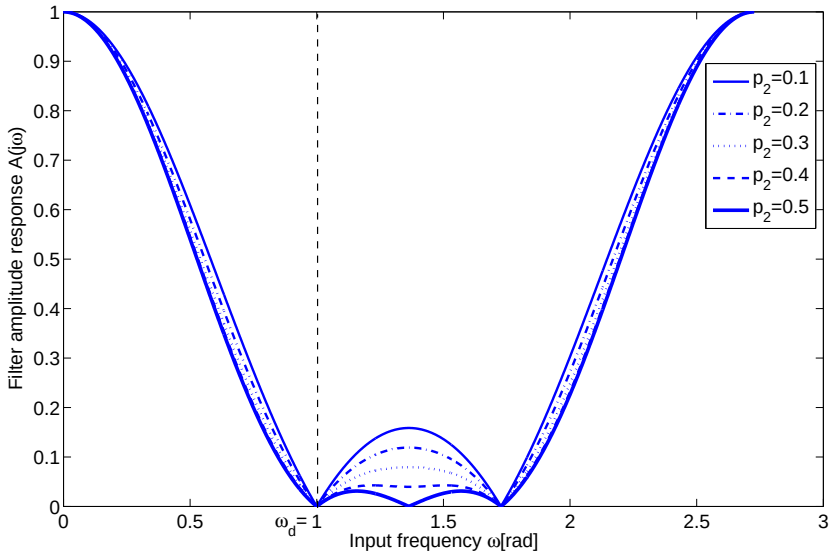

Figure 6.7: Asymmetric filter amplitude response for various values of p_2

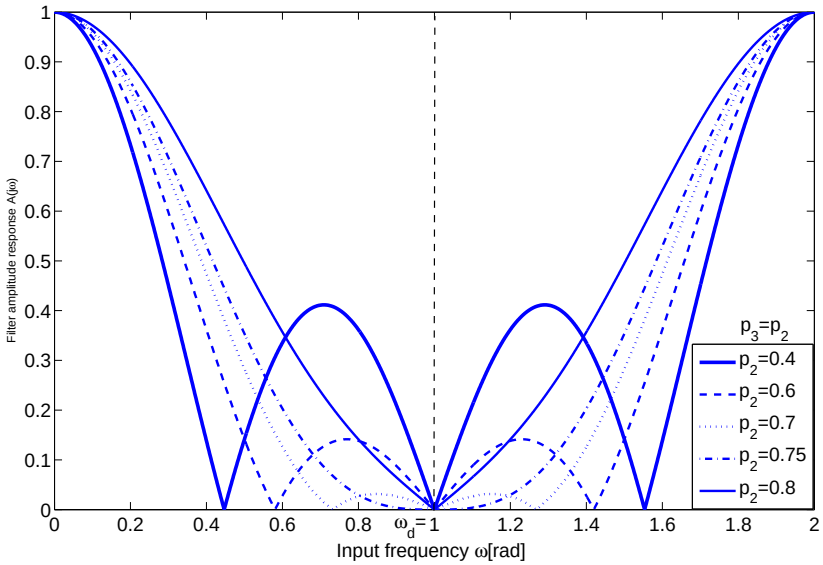

Figure 6.8: Symmetric filter amplitude response for various $p_2 = p_3, p_1 = 0$

The *Insensitivity parameter* p_2 determines the width and the level of attenuation of the filter stopband and thus affects the robustness against the uncertainty in the model of the system resonance (Fig. 6.7). An increase of p_2 results in a wider stopband and

increase of attenuation. For the values $p_2 \in (0.5, 1)$ (region No.1 on figure 6.4), we obtain filters with a frequency response which is identical to the filters from the lower half of the rectangle (regions No.2 and No.3). The only difference is in the transposition of the first and last amplitude (A_1=A_4 and vice versa). Therefore, only regions 2 and 3 should be taken into consideration for practical applications.

The *Additional parameter* p_3 needs to be chosen if p_1 is set to zero. This corresponds to the parametric plane $\{p_2, p_3\}$ which is displayed in figure 6.5. The filter length is fixed to $T_f = 1.5T_d$. There exist a forbidden region in the parametric square which is constrained by function $p_3 = 2 - \frac{1}{p_2}$ (this can be obtained from the condition (6.15)). The choice of p_2 and p_3 inside of this zone produces a negative value of some pulse amplitude A_i. The result is that the filter itself contain an oscillatory dynamics and therefore it is not suitable for the command shaping. The most useful filters can be found by picking the free parameters p_2, p_3 from the diagonal $p_2 = p_3; p_2, p_3 \in < 0, 1 >$. For the values of $p_2 = p_3 \in < 0, 0.75)$ we get robust symmetrical two-hump filters. Again, the value of the free parameters directly affects the shape of the stopband. The choice of $p_2 = p_3 = 0.75$ leads to the standard ZVDD filter. For the higher values the frequency response shrinks and the limit choice $p_2 = p_3 = 1$ corresponds to ZV filter.

The property of amplitude response shaping using the free design parameters was explained on an example of zero damping system for $\xi = 0$. Nonzero damping of the plant resonance leads to a change of the shape of the filter frequency response since the amplitude response of the shaper is generally nonzero for this case. However, the described properties of the filter parameterization are also valid for a more general characteristics which is known as the *shaper sensitivity function* and which expresses a relative amount of induced oscillations. Therefore, the achieved property of clear physical interpretation for the filter parameters in terms of the amount of provided level of vibration attenuation holds for an arbitrary value of the system damping. **The two design parameters may be used for smooth tuning of the filter dynamics and the user can easily find a suitable trade-off between the robustness against the uncertainty in the model of the system resonance and the amount of introduced delay**. Moreover, the standard Zero vibration filters which are commonly referenced in the literature are shown to be special cases of the given set of input shapers.

6.2 Discrete-time implementation of the input-shaping filter

The proposed algorithm was implemented in the form of a functional block in the C language and integrated into the REX control system and in the Matlab-Simulink environment. The universal format of the functional block makes it suitable for an arbitrary platform of a real-time control system which supports the C language.

The functional block interface and principle of interconnection with the identified system is depicted in Fig. (6.9). Feed-forward or feedback connection with the controlled plant is possible (the advantages and drawbacks of these two schemes are discussed in the following section).

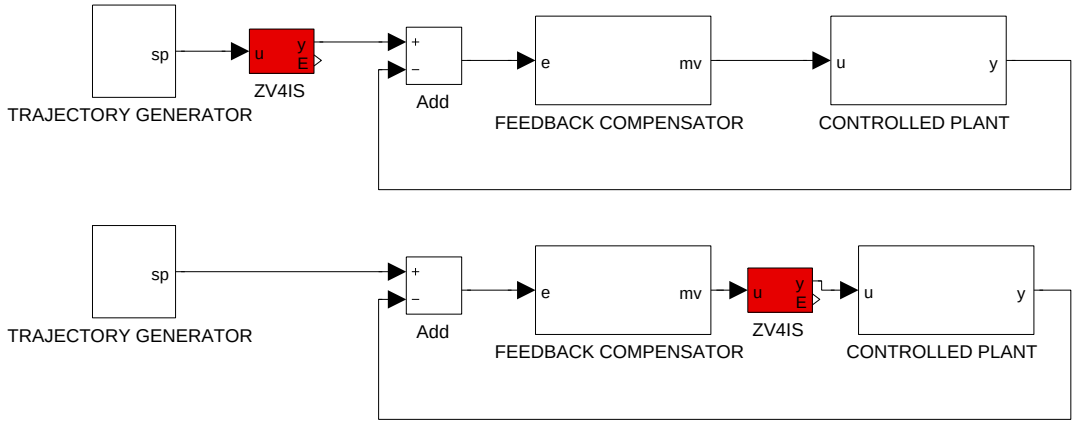

Figure 6.9: ZV4 input shaper - a) feed-forward connection (command shaping), b) feedback connection (manipulating variable shaping)

The user specifies the following set of parameters:

- Natural frequency of the system resonance $\omega_n[rad/s]$
- Relative damping coefficient ξ
- Selection of filter type (basic filters vs full parameterization)
- Three use parameters p_1, p_2, p_3 which determine the shape of the filter frequency response in the case that the full parameterization option has been chosen

The fine-tuning of the filter parameters can be performed either manually or in a special graphical user interface which displays the important plots showing the response of the filter in the time and frequency domains.

The analytical design of the input shaper was performed in the continuous time. Proper discretization of the shaper algorithm is necessary for the implementation in a sampled-data system. The output of the input shaper algorithm is given by equation:

$$y(t) = A_1 u(t - t_1) + A_2 u(t - t_2) + A_3 u(t - t_3) + A_4 u(t - t_4). \tag{6.28}$$

The discrete-time algorithm may be implemented effectively with use of a *cyclic buffer*. One dimensional array of the length corresponding to the largest time delay t_4 stores the samples of the input variable $u(kT_s)$. Proper samples with the time shift corresponding to the individual time-delays are multiplied by the appropriate weights, summed and copied to the block output $y(kT_s)$.

A particular issue of the discrete-time implementation of the equation (6.28) is the **problem of quantization of the applicable time-delay due to the limited resolution** which is given by the sampling period of the algorithm. The general parameterization of the filter which is performed in the continuous-time domain may result in arbitrary

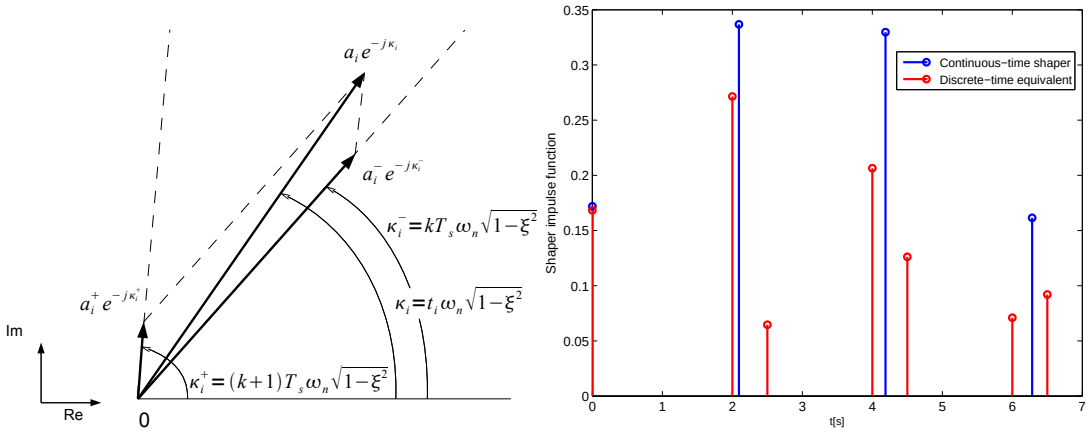

Figure 6.10: Input shaper discretization - left - vector decomposition of the continuous shaper pulse, right - impulse response of the continuous time four-pulse shaper (blue) and its discrete equivalent seven-pulse shaper (red)

values of the time delays t_i which do not necessarily attain integer multiples of the sampling period. Imperfect realization of the precise value of the time-delays may result in de-tuning of the discrete-time filter and may lead to excitation of the unwanted residual oscillations. There are generally three approaches to handling this situation:

1. **Simple round-off of the time-delay values to the nearest integer multiple of the sampling period**
   This approach can work well for fast sampling rates where the effect of the rounding will be negligible. However, significant error may arise in the case of large sample times comparable to the damped period of the oscillations.

2. **Utilization of the proposed parametrization for automatic selection of proper filter length**
   The equation (6.26) for the filter pulses times reveals that the *duration parameter* p_1 directly determines the values of the filter time-delays. For an arbitrary user-specified shaper, the parameter may be automatically adjusted to find a nearest filter with the time-delays which correspond to the integer multiples of the actual sampling period. The resulting filter does not introduce any discretization error. However, its frequency response may differ from the original specification of the user in the case of long sampling periods.

3. **Exact computation of a discrete-time equivalent**
   The problem of the continuous filter discretization can be solved using the geometrical representation of the shaper algorithm. Each pulse and the corresponding time-delay of the filter can be displayed as a vector $a_i e^{-j\kappa_i}$ in the complex plane (see Fig. 6.10 left and the shaper vector diagram 6.1). The base angle from the real axis is given by the value of the particular time-delay and damped

frequency of the controlled system. The discrete-time shaper cannot implement arbitrary values of the time-delay due to the finite sampling period. The idea of exact discretization is to decompose the vector of the continuous shaper into a set of two vectors with the base angles κ_i^+, κ_i^- corresponding to the adjacent sampling times. The vector decomposition is applied to all pulses of the continuous time shaper which do not fit exactly to an integer multiple of the given sampling period. The resulting discrete-time shaper preserves the zero-vibration condition since the last vertex of the polygon which arises from summation of the individual shaper pulses (equations 6.3-6.7) remains in the origin of the complex plane. The obtained discrete-time equivalent is a 7 pulse shaper which approximates the original 4 pulse continuous filter (Fig. 6.10 right).

Exact shaper discretization algorithm

The vector of the continuous-time shaper which needs to be decomposed is given as:

$$v_i = A_i e^{t_i \xi \omega_n} e^{j t_i \omega_n \sqrt{1-\xi^2}} \triangleq a_i e^{j\kappa_i} = a_i \cos(\kappa_i) + j a_i \sin(\kappa_i). \tag{6.29}$$

Vector decomposition is performed to obtain a set of two adjacent vectors with the base angles corresponding to the nearest sampling time instants:

$$v_i^- = a_i^- e^{j\kappa_i^-} = a_i^- \cos(\kappa_i^-) + j a_i^- \sin(\kappa_i^-);\ \kappa_i^- = k T_s \omega_n \sqrt{1-\xi^2}, \tag{6.30}$$

$$v_i^+ = a_i^+ e^{j\kappa_i^+} = a_i^+ \cos(\kappa_i^+) + j a_i^+ \sin(\kappa_i^+);\ \kappa_i^+ = (k+1) T_s \omega_n \sqrt{1-\xi^2}. \tag{6.31}$$

The condition of the vector addition is formulated as:

$$v_i^+ + v_i^- \stackrel{!}{=} v_i. \tag{6.32}$$

Comparison of the real and imaginary parts in (6.32) leads to a set of linear equations for the unknown amplitudes a_i^-, a_i^+:

$$\begin{bmatrix} \cos(\kappa_i^-) & \cos(\kappa_i^+) \\ \sin(\kappa_i^-) & \sin(\kappa_i^+) \end{bmatrix} \begin{bmatrix} a_i^- \\ a_i^+ \end{bmatrix} = \begin{bmatrix} a_i \cos(\kappa_i) \\ a_i \sin(\kappa_i) \end{bmatrix}. \tag{6.33}$$

The analytical solution is obtained in the form of:

$$a_i^- = -\frac{a_i \sin(\kappa_i - \kappa_i^+)}{\sin(\kappa_i^+ - \kappa_i^-)}, \tag{6.34}$$

$$a_i^+ = \frac{a_i \sin(\kappa_i - \kappa_i^-)}{\sin(\kappa_i^+ - \kappa_i^-)}. \tag{6.35}$$

Division by the envelope exponential due to the system damping is necessary to obtain the correct pulse amplitudes:

$$A_i^- = \frac{a_i^-}{e^{k T_s \xi \omega_n}}, \tag{6.36}$$

$$A_i^+ = \frac{a_i^+}{e^{(k+1) T_s \xi \omega_n}}. \tag{6.37}$$

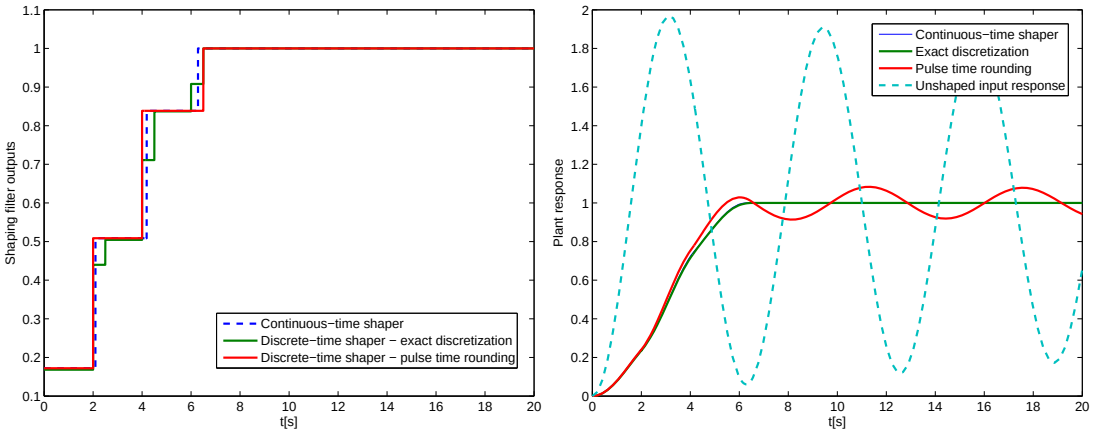

Figure 6.11: Input shaper discretization - rounding vs exact computation, left - shaped input, right - plant output response

Finally, the normalization of the pulse amplitudes has to be performed in order to achieve the unitary steady state gain $\sum_{i=1}^{n} A_i = 1$:

$$A_i = \frac{A_i}{\sum_{i=1}^{n} A_i} \; \forall i. \tag{6.38}$$

The proposed discretization technique is demonstrated on a numerical example. An underdamped second-order oscillatory system with natural frequency $\omega_n = 1\ rad/s$ and damping coefficient $\xi = 0.01$ is considered as the model of the plant resonance. A four-impulse shaper is designed using the proposed parameterization with user specified values $p_1 = 0.5, p_2 = 0.5$. This choice leads to the following values of time-delays and pulse amplitudes:

$$\boldsymbol{t} = \{0, 2.0945, 4.1890, 6.2835\},\ \boldsymbol{A} = \{0.1720, 0.3368, 0.3298, 0.1615\}. \tag{6.39}$$

The step response of the continuous-time filter and the response of the system to the shaped input are shown as blue plots in Fig. (6.11). It can be seen, that the vibrations are completely canceled-out in the finite time at the time instant of the last filter pulse $t = t_4 = 6.2835$ (approximately one period of the unshaped response). The discretization of the shaper is performed using the rounding method for a chosen sampling period $T_s = 0.5s$. This leads to the time-delay values:

$$\boldsymbol{t} = \{0, 2, 4, 6.5\}. \tag{6.40}$$

The pulse amplitudes remain unchanged. The quantization error in the pulse timing introduces an imperfect cancelation of the oscillatory poles of the system and excitation of the vibrations with amplitude about 10% (red plot in Fig. (6.11) right). The

proposed interpolation technique divides the shaper pulses to the couples which occur at the adjacent sampling times (Fig. 6.10 right) leading to the seven-pulse shaper in the form of:

$$\boldsymbol{t} = \{0, 2, 2.5, 4, 4.5, 6, 6.5\},\ \boldsymbol{A} = \{0.1683, 0.2715, 0.0646, 0.2064, 0.1261, 0.071, 0.092\}. \tag{6.41}$$

This leads to the complete elimination of the discretization error. The resulting shaper preserves the zero vibration condition and the level of excited residual oscilations is forced to zero (green lines in Fig. (6.11)).

6.3 Multiple modes input shaping

Industrial motion control systems often exhibit an oscillatory dynamics with multiple resonance modes due to the flexible mechanics. The input shaping method can be adopted even for such cases. There are three possible approaches to passive vibration control of multiple resonance system:

1. **Damping of the first mode**
   The shaping filter can be designed only for the first dominant resonance of the system and the higher modes are ignored. Sufficient damping of the higher resonances may be achieved due to the repetitive nature of the amplitude response of the zero-vibration filters and the performance may be satisfactory.

2. **Convolution of multiple single-mode shapers**
   Multiple input shapers can be designed separately for the individual resonances of the system and be connected in series. The serial connection forms a multi-mode shaper which preserves the zero-vibration conditions for all the resonance frequencies due to the principle of linearity. For a couple of two input shaping filters with the impulse function h_1, h_2 in the form of

   $$h_1(t) = \sum_{i=1}^{n_1} A_i^{(1)} \delta(t - t_i^{(1)}),\ h_2(t) = \sum_{j=1}^{n_2} A_i^{(2)} \delta(t - t_i^{(2)}), \tag{6.42}$$

   we obtain a resulting impulse function h_{12} of their serial connection from the convolution

   $$h_{12}(t) = h_1(t) * h_2(t) = \sum_{i=1}^{n_1} A_i^{(1)} \sum_{j=1}^{n_2} A_j^{(2)} \delta(t - t_i^{(1)} - t_j^{(2)}). \tag{6.43}$$

   The impulse function has an overall length which corresponds to the sum of the lengths of the individual single-mode filters. The number of pulses/time-delays is given as the product of the pulse numbers of the connected filters. *The resulting shaper may be sub-optimal due to the unnecessary large overall length which leads to long rise times in the loop*.

3. **Direct synthesis of a multi-mode shaper**
   A multi-mode shaper can be computed directly from the specification of the system resonances and from the desired shape of the filter sensitivity function. The following section presents a numerical approach based on the linear programming method.

Multi-mode input shaper synthesis using the linear programming approach

The model of the plant resonances is given as a product of the second-order terms corresponding to the individual oscillatory modes:

$$P(s) = \prod_{k=1}^{m} \frac{\omega_k^2}{s^2 + 2\xi_k\omega_k s + \omega_k^2}. \tag{6.44}$$

A general n-impulse shaping filter is described by the transfer function:

$$IS\,(s) = \sum_{i=1}^{n} A_i e^{-t_i s};\ 0 = t_1 < t_2 < ... < t_n,\ t_{k+1} - t_k = const. = T_s\ \forall k. \tag{6.45}$$

Equidistant timing of the filter pulses with a defined spacing T_s is assumed (T_s must not be confused with the sampling period of the discrete-time filter since we are still dealing with the continuous-time domain). This condition reduces the number of unknown variables and simplifies the procedure of the shaper computation. The resulting filter does not necessarily have to be equidistant as some amplitudes may be set to zero. Therefore, this assumption does not pose significant limitation for the achievable shaper dynamics.

Unitary gain of the shaper is required giving the equation:

$$\sum_{i=1}^{n} A_i \stackrel{!}{=} 1. \tag{6.46}$$

Positive values of the filter amplitudes have to be considered in order to achieve a monotonous step response which is necessary for smooth command shaping. This leads to the inequality constraints in the form of:

$$A_i > 0\ \forall i. \tag{6.47}$$

The multi-mode shaper has to fulfill the zero-vibration condition for all the resonances analogously to the single-mode case:

$$IS\left(s = -\xi_k\omega_k \pm j\omega_k\sqrt{1-\xi_k^2}\right) \stackrel{!}{=} 0;\ k = 1, 2, ..., m \tag{6.48}$$

Again, the vibration damping condition (6.48) for a particular mode may be expressed graphically in the form of a vector diagram in the complex plane (Fig. 6.12). Successive

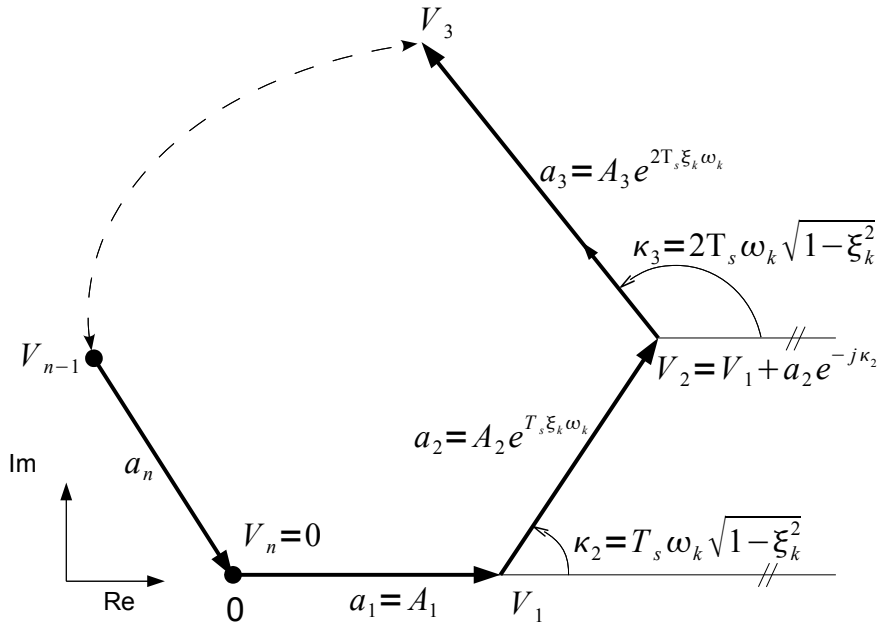

Figure 6.12: Vector diagram of the n-impulse shaper

addition of the individual complex vectors form a polygon whose vertices are obtained by substitution of the condition (6.48) to the transfer function (6.45):

$$
\begin{aligned}
V_1 &= A_1, \\
V_2 &= V_1 + A_2 e^{T_s \xi_k \omega_k} e^{-jT_s \omega_k \sqrt{1-\xi_k^2}}, \\
V_3 &= V_2 + A_3 e^{2T_s \xi_k \omega_k} e^{-j2T_s \omega_k \sqrt{1-\xi_k^2}}, \\
&\vdots \\
V_n &= A_1 + \sum_{l=2}^{n} A_l e^{(l-1)T_s \xi_k \omega_k} \cos(\kappa_l) + j \sum_{l=2}^{n} A_l e^{(l-1)T_s \xi_k \omega_k} \sin(\kappa_l) \\
&\triangleq C(\omega_k, \xi_k) + jS(\omega_k, \xi_k);\ \kappa_l = (l-1)T_s \omega_k \sqrt{1-\xi_k^2},
\end{aligned}
\tag{6.49}
$$

where $C(\omega_k, \xi_k)$ denote the real part of the expression including the cosine terms and $S(\omega_k, \xi_k)$ corresponds to the imaginary part with the sum of sines.

Assuming an apriori chosen pulse spacing time T_s, the m zero vibration conditions (6.48) for the individual resonance modes lead to $2m$ linear equality constraints for the

n unknown amplitudes A_i which are obtained from (6.49) as:

$$\begin{aligned} C(\omega_k, \xi_k) &\stackrel{!}{=} 0 \\ S(\omega_k, \xi_k) &\stackrel{!}{=} 0;\ k = 1, 2, .., m. \end{aligned} \tag{6.50}$$

The number of solutions of the linear equations system depends on the chosen number of shaper pulses. Three distinct cases may occur:

1. $\mathbf{n < 2m}$
   The number of shaper pulses is too low. There is no solution for the given number of resonances and the shaper cannot be computed.

2. $\mathbf{n = 2m}$
   There is exactly one solution which can by computed numerically. The condition of positiveness of the shaper amplitudes (6.47) may be violated for a particular choice of filter spacing time T_s. Furthermore, there are no additional degrees of freedom for a specification of some additional requirements on the shaper dynamics.

3. $\mathbf{n > 2m}$
   There is an infinite number of linearly dependent solutions. Numerical optimization may be used to acquire a particular solution which fulfills some additional design requirements.

The additional degrees of freedom in the case of infinite solutions may be used for a definition of a specified maximum level of the excited vibrations in the case of modelling errors. A suitable tradeoff between the robustness and the introduced delay may be chosen. Moreover, unnecessary pulses of the input shaper may be set to zero to obtain the simplest filter with the shortest length.

One of the useful design requirements is the specification of the robustness to the modelling errors of a particular mode of the system. A model of the $k-th$ resonance of the system (6.44) and the corresponding impulse function are given as:

$$P_k(s) = \frac{\omega_k^2}{s^2 + 2\xi_k\omega_k s + \omega_k^2},\ h_k(t) = \frac{\omega_k}{\sqrt{1-\xi_k^2}} e^{-\xi_k\omega_k t}\sin(\omega_d t);\ \omega_d = \omega_k\sqrt{1-\xi_k^2}. \tag{6.51}$$

The general n-pulse shaper impulse function is defined as:

$$h_s(t) = \sum_{i=1}^{n} A_i \delta(t - t_i). \tag{6.52}$$

The overall impulse response of the $k-th$ mode to the shaped input is obtained from convolution of $h_s(t)$ and $h_k(t)$ as:

$$h(t) = \sum_{i=1}^{n} A_i h_k(t - t_i)\mathbb{1}(t - t_i), \tag{6.53}$$

where $\mathbb{1}(t)$ is the Heaviside step function.
For the time $t > t_n$, we obtain:

$$h(t) = \sum_{i=1}^{n} A_i h_k(t - t_i) = \frac{\omega_k}{\sqrt{1-\xi_k^2}} e^{-\xi_k \omega_k t} \sqrt{C(\omega_k, \xi_k)^2 + S(\omega_k, \xi_k)^2} \sin(\omega_d t - \psi), \tag{6.54}$$

where

$$C(\omega_k, \xi_k) = \sum_{i=1}^{n} A_i e^{\xi_k \omega_k t_i} \cos(\omega_d t_i),\ S = \sum_{i=1}^{n} A_i e^{\xi_k \omega t_i} \sin(\omega_d t_i),\ \psi = \arctan \frac{S}{C}. \tag{6.55}$$

The maximum amplitude of oscillations excited by the shaped input signal is obtained for time $t = t_n$ as:

$$A^s_{max}(\omega_k, \xi_k) = \frac{\omega_k}{\sqrt{1-\xi_k^2}} e^{-\xi_k \omega_k t_n} \sqrt{C(\omega_k, \xi_k)^2 + S(\omega_k, \xi_k)^2}. \tag{6.56}$$

The maximum amplitude of the *unshaped* impulse function which corresponds to the unitary impulse $A_1 = 1$ at $t_1 = 0$ is obtained from (6.51):

$$A^u_{max}(\omega_k, \xi_k) = \frac{\omega_k}{\sqrt{1-\xi_k^2}}. \tag{6.57}$$

The normalized ratio between the shaped and unshaped amplitudes is usually introduced to form a performance index of the shaping filter which specifies the *relative amount of excited vibrations*:

$$A_r(\omega_k, \xi_k) = \frac{A^s_{max}}{A^u_{max}} = e^{-\xi_k \omega_k t_n} \sqrt{C(\omega_k, \xi_k)^2 + S(\omega_k, \xi_k)^2}. \tag{6.58}$$

The zero-vibration condition (6.48) for a particular mode leads to the equality constraint for the shaper amplitudes in the form of:

$$A_r \stackrel{!}{=} 0 \Rightarrow C(\omega_k, \xi_k) \stackrel{!}{=} 0 \ \cap \ S(\omega_k, \xi_k) \stackrel{!}{=} 0. \tag{6.59}$$

Inspection of the vector diagram of the shaper (Fig. 6.12) and the corresponding equations (6.49) reveals that the geometric interpretation of the ZV condition (6.59) implicates the necessity for placement of the last vertex V_n of the shaper in the origin of the complex plane.

The introduced relative vibration damping ratio (6.58) may be used to evaluate the sensitivity of the shaper to the modelling errors. The relative amplitude A_r may be computed for the varying ω_k in a desired frequency range:

$$S(\omega) = A_r(\omega, \xi_k);\ \omega \in \langle 0, \omega_{max} \rangle. \tag{6.60}$$

The resulting plot is often called a *shaper sensitivity function* since it expresses the amount of excited vibrations as a function of a resonance model mismatch. Similarly,

the sensitivity function may be obtained for the varying relative damping coefficient. However, it was shown that the sensitivity to the precision of the damping parameter is relatively low for most of the ZV shapers and the frequency sensitivity function is essential for the evaluation of the filter robustness.

Inequality constraints which define a maximum level of the excited vibrations for particular frequencies may be defined to shape the sensitivity function of the filter:

$$S(\omega_i^s) \leq S_i^{max};\ i = 1, .., s \tag{6.61}$$

where ω_i^s are properly chosen sensitivity function points which can be set in the vicinity of the assumed resonance frequencies to specify the desired width of the shaper stop-band. Geometric interpretation of the inequality (6.61) leads to the limitation of the maximum distance of the last vertex V_n from the origin in the shaper vector diagram. Therefore, we may write:

$$S(\omega_i^s) = e^{-\xi_k \omega_i^s t_n} |V_n(\omega_i^s, \xi_k)| = e^{-\xi_k \omega_i^s t_n} \sqrt{C(\omega_i^s, \xi_k)^2 + S(\omega_i^s, \xi_k)^2} \leq S_i^{max}. \tag{6.62}$$

The constraint (6.62) can be imposed by limiting the absolute value of the sine and cosine terms:

$$|C(\omega_i^s, \xi_k)| \leq \frac{S_i^{max} e^{t_n \xi_k \omega_i^s}}{\sqrt{2}} \cap |S(\omega_i^s, \xi_k)| \leq \frac{S_i^{max} e^{t_n \xi_k \omega_i^s}}{\sqrt{2}}. \tag{6.63}$$

The factor $\sqrt{2}$ is obtained from a square inscribed inside the circle defining the maximum radius of the complex number V_n. The conditions (6.62) define four *linear inequality* constraints for the filter amplitudes A_i for each sensitivity point specification. Another robustness condition may be derived from the requirement of zero derivative of the sensitivity function at the resonance frequency points:

$$\frac{\partial S(\omega_k)}{\partial \omega_k} \stackrel{!}{=} 0. \tag{6.64}$$

This enforces a flat shape of the sensitivity function around the saddle point given by the zero-vibration condition and produces robust shapers which are insensitive to modelling errors. Since the sensitivity function is directly proportional to the magnitude of the complex number V_n, it is clearly seen that the condition (6.64) is fulfilled for zero derivatives of the sine and cosine terms in (6.49). Therefore, we get a set of two conditions:

$$\begin{aligned}
\frac{\partial C(\omega_k, \xi_k)}{\partial \omega_k} &= \sum_{i=1}^{n} A_i t_i \xi_k \mathrm{e}^{t_i \xi_k \omega_k} \cos(t_i \omega_d) - \sum_{i=1}^{n} A_i t_i \mathrm{e}^{t_i \xi_k \omega_k} \sin(t_i \omega_d) \sqrt{1 - {\xi_k}^2} \stackrel{!}{=} 0, \\
\frac{\partial S(\omega_k, \xi_k)}{\partial \omega_k} &= \sum_{i=1}^{n} A_i t_i \xi_k \mathrm{e}^{t_i \xi_k \omega_k} \sin(t_i \omega_d) - \sum_{i=1}^{n} A_i t_i \mathrm{e}^{t_i \xi_k \omega_k} \cos(t_i \omega_d) \sqrt{1 - {\xi_k}^2} \stackrel{!}{=} 0.
\end{aligned} \tag{6.65}$$

Closer inspection of the summations in (6.65) lead to a set of two linear constraints for the unknown amplitudes:

$$\begin{aligned}\sum_{i=1}^{n} A_i t_i \mathrm{e}^{t_i \xi_k \omega_k} \cos\left(t_i \omega_d\right) &\stackrel{!}{=} 0,\\ \sum_{i=1}^{n} A_i t_i e^{t_i \xi_k \omega_k} \sin\left(t_i \omega_d\right) &\stackrel{!}{=} 0.\end{aligned} \tag{6.66}$$

It can easily be shown that the same conditions as in (6.66) are obtained for the derivative of the sensitivity function with respect to the relative damping:

$$\frac{\partial S(\omega_k)}{\partial \xi_k} \stackrel{!}{=} 0. \tag{6.67}$$

Therefore, the robustness is achieved against the modelling errors both in resonance frequency and damping parameters. The robustness can be further improved by forcing the higher derivatives of the sensitivity functions to zero, i.e.:

$$\frac{\partial^l S(\omega_k)}{\partial \omega_k^l} \stackrel{!}{=} 0. \tag{6.68}$$

Continuing in computations of the higher partial derivatives in (6.65) leads to the linear constraints for the shaper amplitudes in the form of:

$$\begin{aligned}\sum_{i=1}^{n} A_i t_i^l \mathrm{e}^{t_i \xi_k \omega_k} \cos\left(t_i \omega_d\right) &\stackrel{!}{=} 0,\\ \sum_{i=1}^{n} A_i t_i^l e^{t_i \xi_k \omega_k} \sin\left(t_i \omega_d\right) &\stackrel{!}{=} 0.\end{aligned} \tag{6.69}$$

Optimization procedure for the multi-mode shaper design

The derived conditions for the robust shaper design can be used for the numerical optimization of the filter parameters. The linearity of the obtained equality and inequality constraints can be used for the formulation of the optimization problem in terms of the **linear programming method** [174]. This allows for utilization of some of the well established and computationally efficient numerical methods e.g. the simplex algorithm or interior point method [207, 208].

The optimization problem is set as a minimization of a linear cost function:

$$J = \boldsymbol{f}^{\boldsymbol{T}} \boldsymbol{x}, \tag{6.70}$$

subject to the linear equality and inequality constraints:

$$\boldsymbol{C_{eq}x} = \boldsymbol{d_{eq}}, \tag{6.71}$$

$$\boldsymbol{Cx} \leq \boldsymbol{d}, \tag{6.72}$$

$$\boldsymbol{lb} \leq \boldsymbol{x} \leq \boldsymbol{ub}. \tag{6.73}$$

The equality constraints (6.71) are obtained in the form of:

- **Zero-vibration conditions**
  Each of the resonance modes which needs to be attenuated gives two equality constraints for the sine and cosine terms in (6.59).
- **Unitary static gain condition**
  The sum of the filter amplitudes has to be equal to one.
- **Sensitivity function derivatives conditions (optional)**
  Each specification of a derivative leads to the two equality constraints (6.66).

The inequality constraints (6.71) are defined as:

- **Specified maximum sensitivity conditions (optional)**
  Each defined upper bound for a sensitivity function value gives four inequality conditions (6.63).
- **First pulse positiveness condition**
  The first pulse should be nonnegative in order to minimize the overall time-delay.

Lower and upper bounds (6.73) are given as:

- **Nonnegative pulse amplitude condition**
  Positive values of the pulse amplitudes are required for the monotonous step response of the filter.
- **Maximum pulse amplitudes conditions (optional)**
  The pulse amplitudes may be limited in order to penalize steep changes in the shaped signal.

The objective function may be set to penalize the higher shaper amplitudes in order to minimize the complexity and overall length of the filter by zeroing unnecessary pulse amplitudes. Two possible weighting schemes are proposed:

$$J_1 = \begin{bmatrix} 0 & 1 & 1 & \dots & 1 \end{bmatrix} \boldsymbol{A^T}, \tag{6.74}$$

$$J_2 = \begin{bmatrix} 1 & k+1 & 2k+1 & \dots & k(n-1)+1 \end{bmatrix} \boldsymbol{A^T};\ k > 0, \tag{6.75}$$

where $\boldsymbol{A}$ is the unknown amplitudes vector. The first scheme uses equal weights for all the shaper amplitudes except the first one (otherwise, the criterion function would be meaningless, since the sum of all pulses is constrained to be equal to one). The second

criterion uses an increasing linear scale for the amplitudes weights and tend to produce filters with shorter overall length and faster rise times.

Finally, the number of shaper amplitudes n and pulse time spacing T_s has to be specified prior to performing the numerical optimization. The following procedure is proposed:

1. Set the pulse spacing time equal to the desired sampling period of the control system $T_s = T$. Set the number of pulses to be greater than the number of the constraint equations $n > dim(\boldsymbol{d_{eq}})$ to achieve sufficient degrees of freedom.

2. Perform the numerical optimization using the linear programming algorithm. If no feasible solution which suits the specified inequality constraints is found, increase the number of the filter pulses by one.

3. Repeat the previous step until a feasible solution is found. The resulting overall filter length is given as $T_f = (n-1)T_s$.

4. Increase the pulse spacing to the next integer multiple of the sampling period $T_s = kT$. Repeat steps 2 and 3. Reasonable upper bound for the maximum feasible time spacing may be obtained from the basic two-pulse shaper for the first resonance mode as $T_s \leq \pi/\omega_{d1}$.

5. Maximum overall filter length T_f, number of shaper pulses n or proper combinations of both criterions can be used for the selection of the final solution which fulfills the design requirements.

Numerical example

An example is given to demonstrate the proposed design method. A three-mode shaper needs to be designed for the resonance modes parameters:

$$\omega_1 = 1\ rad/s,\ \omega_2 = 2.25\ rad/s,\ \omega_3 = 3.4\ rad/s,\ \xi_{1,2,3} = 0.1. \tag{6.76}$$

Specified insensitivity to modelling errors is given in terms of the defined maximum level of excited vibrations to be less than 5% in the range of $\pm 15\%$ around the assumed resonance frequencies. The sampling period is set to $T = 0.01s$. The convolution method is compared to the proposed direct optimal design procedure.

Convolution 3xZVD shaper
The first design uses the conventional approach of independent shaper synthesis for the individual modes. Three ZVD filters are connected in series to form a multi-mode

shaper with parameters:

$$\begin{aligned}\boldsymbol{t} =&\{0, 0.9287, 1.4030, 1.8570, 2.3317, 2.8070, 3.1570, 3.2600, 3.7357, 4.0857, \\ &4.5600, 4.6640, 5.0140, 5.4887, 5.9640, 6.3150, 6.4170, 6.8927, 7.2437, 7.7180, \\ &7.8210, 8.1720, 8.6467, 9.1220, 9.5750, 10.0507, 10.9790\}, \\ \boldsymbol{A} =&\{0.0374, 0.0545, 0.0199, 0.0545, 0.0795, 0.0290, 0.0199, 0.0290, 0.0106, 0.0545, \\ &0.07950.02900.07950.11600.04230.02900.04230.01540.01990.0290 \\ &0.0106, 0.0290, 0.0423, 0.0154, 0.0106, 0.0154, 0.0056\}.\end{aligned} \tag{6.77}$$

The resulting design fulfills the insensitivity requirements. However, the overall shaper length $T_f = 10.979s$ is unnecessarily large as well as the filter complexity in the sense of the number of pulses $n = 3^3 = 27$. Moreover, the resulting pulse times do not respect the chosen sampling period and a discretization error which was discussed in the previous section may occur. The computation of the exact discrete-time equivalent which was proposed in the previous section could be performed for the individual ZVD filter. However, this would lead to the further increase of the filter complexity since the overall number of pulses would be $5^3 = 125$.

Direct multi-mode shaper design Nr. 1
The proposed design procedure is used for the computation of the optimal filter. Three ZV conditions are set for the model of the resonances along with three additional robustness conditions for the first zero derivative of the sensitivity function at the resonance frequencies according to equation (6.64). Second objective function J_2 with scaling coefficient $k = 1$ in (6.75) is selected. A minimum pulse filter is obtained for $n = 14$, $T_s = 0.68s$. The resulting parameters obtained from the optimization algorithm are given as:

$$\begin{aligned}\boldsymbol{t} =&\{0, 0.68, 1.36, 2.04, 2.72, 3.40, 4.08, 4.76, 5.44, 6.12, 6.80, 7.48, 8.16, 8.84\}, \\ \boldsymbol{A} =&\{0.1492, 0, 0.1138, 0.0539, 0.0922, 0.1172, 0.1078, 0.1320, 0.0245, 0.0867, \\ &0.02370.05590.01960.0235\}.\end{aligned} \tag{6.78}$$

A zero amplitude value is computed for the second shaper pulse. Therefore, the inequidistant filter is obtained as a special case of the general equidistant formulation of the optimization problem. The overall length $T_f = 8.84$ is 20% shorter compared to the conventional design (6.77). Moreover, the pulse spacing respects the chosen sampling period and the resulting shaper can be directly implemented in a sampled data system without any discretization error.

Direct multi-mode shaper design Nr. 2
Closer inspection of the shaper sensitivity function for the previous design reveals, that the shaper insensitivity is greater than required. Therefore, further reduction of the filter length is possible by fine tuning of the sensitivity function shape. Direct specification for the desired maximum level of vibrations for the three resonance points is used instead of the general condition of the flatness of the sensitivity function. Six

inequality constraints are obtained in the form of (6.61) for the three pairs of points in the $\pm 15\%$ vicinity of the resonance frequencies. The resulting design is obtained for $n = 14$, $T_s = 0.63s$:

$$\begin{aligned} \boldsymbol{t} =& \{0, 0.63, 1.26, 1.89, 2.52, 3.15, 3.78, 4.41, 5.04, 5.67, 6.30, 6.93, 7.56, 8.1900\}, \\ \boldsymbol{A} =& \{0.2317, 0, 0.0546, 0.1632, 0, 0.1712, 0.0627, 0.1453, 0.0211, 0.0547, \\ & 0.02580.04030.00690.0226\}. \end{aligned} \tag{6.79}$$

The complexity of the shaper is further reduced since there is only 12 nonzero pulse amplitudes. The overall filter length $T_f = 8.19$ is less than 75% of the initial suboptimal convolution design. The number of pulses is reduced by a factor of $5/4$.

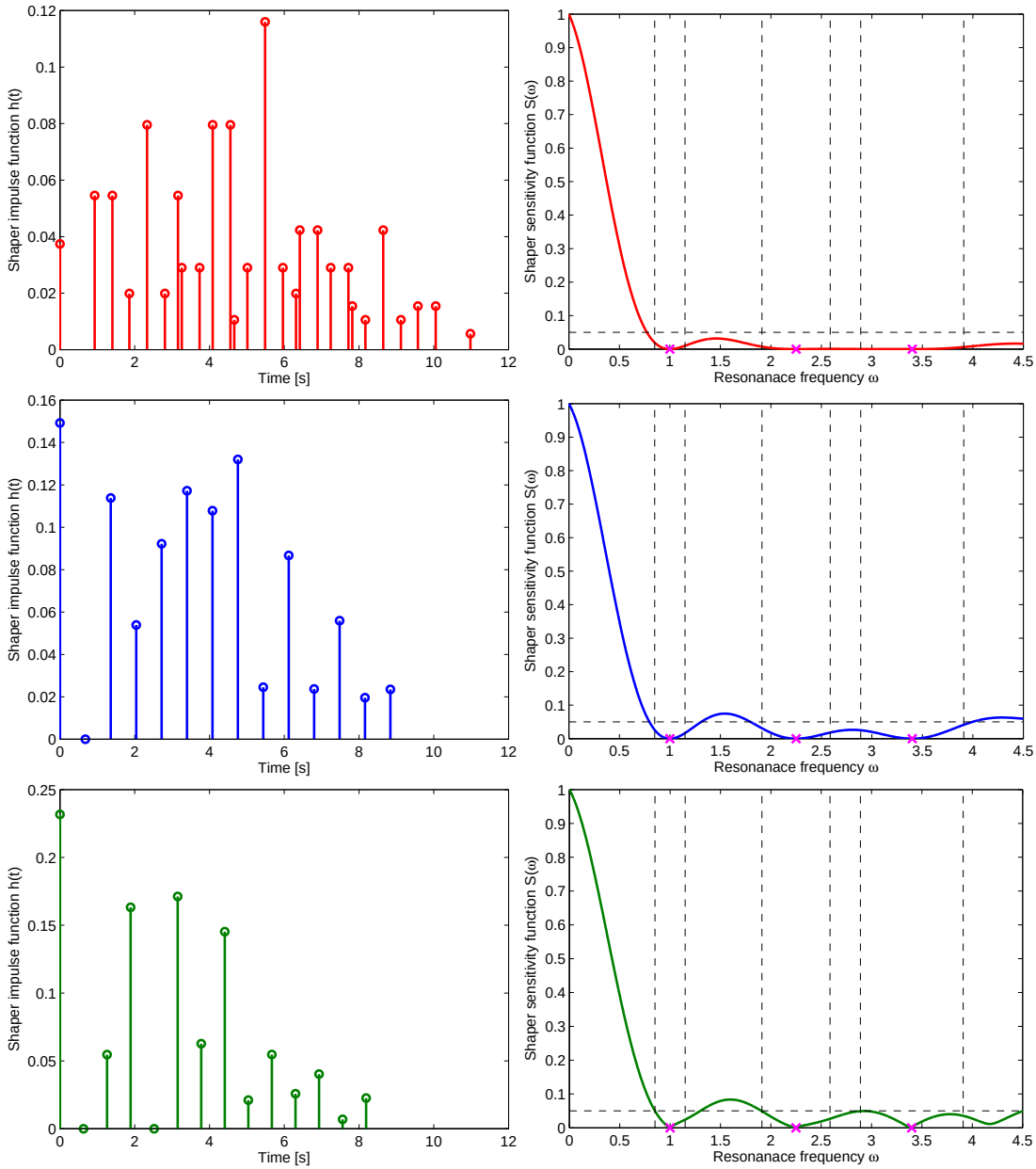

Figure 6.13: Multi-mode shaper design - convolution vs direct optimal design, impulse and sensitivity functions, a) 3xZVD shaper b) optimal design Nr.1 c) optimal design Nr.2, the dashed line represents the desired robustness limits within the $\pm 15\%$ interval around the resonance frequencies

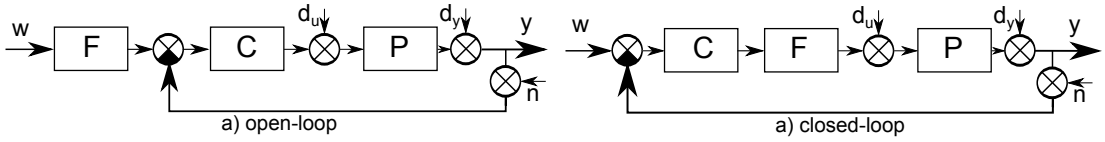

Figure 6.14: Input shaper implementation - open-loop vs closed-loop configuration

6.4 Open-loop vs closed-loop signal shaping

As was mentioned earlier in the thesis, the shaping filter may be used either in an open or closed-loop configuration. Each one offers specific advantages and drawbacks.

The *open-loop* connection (Fig. 6.14a) uses the filter for the shaping of reference commands for the inner feedback motion control loop. The vibration damping properties may be analysed by derivation of important closed-loop transfer functions. The shaping filter, feedback compensator, and controlled plant dynamics can be expressed in the form of transfer functions

$$F(s) = \frac{n_f(s)}{d_f(s)},\ C(s) = \frac{n_c(s)}{d_c(s)},\ P(s) = \frac{b(s)}{a(s)}, \tag{6.80}$$

where $a(s)$ contains the weakly damped poles of the controller system. From (6.80), we obtain the following dynamics of the complementary sensitivity function from the setpoint variable w to the controlled output y as:

$$T_{ol}(s) = \frac{y(s)}{w(s)} = \frac{FCP}{1+CP} = \frac{n_f n_c b}{d_c a + n_c b}. \tag{6.81}$$

The shaper zeros n_f compensate the resonances of the whole closed-loop system given by the weakly damped poles of the polynomial $d_c a + n_c b$. The advantage of this configuration is full exploitation of the FIR structure of the shaping filter. The shaping of the reference trajectories is performed with a finite time delay which is given by the overall filter length. Moreover, the filter does not affect the inner feedback loop in terms of stability and disturbance rejection. The drawback is that the filter causes some tracking error due to the introduced delay in the reference signal. **The shaper cannot provide any damping of vibrations due to the exogenous signals except for the reference variable** (measurement noise, plant input and output disturbances). This can be seen from the corresponding sensitivity, plant sensitivity and noise sensitivity closed-loop transfer functions:

$$S_{ol}(s) = \frac{y(s)}{d_y(s)} = \frac{1}{1+CP} = \frac{d_c a}{d_c a + n_c b}, \tag{6.82}$$

$$PS_{ol}(s) = \frac{y(s)}{d_u(s)} = \frac{P}{1+CP} = \frac{d_c b}{d_c a + n_c b}, \tag{6.83}$$

$$NS_{ol}(s) = \frac{y(s)}{n(s)} = -\frac{CP}{1+CP} = -\frac{n_c b}{d_c a + n_c b}. \tag{6.84}$$

A proper design of the feedback compensator is needed to cope with the damping of the inner loop. There is a risk of residual vibration excitation due to the saturation of the actuator which may lead to distortion of the power spectrum of the plant input. Proper selection of the reference trajectories is needed to make sure that the inner control loop operates in the linear mode to preserve the damping functionality.

The *closed-loop* connection (Fig. 6.14b) utilizes the filter for the shaping of the manipulating variable in the inner feedback loop. The complementary sensitivity function is given as:

$$T_{cl}(s) = \frac{y(s)}{w(s)} = \frac{FCP}{1+FCP} = \frac{n_f n_c b}{d_c d_f a + n_c n_f b}. \tag{6.85}$$

The filter is tuned to the resonances of the physical plant, in this case, and there is a direct cancelation of the weakly damped poles in $a(s)$ and filter zeros $n_f(s)$. The advantage is that the above mentioned actuator saturation problem can easily be solved by introduction of the nonlinearity (saturation, rate-limit etc.), which exists in the physical plant, into the closed loop in front of the shaping filter. Therefore, the resulting spectrum of the filtered manipulating variable is not distorted and does not contain the resonance frequencies which could excite the oscillatory modes of the controlled plant. Lower delay of the Zero vibration filters compared to commonly used notch filters may result in a better control performance. Further properties of the closed-loop configuration can be derived by examining the transfer functions:

$$S_{cl}(s) = \frac{y(s)}{d_y(s)} = \frac{1}{1+FCP} = \frac{d_c d_f a}{d_c d_f a + n_c n_f b}, \tag{6.86}$$

$$PS_{cl}(s) = \frac{y(s)}{d_u(s)} = \frac{P}{1+FCP} = \frac{d_c d_f b}{d_c d_f a + n_c n_f b}, \tag{6.87}$$

$$NS_{cl}(s) = \frac{y(s)}{n(s)} = -\frac{FCP}{1+FCP} = -\frac{n_c n_f b}{d_c d_f a + n_c n_f b}. \tag{6.88}$$

The shaping filter prevents the excitation of the vibrations due to the measurement noise and output disturbance due to the cancelation between weakly damped poles in $a(s)$ and filter zeros in $n_f(s)$. The input disturbance cannot be compensated due to the loss of controllability of the corresponding oscillatory modes. Therefore, the closed-loop connection does not allow any combination with an active vibration damping controller as the filter blocks the transmission of the manipulating variable signal at the resonance frequencies. The infinite order of the shaping filter due to the time delays in its structure complicates the design of the feedback compensator by means of standard methods such as pole placement. The delay introduced by the filter may affect the maximum achievable bandwidth of the closed loop.

A particular problem of the shaping filter design is the motion control of a system with separable rigid feedback loop and additional oscillatory dynamics which is affected by the output of the rigid part (6.15). An example is an overhead crane with a hanging load. Low load to trolley mass ratio or a high amount of friction may prevent

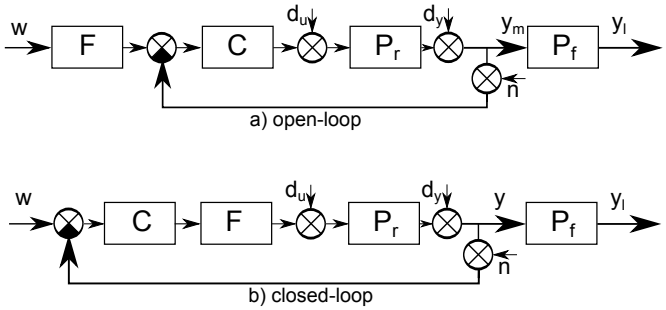

Figure 6.15: Input shaper implementation - system with separable rigid and flexible dynamics, open-loop vs closed-loop configuration

the transfer of the motion induced oscillations to the motor side. The inner feedback loop behaves as a rigid mechanical system while an oscillatory behaviour is observed in the attached load. Another example is a ball screw feed of a CNC machine with significant self-locking which prevents the transmission of the load-side oscillations to the actuating drive. Considering the transfer functions of the shaping filter, feedback compensator, rigid and flexible dynamics transfer functions in the form of

$$F(s) = \frac{n_f(s)}{d_f(s)},\ C(s) = \frac{n_c(s)}{d_c(s)},\ P_r(s) = \frac{b_r(s)}{a_r(s)},\ P_f(s) = \frac{b_f(s)}{a_f(s)}, \tag{6.89}$$

where $P_r(s)$ denotes the rigid actuator-side dynamics and $P_f(s)$ is a flexible load-side dynamics which contains some weakly damped poles in the denominator $a_f(s)$. From (6.89), we obtain the following dynamics of the complementary sensitivity functions from the setpoint variable to the load output

$$T_{ol}(s) = \frac{y_l(s)}{w_l(s)} = \frac{FCP_rP_f}{1+CP_r} = \left(\frac{n_cb_r}{d_ca_r+n_cb_r}\right)\left(\frac{n_fb_f}{d_fa_f}\right), \tag{6.90}$$

$$T_{cl}(s) = \frac{y_l(s)}{w_l(s)} = \frac{FCP_rP_f}{1+FCP_r} = \left(\frac{n_fn_cb_r}{d_fd_ca_r+n_fn_cb_r}\right)\left(\frac{n_fb_f}{d_fa_f}\right). \tag{6.91}$$

It can be seen that the shaping filter has to be tuned for the resonances of the flexible part dynamics for both open-loop and closed-loop configurations. In other words, zeros of the shaper $n_f(s)$ have to cancel the oscillatory poles in $a_f(s)$. Sensitivity and plant sensitivity functions can further be derived to evaluate the effect of external dis-

turbances acting on the actuator side:

$$S_{ol}(s) = \frac{y_l(s)}{d_y(s)} = \frac{P_f}{1 + CP_r} = \left(\frac{d_c a_r}{d_c a_r + n_c b_r}\right)\left(\frac{b_f}{a_f}\right), \tag{6.92}$$

$$S_{cl}(s) = \frac{y_l(s)}{d_y(s)} = \frac{P_f}{1 + FCP_r} = \left(\frac{d_c d_f a_r}{d_c d_f a_r + n_c n_f b_r}\right)\left(\frac{b_f}{a_f}\right), \tag{6.93}$$

$$PS_{ol}(s) = \frac{y_l(s)}{d_u(s)} = \frac{P_r P_f}{1 + CP_r} = \left(\frac{d_c b_r}{d_c a_r + n_c b_r}\right)\left(\frac{b_f}{a_f}\right), \tag{6.94}$$

$$PS_{cl}(s) = \frac{y_l(s)}{d_u(s)} = \frac{P_r P_f}{1 + FCP_r} = \left(\frac{d_c d_f b_r}{d_c d_f a_r + n_c n_f b_r}\right)\left(\frac{b_f}{a_f}\right). \tag{6.95}$$

It can be seen that the **vibrations excited by an input or output disturbance cannot be effectively damped unless the poles in d_c or d_f contain the model of the resonance in a_f.** The noise filtering properties are revealed from the transfer functions:

$$N_{ol}(s) = \frac{y_l(s)}{n(s)} = -\frac{CP_r P_f}{1 + CP_r} = -\left(\frac{n_c b_r}{d_c a_r + n_c b_r}\right)\left(\frac{b_f}{a_f}\right), \tag{6.96}$$

$$N_{cl}(s) = \frac{y_l(s)}{n(s)} = -\frac{FCP_r P_f}{1 + FCP_r} = -\left(\frac{n_c n_f b_r}{d_c d_f a_r + n_c n_f b_r}\right)\left(\frac{b_f}{a_f}\right). \tag{6.97}$$

It is seen that the closed-loop connection can attenuate the load vibrations due to the measurement noise whereas the open-loop configuration provides no damping.

A common approach to the problem of disturbance attenuation is the introduction of a peak filter F which contains the weakly damped poles of the resonance [142]. For a stable closed loop with a feedback compensator designed for the plant FP_r, a vibration damping functionality may be achieved even in the presence of external disturbances. The possibility of utilizing the *inverse Zero-vibration shapers* which perform the function of the peak filter is discussed in papers [209, 210]. To be accurate, the peak filter technique should be considered as an active vibration control scheme since the controller delivers some energy in the frequency range corresponding to the plant resonances.

As a rule of thumb, it may be stated that the open-loop shaper connection is preferable for cases in which a feedback compensator can provide at least some amount of active disturbance rejection. Closed loop configuration is suitable for motion control loops with significant influence of measurement noise and actuator nonlinearities.

6.5 Summary

This section presented a systematic approach to the passive vibration control with the use of Zero vibration filters. A new method for the parameterization of a general four-pulse shaper is proposed. It offers two design parameters with clear physical meaning which can be used for the fine tuning of the shape of the filter frequency response, in order to find a suitable trade-off between the robustness to the modelling errors and

the delay the filter introduces in the signal path. The important result is that all the standard filters which are commonly referenced in the related literature can be obtained as a special case of the derived parameterization. Methods of discretization of the shaper algorithm and the problem of quantization due to a finite sampling period are discussed. An algorithm for the exact transformation of the filter to the discrete-time domain is derived using the geometric approach to the filter design. The problem of optimal design of a multi-mode shaper is solved in the framework of linear programming. The design specifications are given as constraints for the shape of the sensitivity function to impose a specified level of robustness to the modelling errors. Numerical examples show that the optimal filter can outperform a conventional solution which is obtained from the direct convolution of several single-mode shapers. Advantages and disadvantages of various methods for shaper integration in a motion control loop are discussed. The proposed shaping filter is implemented in the form of a functional block in the C language.

7

Active vibration control

This section deals with active vibration control of oscillatory electromechanical systems. Unlike the passive approach which tries to minimize the amount of energy the controlled system receives in the vicinity of the resonance frequencies, the active vibration damping methods use available feedback information to improve overall stiffness of the system even in the presence of external disturbances. This concept brings some inherent advantages:

- **Increase of the mechanical stiffness of the controlled plant**
  From the outer point of view, a properly designed feedback controller may significantly improve the damping of the controlled mechanical system. This allows for higher closed-loop bandwidth of the motion control loops to be achieved. Lightweight construction with lower energy consumption and higher power-mass ratio may be used. Substantial mistakes in the mechanical design may be corrected in terms of the feedback controller.

- **Active compensation of disturbances**
  Motion control systems typically operate under the action of some exogenous disturbances coming from the surrounding environment (gravity, friction effects, cutting forces, reaction forces in contact motions etc.). The external forces/torques which act on the system can excite its oscillatory dynamics and properly designed feedback controller may be necessary for the active compensation.

- **Robustness to modelling errors**
  Passive methods require relatively precise knowledge about the oscillatory dynamics of the system. Modelling errors may lead to significant deterioration in the quality of control. A properly designed active compensator may provide a higher level of robustness due to the feedback information from the sensors.

On the other hand, there are several drawbacks to active vibration control which should be taken into consideration:

- **Difficult compensator design and tuning**
  Simple heuristic rules for compensator tuning or use of overly simplified mathe-

matical models of the controlled system for the compensator design usually fail in the presence of oscillatory dynamics. Advanced model-based techniques may be required for the computation of the compensator parameters.

- **Necessity of complex mathematical model**
  Unlike the passive damping approach which usually requires only information about the location of the plant resonance frequencies, the active methods rely on the knowledge of the full plant model. Analytical modelling is usually infeasible and a proper identification method has to be employed in order to provide a mathematical model which captures the system behaviour with sufficient level of precision, at least in the frequency range of interest.

- **Risk of loop instability**
  The introduction of feedback brings the inherent risk of instability of the closed loop. Stringent performance requirements are in direct conflict with loop stability as the high-gain controllers tend to be more sensitive to the effects of the unmodeled dynamics.

Motivation example

An example of a simple design problem is presented to reveal some of the difficulties with the control of oscillatory systems. The goal is to control the velocity of a single degree of freedom mechanical system with a significantly elastic coupling between the actuator and driven payload. Considering only the first resonance mode which is dominant in the relevant frequency range, its dynamics may be described by a *two-mass model* with the transfer function from motor torque to motor and load velocity given as:

$$P_m(s) = \frac{\omega_m(s)}{T_m(s)} = \frac{I_l s^2 + bs + k}{s[I_m I_l s^2 + b(I_m + I_l)s + k(I_m + I_l)]}, \tag{7.1}$$

$$P_l(s) = \frac{\omega_l(s)}{T_m(s)} = \frac{bs + k}{s[I_m I_l s^2 + b(I_m + I_l)s + k(I_m + I_l)]}. \tag{7.2}$$

For the plant parameters chosen as $I_m = 1,\ I_l = 8,\ b = 0.2,\ k = 8$, we obtain weakly damped oscillatory dynamics described by transfer functions:

$$P_m(s) = \frac{K_1}{s}\frac{s^2 + 2\xi_z\omega_z s + \omega_z^2}{s^2 + 2\xi\omega_n s + \omega_n^2}, \tag{7.3}$$

$$P_l(s) = \frac{K_2}{s}\frac{s + \frac{\omega_z}{2\xi_z}}{s^2 + 2\xi\omega_n s + \omega_n^2}, \tag{7.4}$$

with the resonance and antiresonance frequencies and damping given as

$$\omega_z = 1\ rad/s,\ \xi_z = 0.0125,\ \omega_n = 3\ rad/s,\ \xi = 0.0375. \tag{7.5}$$

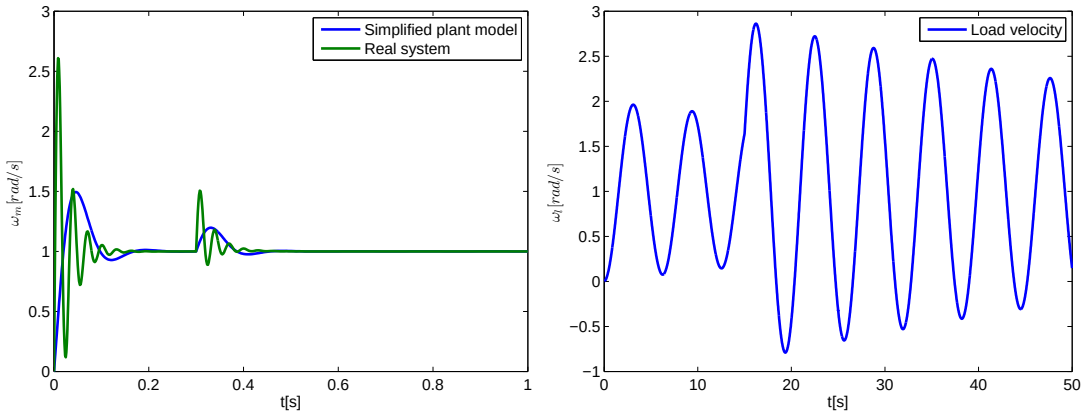

Figure 7.1: Motivation example - Symmetrical Optimum method with an oscillatory two-mass system, left - motor velocity response, right - load velocity response

The velocity PI controller has to be designed and only the motor side feedback is available for the measurement. The controller transfer function is given as:

$$C(s) = K_p + \frac{K_i}{s}. \tag{7.6}$$

There is a low-pass filter which reduces the amount of high-frequency measurement noise in the motor velocity signal. The filter transfer function is assumed as a first order lag

$$F(s) = \frac{1}{\tau_f s + 1}, \tag{7.7}$$

where $\tau_f = 0.01$ is the filter time constant.

The first attempt is to ignore the oscillatory dynamics and design the velocity controller using the standard *Symmetrical Optimum* method. The simplified plant model is obtained from (7.1) and (7.7) by assuming only the rigid mode of the system:

$$P(s) \approx \frac{1}{(I_m + I_l)s} \frac{1}{(\tau_f s + 1)}. \tag{7.8}$$

Using the formulas derived in the previous chapter (3.24) the controller gains are obtained as:

$$K_p = \frac{I_m + I_l}{2\tau_f}, \; K_i = \frac{(I_m + I_l)}{8\tau_f^2}. \tag{7.9}$$

The left plot in Fig. (7.1) shows the motor side velocity response to the setpoint step change at $t = 0s$ and motor load torque step change at $t = 0.3s$. Comparison of data acquired with the simplified rigid plant model (blue line) and the real oscillatory system model (green line) demonstrates that the simplifying assumption of rigid connection of motor and load inertias can lead to poor performance of the closed loop. Although

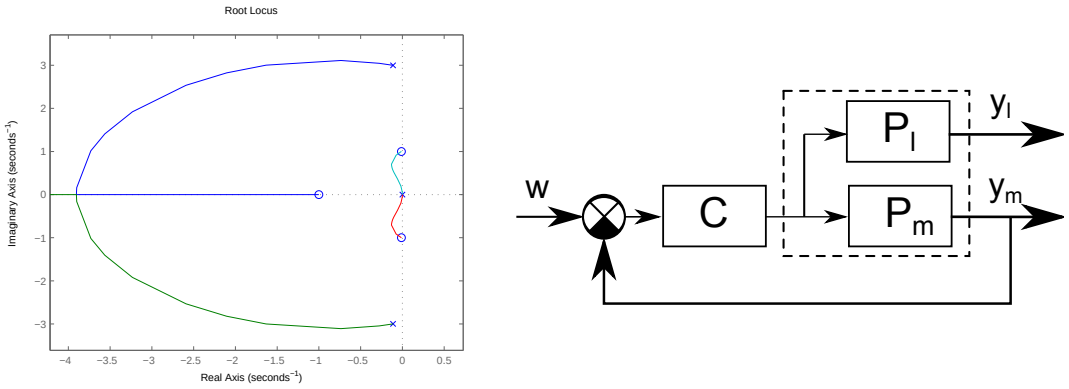

Figure 7.2: Oscillatory system control - left - root locus plot of the actuator loop, right - SITO system problem formulation

there is a significant amount of oscillations in the motor response, the controller is able to stabilize the actuator in a short settling time which is comparable to the ideal response obtained with the simplified model. However, much more serious problem is observed at the load side (Fig. 7.1 right). **The high gain controller which stabilizes the motor loop counteracts the reaction torque coming from the elastic coupling in order to keep low tracking error in the motor velocity**. This leads to weakly damped oscillations of the load due to the setpoint change or in the presence of an external disturbance at $t = 15s$.

This phenomenon can be explained by observing the root locus plot of the oscillatory system with a PI controller (Fig. 7.2 left). It can be seen that for high open-loop gains, two closed-loop poles approach the couple of weakly damped zeros of the system (7.3). Since these closed-loop poles cancel with the open-loop plant zeros which appear in the numerator of the complementary sensitivity function, the motor loop may behave well when only observing the motor side measurement. However, the true objective of the controller design is *to stabilize the load* even in the case that the load output cannot be measured directly. The system structure can be rearranged in the form of a Single Input Two Outputs system (7.2 right) with the plant dynamics appearing in the open-loop connection to the manipulating variable of the controller. Since load transfer function (7.4) does not contain the weakly damped zeros, they do not cancel with the closed loop poles of the motor loop. This leads to **inevitable weakly damped oscillations of the load at the frequency of the system antiresonance**. This result is valid for any high gain controller which is designed for the rigid motor loop only without considering the oscillatory load dynamics (e.g. the popular disturbance observer method and its modifications). The only way of correctly designing the motor feedback compensator, which would actively attenuate the vibrations of both motor and load, is to *assign sufficient damping to all of the closed-loop poles*.

The Symmetrical Optimum method does not offer any free parameters for the con-

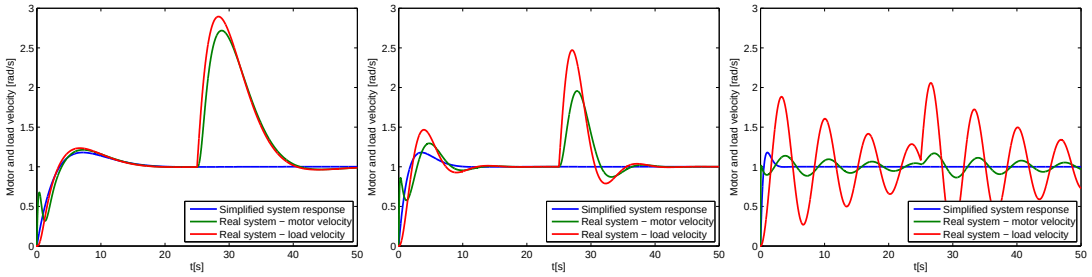

Figure 7.3: Oscillatory system control - pole-placement controller performance for three various settings of the desired closed-loop bandwidth $\omega^* = 0.3, 0.6, 2\ rad/s$

troller tuning which could possibly improve the poor results achieved with the oscillatory system by reducing the controller gains. The **pole placement method** is employed in a second attempt in order to observe the influence of the chosen closed-loop bandwidth on the controller performance. Again, assuming only the rigid dynamics of the system, the plant dynamics may be approximated by transfer function

$$P(s) \approx \frac{1}{(I_m + I_l)s}. \tag{7.10}$$

The given PI controller can be used to freely assign the location of a couple of closed loop poles. According to the equation (3.30), the controller gains are computed as

$$K_p = 2\xi^*\omega^*(I_m + I_l), K_i = (I_m + I_l)(\omega^*)^2, \tag{7.11}$$

where ξ^*, ω^* denote the desired bandwidth and damping of the closed loop. The achieved results are shown for three different settings of desired bandwidth $\omega^* = \{0.3, 0.6, 2\}\ rad/s$ with the damping chosen as $\xi^* = 0.8$. It can be seen that fairly satisfactory results are obtained for the lowest bandwidth. There are no unwanted oscillations and the controller is able to actively damp the external step disturbance which is applied to the load at time $t = 15s$. The load response is close to the response of the simplified rigid model of the system which was used for the compensator design. An increase in the desired bandwidth leads to gradual deterioration of the system performance. For $\omega^* = 2\ rad/s$, there is a significant amount of vibrations both on motor and load side. A further increase in the desired bandwidth lead to similar results which were obtained with the SO method design. **Obviously, there is some limitation on the closed-loop bandwidth which may be achieved with a simple low-order compensator**.

The third attempt uses a **full-order controller** which allows complete assignment of the closed-loop dynamics. Third order compensator with the integrator part to enforce zero steady state error in the case of step reference commands and external disturbances is designed for the system (7.3). Six equal closed-loop poles are assigned in the location $-\omega^*$ for three different bandwidth settings $\omega^* = \{0.6, 2, 4\}\ rad/s$. The simulation results showing the setpoint and load disturbance responses are plotted

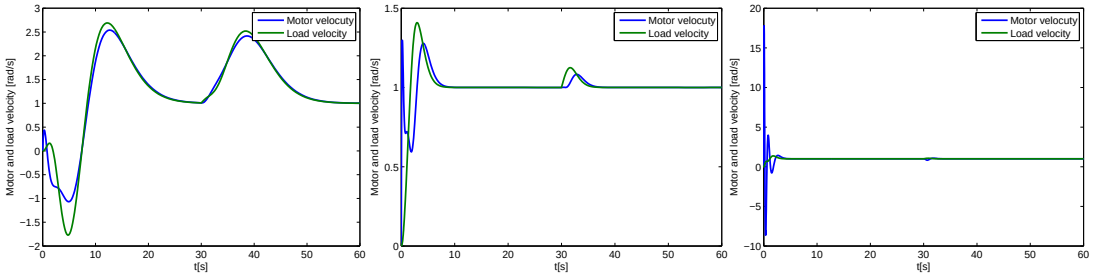

Figure 7.4: Oscillatory system control - full-order compensator performance for three various settings of the desired closed-loop bandwidth $\omega^* = \{0.6, 2, 4\}\ rad/s$

in Fig. (7.4). The first design shows unacceptable undershoot in both motor and load responses. This is caused by nonminimum phase zeros which are obtained in the compensator dynamics. Two DoF structure would have to be used to compensate the unwanted transmission zeros. The second result for the setting $\omega^* = 2$ shows a well behaved response both to setpoint and load disturbance. An increase in the desired bandwidth to $\omega^* = 4$ leads to an excessive response in the motor velocity. Closer inspection of the obtained compensator reveals an unstable pole which would complicate the implementation of the control law. Moreover, **the resulting design is very sensitive to modelling errors**. A small deviation in the plant parameters in the order of a few percent leads to instability of the closed-loop.

The main problems encountered in active vibration control of oscillatory systems can be summarized from the acquired observations:

- Truncation of the oscillatory dynamics in the process of compensator design may lead to severe degradation of closed-loop performance.
- Conventional methods developed for rigid systems fail in the presence of an elastically coupled load.
- Stabilization of the oscillatory mechanics using only a motor side feedback poses a difficult control problem. A high gain controller acting in the motor loop may cause weakly damped oscillations of the load.
- There are fundamental limitations on achievable bandwidth and damping when a low order compensator is used.
- Naive design of a full-order controller can lead to unpredictable results. A systematic approach is needed to cope with the difficult task of load stabilization to obtain a suitable solution.

7.1 PID control of single resonance system

The vast majority of industrial motion controllers use the standard cascade PID control scheme which was described in the introductory chapter (Fig. 3.3). The inner current loop controls the electromagnetic torque generated by the motor. Its time constant is usually negligible compared to the dynamics of the mechanical subsystem. **The velocity control loop is crucial for the purpose of vibration control and its proper tuning respecting the compliance in the attached load is necessary**. The outer position loop ensures proper positioning of the load when needed. Setpoint values are obtained from a higher level of trajectory generator. The advantage of the PID cascade scheme is a low number of parameters, the possibility of successive tuning of individual loops and a simple introduction of the physical limitations on maximum torque, velocity and position.

7.1.1 Fundamental limitations on achievable performance

The PID control structure performs well in the case of rigid mechanics when properly tuned. However, the occurrence of an elastically coupled load may bring severe difficulties with the implementation of this control scheme. Fundamental limitations on achievable quality of control have to be examined in order to determine a class of systems for which this control scheme may be applied.

The starting point is a two-mass system given by the transfer function:

$$P_m(s) = \frac{\omega_m(s)}{T_m(s)} = \frac{1}{s}\frac{(s^2+1)}{(s^2+r^2)}, \tag{7.12}$$

where r is the resonance ratio between the resonance and antiresonance frequencies. Without loss of generality, the system is normalized both in time and gain by setting the unitary gain of the integral term and unitary value of the antiresonance frequency $\omega_z = 1\ rad/s$. Zero modal damping is assumed to evaluate the worst-case scenario of an undamped system and to reduce the number of system parameters which leads to the simplification of the performed analysis. The physical parameters of the normalized two-inertia system with elastic coupling are obtained from (7.12) as:

$$I_m = 1\ [kg.m^2],\ I_l = (r^2-1)\ [kg.m^2],\ k = (r^2-1),\ b = 0,\ R = \frac{I_l}{I_m} = r^2 - 1. \tag{7.13}$$

We assume the 2DoF PI velocity control law with the motor-side feedback which can be described in the $\mathcal{L}$-domain as

$$T_m(s) = K_p\left\{w_p\omega_m^*(s) - \omega_m(s)\right\} + \frac{K_i}{s}\left\{\omega_m^*(s) - \omega_m(s)\right\}, \tag{7.14}$$

where ω_m^* is the setpoint value for the motor velocity and $w_p \in \langle 0, 1\rangle$ is the setpoint weighting factor of the proportional part.

Closed-loop complementary sensitivity functions from the velocity reference to motor and load speed are obtained in the form of:

$$P_m^{cl}(s) = \frac{\omega_m(s)}{\omega_m^*(s)} = \frac{(w_p K_p s + K_i)(s^2+1)}{s^4 + K_p s^3 + (K_i + r^2)s^2 + K_p s + K_i}, \tag{7.15}$$

$$P_l^{cl}(s) = \frac{\omega_l(s)}{\omega_m^*(s)} = \frac{(w_p K_p s + K_i)}{s^4 + K_p s^3 + (K_i + r^2)s^2 + K_p s + K_i}. \tag{7.16}$$

Plant sensitivity functions from the load torque T_l to load and motor speed which expresses the ability of the closed-loop to attenuate external disturbances are obtained as:

$$PS_m^{cl}(s) = \frac{\omega_m(s)}{T_l(s)} = \frac{s}{s^4 + K_p s^3 + (K_i + r^2)s^2 + K_p s + K_i}, \tag{7.17}$$

$$PS_l^{cl}(s) = \frac{\omega_l(s)}{T_l(s)} = \frac{\frac{(s^2 + K_p s + K_i + r^2 - 1)s}{(r^2-1)}}{s^4 + K_p s^3 + (K_i + r^2)s^2 + K_p s + K_i}. \tag{7.18}$$

Since there are only two free parameters of the compensator which affect the poles (the proportional and integral gain), **the closed-loop dynamics cannot be freely assigned**. The location of two poles can be selected arbitrarily whereas the *position of the second remaining pole-pair is determined indirectly* by the system resonance ratio and first pair placement.

The characteristic polynomial $a_{cl}^*(s)$ of the closed-loop (7.15,7.16) can be parameterized by two second order terms:

$$\begin{aligned} a_{cl}^*(s) &= (s^2 + 2\xi^*\omega^* s + {\omega^*}^2)(s^2 + 2\xi_2\omega_2 s + {\omega_2}^2) \\ &= s^4 + (2\xi^*\omega^* + 2\xi_2\omega_2)s^3 + ({\omega^*}^2 + 4\xi^*\omega^*\omega_2\xi_2 + \omega_2^2)s^2 \\ &+ (2{\omega^*}^2\xi_2\omega_2 + 2\xi^*\omega^*\omega_2^2)s + (\omega^*\omega_2)^2, \end{aligned} \tag{7.19}$$

where w^*, ξ^* denote desired damping and natural frequency of two directly assigned poles and $\xi_2,\ \omega_2$ determine the damping and natural frequency of the second indirectly controlled pole pair.

Comparison of (7.19) with the denominator of (7.15,7.16) reveals some constraints which exist between the individual closed-loop poles. By comparing the individual powers of the polynomials and substituting for the controller gains we get:

$$K_p = 2(\xi^*\omega^* + \xi_2\omega_2), \tag{7.20}$$

$$K_i = (\omega^*\omega_2)^2, \tag{7.21}$$

$${\omega^*}^2\omega_2^2 + r^2 = {\omega^*}^2 + 4\xi^*\omega^*\xi_2\omega_2 + \omega_2^2, \tag{7.22}$$

$$\xi^*\omega^* + \xi_2\omega_2 = {\omega^*}^2\xi_2\omega_2 + \xi^*\omega^*\omega_2^2. \tag{7.23}$$

The last equation can be rearranged as:

$$\xi^*\omega^*(1 - \omega_2^2) = \xi_2\omega_2({\omega^*}^2 - 1), \tag{7.24}$$

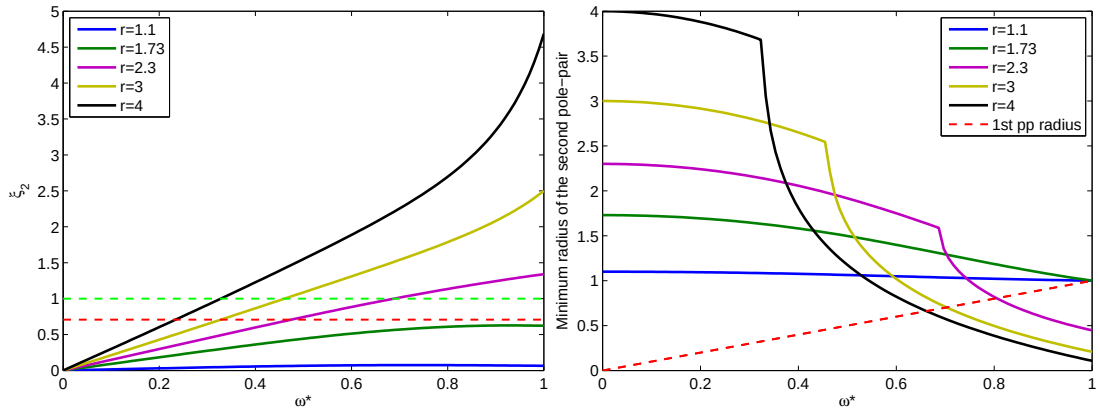

Figure 7.5: Damping and minimal radius of the second pole-pair as a function of the desired bandwidth ω^*

which reveals that ω^* and ω_2 cannot be greater than one at the same time. **There is a fundamental restriction on the closed-loop bandwidth achievable with the PI controller** which is given by the value of the system antiresonance frequency (for the general non-normalized case). Moreover, it is seen that the location of the second pair of the closed-loop poles depends on the parameter of the system resonance ratio. Closer inspection of its influence reveals that there are further performance limitations due to the dynamics of the controlled system.

A solution of the set of two polynomial equations (7.22,7.22) for the unknowns ω_2, ξ_2 may be derived to express the second pole pair location as a function of chosen poles and plant resonance ratio. A positive real solution valid for the range of interest $\omega^* \in \langle 0, 1 \rangle$ is obtained in the form of:

$$\omega_2 = \sqrt{-\frac{\omega^{*2} - \omega^{*4} - 4\,\xi^{*2}\omega^{*2} - r^2 + r^2\omega^{*2}}{4\,\xi^{*2}\omega^{*2} + 1 - 2\,\omega^{*2} + \omega^{*4}}}, \tag{7.25}$$

$$\xi_2 = \frac{\left(r^2 - 1\right)\xi^*\,\omega^*}{\sqrt{-\frac{-\omega^{*4}+\omega^{*2}r^2-4\,\omega^{*2}\xi^{*2}+\omega^{*2}-r^2}{\omega^{*4}+4\,\omega^{*2}\xi^{*2}-2\,\omega^{*2}+1}}}\left(\omega^{*4} + 4\,\omega^{*2}\xi^{*2} - 2\,\omega^{*2} + 1\right). \tag{7.26}$$

The function (7.26) of the achievable damping of the second pole-pair is plotted for different values of the resonance ratio in Fig. (7.5) left as a function of location of the first assigned pole pair. The damping of the assigned poles is fixed to $\xi^* = 0.8$ and the natural frequency is varied in the admissible range $\omega^* \in \langle 0, 1 \rangle$. It can be seen that the sufficient amount of damping (represented by the red dashed line which marks the $\sqrt{2}/2$ level) cannot be provided for low resonance ratio systems which arise for low load to motor inertia ratio R. On the contrary, damping of the high resonance ratio systems tend to increase rapidly up to the level $\xi_2 > 1$ (green dashed line in Fig. (7.5) left). This indicates that the real axis of the complex plane has been reached leading to a couple of real poles. These real poles travel towards the right half plane when

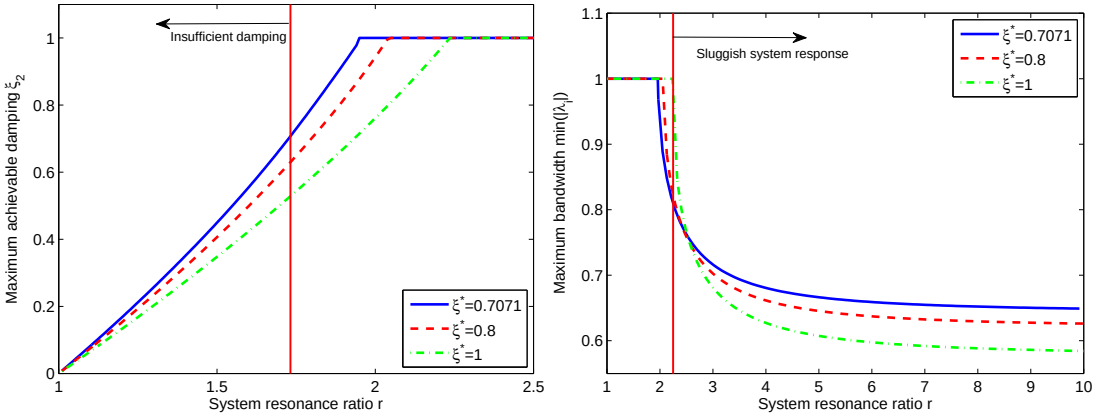

Figure 7.6: Maximum achievable damping and minimum radius of the second pole-pair as a function of the system resonance ratio r

further increasing the radius ω^* and they limit the maximum achievable bandwidth. This behaviour is documented in the right plot in Fig. (7.5) which shows the minimum radius (absolute value) of the second pole-pair. For low values of r, the second pair of poles remains complex and the minimum radius corresponds to the natural frequency ω_2 (eq. 7.25), which is always $\omega_2 \geq 1$ due to the constraint (7.24). When the second pole-pair hits the real axis (the crossing of the left damping plot with the green line), the minimum radius is obtained as the value of the pole with the smallest real part which can be computed as

$$r_{min} = min(|\{\lambda_3, \lambda_4\}|) = \omega_2\big(\xi_2 - \sqrt{(\xi_2^2 - 1)}\big), \tag{7.27}$$

where λ_3, λ_4 denote the couple of indirectly controlled poles.

The radius of the first assigned pole-pair is directly given by the chosen ω^* and is plotted as a red dashed line in the right plot of Fig. (7.5). The intersection of this line with the plot of the minimum radius r_{min} (eq. 7.27) denotes the maximum achievable closed-loop bandwidth ω^*_{max}. It is seen that the poles of high resonance ratio systems approach the real axis more rapidly and thus the maximum bandwidth is significantly limited. Very similar results are obtained for other values of the first pole pair damping ξ^*.

The next couple of plots are introduced to show the dependence of the maximum achievable damping and overall bandwidth as a function of the system resonance ratio (Fig. 7.6). The left plot shows the maximum damping of the second pole-pair ξ_2 which may be achieved in the whole admissible range of ω^*. This can be derived by analyzing the function (7.26) and its derivatives. Full symbolic derivation is omitted as it involves examination of roots of fourth order polynomials which are very lengthy. Three plots are shown for various values of desired damping of the first pole couple ξ^*. It can be seen that low resonance ratio with $r \leq \sqrt{3}$ (red vertical line in the left plot) cannot be effectively controlled as the compensator cannot provide a sufficient

amount of damping. Analytical proof of this statement may be derived by analyzing the constraint equations (7.22,7.23). By assuming equal values of damping of both closed-loop pole-pairs $\xi^* = \xi_2$, the equation (7.23) simplifies to

$$\omega^*(\omega_2^2 - 1) = \omega_2(1 - \omega^{*2}), \tag{7.28}$$

with a single positive solution

$$\omega_2 = \frac{1}{\omega^*}. \tag{7.29}$$

Substitution of (7.29) to (7.22) yields

$$\omega^{*2} + \frac{1}{\omega^{*2}} + 4\xi_2^2 - 1 = r^2. \tag{7.30}$$

Substraction of one from both sides and completion of the square gives:

$$\frac{(\omega^{*2} - 1)^2}{\omega^{*2}} = r^2 - 1 - 4\xi_2^2. \tag{7.31}$$

Since the left side is greater or equal to zero for the admissible range of the first pole-pair radius, we may write

$$\frac{(\omega^{*2} - 1)^2}{\omega^{*2}} \geq 0 \; \forall \omega^* \in \langle 0, 1\rangle \Rightarrow (r^2 - 1 - 4\xi_2^2) \overset{!}{\geq} 0 \Rightarrow \xi_2 \overset{!}{\leq} \frac{\sqrt{r^2 - 1}}{2}. \tag{7.32}$$

The result (7.32) implies that **the resonance ratio of the system has to be** $r \geq \sqrt{3}$ **in order to achieve a reasonable minimum amount of damping** $\xi \geq \frac{\sqrt{2}}{2}$ for all the closed-loop poles.

The right plot in Fig. (7.6) shows the maximum achievable closed-loop bandwidth as a function of the system resonance ratio. The maximum bandwidth for a particular r is seen as the intersection of the minimum radius plot with the first pole pair radius line ω^* in Fig. (7.5). The achievable bandwidth ω^*_{max} is obtained as a positive real solution of the equation

$$r_{min} = \omega_2\big(\xi_2 - \sqrt{(\xi_2^2 - 1)}\big) = \omega^*. \tag{7.33}$$

It can be seen that **the maximum achievable bandwidth decays rapidly for the values** $r \geq \sqrt{5}$ due to the real pole which moves to the right towards the right half plane for increasing ω^*. The range of the resonance ratios for which the maximum pole radius may be obtained can be computed by setting $\omega^* = 1$. Substitution to equations (7.25,7.26) leads to

$$\omega_2 = 1, \; \xi_2 = \frac{r^2 - 1}{4\xi^*}. \tag{7.34}$$

The damping of the second pole-pair has to be less or equal to one to ensure that no real pole from the second couple enters the unitary circle in the complex plane. Therefore, we may write:

$$\xi_2 = \frac{r^2 - 1}{4\xi^*} \overset{!}{\leq} 1 \Rightarrow r \overset{!}{\leq} \sqrt{4\xi^* + 1}. \tag{7.35}$$

For the three choices $\xi^* = \{\sqrt{2}/2, 0.8, 1\}$ we get $r \leq \{1.96, 2.05, 2.24\}$. Rapid decay of the achievable bandwidth is observed for larger values of the resonance ratio. It is important to mention that the plots are shown for the normalized system with the unitary antiresonance frequency and the resulting bandwidth has the meaning of the *relative value with respect to the antiresonance frequency of the original system*. Inspection of the dependence of the frequency response on the physical plant parameters reveals that the antiresonance frequency declines with the increasing inertia of the mechanical load following the relation $\omega_z = \sqrt{\frac{k}{I_l}}$. Therefore, an increase of the load to drive inertia ratio leads to an even more significant decrease of the *absolute* value of the closed-loop bandwidth.

The behaviour of the system may also be observed in terms of the closed-loop root locus plot for the varying bandwidth ω^*. The PI controller gains can be computed from equations (7.20,7.21) as:

$$
\begin{aligned}
&K_p(\xi^*, \omega^*) = \frac{num_p(\xi^*, \omega^*)}{den_{p,i}(\xi^*, \omega^*)},\ K_i(\xi^*, \omega^*) = \frac{num_i(\xi^*, \omega^*)}{den_{p,i}(\xi^*, \omega^*)},\\
&num_p = 2\,\xi^* \omega^{*5} + \left(8\,\xi^{*3} - 4\,\xi^*\right)\omega^{*3} + 2\,\xi^* r^2 \omega^*,\\
&num_i = \omega^{*2}\{\omega^{*4} + \left(4\,\xi^{*2} - r^2 - 1\right)\omega^{*2} + r^2\},\\
&den_{p,i} = \omega^{*4} - \left(2 - 4\,\xi^{*2}\right)\omega^{*2} + 1.
\end{aligned}
\tag{7.36}
$$

The obtained rational functions for the compensator gains represent a **parametrization of a set of stabilizing PI controllers which assign a couple of poles determined by the desired natural frequency and damping** ω^*, ξ^*. Location of the obtained closed-loop poles is plotted in Fig. (7.7). The blue circles denote the position of the directly assigned first pole pair for a chosen $\xi^* = \sqrt{2}/2$ and varying $\omega^* \in \langle 0, 1\rangle$. They start from the two open-loop poles at the origin of the complex plane for $\omega^* = 0$ and follow the two lines with the slope of 45^o until they reach the points $-1 \pm i$ for $\omega^* = 1$. The crosses show the corresponding movement of the second indirectly controlled pole-pair. Three curves are plotted for various values of the resonance ratio parameter. It is seen that a sufficient amount of damping cannot be achieved for a low resonance ratio system (magenta trace for $r = 1.2$). A properly damped response can be obtained for a well controllable system with resonance ratio $r \approx 2$ (green curve). The second pole pair remains complex and approaches the unitary circle with the increasing bandwidth ω^*. For a high resonance ratio (red curve for $r = 4$ in the figure), the second couple of poles hits the real axis and the real poles move towards the right half-plane. At some point, they become the limiting factor for the achievable bandwidth as their minimum radius gets lower than the radius of the first assigned pole pair ω^*.

7.1.2 Stability analysis

Stability of the closed-loop has to be examined for the obtained set of controllers given by the parameterization (7.36) as the indirectly controlled poles can potentially enter

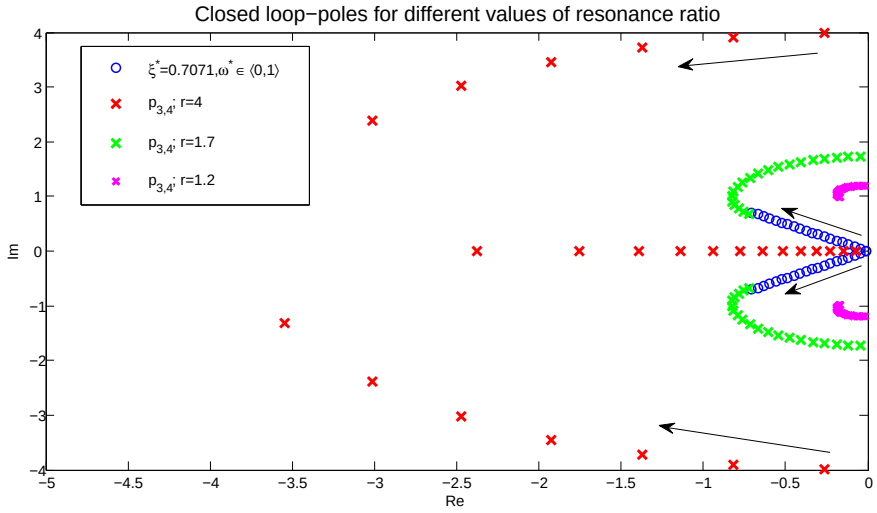

Figure 7.7: PI control of two-mass oscillatory system - location of the closed-loop poles as a function of ω^* with fixed ξ^*, blue circles - assigned pole pair for a chosen ω^*, ξ^*, crossed curves - indirectly controlled second pole pair

the right half plane. Hurwitz criterion may be used for the evaluation of the closed-loop characteristic polynomial in (7.15,7.16).
The Hurwitz matrix is obtained in the form of:

$$H = \begin{bmatrix} K_p & K_p & 0 & 0 \\ 1 & K_i + r^2 & K_i & 0 \\ 0 & K_p & K_p & 0 \\ 0 & 0 & 0 & K_i \end{bmatrix}. \tag{7.37}$$

All the coefficients are positive for $K_p, K_i > 0$ fulfilling the necessary condition of stability. The leading principal minors of H are:

$$\begin{aligned} |H_2| &= K_i\, K_p + K_p \left(r^2 - 1\right), \\ |H_3| &= K_p^2 \left(r^2 - 1\right). \end{aligned} \tag{7.38}$$

Since $r > 1$ for all physically feasible systems, they are positive for all $K_p, K_i > 0$. Therefore, **positiveness of the controller gains gives a sufficient condition of stability**. This condition also appears from the natural demand for stable and minimum-phase controller.

The common denominator $den_{p,i}(\omega^*)$ of the rational functions in (7.36) is positive for $\forall \omega^* \geq 0$ provided that the desired damping of the first pole pair is chosen as $\xi^* \geq \sqrt{2}/2$. This also gives a sufficient condition for the positiveness of the numerator of the proportional gain num_p in (7.36). Positiveness of the integral gain numerator num_i is determined by the sign of the polynomial

$$(\omega^{*4} + \left(4\,\xi^{*2} - r^2 - 1\right)\omega^{*2} + r^2), \tag{7.39}$$

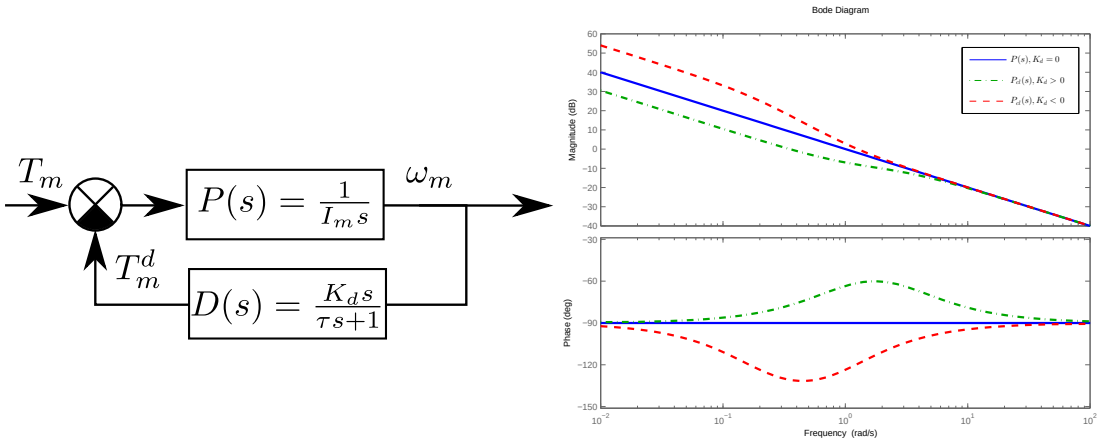

Figure 7.8: Introduction of derivative feedback, left - actuator velocity loop, right - shaping of the motor transfer function in the frequency domain

which can be rewritten in the form of

$$(1 - \omega^{*2})(r^2 - \omega^{*2}) + 4\omega^{*2}\xi^{*2}. \tag{7.40}$$

It is seen that the polynomial is positive for $r > 1$ and $\omega^* \in \langle 0, 1\rangle$. Therefore, **minimum-phase PI controllers with positive proportional and integral gains which stabilize the closed-loop system** are obtained $\forall \omega^* \in \langle 0, 1\rangle,\ \xi^* \geq \sqrt{2}/2$.
There are another important properties of the parametrization (7.36):

$$K_p(\forall \xi^*, \omega^* = 0) = 0, \tag{7.41}$$
$$K_i(\forall \xi^*, \omega^* = 0) = 0, \tag{7.42}$$
$$\frac{\partial K_p(\forall \xi^*, \omega^* = 0)}{\partial \omega^*} = 2\xi^* r^2, \tag{7.43}$$
$$\frac{\partial K_i(\forall \xi^*, \omega^* = 0)}{\partial \omega^*} = 0, \tag{7.44}$$
$$\frac{\partial^2 K_i(\forall \xi^*, \omega^* = 0)}{\partial \omega^{*2}} = 2r. \tag{7.45}$$

Zero controller gains are obtained for $\omega^* = 0$ and the loop is smoothly closing when ω^* is gradually increased up to the maximum bandwidth with positive gains in the whole admissible range up to $\omega^* = 1$.

7.1.3 Introduction of derivative action

When available, the derivative part of the PID controller may be used for improvement of the closed-loop performance. The effect of the derivative feedback may be explained by analyzing the dynamics of the actuator loop (7.8). We assume a drive inertia system

described by the transfer function

$$P(s) = \frac{\omega_m(s)}{T_m(s)} = \frac{1}{I_m s}, \tag{7.46}$$

with an output derivative feedback in the form of

$$D(s) = \frac{T_m^d(s)}{\omega_m(s)} = \frac{K_d s}{\tau s + 1}, \tag{7.47}$$

where τ is the time constant of the low-pass filter which has to be used to form a physically feasible differentiator and which limits the high frequency gain of the feedback. We obtain the complementary sensitivity function as

$$P^{cl}(s) = \frac{\omega_m(s)}{T_m(s)} = \frac{P}{1 + PD} = \frac{\tau s + 1}{s(I_m \tau s + I_m + K_d)}. \tag{7.48}$$

In the frequency range $\omega < 1/\tau$ in which the feedback provides an effective differentiation, $D(s)$ may be approximated as

$$D(s) \approx K_d s, \tag{7.49}$$

and the equation (7.48) reduces to

$$P^{cl}(s) \approx \frac{1}{s(I_m + K_d)}. \tag{7.50}$$

It is seen, that the derivative component which acts as an acceleration feedback in the actuator loop virtually adjusts the motor inertia to a new value $\bar{I}_m = (I_m + K_d)$ in the low frequency region. Therefore, **it may be used to correct an inappropriate resonance ratio in the case of an oscillatory system**.

The derivative part is introduced in the 2DoF PID control law in the form of

$$\begin{aligned} T_m(s) = {} & K_p \left\{ w_p \omega_m^*(s) - \omega_m(s) \right\} + \frac{K_i}{s} \left\{ \omega_m^*(s) - \omega_m(s) \right\} \\ & + \frac{K_d s}{\tau s + 1} \left\{ w_d \omega_m^*(s) - \omega_m(s) \right\}, \; w_p, w_d \in \langle 0, 1 \rangle, \end{aligned} \tag{7.51}$$

where w_d is setpoint weighting factor for the derivative part and τ is a low-pass filter time constant. Provided that the derivative part works effectively in the range of the system resonance frequency ($1/\tau >> r$), the closed-loop dynamics may be approximated as

$$P_m^{cl}(s) = \frac{\omega_m(s)}{\omega_m^*(s)} \approx \frac{(w_d \frac{K_d}{K_d+1} s^2 + w_p \bar{K}_p s + \bar{K}_i)(s^2 + 1)}{s^4 + \bar{K}_p s^3 + (\bar{K}_i + \bar{r}^2) s^2 + \bar{K}_p s + \bar{K}_i}, \tag{7.52}$$

$$P_l^{cl}(s) = \frac{\omega_l(s)}{\omega_m^*(s)} \approx \frac{(w_d \frac{K_d}{K_d+1} s^2 + w_p \bar{K}_p s + \bar{K}_i)}{s^4 + \bar{K}_p s^3 + (\bar{K}_i + \bar{r}^2) s^2 + \bar{K}_p s + \bar{K}_i}, \tag{7.53}$$

where the newly introduced parameters with the bar marking are given as:

$$\bar{K}_p = \frac{K_p}{K_d+1},\ \bar{K}_i = \frac{K_i}{K_d+1},\ \bar{R} = \frac{I_l}{\bar{I}_m} = \bar{r}^2 - 1 = \frac{r^2-1}{K_d+1} = \frac{R}{K_d+1}. \tag{7.54}$$

Comparison of (7.52) and (7.53) with the transfer functions obtained with the PI controller (7.15),(7.16) reveals that the derivative feedback adjusts the *virtual load to drive inertia ratio* $\bar{R} = \frac{I_l}{\bar{I}_m}$ *and the corresponding resonance ratio* $\bar{r} = \sqrt{1+\bar{R}}$.

The procedure of PID compensator design may be decomposed into the subsequent steps:

1. For a difficult controllable system with the resonance ratio parameter outside the range $r \notin \langle\sqrt{2}, \sqrt{5}\rangle$ viable for the PI control, introduce the derivative gain which adjusts the virtual inertia of the motor and shifts the resonance ratio to the new value $\bar{r}$ as:

   $$K_d = \frac{r^2-1}{\bar{r}^2-1} - 1. \tag{7.55}$$

   Positive K_d which decreases the resonance ratio should be used for sluggish systems with large r whereas negative values are suitable for low resonance ratio systems for which the PI controller without the derivative action cannot provide a sufficient level of damping.

2. Compute the PI controller gains $\bar{K}_p, \bar{K}_i$ for the new system with the virtual resonance ratio $\bar{r}$. Both proper damping and maximum closed-loop bandwidth can be achieved now due to the derivative action.

3. Scale the PI gains for the original system according to the equations

   $$K_p = \bar{K}_p(K_d+1),\ K_i = \bar{K}_i(K_d+1). \tag{7.56}$$

The cut-off frequency of the low-pass filter in the derivative part has to be set according to the resonance frequency of the system ($1/\tau > \omega_n$ for the non-normalized case) to allow effective loopshaping in the desired frequency range. The second case for $K_d < 0$ should be used with caution as the positive derivative feedback has a destabilizing effect due to the introduced phase lag (see the dashed Bode plot in Fig. 7.8). Moreover, unstable zeros can appear in the nominator of the closed loop transfer functions (7.52,7.53) which may lead to undesirable behaviour during setpoint tracking. Output derivative feedback (for the setting $w_d = 0$ in the 2DoF control law) may be needed to minimize sudden changes in the motor torque. The range of applicable derivative gain is also limited by the amount of measurement noise. The maximum attainable closed-loop bandwidth is still limited by the value of the first antiresonance of the controlled plant.

7.1.4 Nonzero damping case

The performed analysis can be extended to the more general case of nonzero modal damping. The *normalized* model of the plant is acquired in the form of:

$$P_m(s) = \frac{\omega_m(s)}{T_m(s)} = \frac{1}{s}\frac{(s^2 + 2\xi_z s + 1)}{(s^2 + 2\xi_z r^2 s + r^2)}, \tag{7.57}$$

which is equivalent to the two-mass system with physical parameters:

$$I_m = 1,\ I_l = k = r^2 - 1,\ b = 2\xi_z(r^2 - 1). \tag{7.58}$$

Closed-loop transfer functions for the 2DoF PI controller (7.14) from the reference to motor and load speed are obtained as:

$$P_m^{cl}(s) = \frac{\omega_m(s)}{\omega_m^*(s)} = \frac{(w_p K_p s + K_i)\left(s^2 + 2\xi_z s + 1\right)}{s^4 + a_3 s^3 + a_2 s^2 + a_1 s + a_0}, \tag{7.59}$$

$$P_l^{cl}(s) = \frac{\omega_l(s)}{\omega_m^*(s)} = \frac{(w_p K_p s + K_i)\left(2\xi_z s + 1\right)}{s^4 + a_3 s^3 + a_2 s^2 + a_1 s + a_0}, \tag{7.60}$$

$$\begin{aligned} a_3 &= \left(2\,\xi_z\, r^2 + K_p\right),\ a_2 = \left(2\,\xi_z\, K_p + r^2 + K_i\right), \\ a_1 &= \left(2\,\xi_z\, K_i + K_p\right),\ a_0 = K_i. \end{aligned}$$

Plant sensitivity functions are given as:

$$PS_m^{cl}(s) = \frac{\omega_m(s)}{T_l(s)} = \frac{s(2\xi_z s + 1)}{s^4 + a_3 s^3 + a_2 s^2 + a_1 s + a_0}, \tag{7.61}$$

$$PS_l^{cl}(s) = \frac{\omega_l(s)}{T_l(s)} = \left(\frac{s}{r^2 - 1}\right)\left(\frac{s^2 + (2\xi_z[r^2 - 1] + K_p)s + K_i + r^2 - 1}{s^4 + a_3 s^3 + a_2 s^2 + a_1 s + a_0}\right). \tag{7.62}$$

The solution of the partial pole placement problem can be found using the Jordan form assignment method (see the preliminary chapter or paper [211]). Analytical expressions for the controller gains are obtained in the form of rational functions of the desired location of the assigned closed-loop pole pair ξ^*, ω^*:

$$\begin{aligned} K_p(\xi^*, \omega^*) &= \frac{num_p(\xi^*, \omega^*)}{den_{p,i}(\xi^*, \omega^*)},\ K_i(\xi^*, \omega^*) = \frac{num_i(\xi^*, \omega^*)}{den_{p,i}(\xi^*, \omega^*)}, \\ num_p &= 2\,\xi^*\omega^{*5} + \left(2\xi_z(1 - r^2) - 8\,\xi_z\xi^{*2}\right)\omega^{*4} + \\ &\quad + \left(8\,\xi^{*3} + 8\,{\xi_z}^2\xi^* r^2 - 4\,\xi^*\right)\omega^{*3} - 8\,\xi^{*2}\xi_z\, r^2\omega^{*2} \\ &\quad + 2\,\xi^* r^2\omega^*, \\ num_i &= \omega^{*2}\{\omega^{*4} - 4\,\omega^{*3}\xi^*\xi_z + \left(4\,{\xi_z}^2 r^2 - r^2 + 4\,\xi^{*2} - 1\right)\omega^{*2} \\ &\quad - 4\,\omega^*\xi^*\xi_z\, r^2 + r^2\}, \\ den_{p,i} &= \omega^{*4} - 4\,\xi^*\xi_z\omega^{*3} - \left(2 - 4\,{\xi_z}^2 - 4\,\xi^{*2}\right)\omega^{*2} \\ &\quad - 4\,\xi^*\xi_z\,\omega^* + 1. \end{aligned} \tag{7.63}$$

Stability of the closed-loop system has to be examined analogously to the zero damping case. The Hurwitz matrix for the characteristic polynomial in (7.59) is obtained as:

$$H = \begin{bmatrix} 2\xi_z r^2 + K_p & 2\xi_z K_i + K_p & 0 & 0 \\ 1 & 2\xi_z K_p + K_i + r^2 & K_i & 0 \\ 0 & 2\xi_z r^2 + K_p & 2\xi_z K_i + K_p & 0 \\ 0 & 0 & 0 & K_i \end{bmatrix}. \tag{7.64}$$

All the coefficients are positive for $K_p, K_i > 0$ fulfilling the necessary condition of stability. The leading principal minors of H are:

$$\begin{aligned} |H_2| =& 4\,{\xi_z}^2 K_p\, r^2 + 2\,\xi_z\,{K_p}^2 + 2\,K_i\,\xi_z\,\left(r^2-1\right) \\ & K_i\,K_p + 2\,r^4\xi_z + K_p\,\left(r^2-1\right), \\ |H_3| =& 8\,{\xi_z}^3 K_i\,K_p\,r^2 + \left(4\,K_i\,{K_p}^2 + 4\,r^2{K_p}^2\right){\xi_z}^2 \\ & + 2\,K_p\,\left(r^4 - 2\,K_i + {K_p}^2 + {K_i}^2\right)\xi_z + \\ & \left(4\,{\xi_z}^2{K_i}^2 + {K_p}^2\right)\left(r^2-1\right). \end{aligned} \tag{7.65}$$

Since $r > 1$, they are positive for all $K_p, K_i > 0$. Therefore, positiveness of controller gains provides the sufficient condition of stability and also ensures that a stable minimum-phase controller is obtained. The common denominator $den_{p,i}(\omega^*)$ of rational functions in (7.63) has four roots:

$$\begin{aligned} \omega^*_{1,2} &= \xi^*\,\xi_z + \sqrt{u} \pm \sqrt{2\,{\xi^*}^2{\xi_z}^2 + 2\,\xi^*\,\xi_z\,\sqrt{u} - {\xi_z}^2 - {\xi^*}^2} \\ \omega^*_{3,4} &= \xi^*\,\xi_z - \sqrt{u} \pm \sqrt{2\,{\xi^*}^2{\xi_z}^2 - 2\,\xi^*\,\xi_z\,\sqrt{u} - {\xi_z}^2 - {\xi^*}^2} \\ u &= ({\xi^*}^2 - 1)(\xi_z^2 - 1) \end{aligned} \tag{7.66}$$

Since $u < 0$ for $\xi^* > 1$ and $\xi_z \in (0,1)$, complex roots are obtained and den_p, i is positive $\forall\omega^*$. This also holds for the case $\xi^* \in (0,1\rangle, \xi_z \in (0,1), \xi^* \neq \xi_z$ (follows from inspection of last term under the square-root), which is valid for practical cases of lightly damped systems where $\xi_z << \xi^*$). Special case $\xi^* = \xi_z \in (0,1\rangle$ leads to real roots in $\omega^* = 1$. Therefore, $den_{p,i}$ is positive and the range of applicable controller gains can be determined by inspection of numerators num_p, num_i. The property of gradual closing of the closed-loop which was derived for the zero damping case holds for the parametrization (7.63) as well:

$$\begin{aligned} & K_p(\xi^*, \omega^* = 0) = 0,\ K_i(\xi^*, \omega^* = 0) = 0, \\ & \frac{\partial K_p}{\partial \omega^*} = 2\xi^* r^2, \frac{\partial K_i}{\partial \omega^*} = 0, \frac{\partial^2 K_i}{\partial {\omega^*}^2} = 2r \mid\ \omega^* = 0 \end{aligned} \tag{7.67}$$

Zero gains are obtained for $\omega^* = 0$ and the loop smoothly closes when ω^* is gradually increased. There is always a nonempty range of applicable $\omega^* \in \langle 0, \omega^*_{max}\rangle$ which results in positive controller gains. This range can be found for a chosen ξ^* by computing a first real root of polynomials $num_p(\omega^*), num_i(\omega^*)$ in the admissible interval of $\omega^* \in \langle 0,1\rangle$ (follows from fundamental limitation on achievable bandwidth for

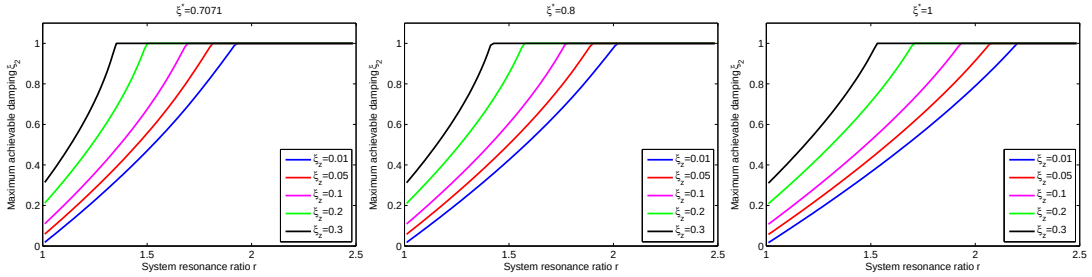

Figure 7.9: Maximum achievable damping of the second indirectly controlled pole-pair as a function of modal damping and resonance ratio, three plots for various setting of first pole pair damping $\xi^* = \{\sqrt{2}/2, 0.8, 1\}$

the normalized plant). This can be done with use of Sturm's theorem and a proper numerical method for isolation of the roots [212]. The maximum allowable radius $\omega^*_{max}(\xi^*) \in \langle 0, 1\rangle$ is the lower bound from these two limits and defines a **permissible range of assignable** $\omega^*(\xi^*) \in \langle 0, \omega^*_{max}\rangle$ **which parameterize all stabilizing PI controllers which are stable and minimum-phase** $(K_p, K_i > 0)$. Computation of ω^*_{max} can be performed automatically in a drive commissioning software.

The derivative action can be used in the same manner as in the previous case of an undamped system. The closed-loop transfer function obtained for the 2DoF PID controller (7.51) can be derived as:

$$P^{cl}_m(s) = \frac{\omega_l(s)}{\omega^*_m(s)} \approx \frac{\left(w_d \frac{K_d}{K_d+1} s^2 + w_p \bar{K}_p s + \bar{K}_i\right)\left(s^2 + 2\xi_z s + 1\right)}{s^4 + a_3 s^3 + a_2 s^2 + a_1 s + a_0}, \tag{7.68}$$

$$P^{cl}_l(s) = \frac{\omega_l(s)}{\omega^*_m(s)} \approx \frac{\left(w_d \frac{K_d}{K_d+1} s^2 + w_p \bar{K}_p s + \bar{K}_i\right)\left(2\xi_z s + 1\right)}{s^4 + a_3 s^3 + a_2 s^2 + a_1 s + a_0}, \tag{7.69}$$

$$a_3 = \left(2\,\xi_z\,\bar{r}^2 + \bar{K}_p\right),\ a_2 = \left(2\,\xi_z\,\bar{K}_p + \bar{r}^2 + \bar{K}_i\right), \bar{K}_p = \frac{K_p}{K_d+1},$$

$$a_1 = \left(2\,\xi_z\,\bar{K}_i + \bar{K}_p\right),\ a_0 = \bar{K}_i,\ \bar{r}^2 - 1 = \frac{r^2-1}{K_d+1}, \bar{K}_i = \frac{K_i}{K_d+1}.$$

Comparison with the PI control transfer functions (7.52,7.53) shows that the adjustment of the resonance ratio can be performed in the same way.
The effect of the modal damping on the achievable closed-loop performance can be studied analogously to the undamped case. Comparison of the closed-loop characteristic polynomial in (7.52,7.53) with the parametrization (7.19) leads to equations:

$$\omega_2 = \frac{\sqrt{K_i}}{\omega^*}, \tag{7.70}$$

$$\xi_2 = \frac{2\xi_z r^2 + K_p - 2\xi^*\omega^*}{2\omega_2}. \tag{7.71}$$

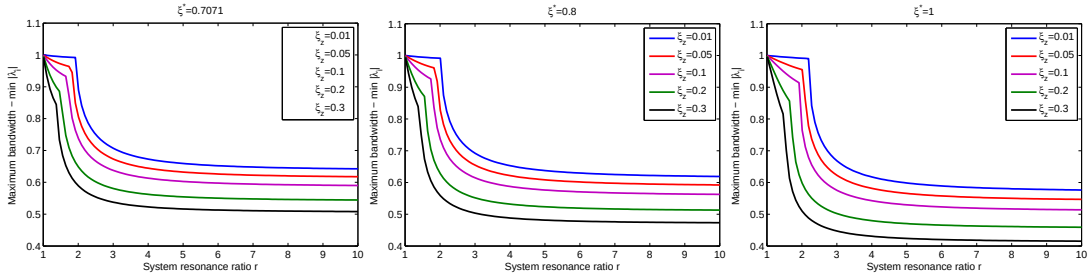

Figure 7.10: Maximum achievable bandwidth in the sense of maximum radius of all closed-loop poles as a function of modal damping and resonance ratio, three plots for various setting of first pole pair damping $\xi^* = \{\sqrt{2}/2, 0.8, 1\}$

Substitution of the controller gains from the obtained parameterization (7.63) can be used to express the natural frequency and damping of the second indirectly controlled pole-pair as a function of the first directly assigned pair location. Maximum achievable damping and bandwidth can be plotted for various values of modal damping ξ_z to study its effect on the closed-loop behaviour. Figure (7.9) shows the maximum attainable damping ξ_2 of the second pole pair with respect to the system resonance ratio. Five curves are plotted for distinct values of the damping ξ_z. Three plots are acquired for a different setting of the first pole pair damping ξ^*. It can be seen that higher level of modal damping allows better controllability in the region of low resonance ratio $r < 2$. On the contrary, high values of damping reduce the maximum achievable bandwidth as can be seen in Fig. (7.10). The reason for that is that better damped poles reach the real axis sooner when increasing the first pole pair radius ω^* and their movement towards the right half plane limits the maximum feedback gains at lower values of ω^*. The conclusion is that **there is still a relatively narrow range of resonance ratios for which both good damping and high bandwidth may be achieved**. This region shifts towards the lower values of r with the increasing values of modal damping. A higher order compensator has to be used outside of this range when a significant improvement of control performance is needed.

Addition of friction model

Further generalization of the two-mass oscillatory system model is obtained by adding motor and load side friction (3.62). The normalized transfer function is given as:

$$P_m(s) = \frac{\omega_m(s)}{T_m(s)} = \frac{1}{s+a}\frac{(s^2 + 2\xi_z s + 1)}{(s^2 + 2\xi r s + r^2)}. \tag{7.72}$$

Physical plant parameters (motor and load inertia, stiffness and damping of the flexible coupling) can be obtained by comparing the normalized model (7.72) with the transfer function (3.62) which was derived for the two-inertia system. The solution is obtained

in the form of:

$$I_m = 1,\ I_l = k = f(\xi_z, r, a),\ b = \xi_z f(\xi_z, r, a) - \frac{1}{2}ar^2 - \xi_z + \frac{1}{2}a + \xi r, \tag{7.73}$$
$$b_l = \xi_z f(\xi_z, r, a) + \frac{1}{2}ar^2 + \xi_z - \frac{1}{2}a - \xi r,\ b_m = -\xi_z f(\xi_z, r, a) + \frac{1}{2}ar^2 - \xi_z + \frac{1}{2}a + \xi r,$$

where $f(\xi_z, r, a)$ is a root of the quadratic equation

$$\begin{aligned} f(\xi_z, r, a) = \mathrm{RootOf}\{&(4\xi_z^2 - 4)x^2 + (8\xi_z^2 - 8\xi r\xi_z - 4\xi_z a + 8a\xi r4 - 4\xi_z ar^2 + 4r^2)x + \\ &+ (r^4a^2 + 4\xi_z^2 + 4a\xi r + a^2 + 4ar^2\xi_z - 8\xi_z\xi r - 4\xi_z a - 2r^2a^2 + 4r^2\xi^2 - 4\xi r^3 a)\} \end{aligned} \tag{7.74}$$

in the variable x. A root which gives positive values of the plant parameters is selected. In the case that both roots lead to some negative values, there is no two-mass system which matches the transfer function (7.72), possibly due to some unmodeled dynamics or an error in the identification procedure.

Knowledge of the physical parameters (7.73) is necessary for the derivation of the closed-loop plant sensitivity function in order to evaluate the level of active load-side disturbance rejection. This serves as a performance criterion for a controller optimization which is proposed in the next section. The closed-loop transfer functions are obtained as:

$$P_m^{cl}(s) = \frac{\omega_m(s)}{\omega_m^*(s)} = \frac{(w_p K_p s + K_i)\left(s^2 + 2\xi_z s + 1\right)}{s^4 + a_3 s^3 + a_2 s^2 + a_1 s + a_0}, \tag{7.75}$$
$$P_l^{cl}(s) = \frac{\omega_l(s)}{\omega_m^*(s)} = \frac{(w_p K_p s + K_i)\left(2\xi_z s + 1\right)}{s^4 + a_3 s^3 + a_2 s^2 + a_1 s + a_0}, \tag{7.76}$$
$$a_3 = \left(2\,\xi\, r + K_p + a\right),\ a_2 = \left(2\,\xi_z\, K_p + r^2 + K_i + 2a\xi r\right),$$
$$a_1 = \left(2\,\xi_z\, K_i + K_p + ar^2\right),\ a_0 = K_i.$$

Plant sensitivity functions are given as:

$$PS_m^{cl}(s) = \frac{\omega_m(s)}{T_l(s)} = \left(\frac{s}{I_l}\right)\left(\frac{bs + I_l}{s^4 + a_3 s^3 + a_2 s^2 + a_1 s + a_0}\right), \tag{7.77}$$
$$PS_l^{cl}(s) = \frac{\omega_l(s)}{T_l(s)} = \left(\frac{s}{I_l}\right)\left(\frac{s^2 + (b + K_p + b_m)s + K_i + I_l}{s^4 + a_3 s^3 + a_2 s^2 + a_1 s + a_0}\right). \tag{7.78}$$

The controller gains are again obtained as rational functions of plant parameters and

first assigned pole pair location:

$$
\begin{aligned}
K_p(\xi^*,\omega^*) &= \frac{num_p(\xi^*,\omega^*)}{den_{p,i}(\xi^*,\omega^*)},\ K_i(\xi^*,\omega^*) = \frac{num_i(\xi^*,\omega^*)}{den_{p,i}(\xi^*,\omega^*)},\\
num_p &= 2\,\xi^*\omega^{*5} + \left(2\xi_z - a - 2\xi r - 8\,\xi_z\xi^{*2}\right)\omega^{*4} +\\
&\quad + \left(8\,\xi_z\,\xi^*\,\xi\,r + 8\,\xi^{*3} - 4\,\xi^* + 4\,\xi_z\,\xi^*\,a\right)\omega^3\\
&\quad + \left(a - 2\,\xi_z\,r^2 - 4\,\xi^{*2}a - 8\,\xi^{*2}\xi\,r + 2\,\xi\,r + r^2a - 4\,\xi_z\,\xi\,r\,a\right)\omega^{*2} +\\
&\quad + \left(4\,\xi^*\,\xi\,r\,a + 2\,\xi^*\,r^2\right)\omega^* - r^2a,\\
num_i &= \omega^{*2}\{\omega^{*4} - 4\,\omega^{*3}\xi^*\xi_z + \left(-1 - 2\xi ra + 4\xi_z\xi r - r^2 + 4\,\xi^{*2} + 2\,\xi_z\,a\right)\omega^{*2}\\
&\quad + (-2\xi^*a + 2\xi^*r^2a - 4\xi^*\xi r)\omega^* + r^2 + 2\xi ra - 2\xi_z r^2 a\},\\
den_{p,i} &= \omega^{*4} - 4\,\xi^*\xi_z\omega^{*3} - \left(2 - 4\,{\xi_z}^2 - 4\,\xi^{*2}\right)\omega^{*2}\\
&\quad - 4\,\xi^*\xi_z\,\omega^* + 1.
\end{aligned}
\tag{7.79}
$$

Comparison with (7.63) reveals, that the common denominator $den_{p,i}$ remains the same as in the frictionless case and again only the positiveness of the numerators num_p, num_i has to be checked to find a set of stable minimum phase controllers with positive gains.

Unlike the previous case, **positiveness of the controller gains does not provide the sufficient condition of the closed-loop stability**. Although the instability occurs only in very rare cases of odd combinations of plant and controller parameters, a fail-safe algorithm which finds a set of stabilizing controllers has to be derived for a proper functionality of the auto-tuning procedure. *Stability of the closed-loop may be examined by observing the constraint equations which relate the location of the poles*.

The characteristic polynomial can be described by two pole pairs with the second indirectly controlled pair being parameterized as a complex couple with natural frequency ω_2 and damping ξ_2

$$
\begin{aligned}
a^*_{cl}(s) &= (s^2 + 2\xi^*\omega^* s + {\omega^*}^2)(s^2 + 2\xi_2\omega_2 s + {\omega_2}^2)\\
&= s^4 + (2\xi^*\omega^* + 2\xi_2\omega_2)s^3 + ({\omega^*}^2 + 4\xi^*\omega^*\omega_2\xi_2 + \omega_2^2)s^2\\
&\quad + (2{\omega^*}^2\xi_2\omega_2 + 2\xi^*\omega^*\omega_2^2)s + (\omega^*\omega_2)^2,
\end{aligned}
\tag{7.80}
$$

or as a couple of real poles p_3, p_4

$$
a^*_{cl}(s) = (s^2 + 2\xi^*\omega^* s + {\omega^*}^2)(s + p_3)(s + p_4) \tag{7.81}
$$

$$
\begin{aligned}
&= s^4 + (2\xi^*\omega^* + p_3 + p_4)s^3 + ({\omega^*}^2 + 2\xi^*\omega^* p_3 + (2 * \xi^*\omega^* + p_3)p_4)s^2\\
&\quad + ({\omega^*}^2 p_3 + ({\omega^*}^2 + 2\xi^*\omega^* p_3)p_4)s + {\omega^*}^2 p_3 p_4.
\end{aligned}
\tag{7.82}
$$

Comparison with the closed-loop transfer function (7.16) leads to equations

$$
(p_3 + p_4) = 2\xi_2\omega_2 = 2\xi r + K_p + a - 2\xi^*\omega^* \tag{7.83}
$$

$$
(p_3 p_4) = \omega_2^2 = \frac{K_i}{\omega^*} \tag{7.84}
$$

It is seen that stable controller with $K_i > 0$ has to be used and the stability of the closed-loop is determined by the sign of the real part of the right side of the equation (7.83). Substitution of K_p from the solution (7.79) leads to inequality

$$2\xi r + \frac{num_p}{den_{p,i}} + a - 2\xi^*\omega^* \overset{!}{>} 0. \tag{7.85}$$

Since $den_{p,i}$ is positive $\forall \xi^*, \omega^* \in \langle 0, 1\rangle$ as shown in the previously performed analysis (7.66), the sufficient condition of stability reduces to

$$(2\xi r + a - 2\xi^*\omega^*)den_{p,i} + num_p \overset{!}{>} 0. \tag{7.86}$$

The left side of (7.86) is a fourth order polynomial in variable ω^*:

$$2\,\xi_z\,(\omega^*)^4 - 8\,\xi^*{\xi_z}^2 + \left(8\,\xi_z\,(\omega^*)^3\,(\xi^*)^2 + 4\,a{\xi_z}^2 - 2\,\xi_z r^2 - 2\,\xi\,r + ar^2 - 4\,\xi_z\xi\,ra + 8\,\xi\,r{\xi_z}^2 - a\right)(\omega^*)^2$$
$$+\left(-2\,\xi^* - 8\,\xi_z\xi^*\xi\,r - 4\,a\xi^*\xi_z + 4\,\xi^*\xi\,ra + 2\,\xi^* r^2\right)\omega^* + a - ar^2 + 2\,\xi\,r \tag{7.87}$$

Examination of its roots (either analytically or numerically) reveals the range of applicable ω^* which leads to a stabilizing controller.

Reparameterization for smooth feedback closing

A particular problem of the parameterization (7.79) is the violation of the property of smooth gradual transition from the open-loop to the closed-loop control with a progressively increasing bandwidth which was demonstrated in the previous case of a frictionless system. Substitution of $\omega^* = 0$ to the controller gains leads to:

$$K_p(\omega^* = 0) = -r^2 a,\ K_i(\omega^* = 0) = 0, \tag{7.88}$$

$$\frac{\partial K_i(\omega^* = 0)}{\partial \omega^*} = 0,\ \frac{\partial^2 K_i(\omega^* = 0)}{\partial {\omega^*}^2} = 4\xi ra - 4\xi_z r^2 a + 2r^2. \tag{7.89}$$

The closed-loop poles do not match the poles of the open loop for the zero bandwidth. There is a discontinuity in the proportional gain which starts at negative values leading to a nonminimum phase compensator. The derivative of the integral gain reveals that an unstable compensator and closed-loop may be obtained for certain plant parameters.

This problem can be solved in two ways:

1. Computation of a minimum value of ω^* which leads to stable minimum phase stabilizing controller.
2. Reparameterization of the location of the first directly assigned pole pair to allow smooth transition from the open loop for low values of closed-loop bandwidth.

The first method may be applied by analyzing the corresponding polynomials in num_p, num_i and the condition (7.86) which determine the sign of the controller gains and stability of the closed-loop. The second approach needs to introduce a parameterization of the closed-loop poles which starts from the open-loop poles location for $\omega^* = 0$. The following algorithm is proposed:

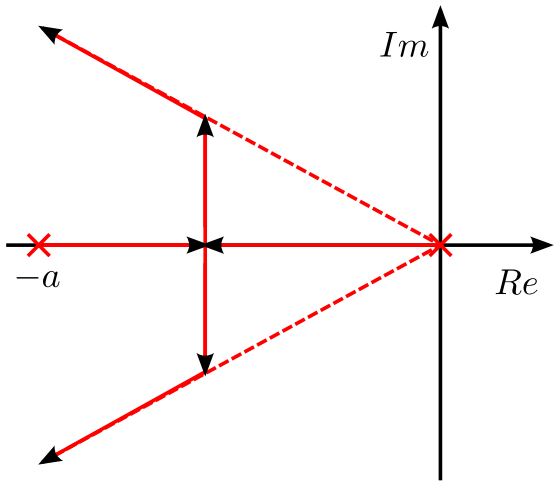

Figure 7.11: Reparametrization of the closed-loop poles for the case of model with friction

- For $\omega^* \leq 0.7a$, the closed-loop poles start from the zero pole in the origin (due to the integrator part of the controller) and stable real pole a of the plant. The two poles move against each other and meet at the location $-0.7a$.

- When $\xi^* = 1$, the couple of double real pole moves together to the left on the real axis for $\omega^* > 0.7a$. For $\xi^* \in \langle\sqrt{2}/2, 1\rangle$, the poles are moved vertically in parallel with the imaginary axis until they reach the half lines corresponding to the chosen ξ^*. After that, they continue along these half lines for further increasing ω^* as in the previous frictionless case.

The pattern of the closed-loop poles movement in the complex plane is depicted in Fig. (7.11). The given parameterization was constructed as an approximation of the solution of the Symmetrical Root Locus which is obtained by synthesis of a LQ optimal controller for a scalar weighted output (see the preliminary chapter). This plot is useful for the examination of the optimal location of the closed-loop poles which lead to a reasonable compromise between the amplitude of the control and system bandwidth given by the quadratic criterion. Although the exact shape of the optimal SRL plot differs with the varying plant dynamics and weighting coefficients in the quadratic criterion, its behaviour for low bandwidth is almost the same for typical values of oscillatory system parameters. The closed-loop poles start from the location of open-loop poles, they meet on the real axis, approach half lines in the complex-plane given by the Butterworth pattern and tend to infinity except for some of them which end in the zeros of the root locus equation. The proposed parameterization allows smooth transition from open to closed-loop with gradual increase of compensator gains and closed-loop bandwidth which may be advantageous especially for a manual tuning.

7.1.5 Controller performance optimization

The previous section presented the algorithm which derives a whole set of admissible PID controllers which are stable, minimum phase and which stabilize a given system. Optimization procedure which selects one particular compensator from the admissible set according to some proper performance criterion may be useful for the purpose of automatic drive commissioning.

The feedback compensator should provide two basic functions:

1. **Reference trajectory tracking**
   The motion of the load which is driven by the actuator should track reference signals which are obtained from a trajectory generator. As was shown in the introductory example, precise actuator motion does not necessarily imply good control of an elastically coupled load. Therefore, *load side dynamics* should be taken into account in the optimization process.

2. **Active compensation of external disturbances**
   The controller should actively damp vibrations excited by external disturbances which typically occur as an external load torque/force acting on the load side of the driven mechanism. Again, load side dynamics is essential for the evaluation of performance of the control system.

These two basic requirements may be contradictory and different compensator settings may be required in distinct applications. Whereas the disturbance compensation is more significant for contact motions of a CNC machine tool, reference tracking may be more important for free space manipulation tasks of a robotic arm. The next section presents an optimization algorithm which is proposed for the automatic controller tuning.

Reference tracking

The first important performance index related to the reference trajectory tracking can be expressed in the frequency domain as a required shape of the load-side complementary sensitivity function. The closed-loop bandwidth (in the standard -3dB sense) with respect to the *load motion* (7.60) is defined as:

$$\begin{aligned} J_1 = \omega_0^{max};\ |P_l^{cl}(i\omega) = \tfrac{\omega_l(i\omega)}{\omega_m^*(i\omega)}| > -3dB,\ \forall\omega \in \langle 0, \omega_0^{max}\rangle \\ \wedge M_T = \|P_l^{cl}(s)\|_\infty = \sup_{\forall\omega}|P_l^{cl}(i\omega)| < M_T^{max}. \end{aligned} \tag{7.90}$$

The limitation of the maximum peak value M_T^{max} is introduced to disqualify closed loops with oscillatory behaviour or excessive overshoot due to weakly damped poles or system zeros. The value of the criterion J_1 may be computed numerically for a particular controller given by desired radius and damping of the assigned pole pair ξ^*, ω^*. **The optimal setting which maximizes J_1 is then selected from the set of admissible compensators**.

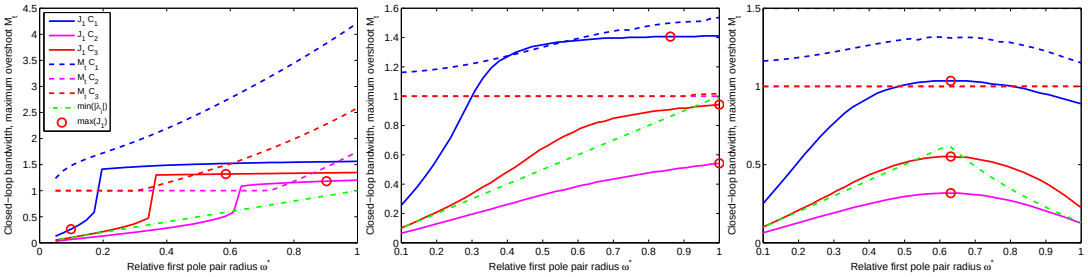

Figure 7.12: Achievable reference tracking performance - closed-loop bandwidth J_1 and maximum overshoot M_t of load-side complementary sensitivity function P_l^{cl} for three different values of resonance ratio $r = \{1.25, 2, 4\}$, blue color - 1DoF PI controller, red color - 2DoF PI controller with $w_p = 0.5$, magenta color - 2DoF PI controller with $w_p = 0$, green color - minimum radius of the closed-loop poles, solid lines - closed-loop bandwidth J_1, dashed lines - max. overshoot M_T, red markers - maximum achievable bandwidth

An example is given for a set of normalized two-mass systems (7.57) with modal damping $\xi_z = 0.01$ and three various values of the resonance ratio $r = \{1.25, 2, 4\}$. Figure (7.12) shows the plots of the closed-loop bandwidth J_1 (solid lines) and maximum overshoot M_T in the amplitude response of the closed-loop transfer function P_l^{cl}. Three different colors show the influence of the weighting factor w_p in the 2DoF PI control law. It is seen that the achievable bandwidth is poor for low resonance ratio systems. This is due to the poor damping of the second pole pair which causes an oscillatory behaviour of the loop and which is seen as an overshoot in the amplitude response of the complementary sensitivity function. This overshoot is even emphasized by the stable real zero $z_1 = K_i/K_p$ introduced by the compensator. Two DoF control law may be beneficial in this case. Lowering the setpoint weighting factor w_p limits the influence of the compensator zero and enhances the range of applicable gains as can be seen in the left plot (indicated by red markers). An optimal value of w_p may be found automatically to achieve the highest possible bandwidth. With the increasing resonance ratio, the advantage of 2DoF control law diminishes and a 1DoF controller may provide higher bandwidth due to the influence of the compensator zero which introduces a phase lead. For high resonance ratio systems, the movement of the closed-loop poles towards the right half plane (indicated by green line which shows the minimum radius of the closed-loop poles) becomes the limiting factor for the maximum achievable bandwidth as can be seen from the last plot for $r = 4$.

The maximum achievable bandwidth J_1 as a function of the system resonance ratio is plotted in Fig. (7.13). Three colors are used to distinguish the 1DoF PI control law (blue), 2DoF control law with the setpoint weighting $w_p = 0.5$ (magenta) and 2DoF control law with proportional output feedback (red). Solid lines show the results for the chosen damping $\xi^* = \sqrt{2}/2$, dashed lines stand for $\xi^* = 1$. It can be seen that the achievable bandwidth drops considerably for $r < \sqrt{2}$ in the case of 1DoF controller. The range of controllable systems with low r can be extended by reduction of the setpoint

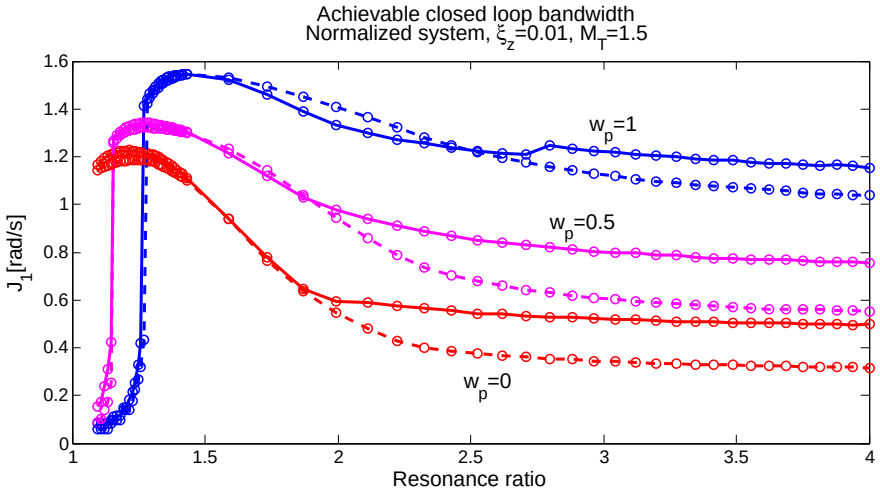

Figure 7.13: Maximum achievable bandwidth - $J_1[rad/s]$ with respect to system resonance ratio, blue - 1DoF control law, magenta - 2DoF control law with $w_p = 0.5$, red - 2DoF control law with $w_p = 0$, solid lines $\xi^* = \frac{\sqrt{2}}{2}$, dashed lines $\xi^* = 1$

weighting factor w_p. The maximum bandwidth drops exponentially for large $r > 2$ due to real poles p_3, p_4 approaching the right half-plane. The compensator zero for higher values of w_p is beneficial in this case as it provides a phase lead. Lower values of ξ^* leads to shorter settling times for a large r whereas its influence is minimal for $r < 2$. The observations are consistent with the analysis of the closed-loop poles behaviour performed in the previous section.

Disturbance rejection

Second performance index is introduced for the evaluation of the *active vibration damping* property of the controller. The disturbance rejection performance may be formulated in the frequency domain with the use of the load-side plant sensitivity function as

$$J_2 = \frac{\|PS_l^{cl}(s)W(s)\|_\infty}{\|PS_l^{ol}(s)W(s)\|_\infty} = \frac{\sup\limits_{\forall\omega}|PS_l^{cl}(i\omega)W(i\omega)|}{\sup\limits_{\forall\omega}|PS_l^{ol}(i\omega)W(i\omega)|}, W(s) = \frac{s}{s+1},$$

where $PS_l^{cl}(s) = \frac{\omega_l(s)}{T_l(s)}$ is the transfer function obtained from (7.17),(7.61) or (7.77), depending on the model type being used and $PS_l^{ol}(s)$ denote the open-loop transfer function of the load side disturbance for the disconnected feedback:

$$PS_l^{ol}(s) = PS_l^{cl}(s) \mid K_p, K_i = 0. \tag{7.91}$$

The high-pass weighting filter $W(s)$ is added to emphasize the region of system antiresonance and resonance frequency which is important for the performance in active

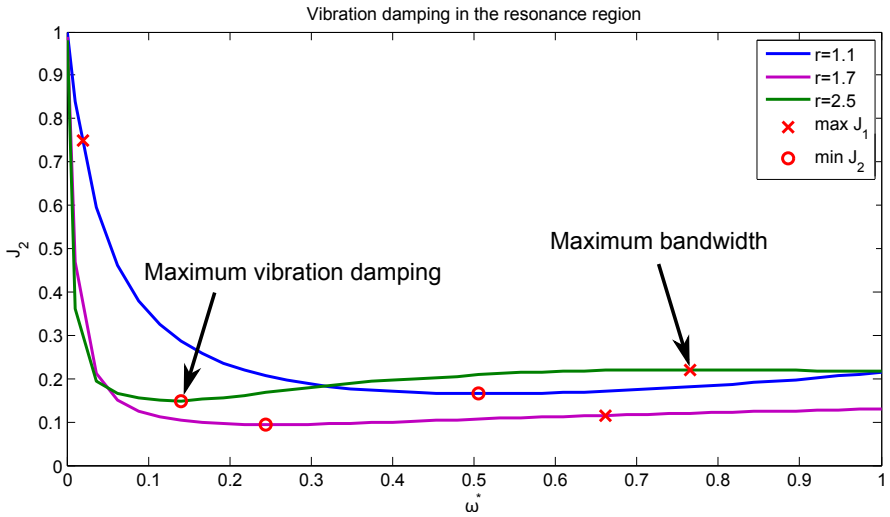

Figure 7.14: Maximum vibration damping - J_2 with respect to system resonance ratio and closed-loop bandwidth ω^*

vibration damping of the load. The normalization with respect to the open-loop is introduced to obtain a reasonable scaling of the index.

The values of J_2 as a function of controller gains $\omega^* \in \langle 0, 1\rangle, \xi^* = 1$ are plotted in Fig.(7.14) for different values of r. The typical shape with exponential decay is caused by increasing damping of the second pole pair. Optimal performance of the controller is achieved in the range $\omega^* \in \langle min(J_2), max(J_1)\rangle$. This interval may be empty for a poorly controllable system for which the poles cannot be damped sufficiently (blue line in Fig.7.14) while achieving reasonable reference tracking.

Robust stability and performance analysis

Maximum achievable bandwidth is often limited in practical motion control applications due to an uncertainty in the system model. Parametric variations due to a change of the operating point, occurrence of higher resonance modes, sensor or actuator lag, sampling effects or measurement noise are typical examples of unmodeled high-frequency dynamics which limits the range of applicable controller gains.

Three typical cases of model uncertainty are analyzed in this section

- Parametric uncertainty in the nominal plant model
- Unknown unstructured high frequency perturbation of the nominal dynamics
- Known high frequency perturbation due to additional dynamics in the loop

The parameter variations in dynamics of flexible mechanical systems are typically caused by changes of load inertia (e.g. due to the varying load during pick and place operations) or alteration of the stiffness of the flexible coupling (see e.g. the example of

nonlinear belt-drive system given in the previous chapter). The parametric perturbations result in a shift of the resonance and antiresonance frequencies and may lead to detuning or even instability of the closed-loop. The condition of robust stability has to be evaluated to make sure that the system can operate well even in the presence of the uncertainty.

As was shown in the previous sections, sufficient condition for robust stability is given by positiveness of the compensator gain for the case of a two-mass system without the motor and load side friction (7.57). This does not hold for the general model with friction for which the stability has to be examined. The analysis of **robustness in stability with respect to parametric uncertainty** can be performed with the use of the *Kharitonov's theorem*. The nominal normalized plant model is assumed in the form of:

$$P_n(s) = \frac{\omega_m(s)}{T_m(s)} = \frac{1}{s + a_n} \frac{(s^2 + 2\xi_{zn} s + 1)}{(s^2 + 2\xi_n r_n s + r_n^2)}. \tag{7.92}$$

A set of stable, minimum phase and stabilizing controllers may be derived using the previously proposed algorithm. An optimal controller may be selected from this set according to the presented optimization algorithm to achieve best reference tracking or vibration attenuation. A model of the perturbed plant with a parametric uncertainty is given as the transfer function

$$P_p(s) = \frac{\omega_m(s)}{T_m(s)} = \frac{K}{s + a} \frac{(s^2 + 2\xi_z s + \omega_z)}{(s^2 + 2\xi\omega s + \omega^2)}, \tag{7.93}$$

where the plant parameters are known to be bounded

$$\begin{aligned} &K \in \langle K_{min}, K_{max} \rangle,\ a \in \langle a_{min}, a_{max} \rangle,\ \xi_z \in \langle \xi_{zmin}, \xi_{zmax} \rangle,\ \omega_z \in \langle \omega_{zmin}, \omega_{zmax} \rangle, \\ &\xi \in \langle \xi_{min}, \xi_{max} \rangle,\ \omega \in \langle \omega_{min}, \omega_{max} \rangle. \end{aligned} \tag{7.94}$$

The closed-loop complementary sensitivity function of the perturbed plant with a PI compensator is given as:

$$\begin{aligned} P_p^{cl} &= \frac{\omega_m(s)}{\omega_m^*(s)} = \frac{(K_p s + K_i) K (s^2 + 2\xi_z s + \omega_z^2)}{s^4 + a_3 s^3 + a_2 s^2 + a_1 s + a_0}, \\ a_3 &= (2\xi\omega + K K_p + a),\ a_2 = (2a\xi\omega + K K_i + \omega^2 + 2K K_p \xi_z) \\ a_1 &= (K K_p \omega_z^2 + a\omega^2 + 2K K_i \xi_z),\ a_0 = K K_i \omega_z^2 \end{aligned} \tag{7.95}$$

Lower and upper bounds for the coefficients of the characteristic polynomial in (7.95) may be found as:

$$a_3 \in \langle \underline{a_3}, \overline{a_3} \rangle,\ a_2 \in \langle \underline{a_2}, \overline{a_2} \rangle,\ a_1 \in \langle \underline{a_1}, \overline{a_1} \rangle,\ a_0 \in \langle \underline{a_0}, \overline{a_0} \rangle, \tag{7.96}$$

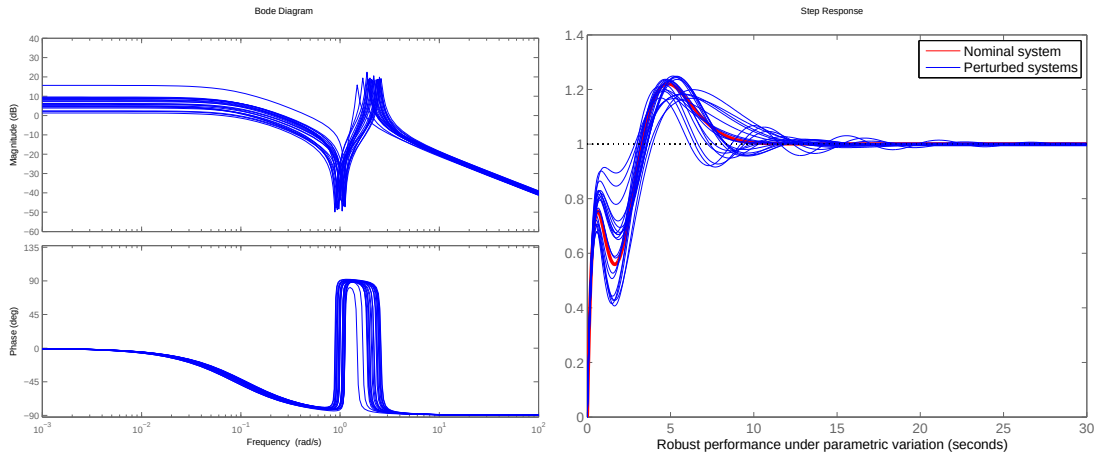

Figure 7.15: Robust performance - example of uncertain plant with parametric variations, left - Bode plot, right - closed loop step response with the robust controller

where the bounds are obtained in the form of:

$$
\begin{aligned}
&\underline{a_3} = 2\xi_{min}\omega_{min} + K_{min}K_p + a_{min},\ \overline{a_3} = 2\xi_{max}\omega_{max} + K_{max}K_p + a_{max}, \\
&\underline{a_2} = 2a_{min}\xi_{min}\omega_{min} + K_{min}K_i + \omega_{min}^2 + 2K_{min}K_p\xi_{zmin}, \\
&\overline{a_2} = 2a_{max}\xi_{max}\omega_{max} + K_{max}K_i + \omega_{max}^2 + 2K_{max}K_p\xi_{zmax}, \\
&\underline{a_1} = K_{min}K_p\omega_{zmin}^2 + a_{min}\omega_{min}^2 + 2K_{min}K_i\xi_{zmin} \\
&\overline{a_1} = K_{max}K_p\omega_{zmax}^2 + a_{max}\omega_{max}^2 + 2K_{max}K_i\xi_{zmax} \\
&\underline{a_0} = K_{min}K_i\omega_{zmin}^2,\ \overline{a_0} = K_{max}K_i\omega_{zmax}^2.
\end{aligned}
\tag{7.97}
$$

According to the Kharitonov's theorem, the characteristic polynomial (7.95) is strictly Hurwitz if and only if each of the four Kharitonov polynomials

$$
\begin{aligned}
k_1(s) &= \underline{a_0} + \underline{a_1}s + \overline{a_2}s^2 + \overline{a_3}s^3 + s^4 \\
k_2(s) &= \overline{a_0} + \overline{a_1}s + \underline{a_2}s^2 + \underline{a_3}s^3 + s^4 \\
k_3(s) &= \overline{a_0} + \underline{a_1}s + \underline{a_2}s^2 + \overline{a_3}s^3 + s^4 \\
k_4(s) &= \underline{a_0} + \overline{a_1}s + \overline{a_2}s^2 + \underline{a_3}s^3 + s^4
\end{aligned}
\tag{7.98}
$$

is stable. Stability of the four polynomials may be examined by checking their roots or with use of some algebraic criterion such as Hurwitz or the Routh-Hurwitz method.

This result may be used for the evaluation of the robustness of the closed-loop with respect to known bounds of a parametric uncertainty. These bounds may be obtained, for example, by the automatic identification experiment in different operating points of a machine or they are based on apriori information about the system operation (e.g. from a known bounds for the varying load inertia).

A numerical example is given to demonstrate this procedure. The normalized plant model is given by the set of nominal parameters $K = 1,\ a = 0.1,\ \xi = 0.02,\ \xi_z = 0.01,$, $\omega = 2, \omega_z = 1$. The parameters can vary in $\pm 10\%$ range around their nominal value except for the resonance frequency which is expected in range $\pm 30\%$. Bode plots of the uncertain model are shown in Fig. (7.15) left. A velocity PI controller is designed for the nominal plant. Optimal reference tracking performance according to the criterion J_1 (7.90) is achieved for $\omega^* = 0.9\omega_z$. Evaluation of the Kharitonov polynomials reveals that the closed-loop system is stable for the given class of transfer functions. The result is verified experimentally using Monte Carlo simulation with samples of the uncertain system (Fig. 7.15 right). It is seen that the compensator is robust with respect to the given class of perturbations and consistent performance of the closed loop is achieved for assumed parameter variations.

Failure of the Kharitonov test does not necessarily mean that the closed-loop system is unstable since the bounds of the polynomial coefficients in (7.96) cannot be reached independently. **Method of gridding** may be applied in the case that the test fails. The parameter space is covered with a grid and stability of the closed loop is evaluated for each point. When the compensator fails to meet the robustness requirements, the procedure is repeated for a lower bandwidth ω^*. Simple bisection algorithm may be used to find a suitable controller setting which fulfills the robustness conditions. A **robust performance** test can be formulated in the frequency domain by setting some constraints on the shape of the important closed-loop transfer functions. Fulfillment of the performance specification may be evaluated for each individual sample in the grid. Considering the relatively low number of plant parameters, the results may be obtained in a reasonable time.

There are other types of unmodeled dynamics which cannot be described simply as a variation of parameters of the nominal plant. An example is a transport delay caused by a communication network which connects a motor power amplifier with the supervisory control system, influence of higher resonance modes which are not assumed in the model or nonlinear dynamics of the mechanical subsystem occurring at higher frequencies. A more general model of the uncertainty is needed as the unmodeled high-frequency dynamics can potentially change the order of the closed loop arbitrarily. Results of the robust control theory may be used to cope with the high-frequency unstructured uncertainty.

The modelling errors can be expressed as a multiplicative uncertainty which perturbs the nominal plant $P_n(s)$ [5],[213]:

$$P(s) = P_n(s)\Big(1 + \Delta(s)W_2(s)\Big), \tag{7.99}$$

where W_2 is a fixed stable transfer function and Δ is a variable stable transfer function satisfying $\|\Delta\|_\infty < 1$. The weighting function W_2 provides a frequency dependent scaling of the level of the relative uncertainty. Since $\|\Delta\|_\infty < 1$, it holds

$$\left|\frac{P(i\omega)}{P_n(i\omega)} - 1\right| \leq |W_2(i\omega)|\ \forall\omega. \tag{7.100}$$

The uncertainty model may be expressed in the frequency domain for each particular frequency as a disc of radius $|P_n(i\omega)W_2(i\omega)|$ which denotes all the possible locations of the frequency response $P(i\omega)$ of the uncertain system. The model of the uncertainty may be obtained automatically from the identification experiment by comparing the frequency response data points with the computed nominal plant transfer function.

The condition of robust stability can be derived with use of the Small gain theorem after some manipulations with the closed loop scheme as [213]:

$$\|\Delta(s)W_2(s)T_n(s)\|_\infty \leq \|W_2(s)T_n(s)\|_\infty \overset{!}{<} 1. \tag{7.101}$$

where $T_n(s)$ is the complementary sensitivity function of the nominal plant. Comparison with (7.90) shows that the robustness in stability with respect to high-frequency perturbations is inversely proportional to the closed-loop bandwidth and criterion J_1 . The same conclusion holds for the injection of a measurement noise.

Performance of the nominal system can be specified in terms of a desired shape of the sensitivity function $S_n(s)$ of the closed-loop as:

$$\|W_1(s)S_n(s)\|_\infty < 1, \tag{7.102}$$

which leads to inequality

$$\left| S_n(i\omega) = \frac{1}{1 + C(i\omega)P_n(i\omega)} \right| \leq |W_1^{-1}(i\omega)| \ \forall\omega. \tag{7.103}$$

Since the bandwidth of the closed-loop is directly controlled by the first pole pair radius ω^*, the weighting filter W_1 may be set as a constant which specifies the maximum peak of the sensitivity function

$$W_1 = \frac{1}{M_S}. \tag{7.104}$$

The sensitivity function of the uncertain plant (7.99) is perturbed to

$$S(s) = \frac{S_n(s)}{1 + \Delta(s)W_2(s)T_n(s)}. \tag{7.105}$$

The **robust performance condition** is formulated as the simultaneous achievement of the desired performance and stability for all admissible perturbations:

$$\|W_1(s)S_n(s)\|_\infty \overset{!}{<} 1 \ \cap \ \left\| \frac{W_1(s)S_n(s)}{1 + \Delta(s)W_2(s)T_n(s)} \right\|_\infty \overset{!}{<} 1 \ \forall \|\Delta(s)\|_\infty \leq 1. \tag{7.106}$$

It can be shown that a necessary and sufficient condition for achievement of the robust performance is [213]:

$$\| |W_1(s)S_n(s)| + |W_2(s)T_n(s)| \|_\infty \overset{!}{<} 1. \tag{7.107}$$

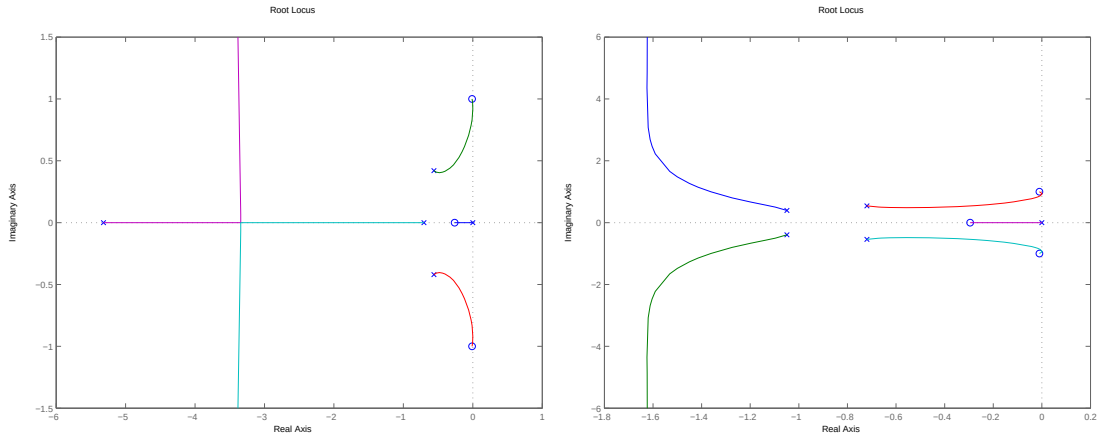

Figure 7.16: Root locus of the position loop closed-loop poles in the cascade PID control structure, two typical shapes obtained for real couple of velocity loop poles (left) or complex pair poles (right)

A robust PID controller can be designed by numerically computing a range of applicable gains $\omega^* \in \langle 0, \omega_{\Delta}^{max} \rangle$ for which the condition (7.107) holds.

The third type of model uncertainty is a **perturbation of the nominal plant by *known linear high-frequency dynamics***. A typical example is the inclusion of the feedback signal filter, a fixed time-delay due to communication between the controller-actuator pair or a known actuator lag. The overall plant dynamics can be described in the form of:

$$P(s) = P_n(s)P_{hf}(s), \tag{7.108}$$

where P_n is the nominal part of the dynamics of the mechanical subsystem and P_{hf} is a known high-frequency dynamics. Utilization of the full plant model (7.108) would complicate or disallow analytical derivation of the controller design e.g. due to an infinite order of the plant in the case of time delay. However, the influence of the perturbation may be insignificant for low controller gains and closed-loop bandwidth which is relatively low with respect to the dominant frequency range of the parasitic dynamics. Therefore, suitable performance may be achieved with the controller obtained for the simplified nominal model P_n. The effect of the high-frequency perturbation is quantified by the inclusion of the full model (7.108) in the optimization process presented in the previous section. The closed-loop performance may be conveniently analyzed in the frequency domain since the proposed optimization procedure evaluates the important closed-loop transfer functions. *Controller gains which meet the design requirements for the full plant dynamics are selected*.

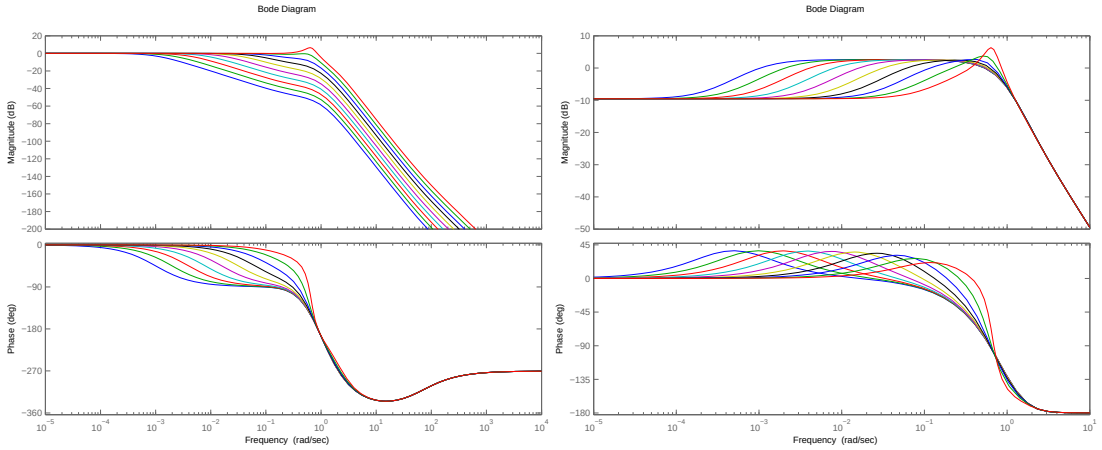

Figure 7.17: Shaping of the closed loop transfer functions - load-side complementary sensitivity function $P_p^{cl}(s)$ (left) and plant sensitivity function $PS_p^{cl}(s)$ (right) for the varying gain of the position controller

7.1.6 Position control

The position control loop is formed in the outer loop of the cascade control scheme (3.3). A simple proportional controller is used in most cases. The open-loop transfer function is obtained in the form of:

$$L(s) = \frac{K_p^p P_m^{cl}(s)}{s}, \tag{7.109}$$

where K_p^p is the proportional gain of the position controller and P_m^{cl} is the closed-loop transfer function of the inner velocity loop.

Behaviour of the dynamics of the position loop can be explained on the root-locus plot of the closed loop system (7.16) which illustrates the effect of position gain adjustment. The root-locus starts from the closed-loop poles of the velocity loop, which are well damped for a properly designed velocity loop, and from zero pole which is introduced by the integrator. The closed-loop bandwidth of the position loop is determined by the dominant stable real pole which moves from the origin to the open-loop zero $z = -\frac{K_i}{w_p K_p}$ introduced by the velocity controller. The first couple of closed-loop poles ends in the weakly damped open-loop zeros of the velocity loop, the second couple tends to infinity. For high values of the position gain, the couple of oscillatory poles becomes dominant leading to oscillatory response. There is even a risk of instability of the closed-loop since the poles may enter the right half-plane.

Optimization of the position loop performance may be performed analogously to the previous case. Since the main goal is to control the position of the load, the most significant closed loop transfer functions are obtained for the load position response φ_l

to position reference φ^* and load-side load torque T_l:

$$P_p^{cl}(s) = \frac{\varphi_l(s)}{\varphi^*(s)} = \frac{K_p^p(bs+k)(w_pK_ps+K_i)}{s^5+a_4s^4+a_3s^3+a_2s^2+a_1s+a_0}, \tag{7.110}$$

$$PS_p^{cl}(s) = \frac{\varphi_l(s)}{T_l(s)} = \frac{s^3I_m+(b+b_m+K_p)s^2+(k+K_p^pK_p+K_i)s+K_iK_p^p}{a_5s^5+a_4s^4+a_3s^3+a_2s^2+a_1s+a_0},$$

$$a_5 = I_l\,I_m,\ a_4 = (b_l\,I_m + I_l\,b_m + I_l\,K_p + I_l\,b + b\,I_m)\,,$$

$$a_3 = \left(K\,I_m + I_l\,K_i + I_l\,K_p^p\,K_p + I_l\,K + b_l\,b + b\,b_m + b\,K_p + b_l\,b_m + b_l\,K_p\right),$$

$$a_2 = \left(I_l\,K_i\,K_p^p + K\,b_m + K\,K_p + b_l\,K + b\,K_p^p\,K_p + K_i\,b + b_l\,K_p^p\,K_p + K_i\,b_l\right),$$

$$a_1 = \left(K_i\,K_p^p\,b + K_i\,K + K_i\,K_p^p\,b_l + K\,K_p^p\,K_p\right),$$

$$a_0 = K_i\,K\,K_p^p.$$

The optimal position controller with respect to the **reference tracking performance** is obtained analogously to the velocity loop case by maximization of the criterion

$$J_1 = \omega_0^{max};\ |P_p^{cl}(i\omega) = \tfrac{\varphi_l(i\omega)}{\varphi^*(i\omega)}| > -3dB,\ \forall\omega \in \langle 0, \omega_0^{max}\rangle$$
$$\wedge \|P_p^{cl}(s)\|_\infty = \sup_{\forall\omega}|P_p^{cl}(i\omega)| \leq 1. \tag{7.111}$$

The amplitude response of the load complementary sensitivity function has to be limited in order to minimize the overshoot which is unacceptable in the position loop as it may lead to dangerous failures during machine operation (e.g. a wrong cut of a CNC machine tool or collision of a robotic arm with an obstacle in the surrounding environment).

The **disturbance rejection performance** may be expressed as a worst-case gain of the load-side plant sensitivity function in terms of the criterion

$$J_2 = \|PS_l^{cl}(s)\|_\infty. \tag{7.112}$$

Frequency weighting and normalization of the performance index is not necessary in this case due to the flat shape of the amplitude response which is obtained for a correctly designed velocity loop.

The typical shape of the important closed-loop transfer functions is shown in Fig. (7.17). The amplitude responses of the load side complementary sensitivity and plant sensitivity functions (7.110) are plotted for the varying gain of the position controller. It is observed that the closed-loop bandwidth gradually increases with the rising gain. The flat shape is preserved until the pole pair which approaches the weakly damped open-loop zeros becomes dominant causing peaks around the antiresonance frequency of the plant both in reference and disturbance response. The functions of bandwidth J_1 and disturbance attenuation J_2 with respect to the position control gain are plotted in Fig. (7.18). Analogously to the velocity loop case, a range of suitable gains may be found for which the feedback loops provides both sufficient damping and reasonable bandwidth. The drop to zero in the red J_1 plot indicates an excess $\|P_p^{cl}(s)\|_\infty > 1$ which signalizes oscillatory behaviour of the loop and marks the maximum allowable

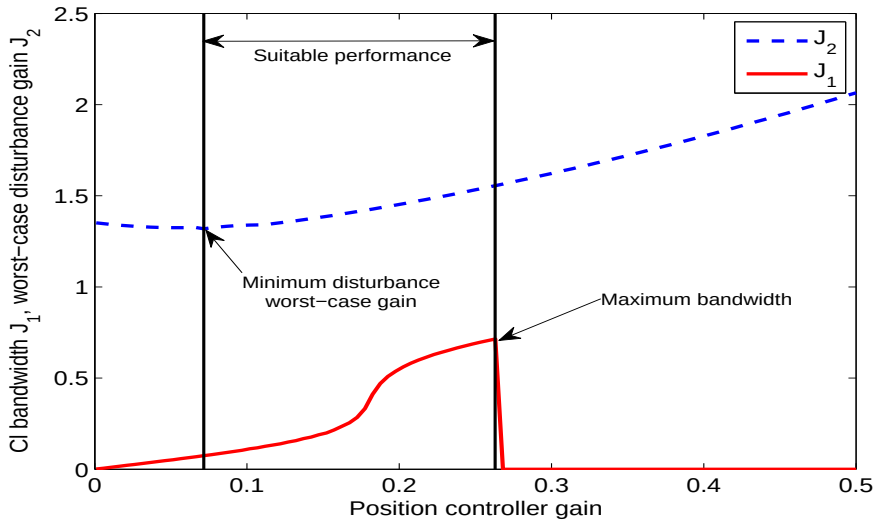

Figure 7.18: Position loop performance criterions - maximum bandwidth J_1 and worst-case disturbance gain J_2 for the varying position controller gain

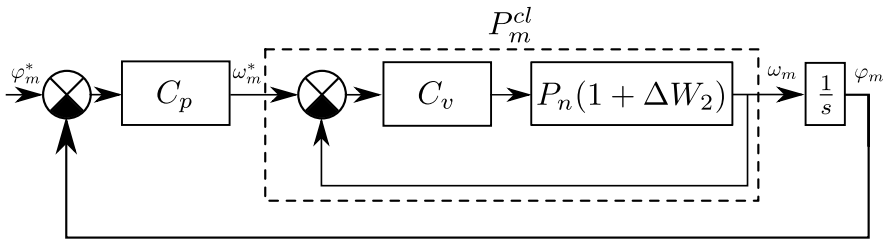

Figure 7.19: Position control of an uncertain system - cascade control with velocity and position control loops

position controller gain. The level of damping J_2 does not vary significantly for a well tuned inner velocity loop and the criterion J_1 gives sufficient information about the closed-loop performance.

Robust performance

The effect of uncertainty in the plant model to closed-loop stability and performance may be analyzed analogously to the previous case of velocity loop tuning. A parametric uncertainty or known high frequency perturbation can be handled in the same way as proposed in the previous section. The analysis of an unstructured uncertainty is more complicated as it involves two cascade feedback loops of velocity and position control (Fig. 7.19). Following section deals with derivation of conditions for robust stability and performance.

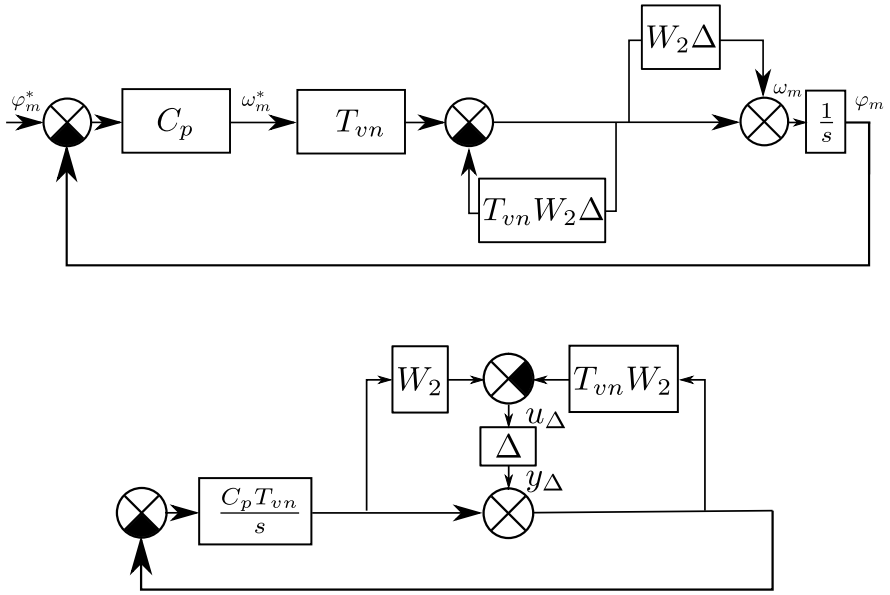

Figure 7.20: Position control of an uncertain system - equivalent diagrams of the closed-loop with a multiplicative perturbation model

The model of the uncertain plant with a multiplicative perturbation is given as:

$$P_p(s) = \frac{\omega_m(s)}{T_m(s)} = P_n(s)\big(1 + \triangle(s)W_2(s)\big), \tag{7.113}$$

where P_n is a nominal model and W_2 is a proper scaling function which express the level of uncertainty. Both of them can be acquired from the identification experiment. Uncertain closed-loop transfer function of the velocity loop is obtained in the form of:

$$P_m^{cl}(s) = \frac{\omega_m(s)}{\omega_m^*(s)} = \frac{C_v(s)P_n(s)\big(1 + \triangle(s)W_2(s)\big)}{1 + C_v(s)P_n(s)\big(1 + \triangle(s)W_2(s)\big)} = \frac{T_{vn}(s)\big(1 + \triangle(s)W_2(s)\big)}{1 + \triangle(s)W_2(s)T_{vn}(s)}, \tag{7.114}$$

where C_v is a velocity controller and T_{vn} is the *nominal* complementary sensitivity function of the velocity loop

$$T_{vn}(s) = \frac{\omega_m(s)}{\omega_m^*(s)} = \frac{C_v(s)P_n(s)}{1 + C_v(s)P_n(s)}. \tag{7.115}$$

The *position control* loop may be partitioned to a known part which contains the nominal dynamics and the uncertain part which models the perturbation. The diagram of the closed-loop circuit (Fig. 7.19) may be redrawn using block manipulations to the configuration in Fig. 7.20. The dynamics of the interconnection system which forms

the feedback loop around the perturbation $\Delta(s)$ is given as:

$$H(s) = \frac{u_\Delta(s)}{y_\Delta(s)} = \frac{W_2(s)T_{vn}(s)}{1 + L_{pn}(s)} - \frac{W_2(s)L_{pn}(s)}{1 + L_{pn}(s)} = W_2(s)T_{vn}(s)S_{pn}(s) - W_2(s)T_{pn}(s), \tag{7.116}$$

where $L_{pn} = \frac{C_p T_{vn}}{s}$ is the *nominal* open loop transfer function of the position loop and S_{pn}, T_{pn} denote the corresponding sensitivity and complementary sensitivity functions. Since $\|\Delta\|_\infty < 1$, the sufficient condition for the internal stability of the closed-loop system according to the *Small gain theorem* is given as:

$$\|H(s)\|_\infty = \|W_2(s)T_{vn}(s)S_{pn}(s) - W_2(s)T_{pn}(s)\|_\infty < 1. \tag{7.117}$$

The inequality (7.117) may be used for the computation of the allowable range of position controller gains which fulfills the **condition of robust stability** with respect to perturbations of the nominal system dynamics given by the uncertainty model.

The **robust performance** condition may be derived as follows. Since the uncertain model (7.113) is acquired from the identification of the motor side dynamics and there is no further apriori information about the way the uncertainty affects the load side dynamics, the controller optimization is performed in the actuator loop. Uncertain open-loop transfer function is obtained from (7.114) as:

$$L_p(s) = \frac{C_p(s)T_{vn}(s)\big(1 + \triangle(s)W_2(s)\big)}{s\big(1 + \triangle(s)W_2(s)T_{vn}(s)\big)}. \tag{7.118}$$

The perturbed complementary sensitivity function is given by equation:

$$T_p(s) = \frac{L_p(s)}{1 + L_p(s)} = \frac{C_p(s)T_{vn}(s)\big(1 + \triangle(s)W_2(s)\big)}{s\big(1 + \triangle(s)W_2(s)T_{vn}(s)\big) + C_p(s)T_{vn}(s)\big(1 + \triangle(s)W_2(s)\big)}. \tag{7.119}$$

The condition of robust performance may be expressed as

$$\|T_p(s)\|_\infty < 1 \; \forall \Delta(s), \tag{7.120}$$

which gives a reasonable requirement for minimization of worst-case gain which leads to oscillatory behaviour of the loop. Assuming proportional controller $C_p(s) = K_{pp}$ in the position loop, the condition (7.120) may be rewritten as:

$$\begin{aligned} &|K_{pp}T_{vn}(i\omega)\big(1 + \triangle(i\omega)W_2(i\omega)\big)| \\ &\overset{!}{\leq} |i\omega\big(1 + \triangle(i\omega)W_2(i\omega)T_{vn}(i\omega)\big) + K_{pp}T_{vn}(i\omega)\big(1 + \triangle(i\omega)W_2(i\omega)\big)|, \; \forall\omega > 0 \end{aligned} \tag{7.121}$$

The upper bound of the left side of the inequality (7.121) may be derived as:

$$|K_{pp}T_{vn}(i\omega)\big(1 + \triangle(i\omega)W_2(i\omega)\big)| \leq K_{pp}\big(|T_{vn}(i\omega)| + |W_2(i\omega)T_{vn}(i\omega)|\big). \tag{7.122}$$

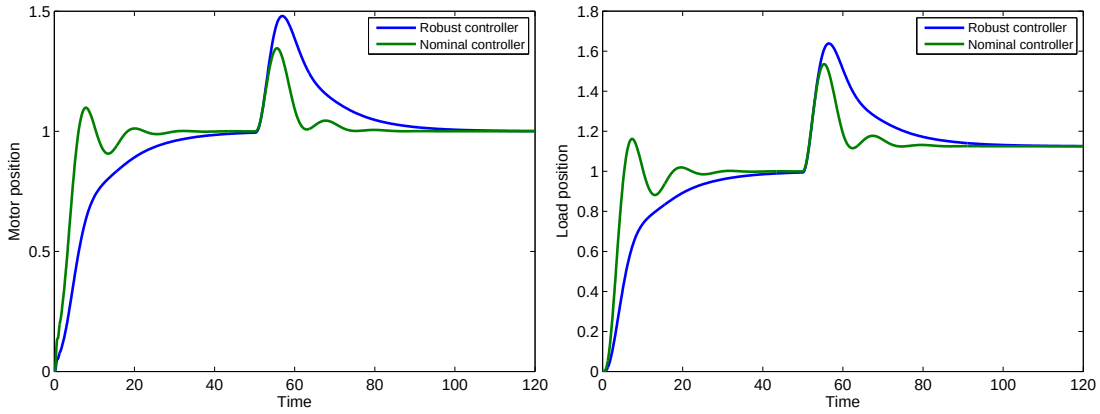

Figure 7.21: Robust performance position control - nominal vs robust design of the position controller, left - motor position response to step in reference command and load side disturbance torque, right - load side response

The lower bound of the right side of (7.121) is obtained by selecting particular $\Delta(i\omega)$ which minimizes the absolute value of the expression:

$$|i\omega\big(1+\triangle(i\omega)W_2(i\omega)T_{vn}(i\omega)\big)+K_{pp}T_{vn}(i\omega)\big(1+\triangle(i\omega)W_2(i\omega)\big)|\geq \\ |i\omega+K_{pp}T_{vn}(i\omega)|-|W_2(i\omega)T_{vn}(i\omega)||i\omega+K_{pp}|. \tag{7.123}$$

Therefore, the **sufficient condition for robust performance** is obtained by combining (7.122) and (7.123):

$$K_{pp}\big(|T_{vn}(i\omega)|+|W_2(i\omega)T_{vn}(i\omega)|\big)\leq |i\omega+K_{pp}T_{vn}(i\omega)|-|W_2(i\omega)T_{vn}(i\omega)||i\omega+K_{pp}|\;\forall\omega>0 \tag{7.124}$$

Numerical evaluation of (7.124) may be used for the derivation of the **maximum position controller gain which leads to robust performance of the closed-loop system under all admissible perturbations of the nominal dynamics**.

A numerical example is given to demonstrate the proposed approach. A nominal two-mass system is perturbed by a time-delay. The normalized transfer function is given in the form of:

$$P_p(s)=\frac{\omega_m(s)}{T_m(s)}=\frac{1}{s}\frac{s^2+2\xi_z s+1}{s^2+2\xi_z r^2 s+r^2}e^{-Ds};\;\xi_z=0.01,\;r=3,\;D=0.15 \tag{7.125}$$

The upper bound of the multiplicative perturbation in the model (7.113) is given by the weighting function $W_2(s)=\frac{2.6s}{s+15}$. The velocity PI controller is obtained from the reference tracking performance optimization according to (7.90) for the nominal system without the time delay. Best performance is achieved for the settings $\omega^*=0.67,\;\xi^*=1$ leading to PI gains $K_p=4.63,\;K_i=0.64$. Since $\|W_2T_{vn}\|_\infty=0.68$ the velocity loop is robustly stable with respect to the given perturbation model. Maximum allowable

position controller gain for the robust stability is obtained from the test as (7.117) $K_{pp} \leq 2$. Maximum gain for the optimal reference tracking according to the *nominal model* is computed from (7.111) as $K_{pp} = 0.3$. This setting leads to unacceptable performance of the perturbed closed-loop with the time-delay as can be seen from the plots in Fig. (7.21) which show reference and disturbance response of the position loop. The highest gain which fulfills the robust performance condition obtained from (7.124) has the value $K_{pp} = 0.11$. The reduction of the gain leads to significant improvement of closed-loop performance as can be seen from Fig. (7.21).

7.1.7 Conclusions for the PID control

The algorithm of the controller synthesis can be summarized as follows:

1. Obtain a nominal plant model from the identification experiment. Estimate the bounds of parametric or unstructured uncertainty or set a known high-frequency dynamics which perturbs the nominal plant.
2. For the normalized nominal plant, compute the set of stable, minimum-phase stabilizing velocity controllers.
3. Adjust the derivative part of the controller (when available) in the case of poorly controllable system to improve the resonance ratio.
4. Compute the range of optimal gains $\langle \omega^*_{J1}, \omega^*_{J2} \rangle$ according to the criterions J_1, J_2 depending on application requirements.
5. Compute the upper bound on ω^* with respect to the model uncertainty (when available).
6. Select a particular controller which meets both performance and robustness requirements.
7. Compute the controller for the original plant by de-normalization in gain and time.
8. Repeat the procedure for the position loop when needed.

All these steps can be performed automatically in the drive commissioning software. The obtained analytical solution for the controller gains can be used for the smooth fine tuning on a real plant using physically intuitive parameters of closed-loop bandwidth and damping.

The performed analysis leads to important conclusions:

- There are fundamental limitations on closed-loop bandwidth and active vibration damping achievable with the conventional PID control. The properties of the closed-loop system are primarily determined by the value of the resonance ratio parameter.

- The maximum achievable bandwidth is limited by the value of the first antiresonance frequency of the system.
- Low resonance ratio systems with $r \leq \sqrt{3}$ cannot be effectively damped whereas sluggish response and low closed-loop bandwidth is ahieved for $r \geq \sqrt{5}$ with the PI velocity compensator.
- The derivative part of the velocity PID controller which serves as motor acceleration feedback can overcome the limitations of low or high resonance ratio systems by changing the virtual inertia of the motor side. Significant improvement compared to the simple PI control may be achieved. The maximum attainable bandwidth is still limited by the value of the first antiresonance of the system. The amount of the derivative action which may be applied is restricted by the level of the measurement noise in the feedback signal.
- The proposed parameterization offers a whole set of suitable stabilizing controllers. The free parameters serve for selection of a particular compensator which meets performance and robustness design requirements. This brings significant simplification compared to direct optimization of the compensator parameters which is a nonlinear and nonconvex problem.
- The load to drive inertia ratio should be kept in the optimal range yet in the phase of mechanical design of the system to prevent from difficulties with vibration control.

7.2 Full-order compensator design

The analysis of the PID control scheme which was performed in the previous section revealed some important performance limitations which arise from the nature of dynamics of the compliantly coupled mechanical load. A fundamental question is, *whether it is possible to improve the quality of control if we do not impose any limitations on the controller structure and order*. The next section deals with fundamental performance limits which hold for any linear controller. Full order velocity and position compensators are derived using methods of optimal and robust control in order to quantify possible performance improvement.

7.2.1 Fundamental limitations on achievable performance

Precise motion control of compliantly coupled load with utilization of motor side feedback only is a difficult control problem. There are fundamental limitations on achievable quality of control which arise from basic constraints which exist in every linear feedback loop. The main issues can be explained using the important closed loop transfer functions. We assume the motor and load side dynamics in the form of:

$$P_m(s) = \frac{\omega_m(s)}{T_m(s)} = \frac{b_m(s)}{a(s)},\ P_l(s) = \frac{\omega_l(s)}{T_m(s)} = \frac{b_l(s)}{a(s)}. \tag{7.126}$$

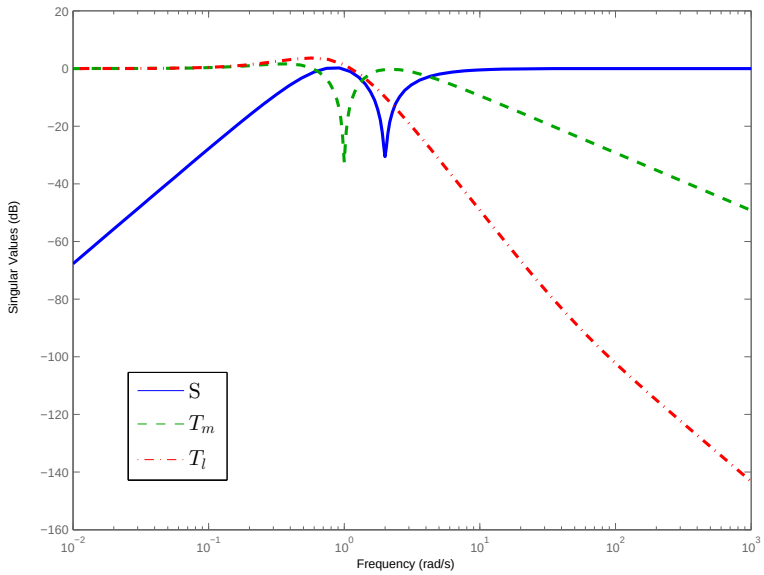

Figure 7.22: Fundamental limitations on achievable performance - proper shape of the amplitude response of important closed-loop transfer functions of a normalized compliant system

The plant is controlled by a linear compensator $C(s) = \frac{T_m(s)}{\omega^*(s) - \omega_m(s)} = \frac{d(s)}{c(s)}$ which uses the motor side feedback only. Closed-loop sensitivity and complementary sensitivity functions which are important for stability and robustness of the loop are given as:

$$S(s) = \frac{1}{1 + C(s)P_m(s)} = \frac{a(s)c(s)}{a(s)c(s) + b_m(s)d(s)}, \tag{7.127}$$

$$T_m(s) = \frac{C(s)P_m(s)}{1 + C(s)P_m(s)} = \frac{b_m(s)d(s)}{a(s)c(s) + b_m(s)d(s)}. \tag{7.128}$$

Load-side complementary sensitivity function which describes the performance of the motion control system is obtained as (see the SITO problem formulation in the introductory section of this chapter):

$$T_l(s) = C(s)S(s)P_l(s) = \frac{b_l(s)d(s)}{a(s)c(s) + b_m(s)d(s)}. \tag{7.129}$$

A properly tuned feedback controller should lead to the shape of the amplitude frequency response of the closed-loop transfer function which is depicted in Fig. (7.22). The sensitivity function S contains weakly damped poles $a(s)$ of the compliant mechanical load in the numerator. All the closed-loop poles have to be properly damped for the correct *active vibration damping* functionality. Therefore, weakly damped poles of the characteristic polynomial $a(s)c(s) + b_m(s)d(s)$ *must not appear in the resonance region* and a notch in the magnitude of $S(i\omega)$ has to be present due to weakly damped zeros of

$a(s)$. Analogously, the complementary sensitivity function T_m should resemble a notch filter characteristics in the vicinity of the *antiresonance* frequency since its numerator contains the weakly damped zeros of the system due to the polynomial $b_m(s)$.

These observations lead to important conclusions:

1. The **problem with controllability of low resonance ratio systems** which was observed in the case of PID control is valid for any linear compensator. As the resonance ratio parameter r gets close to one, the magnitude of both $S(i\omega)$ and $T_m(i\omega)$ would have to be *significantly less than one in the same frequency range* in order to properly damp all the closed-loop poles (without allowing some undesirable peaks in the frequency response functions). This is physically infeasible due to the constraint $S + T_m = 1$. The closed-loop system must have some weakly damped poles either in the vicinity of the antiresonance frequency or in the resonance region. Both cases inevitably lead to an oscillatory response of the load motion since the poles cannot be canceled by the corresponding zeros in T_l. The polynomial $b_l(s)$ contains a stable real zero which is far beyond the frequency range of the closed-loop bandwidth for weakly damped systems and $d(s)$ cannot contain weakly damped zeros around the resonance frequency since this would introduce a notch filter characteristics in the compensator dynamics and violate the requirement of active vibration control.

2. The **closed-loop bandwidth in terms of the load-side tracking performance is limited by the value of the *antiresonance* frequency**. Since the magnitude of $T_m(i\omega)$ has to be significantly less than one in the antiresonance region, magnitude of $S(i\omega)$ has to be close to unity in this frequency range. Therefore, *all the closed-loop poles cannot be shifted far beyond the value of the antiresonance at the same time* without allowing an excessive peaking in the sensitivity functions. This leads to inevitable constraint on the achievable bandwidth of T_l which is given mainly by the dominant closed-loop poles.

3. The **closed-loop bandwidth in the actuator loop cannot be significantly lower than the value of the *resonance* frequency of the system**. The magnitude of $S(i\omega)$ has to be substantially less than one in the resonance region. Therefore, $|T_m(i\omega)|$ has to be close to unity at the same time. *All the closed-loop poles cannot be significantly slower than the value of the resonance frequency at the same time*. This imposes a limitation on achievable robustness in stability and performance with respect to an unmodeled high-frequency dynamics which is mainly determined by the bandwidth of T_m. This problem is emphasized for high values of resonance ratio parameter.

The fundamental limitations cannot be overcome by any linear controller. Two methods of modern control theory, LQG control and H_∞ optimization, are employed to quantify a possible improvement of the closed-loop performance compared to the conventional PID control scheme.

7.2.2 LQG control

One of the classical results of the optimal control theory is the derivation of a compensator which minimizes a quadratic cost function describing the closed-loop performance. The optimal controller has a form of static state feedback whose gains are computed from the Algebraic Riccati equation according to the specified cost function weights (see the preliminary chapter). In the case that some of the state vector components cannot be directly measured, the state controller is complemented by a linear observer. An optimal observer which minimizes the steady state error covariance when the state and output equations are perturbed by a stochastic white noise is known as the Kalman filter. The procedure of state feedback and observer design can be approached as two independent problems due to the *separation theorem*.

The most problematic part of the LQ design procedure is the choice of the weighting matrices in the controller and observer cost functions. Although some heuristic rules for the weights selections are known, the controller tuning is usually performed iteratively according to the numerical simulations of the closed-loop system. The goal of the thesis was to derive a weighting scheme which would be applicable for a wide range of compliant systems with different values of the resonance ratio parameters and which would provide a reasonable compromise between closed-loop bandwidth and robustness to modelling errors.

The starting point is the velocity compensator. The first step is the design of the optimal state regulator, which minimizes the quadratic cost:

$$J = \int_0^\infty \boldsymbol{x}^T \boldsymbol{Q} \boldsymbol{x} + \rho u^2 dt. \tag{7.130}$$

The state space model of a two-mass system can be obtained from the equations of motion in the form of:

$$\dot{\boldsymbol{x}} = \begin{bmatrix} \dot{\omega}_m \\ \dot{\omega}_l \\ \dot{T}_s \\ \dot{x}_i \end{bmatrix} = \begin{bmatrix} -\frac{b}{I_m} & \frac{b}{I_m} & -\frac{1}{I_m} & 0 \\ \frac{b}{I_l} & -\frac{b}{I_l} & \frac{1}{I_l} & 0 \\ k & -k & 0 & 0 \\ -1 & 0 & 0 & 0 \end{bmatrix} \boldsymbol{x} + \begin{bmatrix} \frac{1}{I_m} \\ 0 \\ 0 \\ 0 \end{bmatrix} T_m, \tag{7.131}$$

where the plant parameters are obtained from the **normalized frequency response function** computed from the identification experiment as:

$$I_m = 1,\ I_l = k = r^2 - 1,\ b = 2\xi_z(r^2 - 1). \tag{7.132}$$

A frictionless system is assumed to simplify the explanation. Again, the concept of **normalization in gain and time** is used to obtain a universally applicable solution which does not depend on the time-scale and amplitude of the input. Step disturbance and reference model is introduced by extending the state space model with the integrator term which corresponds to the last state x_i.

The weights of the quadratic criterion are chosen as:

$$\rho = \frac{k_{bw}}{c^2},\ Q = diag\{0,\ 20, \frac{k_{bw}}{c^2},\ 20\};\ c = \frac{r^2}{2}. \tag{7.133}$$

The variable c is the scaling parameter which needs to be introduced in order to **normalize the cost function with respect to the resonance ratio parameter**. Since the overall inertia of the normalized system is equal to $I_m + I_l = r^2$, the weighting terms which penalize the shaft torque and driving motor torque should be adjusted in this ratio to make the closed-loop behaviour independent on the absolute value of r. The parameter k_{bw} determines the overall bandwidth of the closed loop.

The Kalman filter is designed for the extended plant model in the form of:

$$\begin{aligned} \dot{\boldsymbol{x}} &= \begin{bmatrix} \dot{\omega}_m \\ \dot{\omega}_l \\ \dot{T}_s \\ \dot{T}_l \end{bmatrix} = \begin{bmatrix} -\frac{b}{I_m} & \frac{b}{I_m} & -\frac{1}{I_m} & 0 \\ \frac{b}{I_l} & -\frac{b}{I_l} & \frac{1}{I_l} & \frac{1}{I_l} \\ k & -k & 0 & 0 \\ 0 & 0 & 0 & 0 \end{bmatrix} \boldsymbol{x} + \begin{bmatrix} \frac{1}{I_m} \\ 0 \\ 0 \\ 0 \end{bmatrix} T_m + \begin{bmatrix} 1 & 0 \\ 0 & 0 \\ 0 & 0 \\ 0 & 1 \end{bmatrix} \boldsymbol{w}, \\ y &= \omega_m + v, \end{aligned} \tag{7.134}$$

where $\boldsymbol{w}$ and v represent state and output zero mean white noise with covariance parameters chosen as:

$$E(\boldsymbol{w}\boldsymbol{w}^{\boldsymbol{T}}) = diag\{1,\ 1\},\ E(v^2) = 0.1. \tag{7.135}$$

The state of the integral term x_i does not have to be reconstructed by the observer as it is the part of the controller itself. An integrator model of the load-side disturbance torque is added in order to improve the observer response in the case of external load torques acting on the system.

The noise intensities are considered merely as tuning parameters since it is usually impossible to derive a meaningful noise model which would describe the uncertainty in the real system. The noise covariances were chosen in such a way that the closed-loop responses resemble the behaviour achieved with the full LQR state feedback. The standard algorithm for the achievement of Loop transfer recovery [214] which is recommended for the improvement of the robustness of the LQG controlled loops does not work well in this case as an extensive increase of the state noise intensities lead to observer poles which approach the location of weakly damped open-loop zeros resulting in poor performance.

State feedback and observer innovation gains are computed from the corresponding Riccati equations (see the section 2.2). A feed-forward term k_{ff} from the reference speed to motor torque is introduced in order to extend the closed-loop bandwidth. Its gain is computed numerically as the largest allowable value which leads to a maximum specified peak of the load-side complementary sensitivity function $\|T_l(s)\|_\infty < M_T$. The overall structure of the controller is shown in Fig. (7.23) left. The motor velocity feedback can be taken directly from the motor measurement instead of the Kalman

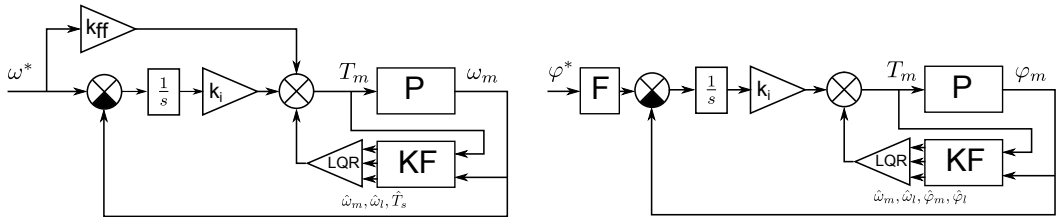

Figure 7.23: LQG compensator structure - left velocity controller, right position controller, P - plant, KF - Kalman filter, k_i - integral feedback gain, k_{ff} - proportional feedforward gain, F - reference command prefilter, LQR - optimal static state feedback

filter as it enters the integral part of the compensator which limits the high frequency gain and therefore the amplification of the measurement noise. The overall order of the compensator is five.

A **position controller** may be designed in a similar manner. A higher order model which includes the position variables has to be used in this case. The state equation is given in the form of:

$$\dot{\boldsymbol{x}} = \begin{bmatrix} \dot{\varphi}_m \\ \dot{\omega}_m \\ \dot{\varphi}_l \\ \dot{\omega}_l \\ \dot{x}_i \end{bmatrix} = \begin{bmatrix} 0 & 1 & 0 & 0 & 0 \\ -\frac{k}{I_m} & -\frac{b}{I_m} & \frac{k}{I_m} & \frac{b}{I_m} & 0 \\ 0 & 0 & 0 & 1 & 0 \\ \frac{k}{I_l} & \frac{b}{I_l} & -\frac{k}{I_l} & -\frac{b}{I_l} & 0 \\ -1 & 0 & 0 & 0 & 0 \end{bmatrix} \boldsymbol{x} + \begin{bmatrix} 0 \\ \frac{1}{I_m} \\ 0 \\ 0 \\ 0 \end{bmatrix} T_m. \quad (7.136)$$

Again an integral term is added in the model to impose integral action of the compensator. The weights of the quadratic criterion are chosen as:

$$\rho = \frac{k_{bw}}{c^2},\ Q = diag\{1,\ 1,\ 20,\ 20,\ 5\};\ c = \frac{r^2}{2}. \quad (7.137)$$

The scaling parameter is now present only in the control action penalization term since the state variables do not change their dimension with the varying resonance ratio. The state space model for the estimator part is given as:

$$\begin{aligned} \dot{\boldsymbol{x}} &= \begin{bmatrix} \dot{\varphi}_m \\ \dot{\omega}_m \\ \dot{\varphi}_l \\ \dot{\omega}_l \\ \dot{x}_i \end{bmatrix} = \begin{bmatrix} 0 & 1 & 0 & 0 & 0 \\ -\frac{k}{I_m} & -\frac{b}{I_m} & \frac{k}{I_m} & \frac{b}{I_m} & 0 \\ 0 & 0 & 0 & 1 & 0 \\ \frac{k}{I_l} & \frac{b}{I_l} & -\frac{k}{I_l} & -\frac{b}{I_l} & \frac{1}{I_l} \\ 0 & 0 & 0 & 0 & 0 \end{bmatrix} \boldsymbol{x} + \begin{bmatrix} 0 \\ \frac{1}{I_m} \\ 0 \\ 0 \\ 0 \end{bmatrix} T_m + \\ &\quad +\mathrm{diag}\{1,1,1,1,1\}\boldsymbol{w}, \\ y &= \varphi_m + v. \end{aligned} \quad (7.138)$$

The covariances of the state and measurement noises are chosen as:

$$E(\boldsymbol{w}\boldsymbol{w}^{\boldsymbol{T}}) = diag\{1,\ 1\ ,1,\ 1,\ 1\},\ E(v^2) = 0.01. \quad (7.139)$$

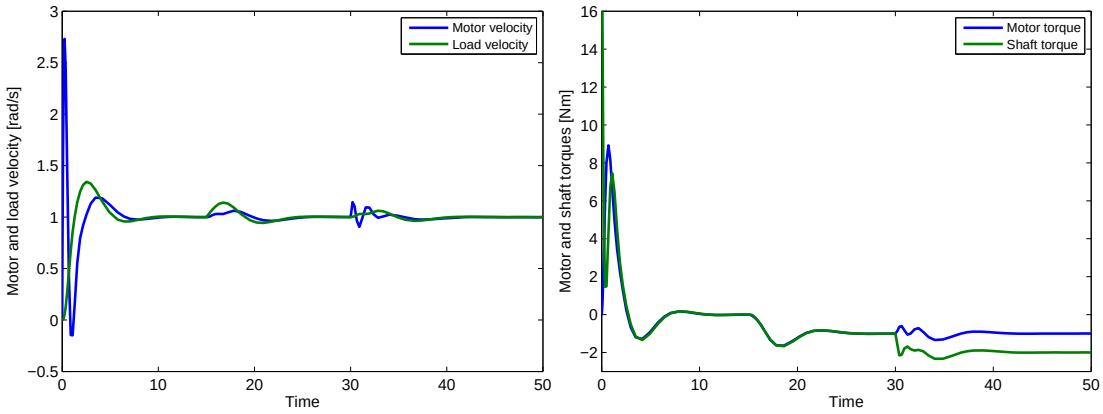

Figure 7.24: LQG velocity control performance - left motor and load velocity, right motor and shaft torque

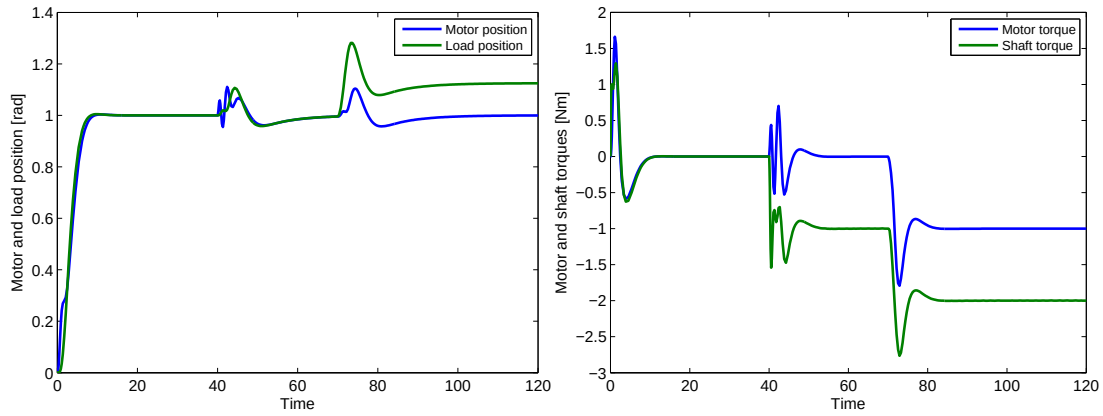

Figure 7.25: LQG position control performance - left motor and load position, right motor and shaft torque

The feedback controller has to be supplemented by a preshaping filter which shapes the reference position commands in order to reduce an overshoot which arises due to the integral part. Simple first order lag is sufficient. Its time constant may be computed numerically from the condition $\|T_l(s)\|_\infty < 1$. The structure of the controller is shown in Fig. (7.23) right. The overall order is six plus the order of the preshaping filter.

An alternative approach to position controller design is employment of the cascade control scheme with LQG velocity controller and proportional position controller. The advantage is the possibility of successive tuning of the individual loops, easier implementation of velocity saturation limits and lower order of the resulting compensator. Practical experiments show that the full order LQG position controller achieves slightly better nominal performance whereas the cascade scheme is more robust to modelling errors.

Performance of the LQG velocity and position controller is shown in figures (7.24)

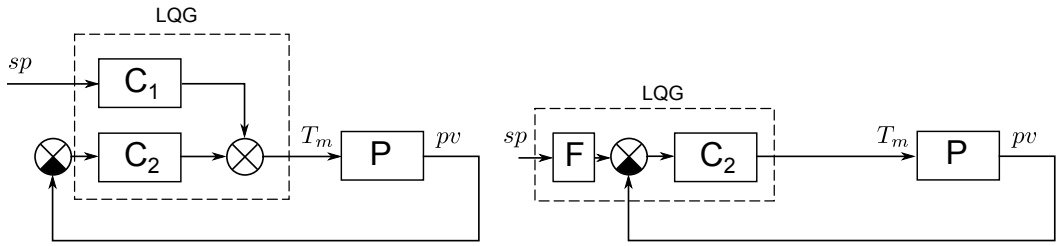

Figure 7.26: Equivalent 2DoF structures of the LQG compensator used for the robustness analysis

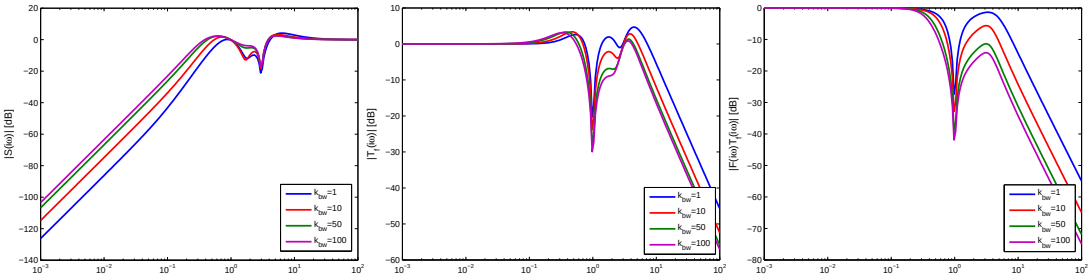

Figure 7.27: LQG loopshaping - amplitude frequency response of the closed-loop sensitivity function $|S(i\omega)|$, complementary sensitivity function of the inner loop $|T_f(i\omega)|$ and 2DoF complementary sensitivity function $|F(i\omega)T_f(i\omega)|$ for varying bandwidth k_{bw}, normalized system with resonance ratio $r = 3$

and (7.25). A normalized system with resonance ratio $r = 3$ and modal damping $\xi_z = 0.01$ was used for simulation. The controller is tuned for the bandwidth setting $k_{bw} = 1$. The left plots show the response of motor and load side velocity and position. The right plot shows the control effort in terms of the generated motor torque and the shaft torque which expresses the stress induced in the compliant coupling. The closed-loop system follows unitary step change in the reference variable and the plant is disturbed by external load torques acting on the motor and load side ($t = 15, 30$) in the velocity control loop and ($t = 40, 70$) for the position loop). It can be seen that the compensator is able to follow reference commands and actively compensate external disturbances achieving well damped closed-loop responses. Very similar plots are obtained for other values of the resonance ratio thanks to the normalization introduced in the weighting functions. The nonzero tracking error of the load side position can be suppressed by closing the feedback loop of the integral part from the estimated *load-side* position at the cost of reduced robustness to modelling errors.

Evaluation of **robust stability and performance** in the presence of model uncertainty can be performed in a similar manner as in the case of the PID controller. The LQG compensator can be transformed from the observer plus state feedback structure into the standard 2DoF form with feedforward and feedback parts (7.26). The aug-

mented state representation may be derived in the form of

$$\begin{aligned} \dot{\boldsymbol{x}}_{\boldsymbol{c}} &= \boldsymbol{A_c x_c} + \boldsymbol{B_1}sp + \boldsymbol{B_2}pv, \\ T_m &= \boldsymbol{C_c x_c}, \end{aligned} \tag{7.140}$$

where pv is the process variable (position or velocity) and sp is the corresponding setpoint signal. The transfer function of the equivalent 2DoF structures (Fig. 7.26) are obtained as:

$$C_1(s) = \boldsymbol{C_c}(s\boldsymbol{I} - \boldsymbol{A_c})^{-1}\boldsymbol{B_1} = \frac{num_1(s)}{den_{1,2}(s)}, \tag{7.141}$$

$$C_2(s) = \boldsymbol{C_c}(s\boldsymbol{I} - \boldsymbol{A_c})^{-1}\boldsymbol{B_2} = \frac{num_2(s)}{den_{1,2}(s)}, \tag{7.142}$$

$$F(s) = \frac{num_1(s)}{num_2(s)}. \tag{7.143}$$

The **robust stability test** is performed for the inner feedback loop only considering the C_2 compensator analogously to the PID control case. For the robust performance evaluation, also the feedforward dynamics of the prefilter has to be taken into account. Considering the multiplicative uncertainty model

$$P(s) = \frac{pv(s)}{T_m(s)} = P_n(s)\big(1 + \Delta(s)W_2(s)\big), \tag{7.144}$$

the nominal performance specification may be given in terms of the desired shape of the complementary sensitivity function:

$$\|W_1(s)T(s)\|_\infty < 1;\ T(s) = \frac{pv(s)}{sp(s)} = \frac{F(s)C_2(s)P(s)}{1 + C_2(s)P(s)} \triangleq F(s)T_f(s). \tag{7.145}$$

The weighting function can be chosen simply as a constant defining a maximum peak of the complementary sensitivity function:

$$W_1 = \frac{1}{M_T^{max}}. \tag{7.146}$$

The perturbed complementary sensitivity function is given as:

$$T_p(s) = \frac{F(s)\big(1 + \Delta(s)W_2(s)\big)T_f(s)}{1 + \Delta(s)W_2(s)T_f(s)}. \tag{7.147}$$

Therefore, the condition of robust performance is formulated from 7.145 and 7.147 as:

$$|W_1F(s)\big(1 + \Delta(s)W_2(s)\big)T_f(s)| < |1 + \Delta(s)W_2(s)T_f(s)|\ \forall\omega. \tag{7.148}$$

Since the uncertainty model is scaled such that $\|\Delta(s)\|_\infty < 1$, we may write

$$\begin{aligned} |W_1F(s)\big(1 + \Delta(s)W_2(s)\big)T_f(s)| &\le |W_1F(s)T_f(s)|\big(1 + |W_2(s)|\big), \\ 1 - |W_2(s)T_f(s)| &\le |1 + \Delta(s)W_2(s)T_f(s)|\ \forall\omega. \end{aligned} \tag{7.149}$$

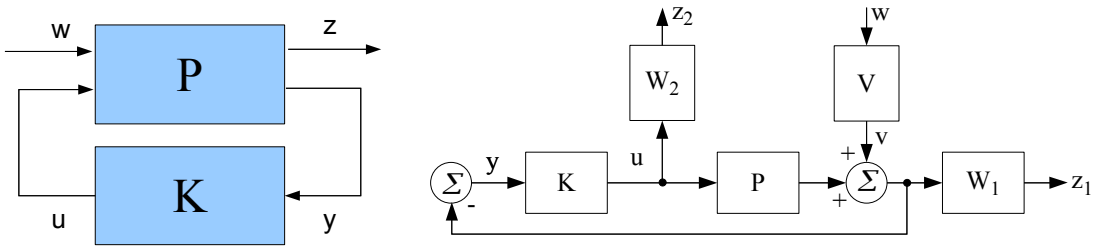

Figure 7.28: H_∞ **optimization** - left general optimization problem, right modified mixed sensitivity problem, $\boldsymbol{w}$ - input variables, $\boldsymbol{z}$ - control errors, $\boldsymbol{u}$ - control inputs, $\boldsymbol{y}$ - observed outputs

From (7.149), the sufficient condition for the robust performance is obtained as:

$$\left\| \frac{W_1 F(s) T_f(s)(1 + |W_2(s)|)}{1 - |W_2(s) T_f(s)|} \right\|_\infty < 1. \tag{7.150}$$

The condition (7.150) can be evaluated numerically for a particular compensator. The parameter k_{bw} which is proposed in the introduced weighting scheme serves as an effective tool for shaping of the important closed-loop frequency response functions (see Fig. 7.27). The optimal solution is found by using a search procedure which adjusts k_{bw} to achieve the highest possible bandwidth for which the robust performance condition holds. As was explained in the analysis of fundamental limitations, the bandwidth of the inner feedback loop cannot be significantly lower than the value of the first resonance frequency. Therefore, *the active vibration damping property may be unattainable when there is a significant amount of uncertainty*. The passive vibration control strategy has to be employed in such case.

7.2.3 H_∞ control

The H_∞ optimization is chosen as another possible approach to full order compensator design. The problem is formulated as a *Mixed sensitivity* optimization which allows to gain control over the shape of the important closed-loop frequency response functions. A modified version of the standard mixed sensitivity problem which was proposed in [5, 215] is used as it allows precise fine tuning of the resulting design.

The *general* H_∞ *optimization problem* (Fig. (7.28) left) is formulated as a search for a controller K which:

1. Internally stabilizes the plant P
2. Minimizes the $\infty - norm$ of the closed-loop matrix H from the external input w to the control error z

The *Mixed sensitivity problem* (Fig. (7.28) right) is set up for a particular choice of weighted input and output variables. The input w is chosen as an output plant disturbance, controlled outputs z_1, z_2 are chosen as weighted output error and manipulating variable. The closed-loop transfer matrix H is obtained in the form of

$$\boldsymbol{H} = \frac{\boldsymbol{z}}{w} = \begin{bmatrix} W_1SV \\ -W_2UV \end{bmatrix}, \tag{7.151}$$

where $S = (1+PK)^{-1}$ is the sensitivity function and $U = K(1+PK)^{-1}$ is the controller sensitivity function. The optimization procedure involves a search for a compensator which gives a minimal value of criterion function γ given as:

$$\gamma = \|H\|_\infty = \sqrt{\sup_{\forall\omega\in R}\left(|W_1(i\omega)S(i\omega)V(i\omega)|^2 + |W_2(i\omega)U(i\omega)V(i\omega)|^2\right)}. \tag{7.152}$$

Supposing that the optimal controller may be computed, the equation (7.152) imposes constraints on the shape of the closed-loop transfer functions:

$$|S(i\omega)| \leq \frac{\gamma}{|W_1(i\omega)V(i\omega)|}, |U(i\omega)| \leq \frac{\gamma}{|W_2(i\omega)V(i\omega)|}, |T(i\omega)| \leq \frac{\gamma|P(i\omega)|}{|W_2(i\omega)V(i\omega)|}\ \forall\omega \in R. \tag{7.153}$$

Proper selection of the weighting functions may be used for effective shaping of the important closed-loop transfer functions in the frequency domain. Although the optimal solution cannot be computed directly, effective algorithms exist for the derivation of a suboptimal compensator which leads to a particular value of γ [5]. The optimal solution can be approached by iterating γ to a minimum value for which the compensator may be found.

As in the previous case, the most important part of the design is the selection of the appropriate weighting scheme. The normalized models of the plant dynamics on the motor and load side obtained from the identification are given as:

$$P(s) = \frac{1}{s}\frac{(s^2+2\xi_z s+1)}{(s^2+2\xi_z r^2 s+r^2)},\ P_l(s) = \frac{1}{s}\frac{(2\xi_z s+1)}{(s^2+2\xi_z r^2 s+r^2)}. \tag{7.154}$$

Again, a frictionless system is assumed to simplify the explanation. Extension to the more general case with friction is straightforward. The plant has to be extended by an integral term to impose integral action in the resulting controller:

$$P_e(s) = \frac{P(s)}{s} = \frac{1}{s^2}\frac{(s^2+2\xi_z s+1)}{(s^2+2\xi_z r^2 s+r^2)},\ P_{el}(s) = \frac{P(s)}{s} = \frac{1}{s^2}\frac{(2\xi_z s+1)}{(s^2+2\xi_z r^2 s+r^2)}. \tag{7.155}$$

When no model of the uncertainty is known, the reasonable design requirements for the nominal plant may be formulated as:

- Maximize the closed-loop bandwidth in terms of the load side motion tracking performance, which is expressed by complementary sensitivity function $T_l(s)$ from reference value to the load motion

- At the same time, make sure that there is no excessive peak in T_l which would signalize an oscillatory behaviour of the loop by setting $\|T_l\|_\infty \leq M_t$
- Limit the maximum peak of the actuator loop sensitivity function in order to achieve sufficient robustness in stability and limit oscillatory behaviour at the motor side by setting $\|S\|_\infty \leq M_s$
- Avoid excessive bandwidth in the actuator loop to make the closed-loop robust to unmodeled high-frequency dynamics
- Make sure that active vibration control function is achieved

Follolwing weighting filters are chosen to fulfill the design requirements:

$$\begin{aligned} W_1 &= \frac{1}{M_s}, \\ W_2 &= \frac{1}{M_t}\frac{(s+\omega_0^T)^2(s+r)^2}{(s+\omega_0^S)^2(s^2+2\xi_v r s+r^2)(\omega_0^T r)^2}, \\ V &= \frac{(s+\omega_0^S)^2(s^2+2\xi_v r s+r^2)}{s^2(s^2+2\xi_z r^2 s+r^2)}. \end{aligned} \tag{7.156}$$

This choice utilizes a special property of the modified Mixed sensitivity problem which is known as a *partial pole placement* [5]. The well known nature of the solutions to H_∞ optimization problems is, that the resulting compensators cancel the stable plant poles with controller zeros. This is unacceptable in the case of weakly damped system as the resulting compensator would resemble the notch filter characteristics in the vicinity of system resonance and the property of *active* vibration control would be lost. Moreover, the compensator zero in the origin would cancel the intended integral action. It was shown that both these problems are avoided by selecting the denominator of V equal to open loop poles and the numerator of V equal to their desired location in the closed-loop. The resulting compensator does not cancel the open loop poles and part of the closed-loop poles are assigned to the location of the numerator of V. By properly adjusting the remaining weighting filters W_1, W_2, the assigned poles may become the *dominant poles* which determine the overall closed-loop bandwidth.

The proposed weighting scheme leads to the loopshaping inequalities:

$$|S(i\omega)| \leq \frac{\gamma}{|V(i\omega)|} = \gamma M_s \left| \left(\frac{s^2}{(s+\omega_0^S)^2} \right) \left(\frac{s^2+2\xi_z r^2 s+r^2}{s^2+2\xi_v r s+r^2} \right) \right|_{s=i\omega}, \tag{7.157}$$

$$|T_m(i\omega)| \leq \frac{\gamma|P_e(i\omega)|}{|V(i\omega)W_2(i\omega)|} = \gamma M_t \left| \frac{(s^2+2\xi_z s+1)(\omega_0^T r)^2}{(s+\omega_0^T)^2(s+r)^2} \right|_{s=i\omega}, \tag{7.158}$$

$$|T_l(i\omega)| \leq \frac{\gamma|P_{el}(i\omega)|}{|V(i\omega)W_2(i\omega)|} = \gamma M_t \left| \frac{(2\xi_z s+1)(\omega_0^T r)^2}{(s+\omega_0^T)^2(s+r)^2} \right|_{s=i\omega}. \tag{7.159}$$

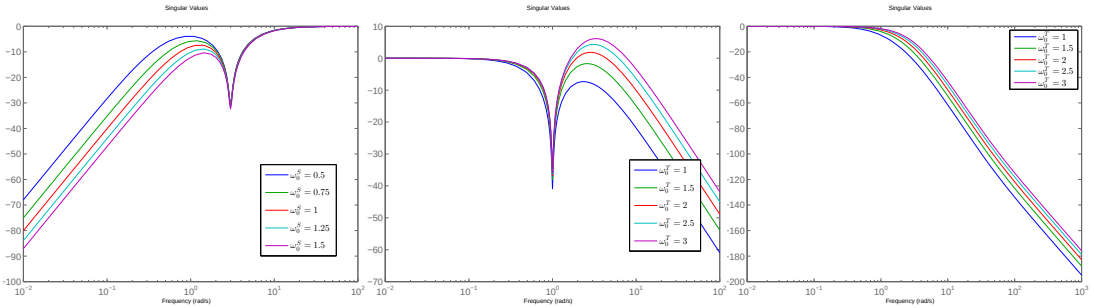

Figure 7.29: H_∞ weighting functions - example of shaping functions for $|S(i\omega)|$, $|T_m(i\omega)|$,$|T_l(i\omega)|$ for varying parameters ω_0^S, ω_0^T

The desired shape of the sensitivity function S is formed as a **high-pass filter plus a notch-filter element at the resonance frequency** of the plant (Fig. 7.29 left). This shape is necessary for the purpose of active vibration damping as was discussed in the previous section related to fundamental limitations on achievable performance. The bandwidth is controlled by the parameter ω_0^S while the depth of the notch is determined by the choice of ξ_v. Since ξ_v also determines damping of one couple of the closed-loop poles, a reasonable choice is between $\xi_v \in \langle\sqrt{2}/2, 1\rangle$. The maximum amplitude is given by the parameter M_s.

The weight for the complementary sensitivity function of the actuator loop T_m has a character of a **low-pass filter with a notch region around the antiresonance frequency** of the plant (Fig. 7.29 in the center). Again, this is the shape necessary for the purpose of active vibration control. The bandwidth of T_m is determined by the value of ω_0^T. Maximum amplitude is given by the parameter M_t.

The shape of the complementary sensitivity function of the load T_l is given as a low-pass filter with the cut-off frequency equal to the lower value of the pair ω_0^T, r. As follows from the analysis of fundamental limitations, ω_0^T cannot be significantly higher than the antiresonance frequency and therefore ω_0^T determines the bandwidth with respect to the tracking performance of the load motion.

There are two parameters which have to be specified prior to execution of the H_∞ optimization process. The value ω_0^S determines the performance of the closed-loop by specifying the location of the couple of two dominant closed-loop poles. The parameter ω_0^T specifies the upper bound on the closed-loop bandwidth which is essential for the robustness w.r.t. unmodeled dynamics.

Following procedure which automates the search for optimal parameters is proposed:

1. Start with a low value of the desired bandwidth ω_0^S somewhere in the interval $\langle 0, 1\rangle$

2. Set ω_0^T to r (the minimum bandwidth of the motor loop which follows from constraint $S + T_m = 1$)

3. Perform the H_∞ optimization for the extended plant model P_e and acquire a compensator K_0. The compensator for the original plant P is obtained as $K = K_0/s$. If $\gamma < 1$ the design requirements are achieved. Otherwise, check whether the conditions $\|S\|_\infty \leq M_s,\ \|T_l\|_\infty \leq M_t$ are fulfilled with the controller K.

4. When the test in the previous step succeeds, go to step 1 and increase the bandwidth ω_0^S. Otherwise relax the restriction on maximum bandwidth of T_m by increasing ω_0^T and repeat step 3.

5. Repeat previous steps as long as a suitable controller can be found for an actual ω_0^S. The compensator with the highest bandwidth of $T_l(s)$ is selected as an optimal one.

When there is an unstructured uncertainty model known from the identification experiment, the same procedure can be used for the computation of a **robust controller**. The same algorithm is used except for the step 2, in which a computation of the infinity norm of S and T_l is replaced by the evaluation of the robust stability or robust performance conditions (see the PID control section for detailed derivation). If there is a known additional dynamics, its description may be added to the plant model. However, this increases the overall order of the compensator. Alternatively, the controller may be designed for the simplified model while the loop performance check in the step 2 of the algorithm is performed with the closed-loop transfer functions computed from the full plant model.

Position controller can be designed in the same manner for the extended plant model:

$$P_e(s) = \frac{1}{s^3}\frac{(s^2+2\xi_z s+1)}{(s^2+2\xi_z r^2 s+r^2)},\ P_{el}(s) = \frac{1}{s^3}\frac{(2\xi_z s+1)}{(s^2+2\xi_z r^2 s+r^2)}. \tag{7.160}$$

The weighting scheme is adjusted to:

$$\begin{aligned} W_1 &= \frac{1}{M_s}, \\ W_2 &= \frac{1}{M_t}\frac{(s+\omega_0^T)^3(s+r)^2}{(s+\omega_0^S)^3(s^2+2\xi_v r s+r^2)(\omega_0^{T^3} r^2)}, \\ V &= \frac{(s+\omega_0^S)^3(s^2+2\xi_v r s+r^2)}{s^3(s^2+2\xi_z r^2 s+r^2)}. \end{aligned} \tag{7.161}$$

Setpoint preshaping filter may be needed as in the case of the LQG controller. Alternatively, cascade structure with proportional position controller may be used as well. Fifth order velocity controller and sixth order position controller is obtained from the optimization algorithm.

Performance of the H_∞ velocity and position controller is shown in figures (7.30, 7.31) for the same system which was used in the LQG section. The LQG controller achieves faster settling times due to the reference step change at cost of slower disturbance compensation. Very similar results are obtained for various resonance ratio

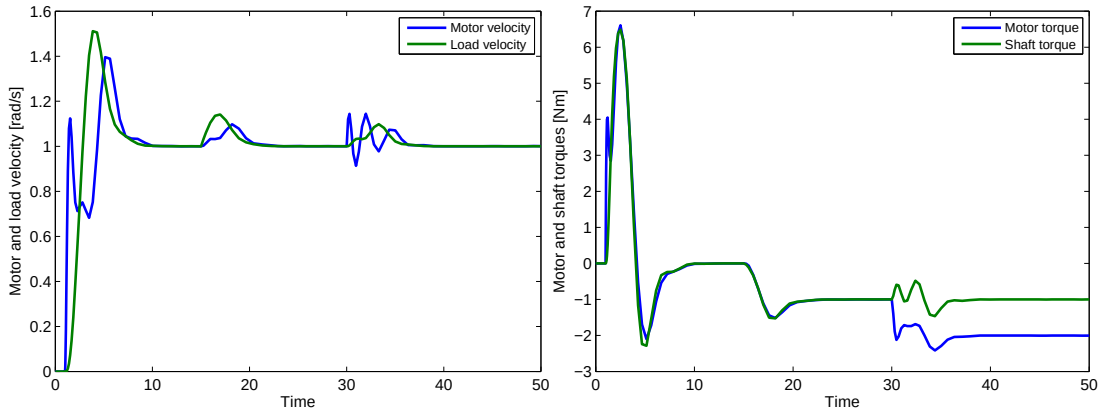

Figure 7.30: H_∞ **velocity control performance** - left motor and load velocity, right motor and shaft torque

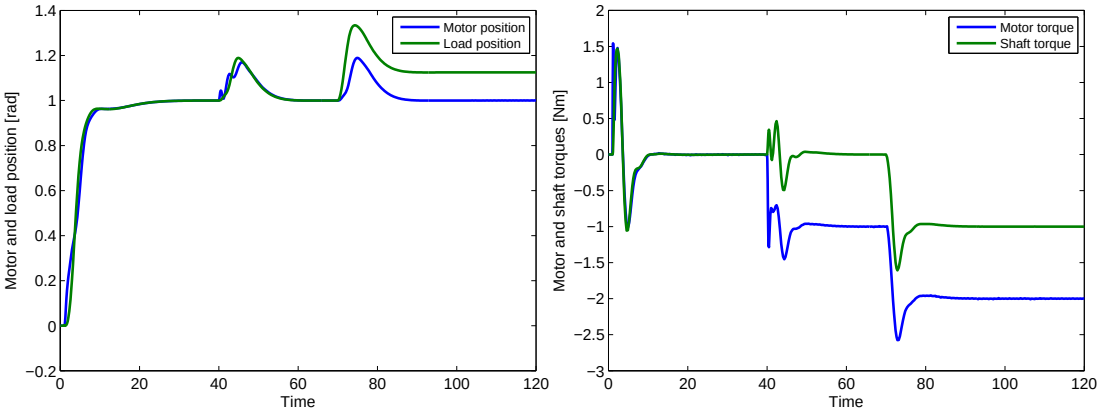

Figure 7.31: H_∞ **position control performance** - left motor and load position, right motor and shaft torque

values except for very low r for which even a full-order compensator cannot achieve suitable performance. The advantage of the H_∞ controller is that the frequency response shaping is more straightforward than the tuning of the quadratic cost function in the case of the LQG controller. The tuning parameters ω_0^S and ω_0^T have direct physical interpretation of closed-loop bandwidth and control effort and they can be used even for a manual fine tuning of the compensator. The disadvantage is, that an unstable compensator may be obtained from the optimization algorithm. Care should be taken to proper implementation of such controller.

7.3 Comparison of the proposed control schemes

All the presented control strategies, i.e. PI, PID, LQG and H-infinity control, are compared in terms of tracking performance and disturbance rejection in order to quantify a

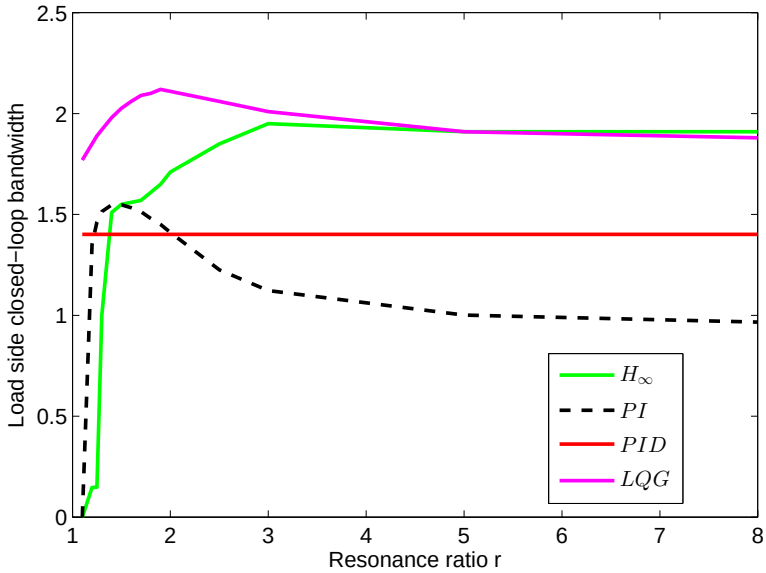

Figure 7.32: Reference tracking performance - maximum achievable closed-loop bandwidth for the individual control schemes as a function of the resonance ratio parameter, relative values w.r.t. the antiresonance frequency

possible advantage of utilization of higher order compensator. It is difficult to compare the individual design methods since they rely on different specifications of the closed-loop performance. Whereas the PI and PID controllers are based on the pole-placement method, LQG minimizes a quadratic cost functional and H_∞ uses the idea of loopshaping. To obtain some comparable results, the velocity compensators were tuned to meet following design requirements:

- Achieve maximum reference tracking performance in terms of the bandwidth of the transfer function T_l from the reference value to the load side motion
- Achieve properly damped response by limiting the peak $\|T_l\|_\infty \leq 1.5$
- Achieve a reasonable robustness in stability by limiting $\|S\|_\infty \leq 1.5$

All the controllers were tuned automatically based on the algorithms and weighting schemes presented in the previous sections. The procedure was repeated for different systems with the resonance ratio parameter varied in the range $r \in \langle 1.1, 8 \rangle$.

The results are shown in figures (7.32) and (7.33). The first plot shows the maximum achieved bandwidth of T_l as a function of the resonance ratio parameter. Relative values with respect to the antiresonance frequency are shown. The remaining two plots evaluate the disturbance rejection performance. The left plot shows the worst-case gain of the frequency response function from load-side disturbance torque to load velocity in the sense of the norm $\|\frac{\omega_l(s)}{T_l(s)}\|_\infty$. It expresses the level of attenuation the controller

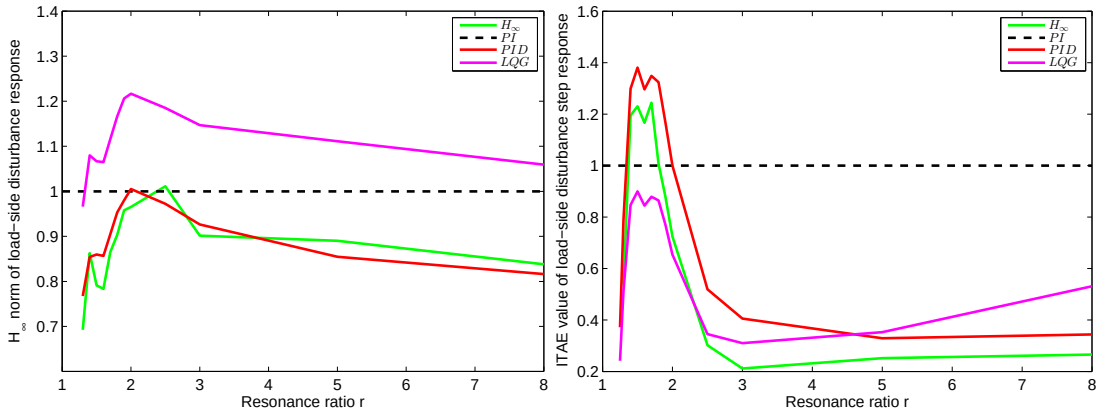

Figure 7.33: Disturbance rejection performance for the individual control schemes as a function of resonance ratio parameter, left worst case gain of the load-side disturbance frequency response function, right value of the ITAE criterion of load-side load torque step response

is able to provide in the closed-loop. The right plot shows the value of the ITAE cost function $\int_{t=0}^{\infty} t|\omega_l(t)|dt$ of the response to the unitary step in the load torque. It demonstrates the ability of the closed-loop to recover from disturbance in the time domain. Since the absolute values of these two performance indices change considerably with the varying r, the plots in Fig. (7.33) show the *relative* values with respect to the results achieved with the PI controller, for better readability.

The results lead to the following conclusions:

- The problem with controllability of low resonance ratio systems with $r < 1.3$ cannot be solved by using a higher order compensator. There are inherent fundamental limitations which arise from the nature of the system dynamics and from basic constraints of the feedback loop. The only way to avoid these problems is proper mechanical design of the system.

- Very similar results are achieved for well controllable systems in the range $r \in \langle 1.7, 2.3\rangle$ for all the control schemes. The LQG controller achieves the highest bandwidth at cost of slower disturbance rejection in this range. The improvement of the full order controllers compared to the PI compensator are questionable. Slight improvement of the disturbance attenuation is observed in the lower range $r \in \langle 1.3, 1.7\rangle$.

- The full advantage of the full order compensators can be exploited for high values of $r > 2.3$ where the performance of the basic PI control drops considerably. The PID controller was tuned to achieve the virtual resonance ratio $r = 2$. The addition of the derivative action in the PID controller allows to extend the range of applicable gains and recover the properties of lower resonance ratio systems.

The PID controller achieves up to 45% higher bandwidth with respect to the PI compensator. Up to 100% increase in bandwidth is observed for LQG and H_∞ controllers. The H_∞ controller is superior to the other control schemes in this range.

7.4 Control of multiple resonance system

Every real-world compliant mechanism is a distributed parameter system. Therefore, its dynamics can theoretically contain an infinite number of resonance modes. A linear lumped parameter model is always only an approximation of the overall system behaviour in a certain frequency range. The basic issue for the design of the motion control system is the *distribution of the individual resonance frequencies*. **Their location with respect to the desired bandwidth of the closed-loop system as well as their individual spacing determines proper control strategy which should be used**. As was explained in the introductory chapter, the system dynamics of a multi-mode system with colocated feedback can be written in the form of transfer function:

$$P(s) = \frac{\omega_m(s)}{T_m(s)} = \frac{K}{s} \frac{\prod_{i=1}^{n}(s^2 + 2\xi_{zi}\omega_{zi}s + \omega_{zi}^2)}{\prod_{i=1}^{n}(s^2 + 2\xi_i\omega_i s + \omega_i^2)}. \tag{7.162}$$

When the desired closed-loop bandwidth is much lower than the resonance and antiresonance frequencies of the first mode ω_{zi}, ω_i, the system can be considered as a rigid body and a feedback controller can be designed for the simplified model:

$$P(s) \approx \frac{K}{s} \frac{\prod_{i=1}^{n} \omega_{zi}^2}{\prod_{i=1}^{n} \omega_i^2}. \tag{7.163}$$

If the desired bandwidth overlaps with the first resonance mode location, its behaviour has to be taken into account by proper adjustment of the controller gains or structure. Carefully designed feedback compensator can actively compensate the resonance mode by relocation of its weakly damped poles. In this case we talk about **phase stabilization** since the controller performs a shaping of the loop transfer function in the vicinity of the crossover frequency to achieve stable and well damped closed-loop dynamics (Fig. 7.34).

When there are another resonance modes far enough from the crossover range, their contribution to the closed-loop dynamics is negligible as the excitation in the high frequency range drops off considerably due to the inherent low-pass nature of the mechanical systems and optionally thanks to an additional high-frequency roll-off provided by the compensator. The higher modes are **gain stabilized** in this case and only the first mode can be assumed in the simplified plant model.

The situation gets complicated when the second resonance mode approaches the first one. If there is enough loop transfer gain around the second resonance frequency, the mode receives enough energy to demonstrate the corresponding shape of vibrations leading to oscillatory closed-loop dynamics or even instability of the loop (so called spillover effect).

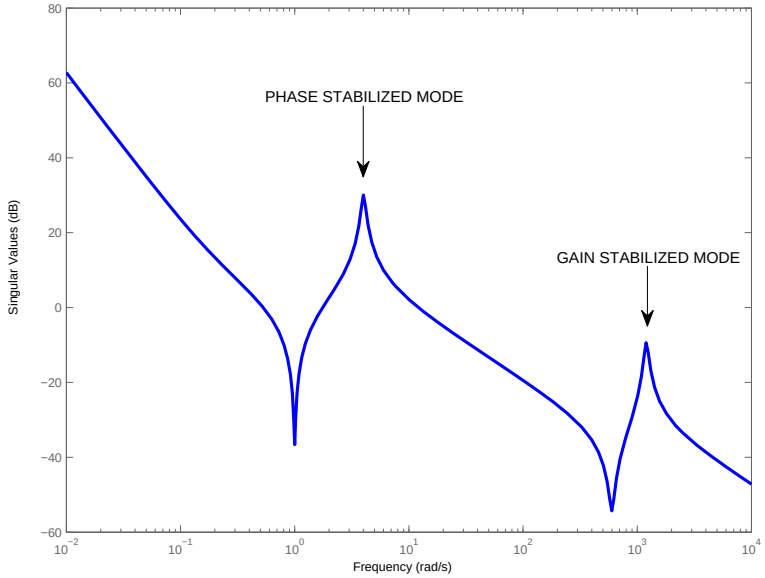

Figure 7.34: Multiple resonance control - phase vs gain stabilization

There are two fundamental approaches to correct this unwanted behaviour:

- **Reduction of the high-frequency loop transfer gain** to passively stabilize the higher modes
- **Addition of the dominant higher modes to the plant model** and adjustment of the compensator in such a way that phase stabilization is achieved

The first approach may be used with utilization of the active vibration methods proposed in the previous section. The design procedure is summarized in the following steps:

1. Truncate the high-frequency dynamics and use the single resonance mode model for the controller synthesis.
2. For the obtained compensator, evaluate the closed-loop performance with the *full plant model* including the higher resonance modes.
3. When the resulting closed-loop design does not meet the performance requirements, reduce the compensator gain by lowering the desired closed-loop bandwidth. This is done directly by the adjustment of the parameter ω^* in the PID control method, k_{bw} in the LQG scheme and ω_0^S in the case of H_∞ controller.
4. The bandwidth of the system cannot be reduced arbitrarily due to the fundamental limitations imposed by the first resonance mode. The closed-loop bandwidth cannot be significantly lower than the value of the first antiresonance frequency

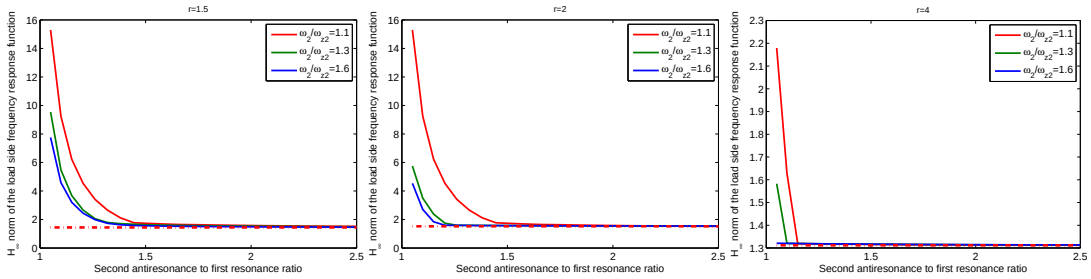

Figure 7.35: Multiple resonance PID control - performance deterioration of the closed loop designed with the simplified one mode model as the second resonance mode approaches the first one (the ratio ω_{z2}/ω_1 gets close to one), dot-dashed lines denote the nominal performance achieved for the single resonance system

when requesting active vibration damping. If the performance requirements still cannot be achieved by simple retuning of the controller, employ a shaping filter, preferably with a notch filter characteristics, which selectively reduces the loop gain around the higher resonance frequencies. The filter can shape the setpoint command in the feedforward path or the manipulating variable in the feedback loop. The advantages and drawbacks of each type of connection were discussed in the previous chapter related to the signal shaping. This approach can be designated as *composite vibration control*, as both active and passive stabilization via signal shaping is used simultaneously.

The second approach involves a controller design for the *extended plant model which includes all resonance modes appearing in the target range of the closed-loop bandwidth*. The analytical solution which was derived for the **PID controller** with the single mode system cannot be computed in the case of multiple resonance modes due to the exponential increase in complexity of the corresponding set of polynomial equations. The solution of the partial pole placement problem can be obtained numerically for a particular plant model. However, practical experiments show that the controller parameterization computed for the single mode model is very robust with respect to the perturbation by higher modes dynamics. The error in the precise placement of the assigned dominant poles due to the unmodeled dynamics is negligible compared to the contribution of weakly damped poles of higher resonances which cannot be sufficiently damped by the low order compensator and which may eventually cause an oscillatory behaviour when there is enough loop transfer gain.

This is demonstrated by the plots in Fig. (7.35) which show the performance deterioration in the presence of a second oscillatory mode. Each plot shows the peak of the load-side complementary sensitivity function $\|T_l(s)\|_\infty$ which expresses the amount of oscillations as a function of relative location of the second oscillatory mode with respect to the first one (the ratio of the second antiresonance frequency ω_{z2} to the first resonance frequency ω_1). Three colours in each plot denote the results achieved for various second resonance ratios ω_2/ω_{z2}. Three plots are shown for different values of

the first resonance ratio parameter $r = \omega_1/\omega_{z1}$. It is seen that nominal performance achievable with the single mode system (red dot-dashed line) is preserved until the second resonance mode gets very close to the first one. The performance deterioration is caused by the second pair of weakly damped poles which cannot be efficiently damped with the PID compensator. The situation is worse for poor controllable systems with low resonance ratios r and r_2. The performance may be improved by retuning of the controller for a lower closed-loop bandwidth. As the ratio ω_{z2}/ω_1 gets close to one, the first resonance mode becomes unobservable and its active stabilization is impossible with the use colocated motor side feedback. The only solution in this case is the *passive stabilization* with the use of the notch filter type shaping filter.

Active stabilization of multiple resonance modes is possible with the use of a full order compensator. The design of the LQG controller can be performed analogously to the single mode case by extending the plant model with the dynamics of the higher modes. The property of *pole-zero cancelation* in the case of the H_∞ optimization can be used for the derivation of controller which *combines active and passive stabilization* of the individual modes (e.g. active damping of the first resonance and passive stabilization of the second one). The same weighting scheme which was proposed for the single mode system can be used. The only difference is the extension of the plant model with the higher resonance modes description (7.162). The resulting compensator always cancels the weakly damped poles of the second and higher resonances and achieves their passive stabilization while the first mode is phase stabilized due to the specification of the partial pole placement in the weighting function $V(s)$. For each additional resonance mode, the overall order of the compensator is raised by two. **In most practical cases, the assumption of first two dominant resonance modes is sufficient for the purpose of vibration control**. This leads to a seventh order velocity controller and eighth order position controller. Order reduction techniques may be used to reduce the controller complexity and to simplify its implementation. Method of balanced state representations gives good results [216]. Active stabilization of multiple resonance modes may be achieved with the *partial pole-placement method* by proper adjustment of the output disturbance weighting function V. An example is given for a two mode system, for which the weighting filter becomes:

$$V(s) = \frac{(s+\omega_0^S)^2(s^2+2\xi_v\omega_1 s+\omega_1^2)(s^2+2\xi_{v2}\omega_2 s+\omega_2^2)}{s^2(s^2+2\xi_1\omega_1 s+\omega_1^2)(s^2+2\xi_2\omega_2 s+\omega_2^2)}. \tag{7.164}$$

Damping of the open loop poles is changed to the specified level given by coefficients ξ_v, ξ_{v2}.

The proposed method is demonstrated on an example of a two mode system with parameters:

$$\omega_{z1}=1,\ \xi_{z1}=0.01,\ \omega_1=4,\ \xi_1=0.04,\ \omega_{z2}=6,\ \xi_{z2}=0.01,\ \omega_2=12,\ \xi_2=0.02. \tag{7.165}$$

Three compensator designs are compared. The first one is a velocity PI compensator designed for the truncated model with the first resonance mode only. Second one

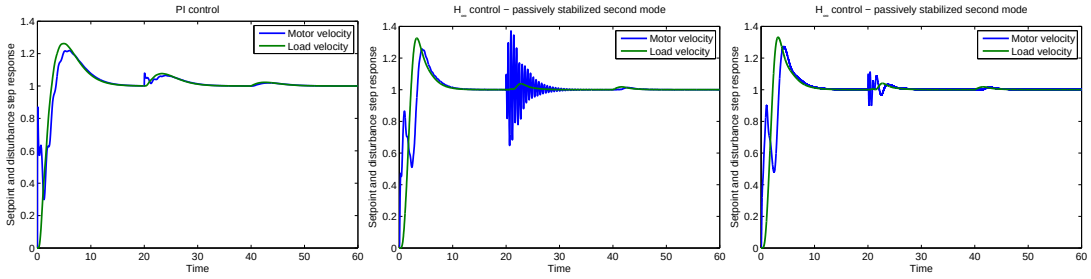

Figure 7.36: Two resonance system control - setpoint and disturbance response for three different compensator designs - left PI controller, center H_∞ controller with passive stabilization of the second resonance, right H_∞ controller with active compensation of both modes

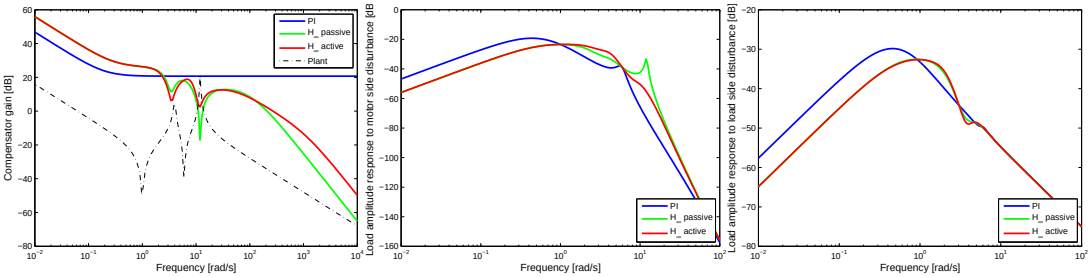

Figure 7.37: Two resonance system control - compensator, motor side disturbance and load disturbance amplitude frequency response functions for three controller designs

is a H_∞ compensator designed for the full two mode model with the weighting scheme proposed for active stabilization of the *first mode only*. The third one is H_∞ controller designed for active stabilization of *both resonance modes*. Setpoint change and disturbance response to both motor and load side external torques is shown in Fig. (7.36). Even the simplest PI controller can achieve sufficient performance and well damped setpoint and disturbance response. The second resonance mode is gain stabilized and its influence on the dynamics of the closed-loop is negligible. The only drawback is relatively low closed-loop bandwidth which is limited by the first antiresonance frequency.

Almost two times faster closed-loop response is achieved with the H_∞ controllers. The first design shows poor damping of the motor side disturbances since the second resonance is canceled by compensator zeros leading to loss of controllability. When no significant disturbances are present in a real system the passive controller may work well as the load side disturbances are damped sufficiently. The second design shows active compensation of both motor and load side external torques thanks to phase stabilization of both resonance modes.

The properties of the individual designs can be seen in the frequency domain by plotting the amplitude of the compensators frequency response function which demonstrates how the loopshaping is achieved (Fig.7.37 left). The simple structure of the PI controller does not allow significant changes in its gain over the frequency range

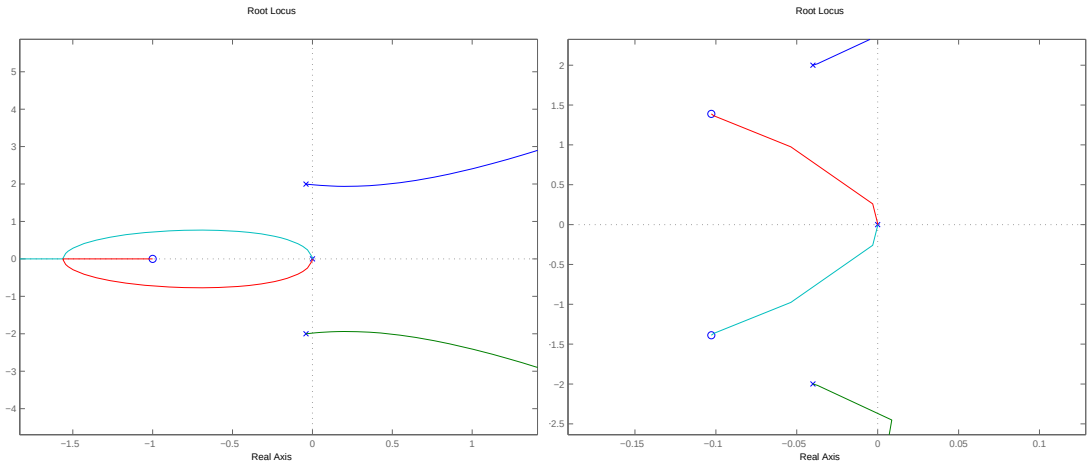

Figure 7.38: Load side-feedback utilization - root locus plots for the PI (left) and PID controller (right) used for the load-side feedback stabilization of a two-mass compliant system

which leads to limitation on achievable bandwidth. Higher order of the H_∞ compensators offers more degrees in freedom in shaping of the loop transfer function. Both H_∞ controllers apply higher low frequency gains which leads to faster closed-loop response. They actively compensate the first resonance mode which is seen by drop of the compensator gain in its region. Their amplitude response becomes different at the higher frequencies. The first design cancels the weakly damped poles of the second mode which leads to deep notch around its resonance frequency. On the contrary, the amplitude of the second design is much larger indicating the active compensation. The passive cancelation is demonstrated by the peak in the amplitude frequency response of the motor side disturbance which explains the oscillations observed in the time domain. The active stabilization of the second mode is achieved at the cost of increased high-frequency gain of the compensator.

7.5 Load side feedback utilization

Installation of an additional load side velocity or position sensor can overcome some performance limitations of the motor side feedback. The main advantages are:

- **Direct measurement of the controlled output**
  Since the main objective is the motion control of the load side, it is natural to use the load measurement as a feedback signal. This eliminates the steady state position error due to the compliance in the drivetrain.

- **Elimination of the antiresonance dynamics**
  The load side dynamics does not contain the weakly damped antiresonance zeros

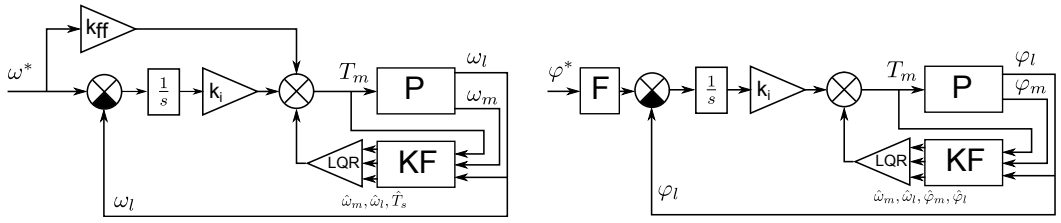

Figure 7.39: LQG compensator with combined motor and load feedback - left velocity controller, right position controller, P - plant, KF - Kalman filter, k_i - integral feedback gain, k_{ff} - proportional feed-forward gain, F - reference command prefilter, LQR - optimal static state feedback

which complicate the identification and which significantly affect the range of applicable feedback gains. There is no problem with the pole-zero cancelation, the system is stable and minimum phase and thus there are no theoretical limitations on achievable performance.

On the contrary, some important drawbacks of the load side feedback should be considered:

- **Problem with controllability using low order controllers**
  It can be shown that the system cannot be effectively stabilized by a low order PI or PID compensator. This is demonstrated in Fig. (7.38) which shows the root locus plots for the two-mass compliant system with the load-side feedback. Due to the lack of open-loop zeros, the closed-loop poles inevitably approach the right half-plane regardless of the controller parameters. A full order compensator has to be used in this case.

- **Practical limitation on achievable bandwidth**
  The closed-loop bandwidth cannot be much higher than the value of the first resonance frequency without having a perfect feedback sensor and model of the plant. As there is a large drop of the gain and phase beyond the system resonance, this must be compensated by large amount of high frequency gain in the controller making the closed-loop very sensitive to the measurement noise and modelling errors.

The next section presents the procedure of load-side feedback controller synthesis in the LQG and H_∞ framework.

7.5.1 LQG control

The compensator can be designed in the same manner as in the case of the motor side feedback. The only difference is the integral part which is now introduced from the load side process variable to impose the zero steady state error. Velocity controller

design is given as an example. The state space model for the LQ optimal state feedback design is changed to:

$$\dot{\boldsymbol{x}} = \begin{bmatrix} \dot{\omega}_m \\ \dot{\omega}_l \\ \dot{T}_s \\ \dot{x}_i \end{bmatrix} = \begin{bmatrix} -\frac{b}{I_m} & \frac{b}{I_m} & -\frac{1}{I_m} & 0 \\ \frac{b}{I_l} & -\frac{b}{I_l} & \frac{1}{I_l} & 0 \\ k & -k & 0 & 0 \\ 0 & -1 & 0 & 0 \end{bmatrix} \boldsymbol{x} + \begin{bmatrix} \frac{1}{I_m} \\ 0 \\ 0 \\ 0 \end{bmatrix} T_m. \tag{7.166}$$

The quadratic cost function remains unchanged compared to the motor feedback case (Eq. 7.137). Again, the single parameter k_{bw} is used for the tuning of the closed-loop bandwidth. The Kalman filter **can be easily adapted to use both motor and load side feedback signals**. This allows the use of all available information on the state of the system. The observer is designed for the extended plant model in the form of:

$$\begin{aligned} \dot{\boldsymbol{x}} &= \begin{bmatrix} \dot{\omega}_m \\ \dot{\omega}_l \\ \dot{T}_s \\ \dot{T}_l \end{bmatrix} = \begin{bmatrix} -\frac{b}{I_m} & \frac{b}{I_m} & -\frac{1}{I_m} & 0 \\ \frac{b}{I_l} & -\frac{b}{I_l} & \frac{1}{I_l} & \frac{1}{I_l} \\ k & -k & 0 & 0 \\ 0 & 0 & 0 & 0 \end{bmatrix} \boldsymbol{x} + \begin{bmatrix} \frac{1}{I_m} \\ 0 \\ 0 \\ 0 \end{bmatrix} T_m + \begin{bmatrix} 1 & 0 \\ 0 & 0 \\ 0 & 0 \\ 0 & 1 \end{bmatrix} \boldsymbol{w}, \\ \boldsymbol{y} &= \begin{bmatrix} \omega_m \\ \omega_l \end{bmatrix} + \boldsymbol{v}, \end{aligned} \tag{7.167}$$

with the noise covariance parameters chosen as:

$$E(\boldsymbol{w}\boldsymbol{w}^{\boldsymbol{T}}) = diag\{1,\ 1\},\ E(\boldsymbol{v}\boldsymbol{v}^{\boldsymbol{T}}) = diag\{0.1, 0.1\}. \tag{7.168}$$

The overall structure of the controller can be seen in Fig. (7.39). With an equal closed-loop bandwidth setting, the nominal performance is almost identical to that obtained with the motor feedback only. However, the introduction of the second feedback signal *considerably improves the robustness of the closed-loop to the modelling errors and external disturbances*. This is shown in tables (7.1) and (7.2) which quantify the amount of parametric variations which are allowed prior to the loss of closed-loop performance and stability. Both controllers were tuned for the same bandwidth approximately equal to the value of the first antiresonance frequency achieving the same nominal setpoint and disturbance response. Changes of the load side inertia and stiffness of the drive-train were assumed as the most common form of parametric uncertainty occurring in the industrial motion control systems. This shifts both resonance and antiresonance frequencies as well as static gain of the system. Robustness to an unmodeled high-frequency dynamics was also evaluated by adding a time-delay which models a sensor or actuator lag. Robust performance was considered to be achieved when the overshoot in the setpoint step response was less than 30% and settling time was at most twice as long as in the nominal case. **Significant improvement of the robustness to both structured and unstructured uncertainty is observed over a wide range of resonance ratio parameter.**

r	**1.5**	**2**	**3**	**5**	**8**
Motor side feedback					
${}^1\overline{\boldsymbol{I_{lp}}} = max(\frac{I_{lp}}{I_{ln}})$	$+\infty$	22	6	7.13	5.9
${}^1\boldsymbol{I_{lp}} = min(\frac{I_{lp}}{I_{ln}})$	0.46	0.54	0.37	0.19	0.09
${}^1\overline{\boldsymbol{k_p}} = max(\frac{k_p}{k_n})$	2.04	1.67	1.85	3.2	6.2
${}^1\boldsymbol{k_p} = min(\frac{k_p}{k_n})$	0.11	0	0	0.38	0.55
${}^1\overline{\boldsymbol{T_D^{max}}}$	0.2	0.16	0.12	0.09	0.07
Motor+load feedback					
${}^2\overline{\boldsymbol{I_{lp}}} = max(\frac{I_{lp}}{I_{ln}})$	$+\infty$	$+\infty$	150	7.5	6.85
${}^2\boldsymbol{I_{lp}} = min(\frac{I_{lp}}{I_{ln}})$	0.52	0.42	0.16	0.04	0.03
${}^2\overline{\boldsymbol{k_p}} = max(\frac{k_p}{k_n})$	$+\infty$	$+\infty$	$+\infty$	$+\infty$	$+\infty$
${}^2\boldsymbol{k_p} = min(\frac{k_p}{k_n})$	0.18	0.29	0.26	0.08	0.03
${}^2\overline{\boldsymbol{T_D^{max}}}$	0.25	0.335	0.395	0.19	0.19
Load side feedback improvement					
$\boldsymbol{\Delta\overline{I_{lp}}} = ({}^2\overline{\boldsymbol{I_{lp}}} - {}^1\overline{\boldsymbol{I_{lp}}}).100\%$	0	$+\infty$	$+14400\%$	$+37\%$	$+95\%$
$\boldsymbol{\Delta I_{lp}} = ({}^1\boldsymbol{I_{lp}} - {}^2\boldsymbol{I_{lp}}).100\%$	-6%	$+12\%$	$+21\%$	$+15\%$	$+6\%$
$\boldsymbol{\Delta\overline{k_p}} = ({}^2\overline{\boldsymbol{k_p}} - {}^1\overline{\boldsymbol{k_p}}).100\%$	$+\infty$	$+\infty$	$+\infty$	$+\infty$	$+\infty$
$\boldsymbol{\Delta k_p} = ({}^1\boldsymbol{k_p} - {}^2\boldsymbol{k_p}).100\%$	-7%	-29%	-26%	$+30\%$	$+52\%$
$\boldsymbol{\Delta\overline{T_D^{max}}} = ({}^2\overline{\boldsymbol{T_D^{max}}}/{}^1\overline{\boldsymbol{T_D^{max}}}).100\%$	125%	209%	329%	211%	271%

Table 7.1: Robustness in *stability* w.r.t. parameter variations and unmodelled dynamics

7.5.2 H_∞ control

The H_∞ controller can be designed for the load side feedback similarly to the collocated sensor case. The velocity compensator is given as an example. The normalized extended plant model for the load dynamics augmented with the integrator is given as:

$$P_{el}(s) = \frac{P(s)}{s} = \frac{1}{s^2}\frac{(2\xi_z s + 1)}{(s^2 + 2\xi_z r^2 s + r^2)}. \tag{7.169}$$

The weighting scheme for the Mixed sensitivity optimization is chosen as:

$$\begin{aligned} W_1 &= \frac{1}{M_s}, \\ W_2 &= \frac{1}{M_t}\frac{(s+\omega_0^T)^4}{(s+\omega_0^S)^2(s^2+2\xi_v r s + r^2)(\omega_0^T r)^2}, \\ V &= \frac{(s+\omega_0^S)^2(s^2+2\xi_v r s + r^2)}{s^2(s^2+2\xi_z r^2 s + r^2)}. \end{aligned} \tag{7.170}$$

The weighting functions are almost identical to that used in the motor feedback case except for the numerator of $W_2(s)$ which sets the maximum closed-loop bandwidth.

r	1.5	2	3	5	8
Motor side feedback					
${}^1\overline{\boldsymbol{I_{lp}}} = max(\frac{I_{lp}}{I_{ln}})$	1.4	1.55	1.6	1.5	1.6
${}^1\boldsymbol{I_{lp}} = min(\frac{I_{lp}}{I_{ln}})$	0.49	0.69	0.72	0.26	0.18
${}^1\overline{\boldsymbol{k_p}} = max(\frac{k_p}{k_n})$	1.7	1.35	1.34	2.7	5.1
${}^1\boldsymbol{k_p} = min(\frac{k_p}{k_n})$	0.65	0.7	0.65	0.53	0.53
${}^1\boldsymbol{T_D^{max}}$	0.2	0.16	0.12	0.09	0.07
Motor+load feedback					
${}^2\overline{\boldsymbol{I_{lp}}} = max(\frac{I_{lp}}{I_{ln}})$	2.05	2.5	2.7	1.5	1.5
${}^2\boldsymbol{I_{lp}} = min(\frac{I_{lp}}{I_{ln}})$	0.2	0.51	0.63	0.1	0.07
${}^2\overline{\boldsymbol{k_p}} = max(\frac{k_p}{k_n})$	$+\infty$	$+\infty$	$+\infty$	$+\infty$	$+\infty$
${}^2\boldsymbol{k_p} = min(\frac{k_p}{k_n})$	0.36	0.51	0.49	0.25	0.13
${}^2\boldsymbol{T_D^{max}}$	1.15	1.2	1.3	1.3	1.28
Load side feedback improvement					
$\boldsymbol{\Delta\overline{I_{lp}}} = ({}^2\overline{\boldsymbol{I_{lp}}} - {}^1\overline{\boldsymbol{I_{lp}}}).100\%$	+65%	+95%	+110%	0	-10%
$\boldsymbol{\Delta I_{lp}} = ({}^1\boldsymbol{I_{lp}} - {}^2\boldsymbol{I_{lp}}).100\%$	+29%	+18%	+9%	+16%	+11%
$\boldsymbol{\Delta\overline{k_p}} = ({}^2\overline{\boldsymbol{k_p}} - {}^1\overline{\boldsymbol{k_p}}).100\%$	$+\infty$	$+\infty$	$+\infty$	$+\infty$	$+\infty$
$\boldsymbol{\Delta k_p} = ({}^1\boldsymbol{k_p} - {}^2\boldsymbol{k_p}).100\%$	+29%	+19%	+16%	+28%	+40%
$\boldsymbol{\Delta\overline{T_D^{max}}} = ({}^2\overline{\boldsymbol{T_D^{max}}}/{}^1\overline{\boldsymbol{T_D^{max}}}).100\%$	575%	774%	1083%	1477%	1855%

Table 7.2: Robustness in *performance* w.r.t. parameter variations and unmodelled dynamics

As there is no fundamental limitation on the achievable bandwidth, the numerator is adjusted to set the cutoff frequency of the complementary sensitivity function to the value of the parameter ω_0^T. Its value along with the performance specification parameter ω_0^S is obtained automatically in the optimization routine which searches for the fastest compensator which meets the constraints $M_s,\ M_t$ for the peak values of the closed-loop sensitivity functions. Alternatively, the setting of $\omega_0^S,\ \omega_0^T$ may be left as a tuning parameter for the manual adjustment of the controller.

The advantage of the load-side feedback is the possibility of arbitrary adjustment of the closed-loop bandwidth without any restrictions imposed by the antiresonance dynamics. However, **the high-frequency gain of the resulting compensator increases considerably when pushing the bandwidth beyond the value of the first resonance frequency** (Fig. 7.40). This becomes a limiting factor due to the amplification of the measurement noise and possible excitation of an unmodeled high-frequency dynamics. Practical experiments have shown that both nominal performance and robustness is worse compared to the LQG controller with the composite motor and load feedback. A multivariable H_∞ controller which uses both feedback signals can be designed as well. However the choice of the weighting scheme is not so straightforward as in the

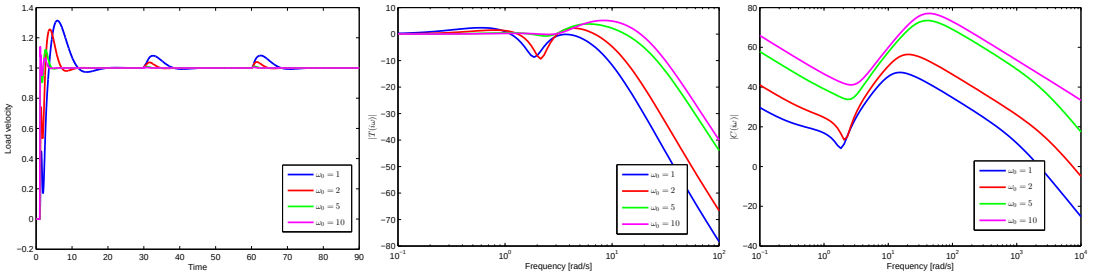

Figure 7.40: H_∞ load side feedback compensator - left setpoint and disturbance response of the load velocity, center gain of the load-side complementary sensitivity function $|T(i\omega)|$, right controller amplitude frequency response $|C(i\omega)|$ for the different settings of the bandwidth $\omega_0^S = \{1, 2, 5, 10\} rad/s$, ω_0^T is tuned automatically to achieve $M_s, M_t \leq 1.8$

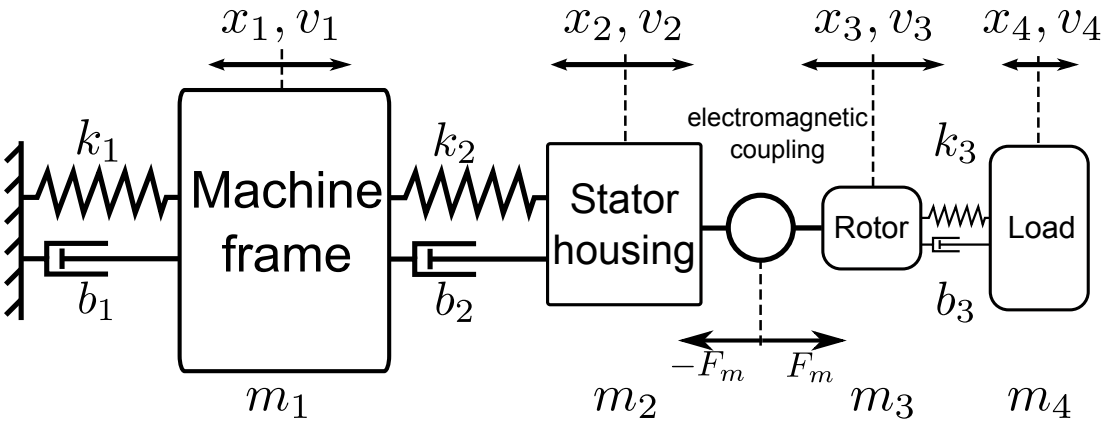

Figure 7.41: Flexible frame model - mechanical setup with compliantly coupled load, flexible frame and actuator mounting

SISO case and no suitable set of weighting functions with a small number of physically intuitive parameters which would be useful for the purpose of automatic tuning was found until now. This is left for a future research.

7.6 Flexible frame modelling and control

A compliant coupling between the actuator and a driven load is not the only potential source of mechanical oscillations in motion control systems. Low stiffness of the machine frame or an improper dimensioning of the actuator mounting may lead to the unwanted vibrations as well. Precise identification of complex machine dynamics requires very specific knowledge about its mechanical structure. However, a relatively simple problem oriented model may be constructed for the purpose of a qualitative analysis of the influence of the frame flexibility on the achievable quality of control.

A **four-mass flexible frame model** is introduced in Fig. (7.41). The static part of the system is represented by a machine frame and an actuator stator bodies. They are connected by compliant spring-damper elements to each other and to the ground. The moving part is modeled as a two-mass flexible system consisting of rotor and load inertias which is coupled with the static part through an electromagnetic force/torque produced by the actuator. The system dynamics is governed by a linear state space model:

$$\dot{\boldsymbol{x}} = \begin{bmatrix} \dot{x_1} \\ \dot{v_1} \\ \dot{x_2} \\ \dot{v_2} \\ \dot{x_3} \\ \dot{v_3} \\ \dot{x_4} \\ \dot{v_4} \end{bmatrix} = \begin{bmatrix} 0 & 1 & 0 & 0 & 0 & 0 & 0 & 0 \\ \frac{-k_1-k_2}{m_1} & \frac{-b_1-b_2}{m_1} & \frac{k_2}{m_1} & \frac{b_2}{m_1} & 0 & 0 & 0 & 0 \\ 0 & 0 & 0 & 1 & 0 & 0 & 0 & 0 \\ \frac{k_2}{m_2} & \frac{b_2}{m_2} & -\frac{k_2}{m_2} & -\frac{b_2}{m_2} & 0 & 0 & 0 & 0 \\ 0 & 0 & 0 & 0 & 0 & 1 & 0 & 0 \\ 0 & 0 & 0 & 0 & -\frac{k_3}{m_3} & -\frac{b_3}{m_3} & \frac{k_3}{m_3} & \frac{b_3}{m_3} \\ 0 & 0 & 0 & 0 & 0 & 0 & 0 & 1 \\ 0 & 0 & 0 & 0 & \frac{k_3}{m_4} & \frac{b_3}{m_4} & -\frac{k_3}{m_4} & -\frac{b_3}{m_4} \end{bmatrix} \boldsymbol{x} + \\ + \begin{bmatrix} 0 & 0 & 0 \\ 0 & 0 & 0 \\ 0 & 0 & 0 \\ -\frac{1}{m_2} & 0 & \frac{1}{m_2} \\ 0 & 0 & 0 \\ \frac{1}{m_3} & 0 & 0 \\ 0 & 0 & 0 \\ 0 & \frac{1}{m_4} & 0 \end{bmatrix} \begin{bmatrix} F_m \\ F_l \\ F_s \end{bmatrix}, \; \boldsymbol{y} = \begin{bmatrix} v_3 - v_2 \\ v_4 - v_2 \\ x_3 - x_2 \\ x_4 - x_2 \end{bmatrix} = \begin{bmatrix} v_r^s \\ v_l^s \\ p_r^s \\ p_l^s \end{bmatrix}, \tag{7.171}$$

where F_m is the electromagnetic force/torque produced by the motor, F_l, F_s denote external disturbances acting on the load and actuator and the outputs are defined as the relative position and velocities in the *stator coordinates* which are measured by installed motor or load-side sensors.

Considering the motor side feedback, we obtain a following transfer function from the motor force to the measured rotor velocity:

$$\begin{aligned} P(s) = \frac{v_r^s(s)}{F_m(s)} &= \frac{m_4 s^2 + b_3 s + k_3}{s(m_4 m_3 s^2 + b_3(m_3 + m_4)s + k_3(m_3 + m_4))} + \\ &+ \frac{s(m_1 s^2 + (b_1 + b_2)s + k_1 + k_2)}{m_2 m_1 s^4 + (m2(b_1 + b_2) + b_2 m_1)s^3 + (k_2(m_2 + m_1) + b_2 b_1 + m_2 k_1)s^2 + (k_2 b_1 + b_2 k_1)s + k_2 k_1} \\ &\triangleq P_m(s) + P_f(s). \end{aligned} \tag{7.172}$$

It is seen that the overall dynamics seen on the motor shaft encoder consists from the flexible motor+load part $P_m(s)$ which corresponds to the standard two-mass compliant system and an additive dynamics of the flexible frame and stator $P_f(s)$. Assuming a weakly damped systems both on the stator and rotor side, the transfer functions may

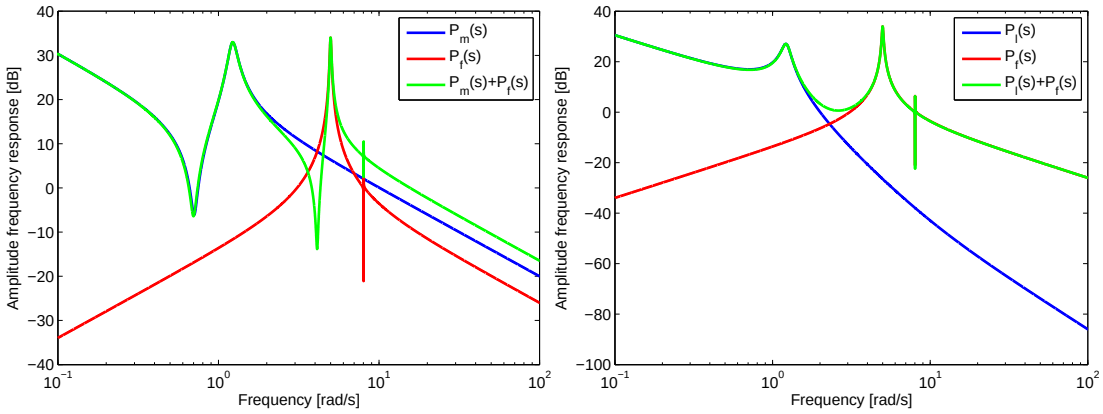

Figure 7.42: Flexible frame system dynamics - amplitude frequency response functions for the motor (left) and load (right) side velocities

be rewritten in terms of the corresponding resonance and antiresonance frequencies:

$$P_m(s) = \frac{K_1}{s}\frac{(s^2+2\xi_z\omega_z s+\omega_z^2)}{(s^2+2\xi_m\omega_m s+\omega_m^2)} = \frac{b_m(s)}{a_m(s)},$$
$$P_f(s) = \frac{K_2 s(s^2+2\xi_{zs}\omega_{zs} s+\omega_{zs}^2)}{(s^2+2\xi_{s1}\omega_{s1} s+\omega_{s1}^2)(s^2+2\xi_{s2}\omega_{s2} s+\omega_{s2}^2)} = \frac{b_s(s)}{a_s(s)}. \tag{7.173}$$

The overall dynamics is obtained as:

$$P(s) = P_m(s)+P_f(s) = \frac{b_m(s)a_s(s)+b_s(s)a_m(s)}{a_s(s)a_m(s)} =$$
$$= \frac{K_3(s^2+2\overline{\xi}_{z1}\overline{\omega}_{z1}s+\overline{\omega}_{z1})(s^2+2\overline{\xi}_{z2}\overline{\omega}_{z2}s+\overline{\omega}_{z2})(s^2+2\overline{\xi}_{z3}\overline{\omega}_{z3}s+\overline{\omega}_{z3})}{s(s^2+2\xi\omega s+\omega^2)(s^2+2\xi_{s1}\omega_{s1}s+\omega_{s1}^2)(s^2+2\xi_{s2}\omega_{s2}s+\omega_{s2}^2)}. \tag{7.174}$$

The system contains three flexible modes, two of them corresponding to the frame and one coming from the compliant load. Their contribution to the overall dynamics is indistinguishable from the motor side measurement only. However, from the control point of view, it is not necessary to identify the main source of oscillations but to stabilize the overall system. In most cases, the load side dynamics will determine the dominant first resonance of the system unless there is a poor mechanical design of the machine frame and actuator mounting. **The plant can be treated as a general three mode system and all the previously mentioned methods for the compensator design can be used as well**. The relative placement of the individual resonance and antiresonance frequencies determines a suitable control strategy.

A numerical exampleis given to demonstrate three different design methods for a flexible frame system. The four-mass model (7.171) is assumed with the rotor feedback only available for the measurement. The system parameters are given as:

$$m_1 = 70,\ k_1 = 4500,\ b_1 = 0.01,\ m_2 = 0.2,\ k_2 = 5,\ b_2 = 0.02,\ m_3 = 0.1,\ k_3 = 0.1,\ b_3 = 0.01, \tag{7.175}$$

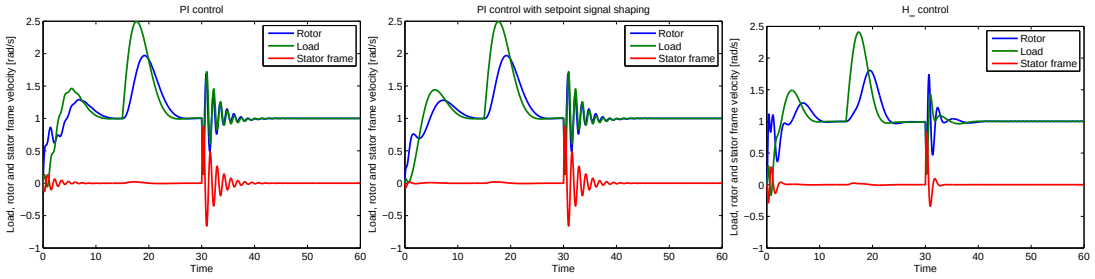

Figure 7.43: Flexible frame system control - comparison of closed-loop performance, left PI velocity controller designed for the active stabilization of the first load resonance mode only, center - PI controller + setpoint signal shaper for the passive stabilization of the second frame resonance, right - $H\infty$ controller designed for the active vibration damping of both load and frame resonances

which leads to the resonance and antiresonance values:

$$\omega_m = 1.22,\ \omega_{s1} = 5,\ \omega_{s2} = 8.03,\ \overline{\omega}_{z1} = 0.7,\ \overline{\omega}_{z2} = 4.12,\ \overline{\omega}_{z3} = 8.02. \tag{7.176}$$

The amplitude frequency response function of the system is shown in Fig. (7.42) which shows the overall dynamics of the rotor and load velocity with respect to the actuator input. Contribution of the motor and frame part of the dynamics is demonstrated as well. The low-frequency behaviour of the system is mainly determined by the load resonance. The frame compliance adds another two resonance modes. The last of them is poorly observable both from rotor and load-side velocity measurement due to the poor resonance ratio $\omega_{s2}/\overline{\omega}_{z3} \approx 1$. Its stabilization is practically infeasible without installing an additional instrumentation, e.g. an accelerometer attached to the machine frame.

The first control strategy is to truncate the higher resonance modes dynamics and employ the standard PI velocity controller for the active stabilization of the first resonance only. Using the proposed partial pole-placement method, a compensator with control gains tuned as $K_p = 1.94,\ K_i = 0.4$ is obtained. Closed-loop setpoint and disturbance response can be seen in Fig. (7.43) left. Rotor, load and stator velocities are plotted with the step change in the reference command at $t = 0$, step in the load disturbance force F_l occuring at $t = 15$ and stator disturbance force F_l step comming at $t = 30$. It is seen that the controller is able to stabilize the resonance of the load. The frame compliance is not compensated. The control performance can be improved by adding a setpoint preshaping filter tuned for the second resonance frequency. This eliminates the oscillations of the frame due to the setpoint tracking (Fig. 7.43 center), disturbance response at the stator side remains oscillatory. Active stabilization of both load and frame resonances can be achieved with the proposed H_∞ controller. Fifth order compensator is obtained after order reduction in the form of transfer function $K(s) = \frac{-0.067(s-146)(s+0.27)(s^2+0.52s+2.02)}{s(s^2-0.96s+2.9)(s^2+22.35s+274.2)}$. It is seen that both load and frame side disturbances are compensated and the first resonances are actively stabilized.

The four-mass model may be adjusted to cover an arbitrary number of load and frame resonance modes by simply adding or removing the appropriate number of mass elements from the kinematic chain. By setting $k_1 = \infty$, the dynamics reduces to a three-mass system with one load and one frame resonances. Assuming $k_1 = \infty,\ k_3 = \infty$, we get a two-mass system consisting of a rigid load with compliant actuator mounting which can be transformed to an equivalent flexible shaft system described in the previous chapter. The simplest case is obtained for $k_1 = k_2 = k_3 = \infty$ which leads to a standard 1DoF rigid motor-load system. The important conclusion of the provided analysis is that *the knowledge of a particular structure of the mechanical system is not required for the purpose of vibration control and the automatic identification and compensator design can be performed conveniently in the frequency domain for a wide class of physical plants*.

7.7 Summary

This section presented a systematic approach to active vibration control of oscillatory electromechanical systems. Special attention is paid to the cascade PID control structure which is prevalent in industrial applications. There are fundamental limitations on the closed-loop performance achievable with a low-order compensator when requesting the active vibration functionality. The attainable quality if control is dominantly influenced by the *resonance ratio* of the flexible modes of the system. Low resonance ratio systems are difficult to stabilize due to the loss of observability of the resonance modes whereas high resonance ratio leads to lower closed-loop bandwidth. A partial pole-placement method is used for the derivation of the whole set of admissible stabilizing PID controllers. A particular compensator is selected from the admissible set in the second optimization step according to a proper performance index. The derivative action of the PID control may be used to adjust the inappropriate resonance ratio and up to approximately 50% increase in bandwidth can be achieved compared to the PI control. The closed-loop performance can be further improved by using higher order compensators. Two design methods are proposed in the framework of optimal and robust control theory. The developed weighting schemes are universally applicable for a wide range of systems thanks to the introduced normalization in gain and time and proper adjustment of the performance criterions. The LQG and H_∞ compensators can achieve up to 100% bandwidth improvement compared to the conventional PI control. Robust controller can be designed for an uncertainty model obtained during the identification experiment. The final part of the chapter discusses the possibility of utilization of the load side feedback and machine frame vibration damping.

8

Application results

This chapter presents some of the application results which use the theoretical methods developed in the thesis. Most of them were achieved in terms of various R&D projects conducted at the University of West Bohemia in collaboration with industrial partners. Detailed description can be found in the referenced literature.

8.1 Gantry crane control

Gantry cranes are extensively used for various manipulation tasks all over the world. One of the particular problems concerning the motion control is the flexibility of the rope which which brings an inherent issue of hanging load oscillations which can be excited by the crane movement. Unwanted sway of the load during the process of manipulation may cause a collision with an obstacle or a damage to the cargo. Precise motion control may be achieved by employing the signal shaping techniques presented in the thesis.

The 1DoF gantry crane model is shown in Fig. (8.1). The equation of motion can be derived using the Lagrange's equation method [180]. The kinetic energy of the system is defined as:

$$\begin{aligned} T &= \frac{1}{2} m \dot{\boldsymbol{r}} \cdot \dot{\boldsymbol{r}} = \frac{1}{2} m (\dot{r}_x^2 + \dot{r}_y^2) = \frac{1}{2} m \left[\dot{x}^2 + 2 \dot{x} \dot{\theta} l \cos(\theta) + (\dot{\theta} l)^2 \right]; \\ \mathbf{r} &= \begin{bmatrix} r_x \\ r_y \end{bmatrix} = \begin{bmatrix} x + l \sin(\theta) \\ l(1 - \cos(\theta)) \end{bmatrix}, \end{aligned} \tag{8.1}$$

where m is the mass of the hanging load, x is the crane position, l is the rope length, θ is the swing angle and $\boldsymbol{r}$ is the load radius vector.

The potential energy is computed as:

$$V = mgl\big(- \cos(\theta)\big). \tag{8.2}$$

The Euler-Lagrange euqation of the system is formed as:

$$\frac{d}{dt} \left(\frac{\partial L}{\partial \dot{\theta}} \right) - \frac{\partial L}{\partial \theta} = - \frac{\partial D}{\partial \dot{\theta}}, \tag{8.3}$$

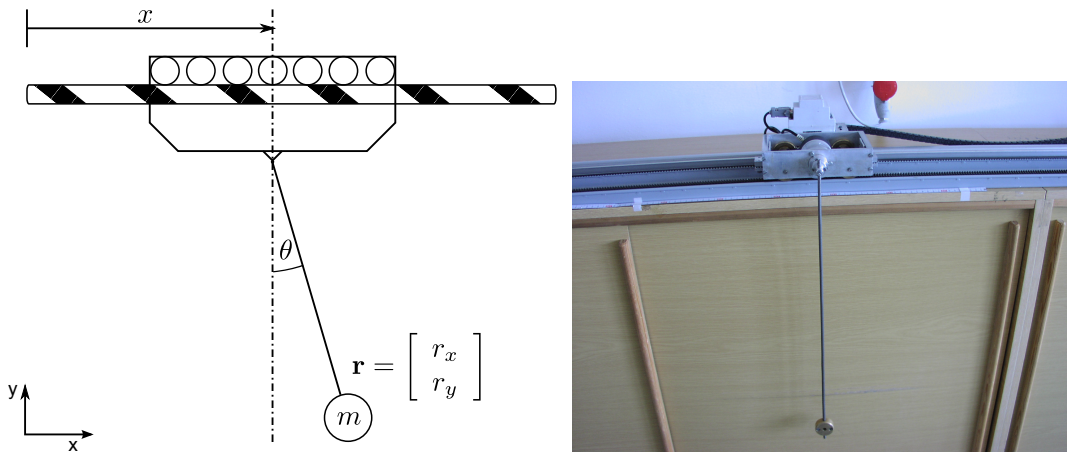

Figure 8.1: Gantry crane system - left kinematic setup, right experimental laboratory model

where $L = T - V$ is the Lagrangian and $D = \frac{1}{2}b\dot{\theta}^2$ is the Rayleigh dissipation function which describes the effect of the viscous friction b in the joint. Substitution from (8.1) and (8.2) yields:

$$\ddot{\theta} + \frac{b}{ml^2}\dot{\theta} + \frac{g}{l}\sin(\theta) = -\frac{1}{l}\ddot{x}\cos(\theta). \tag{8.4}$$

Considering the stable lower position of the load around $\theta \approx 0$, we may assume that $\sin(\theta) \approx \theta,\ \cos(\theta) \approx 1$ and the equation (8.4) reduces to a linear system:

$$\ddot{\theta} + \frac{b}{ml^2}\dot{\theta} + \frac{g}{l}\theta = -\frac{1}{l}\ddot{x}. \tag{8.5}$$

Assuming a crane system with a velocity control loop of the cart and applying the Laplace transform to (8.5), we obtain the transfer function from the cart speed to the load sway as:

$$P(s) = \frac{\theta(s)}{\dot{x}(s)} = -\frac{\frac{1}{l}s}{s^2 + \frac{b}{ml^2}s + \frac{g}{l}} = \frac{Ks}{s^2 + 2\xi\omega_n s + \omega_n^2};\ \omega_n = \sqrt{\frac{g}{l}},\ \xi = \frac{b}{2m\sqrt{gl^3}},\ K = -\frac{1}{l}. \tag{8.6}$$

Since there is usually no sensor measuring the sway angle, a convenient way to reduce the load oscillations is to use a setpoint shaping filter which processes the reference commands coming from a trajectory generator or from a human operator.

Figure (8.2) shows the experimental results obtained with the laboratory gantry crane model (Fig. 8.1 right). The cart is driven by a three-phase AC induction motor controlled by a frequency inverter. Standard cascade PID position control is implemented using the feedback from the incremental encoder installed on the motor shaft. A four-pulse ZV4 input shaper which filters the position reference command was designed with the tuning parameters chosen as $p_1 = 0.3, p_2 = 0.5$. The plant parameters $w_n = 4.22rad/s,\ \xi = 0.0079$ were obtained from the experimental identification. The

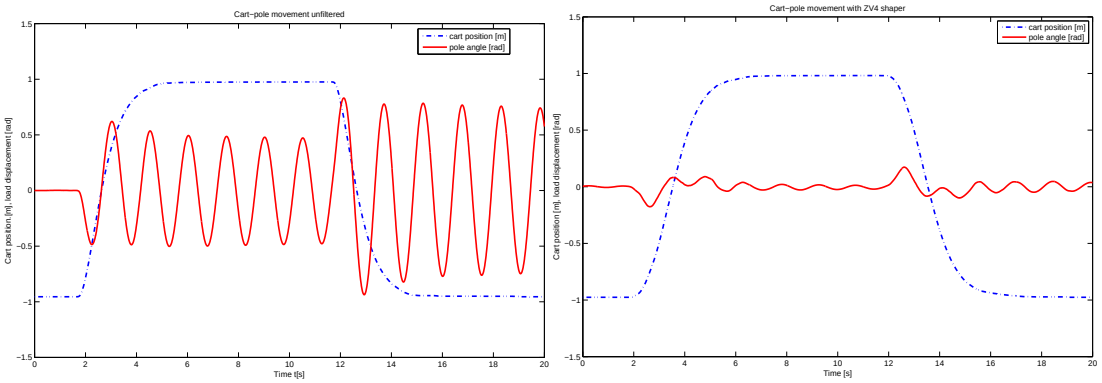

Figure 8.2: Motion control of the experimental gantry crane model - left no signal filtering, right reference command shaping using the ZV4 input shaper

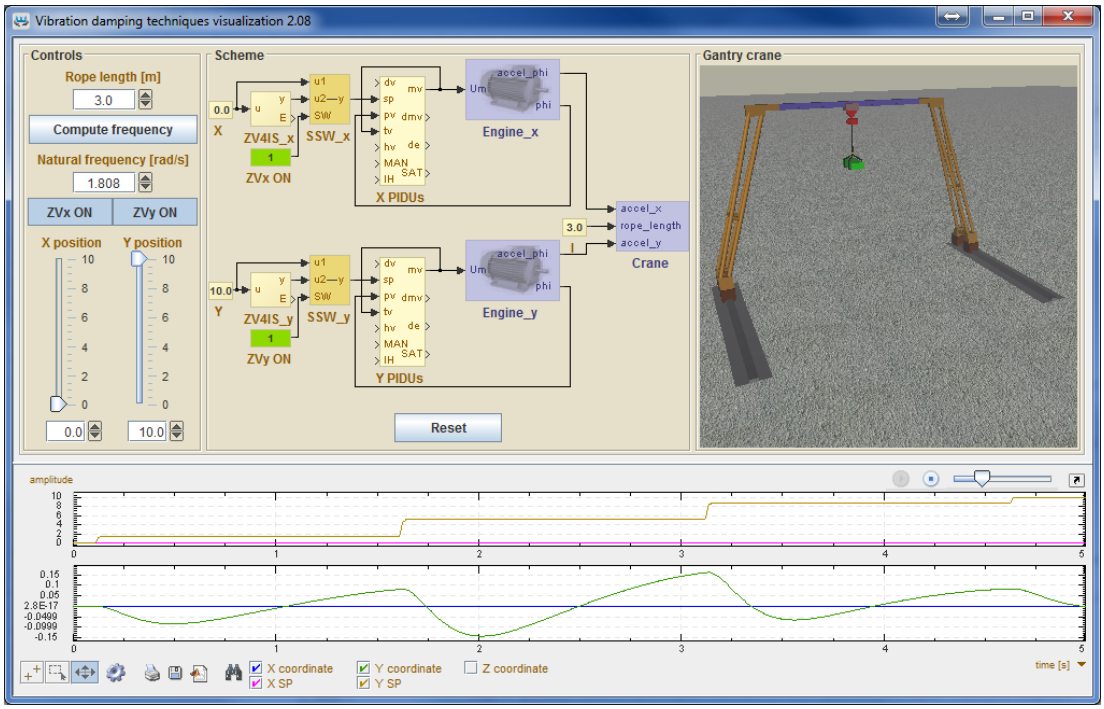

Figure 8.3: Zero vibration shaping virtual laboratory - feedforward vibration control of an overhead gantry crane, available at *http://www.contlab.eu/en/zv4is-demo*

load sway angle was not used as a feedback for the controller and it served only for the evaluation of the results. The cart was commanded to perform two point-to-point movements. It is seen that the amount excited oscillations of the hanging load was vastly reduced with the use of the shaping filter at the cost of slightly slower motion of the crane. Small level of residual vibration was still present due to the imperfect

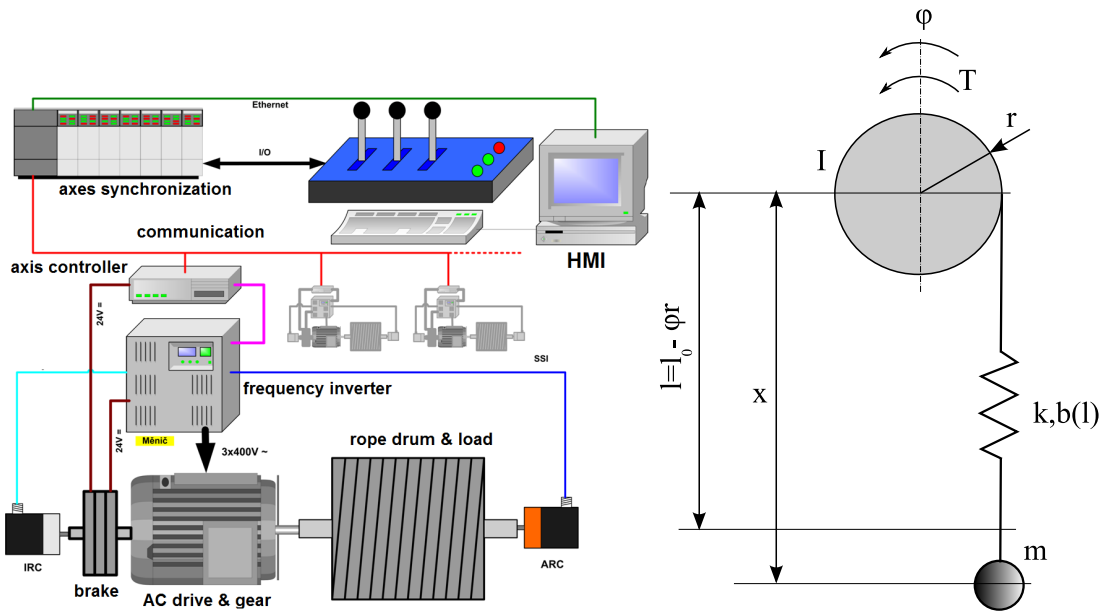

Figure 8.4: Rope drum system control - left typical structure of stage motion control system, right rope drum configuration

shape of the cart rail causing external disturbances which cannot be compensated in the feedforward manner. More details can be found in the papers [87, 206].

The concept of the overhead gantry control can be easily extended to the three-dimensional case by adding a second orthogonal axis. Virtual laboratory presenting the input shaping filters was developed at the University of West Bohemia [217]. Virtual reality 3D model was implemented using the Java3D rendering package and Virtual Reality Modeling Language (VRML). The interactive tool is freely accessible at *www.contlab.eu*. Detailed description can be found in the thesis [218].

8.2 Rope drum system control

Stage motion control system is an essential part of a modern theater. It consist of several technical devices including rope drums, moving walls, turntables and drop curtains which allow to create and change a shape of the stage during a break or ”on the fly” within a running performance. Rope drums serve for manipulation with various loads in the form of scenes performing variety of motions ranging from simple rest-to-rest manoeuvres in one direction to complicated multidimensional trajectories with multiple synchronized ropes. Particular problem is the flexibility of the rope which may lead to unwanted motion induced oscillations of the hanging load. The problem of vibration control of a rope drum system was solved in terms of an R&D project in cooperation with ZAT a.s. company. Detailed description can be found in the paper [211].

Typical structure of the control system is shown in Fig. (8.4 left). The rope drum is driven by an electrical drive, usually an AC induction motor with a corresponding frequency inverter. The axis controller is responsible for the desired trajectory tracking and serves as the position controller. The setpoint values for the desired position, velocity and acceleration of each axis are received from the motion planning level ensuring the trajectory generation and proper synchronization during multi-axes motions. The system is parameterized and supervised by an operator using a human-machine-interface.

The rope-drum system consists of rotational drum, flexible rope and a hanging load (Fig. 8.4 right). To obtain a finite-order model suitable for the control law design, some simplifications have to be made. We assume that the elastic rope with a load can be modelled as a mass-spring-damper system. The values of the spring constant k and viscous damping coefficient b are generally time varying. Under some simplifying assumptions, we may write:

$$k = \frac{k_0}{l}, b = \frac{b_0}{l}, \tag{8.7}$$

where k_0 corresponds to the stiffness of the unit length of the rope and l is the actual length in dependence on drum position φ

$$l = l_0 - \varphi r. \tag{8.8}$$

The equations of motion can be derived using the Newton-Euler method in the form of:

$$\begin{aligned} T - \tfrac{k_0}{l_0-\varphi r}(x - l_0 + \varphi r)r - br(\dot{x} + r\dot{\varphi}) = I\ddot{\varphi} \quad , \\ mg - \tfrac{k_0}{l_0-\varphi r}(x - l_0 + \varphi r) - b(\dot{x} + r\dot{\varphi}) = m\ddot{x} \quad . \end{aligned} \tag{8.9}$$

Introduction of state variables $x = [x_1\ x_2\ x_3\ x_4]^T = [x\ \varphi\ \dot{x}\ \dot{\varphi}]^T$ and linearisation around some operating point corresponding to a fixed rope length l leads to the LTI model with the system matrices given as:

$$A = \begin{bmatrix} 0 & 0 & 1 & 0 \\ 0 & 0 & 0 & 1 \\ -\frac{k_0}{ml} & -\frac{r(k_0+gm)}{ml} & -\frac{b_0}{ml} & -\frac{b_0 r}{ml} \\ -\frac{k_0 r}{Il} & -\frac{r^2(k_0+gm)}{Il} & -\frac{b_0 r}{Il} & -\frac{b_0 r^2}{Il} \end{bmatrix},\ B = \begin{bmatrix} 0 \\ 0 \\ 0 \\ \frac{1}{I} \end{bmatrix},\ C = \begin{bmatrix} 0 & 1 & 0 & 0 \\ 0 & 0 & 0 & 1 \end{bmatrix}. \tag{8.10}$$

The transfer function from the motor torque to the motor speed is obtained as

$$\begin{aligned} P(s) &= \frac{mls^2 + b_0 s + k_0}{s(Jlms^2 + (b_0 r^2 m + Jb_0)s + (r^2 k_0 m + r^2 g m^2))} \\ &= \frac{K}{s}\frac{s^2 + 2\xi_z\omega_{nz}s + \omega_{nz}^2}{s^2 + 2\xi_p\omega_{np}s + \omega_{np}^2}, \end{aligned} \tag{8.11}$$

which has a structure of a flexible two-mass system. Therefore, passive or active vibration control methods presented in the thesis may be used in this case. The resonance

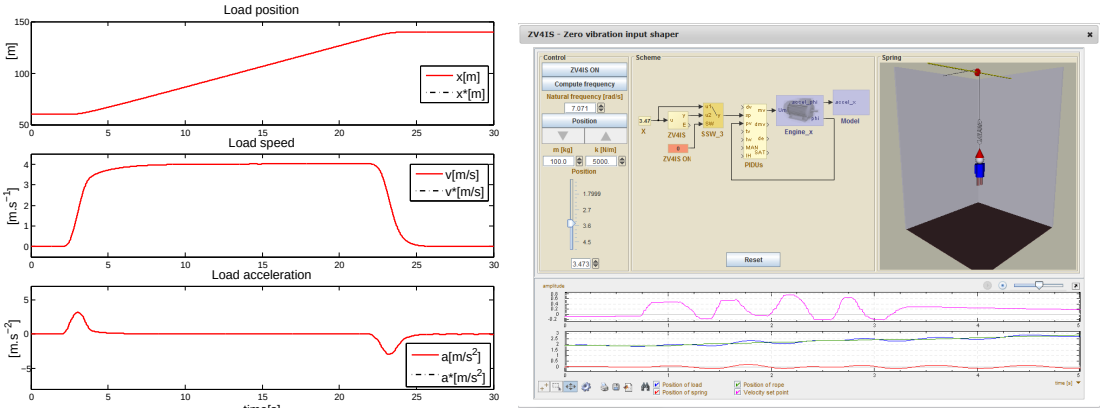

Figure 8.5: Left - position tracking of a nonlinear rope drum system, right - virtual laboratory presenting the vibration control schemes

frequency may differ considerably when significantly changing the length of the rope. Gain scheduling techniques may be used for the adaptation of controller parameters in this case. Example of position tracking of the flexible rope drum system is shown in Fig. (8.5 left). Composite vibration controller consisting of gain-scheduled PID compensator tuned for the active vibration control combined with a setpoint reference shaping filter was used to perform a rest-to-rest movement with a hanging load without excitation of any unwanted vibrations [211]. Interactive virtual laboratory presenting the rope drum system problem is available at *http://www.contlab.eu/en/zv4is-demo-2* [219]. The developed vibration control algorithms has become a part of a patented solution of the flexible rope controller [220].

8.3 Robotic manipulator for testing of shifting system

Intensive testing is currently an integral part of the research and development of new automotive components. A joint project was conducted at the UWB in cooperation with ZF Engineering company. The goal was to develop a test bench for the automated testing of automobile shifting systems. The work on the project involved a complete model-based design cycle - system modelling, control system design, development of a real-time Hardware-in-the-loop simulator and final commissioning of the control system. Detailed description can be found in the paper [221]. Particular problem of vibration control was solved using the proposed input shaping algorithms.

The test bench uses a two degrees of freedom manipulator with the serial connection of one translational and one rotational axis for the motion control of the lever of an automatic transmission unit (Fig. 8.6, 8.7). The goal is to perform automated operational tests consisting of precisely defined motion sequences simulating a typical service load. Two independent manipulators are used in order to allow simultaneous testing of two transmission units. The gear selectors are placed inside of an environmental

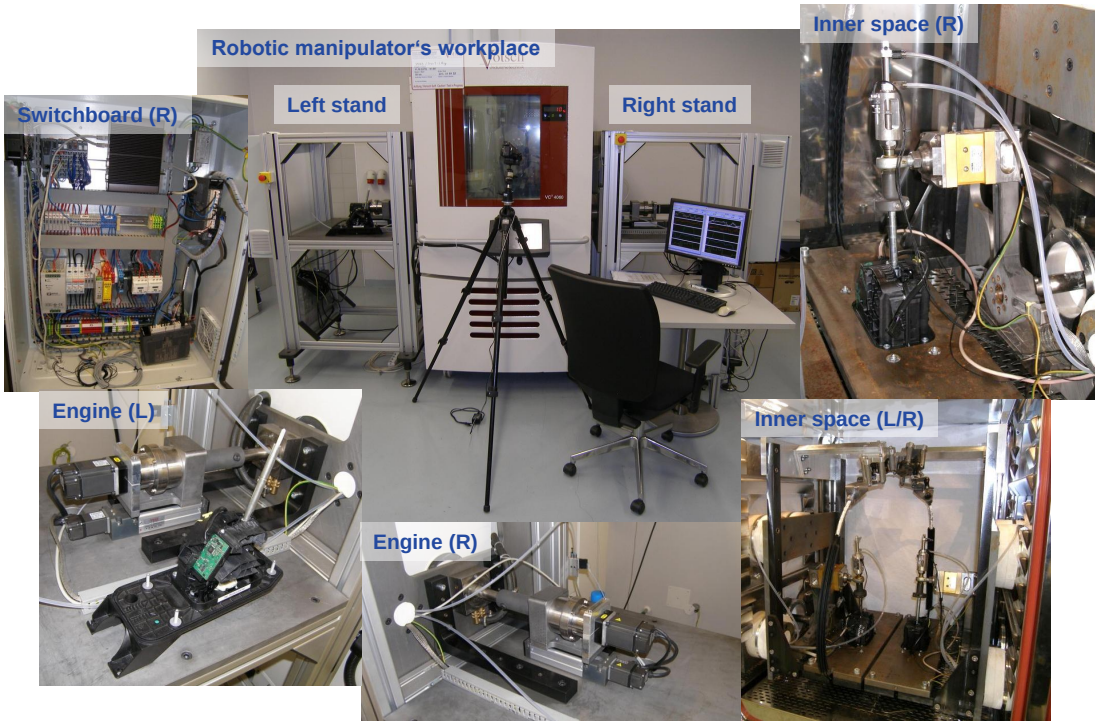

Figure 8.6: Robotic shifting system - test bench structure

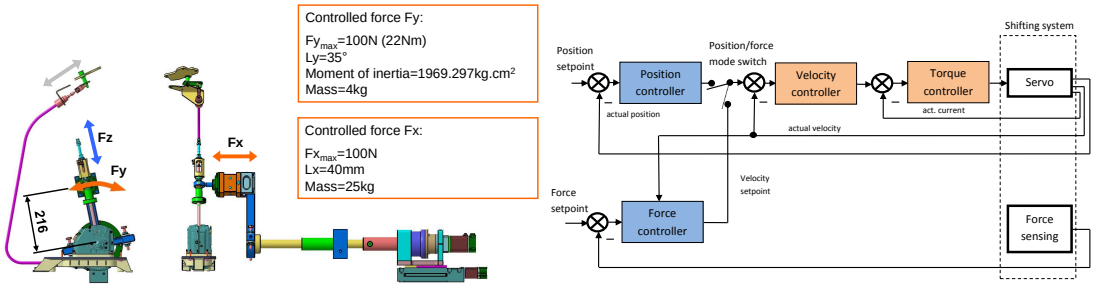

Figure 8.7: Robotic shifting system - left mechanical configuration of the manipulator, right control system structure

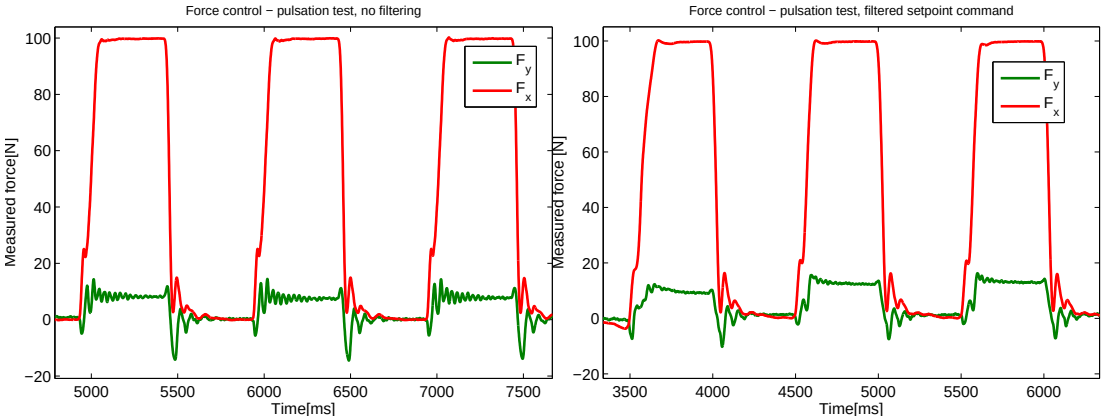

Figure 8.8: Force control - reduction of test bench chassis vibrations during the force pulsation test using setpoint command shaping, left no reference signal filter, right force setpoint processed by ZV4 input shaper tuned for the chassis resonance frequency

chamber which simulates various temperature and humidity conditions. Hybrid position/force control algorithm was developed since some parts of the testing sequence require motions with a defined contact force. The control system switches between position and force regimes according to the actual executed motion (Fig. 8.7 right).

One of the durability tests includes so called *Pulsation test* which is defined as an application of a defined contact force (usually 100N) repeatedly in various directions and gear positions. In most cases, the position of the lever is fixed and all the motion is caused by the elastic deformation of the lever and transmission box. Motion induced oscillations of the whole test bench were observed during this test. The vibrations were visible to the eye and readable in the force feedback signal provided by a three axial force sensor installed on the end of the robotic arm. Low stiffness of the mechanical construction of the actuator mounting was identified as the main reason for this behaviour. Although the observed vibrations did not affect the quality of control during the operational test, they could cause an increased wear of the mechanical components of the system during a long term operation. The amount of excited vibrations was significantly reduced by employing the ZV4 input shaper in the force reference signal path. This is indicated in Fig. (8.8) which compares the force sensor feedback during the pulsation test without any reference filtering and after the application of the shaping filter. The test bench chassis oscillations are visible in the time intervals in which $F_x = 100N$ (after the lever is pushed). The oscillatory transient when the contact force reaches zero level is caused by nonlinear dynamics of the lever and transition from contact to noncontact motion and it is not related to chassis vibrations. Manipulator motion during a testing sequence can be seen in the movie avaliable at *http://www.rexcontrols.com/control-system-for-shifting-stand-manipulator*.

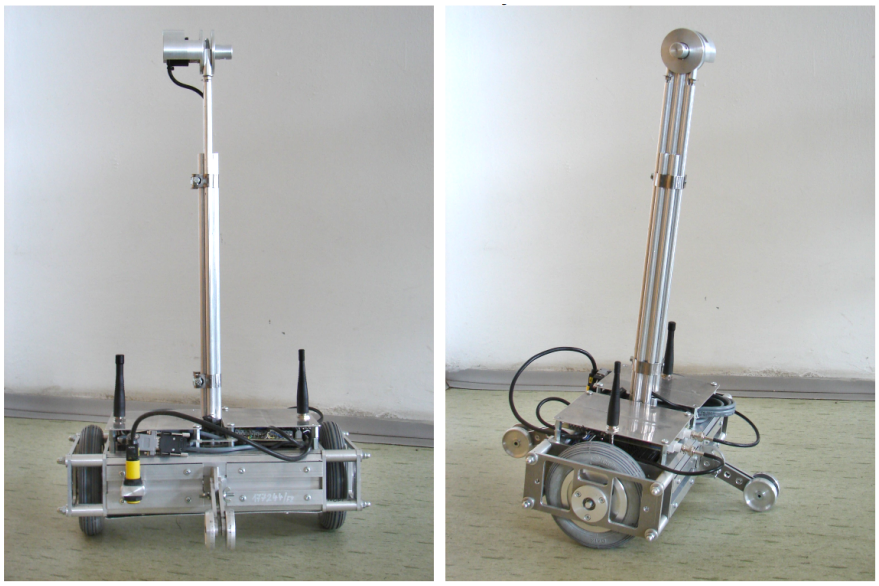

Figure 8.9: Two-wheeled robotic platform

8.4 Two-wheeled self balancing robotic platform

Two-wheeled self balancing platform was developed at the Department of Cybernetics for educational purposes (Fig. 8.9). The robot resembles the well known Segway electric vehicle which is used as a personal transporter. The robot is being used for the demonstration of various motion control concepts including robust unstable system stabilization, trajectory planning and tracking and vision-based control. A wireless communication allows the implementation of a remote human-machine interface. A camera can be attached to the platform to provide a visual feedback for the purpose of teleoperation. Autonomous operation can be achieved by implementing proper image processing and decision making algorithms.

The control system of the robot consist of several layers (Fig. 8.10 left). The lowest level provides current and velocity control of two brushless DC motors. The sway controller in the next level is responsible for the stabilization of the platform in the upward unstable position. Cruise and direction controller tracks desired motion profiles received by the trajectory generator. The actual required motion is obtained from the operator through the remote HMI or from the visual feedback in the autonomous mode. Detailed description of the system modelling and control design can be found in [222, 223].

Difficulties with mechanical vibrations arised during the implementation of the sway control algorithm. Sudden changes in the motor torque along with a backlash of the gears caused an excitation of a flexible mode of the robot chassis at the frequency approximately 8 Hz. Visible and audible oscillations of the machine frame were

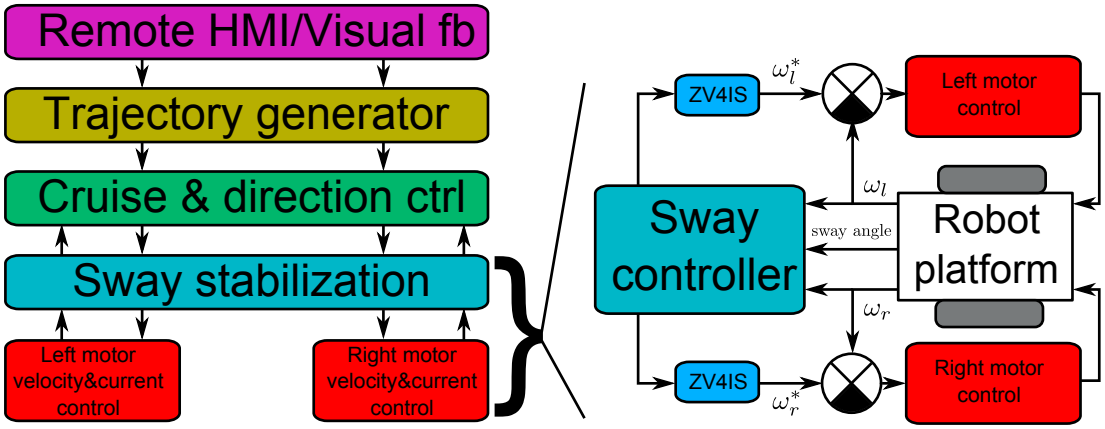

Figure 8.10: Two-wheeled robot control scheme - left - motion control layers, right - details of the sway stabilization control loop

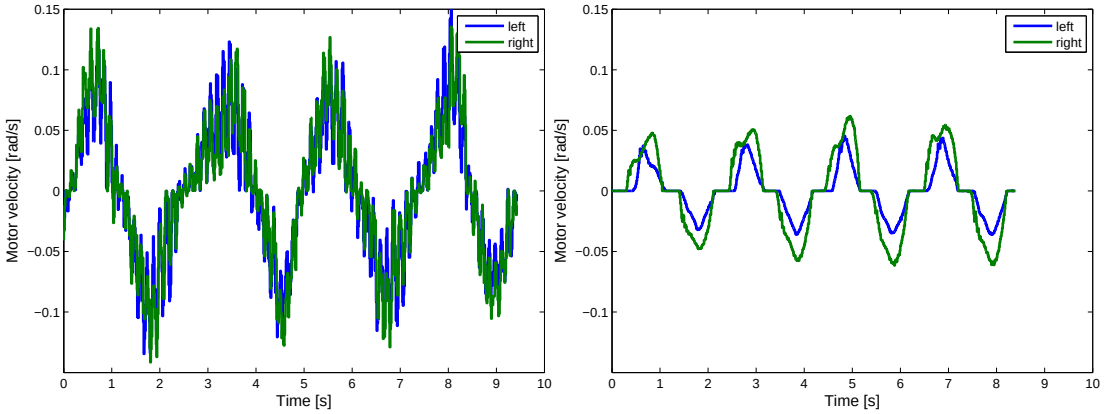

Figure 8.11: Two-wheeled robot vibration damping - left - steady state frame oscillations excited during platform stabilization, right - vibration damping achieved by applying the ZV4IS shaping filter in the sway control loop

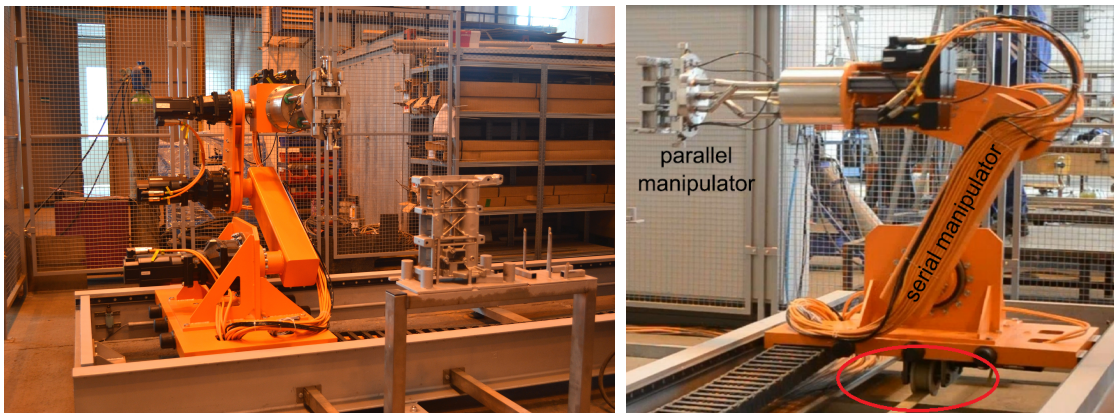

Figure 8.12: AGEBOT industrial manipulator - 7DoF machine kinematics consisting of 4DoF serial part and 3DoF parallel spherical wrist, on the right - flexible toothed belt, source of oscillations of the translational axis

observed also in the motor velocity signals acquired from the quadrature encoders (Fig. 8.11 left). The developed ZV4IS filter was used to suppress the unwanted oscillations. The shaping filters were placed inside the sway control loop to prevent from the flexible mode excitation due to external disturbances and nonlinearities in the system dynamics (Fig. 8.10 right). Figure (8.11) shows considerable improvement of the quality of control. The vibrations of the robot frame were completely suppressed. The observed limit cycle is caused by a small amount of stiction in the motors, gears and wheel bearings and could not be completely eliminated. However, the sway controller performed well and the problem of platform stabilization was successfully solved.

8.5 Industrial manipulator for chemically aggressive environment

Utilization of industrial robots in modern automated factories has grown dramatically in recent decades. There is variety of industrial robots available on the market which are well established in standard applications such as welding, soldering, palletizing, material handling. However, the most commonly used universal robots may fail in the case of some specific requirements and a special design may be needed. One of such nonstandard applications is a technology for the robot supported parts cleaning which is essential in several fields of industry and mass production. A robot operates a degreasing or paint removal machine and manipulates with metal or nonmetal parts which have to be cleaned precisely. The goal is to remove all the remains of grease, cutting or tempering oil or any kind of mechanical dirt in order to prepare the parts for further processing. Strong chemicals such as acid, lye or special degreasing lotions are typically used to achieve a high level of surface cleanness. These highly aggressive

chemicals are dangerous not only for the human staff but also for a robot which is used for the manipulation and precise positioning of the parts inside a cleaning chamber. The sensitive parts of the robot such as drives, electronics or wiring can easilly be damaged and most of the commonly available robots are not suitable for this task. Therefore, a serio-parallel manipulator which is called AGEBOT (AGgressive Environment roBOT) has been developed in cooperation with EuroTec JKR company for the specific operation in the chemically aggressive environment. The research and development involved model-based design and optimization of the mechanical construction, derivation of kinematic and dynamic models and control system design and implementation [114, 224, 225].

AGEBOT is designed as a special robotic architecture which consists of two main parts - serial manipulator (SM) and parallel manipulator (PM). SM ensures basic positioning of the end effector including the translations in x, y, z axes and orientation of the longitudinal axis of the PM. This motion is used for the handling of parts which are to be processed in cleaning chambers. Parallel spherical wrist of the PM holds the end effector platform and performs precise positioning of the cleaned parts with complex geometry towards cleaning jets inside the chamber by changing their orientation. The main advantage of this kinematic structure is the ability of waterproof separation of the vulnerable components (motors, sensors, etc.) from the aggressive environment and an additional degree of freedom allowing more complex motions.

Particular problem of mechanical vibrations was encountered during the commissioning of the prototype manipulator. Strong oscillations of the robot platform were observed during the translational movements along the rail. The vibrations were caused by elasticity of the toothed belt which connects the platform with the manipulator base. Initial tuning of the motion control loop in which an ideal rigid connection was assumed led to a very nice closed-loop response measured by the motor side feedback sensor (Fig. 8.13 left). However, significant vibrations were induced at the load side of the robot platform. The oscillations were also visible in the records of the motor current (8.8 right). This was caused by the *pole-zero cancelation phenomenon* occurring in a compliant system driven by a high gain compensator with the motor feedback only.

Experimental identification was carried out to acquire the information about the system dynamics. Two-mass flexible system model was obtained with resonance and antiresonance frequencies $f_n,\ f_z$ given as:

$$f_z = 4.5Hz,\ f_n = 12.1Hz,\ r = \frac{f_n}{f_z} = 2.7. \tag{8.12}$$

The velocity PI controller was redesigned according to the flexible dynamics model to achieve the active vibration damping functionality. The resulting closed-loop response can be seen in Fig. (8.14). The motion induced oscillations were eliminated completely at the cost of reduced achievable bandwidth. The compensator is able to damp the oscillations even in the presence of external disturbances (red mark in Fig. 8.14 right indicating application of external force to the manipulator base). The feedback compensator was supplemented with the ZV4IS shaping filter which processed

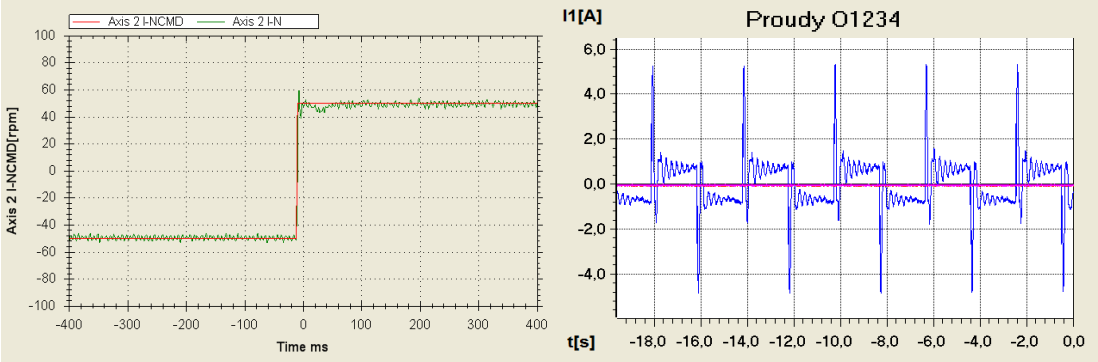

Figure 8.13: High gain PI velocity controller designed for an ideal rigid model, left - velocity setpoint response measured at the motor side, right - motor current during rectangular setpoint signal tracking indicating the load vibrations

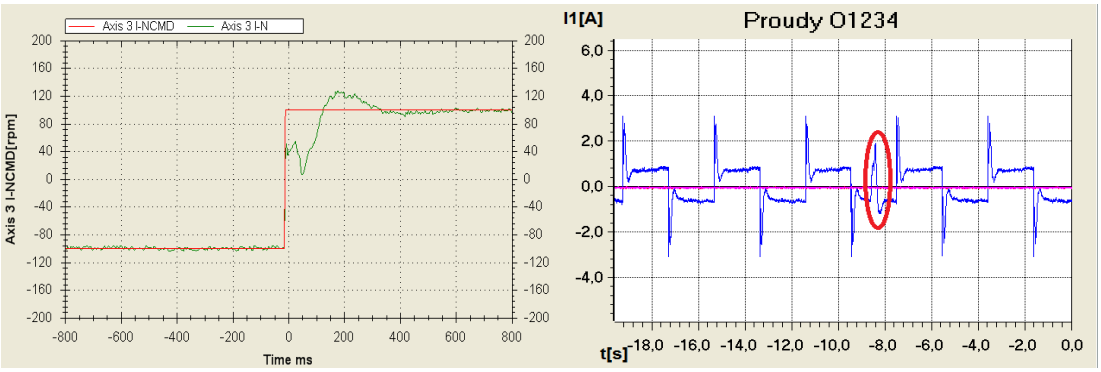

Figure 8.14: Reduced gain PI velocity controller designed for the compliant system model, left - velocity setpoint response measured at the motor side, right - motor current during rectangular setpoint signal tracking showing the active vibration damping, red mark denotes the active compensation of external disturbance

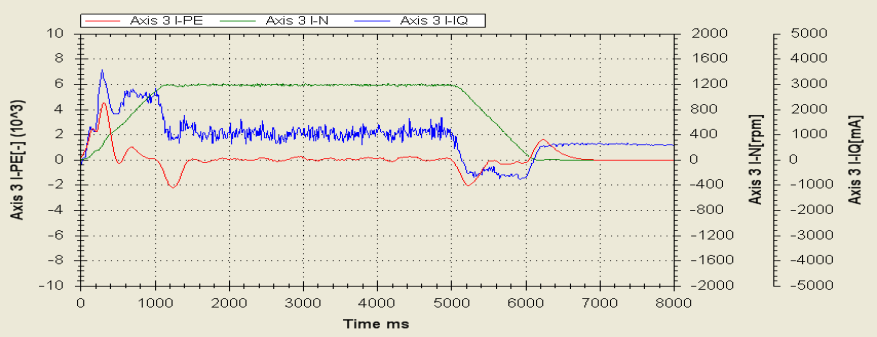

Figure 8.15: Position profile tracking during a point to point movement, motor velocity (green), motor current (blue) and position tracking error (red)

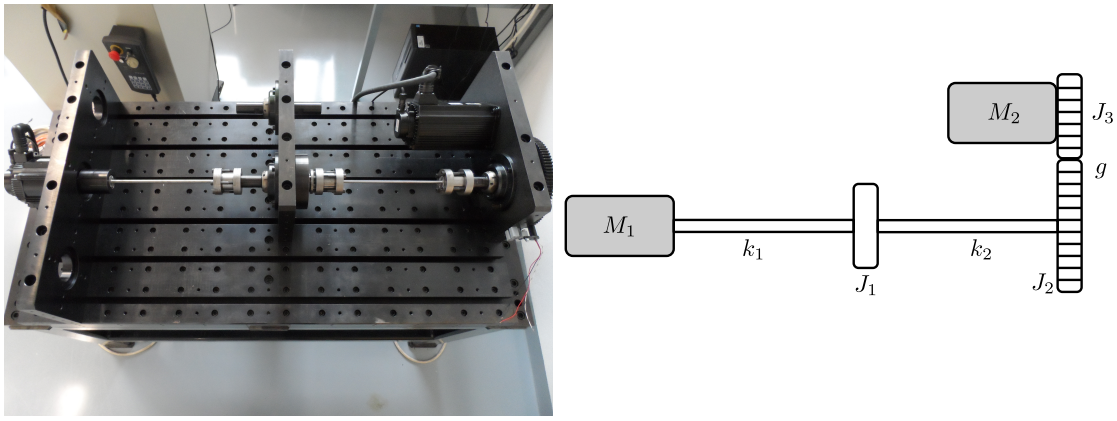

Figure 8.16: Dynamic test bed overview - left picture of the actual configuration, right system structure; M_1, M_2 input and output actuator, $J_{1,2,3}$ load inertias, $k_{1,2}$ flexible shafts, g gearing.

the reference trajectories sent to the servo drive in order to further reduce the amount of transient and residual oscillations. Position profile tracking during a point to point movement is captured in the plot (8.15) which shows the performance of the composite vibration control scheme. The vibrations are effectively damped in all phases of the robot trajectory. The closed-loop performance could be further improved with the use of a higher order compensator. However, the achieved quality of control was satisfactory for the customer. Therefore, the default cascade PID control scheme implemented in the frequency inverters was used without changes.

8.6 Dynamic test bed for compliant systems control

A mechanical test bench was constructed for the evaluation of vibration control methods with the aid of VÚTS a.s. company which has lent the mechanical and electrical components (the support is gratefully acknowledged). The test bed structure is shown in Fig. (8.16). The system consists of two electrical drives (Yaskawa permanent magnets synchronnous servomotors) acting as input and output actuators, two elastic torsional bars, gearing and inertial loads. The system simulates a compliant load with two resonance modes. The location of the resonance frequencies can be adjusted by changing the stiffness of the installed shafts and moment of inertias of the flywheels.

Experimental identification was performed using the proposed algorithm. The developed method was implemented in the form of a functional block in the REX real-time control system. Both identification and control algorithms are executed in the LEC industrial PC with a real-time operating system Linux-Xenomai. The controller communicates with two Yaskawa frequency inverters using EtherCAT serial bus with the update rate of 2kHz.

Figure (8.17) shows the result of the frequency identification experiment. Twenty

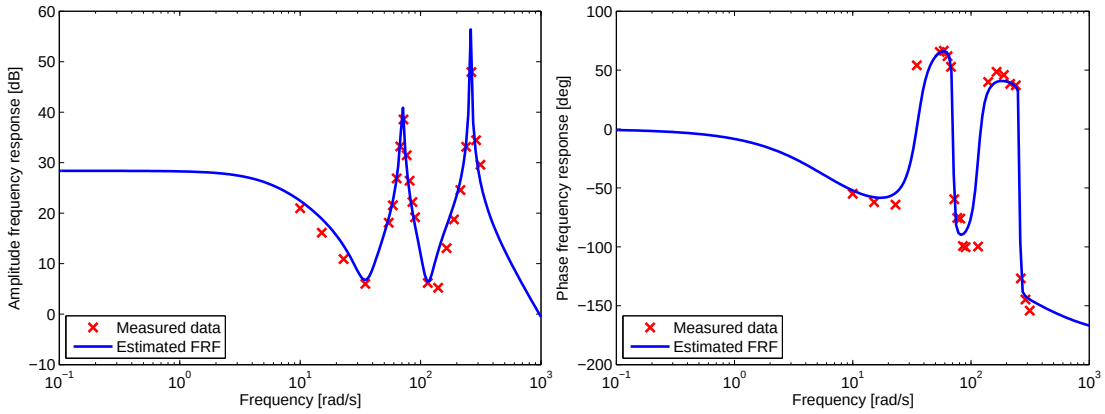

Figure 8.17: Frequency response identification - measured and estimated frequency response function, left amplitude response, right phase response

points of measured frequency response were processed with the proposed approximation algorithm which was used for the numerical computation of a 6th order transfer function. The resulting plant model was obtained in the form of:

$$P(s) = \frac{\omega_m(s)}{T_m(s)} = \underbrace{\left(\frac{K}{s+\tau_1}\right)}_{\text{rigid mode}} \underbrace{\left(\frac{s^2+2\xi_{z1}\omega_{z1}s+\omega_{z1}^2}{s^2+2\xi_1\omega_1 s+\omega_1^2}\right)}_{1^{st}\text{ resonance}} \underbrace{\left(\frac{s^2+2\xi_{z2}\omega_{z2}s+\omega_{z2}^2}{s^2+2\xi_2\omega_2 s+\omega_2^2}\right)}_{2^{nd}\text{ resonance}} \underbrace{\left(\frac{1}{s+\tau_2}\right)}_{\substack{\text{additional}\\ \text{dynamics}}},$$

$$K = 544.6,\ \tau_1 = 0.16s,\ \tau_2 = 0.0038s,\ \xi_{z1} = 0.19,\ \omega_{z1} = 35.3\frac{rad}{s},$$
$$\xi_1 = 0.02,\ \omega_1 = 70.8\frac{rad}{s},\ \xi_{z2} = 0.11,\ \omega_{z2} = 114.6\frac{rad}{s},\ \xi_2 = 0.005,\ \omega_2 = 260.1\frac{rad}{s}. \tag{8.13}$$

The first three parts of the plant transfer function describe the dynamics of the three modes of the mechanical system. The second time constant τ_2 covers additional parasitic effects such as time delay due to digital sampling, communication delay and actuator lag.

Three different velocity controllers were designed using the algorithms proposed in the thesis with the use of motor side feedback only. The design specifications were set to achieve the highest possible bandwidth while limiting the peaks in the sensitivity and complementary sensitivity functions to $M_S, M_T < 2.5$. The first one is a PI controller which was computed for the truncated model containing only the first resonance mode dynamics. The simulation of step reference and disturbance responses is shown in Fig. (8.18) left. It is seen that the controller is able to damp the oscillatory system although a truncated model was used for its computation. Since the resonance ratio $r \approx 2$ is in the optimal range for the PI control, there is no need for introduction of the derivative part. The two other plots in Fig. (8.18) show the results achieved with the

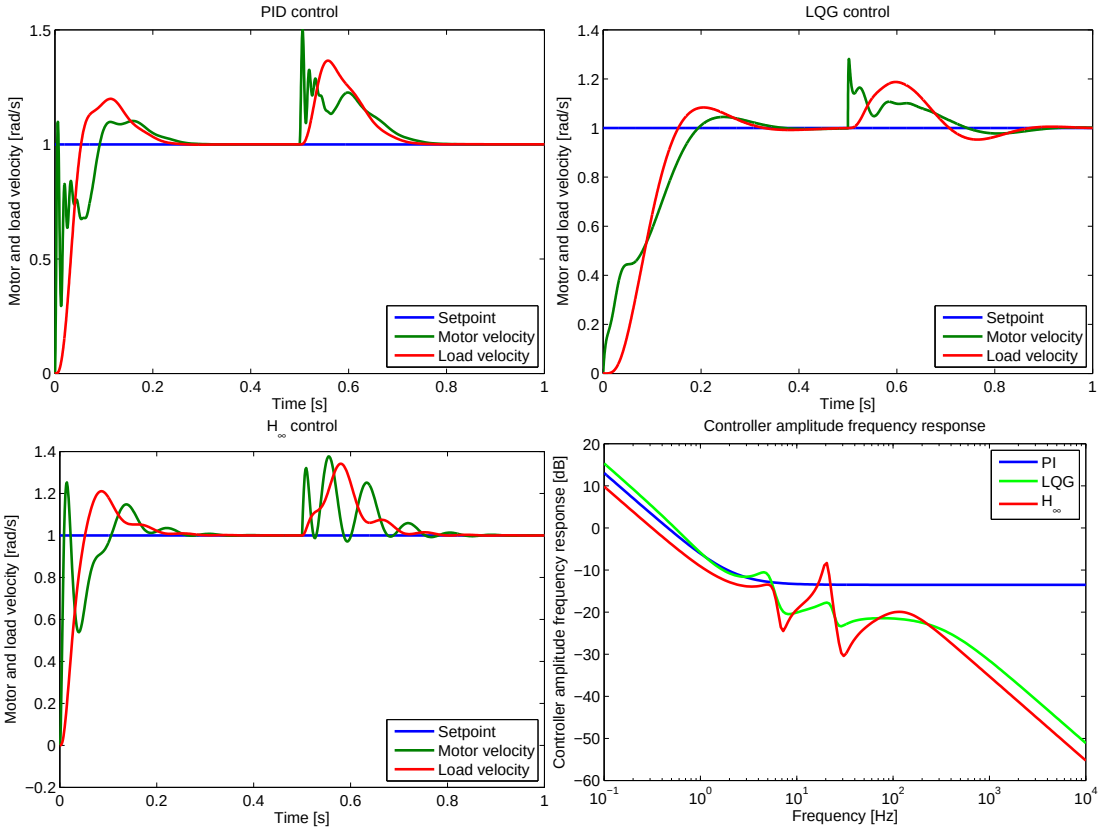

Figure 8.18: Three compensator designs comparison - simulated reference and disturbance step response, controller amplitude frequency response

LQG and H_∞ controllers designed for the full plant model. It is seen that the performance is comparable to the PI controller and there is no significant advantage in terms of achievable bandwidth when using a full order compensator. However, there is a significant **improvement in the achieved high-frequency roll-off** which can be observed in the comparison of the amplitude frequency responses of the obtained compensators (last plot in Fig. 8.18). *Lower high-frequency gain of the compensator is desirable for the attenuation of the measurement noise and improvement of robustness to unmodeled dynamics*.

This is confirmed by experimental results obtained at the test bed (Fig. 8.21) which compare the PI and H_∞ compensators in terms of setpoint tracking and disturbance rejection performance. The first row shows motor and load velocity response to step change in the setpoint variable, the second one tracks the response to step changes in the disturbance torque generated on the motor and load side. Both controllers achieve similar settling times, the closed loop bandwidth is identical. Much higher variance of the generated motor torque is observed in the case of the PI controller due to its higher high-frequency gain. The quantization noise in the motor velocity feedback is amplified

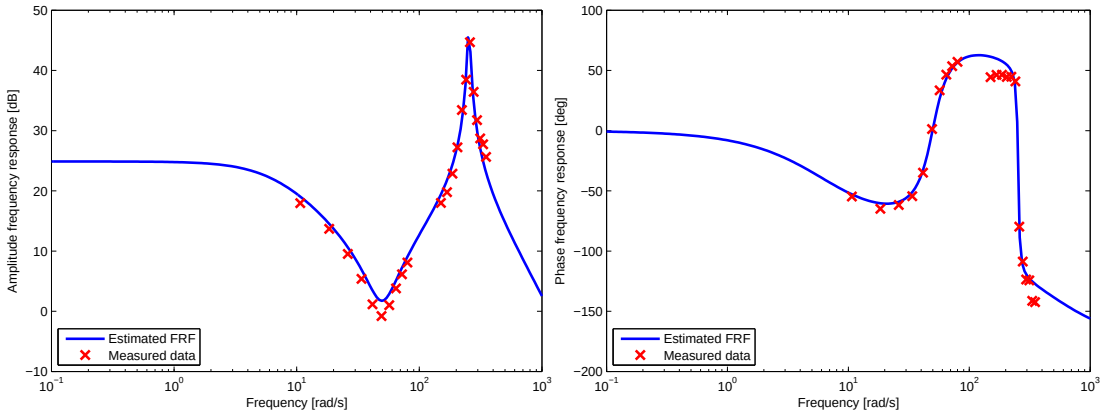

Figure 8.19: Frequency response identification - measured and estimated frequency response function for the second configuration of the test bench

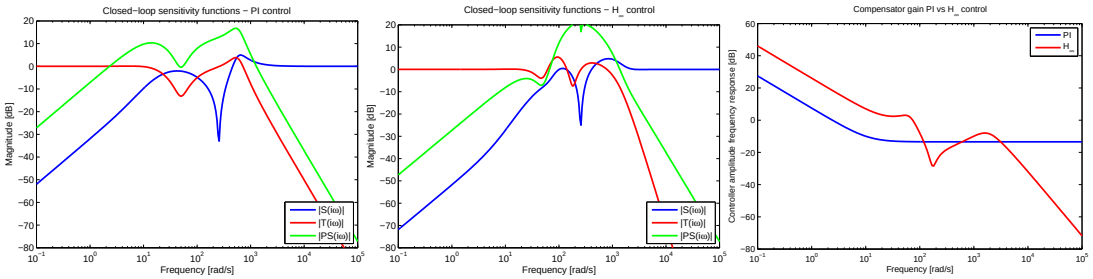

Figure 8.20: Closed-loop sensitivity functions - amplitude frequency response of the sensitivity function $|S(i\omega)|$, complementary sensitivity function $|T(i\omega)|$ and plant sensitivity function $|PS(i\omega)|$ for the two compared control schemes - PI and H_∞ control

by the compensator and causes oscillations at the motor side. Analysis of the *amplitude spectrum of the regulation error signal* with the use of fast Fourier transform reveals that there is a significant amount of energy in the motor side signal in the frequency range around $\approx 100\ Hz$ (Fig. 8.22 left). Amplification of the measurement noise is much lower in the case of the H_∞ controller. The peaks observed at frequencies of 210 and 420 Herzes are caused by unmodeled flexible modes of the test bed frame. The load side amplitude spectrum is almost identical as the load inertia works as a low-pass filter which attenuates the high frequency motor side oscillations. Thus, the **main advantage of the higher order controller is a smoother run of the drive in this case**.

A second experiment is performed with a different mechanical configuration of the test bed. The second compliant torsional bar is replaced by a rigid link. The overall dynamics now resembles a single resonant mode system with a high resonance ratio value. The result of the frequency identification and model fitting is seen in Fig. (8.19).

Fourth order transfer function is obtained in the form of:

$$P(s) = \frac{\omega_m(s)}{T_m(s)} = \left(\frac{K}{s+\tau_1}\right)\left(\frac{s^2 + 2\xi_{z1}\omega_{z1}s + \omega_{z1}^2}{s^2 + 2\xi_1\omega_1 s + \omega_1^2}\right)\left(\frac{1}{s+\tau_2}\right), \tag{8.14}$$

$$K = 454.5,\ \tau_1 = 0.15s,\ \tau_2 = 0.0022s,\ \xi_{z1} = 0.24,\ \omega_{z1} = 49.9\frac{rad}{s},$$

$$\xi_1 = 0.02,\ \omega_1 = 254\frac{rad}{s}.$$

The high value of the resonance ratio parameter $r \approx 5$ limits the performance achievable with the conventional PI control. The advantage of higher order compensator can be fully exploited in this case. This is shown on the example of the H_∞ controller. Again, both compensators were tuned to achieve highest possible bandwidth while keeping the peaks of the sensitivity functions below the specified level $M_S, M_T < 2.5$. Comparison of the compensators amplitude frequency response functions (Fig. 8.19 right) reveals that that the H_∞ controller achieves higher values of low-frequency gain and improved high-frequency roll-off which indicates an improvement in both closed-loop bandwidth and noise rejection.

This is confirmed by numerical simulations and experimental results. Figure (8.23) compares the closed-loop performance of the two control schemes. Approximately two-times faster settling times, much better disturbance rejection and slight improvement of noise attenuation is achieved with the H_∞ compensator which outperforms the conventional PI controller. This coincides with the theoretical analysis provided in the previous chapter which state that the **advantage of higher order compensators compared to the PID control are remarkable for high resonance ratio systems**. Further improvement of closed-loop performance is not possible without using both motor and load-side measurement for feedback in this case.

8.7 Summary

This chapter demonstrated a successful employment of the proposed vibration damping methods. Various examples of laboratory setups and industrial applications show the possibilities of feedforward and feedback vibration control concepts. The experimental results confirmed the theoretical analysis which was performed in the preceding sections of the thesis. A properly designed algorithm embedded in the control system can significantly enhance the overall closed-loop performance, provided that a mathematical model can be obtained with a sufficient precision. However, there are some fundamental limitations on the achievable quality control resulting from the nature of the problem that can not be overcome by any linear compensator.

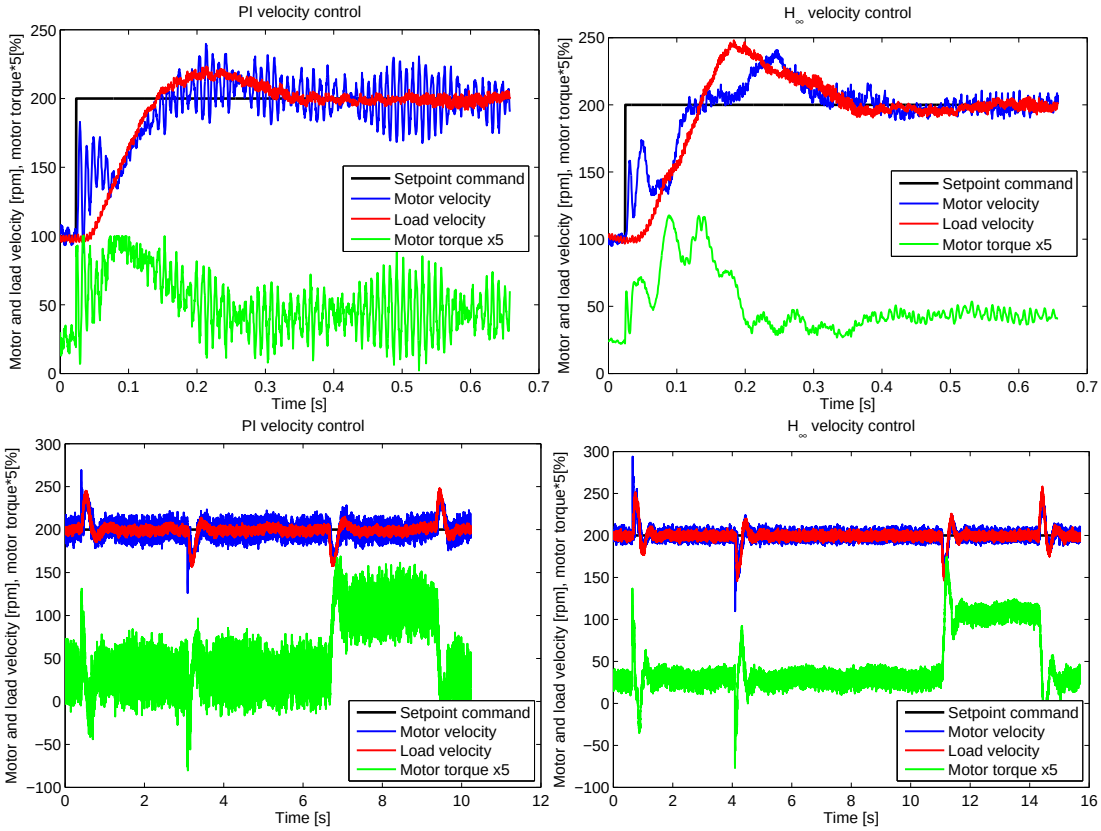

Figure 8.21: Dynamic test bed experiment Nr.1 - closed-loop response of two feedback compensator schemes, up setpoint tracking, down disturbance rejection, left PI control, right H_∞ control

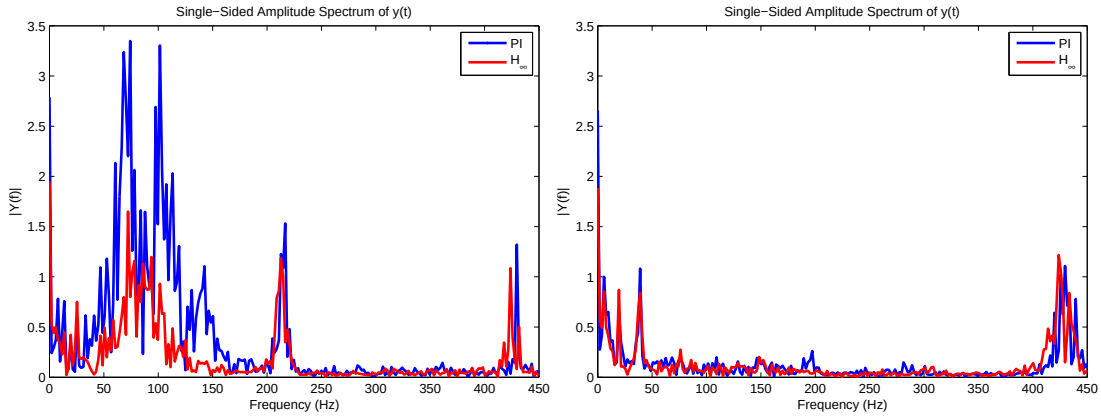

Figure 8.22: Dynamic test bed experiment Nr.1 - amplitude spectrum of steady-state regulation error signal acquired at 200 rpms, left motor side velocity measurement, right load side signal, blue color PI controller, red color H_∞ controller; significant reduction of motor side oscillations is observed when using the higher order H_∞ controller due to the improved high-frequency roll-off, the load side behaviour is almost identical for both control schemes

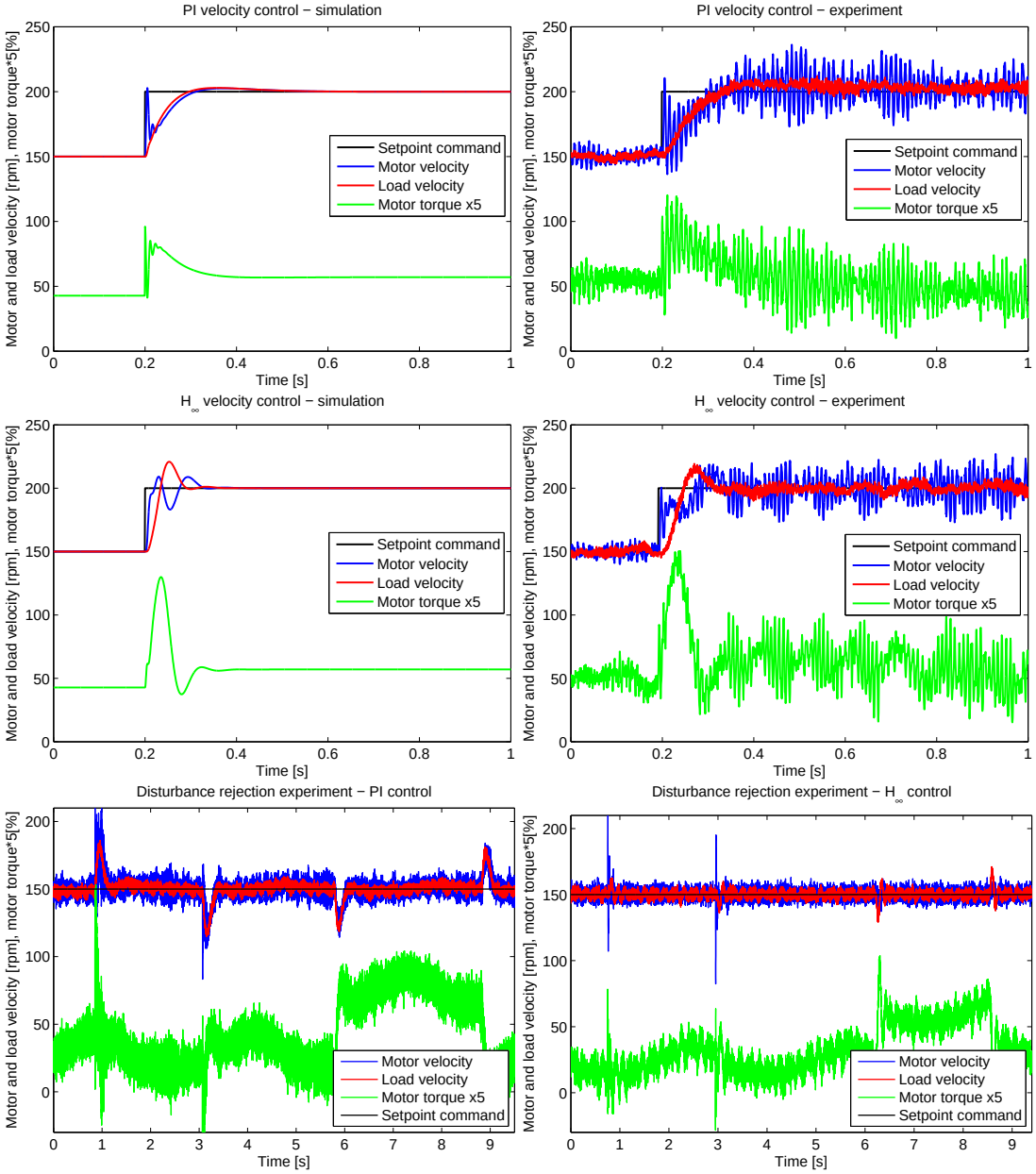

Figure 8.23: Dynamic test bed experiment Nr.2 - closed-loop response of two feedback compensator schemes, setpoint tracking and disturbance rejection performance, the H_∞ controller can achieve higher bandwidth and better noise suppression in the case of high resonance ratio system, the observed steady state oscillations in the driving torque are caused by imperfect balancing of the mounted gearwheels which produces a periodic disturbance

9

Discussion and final conclusions

The thesis deals with the problem of motion control of compliant electromechanical systems. The proposed methods and algorithms cover the issues of automatic identification and robust controller design for both passive and active vibration damping. The main theoretical results can be summarized as follows:

- **Development of novel frequency identification method**
  The key idea is the utilization of a swept sine signal with varying frequency, amplitude and DC component in conjunction with the time-varying observer which estimates the system frequency response. The main advantage of the proposed approach is the possibility of precise control over the energy of the excitation signal at each particular frequency which can be adapted online according to the actual operating conditions. This is beneficial due to possible occurrence of nonlinearities in the mechanical subsystem and large gain variations arising in oscillatory plants. Additional benefits include the possibility of real-time frequency response estimation and closed-loop identification. The disadvantage is a longer execution time of the identification experiment compared to a wideband excitation signals.

- **Feature-based parameterization of single-mode zero vibration input shaping filters**
  The proposed parametrization of all equidistant four impulse zero vibration shapers allows fine tuning of the shaper sensitivity function which describes the level of excited vibrations in the case of modelling errors. Suitable compromise between robustness and introduced dynamical lag may be found by adjusting the set of two user parameters with a clear physical meaning. All the standard zero vibration shapers commonly referenced in the literature are shown to be a particular case of the given parameterization.

- **General algorithm for multiple mode shaper design**
  A general algorithm for the multimode shaper design is proposed. The design problem is formulated in terms of the desired shape of the shaper sensitivity

function around the individual resonance frequencies. An optimal shaping filter is computed using the linear programming method.

- **Analysis of fundamental limitations on achievable quality of feedback vibration control**
  The limitations on achievable quality of control are analyzed both for conventional PID control and a general linear compensator.

- **Analytical derivation of set of stabilizing PID controllers for active feedback control of oscillatory systems**
  The partial pole-placement method is used for the computation of a whole set of controllers which stabilize the system and assign a chosen dominant pair of closed-loop poles. A particular compensator can be selected from the computed set based on a proper performance index. Robust controller can be designed for a specified parametric, structured or unstructured uncertainty. The parameterization of the feedback controllers allows precise fine tuning of the closed-loop with the physically intuitive parameters of bandwidth and damping.

- **Full order compensator design method based on LQG and H_∞ framework**
  Full order compensators which can enhance the achievable closed-loop performance are designed using the methods of modern control theory. The proposed weighting schemes are universally applicable for arbitrary oscillatory system due to the introduced normalization in gain, time and resonance ratio parameter. The user specifies the maximum peaks of closed-loop sensitivity functions and desired bandwidth, the controller is computed numerically.

The achieved results can be applied for a class of electromechanical systems which can be described by a linear model with a rigid mode and multiple resonance modes at least around some operating point. The results were verified in several laboratory experiments and industrial applications.

The main *practical implications* of the research carried out in this field are formulated in the following *theses*:

- ***A wide range of compliant electromechanical systems can be described by relatively simple linear models.*** *A precise mathematical model of a particular mechanical plant to be controlled is not needed in most practical cases. Local problem oriented model which describes the contribution of the individual modes of the system in the frequency range relevant for the target bandwidth may be used for the purpose of control system design.*

- ***The mechanical compliance significantly affects the closed-loop performance***. *If possible, proper mechanical design should ensure that the resonant frequencies of the mechanism do not overlap with the target closed-loop bandwidth.*

- ***Nonlinearities typically appearing in mechanical systems such as friction, backlash or hysteresis complicate the process of system identification***. *Standard methods developed for the linear systems may fail in the case of nonlinear*

mechanics. Utilization of proper excitation signal may suppress the effects of nonlinearities in order to extract the information about the linear part of system dynamics.

- ***There are two fundamental approaches to vibration control - passive and active, each offering a specific advantages and drawbacks**. Selection of proper control strategy or the combination of both approaches is a matter of a particular system. Several factors have to be taken into consideration including the location of the resonance modes, nonlinearities in the loop, precision of the system model or given instrumentation. Advanced software tools which automate most of the steps required in the control algorithm design can significantly simplify the process of machine commissioning.*

- ***There are fundamental limitations on achievable quality of control when using only the motor side feedback due to the rapid drop of the open-loop gain in the antiresonance regions**. The most important parameter which indicates the achievable performance is the resonance ratio. Very low resonance ratio systems with $r \approx 1$ are practically uncontrollable due to the loss of observability of the given resonance mode. This situation may be caused by improper dimensioning of the actuator with respect to the driven load. Passive damping methods should be used in this case.*

- ***Low and high resonance ratio systems** $r \notin \langle \sqrt{3}, \sqrt{5} \rangle$ **are poorly controllable with the conventional PI velocity controller** due to the inherent constraints between the closed-loop poles imposed by the controller structure. Poor damping or sluggish closed-loop response is achieved outside of this region.*

- ***The optimal value of the resonance ratio for the conventional PI control s** $r \approx 2$. The achievable bandwidth is approximately 150% of the first antiresonance frequency. There is no significant advantage of higher order compensator apart from improved noise rejection.*

- ***The derivative feedback of the PID controller may be used to virtually shift the resonance ratio of the system**. This allows to recover the performance achievable in the optimal range of $r = 2$. However, the amount of derivative action is limited by the level of the measurement noise and by unmodelled high-frequency dynamics.*

- ***The full advantage of higher order controllers can be fully exploited for high resonance ratio systems with** $r >> \sqrt{5}$. There are still some fundamental limitations on achievable bandwidth which is approximately 200% of the first antiresonance frequency (up to a double compared to the PI control).*

- ***There are no theoretical limitations on achievable quality of control when using the load-side feedback**. However, robustness of the closed-loop drops rapidly when extending the bandwidth beyond the value of the first resonance of the system.*

There are still some unresolved questions which outline possible directions for a future research in this field. The identification algorithm could be extended to **cover the nonlinear part of the system dynamics**, possibly in the second step of the identification experiment once the linear part has been identified. Any knowledge about the friction characteristics and amount of backlash or hysteresis could be used to improve the quality of closed-loop control and to suppress some negative phenomena appearing in motion control systems such as steady state oscillations or limit cycling.

The vibration damping concepts could be **extended for multiaxes compliant systems** (e.g. robotic manipulators). However, nonlinear dynamic coupling between the individual axes calls for utilization of nonlinear methods.

The provided analysis of controllability revealed some fundamental limitations of the linear feedback. The question is, **whether some of these constraints may be overcome by a nonlinear controller**. Sliding mode or passivity based approach could offer an alternative to the linear compensators.

The robust controller design methods proposed in the thesis are focused on unstructured perturbation of the nominal dynamic model. **Combination of an unstructured uncertainty with parametric variations** is treated by brute force with the method of gridding applied in the assumed parameter subspace. The framework of μ analysis could provide a more effective process for the derivation of the robust controller when various types of uncertainty should be assumed at the same time.

10

Appendix

10.1 Synthesis of observer for frequency identification

Butterworth pattern of closed-loop poles s_m for the observer (5.5) is obtained in the form of:

$$s_m = \alpha_0 \omega e^{\frac{i(2m+11-1)\pi}{2\cdot 11}};\ m = 1, 2, 3, ..., 11 \tag{10.1}$$

Solution of the pole-placement problem leads to closed-form formulas in the form:

$$k_m = k_m^0(\alpha_0)\omega;\ m = 1, 2, 3, ..., 11 \tag{10.2}$$

where $num(\alpha_0), den(\alpha_0)$ are polynomial functions of α_0.

The polynomials k_m^0 are given as:

$$\begin{aligned} k_1^0 =& \frac{1}{43200000000000000000000000000000000000000000} \alpha_0 \cdot \\ & (-6162137660593439769226000000000000000000\, {\alpha_0}^4 \\ & + 4999441708897943361224517686884511889\, {\alpha_0}^{10} \\ & - 123427161019929267191958384385881182800\, {\alpha_0}^8 \\ & + 47966848970270895630850448018400000000\, {\alpha_0}^6 \\ & + 28510583873976000000000000000000000000\, {\alpha_0}^2 \\ & - 35134000000000000000000000000000000000) \end{aligned}$$

$$
\begin{aligned}
k_2^0 = &- \frac{11710117031201997339471410648065031563}{144000000000000000000000000000000000000000} {\alpha_0}^{10} \\
&+ \frac{14254356089314209420185796515628 53}{216000000000000000000000000000000000000} {\alpha_0}^{8} \\
&- \frac{30810267811181666243107861}{216000000000000000000000000} {\alpha_0}^{6} \\
&+ \frac{959375789654233277}{86400000000000000000} {\alpha_0}^{4} \\
&- \frac{411459911}{144000000000} {\alpha_0}^{2} \\
&+ \frac{1}{8640}
\end{aligned}
$$

$$
\begin{aligned}
k_3^0 = &- \frac{1}{75600000000000000000000000000000000000000000} \cdot \\
&(4999441708897943361224517686884511889\,{\alpha_0}^{10} \\
&- 49370864407971706876783353754352473 1200\,{\alpha_0}^{8} \\
&+ 76746958352433433009360716829440000000 00\,{\alpha_0}^{6} \\
&- 39437681027798014523046400000000000000 0000\,{\alpha_0}^{4} \\
&+ 72987094717378560000000000000000000000 0000\,{\alpha_0}^{2} \\
&- 35977216000000000000000000000000000000 0000)\alpha_0
\end{aligned}
$$

$$
\begin{aligned}
k_4^0 = &\frac{11710117031201997339471410648065031563}{126000000000000000000000000000000000000000000} {\alpha_0}^{10} \\
&- \frac{14254356089314209420185796515628 53}{472500000000000000000000000000000000} {\alpha_0}^{8} \\
&+ \frac{44014668301688094633011 23}{16875000000000000000000000} {\alpha_0}^{6} \\
&- \frac{959375789654233277}{1181250000000000000} {\alpha_0}^{4} \\
&+ \frac{411459911}{492187500} {\alpha_0}^{2} \\
&- \frac{128}{945}
\end{aligned}
$$

$$
\begin{aligned}
k_5^0 =& \frac{1}{22400000000000000000000000000000000000000} \cdot \\
& (5554935232108825956916130763205013 21\,{\alpha_0}^{10} \\
& - 12342716101992926719195838438588118 2800\,{\alpha_0}^{8} \\
& + 43170164073243806067765403216560000000 00\,{\alpha_0}^{6} \\
& - 49913315050806862130730600000000000000 0000\,{\alpha_0}^{4} \\
& + 20784215644128504000000000000000000000 0000000\,{\alpha_0}^{2} \\
& - 23051417400000000000000000000000000000 0000000)\alpha_0
\end{aligned}
$$

$$
\begin{aligned}
k_6^0 =& - \frac{11710117031201997339471410648065031563}{22400000000000000000000000000000000000000000}\,{\alpha_0}^{10} \\
& + \frac{42763068267942628260557389546885 59}{11200000000000000000000000000000000000000}\,{\alpha_0}^{8} \\
& - \frac{11883960441455785550913032 1}{16000000000000000000000000000}\,{\alpha_0}^{6} \\
& + \frac{233128316885978686311}{44800000000000000000}\,{\alpha_0}^{4} \\
& - \frac{2699588476071}{224000000000}\,{\alpha_0}^{2} \\
& + \frac{19683}{4480}
\end{aligned}
$$

$$
\begin{aligned}
k_7^0 =& - \frac{1}{90720000000000000000000000000000000000000000} \cdot \\
& (4999441708897943361224517686884511889\,{\alpha_0}^{10} \\
& - 19748345763188682750713341501740989248 00\,{\alpha_0}^{8} \\
& + 12279513336389349281497714692710400000000 0\,{\alpha_0}^{6} \\
& - 25240115857790729294749696000000000000000 00\,{\alpha_0}^{4} \\
& + 18684696247648911360000000000000000000000 00000\,{\alpha_0}^{2} \\
& - 36840669184000000000000000000000000000000 0000000)\alpha_0
\end{aligned}
$$

$$
\begin{aligned}
k_8^0 =& \frac{11710117031201997339471410648065031563}{75600000000000000000000000000000000000000000000}\,{\alpha_0}^{10} \\
& - \frac{14254356089314209420185796515628 53}{70875000000000000000000000000000000000}\,{\alpha_0}^{8} \\
& + \frac{44014668301688094633011 23}{63281250000000000000000000}\,{\alpha_0}^{6} \\
& - \frac{959375789654233277}{110742187500000000}\,{\alpha_0}^{4} \\
& + \frac{13166717152}{369140625}\,{\alpha_0}^{2} \\
& - \frac{65536}{2835}
\end{aligned}
$$

$$
\begin{aligned}
k_9^0 = & \frac{1}{907200000000000000000000000000000000000000000} \\
& (4999441708897943361224517686884511889\,{\alpha_0}^{10} \\
& - 308567902549823167979895960964702957000 0\,{\alpha_0}^{8} \\
& + 299792806064193097692815300115000000000000\,{\alpha_0}^{6} \\
& - 962834009467724963941562500000000000000000\,{\alpha_0}^{4} \\
& + 111369468257718750000000000000000000000000000\,{\alpha_0}^{2} \\
& - 34310546875000000000000000000000000000000000)\alpha_0
\end{aligned}
$$

$$
\begin{aligned}
k_{10}^0 = & \frac{11710117031201997339471410648065031563}{60480000000000000000000000000000000000000000}\,{\alpha_0}^{10} \\
& + \frac{14254356089314209420185796515628 53}{36288000000000000000000000000000000000}\,{\alpha_0}^{8} \\
& - \frac{4401466830168809463301123}{20736000000000000000000000}\,{\alpha_0}^{6} \\
& + \frac{959375789654233277}{232243200000000000}\,{\alpha_0}^{4} \\
& - \frac{411459911}{15482880}\,{\alpha_0}^{2} \\
& + \frac{1953125}{72576}
\end{aligned}
$$

$$
k_{11}^0 = -\frac{5554935232108825956916130763205013 21}{80000000000000000000000000000000000000000000}\,{\alpha_0}^{11}
$$

10.2 Data fitting and model synthesis

The data fitting algorithm using the **interpolation** of the measured points of the frequency response was explained in the section (5.3) on the example of the two-mass flexible system. The system model is assumed in the form:

$$
P(s) = \frac{v_m(s)}{T_m(s)} = \left(\frac{K}{s+a}\right)\left(\frac{s^2 + 2\xi_z\omega_z s + \omega_z^2}{s^2 + 2\xi_n\omega_n s + \omega_n^2}\right) = \frac{b_2 s^2 + b_1 s + b_0}{s^3 + a_2 s^2 + a_1 s + a_0}. \qquad (10.3)
$$

The analytical solution for the transfer function coefficients is derived from the set of polynomial equations $P(i\omega_l) \stackrel{!}{=} \hat{P}(i\omega_l);\ l = 1, 2, 3$ in the form of:

$$
\begin{aligned}
a_0 =& \{+2\,im_1\,im_2\,re_3\,\omega_1\,\omega_2\,{\omega_3}^4 - 2\,im_1\,im_3\,re_2\,{\omega_1}^3{\omega_2}^2\omega_3 + 2\,im_1\,im_3\,re_2\,\omega_1\,{\omega_2}^4\omega_3 \\
&- 2\,im_1\,im_3\,re_2\,\omega_1\,{\omega_2}^2{\omega_3}^3 - {im_2}^2 re_1\,{\omega_1}^4{\omega_2}^2 + {im_2}^2 re_1\,{\omega_1}^2{\omega_2}^4 \\
&- {im_2}^2 re_1\,{\omega_2}^4{\omega_3}^2 - {im_2}^2 re_3\,{\omega_1}^2{\omega_2}^4 + {im_2}^2 re_3\,{\omega_2}^4{\omega_3}^2 - {im_2}^2 re_3\,{\omega_2}^2{\omega_3}^4 \\
&- {im_3}^2 re_1\,{\omega_1}^4{\omega_3}^2 + {im_3}^2 re_1\,{\omega_1}^2{\omega_3}^4 - {im_3}^2 re_1\,{\omega_2}^2{\omega_3}^4 - {im_3}^2 re_2\,{\omega_1}^2{\omega_3}^4 \\
&- {im_3}^2 re_2\,{\omega_2}^4{\omega_3}^2 + {im_3}^2 re_2\,{\omega_2}^2{\omega_3}^4 + {re_1}^2 re_2\,{\omega_1}^4{\omega_2}^2 - {re_1}^2 re_2\,{\omega_1}^4{\omega_3}^2 \\
&- {re_1}^2 re_2\,{\omega_1}^2{\omega_2}^4 - {re_1}^2 re_3\,{\omega_1}^4{\omega_2}^2 + {re_1}^2 re_3\,{\omega_1}^4{\omega_3}^2 - {re_1}^2 re_3\,{\omega_1}^2{\omega_3}^4 \\
&- re_1\,{re_2}^2{\omega_1}^4{\omega_2}^2 + re_1\,{re_2}^2{\omega_1}^2{\omega_2}^4 - re_1\,{re_2}^2{\omega_2}^4{\omega_3}^2 - re_1\,{re_3}^2{\omega_1}^4{\omega_3}^2 \\
&+ re_1\,{re_3}^2{\omega_1}^2{\omega_3}^4 - re_1\,{re_3}^2{\omega_2}^2{\omega_3}^4 - {re_2}^2 re_3\,{\omega_1}^2{\omega_2}^4 + {re_2}^2 re_3\,{\omega_2}^4{\omega_3}^2 \\
&- {re_2}^2 re_3\,{\omega_2}^2{\omega_3}^4 - re_2\,{re_3}^2{\omega_1}^2{\omega_3}^4 - re_2\,{re_3}^2{\omega_2}^4{\omega_3}^2 + re_2\,{re_3}^2{\omega_2}^2{\omega_3}^4 \\
&+ {im_1}^2 re_2\,{\omega_1}^4{\omega_2}^2 - {im_1}^2 re_2\,{\omega_1}^4{\omega_3}^2 - {im_1}^2 re_2\,{\omega_1}^2{\omega_2}^4 - {im_1}^2 re_3\,{\omega_1}^4{\omega_2}^2 \\
&+ {im_1}^2 re_3\,{\omega_1}^4{\omega_3}^2 - {im_1}^2 re_3\,{\omega_1}^2{\omega_3}^4 + 2\,im_1\,im_2\,re_3\,{\omega_1}^3{\omega_2}^3 \\
&+ 2\,im_1\,im_3\,re_2\,{\omega_1}^3{\omega_3}^3 + {im_2}^2 re_1\,{\omega_1}^2{\omega_2}^2{\omega_3}^2 + {im_2}^2 re_3\,{\omega_1}^2{\omega_2}^2{\omega_3}^2 \\
&+ 2\,im_2\,im_3\,re_1\,{\omega_2}^3{\omega_3}^3 + {im_3}^2 re_1\,{\omega_1}^2{\omega_2}^2{\omega_3}^2 + {im_3}^2 re_2\,{\omega_1}^2{\omega_2}^2{\omega_3}^2 \\
&+ {re_1}^2 re_2\,{\omega_1}^2{\omega_2}^2{\omega_3}^2 + {re_1}^2 re_3\,{\omega_1}^2{\omega_2}^2{\omega_3}^2 + re_1\,{re_2}^2{\omega_1}^2{\omega_2}^2{\omega_3}^2 \\
&+ re_1\,re_2\,re_3\,{\omega_1}^4{\omega_2}^2 + re_1\,re_2\,re_3\,{\omega_1}^4{\omega_3}^2 + re_1\,re_2\,re_3\,{\omega_1}^2{\omega_2}^4 \\
&+ re_1\,re_2\,re_3\,{\omega_1}^2{\omega_3}^4 + re_1\,re_2\,re_3\,{\omega_2}^4{\omega_3}^2 + re_1\,re_2\,re_3\,{\omega_2}^2{\omega_3}^4 \\
&+ re_1\,{re_3}^2{\omega_1}^2{\omega_2}^2{\omega_3}^2 + {re_2}^2 re_3\,{\omega_1}^2{\omega_2}^2{\omega_3}^2 + re_2\,{re_3}^2{\omega_1}^2{\omega_2}^2{\omega_3}^2 \\
&+ {im_1}^2 re_2\,{\omega_1}^2{\omega_2}^2{\omega_3}^2 + {im_1}^2 re_3\,{\omega_1}^2{\omega_2}^2{\omega_3}^2)\}/\{-6\,im_1\,im_2\,im_3\,{\omega_1}^2{\omega_2}^2{\omega_3}^2 \\
&+ 2\,im_1\,re_2\,re_3\,{\omega_1}^4\omega_2\,\omega_3 - 2\,im_1\,re_2\,re_3\,{\omega_1}^2{\omega_2}^3\omega_3 - 2\,im_1\,re_2\,re_3\,{\omega_1}^2\omega_2\,{\omega_3}^3 \\
&- 2\,im_2\,re_1\,re_3\,{\omega_1}^3{\omega_2}^2\omega_3 + 2\,im_2\,re_1\,re_3\,\omega_1\,{\omega_2}^4\omega_3 - 2\,im_2\,re_1\,re_3\,\omega_1\,{\omega_2}^2{\omega_3}^3 \\
&- 2\,im_3\,re_1\,re_2\,{\omega_1}^3\omega_2\,{\omega_3}^2 - 2\,im_3\,re_1\,re_2\,\omega_1\,{\omega_2}^3{\omega_3}^2 + 2\,im_3\,re_1\,re_2\,\omega_1\,\omega_2\,{\omega_3}^4 \\
&- im_3\,{re_2}^2{\omega_1}^3{\omega_2}^3 - {im_1}^2 im_3\,{\omega_1}^3{\omega_2}^3 - {im_2}^2 im_3\,{\omega_1}^3{\omega_2}^3 - im_3\,{re_1}^2{\omega_1}^3{\omega_2}^3 \\
&- {im_1}^2 im_2\,{\omega_1}^3{\omega_3}^3 - im_2\,im_3^2{\omega_1}^3{\omega_3}^3 - im_2\,{re_1}^2{\omega_1}^3{\omega_3}^3 - im_2\,{re_3}^2{\omega_1}^3{\omega_3}^3 \\
&- im_1\,{im_2}^2{\omega_2}^3{\omega_3}^3 - im_1\,im_3^2{\omega_2}^3{\omega_3}^3 - im_1\,{re_2}^2{\omega_2}^3{\omega_3}^3 - im_1\,{re_3}^2{\omega_2}^3{\omega_3}^3 \\
&+ im_1\,im_2\,im_3\,{\omega_1}^4{\omega_2}^2 + im_1\,im_2\,im_3\,{\omega_1}^2{\omega_2}^4 + im_1\,im_2\,im_3\,{\omega_1}^4{\omega_3}^2 \\
&+ im_1\,im_2\,im_3\,{\omega_1}^2{\omega_3}^4 + 2\,im_3\,re_1\,re_2\,{\omega_1}^3{\omega_2}^3 + im_1\,im_2\,im_3\,{\omega_2}^4{\omega_3}^2 \\
&+ im_1\,im_2\,im_3\,{\omega_2}^2{\omega_3}^4 + 2\,im_2\,re_1\,re_3\,{\omega_1}^3{\omega_3}^3 + 2\,im_1\,re_2\,re_3\,{\omega_2}^3{\omega_3}^3 \\
&- im_2\,im_3^2\omega_1\,{\omega_2}^4\omega_3 + im_2\,im_3^2\omega_1\,{\omega_2}^2{\omega_3}^3 + im_2\,{re_1}^2{\omega_1}^3{\omega_2}^2\omega_3 - im_2\,{re_1}^2\omega_1\,{\omega_2}^4\omega_3 \\
&+ im_2\,{re_1}^2\omega_1\,{\omega_2}^2{\omega_3}^3 + im_2\,{re_3}^2{\omega_1}^3{\omega_2}^2\omega_3 - im_2\,{re_3}^2\omega_1\,{\omega_2}^4\omega_3 + im_2\,{re_3}^2\omega_1\,{\omega_2}^2{\omega_3}^3 \\
&+ im_3\,{re_1}^2{\omega_1}^3\omega_2\,{\omega_3}^2 + im_3\,{re_1}^2\omega_1\,{\omega_2}^3{\omega_3}^2 - im_3\,{re_1}^2\omega_1\,\omega_2\,{\omega_3}^4 + im_3\,{re_2}^2{\omega_1}^3\omega_2\,{\omega_3}^2 \\
&- im_1\,{re_3}^2{\omega_1}^4\omega_2\,\omega_3 + im_1\,{re_3}^2{\omega_1}^2{\omega_2}^3\omega_3 + im_1\,{re_3}^2{\omega_1}^2\omega_2\,{\omega_3}^3 + {im_2}^2 im_3\,{\omega_1}^3\omega_2\,{\omega_3}^2 \\
&+ {im_2}^2 im_3\,\omega_1\,{\omega_2}^3{\omega_3}^2 - {im_2}^2 im_3\,\omega_1\,\omega_2\,{\omega_3}^4 + im_2\,im_3^2{\omega_1}^3{\omega_2}^2\omega_3 \\
&+ im_3\,{re_2}^2\omega_1\,{\omega_2}^3{\omega_3}^2 - im_3\,{re_2}^2\omega_1\,\omega_2\,{\omega_3}^4 + {im_1}^2 im_2\,{\omega_1}^3{\omega_2}^2\omega_3 - {im_1}^2 im_2\,\omega_1\,{\omega_2}^4\omega_3 \\
&+ {im_1}^2 im_2\,\omega_1\,{\omega_2}^2{\omega_3}^3 + {im_1}^2 im_3\,{\omega_1}^3\omega_2\,{\omega_3}^2 + {im_1}^2 im_3\,\omega_1\,{\omega_2}^3{\omega_3}^2 \\
&- {im_1}^2 im_3\,\omega_1\,\omega_2\,{\omega_3}^4 - im_1\,{im_2}^2{\omega_1}^4\omega_2\,\omega_3 + im_1\,{im_2}^2{\omega_1}^2{\omega_2}^3\omega_3 \\
&+ im_1\,{im_2}^2{\omega_1}^2\omega_2\,{\omega_3}^3 - im_1\,im_3^2{\omega_1}^4\omega_2\,\omega_3 + im_1\,im_3^2{\omega_1}^2{\omega_2}^3\omega_3 \\
&+ im_1\,im_3^2{\omega_1}^2\omega_2\,{\omega_3}^3 - im_1\,{re_2}^2{\omega_1}^4\omega_2\,\omega_3 + im_1\,{re_2}^2{\omega_1}^2{\omega_2}^3\omega_3 \\
&+ im_1\,{re_2}^2{\omega_1}^2\omega_2\,{\omega_3}^3\},
\end{aligned}
\tag{10.4}
$$

$$
\begin{aligned}
a_1 = \{&-im_1 re_3{}^2 \omega_1{}^4 \omega_2 \omega_3{}^3 + im_1 re_2 re_3 \omega_2{}^3 \omega_3{}^5 + im_1 re_2 re_3 \omega_2{}^5 \omega_3{}^3 + im_1 re_2{}^2 \omega_1{}^2 \omega_2{}^5 \omega_3 \\
&+ im_1 re_2{}^2 \omega_1{}^2 \omega_2{}^3 \omega_3{}^3 - im_1 re_2{}^2 \omega_1{}^4 \omega_2{}^3 \omega_3 + im_1 im_3{}^2 \omega_1{}^2 \omega_2 \omega_3{}^5 - im_1 im_3{}^2 \omega_1{}^4 \omega_2 \omega_3{}^3 \\
&+ im_1 im_3{}^2 \omega_1{}^2 \omega_2{}^3 \omega_3{}^3 + 2\, im_1 im_2 im_3 \omega_2{}^4 \omega_3{}^4 + 2\, im_1 im_2 im_3 \omega_1{}^4 \omega_2{}^4 + 2\, im_1 im_2 im_3 \omega_1{}^4 \omega_3{}^4 \\
&+ im_1 im_2{}^2 \omega_1{}^2 \omega_2{}^5 \omega_3 + im_1 im_2{}^2 \omega_1{}^2 \omega_2{}^3 \omega_3{}^3 - im_1{}^2 im_3 \omega_1{}^3 \omega_2 \omega_3{}^4 - im_1 im_2{}^2 \omega_1{}^4 \omega_2{}^3 \omega_3 \\
&+ im_1{}^2 im_3 \omega_1{}^5 \omega_2 \omega_3{}^2 + im_1{}^2 im_3 \omega_1{}^3 \omega_2{}^3 \omega_3{}^2 + im_1{}^2 im_2 \omega_1{}^5 \omega_2{}^2 \omega_3 - im_1{}^2 im_2 \omega_1{}^3 \omega_2{}^4 \omega_3 \\
&+ im_1{}^2 im_2 \omega_1{}^3 \omega_2{}^2 \omega_3{}^3 + im_3 re_1 re_2 \omega_1{}^3 \omega_2{}^5 + im_3 re_2{}^2 \omega_1{}^3 \omega_2{}^3 \omega_3{}^2 + im_3 re_2{}^2 \omega_1 \omega_2{}^5 \omega_3{}^2 \\
&- im_3 re_2{}^2 \omega_1 \omega_2{}^3 \omega_3{}^4 + im_3 re_1 re_2 \omega_1{}^5 \omega_2{}^3 - im_3 re_1{}^2 \omega_1{}^3 \omega_2 \omega_3{}^4 + im_3 re_1{}^2 \omega_1{}^3 \omega_2{}^3 \omega_3{}^2 \\
&+ im_3 re_1{}^2 \omega_1{}^5 \omega_2 \omega_3{}^2 + im_2 re_3{}^2 \omega_1 \omega_2{}^2 \omega_3{}^5 - im_2 re_3{}^2 \omega_1 \omega_2{}^4 \omega_3{}^3 + im_2 re_3{}^2 \omega_1{}^3 \omega_2{}^2 \omega_3{}^3 \\
&+ im_2 re_1 re_3 \omega_1{}^3 \omega_3{}^5 + im_2 re_1 re_3 \omega_1{}^5 \omega_3{}^3 + im_2 re_1{}^2 \omega_1{}^3 \omega_2{}^2 \omega_3{}^3 - im_2 re_1{}^2 \omega_1{}^3 \omega_2{}^4 \omega_3 \\
&+ im_2 re_1{}^2 \omega_1{}^5 \omega_2{}^2 \omega_3 + im_2 im_3{}^2 \omega_1 \omega_2{}^2 \omega_3{}^5 - im_2 im_3{}^2 \omega_1 \omega_2{}^4 \omega_3{}^3 + im_2 im_3{}^2 \omega_1{}^3 \omega_2{}^2 \omega_3{}^3 \\
&- im_2{}^2 im_3 \omega_1 \omega_2{}^3 \omega_3{}^4 + im_2{}^2 im_3 \omega_1 \omega_2{}^5 \omega_3{}^2 + im_2{}^2 im_3 \omega_1{}^3 \omega_2{}^3 \omega_3{}^2 + im_1 re_3{}^2 \omega_1{}^2 \omega_2 \omega_3{}^5 \\
&+ im_1 re_3{}^2 \omega_1{}^2 \omega_2{}^3 \omega_3{}^3 + im_2 re_1 re_3 \omega_1 \omega_2{}^4 \omega_3{}^3 - im_1 re_2 re_3 \omega_1{}^2 \omega_2{}^5 \omega_3 + im_1 re_2 re_3 \omega_1{}^4 \omega_2{}^3 \omega_3 \\
&+ im_1 re_2 re_3 \omega_1{}^4 \omega_2 \omega_3{}^3 - 2\, im_1 im_2 im_3 \omega_1{}^2 \omega_2{}^2 \omega_3{}^4 - 2\, im_1 im_2 im_3 \omega_1{}^4 \omega_2{}^2 \omega_3{}^2 - 2\, im_1 im_2 im_3 \omega_1{}^2 \omega_2{}^4 \omega_3{}^2 \\
&+ im_3 re_1 re_2 \omega_1 \omega_2{}^3 \omega_3{}^4 + im_3 re_1 re_2 \omega_1{}^3 \omega_2 \omega_3{}^4 - im_3 re_1 re_2 \omega_1 \omega_2{}^5 \omega_3{}^2 - im_2 re_1 re_3 \omega_1 \omega_2{}^2 \omega_3{}^5 \\
&- im_3 re_1 re_2 \omega_1{}^5 \omega_2 \omega_3{}^2 - 2\, im_3 re_1 re_2 \omega_1{}^3 \omega_2{}^3 \omega_3{}^2 - 2\, im_1 re_2 re_3 \omega_1{}^2 \omega_2{}^3 \omega_3{}^3 - im_1 re_2 re_3 \omega_1{}^2 \omega_2 \omega_3{}^5 \\
&- im_2 re_1 re_3 \omega_1{}^5 \omega_2{}^2 \omega_3 + im_2 re_1 re_3 \omega_1{}^3 \omega_2{}^4 \omega_3 - 2\, im_2 re_1 re_3 \omega_1{}^3 \omega_2{}^2 \omega_3{}^3 - im_1{}^2 im_2 \omega_1{}^5 \omega_3{}^3 \\
&- im_1{}^2 im_3 \omega_1{}^5 \omega_2{}^3 - im_1 im_2{}^2 \omega_2{}^5 \omega_3{}^3 - im_1 im_3{}^2 \omega_2{}^3 \omega_3{}^5 - im_1 re_2{}^2 \omega_2{}^5 \omega_3{}^3 \\
&- im_1 re_3{}^2 \omega_2{}^3 \omega_3{}^5 - im_2{}^2 im_3 \omega_1{}^3 \omega_2{}^5 - im_3 re_1{}^2 \omega_1{}^5 \omega_2{}^3 - im_3 re_2{}^2 \omega_1{}^3 \omega_2{}^5 \\
&- im_2 im_3{}^2 \omega_1{}^3 \omega_3{}^5 - im_2 re_1{}^2 \omega_1{}^5 \omega_3{}^3 - im_2 re_3{}^2 \omega_1{}^3 \omega_3{}^5\} / \{im_1 im_2 im_3 \omega_1{}^4 \omega_2{}^2 \\
&+ im_1 im_2 im_3 \omega_1{}^2 \omega_2{}^4 + im_1 im_2 im_3 \omega_1{}^4 \omega_3{}^2 + im_1 im_2 im_3 \omega_1{}^2 \omega_3{}^4 + 2\, im_3 re_1 re_2 \omega_1{}^3 \omega_2{}^3 \\
&+ im_1 im_2 im_3 \omega_2{}^4 \omega_3{}^2 - im_3 re_1{}^2 \omega_1 \omega_2 \omega_3{}^4 + im_3 re_2{}^2 \omega_1{}^3 \omega_2 \omega_3{}^2 + im_1 im_2 im_3 \omega_2{}^2 \omega_3{}^4 \\
&+ 2\, im_2 re_1 re_3 \omega_1{}^3 \omega_3{}^3 + 2\, im_1 re_2 re_3 \omega_2{}^3 \omega_3{}^3 + im_3 re_1{}^2 \omega_1 \omega_2{}^3 \omega_3{}^2 - im_2 re_1{}^2 \omega_1 \omega_2{}^4 \omega_3 \\
&+ im_2 re_1{}^2 \omega_1 \omega_2{}^2 \omega_3{}^3 + im_2 re_3{}^2 \omega_1{}^3 \omega_2{}^2 \omega_3 - im_2 re_3{}^2 \omega_1 \omega_2{}^4 \omega_3 + im_2 re_3{}^2 \omega_1 \omega_2{}^2 \omega_3{}^3 \\
&+ im_3 re_1{}^2 \omega_1{}^3 \omega_2 \omega_3{}^2 + im_2 im_3{}^2 \omega_1{}^3 \omega_2{}^2 \omega_3 - im_2{}^2 im_3 \omega_1 \omega_2 \omega_3{}^4 + im_2{}^2 im_3 \omega_1 \omega_2{}^3 \omega_3{}^2 \\
&+ im_2{}^2 im_3 \omega_1{}^3 \omega_2 \omega_3{}^2 + im_1 re_3{}^2 \omega_1{}^2 \omega_2 \omega_3{}^3 + im_1 re_3{}^2 \omega_1{}^2 \omega_2{}^3 \omega_3 + im_3 re_2{}^2 \omega_1 \omega_2{}^3 \omega_3{}^2 \\
&- im_3 re_2{}^2 \omega_1 \omega_2 \omega_3{}^4 - im_2 im_3{}^2 \omega_1 \omega_2{}^4 \omega_3 + im_2 im_3{}^2 \omega_1 \omega_2{}^2 \omega_3{}^3 + im_2 re_1{}^2 \omega_1{}^3 \omega_2{}^2 \omega_3 \\
&- im_1 re_3{}^2 \omega_1{}^4 \omega_2 \omega_3 + im_1 re_2{}^2 \omega_1{}^2 \omega_2 \omega_3{}^3 + im_1 re_2{}^2 \omega_1{}^2 \omega_2{}^3 \omega_3 - im_1 re_2{}^2 \omega_1{}^4 \omega_2 \omega_3 \\
&+ im_1 im_3{}^2 \omega_1{}^2 \omega_2 \omega_3{}^3 + im_1 im_3{}^2 \omega_1{}^2 \omega_2{}^3 \omega_3 - im_1 im_3{}^2 \omega_1{}^4 \omega_2 \omega_3 + im_1 im_2{}^2 \omega_1{}^2 \omega_2 \omega_3{}^3 \\
&+ im_1 im_2{}^2 \omega_1{}^2 \omega_2{}^3 \omega_3 - im_1 im_2{}^2 \omega_1{}^4 \omega_2 \omega_3 - im_1{}^2 im_3 \omega_1 \omega_2 \omega_3{}^4 + im_1{}^2 im_3 \omega_1 \omega_2{}^3 \omega_3{}^2 \\
&+ im_1{}^2 im_3 \omega_1{}^3 \omega_2 \omega_3{}^2 - im_1{}^2 im_2 \omega_1 \omega_2{}^4 \omega_3 + im_1{}^2 im_2 \omega_1 \omega_2{}^2 \omega_3{}^3 + im_1{}^2 im_2 \omega_1{}^3 \omega_2{}^2 \omega_3 \\
&+ 2\, im_2 re_1 re_3 \omega_1 \omega_2{}^4 \omega_3 - 2\, im_2 re_1 re_3 \omega_1 \omega_2{}^2 \omega_3{}^3 + 2\, im_3 re_1 re_2 \omega_1 \omega_2 \omega_3{}^4 - 2\, im_3 re_1 re_2 \omega_1{}^3 \omega_2 \omega_3{}^2 \\
&- 2\, im_3 re_1 re_2 \omega_1 \omega_2{}^3 \omega_3{}^2 - 2\, im_1 re_2 re_3 \omega_1{}^2 \omega_2{}^3 \omega_3 - 2\, im_1 re_2 re_3 \omega_1{}^2 \omega_2 \omega_3{}^3 - 2\, im_2 re_1 re_3 \omega_1{}^3 \omega_2{}^2 \omega_3 \\
&- 6\, im_1 im_2 im_3 \omega_1{}^2 \omega_2{}^2 \omega_3{}^2 + 2\, im_1 re_2 re_3 \omega_1{}^4 \omega_2 \omega_3 - im_3 re_2{}^2 \omega_1{}^3 \omega_2{}^3 - im_1{}^2 im_3 \omega_1{}^3 \omega_2{}^3 \\
&- im_2{}^2 im_3 \omega_1{}^3 \omega_2{}^3 - im_3 re_1{}^2 \omega_1{}^3 \omega_2{}^3 - im_1{}^2 im_2 \omega_1{}^3 \omega_3{}^3 - im_2 im_3{}^2 \omega_1{}^3 \omega_3{}^3 \\
&- im_2 re_1{}^2 \omega_1{}^3 \omega_3{}^3 - im_2 re_3{}^2 \omega_1{}^3 \omega_3{}^3 - im_1 im_2{}^2 \omega_2{}^3 \omega_3{}^3 - im_1 im_3{}^2 \omega_2{}^3 \omega_3{}^3 \\
&- im_1 re_2{}^2 \omega_2{}^3 \omega_3{}^3 - im_1 re_3{}^2 \omega_2{}^3 \omega_3{}^3\},
\end{aligned}
\tag{10.5}
$$

$$
\begin{aligned}
a_2 = &- \{-re_1 re_2{}^2 \omega_1 \omega_2{}^3 \omega_3{}^3 - re_1 re_3{}^2 \omega_1{}^5 \omega_2 \omega_3 + im_1{}^2 re_2 \omega_1{}^3 \omega_2{}^3 \omega_3 - im_1{}^2 re_2 \omega_1{}^3 \omega_2 \omega_3{}^3 \\
&- im_1{}^2 re_2 \omega_1 \omega_2{}^5 \omega_3 + re_1 re_3{}^2 \omega_1{}^3 \omega_2{}^3 \omega_3 + re_1 re_3{}^2 \omega_1{}^3 \omega_2 \omega_3{}^3 - re_1 re_3{}^2 \omega_1 \omega_2{}^3 \omega_3{}^3 \\
&- re_2{}^2 re_3 \omega_1{}^3 \omega_2{}^3 \omega_3 + re_2{}^2 re_3 \omega_1{}^3 \omega_2 \omega_3{}^3 + re_2{}^2 re_3 \omega_1 \omega_2{}^3 \omega_3{}^3 - re_2{}^2 re_3 \omega_1 \omega_2 \omega_3{}^5 \\
&+ re_2 re_3{}^2 \omega_1{}^3 \omega_2{}^3 \omega_3 - re_2 re_3{}^2 \omega_1{}^3 \omega_2 \omega_3{}^3 - re_2 re_3{}^2 \omega_1 \omega_2{}^5 \omega_3 + re_2 re_3{}^2 \omega_1 \omega_2{}^3 \omega_3{}^3 \\
&- im_1 im_2 re_3 \omega_2{}^4 \omega_3{}^3 + im_1 im_2 re_3 \omega_2{}^2 \omega_3{}^5 - im_1 im_3 re_2 \omega_1{}^4 \omega_2{}^3 + im_1 im_3 re_2 \omega_1{}^2 \omega_2{}^5 \\
&+ im_1{}^2 re_2 \omega_1 \omega_2{}^3 \omega_3{}^3 - im_1{}^2 re_3 \omega_1{}^3 \omega_2{}^3 \omega_3 + im_1{}^2 re_3 \omega_1{}^3 \omega_2 \omega_3{}^3 + im_1{}^2 re_3 \omega_1 \omega_2{}^3 \omega_3{}^3 \\
&- im_1{}^2 re_3 \omega_1 \omega_2 \omega_3{}^5 - im_1 im_2 re_3 \omega_1{}^4 \omega_3{}^3 + im_1 im_2 re_3 \omega_1{}^2 \omega_3{}^5 + im_1 im_3 re_2 \omega_2{}^5 \omega_3{}^2 \\
&- im_1 im_3 re_2 \omega_2{}^3 \omega_3{}^4 - im_2{}^2 re_1 \omega_1{}^5 \omega_2 \omega_3 + im_2{}^2 re_1 \omega_1{}^3 \omega_2{}^3 \omega_3 + im_2{}^2 re_1 \omega_1{}^3 \omega_2 \omega_3{}^3 \\
&- im_2{}^2 re_1 \omega_1 \omega_2{}^3 \omega_3{}^3 - im_2{}^2 re_3 \omega_1{}^3 \omega_2{}^3 \omega_3 + im_2{}^2 re_3 \omega_1{}^3 \omega_2 \omega_3{}^3 + im_2{}^2 re_3 \omega_1 \omega_2{}^3 \omega_3{}^3 \\
&- im_2{}^2 re_3 \omega_1 \omega_2 \omega_3{}^5 + im_2 im_3 re_1 \omega_1{}^5 \omega_2{}^2 + im_2 im_3 re_1 \omega_1{}^5 \omega_3{}^2 - im_2 im_3 re_1 \omega_1{}^3 \omega_2{}^4 \\
&- im_2 im_3 re_1 \omega_1{}^3 \omega_3{}^4 - im_3{}^2 re_1 \omega_1{}^5 \omega_2 \omega_3 + im_3{}^2 re_1 \omega_1{}^3 \omega_2{}^3 \omega_3 + im_3{}^2 re_1 \omega_1{}^3 \omega_2 \omega_3{}^3 \\
&- im_3{}^2 re_1 \omega_1 \omega_2{}^3 \omega_3{}^3 + im_3{}^2 re_2 \omega_1{}^3 \omega_2{}^3 \omega_3 - im_3{}^2 re_2 \omega_1{}^3 \omega_2 \omega_3{}^3 - im_3{}^2 re_2 \omega_1 \omega_2{}^5 \omega_3 \\
&+ im_3{}^2 re_2 \omega_1 \omega_2{}^3 \omega_3{}^3 + re_1{}^2 re_2 \omega_1{}^3 \omega_2{}^3 \omega_3 - re_1{}^2 re_2 \omega_1{}^3 \omega_2 \omega_3{}^3 - re_1{}^2 re_2 \omega_1 \omega_2{}^5 \omega_3 \\
&+ re_1{}^2 re_2 \omega_1 \omega_2{}^3 \omega_3{}^3 - re_1{}^2 re_3 \omega_1{}^3 \omega_2{}^3 \omega_3 + re_1{}^2 re_3 \omega_1{}^3 \omega_2 \omega_3{}^3 + re_1{}^2 re_3 \omega_1 \omega_2{}^3 \omega_3{}^3 \\
&- re_1{}^2 re_3 \omega_1 \omega_2 \omega_3{}^5 - re_1 re_2{}^2 \omega_1{}^5 \omega_2 \omega_3 + re_1 re_2{}^2 \omega_1{}^3 \omega_2{}^3 \omega_3 + re_1 re_2{}^2 \omega_1{}^3 \omega_2 \omega_3{}^3 \\
&+ im_1 im_3 re_2 \omega_1{}^4 \omega_2 \omega_3{}^2 + 2\, re_1 re_2 re_3 \omega_1 \omega_2{}^5 \omega_3 + 2\, re_1 re_2 re_3 \omega_1 \omega_2 \omega_3{}^5 \\
&- 2\, re_1 re_2 re_3 \omega_1{}^3 \omega_2 \omega_3{}^3 - 2\, re_1 re_2 re_3 \omega_1{}^3 \omega_2{}^3 \omega_3 + im_2 im_3 re_1 \omega_1 \omega_2{}^4 \omega_3{}^2 - 2\, im_2 im_3 re_1 \omega_1{}^3 \omega_2{}^2 \omega_3{}^2 \\
&+ im_1 im_3 re_2 \omega_1{}^2 \omega_2 \omega_3{}^4 - 2\, im_1 im_3 re_2 \omega_1{}^2 \omega_2{}^3 \omega_3{}^2 + im_1 im_2 re_3 \omega_1{}^2 \omega_2{}^4 \omega_3 + im_2 im_3 re_1 \omega_1 \omega_2{}^2 \omega_3{}^4 \\
&+ im_1 im_2 re_3 \omega_1{}^4 \omega_2{}^2 \omega_3 - 2\, re_1 re_2 re_3 \omega_1 \omega_2{}^3 \omega_3{}^3 - 2\, im_1 im_2 re_3 \omega_1{}^2 \omega_2{}^2 \omega_3{}^3 + 2\, re_1 re_2 re_3 \omega_1{}^5 \omega_2 \omega_3\} / \\
&\{im_1 im_2 im_3 \omega_1{}^4 \omega_2{}^2 + im_1 im_2 im_3 \omega_1{}^2 \omega_2{}^4 + im_1 im_2 im_3 \omega_1{}^4 \omega_3{}^2 + im_1 im_2 im_3 \omega_1{}^2 \omega_3{}^4 \\
&+ 2\, im_3 re_1 re_2 \omega_1{}^3 \omega_2{}^3 + im_1 im_2 im_3 \omega_2{}^4 \omega_3{}^2 - im_3 re_1{}^2 \omega_1 \omega_2 \omega_3{}^4 + im_3 re_2{}^2 \omega_1{}^3 \omega_2 \omega_3{}^2 \\
&+ im_1 im_2 im_3 \omega_2{}^2 \omega_3{}^4 + 2\, im_2 re_1 re_3 \omega_1{}^3 \omega_3{}^3 + 2\, im_1 re_2 re_3 \omega_2{}^3 \omega_3{}^3 + im_3 re_1{}^2 \omega_1 \omega_2{}^3 \omega_3{}^2 \\
&- im_2 re_1{}^2 \omega_1 \omega_2{}^4 \omega_3 + im_2 re_1{}^2 \omega_1 \omega_2{}^2 \omega_3{}^3 + im_2 re_3{}^2 \omega_1{}^3 \omega_2{}^2 \omega_3 - im_2 re_3{}^2 \omega_1 \omega_2{}^4 \omega_3 \\
&+ im_2 re_3{}^2 \omega_1 \omega_2{}^2 \omega_3{}^3 + im_3 re_1{}^2 \omega_1{}^3 \omega_2 \omega_3{}^2 + im_2 im_3{}^2 \omega_1{}^3 \omega_2{}^2 \omega_3 - im_2{}^2 im_3 \omega_1 \omega_2 \omega_3{}^4 \\
&+ im_2{}^2 im_3 \omega_1 \omega_2{}^3 \omega_3{}^2 + im_2{}^2 im_3 \omega_1{}^3 \omega_2 \omega_3{}^2 + im_1 re_3{}^2 \omega_1{}^2 \omega_2 \omega_3{}^3 + im_1 re_3{}^2 \omega_1{}^2 \omega_2{}^3 \omega_3 \\
&+ im_3 re_2{}^2 \omega_1 \omega_2{}^3 \omega_3{}^2 - im_3 re_2{}^2 \omega_1 \omega_2 \omega_3{}^4 - im_2 im_3{}^2 \omega_1 \omega_2{}^4 \omega_3 + im_2 im_3{}^2 \omega_1 \omega_2{}^2 \omega_3{}^3 \\
&+ im_2 re_1{}^2 \omega_1{}^3 \omega_2{}^2 \omega_3 - im_1 re_3{}^2 \omega_1{}^4 \omega_2 \omega_3 + im_1 re_2{}^2 \omega_1{}^2 \omega_2 \omega_3{}^3 + im_1 re_2{}^2 \omega_1{}^2 \omega_2{}^3 \omega_3 \\
&- im_1 re_2{}^2 \omega_1{}^4 \omega_2 \omega_3 + im_1 im_3{}^2 \omega_1{}^2 \omega_2 \omega_3{}^3 + im_1 im_3{}^2 \omega_1{}^2 \omega_2{}^3 \omega_3 - im_1 im_3{}^2 \omega_1{}^4 \omega_2 \omega_3 \\
&+ im_1 im_2{}^2 \omega_1{}^2 \omega_2 \omega_3{}^3 + im_1 im_2{}^2 \omega_1{}^2 \omega_2{}^3 \omega_3 - im_1 im_2{}^2 \omega_1{}^4 \omega_2 \omega_3 - im_1{}^2 im_3 \omega_1 \omega_2 \omega_3{}^4 \\
&+ im_1{}^2 im_3 \omega_1{}^3 \omega_2 \omega_3{}^2 - im_1{}^2 im_2 \omega_1 \omega_2{}^4 \omega_3 + im_1{}^2 im_2 \omega_1 \omega_2{}^2 \omega_3{}^3 + im_1{}^2 im_2 \omega_1{}^3 \omega_2{}^2 \omega_3 \\
&+ 2\, im_2 re_1 re_3 \omega_1 \omega_2{}^4 \omega_3 - 2\, im_2 re_1 re_3 \omega_1 \omega_2{}^2 \omega_3{}^3 + 2\, im_3 re_1 re_2 \omega_1 \omega_2 \omega_3{}^4 - 2\, im_3 re_1 re_2 \omega_1{}^3 \omega_2 \omega_3{}^2 \\
&- 2\, im_3 re_1 re_2 \omega_1 \omega_2{}^3 \omega_3{}^2 - 2\, im_1 re_2 re_3 \omega_1{}^2 \omega_2{}^3 \omega_3 - 2\, im_1 re_2 re_3 \omega_1{}^2 \omega_2 \omega_3{}^3 - 2\, im_2 re_1 re_3 \omega_1{}^3 \omega_2{}^2 \omega_3 \\
&- 6\, im_1 im_2 im_3 \omega_1{}^2 \omega_2{}^2 \omega_3{}^2 + 2\, im_1 re_2 re_3 \omega_1{}^4 \omega_2 \omega_3 - im_3 re_2{}^2 \omega_1{}^3 \omega_2{}^3 - im_1{}^2 im_3 \omega_1{}^3 \omega_2{}^3 \\
&+ im_1{}^2 im_3 \omega_1 \omega_2{}^3 \omega_3{}^2 - im_2{}^2 im_3 \omega_1{}^3 \omega_2{}^3 - im_3 re_1{}^2 \omega_1{}^3 \omega_2{}^3 - im_1{}^2 im_2 \omega_1{}^3 \omega_3{}^3 \\
&- im_2 im_3{}^2 \omega_1{}^3 \omega_3{}^3 - im_2 re_1{}^2 \omega_1{}^3 \omega_3{}^3 - im_2 re_3{}^2 \omega_1{}^3 \omega_3{}^3 - im_1 im_2{}^2 \omega_2{}^3 \omega_3{}^3 \\
&- im_1 im_3{}^2 \omega_2{}^3 \omega_3{}^3 - im_1 re_2{}^2 \omega_2{}^3 \omega_3{}^3 - im_1 re_3{}^2 \omega_2{}^3 \omega_3{}^3\},
\end{aligned}
\tag{10.6}
$$

$$
\begin{aligned}
b_0 =\{&(-im_1{}^2re_2re_3\omega_2{}^2\omega_3{}^4 - 2\,im_1{}^2re_3{}^2\omega_1{}^2\omega_2{}^2\omega_3{}^2 - 2\,re_1{}^2\omega_3{}^3\omega_2{}^3im_3im_2 - 2\,re_1{}^2\omega_2{}^2im_2{}^2\omega_1{}^2\omega_3{}^2\\
&- 2\,re_1{}^2\omega_2{}^2im_3{}^2\omega_1{}^2\omega_3{}^2 - 2\,\omega_2{}^2im_3{}^2\omega_1{}^2\omega_3{}^2im_1{}^2 - 2\,\omega_2{}^2im_2{}^2\omega_1{}^2\omega_3{}^2im_1{}^2 - 2\,im_3{}^2re_2{}^2\omega_1{}^2\omega_2{}^2\omega_3{}^2\\
&- 2\,im_2{}^2im_3{}^2\omega_1{}^2\omega_2{}^2\omega_3{}^2 - im_2{}^2re_1re_3\omega_2{}^4\omega_3{}^2 - im_2{}^2re_1re_3\omega_1{}^4\omega_3{}^2 - 2\,im_2{}^2re_3{}^2\omega_1{}^2\omega_2{}^2\omega_3{}^2\\
&- im_3{}^2re_1re_2\omega_1{}^4\omega_2{}^2 - im_3{}^2re_1re_2\omega_2{}^2\omega_3{}^4 - 2\,im_1im_2re_3{}^2\omega_1{}^3\omega_2{}^3 - 2\,im_1im_3re_2{}^2\omega_1{}^3\omega_3{}^3\\
&+ im_2{}^2re_1re_3\omega_1{}^4\omega_2{}^2 - im_2{}^2re_1re_3\omega_1{}^2\omega_2{}^4 - im_2{}^2re_1re_3\omega_1{}^2\omega_3{}^4 + im_2{}^2re_1re_3\omega_2{}^2\omega_3{}^4\\
&+ im_3{}^2re_1re_2\omega_1{}^4\omega_3{}^2 - im_3{}^2re_1re_2\omega_1{}^2\omega_2{}^4 - im_3{}^2re_1re_2\omega_1{}^2\omega_3{}^4 + im_3{}^2re_1re_2\omega_2{}^4\omega_3{}^2\\
&- re_1{}^2re_2re_3\omega_1{}^4\omega_2{}^2 - re_1{}^2re_2re_3\omega_1{}^4\omega_3{}^2 + re_1{}^2re_2re_3\omega_1{}^2\omega_2{}^4 + re_1{}^2re_2re_3\omega_1{}^2\omega_3{}^4\\
&- 2\,re_1{}^2re_2{}^2\omega_1{}^2\omega_2{}^2\omega_3{}^2 - re_1{}^2re_2re_3\omega_2{}^4\omega_3{}^2 - re_1{}^2re_2re_3\omega_2{}^2\omega_3{}^4 - 2\,re_1{}^2re_3{}^2\omega_1{}^2\omega_2{}^2\omega_3{}^2\\
&+ re_1re_2{}^2re_3\omega_1{}^4\omega_2{}^2 - re_1re_2{}^2re_3\omega_1{}^4\omega_3{}^2 - re_1re_2{}^2re_3\omega_1{}^2\omega_2{}^4 - re_1re_2{}^2re_3\omega_1{}^2\omega_3{}^4\\
&- re_1re_2{}^2re_3\omega_2{}^4\omega_3{}^2 + re_1re_2{}^2re_3\omega_2{}^2\omega_3{}^4 - re_1re_2re_3{}^2\omega_1{}^4\omega_2{}^2 + re_1re_2re_3{}^2\omega_1{}^4\omega_3{}^2\\
&- re_1re_2re_3{}^2\omega_1{}^2\omega_2{}^4 - re_1re_2re_3{}^2\omega_1{}^2\omega_3{}^4 + re_1re_2re_3{}^2\omega_2{}^4\omega_3{}^2 - re_1re_2re_3{}^2\omega_2{}^2\omega_3{}^4\\
&- 2\,re_2{}^2re_3{}^2\omega_1{}^2\omega_2{}^2\omega_3{}^2 - 2\,im_1{}^2re_2{}^2\omega_1{}^2\omega_2{}^2\omega_3{}^2 - im_1{}^2re_2re_3\omega_1{}^4\omega_2{}^2 - im_1{}^2re_2re_3\omega_1{}^4\omega_3{}^2\\
&+ im_1{}^2re_2re_3\omega_1{}^2\omega_2{}^4 + im_1{}^2re_2re_3\omega_1{}^2\omega_3{}^4 - im_1{}^2re_2re_3\omega_2{}^4\omega_3{}^2 - 2\,im_2{}^2im_3\omega_1{}^3\omega_3{}^3im_1\\
&- 2\,\omega_3{}^3\omega_2{}^3im_3im_2im_1{}^2 - 2\,im_2im_3{}^2\omega_1{}^3\omega_2{}^3im_1 + 2\,im_3{}^2re_1re_2\omega_1{}^2\omega_2{}^2\omega_3{}^2\\
&+ 2\,im_2{}^2re_1re_3\omega_1{}^2\omega_2{}^2\omega_3{}^2 + 2\,\omega_2{}^3im_2im_3\omega_1{}^2\omega_3im_1{}^2 - 2\,\omega_2im_2im_3\omega_1{}^4\omega_3im_1{}^2\\
&+ 2\,\omega_2\omega_3{}^3im_2im_3\omega_1{}^2im_1{}^2 + 2\,im_2{}^2im_3\omega_1\omega_2{}^2\omega_3{}^3im_1 - 2\,im_2im_3{}^2\omega_1\omega_2\omega_3{}^4im_1\\
&+ im_2{}^2im_3{}^2\omega_1{}^2\omega_3{}^4 + re_1{}^2\omega_3{}^2\omega_2{}^4im_2{}^2 + re_1{}^2\omega_3{}^4\omega_2{}^2im_3{}^2 + re_1{}^2im_2{}^2\omega_1{}^4\omega_3{}^2 + re_1{}^2\omega_2{}^2im_3{}^2\omega_1{}^4\\
&+ 2\,im_2{}^2im_3\omega_1{}^3\omega_2{}^2\omega_3im_1 + im_2{}^2im_3{}^2\omega_1{}^2\omega_2{}^4 + im_3{}^2re_2{}^2\omega_1{}^2\omega_2{}^4 + im_3{}^2re_2{}^2\omega_1{}^2\omega_3{}^4\\
&+ re_1{}^2re_2{}^2\omega_1{}^4\omega_3{}^2 + re_1{}^2re_2{}^2\omega_2{}^4\omega_3{}^2 + re_1{}^2re_3{}^2\omega_1{}^4\omega_2{}^2 + re_1{}^2re_3{}^2\omega_2{}^2\omega_3{}^4 + re_2{}^2re_3{}^2\omega_1{}^2\omega_2{}^4\\
&+ re_2{}^2re_3{}^2\omega_1{}^2\omega_3{}^4 + im_1{}^2re_2{}^2\omega_1{}^4\omega_3{}^2 + im_1{}^2re_2{}^2\omega_2{}^4\omega_3{}^2 + im_1{}^2re_3{}^2\omega_1{}^4\omega_2{}^2 + im_1{}^2re_3{}^2\omega_2{}^2\omega_3{}^4\\
&+ im_2{}^2re_3{}^2\omega_1{}^2\omega_2{}^4 + im_2{}^2re_3{}^2\omega_1{}^2\omega_3{}^4 + im_2{}^2\omega_1{}^4\omega_3{}^2im_1{}^2 + \omega_2{}^2im_3{}^2\omega_1{}^4im_1{}^2 + \omega_3{}^2\omega_2{}^4im_2{}^2im_1{}^2\\
&+ \omega_3{}^4\omega_2{}^2im_3{}^2im_1{}^2 - 2\,im_2{}^2im_3\omega_1\omega_2{}^4\omega_3im_1 + 2\,im_2im_3{}^2\omega_1\omega_2{}^3\omega_3{}^2im_1 + 2\,im_2im_3{}^2\omega_1{}^3\omega_2\omega_3{}^2im_1\\
&+ 2\,re_1{}^2\omega_2{}^3im_2im_3\omega_1{}^2\omega_3 - 2\,re_1{}^2\omega_2im_2im_3\omega_1{}^4\omega_3 + 2\,re_1{}^2\omega_2\omega_3{}^3im_2im_3\omega_1{}^2\\
&+ 2\,im_1im_2re_3{}^2\omega_1{}^3\omega_2\omega_3{}^2 + 2\,im_1im_2re_3{}^2\omega_1\omega_2{}^3\omega_3{}^2 - 2\,im_1im_2re_3{}^2\omega_1\omega_2\omega_3{}^4\\
&+ 2\,im_1im_3re_2{}^2\omega_1{}^3\omega_2{}^2\omega_3 - 2\,im_1im_3re_2{}^2\omega_1\omega_2{}^4\omega_3 + 2\,im_1im_3re_2{}^2\omega_1\omega_2{}^2\omega_3{}^3\\
&+ 2\,re_1{}^2re_2re_3\omega_1{}^2\omega_2{}^2\omega_3{}^2 + 2\,re_1re_2{}^2re_3\omega_1{}^2\omega_2{}^2\omega_3{}^2 + 2\,re_1re_2re_3{}^2\omega_1{}^2\omega_2{}^2\omega_3{}^2\\
&+ 2\,im_1{}^2re_2re_3\omega_1{}^2\omega_2{}^2\omega_3{}^2)\omega_2\omega_1\omega_3\}/\{im_1im_2im_3\omega_1{}^4\omega_2{}^2\\
&+ im_1im_2im_3\omega_1{}^2\omega_2{}^4 + im_1im_2im_3\omega_1{}^4\omega_3{}^2 + im_1im_2im_3\omega_1{}^2\omega_3{}^4 + 2\,im_3re_1re_2\omega_1{}^3\omega_2{}^3\\
&+ im_1im_2im_3\omega_2{}^4\omega_3{}^2 - im_3re_1{}^2\omega_1\omega_2\omega_3{}^4 + im_3re_2{}^2\omega_1{}^3\omega_2\omega_3{}^2 + im_1im_2im_3\omega_2{}^2\omega_3{}^4\\
&+ 2\,im_2re_1re_3\omega_1{}^3\omega_3{}^3 + 2\,im_1re_2re_3\omega_2{}^3\omega_3{}^3 + im_3re_1{}^2\omega_1\omega_2{}^3\omega_3{}^2\\
&- im_2re_1{}^2\omega_1\omega_2{}^4\omega_3 + im_2re_1{}^2\omega_1\omega_2{}^2\omega_3{}^3 + im_2re_3{}^2\omega_1{}^3\omega_2{}^2\omega_3 - im_2re_3{}^2\omega_1\omega_2{}^4\omega_3\\
&+ im_2re_3{}^2\omega_1\omega_2{}^2\omega_3{}^3 + im_3re_1{}^2\omega_1{}^3\omega_2\omega_3{}^2 + im_2im_3{}^2\omega_1{}^3\omega_2{}^2\omega_3 - im_2{}^2im_3\omega_1\omega_2\omega_3{}^4\\
&+ im_2{}^2im_3\omega_1\omega_2{}^3\omega_3{}^2 + im_2{}^2im_3\omega_1{}^3\omega_2\omega_3{}^2 + im_1re_3{}^2\omega_1{}^2\omega_2\omega_3{}^3 + im_1re_3{}^2\omega_1{}^2\omega_2{}^3\omega_3\\
&+ im_3re_2{}^2\omega_1\omega_2{}^3\omega_3{}^2 - im_3re_2{}^2\omega_1\omega_2\omega_3{}^4 - im_2im_3{}^2\omega_1\omega_2{}^4\omega_3 + im_2im_3{}^2\omega_1\omega_2{}^2\omega_3{}^3\\
&+ im_2re_1{}^2\omega_1{}^3\omega_2{}^2\omega_3 - im_1re_3{}^2\omega_1{}^4\omega_2\omega_3 + im_1re_2{}^2\omega_1{}^2\omega_2\omega_3{}^3 + im_1re_2{}^2\omega_1{}^2\omega_2{}^3\omega_3\\
&- im_1re_2{}^2\omega_1{}^4\omega_2\omega_3 + im_1im_3{}^2\omega_1{}^2\omega_2\omega_3{}^3 + im_1im_3{}^2\omega_1{}^2\omega_2{}^3\omega_3 - im_1im_3{}^2\omega_1{}^4\omega_2\omega_3\\
&+ im_1im_2{}^2\omega_1{}^2\omega_2\omega_3{}^3 + im_1im_2{}^2\omega_1{}^2\omega_2{}^3\omega_3 - im_1im_2{}^2\omega_1{}^4\omega_2\omega_3 - im_1{}^2im_3\omega_1\omega_2\omega_3{}^4\\
&+ im_1{}^2im_3\omega_1\omega_2{}^3\omega_3{}^2 + im_1{}^2im_3\omega_1{}^3\omega_2\omega_3{}^2 - im_1{}^2im_2\omega_1\omega_2{}^4\omega_3 + im_1{}^2im_2\omega_1\omega_2{}^2\omega_3{}^3\\
&+ im_1{}^2im_2\omega_1{}^3\omega_2{}^2\omega_3 + 2\,im_2re_1re_3\omega_1\omega_2{}^4\omega_3 - 2\,im_2re_1re_3\omega_1\omega_2{}^2\omega_3{}^3 + 2\,im_3re_1re_2\omega_1\omega_2\omega_3{}^4\\
&- 2\,im_3re_1re_2\omega_1{}^3\omega_2\omega_3{}^2 - 2\,im_3re_1re_2\omega_1\omega_2{}^3\omega_3{}^2 - 2\,im_1re_2re_3\omega_1{}^2\omega_2{}^3\omega_3 - 2\,im_1re_2re_3\omega_1{}^2\omega_2\omega_3{}^3\\
&- 2\,im_2re_1re_3\omega_1{}^3\omega_2{}^2\omega_3 - 6\,im_1im_2im_3\omega_1{}^2\omega_2{}^2\omega_3{}^2 + 2\,im_1re_2re_3\omega_1{}^4\omega_2\omega_3 - im_3re_2{}^2\omega_1{}^3\omega_2{}^3\\
&- im_1{}^2im_3\omega_1{}^3\omega_2{}^3 - im_2{}^2im_3\omega_1{}^3\omega_2{}^3 - im_3re_1{}^2\omega_1{}^3\omega_2{}^3 - im_1{}^2im_2\omega_1{}^3\omega_3{}^3\\
&- im_2im_3{}^2\omega_1{}^3\omega_3{}^3 - im_2re_1{}^2\omega_1{}^3\omega_3{}^3 - im_2re_3{}^2\omega_1{}^3\omega_3{}^3 - im_1im_2{}^2\omega_2{}^3\omega_3{}^3\\
&- im_1im_3{}^2\omega_2{}^3\omega_3{}^3 - im_1re_2{}^2\omega_2{}^3\omega_3{}^3 - im_1re_3{}^2\omega_2{}^3\omega_3{}^3\},
\end{aligned}
\tag{10.7}
$$

$$
\begin{aligned}
b_1 =&\{\omega_1{\omega_2}^5 im_3{im_2}^2 re_1{\omega_3}^2+{\omega_1}^5\omega_2 im_3{re_1}^2 re_2{\omega_3}^2+\omega_1{\omega_2}^5 im_3 re_1{re_2}^2{\omega_3}^2+re_2 im_1 im_3{}^2{\omega_1}^2\omega_2{\omega_3}^5\\
&-re_2 im_3{re_1}^2{\omega_1}^3\omega_2{\omega_3}^4-im_3 re_1{re_2}^2{\omega_1}^5\omega_2{\omega_3}^2+im_3 re_1{re_2}^2{\omega_1}^3\omega_2{\omega_3}^4-re_2 im_1{}^2 im_3{\omega_1}^3\omega_2{\omega_3}^4\\
&-re_3 im_2{re_1}^2{\omega_1}^3{\omega_2}^4\omega_3-re_2{\omega_2}^3 im_3 re_1\omega_1{\omega_3}^4-re_2{\omega_2}^5 im_3{re_1}^2\omega_1{\omega_3}^2+re_2{\omega_2}^3 im_3{re_1}^2\omega_1{\omega_3}^4\\
&-re_2{\omega_2}^5 im_1{}^2 im_3\omega_1{\omega_3}^2+re_2{\omega_2}^3 im_1{}^2 im_3\omega_1{\omega_3}^4-im_2 re_1{re_3}^2{\omega_1}^5{\omega_2}^2\omega_3+im_2 re_1{re_3}^2{\omega_1}^3{\omega_2}^4\omega_3\\
&+im_1 re_2{re_3}^2{\omega_1}^4{\omega_2}^3\omega_3-im_1 re_2{re_3}^2{\omega_1}^2{\omega_2}^5\omega_3-re_3 im_1{}^2 im_2{\omega_1}^3{\omega_2}^4\omega_3+re_3 im_1 im_2{}^2{\omega_1}^2{\omega_2}^5\omega_3\\
&-re_3 im_1{re_2}^2{\omega_1}^4{\omega_2}^3\omega_3+re_3 im_1{re_2}^2{\omega_1}^2{\omega_2}^5\omega_3+{\omega_3}^5 re_3{}^2 im_1 re_2{\omega_1}^2\omega_2-{\omega_3}^3 re_3{}^2 im_2 re_1\omega_1{\omega_2}^4\\
&-{\omega_3}^5 re_3 im_1{re_2}^2{\omega_1}^2\omega_2+{\omega_3}^3 re_3 im_2{re_1}^2\omega_1{\omega_2}^4+{\omega_1}^4{\omega_3}^3 im_2{}^2 im_1 re_3\omega_2+\omega_1{\omega_3}^5 im_2{re_1}^2 re_3{}^2{\omega_2}^2\\
&-\omega_1{\omega_3}^4 im_2{}^2 im_3 re_1{\omega_2}^3-{\omega_1}^5{\omega_3}^2 im_2{}^2 im_3 re_1\omega_2+{\omega_1}^3{\omega_3}^4 im_2{}^2 im_3 re_1\omega_2+{\omega_1}^5\omega_3 im_2 im_1{}^2 re_3{\omega_2}^2\\
&-{\omega_1}^4\omega_3 im_2{}^2 im_1 re_3{\omega_2}^3+{\omega_3}^3 re_3 im_1{re_2}^2{\omega_1}^4\omega_2-{\omega_3}^5 re_3 im_1{}^2 im_2\omega_1{\omega_2}^2+{\omega_1}^5\omega_3 im_2{re_1}^2 re_3{\omega_2}^2\\
&+\omega_1{\omega_3}^5 im_2 im_3{}^2 re_1{\omega_2}^2+{\omega_3}^3 re_3 im_1{}^2 im_2\omega_1{\omega_2}^4-{\omega_3}^5 re_3 im_2{re_1}^2\omega_1{\omega_2}^2-{\omega_1}^2{\omega_2}^5 im_3{}^2 im_1 re_2\omega_3\\
&-{\omega_1}^2{\omega_3}^5 im_2{}^2 im_1 re_3\omega_2-{\omega_3}^3 re_3{}^2 im_1 re_2{\omega_1}^4\omega_2-\omega_1{\omega_2}^4 im_3{}^2 im_2 re_1{\omega_3}^3-{\omega_1}^5{\omega_2}^2 im_3{}^2 im_2 re_1\omega_3\\
&+{\omega_1}^3{\omega_2}^4 im_3{}^2 im_2 re_1\omega_3+{\omega_1}^5\omega_2 im_3 im_1{}^2 re_2{\omega_3}^2+{\omega_1}^4{\omega_2}^3 im_3{}^2 im_1 re_2\omega_3-{\omega_1}^4\omega_2 im_3{}^2 im_1 re_2{\omega_3}^3\\
&+re_2{\omega_2}^5 im_1 im_3{}^2{\omega_3}^3-re_2 im_1 im_3{}^2{\omega_2}^3{\omega_3}^5+{\omega_3}^5 re_3 im_1{re_2}^2{\omega_2}^3+im_1 re_2{re_3}^2{\omega_2}^5{\omega_3}^3\\
&-re_3 im_1 im_2{}^2{\omega_2}^5{\omega_3}^3-re_3 im_1{re_2}^2{\omega_2}^5{\omega_3}^3-{\omega_3}^5 re_3{}^2 im_1 re_2{\omega_2}^3+{\omega_3}^5 re_3 im_1 im_2{}^2{\omega_2}^3\\
&-{\omega_1}^5{\omega_2}^3 im_3 re_1{}^2 re_2+{\omega_1}^3{\omega_2}^5 im_3{re_1}^2 re_2+{\omega_1}^5{\omega_2}^3 im_3 re_1{re_2}^2-{\omega_1}^3{\omega_2}^5 im_3 re_1{re_2}^2\\
&-{\omega_1}^5{\omega_2}^3 im_3 im_1{}^2 re_2+{\omega_1}^3{\omega_2}^5 im_3 im_1{}^2 re_2+{\omega_1}^5{\omega_3}^3 im_2 im_3{}^2 re_1-{\omega_1}^3{\omega_3}^5 im_2 im_3{}^2 re_1\\
&-{\omega_1}^5{\omega_3}^3 im_2{re_1}^2 re_3+{\omega_1}^3{\omega_3}^5 im_2{re_1}^2 re_3+{\omega_1}^5{\omega_3}^3 im_2 re_1 re_3{}^2-{\omega_1}^3{\omega_3}^5 im_2 re_1 re_3{}^2\\
&-{\omega_1}^5{\omega_3}^3 im_2 im_1{}^2 re_3+{\omega_1}^3{\omega_3}^5 im_2 im_1{}^2 re_3+{\omega_1}^5{\omega_2}^3 im_3 im_2{}^2 re_1-{\omega_1}^3{\omega_2}^5 im_3 im_2{}^2 re_1\}/\\
&\{-im_3{re_2}^2{\omega_1}^3{\omega_2}^3-im_1{}^2 im_3{\omega_1}^3{\omega_2}^3-im_2{}^2 im_3{\omega_1}^3{\omega_2}^3-im_3{re_1}^2{\omega_1}^3{\omega_2}^3-im_1{}^2 im_2{\omega_1}^3{\omega_3}^3\\
&-im_2 im_3{}^2{\omega_1}^3{\omega_3}^3-im_2{re_1}^2{\omega_1}^3{\omega_3}^3-im_2{re_3}^2{\omega_1}^3{\omega_3}^3-im_1 im_2{}^2{\omega_2}^3{\omega_3}^3-im_1 im_3{}^2{\omega_2}^3{\omega_3}^3\\
&-im_1{re_2}^2{\omega_2}^3{\omega_3}^3-im_1{re_3}^2{\omega_2}^3{\omega_3}^3-6\,im_1 im_2 im_3\omega_1{}^2{\omega_2}^2{\omega_3}^2+2\,im_1 re_2 re_3{\omega_1}^4\omega_2\omega_3\\
&-2\,im_1 re_2 re_3\omega_1{}^2{\omega_2}^3\omega_3-2\,im_1 re_2 re_3\omega_1{}^2\omega_2{\omega_3}^3-2\,im_2 re_1 re_3{\omega_1}^3{\omega_2}^2\omega_3+2\,im_2 re_1 re_3\omega_1{\omega_2}^4\omega_3\\
&-2\,im_2 re_1 re_3\omega_1\omega_2{}^2{\omega_3}^3-2\,im_3 re_1 re_2{\omega_1}^3\omega_2{\omega_3}^2-2\,im_3 re_1 re_2\omega_1{\omega_2}^3{\omega_3}^2+2\,im_3 re_1 re_2\omega_1\omega_2{\omega_3}^4\\
&+im_1 im_2 im_3{\omega_1}^4{\omega_2}^2+im_1 im_2 im_3{\omega_1}^2{\omega_2}^4+im_1 im_2 im_3{\omega_1}^4{\omega_3}^2+im_1 im_2 im_3{\omega_1}^2{\omega_3}^4\\
&+2\,im_3 re_1 re_2{\omega_1}^3{\omega_2}^3+im_1 im_2 im_3{\omega_2}^4{\omega_3}^2+im_1 im_2 im_3{\omega_2}^2{\omega_3}^4+2\,im_2 re_1 re_3{\omega_1}^3{\omega_3}^3\\
&+2\,im_1 re_2 re_3{\omega_2}^3{\omega_3}^3-im_2 im_3{}^2\omega_1{\omega_2}^4\omega_3+im_2 im_3{}^2\omega_1{\omega_2}^2{\omega_3}^3+im_2{re_1}^2{\omega_1}^3{\omega_2}^2\omega_3-im_2{re_1}^2\omega_1{\omega_2}^4\omega_3\\
&+im_2{re_1}^2\omega_1{\omega_2}^2{\omega_3}^3+im_2{re_3}^2{\omega_1}^3{\omega_2}^2\omega_3-im_2{re_3}^2\omega_1{\omega_2}^4\omega_3+im_2{re_3}^2\omega_1{\omega_2}^2{\omega_3}^3+im_1{}^2 im_2\omega_1{\omega_2}^2{\omega_3}^3\\
&+im_3{re_1}^2{\omega_1}^3\omega_2{\omega_3}^2+im_3{re_1}^2\omega_1{\omega_2}^3{\omega_3}^2-im_3{re_1}^2\omega_1\omega_2{\omega_3}^4+im_3{re_2}^2{\omega_1}^3\omega_2{\omega_3}^2-im_1{}^2 im_2\omega_1{\omega_2}^4\omega_3\\
&-im_1{re_3}^2{\omega_1}^4\omega_2\omega_3+im_1{re_3}^2{\omega_1}^2{\omega_2}^3\omega_3+im_1{re_3}^2{\omega_1}^2\omega_2{\omega_3}^3+im_2{}^2 im_3{\omega_1}^3\omega_2{\omega_3}^2+im_1{}^2 im_2{\omega_1}^3{\omega_2}^2\omega_3\\
&+im_2{}^2 im_3\omega_1{\omega_2}^3{\omega_3}^2-im_2{}^2 im_3\omega_1\omega_2{\omega_3}^4+im_2 im_3{}^2{\omega_1}^3{\omega_2}^2\omega_3+im_3{re_2}^2\omega_1{\omega_2}^3{\omega_3}^2-im_3{re_2}^2\omega_1\omega_2{\omega_3}^4\\
&+im_1{}^2 im_3{\omega_1}^3\omega_2{\omega_3}^2+im_1{}^2 im_3\omega_1{\omega_2}^3{\omega_3}^2-im_1{}^2 im_3\omega_1\omega_2{\omega_3}^4-im_1 im_2{}^2{\omega_1}^4\omega_2\omega_3+im_1 im_2{}^2{\omega_1}^2{\omega_2}^3\omega_3\\
&+im_1 im_2{}^2{\omega_1}^2\omega_2{\omega_3}^3-im_1 im_3{}^2{\omega_1}^4\omega_2\omega_3+im_1 im_3{}^2{\omega_1}^2{\omega_2}^3\omega_3+im_1 im_3{}^2{\omega_1}^2\omega_2{\omega_3}^3-im_1{re_2}^2{\omega_1}^4\omega_2\omega_3\\
&+im_1{re_2}^2{\omega_1}^2{\omega_2}^3\omega_3+im_1{re_2}^2{\omega_1}^2\omega_2{\omega_3}^3\},
\end{aligned}
\tag{10.8}
$$

$$
\begin{aligned}
b_2 =\{&-im_1 im_2{}^2 im_3\omega_1{}^2\omega_2\omega_3{}^4 - im_1 im_2 im_3{}^2\omega_1{}^4\omega_2{}^2\omega_3 - im_1 im_2 im_3{}^2\omega_1{}^2\omega_2{}^4\omega_3 + 2\, im_1 im_2 im_3{}^2\omega_1{}^2\omega_2{}^2\omega_3{}^3 \\
&- im_1 im_2 re_3{}^2\omega_1{}^4\omega_2{}^2\omega_3 - im_1 im_2 re_3{}^2\omega_1{}^2\omega_2{}^4\omega_3 + 2\, im_1 im_2 re_3{}^2\omega_1{}^2\omega_2{}^2\omega_3{}^3 - im_1 im_3 re_2{}^2\omega_1{}^4\omega_2\omega_3{}^2 \\
&+ 2\, im_1 im_3 re_2{}^2\omega_1{}^2\omega_2{}^3\omega_3{}^2 - im_1 im_3 re_2{}^2\omega_1{}^2\omega_2\omega_3{}^4 + 2\, im_2{}^2 re_1 re_3\omega_1{}^3\omega_2{}^3\omega_3 - 2\, im_2{}^2 re_1 re_3\omega_1{}^3\omega_2\omega_3{}^3 \\
&- 2\, im_2{}^2 re_1 re_3\omega_1\omega_2{}^5\omega_3 + 2\, im_2{}^2 re_1 re_3\omega_1\omega_2{}^3\omega_3{}^3 - 2\, re_1 re_2{}^2 re_3\omega_1\omega_2{}^5\omega_3 + 2\, re_1 re_2{}^2 re_3\omega_1\omega_2{}^3\omega_3{}^3 \\
&+ 2\, im_2 im_3 re_1{}^2\omega_1{}^3\omega_2{}^2\omega_3{}^2 - 2\, re_1{}^2 re_2 re_3\omega_1\omega_2{}^3\omega_3{}^3 + 2\, re_1 re_2{}^2 re_3\omega_1{}^3\omega_2{}^3\omega_3 - 2\, re_1 re_2{}^2 re_3\omega_1{}^3\omega_2\omega_3{}^3 \\
&+ 2\, im_3{}^2 re_1 re_2\omega_1{}^3\omega_2\omega_3{}^3 + 2\, im_3{}^2 re_1 re_2\omega_1\omega_2{}^3\omega_3{}^3 - 2\, im_3{}^2 re_1 re_2\omega_1\omega_2\omega_3{}^5 - 2\, re_1{}^2 re_2 re_3\omega_1{}^5\omega_2\omega_3 \\
&+ 2\, re_1{}^2 re_2 re_3\omega_1{}^3\omega_2{}^3\omega_3 + 2\, re_1{}^2 re_2 re_3\omega_1{}^3\omega_2\omega_3{}^3 - im_1{}^2 im_2 im_3\omega_1\omega_2{}^2\omega_3{}^4 + 2\, re_1 re_2 re_3{}^2\omega_1\omega_2{}^3\omega_3{}^3 \\
&- 2\, re_1 re_2 re_3{}^2\omega_1\omega_2\omega_3{}^5 - 2\, im_3{}^2 re_1 re_2\omega_1{}^3\omega_2{}^3\omega_3 - im_2 im_3 re_1{}^2\omega_1\omega_2{}^2\omega_3{}^4 - im_2 im_3 re_1{}^2\omega_1\omega_2{}^4\omega_3{}^2 \\
&- 2\, im_1{}^2 re_2 re_3\omega_1{}^5\omega_2\omega_3 + 2\, im_1 im_2{}^2 im_3\omega_1{}^2\omega_2{}^3\omega_3{}^2 - 2\, re_1 re_2 re_3{}^2\omega_1{}^3\omega_2{}^3\omega_3 + 2\, re_1 re_2 re_3{}^2\omega_1{}^3\omega_2\omega_3{}^3 \\
&+ 2\, im_1{}^2 im_2 im_3\omega_1{}^3\omega_2{}^2\omega_3{}^2 - im_1{}^2 im_2 im_3\omega_1\omega_2{}^4\omega_3{}^2 + 2\, im_1{}^2 re_2 re_3\omega_1{}^3\omega_2{}^3\omega_3 + 2\, im_1{}^2 re_2 re_3\omega_1{}^3\omega_2\omega_3{}^3 \\
&- 2\, im_1{}^2 re_2 re_3\omega_1\omega_2{}^3\omega_3{}^3 - im_1 im_2{}^2 im_3\omega_1{}^4\omega_2\omega_3{}^2 + im_2{}^2 re_3{}^2\omega_1\omega_2{}^5\omega_3 + im_2{}^2 re_1{}^2\omega_1\omega_2{}^5\omega_3 \\
&+ im_3{}^2 re_2{}^2\omega_1\omega_2{}^5\omega_3 + im_3{}^2 re_1{}^2\omega_1\omega_2\omega_3{}^5 - 2\, im_3{}^2 re_1{}^2\omega_1{}^3\omega_2\omega_3{}^3 + im_3{}^2 re_1{}^2\omega_1{}^5\omega_2\omega_3 \\
&- 2\, im_2{}^2 re_1{}^2\omega_1{}^3\omega_2{}^3\omega_3 - 2\, im_1{}^2 im_2{}^2\omega_1{}^3\omega_2{}^3\omega_3 + im_1{}^2 im_2{}^2\omega_1\omega_2{}^5\omega_3 - im_1{}^2 im_2 im_3\omega_1{}^5\omega_2{}^2 \\
&- im_1{}^2 im_2 im_3\omega_1{}^5\omega_3{}^2 + im_1{}^2 im_2 im_3\omega_1{}^3\omega_2{}^4 + im_1{}^2 im_2 im_3\omega_1{}^3\omega_3{}^4 + im_1{}^2 im_3{}^2\omega_1{}^5\omega_2\omega_3 \\
&- 2\, im_1{}^2 im_3{}^2\omega_1{}^3\omega_2\omega_3{}^3 + im_1{}^2 im_3{}^2\omega_1\omega_2\omega_3{}^5 + im_1{}^2 re_2{}^2\omega_1{}^5\omega_2\omega_3 - 2\, im_1{}^2 re_2{}^2\omega_1{}^3\omega_2{}^3\omega_3 \\
&+ im_1{}^2 re_2{}^2\omega_1\omega_2{}^5\omega_3 + im_1{}^2 re_3{}^2\omega_1{}^5\omega_2\omega_3 - 2\, im_1{}^2 re_3{}^2\omega_1{}^3\omega_2\omega_3{}^3 + im_1{}^2 re_3{}^2\omega_1\omega_2\omega_3{}^5 \\
&+ im_1 im_2{}^2 im_3\omega_1{}^4\omega_2{}^3 - im_1 im_2{}^2 im_3\omega_1{}^2\omega_2{}^5 - im_1 im_2{}^2 im_3\omega_2{}^5\omega_3{}^2 + im_1 im_2{}^2 im_3\omega_2{}^3\omega_3{}^4 \\
&+ im_1 im_2 im_3{}^2\omega_1{}^4\omega_3{}^3 - im_1 im_2 im_3{}^2\omega_1{}^2\omega_3{}^5 + im_1 im_2 im_3{}^2\omega_2{}^4\omega_3{}^3 - im_1 im_2 im_3{}^2\omega_2{}^2\omega_3{}^5 \\
&+ im_1 im_2 re_3{}^2\omega_1{}^4\omega_3{}^3 - im_1 im_2 re_3{}^2\omega_1{}^2\omega_3{}^5 + im_1 im_2 re_3{}^2\omega_2{}^4\omega_3{}^3 - im_1 im_2 re_3{}^2\omega_2{}^2\omega_3{}^5 \\
&+ im_1 im_3 re_2{}^2\omega_1{}^4\omega_2{}^3 - im_1 im_3 re_2{}^2\omega_1{}^2\omega_2{}^5 - im_1 im_3 re_2{}^2\omega_2{}^5\omega_3{}^2 + im_1 im_3 re_2{}^2\omega_2{}^3\omega_3{}^4 \\
&+ im_2{}^2 im_3{}^2\omega_1\omega_2{}^5\omega_3 - 2\, im_2{}^2 im_3{}^2\omega_1\omega_2{}^3\omega_3{}^3 + im_2{}^2 im_3{}^2\omega_1\omega_2\omega_3{}^5 + im_2{}^2 re_1{}^2\omega_1{}^5\omega_2\omega_3 \\
&+ re_2{}^2 re_3{}^2\omega_1\omega_2\omega_3{}^5 + im_1{}^2 im_2{}^2\omega_1{}^5\omega_2\omega_3 - 2\, im_3{}^2 re_2{}^2\omega_1\omega_2{}^3\omega_3{}^3 + im_3{}^2 re_2{}^2\omega_1\omega_2\omega_3{}^5 \\
&+ re_1{}^2 re_2{}^2\omega_1{}^5\omega_2\omega_3 - 2\, re_1{}^2 re_2{}^2\omega_1{}^3\omega_2{}^3\omega_3 + re_1{}^2 re_2{}^2\omega_1\omega_2{}^5\omega_3 + re_1{}^2 re_3{}^2\omega_1{}^5\omega_2\omega_3 - 2\, re_1{}^2 re_3{}^2\omega_1{}^3\omega_2\omega_3{}^3 \\
&+ re_1{}^2 re_3{}^2\omega_1\omega_2\omega_3{}^5 + re_2{}^2 re_3{}^2\omega_1\omega_2{}^5\omega_3 + im_2 im_3 re_1{}^2\omega_1{}^3\omega_3{}^4 + im_2 im_3 re_1{}^2\omega_1{}^3\omega_2{}^4 - im_2 im_3 re_1{}^2\omega_1{}^5\omega_3{}^2 \\
&- 2\, re_2{}^2 re_3{}^2\omega_1\omega_2{}^3\omega_3{}^3 - im_2 im_3 re_1{}^2\omega_1{}^5\omega_2{}^2 + im_2{}^2 re_3{}^2\omega_1\omega_2\omega_3{}^5 - 2\, im_2{}^2 re_3{}^2\omega_1\omega_2{}^3\omega_3{}^3\}/ \\
\{&-im_3 re_2{}^2\omega_1{}^3\omega_2{}^3 - im_1{}^2 im_3\omega_1{}^3\omega_2{}^3 - im_2{}^2 im_3\omega_1{}^3\omega_2{}^3 - im_3 re_1{}^2\omega_1{}^3\omega_2{}^3 - im_1{}^2 im_2\omega_1{}^3\omega_3{}^3 \\
&- im_2 im_3{}^2\omega_1{}^3\omega_3{}^3 - im_2 re_1{}^2\omega_1{}^3\omega_3{}^3 - im_2 re_3{}^2\omega_1{}^3\omega_3{}^3 - im_1 im_2{}^2\omega_2{}^3\omega_3{}^3 - im_1 im_3{}^2\omega_2{}^3\omega_3{}^3 \\
&- im_1 re_2{}^2\omega_2{}^3\omega_3{}^3 - im_1 re_3{}^2\omega_2{}^3\omega_3{}^3 - 6\, im_1 im_2 im_3\omega_1{}^2\omega_2{}^2\omega_3{}^2 + 2\, im_1 re_2 re_3\omega_1{}^4\omega_2\omega_3 \\
&- 2\, im_1 re_2 re_3\omega_1{}^2\omega_2{}^3\omega_3 - 2\, im_1 re_2 re_3\omega_1{}^2\omega_2\omega_3{}^3 - 2\, im_2 re_1 re_3\omega_1{}^3\omega_2{}^2\omega_3 + 2\, im_2 re_1 re_3\omega_1\omega_2{}^4\omega_3 \\
&- 2\, im_2 re_1 re_3\omega_1\omega_2{}^2\omega_3{}^3 - 2\, im_3 re_1 re_2\omega_1{}^3\omega_2\omega_3{}^2 - 2\, im_3 re_1 re_2\omega_1\omega_2{}^3\omega_3{}^2 + 2\, im_3 re_1 re_2\omega_1\omega_2\omega_3{}^4 \\
&+ im_1 im_2 im_3\omega_1{}^2\omega_2{}^4 + im_1 im_2 im_3\omega_1{}^4\omega_3{}^2 + im_1 im_2 im_3\omega_1{}^2\omega_3{}^4 + 2\, im_2 re_1 re_3\omega_1{}^3\omega_2{}^3 \\
&+ im_1 im_2 im_3\omega_2{}^4\omega_3{}^2 + im_1 im_2 im_3\omega_2{}^2\omega_3{}^4 + 2\, im_2 re_1 re_3\omega_1{}^3\omega_3{}^3 + 2\, im_1 re_2 re_3\omega_2{}^3\omega_3{}^3 \\
&- im_2 im_3{}^2\omega_1\omega_2{}^4\omega_3 + im_2 im_3{}^2\omega_1\omega_2{}^2\omega_3{}^3 + im_2 re_1{}^2\omega_1{}^3\omega_2{}^2\omega_3 - im_2 re_1{}^2\omega_1\omega_2{}^4\omega_3 + im_3 re_1{}^2\omega_1\omega_2{}^3\omega_3{}^2 \\
&+ im_2 re_1{}^2\omega_1\omega_2{}^2\omega_3{}^3 + im_2 re_3{}^2\omega_1{}^3\omega_2{}^2\omega_3 - im_2 re_3{}^2\omega_1\omega_2{}^4\omega_3 + im_2 re_3{}^2\omega_1\omega_2{}^2\omega_3{}^3 + im_3 re_1{}^2\omega_1{}^3\omega_2\omega_3{}^2 \\
&- im_3 re_1{}^2\omega_1\omega_2\omega_3{}^4 + im_3 re_2{}^2\omega_1{}^3\omega_2\omega_3{}^2 - im_1 re_3{}^2\omega_1{}^4\omega_2\omega_3 + im_1 re_3{}^2\omega_1{}^2\omega_2{}^3\omega_3 + im_1 re_3{}^2\omega_1{}^2\omega_2\omega_3{}^3 \\
&+ im_2{}^2 im_3\omega_1{}^3\omega_2\omega_3{}^2 + im_2{}^2 im_3\omega_1\omega_2{}^3\omega_3{}^2 - im_2{}^2 im_3\omega_1\omega_2\omega_3{}^4 + im_2 im_3{}^2\omega_1{}^3\omega_2{}^2\omega_3 + im_3 re_2{}^2\omega_1\omega_2{}^3\omega_3{}^2 \\
&- im_3 re_2{}^2\omega_1\omega_2\omega_3{}^4 + im_1{}^2 im_2\omega_1{}^3\omega_2{}^2\omega_3 - im_1{}^2 im_2\omega_1\omega_2{}^4\omega_3 + im_1{}^2 im_2\omega_1\omega_2{}^2\omega_3{}^3 + im_1{}^2 im_3\omega_1{}^3\omega_2\omega_3{}^2 \\
&+ im_1{}^2 im_3\omega_1\omega_2{}^3\omega_3{}^2 - im_1{}^2 im_3\omega_1\omega_2\omega_3{}^4 - im_1 im_2{}^2\omega_1{}^4\omega_2\omega_3 + im_1 im_2{}^2\omega_1{}^2\omega_2{}^3\omega_3 + im_1 im_2{}^2\omega_1{}^2\omega_2\omega_3{}^3 \\
&- im_1 im_3{}^2\omega_1{}^4\omega_2\omega_3 + im_1 im_3{}^2\omega_1{}^2\omega_2{}^3\omega_3 + im_1 im_3{}^2\omega_1{}^2\omega_2\omega_3{}^3 - im_1 re_2{}^2\omega_1{}^4\omega_2\omega_3 + im_1 re_2{}^2\omega_1{}^2\omega_2{}^3\omega_3 \\
&+ im_1 re_2{}^2\omega_1{}^2\omega_2\omega_3{}^3 + im_1 im_2 im_3\omega_1{}^4\omega_2{}^2\},
\end{aligned}
\tag{10.9}
$$

where re_j, im_j denote the real and imaginary part of the measured frequency response $\hat{P}(i\omega_j), j = 1, 2, 3.$

References

[1] R. Isermann. **On the Design and Control of Mechatronic Systems - A Survey**. *IEEE Transactions on industrial electronics*, **43**, 1996. 1, 26

[2] R. Isermann. **Modeling and Design Methodology for Mechatronic Systems**. *IEEE Transactions on Mechatronics*, **1**, 1996. 1, 26

[3] R. Isermann. **Mechatronic systems - A challenge for control engineering**. *Proceedings of the American Control Conference, Albuquerque, New Mexico*, 1997. 1, 2, 26, 29, 82

[4] N. Kyura and H. Oho. **Mechatronics - An Industrial Perspective**. *IEEE Transactions on Mechatronics*, **1**, 1996. 1

[5] O. H. Bosgra, H. Kwakernaak, and G. Meinsma. *Design methods for control systems*. Dutch Institute of Systems and Control, 2004. 5, 8, 16, 17, 223, 242, 243, 244

[6] H. T. Toivonen. *Robust control methods*. Åbo Akademi University, 1998. 5, 7

[7] Gene F. Franklin, J. David Powell, and Michael L. Workman. *Digital Control of Dynamic Systems*. Ellis-Kagle Press, 1998. 8, 11, 146

[8] G. F. Franklin, J. D. Powell, and A. Emami-Naeini. *Feedback Control of Dynamic Systems*. Prentice Hall, 2001. 8, 11

[9] G. Goodwin, S. F. Graebe, and M. E. Salgado. *Control System Design*. Prentice Hall, 2000. 8, 11

[10] K. J. Åström and B. Wittenmark. *Computer Controlled Systems*. Prentice Hall, 1997. 8, 11

[11] R. E. Kalman and R. S. Bucy. **New results in linear filtering and prediction theory**. *Trans. ASME, Ser. D, J. Basic Eng*, page 109, 1961. 10, 28

[12] J.C. Willems. **Deterministic least squares filtering**. *Journal of Econometrics*, **118**(12):341 – 373, 2004. 10

[13] M.G. Safonov and M. Athans. **Gain and phase margin for multiloop LQG regulators**. In *IEEE Conference on Decision and Control including the 15th Symposium on Adaptive Processes*, **15**, pages 361–368, Dec 1976. 11

[14] J.C. Doyle. **Guaranteed margins for LQG regulators**. *IEEE Transactions on Automatic Control*, **23**(4):756–757, Aug 1978. 11

[15] T. Kailath. *Linear Systems*. Prentice Hall, 1980. 11

[16] H. H. Rosenbrock. **Distinctive problems of process control**. *Chemical Engineering Prog.*, **58**, 1962. 12

[17] W. M. Wohnham. **On pole assignment in multi-input controllable linear systems, Technical Report 67-2**. Technical report, Division of Applied Mathematics, Brown University, 1967. 12

[18] B. D. O. Anderson and D. G. Luenberger. **Design of multivariable feedback systems**. *Proc. IEE*, **114**, 1967. 12

[19] S. P. Bhattacharyya and E. De Sousa. **Pole Assignment via Sylvester's Equation**. *Systems and Control Letters*, **1**:261–263, 1982. 12

[20] G. R. Duan. **Parametric Eigenstructure Assignment via Output Feedback Based on Singular Value Decomposition**. In *Proceedings of the 40th IEEE Conference on Decision and Control, Florida, USA*, 2001. 12

[21] M. Schlegel. *Modal control of finite-order linear systems, PhD thesis*. VŠSE Pilsen, 1984. 12, 13

[22] M. Schlegel. **A generalization of Rosenbrock's theorem**. *IEEE Transaction on Automatic Control*, **AC-27**, 1987. 12, 13

[23] M. Schlegel. **Parametrization of the class of deadbeat controllers**. *IEEE Transaction on Automatic Control*, **AC-27**:727–729, 1982. 12, 13

[24] M. Schlegel and J. Königsmarková. **Parametric Jordan Form Assignment Revisited**. *Proceedings of IFAC World Congress, Milano 2011*, 2011. 13, 15

[25] J. Königsmarková. *Robustní přiřazení pólů stavovou a výstupní zpětnou vazbou*. University of West Bohemia, Master Thesis, 2013. 13, 15

[26] D. Cox, J. Little, and D. O'Shea. *Ideals, varietes and algorithms: An Intoduction to Computational Algebraic Geometry and Commutative Algebra*. Springer, 1997. 14

[27] J.C. Doyle, K. Glover, P.P. Khargonekar, and B.A. Francis. **State-space solutions to standard H_2 and H_∞ control problems**. *IEEE Transactions on Automatic Control*, **34**(8):831–847, Aug 1989. 17

[28] K. Madsen, H.B. Nielsen, and O. Tingleff. *Methods for Nonlinear Least Squares Problems*. Technical University of Denmark, 2004. 19, 20, 21, 130

[29] H. P. Gaivn. *The Levenberg-Marquardt method for nonlinear least squares curve-fitting problems*. Duke University, 2013. 19, 130

[30] B. A. Gregory. *An Introduction to Electrical Instrumentation and Measurment Systems*. MacMillan, New York, 1981. 26

[31] A. S. Morris. *Principles of Measurment and Instrumentation*. Prentice Hall, London, 1988. 26

[32] J. G. Webster. *The Measurement, Instrumentation and Sensors Handbook*. CRC Press, 1999. 26

[33] D. G. Luenberger. **An Introduction to Observers**. *IEEE Transactions on Automatic Control*, **6**, 1971. 28

[34] B. D. O. Anderson and J. B. Moore. *Optimal Control Linear Quadratic Methods*. Prentice Hall, 2007. 28

[35] K. J. Åström. *Feedback systems*. Princeton University Press, 2009. 28, 77, 80

[36] K. J. Åström. *Introduction to Stochastic Control Theory*. Dover, New York, 2006. 28

[37] O. Roubíček. *Elektrické motory a pohony*. BEN, Praha, 2004. 31

[38] T. Kenjo and S. Nagamori. *Brushless Motors - Advanced Theory and Modern Applications*. Sogo Electronics Press, 2003. 31

[39] H. A. Toliyat and S. G. Campbell. *DSP-based Electromechanical Motion Control*. CRC Press, 2004. 31, 32, 33, 44, 46, 47

[40] R. Isermann. *Supervision, Fault Detection and Fault Diagnosis Methods*. Control Engineering Practice, 1997. 35

[41] R. Siegwart and I. R. Nourbakh. *Introduction to Autonomous Mobile Robots*. MIT Press, 2004. 35

[42] H. Choset. *Principles of Robot Motion: Theory, Algorithms, and Implementations*. MIT Press, 2005. 35

REFERENCES

[43] T. R. KURFESS. *Robotics and Automation Handbook*. CRC Press, 2004. 35, 38, 41, 59, 63, 80

[44] R. KELLY ET AL. *Control of Robot Manipulators in Joint Space*. Springer, 2005. 35, 38, 41

[45] K. ERKORKMAZ. *Optimal Trajectory Generation and Precision Tracking Control for Multi-axis Machines*. University of British Columbia, 2004. 35, 37

[46] B. SENCER. *Smooth Trajectory Generation and Precision Control of 5-Axis CNC Machine Tools*. University of British Columbia, 2009. 35, 37

[47] J.E. BOBROW, S. DUBOWSKY, AND J.S. GIBSON. **Time-optimal control of robotic manipulators along specified paths**. *International Journal of Robotic Research*, 1985. 36

[48] Z. SHILLER AND H.H. LU. **Computation of path constrained time optimal motions with dynamic singularities**. *ASME Journal of Dynamic Systems*, **114**:34–40, 1992. 36

[49] K.G. SHIN AND N.D. MCKAY. **Minimum-time control of robotic manipulators with geometric constraints**. *IEEE Transactions on Automatic Control*, **AC-30(6)**:531–541, 1985. 36

[50] B. CAO, G.I. DOODS, AND G.W. IRWIN. **Time-optimal and smooth constrained path planning for robot manipulators**. *IEEE International Conference on Robotics and Automation*, 1994. 36

[51] S. MACFARLANE AND S. CROFT. **Jerk-bounded manipulator trajectory planning: design for real-time applications**. *IEEE International Conference on Robotics and Automation*, **19**, 2003. 36

[52] M. SCHLEGEL, J. MOŠNA, AND L. BLÁHA. **Optimal control of chain of integrators with constraints**. *Proceedings of 17th International Conference on Process Control 2009*, 2009. 36

[53] O. J. M. SMITH. **Posicast Control of Damped Oscillatory Systems**. *Proceedings of the IRE*, **45/9**:1249–1255, 1957. 36

[54] W. E. SINGHOSE. *Command Generation for Flexible Systems, PhD thesis*. MIT , Dept. of Mechanical Engineering, 1997. 36, 41, 93

[55] N. C. SINGER AND W.P. SEERING. **Preshaping Comman Inputs to Reduce System Vibration**. *A.I. Memo*, **1027**:1–23, 1988. 36, 41

[56] J. R. HUEY, K.L. SORENSEN, AND W. E. SINGHOSE. **Usefull Applications of Closed-loop Shaping Controllers**. *Control Engineering Practice*, **16**:836–846, 2007. 36, 41, 93

[57] S. S. GÜRLEYÜK AND S. CINAL. **Robust Three-impulse Sequence Input Shaper Design**. *Journal of Vibration and Control*, **13**:1807–1818, 2007. 36, 41, 159

[58] PLCOPEN. *Function blocks for motion control, Version 1.1*. PLCopen, Technical Committee 2, 2005. 36, 38

[59] M. MANDAL AND T. K. NASKAR. **Introduction of control points in splines for synthesis of optimized cam motion program**. *Mechanism and Machine Theory, Elsevier*, 2008. 37

[60] QIU ET AL. **A universal optimal approach to cam curve design and its applications**. *Mechanism and Machine Theory, Elsevier*, 2005. 37

[61] A. IGLESIAS. **B-Splines and NURBS curves and surfaces**. *Lectures in computer-aided geometric design and surfaces, University of Cantabria*, 2001. 37

[62] M. HENG. *Smooth and time optimal trajectory generation for high-speed machine tools*. University of Waterloo, 2008. 37

[63] F. JEŽEK. *Geometrické a počítačové modelování*. Západočeská univerzita v Plzni, 2006. 37

[64] R. L. NORTON. *Cam Design and Manufacturing Handbook*. Industrial Press, Inc., New York, 2002. 37

[65] P. SMID. *CNC Programming Handbook*. Industrial Press, Inc., New York, 2008. 37, 38

[66] P. SMID. *CNC Programming Techniques*. Industrial Press, Inc., New York, 2005. 37, 38

[67] J. N. PIRES. *Industrial Robots Programming*. Springer, 2007. 38, 41

[68] B. SICILIANO AND K. P. VALAVANIS. *Control Problems in Robotics and Automation*. Springer, 1998. 38, 41, 59, 80

[69] L. SCIAVICCO AND B. SICILIANO. *Modelling and Control of Robot Manipulators*. Springer, 1999. 38, 41, 59, 62, 63

[70] G. WILLIAMS. *CNC Robotics*. McGraw-Hill, 2003. 38

[71] P. KELLER. *Programování a řízení CNC strojů*. Technická univerzita v Liberci, Fakulta strojní, 2005. 38

[72] S.J. KWON AND W.K. CHUNG. *Perturbation Compensator based Robust Tracking Control and State Estimation of Mechanical Systems*. Springer, 2004. 40, 58, 63, 80

[73] K. OHNISHI, M. SHIBATA, AND T. MURAKAMI. **Motion control for advanced mechatronics**. *IEEE Transaction on mechatronics*, 1996. 40, 41, 58

[74] G. YHANG AND J. CHEN. **Identifier-Based Adaptive Robust Control for Servomechanisms With Improved Transient Performance**. *IEEE Transaction on Industrial Electronics*, **57**, 2010. 40

[75] K.K. BONG AND CH.K. WAN. **Motion control of precision positioning systems using adaptive compensation**. *Proceedings of the American Control Conference, Anchorage*, 2002. 40, 58

[76] Y. ALTINTAS, K. ERKORKMAZ, AND W.-H. ZHU. **Sliding mode controller design for high-speed drives**. *Annals of the CIRP*, **49**, 2000. 40, 58

[77] V. UTKIN, J. GULDNER, AND J. SHI. *Sliding Mode Control in Electromechanical Systems*. CRC Press, 1999. 40, 46, 58

[78] A. ŠABANOVIĆ AND K. OHNISHI. *Motion Control Systems*. IEEE Press, 2011. 40, 58

[79] S.-J. HUANG AND CH.-F. HU. **Predictive fuzzy controller for robotic motion control**. *Industry applications conference IAS'95*, 1995. 40, 58

[80] J.B. MBEDE, X. HUANG, AND M. WANG. **Robust neuro-fuzzy sensor-based motion control among dynamic obstacles for robot manipulators**. *IEEE Transactions on Fuzzy Systems*, **11**, 2003. 40, 58

[81] B. ARMSTRONG-HELOUVRY, P. DUPONT, AND C.C. DE WIT. **A Survey of Models, Analysis Tools and Compensation Methods for the Control of Machines with Friction**. *Automatica*, **30**, 1994. 40, 134, 140

[82] N. E. EHRICH. *An Investigation of Control Strategies for Friction Compensation*. University of Maryland, 1991. 40

[83] C. C. DE WIT AND V. SERONT. **Robust adaptive friction compensation**. *IEEE International Conference on Robotics and Automation*, **2**:1383–1388, 1990. 40

[84] E. G. PAPADOPOULOS AND G. C. CHASPARIS. **Analysis and Model-based Control of Servomechanisms with Friction**. *International Conference on Intelligent Robots and Systems, Lausanne, Switzerland*, 2002. 40, 140

[85] D. RIJLAARSDAM, B. VAN LOON, P. NUIJ, AND M. STEINBUCH. **Nonlinearities in Industrial Motion Stages - Detection and Classification**. *American Control Conference*, 2010. 40

[86] K. OHNISHI, M. SHIBATA, AND T. MURAKAMI. **Motion control for advanced mechatronics**. *IEEE Transaction on mechatronics*, 1996. 40, 66, 97

[87] M. GOUBEJ, M. SCHLEGEL, AND R. ŠKARDA. **Input Shaping Filters for the Control of Electrical Drive with Flexible Load**. *AT&P Journal PLUS*, **2**:116–121, 2009. 41, 159, 268

[88] M. GOUBEJ AND M. SCHLEGEL. **Feature-based parametrization of input shaping filters with time delays**. *IFAC Workshop on time delay systems, Prague*, 2010. 41

[89] S. L. VUKOSAVIĆ. *Digital Control of Electrical Drives*. Springer, 2007. 41, 49, 82, 95, 158

[90] F. SCHÜTTE. *Automatisierte Reglerbetriebnahme für elektrische Antriebe mit schwingungsfähiger Mechanik*. Universität Padeborn, 2002. 41, 42, 80

[91] K. TAMMI. *Active control of radial rotor vibrations: Identification, feedback, feedforward and repetitive control methods*. VTT Technical Research Centre of Finland, 2004. 41, 58, 80

[92] K. SUGIURA AND Y. HORI. **Vibration Suppresion in 2- and 3-Mass system based on the feedback of imperfect derivative of the estimated torsional torque**. *IEEE Transactions on Industrial Electronics*, **43**, 1996. 41, 97

[93] J. WEISSBACHER, E. GRÜNBACHER, AND M. HORN. **Automatic tuning of a servo drive speed controller for industrial applications**. In *Proceedings of IEEE Conference on Mechatronics, Vicenza, Italy*, 2013. 42, 88

[94] M. PACAS, S. VILLWOCK, AND T. EUTEBACH. **Identification of the Mechanical Resonances of Electrical Drives for Automatic Commissioning**. *Journal of Power Electronics*, **5**, 2005. 42, 84

[95] SHENG-MING YANG AND YU-JYE DENG. **Observer-based inertial identification for auto-tuning servo motor drives**. In *Conference Record of the 2005 Industry Applications Conference, 2005. Fourtieth IAS Annual Meeting.*, **2**, pages 968–972 Vol. 2, 2005. 42

[96] F. SCHÜTTE, S. BEINEKE, AND H. GROTSTOLLEN. **Knowledge based controller selection for electrical drives with imperfect mechanics**. In *Proceedings of the 24th Annual Conference of the IEEE Industrial Electronics Society, 1998. IECON '98.*, **3**, pages 1445–1450 vol.3, 1998. 42

[97] H. WERTZ, S. BEINEKE, N. FROHLEKE, S. BOLOGNANI, K. UNTERKOFLER, M. ZIGLIOTTO, AND M. ZORDAN. **Computer aided commissioning of speed and position control for electrical drives with identification of mechanical load**. In *Conference Record of the 1999 IEEE Industry Applications Conference, 1999. Thirty-Fourth IAS Annual Meeting.*, **4**, pages 2372–2379 vol.4, 1999. 42

[98] L. PERETTI AND M. ZIGLIOTTO. **Identification of mechanical load for electrical drives commissioning - Labelling machine case study**. In *EUROCON 2009, EUROCON '09. IEEE*, pages 797–803, 2009. 42

[99] M. GOUBEJ. *Sliding mode control of electronically commutated drives*. Master Thesis, UWB Pilsen, 2008. 46

[100] S. V. PAURCA, M. COVRIG, AND L. MELCESCU. **Direct Torque Control of Permanent Magnet Synchronous Motor - an approach by using Space Vector Modulation**. In *Proceedings of the 6th WSEAS/IASME Conference on Electric Power Systems, Spain*, 2006. 48

[101] I. TAKAHASHI AND T. NOGUCHI. **A new Quick-reponse and High efficiency Control Strategy of an Induction Motor**. *IEEE Transaction on Industrial Applications*, **22**:820–827, 1986. 48

[102] K. J. ÅSTRÖM AND T. HÄGGLUND. *PID Controllers. Theory, Design and Tuning*. Research Triangle Park, North Carolina, 1995. 49

[103] C. BAJRACHARYA, M. MOLINAS, J. A. SUUL, AND T. M. UNDELAND. **Understanding of tuning techniques of converter controllers for VSC-HVDC**. In *Nordic Workshop on Power and Industrial Electronics*, 2008. 49, 51

[104] S. PREITL AND R. E. PRECUP. **An Extension of Tuning Relations after Symmetrical Optimum Method for PI and PID Controllers**. *Automatica*, **35**:1731–1736, 1999. 49, 51

[105] M. ČECH AND M. SCHLEGEL. **Computing PID tuning regions based on fractional-order model set**. In *2nd IFAC Conference on Advances in PID Control, Brescia, Italy*, 2012. 55

[106] M. SCHLEGEL AND M. ČECH. **Computing value sets from one point of frequency response with applications**. In *Proceedings of the 16th IFAC World Congress*, 2005. 55

[107] M. ČECH AND M. SCHLEGEL. **Interval PID Tuning Rules for a Fractional-Order Model Set**. In *Proceedings of the 18th IFAC World Congress*, 2011. 55

[108] M. SCHLEGEL, P. BALDA, AND M. ŠTĚTINA. **Robust PID Autotuner - method of moments**. *Automatizace*, **46**, 2000. 57

[109] J. A. BUTTERWORTH, L. Y. PAO, AND D. Y. ABRAMOVITCH. **Analysis and comparison of three discrete-time feedforward model-inverse control techniques for nonminimum-phase systems**. *Mechatronics, Elsevier*, **22**:577–587, 2012. 59

[110] X. LIU, Y. WU, AND Y. LIU. **Digital Servo Control Based on Adaptive Zero Phase Error Tracking Controller & Zero Phase Prefilter**. In *Chinese Control and Decision Conference*, 2010. 59

[111] M. TOMIZUKA. **Zero Phase Error Tracking Algorithm for Digital Control**. *Journal of Dynamic Systems, Measurement and Control*, **109**, 1987. 59

[112] H. R. HARRISON AND T. NETTLETON. *Advanced Engineering Dynamics*. John Wiley & Sons Inc., New York, 1997. 59

[113] A. DE LUCA. *Robotics 2, course materials*. Universitá di Roma, 2013. 59, 63

[114] M. GOUBEJ. AND M. ŠVEJDA. **Dynamic analysis and control of robotic manipulator for chemically aggressive environments**. In *IEEE Internetnetional Conference on Mechatronics, Vicenza, Italy*, 2013. 62, 276

[115] A. SABANOVIC. **Variable structure systems with sliding modes in motion control**. *IEEE Transactions on industrial electronics*, 2011. 63

[116] M. GÉRADIN AND A. CARDONA. *Flexible Multibody Dynamics: A Finite Element Approach*. John Wiley & Sons Inc., New York, 2001. 66

[117] E. SÜLI. *Lecture Notes on Finite Element Methods for Partial Differential Equations*. University of Oxford, 2012. 66

[118] M.O. TOKHI AND A. K. M. AZAD, editors. *Flexible Robot Manipulators, Modelling, simulation and control*. The Institution of Engineering and Technology, London, UK, 2008. 66, 70, 95

[119] M. ROGNANT, E. COURTEILLE, AND P. MAURINE. **A systematic procedure for the elasto-dynamic modeling and identification of robot manipulators**. *IEEE Transaction on Robotics*, **26**:1085–1093, 2010. 66

[120] W. KHALIL AND M. GAUTIER. **Modeling of Mechanical Systems with Lumped Elasticity**. In *Proceedings of the IEEE International Conference on Robotics & Automation*, 2000. 66, 79

[121] C. CANUDAS DE WIT, B. SICILIANO, AND G. BASTIN. *Theory of Robot Control*. Springer, 1996. 66

[122] S. M. HAN, H. BENAROYA, AND T. WEI. **Dynamics of Transversely Vibrating Beams Using Four Engineering Theories**. *Journal of Sound and Vibration*, **225**:935–988, 1999. 66

[123] W. CHEN. **Dynamic modelling of multi-link flexible robotic manipulators**. *Computers and Structures*, **79**:183–195, 2001. 66

[124] A. DE LUCA. *Trajectory Control of Flexible Manipulators*. Universitá degli Studi di Roma. 66, 78, 79

[125] A. D. LUCA AND B. SICILIANO. **Closed-form dynamic model of planar multilink lightweight robots**. *IEEE Transactions on Systems, Man and Cybernetics*, **21**:826–839, 1991. 66

[126] A. PREUMONT. *Vibration Control of Active Structures*. Springer, 2011. 66, 70, 75, 78, 80, 95

[127] G. ELLIS AND R. D. LORENZ. **Resonant load control methods for industrial servo drives**. In *Conference Record of the IEEE Industry Applications Conference*, 2000. 66, 80

[128] S. KATSURA AND K. OHNISHI. **Absolute Stabilization of Multi-mass Resonant System by Phase-Lead Compensator Based on Disturbance Observer**. *IEEE Transactions on Industrial Electronics*, **54**:3389–3396, 2007. 66, 80

[129] A. HACE, K. JEZERNIK, AND A. SABANOVIC. **SMC With Disturbance Observer for a Linear Belt Drive**. *IEEE Transactions on Industrial Electronics*, **54**(6):3402–3412, 2007. 77, 80, 97

[130] M. JOKINEN. *Centralized Motion Control of a Linear Tooth-belt drive: Analysis of the Performance and Limitations*. Lappeenranta University of Technology, PhD. Thesis, 2010. 77, 80

[131] W. BERNZEN. **Active Vibration Control of Flexible Robots Usign Virtual Spring-damper Systems**. *Journal of Intelligent and Robotic Systems*, **24**:69–88, 1999. 78, 80

[132] G. FERRETTI, G. MAGNANI, AND P. ROCCO. **Alternatives in Precise Load Motion Control of Two-Mass Servomechanisms**. In *Advanced Intelligent Mechatronics Proceedings*, 2001. 80

[133] K. PETER AND B. ORLIK. **H_∞ Position Control with Robust Friction Compensation for a Two-Mass System**. In *IEEE IAS Annual Meeting*, 2004. 80, 83, 97, 98

[134] J.K. JI AND S.K. SUL. **Kalman filter and LQ based speed controller for torsional vibration suppression in a 2-mass motor drive system**. *IEEE Transactions on Industrial Electronics*, **42**:564–571, 1995. 80, 97

[135] S.A.A. MOOSAVIAN AND E. MOHAMMADIASL. **Backlash Detection in CNC Machines Based on Experimental Vibration Analysis**. In *Robotics, Automation and Mechatronics, 2008 IEEE Conference on*, pages 393–398, 2008. 80

[136] P.V. KROT. **Transient torsional vibrations control in the geared drive trains of the hot rolling mills**. In *Control Applications, (CCA) Intelligent Control, (ISIC), 2009 IEEE*, pages 1368–1373, 2009. 80

[137] M.A. VALENZUELA, J.M. BENTLEY, AND R.D. LORENZ. **Evaluation of torsional oscillations in paper machine sections**. *Industry Applications, IEEE Transactions on*, **41**(2):493–501, 2005. 80

[138] D. G. MACMARTIN, P. M. THOMPSON, M. M. COLAVITA, AND M. J. SIROTA. **Dynamic Analysis of the Actively-Controlled Segmented Mirror of the Thirty Meter Telescope**. *Control Systems Technology, IEEE Transactions on*, **PP**(99):1–1, 2013. 80

[139] Y. ACHKIRE AND A. PREUMONT. **Active tendon control of cable-stayed bridges**. *Earthquake Engineering and Structural Dynamics*, **25**:585–597, 1196. 80

[140] YAOJUNG SHIAO, C. LAI, AND Q. NGUYEN. **The analysis of a semi-active suspension system**. In *SICE Annual Conference 2010, Proceedings of*, pages 2070–2082, 2010. 80

[141] A. G. ULSOY, H. PENG, AND M. ÇAKMAKCI. *Automotive Control Systems*. Cambridge University Press, 2012. 80

[142] C. DU AND L. XIE. *Modeling and Conbtrol of Vibration in Mechanical Systems*. CRC Press, 2010. 80, 190

[143] R. ANTONELLO, R. OBOE, D. PILASTRO, S. VIOLA, K. ITO, AND A. CENEDESE. **IMU-based image stabilization in a HSM-driven camera positioning unit**. In *Mechatronics (ICM), 2013 IEEE International Conference on*, pages 156–161, 2013. 80

[144] HWY-KUEN KWAK, YOUNG JUN CHOI, KUN HWAN YU, JOON LYOU, AND MIN SIG KANG. **Dual stage and digital image based method for sight stabilization**. In *Industrial Electronics, 2008. ISIE 2008. IEEE International Symposium on*, pages 1114–1119, 2008. 80

[145] G. SCHITTER, P. MENOLD, H. F. KNAPP, F. ALLGOWER, AND A. STEMMER. **High performance feedback for fast scanning atomic force microscopes**. *Review of Scientific Instruments*, **72**, 2001. 80

[146] ARMSTRONG-HÉLOUVRY. *Control of Machines with Friction*. Kluwer Academic Press, 1991. 81, 82, 134

[147] T. WESCOTT. *Applied Control Theory for Embedded Systems*. Elsevier, 2006. 82, 83

[148] H. OLSSON, K. J. ÅASTRÖM, C. C. DE WIT, M. GÄFVERT, AND P. LISCHINSKY. *Friction Models and Friction Compensation*. Department of Automatic Control, Lund Institute of Technology, Lund University, Sweden, 1997. 82

[149] H. OLSSON. *Control Systems with Friction*. Department of Automatic Control, Lund Institute of Technology, Lund University, Sweden, 1996. 82

[150] S.N. HUANG, K.K. TAN, AND T.H. LEE. **Adaptive friction compensation using neural network approximations**. *IEEE Transactions on Systems, Man, and Cybernetics, Part C: Applications and Reviews,*, **30**(4):551–557, Nov 2000. 82

[151] LI XU AND BIN YAO. **Adaptive Robust Control of Mechanical Systems with Nonlinear Dynamic Friction Compensation**. In *PROCEEDINGS OF THE AMERICAN CONTROL CONFERENCE*, pages 2595–2599, 2000. 82

[152] L. LJUNG. *System Identification - Theory for the User*. Prentice-Hall, 1999. 83, 90

[153] G. GOODWIN AND R. PAYNE. *Dynamic System Identification*. Academic Press, New York, 1977. 83

[154] M. VILKKO AND T. ROINILA. **Designing Maximum Length Sequence Signal for Frequency Response Measurement of Switched Mode Converters**. *Nordic Workshop on Power and Insutrial Electronics*, 2008. 84

[155] S. VILLWOCK, A. BAUMULLER, M. PACAS, F.-R. GOTZ, BIAO LIU, AND V. BARINBERG. **Influence of the power density spectrum of the excitation signal on the identification of drives**. In *34th Annual Conference of IEEE Industrial Electronics, IECON 2008.*, pages 1252–1257, 2008. 84, 85, 88

[156] S.E. SAARAKKALA, T. LEPPINEN, M. HINKKANEN, AND J. LUOMI. **Parameter Estimation of Two-Mass Mechanical Loads in Electric Drives**. In *The 12th IEEE International Workshop on Advanced Motion Control, Sarajevo, Bosnia and Herzegovina*, 2012. 84, 87

[157] S. BEINEKE, F. SCHÜTTE, H. WERTZ, AND H. GROTSTOLLEN. **Comparison of Parameter Identification Schemes for Self-Commisioning Drive Control of Nonlinear Two-Mass Systems**. In *IEEE Industry Applications Society Annual Meeting, New Orleans, Lousiana*, 1997. 87, 88, 89, 90, 134

[158] M. ÖSTRING, S. GUNNARSSON, AND M. NORRLÖF. **Closed-loop identification of an industrial robot containing flexibilities**. *Control Engineering Practice*, **11**:291–300, 2003. 87

[159] YUJIE GUO, LIPEI HUANG, AND M. MURAMATSU. **Research on inertia identification and auto-tuning of speed controller for AC servo system**. In *Proceedings of the Power Conversion Conference, 2002. PCC-Osaka 2002.*, **2**, pages 896–901 vol.2, 2002. 87

[160] I. EKER AND M. VURAL. **Experimental online identification of a three-mass mechanical system**. In *Proceedings of 2003 IEEE Conference on Control Applications, 2003. CCA 2003.*, **1**, pages 60–65 vol.1, 2003. 88

[161] S. VILLWOCK. *Identifikationsmethoden für die automatisierte Inbetriebnahme und Zustandsüberwachung elektrischer Antriebe*. PhD thesis, Universität Siegen, 2007. 88, 89

[162] M.S. BARLETT. **Smoothing Periodograms from Time-Series with Continuous Spectra**. *Nature*, **161**:686–687, 1948. 89

[163] PETER D. WELCH. **The use of fast Fourier transform for the estimation of power spectra: A method based on time averaging over short, modified periodograms**. *IEEE Transactions on Audio and Electroacoustics*, **15**(2):70–73, 1967. 89

[164] S. VILLWOCK, M. PACAS, AND T. EUTEBACH. **Application of the Welch-method for the automatic parameter identification of electrical drives**. In *31st Annual Conference of IEEE Industrial Electronics Society, 2005. IECON 2005.*, pages 6 pp.–, 2005. 89

[165] S. VILLWOCK AND M. PACAS. **Application of the Welch-Method for the Identification of Two- and Three-Mass-Systems**. *IEEE Transactions on Industrial Electronics*, **55**(1):457–466, 2008. 89

[166] U. WITKOSSKI, S. RUPING, U. RUCKERT, F. SCHUTTE, S. BEINEKE, AND H. GROTSTOLLEN. **System identification using selforganizing feature maps**. In *Fifth International Conference on Artificial Neural Networks,*, pages 100–105, 1997. 89

[167] D. STROBL. *Identifikation nichtlinearer mechatronischer Systeme mittels neuronaler Beobachter*. PhD Thesis, TU München, 1999. 90

[168] D. STROBL AND D. SCHROEDER. **Neural Observers for the Identification of Backlash in Electromechanical Systems**. In *IFAC International Workshop on Motion Control, Grenoble, France*, 1998. 90

[169] D. SCHROEDER. *Intelligent Observer and Control Design for Nonlinear Systems*. Springer, 2000. 90

[170] F. SCHUTTE, S. BEINEKE, H. ROLFSMEIER, AND H. GROTSTOLLEN. **Online Identification of Mechanical Parameters Using Extended Kalman filters**. In *IEEE Industry Applications Society Annual Meeting, New Orleans, Lousiana*, 1997. 90

[171] S. BEINEKE, F. SCHUTTE, AND H. GROTSTOLLEN. **Online identification of nonlinear mechanics using extended Kalman filters with basis function networks**. In *23rd International Conference on Industrial Electronics, Control and Instrumentation, 1997. IECON 97.*, **1**, pages 316–321 vol.1, 1997. 90

[172] R. ESHLEMAN. *Machinery Vibration Analysis: Diagnostics, Condition Evaluation and Correction*. Vibration Institute, 2002. 91

[173] O. J. M. SMITH. **Posicast Control of Damped Oscillatory Systems**. *Proceedings of the IRE*, **45/9**:1249–1255, 1957. 93

[174] N. C. SINGER AND W.P. SEERING. **Preshaping Comman Inputs to Reduce System Vibration**. *A.I. Memo*, **1027**:1–23, 1988. 93, 181

[175] J. V. VAUGHAN, A. YANO, AND W. E. SINGHOSE. **Comparison of Robust input shapers**. *Journal of Sound and Vibration*, **315**:797–815, 2008. 93, 95, 167

[176] WILLIAM SINGHOSE. **Command shaping for flexible systems: A review of the first 50 years**. *International journal of precision engineering and manufacturing*, **10**(4):153–168, 2009. 93, 95

[177] D.P. MAGEE, D.W. CANNON, AND W.J. BOOK. **Combined command shaping and inertial damping for flexure control**. In *American Control Conference, 1997. Proceedings of the 1997*, **3**, pages 1330–1334 vol.3, 1997. 95

[178] D.P. MAGEE AND W.J. BOOK. **Filtering micro-manipulator wrist commands to prevent flexible base motion**. In *Proceedings of the 1995 American Control Conference,*, **1**, pages 924–928 vol.1, 1995. 95

[179] J. R. HUEY, K.L. SORENSEN, AND W. E. SINGHOSE. **Usefull Applications of Closed-loop Shaping Controllers**. *Control Engineering Practice*, **16**:836–846, 2007. 95, 158

[180] R.D. ROBINETT III, J. FEDDEMA, G.R. EISLER, C. DOHRMANN, G.G. PARKER, D.G. WILSON, AND D. STOKES. *Flexible Robot Dynamics and Controls*. Kluwer Academic Press, 2002. 95, 265

[181] S.N. VUKOSAVIC AND M.R. STOJIC. **Suppression of torsional oscillations in a high-performance speed servo drive**. *IEEE Transactions on Industrial Electronics*, **45**(1):108–117, 1998. 95

[182] G. ZHANG AND J. FURUSHO. **Speed control of two-inertia system by PI/PID control**. *IEEE Transactions on Industrial Electronics*, **47**(3):603–609, 2000. 97

[183] SANG-HUN LEE, JONG-SUNG HUR, HYUN-CHUL CHO, AND JONG-HYEON PARK. **A PID-Type Robust Controller Design for Industrial Robots with Flexible Joints**. In *SICE-ICASE International Joint Conference*, pages 5905–5910, 2006. 97

[184] S. COLOMBI AND T. RAIMONDI. **Compliance compensation in mechatronic systems**. In *20th International Conference on Industrial Electronics, Control and Instrumentation, 1994. IECON '94.*, **2**, pages 946–951 vol.2, Sep 1994. 97

[185] J.Y. HUNG. **Control of industrial robots that have transmission elasticity**. In *16th Annual Conference of IEEE Industrial Electronics Society, 1990. IECON '90.*, pages 198–203 vol.1, Nov 1990. 97

[186] K. GIERLOTKA, P. ZALESNY, AND M. HYLA. **Additional Feedback Loops in the Drives with Elastic Joint**. In *International Conference on Electrical Drives and Power Electronics*, 1996. 97

[187] K. SZABAT AND T. ORLOWSKA-KOWALSKA. **Vibration Suppression in a Two-Mass Drive System Using PI Speed Controller and Additional Feedbacks - Comparative Study**. *IEEE Transactions on Industrial Electronics,*, **54**(2):1193–1206, April 2007. 97

[188] G. ZHANG. **Comparison of control schemes for two-inertia system**. In *Proceedings of the IEEE 1999 International Conference on Power Electronics and Drive Systems, 1999. PEDS '99.*, **1**, pages 573–578 vol.1, 1999. 97

[189] KARSTEN PETER, I. SCHOLING, AND B. ORLIK. **Robust output-feedback H_∞ control with a nonlinear observer for a two-mass system**. *IEEE Transactions on Industry Applications*, **39**(3):637–644, May 2003. 97

[190] S. KATSURA AND K. OHNISHI. **Force Servoing by Flexible Manipulator Based on Resonance Ratio Control**. *IEEE Transactions on Industrial Electronics*, **54**(1):539–547, 2007. 97

[191] P. KORONKI, H. HASHIMOTO, AND V. UTKIN. **Direct torsion control of flexible shaft in an observer-based discrete-time sliding mode**. *IEEE Transactions on Industrial Electronics*, **45**(2):291–296, Apr 1998. 97

[192] K. ERENTURK. **Nonlinear two-mass system control with sliding-mode and optimised proportional-integral derivative controller combined with a grey estimator**. *Control Theory Applications, IET*, **2**(7):635–642, July 2008. 97

[193] S. THOMSEN, N. HOFFMANN, AND F.W. FUCHS. **PI Control, PI-Based State Space Control, and Model-Based Predictive Control for Drive Systems With Elastically Coupled Loads; A Comparative Study**. *IEEE Transactions on Industrial Electronics*, **58**(8):3647–3657, 2011. 97

[194] M. CYCHOWSKI, K. SZABAT, AND T. ORLOWSKA-KOWALSKA. **Constrained Model Predictive Control of the Drive System With Mechanical Elasticity**. *IEEE Transactions on Industrial Electronics*, **56**(6):1963–1973, June 2009. 97

[195] B.K. BOSE. **Expert system, fuzzy logic, and neural network applications in power electronics and motion control**. *Proceedings of the IEEE*, **82**(8):1303–1323, Aug 1994. 97

[196] T. ORLOWSKA-KOWALSKA AND K. SZABAT. **Neural-Network Application for Mechanical Variables Estimation of a Two-Mass Drive System**. *IEEE Transactions on Industrial Electronics*, **54**(3):1352–1364, June 2007. 97

[197] M. KAMINSKI AND T. ORLOWSKA-KOWALSKA. **Comparison of bayesian regularization and Optimal Brain Damage methods in optimization of neural estimators for two-mass drive system**. In *2010 IEEE International Symposium on Industrial Electronics (ISIE)*, pages 102–107, July 2010. 97

[198] I. SCHOLING AND B. ORLIK. **Control of a nonlinear two-mass system with uncertain parameters and unknown states**. In *Conference Record of the 2000 IEEE Industry Applications Conference*, **2**, pages 1096–1103 vol.2, 2000. 98

[199] M. F. M. YAKUB, A. QADIR, AND B.A. AMINUDIN. **Comparative Study on Control Method for Two-Mass Systems**. *International Journal on Information Technology*, **2**, 2012. 98

[200] M. SCHLEGEL AND O. VEČEREK. **Samonastavující se regulátor pro velmi slabě tlumené kmitavé systémy**. In *MATLAB Conference, Humusoft*, 2002. 103

[201] M. GOUBEJ, A. KREJCI, AND M. SCHLEGEL. **Robust frequency identification of oscillatory electromechanical systems**. In *2013 International Conference on Process Control*, pages 79–84, 2013. 103

[202] A. ICHIKAWA AND H. KATAYAMA. *Linear Time-varying Systems and Sampled-data Systems*. Springer, 2001. 126, 148

[203] J.-J. E. SLOTINE AND W. LI. *Applied Nonlinear Control*. Prentice Hall, 1991. 137

[204] D. KARNOPP. **Computer simulation of stick-slip friction in mechanical dynamic systems**. *Journal of Dynamic Systems and Measurement*, **107**, 1985. 139

[205] S. CH. D. ROY, B. KUMAR, AND S. B. JAIN. **FIR Notch Filter design - A Review**. *Electronics and Energetics*, **14**:295–327, 2001. 158

[206] M. GOUBEJ AND M. SCHLEGEL. **Feature-based parametrization of input shaping filters with time delays**. *IFAC Workshop on time delay systems, Prague*, 2010. 159, 268

[207] G. B. DANTZIG, A. ORDEN, AND P. WOLFE. **Generalized Simplex Method for Minimizing a Linear from Under Linear Inequality Constraints**. *Pacific Journal Math.*, **5**:183–195. 181

[208] Y. ZHANG. **Solving Large-Scale Linear Programs by Interior-Point Methods Under the MATLAB Environment**. *University of Maryland*, 1995. 181

[209] T. VYHLÍDAL, M. HROMČÍK, AND V. KUČERA. **Inverse signal shapers in effective feedback architecture**. In *2013 European Control Conference (ECC)*, pages 4418–4423, July 2013. 190

[210] T. VYHLÍDAL, V. KUČERA, AND M. HROMČÍK. **Zero vibration shapers with distributed delays of various types**. In *2013 IEEE 52nd Annual Conference on Decision and Control (CDC)*, pages 940–945, Dec 2013. 190

[211] M. SCHLEGEL, M. GOUBEJ, AND J. KÖNIGSMARKOVÁ. **Active vibration control of two-mass flexible system using parametric Jordan form assignment**. In *2nd IFAC Conference on Advances in PID Control*, 2012. 209, 268, 270

[212] H. DÖRRIE. **Sturm's Problem of the Number of Roots**. *100 Great Problems of Elementary Mathematics*, 1965. 211

[213] J. DOYLE, FRANCIS. B., AND A. TANNENBAUM. *Feedback Control Theory*. MacMillan, New York, 1990. 223, 224

[214] G. STEIN AND M. ATHANS. **The LQG/LTR procedure for multivariable feedback control design**. *IEEE Transactions on Automatic Control*, **32**(2):105–114, Feb 1987. 237

[215] HUIBERT KWAKERNAAK. **Minimax frequency domain performance and robustness optimization of linear feedback systems**. *IEEE Transactions on Automatic Control*, **30**(10):994–1004, Oct 1985. 242

[216] A.J. LAUB, M.T. HEATH, C. PAIGE, AND R. WARD. **Computation of system balancing transformations and other applications of simultaneous diagonalization algorithms**. *IEEE Transactions on Automatic Control*, **32**(2):115–122, Feb 1987. 253

[217] J. REITINGER, M. ČECH, AND M. GOUBEJ. **Advanced input shaping filter 3D virtual laboratory**. In *2013 International Conference on Process Control*, pages 528–533, June 2013. 268

[218] JAN REITINGER. *Interactive virtual laboratories presenting techniques for vibration damping*. University of West Bohemia, Master Thesis, 2012. 268

[219] JAN REITINGER. **New tools for teaching vibration damping concepts: ContLab.eu**. *IFAC World Congress 2014, Cape Town, Republic of South Africa*, 2014. 270

[220] M. SCHLEGEL, P. BALDA, A. JÁGER, M. KUČERA, AND J. JANČÍK. *Controller of the cable manipulator with flexible rope*. Úřad průmyslového vlastnictví, 2012. 270

[221] M. GOUBEJ, J. MERTL, AND P. BALDA. **Control system design of robotic manipulator for testing of shifting system**. In *2013 International Conference on Process Control*, pages 241–246, June 2013. 270

[222] L. BLÁHA. *Stabilizace a automaticé řízení pohybu dvoukolky*. Diplomová práce, ZČU v Plzni, ZČU v Plzni, 2007. 273

[223] A. JÁGER. *Návrh řídícího systému robustní stabilizace dvoukolky*. Diplomová práce, ZČU v Plzni, 2011. 273

[224] M. ŠVEJDA AND M. GOUBEJ. **Innovative design and control of robotic manipulator for chemically aggressive environments**. In *2012 13th International Carpathian Control Conference (ICCC)*, pages 715–720, May 2012. 276

[225] M. GOUBEJ AND M. ŠVEJDA. **Research and design of modular robotic manipulator for chemical aggressive environment**. In *2011 12th International Carpathian Control Conference (ICCC)*, pages 374–378, May 2011. 276

Curriculum Vitae

Martin Goubej was born in 1983 in Pilsen, Czech Republic. He received his B.Sc. and M.Sc. degrees in cybernetics and automatic control at Department of Cybernetics, Faculty of applied sciences, University of West Bohemia in Pilsen, Czech Republic in 2005 and 2008, respectively. Since 2006, he has been conducting basic and applied research in terms of national and internetional R&D projects at University of West Bohemia in Pilsen. His main research interests include automation and control systems, robotics, mechatronics, electrical drives, robust control of linear systems and sliding mode control.

Address: University of West Bohemia, Univerzitní 8, 301 00, Pilsen
E-mail: mgoubej@ntis.zcu.cz
Web: https://www.linkedin.com/in/mgoubej

List of author's publications

[1] M. Goubej and M. Schlegel. **Robust PID Control of Electrical Drive with Compliant Load**, *IFAC 19th World Congress 2014*, Cape Town, South Africa, 2014.

[2] A. Krejčí, T. Popule and M. Goubej. **Closing the motion control loops via industrial ethernet network**, *Proceedings of the 15th International Carpathian Control Conference ICCC 2014, pp. 273-278.*, 2014.

[3] M. Goubej, J. Mertl and P. Balda. **Control system design of robotic manipulator for testing of shifting system**, *Proceedings of the 2013 International Conference on Process Control PC 2013*, pp. 241-246, 2013.

[4] M. Goubej, A. Krejčí and M. Schlegel. **Robust frequency identification of oscillatory electromechanical systems**, *Proceedings of the 2013 International Conference on Process Control PC 2013*, pp. 79-84, 2013.

[5] J. Reitinger, M. Čech and M. Goubej. **Advanced input shaping filter 3D virtual laboratory**, *Proceedings of the 2013 International Conference on Process Control PC 2013*, pp. 528-533, 2013.

[6] M. Goubej and M. Švejda. **Dynamic analysis and control of robotic manipulator for chemically aggressive environments**, *2013 IEEE International Conference on Mechatronics, ICM 2013*, pp. 273-278, 2013.

[7] M. Goubej, M. Schlegel and J. Königsmarková. **Active vibration control of two-mass flexible system using parametric Jordan form assignment**, *IFAC Conference on Advances in PID control*, Brescia, Italy, 2012.

[8] O. Severa, R. Pišl, M. Čech, M. Goubej, M. Štětina and M. Schlegel. **New 3D HMI tool for robot path planning based on latest W3C standards**, *Proceedings of the 2012 13th International Carpathian Control Conference, ICCC 2012*, 2012.

[9] M. Švejda and M. Goubej. **Innovative design and control of robotic manipulator for chemically aggressive environments**, *Proceedings of the 2012 13th International Carpathian Control Conference, ICCC 2012*, 2012.

[10] M. Goubej, M. Schlegel and R. Škarda. **Mechatronic models for education - Robotic sea lion**, *IFAC 18th World Congress 2011*, Milano, Italy, 2011.

[11] M. Švejda and M. Goubej. **Research and design of modular robotic manipulator for chemically aggressive environments**, *Proceedings of the 2011 12th International Carpathian Control Conference, ICCC 2011*, 2011.

[12] M. Schlegel and M. Goubej. **Feature-based parametrization of input shaping filters with time delays**, *IFAC Workshop on Time Delay Systems*, Prague, 2010.

[13] M. Goubej, R. Škarda and M. Schlegel. **Input shaping filters for the control of electrical drive with flexible load**, *AT&P Journal PLUS*, 2010.

[14] R. Škarda and M. Goubej. **Self tuning algorithm for motion control applications using extremum seeking method**, *Proceedings of the 2010 11th International Carpathian Control Conference, ICCC 2010*, 2010.

[15] M. Štětina, P. Balda, R. Pišl and M. Goubej **Motion control algorithms in the new version of the REX control system**, *Proceedings of the 2010 International Conference on Process Control, PC 2010*, 2010.

[16] M. Goubej **Polynomial interpolation methods for synthesis of electronic cam profiles** , *SVK conference*, UWB Pilsen, 2010.

[17] M. Goubej, R. Škarda and M. Schlegel. **Input shaping filters for the control of electrical drive with flexible load**, *Proceedings of the 2009 International Conference on Process Control, PC 2009*, 2009.

Declaration

I herewith declare that I have produced this thesis without the prohibited assistance of third parties and without making use of aids other than those specified; notions taken over directly or indirectly from other sources have been identified as such. This thesis has not previously been presented in identical or similar form to any other Czech or foreign examination board.

The thesis work was conducted from 2009 to 2014 under the supervision of Prof. Ing. Miloš Schlegel at University of West Bohemia.

Pilsen,